LIVER REGENERATION AND CELLULAR ADAPTATION TO CHRONIC DISEASES: A SYSTEMS BIOLOGY INVESTIGATION

by

Daniel J. Cook

A dissertation submitted to the Faculty of the University of Delaware in partial fulfillment of the requirements for the degree of Doctor of Philosophy in Chemical Engineering

Fall 2016

LIVER REGENERATION AND CELLULAR ADAPTATION TO CHRONIC DISEASES: A SYSTEMS BIOLOGY INVESTIGATION

by

Daniel J. Cook

Approved: _____

Abraham M. Lenhoff, Ph.D.
Chair of the Department of Chemical and Biomolecular Engineering

Approved: _____

Babatunde A. Ogunnaike, Ph.D.
Dean of the College of Engineering

Approved: _____

Ann L. Ardis, Ph.D.
Senior Vice Provost for Graduate and Professional Education

I certify that I have read this dissertation and that in my opinion it meets the academic and professional standard required by the University as a dissertation for the degree of Doctor of Philosophy.

Signed: _____

Babatunde A. Ogunnaike, Ph.D.
Professor in charge of dissertation

I certify that I have read this dissertation and that in my opinion it meets the academic and professional standard required by the University as a dissertation for the degree of Doctor of Philosophy.

Signed: _____

Rajanikanth Vadigepalli, Ph.D.
Professor in charge of dissertation

I certify that I have read this dissertation and that in my opinion it meets the academic and professional standard required by the University as a dissertation for the degree of Doctor of Philosophy.

Signed: _____

Jan Hoek, Ph.D.
Member of dissertation committee

I certify that I have read this dissertation and that in my opinion it meets the academic and professional standard required by the University as a dissertation for the degree of Doctor of Philosophy.

Signed: _____

Prasad S. Dhurjati, Ph.D.

Member of dissertation committee
I certify that I have read this dissertation and that in my opinion it meets the academic and professional standard required by the University as a dissertation for the degree of Doctor of Philosophy.

Signed: _____

April Kloxin, Ph.D.
Member of dissertation committee

ACKNOWLEDGMENTS

Three of the most important decisions in my life have made me into the person I am today: (1) First and foremost, my decision to follow Christ. With him all things are possible; without him, I am nothing. (2) My decision to marry my wife, Jiadi. Her love of people, kindness, tenderness, and intelligence inspire me to want to do better and be better. (3) My decision to be an engineer working in systems biology. I came to biology as a true outsider, not having had a biology class since freshman year of high school. Thank you to my professors, mentors, and peers who took the time to train me and teach me during my time at Thomas Jefferson University and the University of Delaware.

I acknowledge the support and guidance of my thesis advisors: Dr. Rajanikanth Vadigepalli and Dr. Babatunde Ogunnaike. Thank you for training me to be a scientist and showing me how far I still have to go. I also acknowledge the support of the many faculty members who took the time to mentor me. Special thanks goes to Dr. Jim Schwaber for taking the time to mentor me, Dr. Prasad Dhurjati for taking me under his wing when I was adrift, to Dr. Nancy Philp for making me included at Thomas Jefferson University, and to Dr. Jan Hoek for always treating me like I was in his research group. Thank you to Dr. April Kloxin for providing feedback and excitement for my research project and for showing how to balance a career with life. Thank you to Dr. Abhi Singh and Dr. Pak-Wing Fok for working with me during the Systems Biology class and to the students who put up with my sometimes-absent TAing.

I have had the opportunity to work with some exceptional young undergraduate students who have enriched my study and taught me as much or more than I was able to teach them. Thank you to Bronson Weston, Ben Fogal, Ryan Downs, Jon Perna, Andrew Vitelli, and Sean Mack. Thank you for sticking with me even when I was not readily available (or in China).

Thank you to the former Ogunnaike group members who have offered me support and encouragement: Dr. Mary McDonald Staehle, Dr. Marc Birtwistle, Dr. Seung-Wook Chung, Dr. Jake McGill, Dr. Melissa St. Amand McGill, Dr. Qian Gou, Dr. Zach Whiteman, Dr. Robert Lovelett. Thank you to the current Ogunnaike group and Vadigepalli group for all the help, encouragement, and friendship: Dr. Chia-Hun Tsai, Devesh Radhakrishnan, Austin Parrish, Dr. Warren Anderson, and Dr. Danielle DeCicco. Special thanks are in order for Dr. Lakshmi Kuttippurathu, who taught me how to analyze data and how to become a PhD student; Sirisha Achanta and her husband (also a group member) Aalap Verma, who spent thankless hours in the lab with me and became my friends; and my partner in crime, James Park. James, you always drive me to be a better researcher. Thank you also to my fellow UD students and friends for your support during the PhD program, specifically Scott Horton, who always put up with me even though he graduated from UVA.

Thank you to my friends and mentors for showing me that this task was possible and for believing in me: Dr. John Meade, Dr. Zach Frye, Dr. Sherri Cook, Dr. Joanna Wen, Dr. Julie Cushen, and Mr. Harold Metz, you guys are great, I am honored to call you friends. Dick Farms, Jason Lamb, Jim Apple, Steve Puchalla, Kory Rose, and Scott Robinson, thank you for training me and believing in me. Thank you to my

oldest friends: Andrew Stevens, Nathaniel Barton, Dan Jeter, and Steve Harrison. You were my friends before I know how to be a friend.

Finally, I thank my family for making me the person I am today, for supporting me, and for loving me (faults and all). Mom and Dad, thank you for teaching me what is important in life and for instilling in me a questioning spirit, a love of learning, and a work ethic to be able to answer tough questions. Dave and Lauren, Becky and Paul, and Aaron, you are the greatest siblings it is possible to have. Thank you to everyone who sacrificed to take care of the twins while I was working on this thesis: Mom and Zhe, you made this work possible. Jiadi, thank you for our daughters Anna and Emma. Thank you for supporting me, for caring about me, and for loving me. Thank you for keeping me sharp and on my toes (the few I have left). Thank you for making me be a better person than I am.

The last one was not final, but this one is. Thank you to the US taxpayers whose money funded this work through the NIH. I hope if you find this work, you consider it worthwhile.

TABLE OF CONTENTS

LIST OF TABLES xvii
LIST OF FIGURES xix
ABSTRACT xlix

Chapter

1 INTRODUCTION 1

1.1 Therapeutic Significance of Liver Regeneration 1
1.2 Features of Liver Regeneration 2
1.3 Effects of Chronic Diseases on Regeneration Capacity 4
1.4 Thesis Overview 7

2 NF-κB BINDING DURING THE PRIMING PHASE OF LIVER REGENERATION IN RATS 10

2.1 Introduction 10
2.2 Methods 13

2.2.1 Animals 13
2.2.2 Chromatin Immunoprecipitation (ChIP) 14
2.2.3 Identification of NF-κB Binding Sites using Microarrays (ChIP-chip) 16
2.2.4 Genome-wide Mapping and Peak Detection: Identification of Binding Sites 17
2.2.5 Peak Annotation 18
2.2.6 Dynamic Pattern Analysis 19
2.2.7 Integration with Expression Data 24
2.2.8 Pathway Analysis and Functional Association Identification 26
2.2.9 Motif Discovery 26
2.2.10 Quantitative PCR Validation of NF-κB Binding 27

2.3 RESULTS 29

2.3.1 NF-κB binding following partial hepatectomy 29
2.3.2 Dynamic Pattern Analysis of NF-κB binding 31

2.3.3 Functional Pathways Represented by Genes Bound by NF-κB post-PHx 33
2.3.4 NF-κB Switches Co-ordinate Dynamic Tissue Function post-PHx 37
2.3.5 NF-κB Binding Motif Analysis 41
2.3.6 AP-1 as a Co-regulator of NF-κB Bound Genes Following PHx 46
2.3.7 Validation of Selected NF-κB Binding Dynamics Using ChIP-qPCR 47

2.4 DISCUSSION 50

3 PREDICTING MOLECULAR REGULATION OF LIVER REGENERATION IN ADIPONECTIN KNOCKOUT MICE USING AN EXISTING COMPUTATIONAL MODEL 55

3.1 Introduction 55
3.2 Materials and Methods 58

3.2.1 Animals 58
3.2.2 Histological analysis 60
3.2.3 Biochemical analysis 60
3.2.4 Computational modeling of liver regeneration 61
3.2.5 Sensitivity analyses for identifying key factors controlling regeneration phenotype 61
3.2.6 Parameter estimation to match Adn-/- regeneration phenotype 62

3.3 Results 63

3.3.1 Hepatocyte proliferation is delayed after PHx in Adn -/- mice 63
3.3.2 Pulsatile Sensitivity Analysis reveals critical time-windows of molecular effects on liver regeneration 65
3.3.3 Computational modeling of the altered regenerative response in the Adn -/- mice reveals the key controlling molecular regulatory balances 75

3.4 Discussion 81

4 TESTING MODEL PREDICTIONS IN ADIPONECTIN KNOCKOUT MICE AND CONTROLS 83

4.1 Introduction 83
4.2 Materials and Methods 84

4.2.1 Animals 84
4.2.2 Biochemical analysis 85

4.3 Results 87

4.3.1 Biochemical analysis revealed an altered balance of cytokine and growth factor profiles in Adn-/- mice, consistent with computational model predictions 87
4.3.2 Computational analysis predicts that overexpression of adiponectin disrupts the regeneration by dysregulating the cytokine and growth factor profiles 91
4.3.3 Rosiglitazone-induced super-physiological levels of adiponectin inhibited hepatocyte replication in WT but not Adn-/- mice 93

4.4 Discussion 96

5 AN UNBIASED COMPARISON OF MOLECULAR REGULATION OF PRIMING IN ADN-/- MICE AND CONTROLS 101

5.1 Introduction 101
5.2 Materials and Methods 104

5.2.1 Animals 104
5.2.2 Biochemical analysis 104
5.2.3 Data normalization and batch correction 104
5.2.4 Multivariate data analysis 105
5.2.5 Correlation network analysis 105

5.3 Results 106

5.3.1 Adn-/- mice dynamically regulate protein levels differently following resection than wild-type controls 106
5.3.2 Adn knockout preconditions tissue microenvironment 108

5.3.2.1 Proteins highly down-regulated in Adn-/- mice may inhibit liver responsiveness to PHx 108
5.3.2.2 Proteins down-regulated in Adn-/- mice may cause impaired neutrophil and NKT cell recruitment 110
5.3.2.3 Proteins up-regulated in Adn-/- mice may modify non-parenchymal cell state balances 111
5.3.2.4 Protein variability in the homeostatic liver suggests constrained and deregulated control in Adn-/- mice .. 114

5.3.3 Protein level responses following PHx are constrained into dynamic expression modes 115

5.3.3.1 Mode 1: Rising 118
5.3.3.2 Mode 2: Rising with a peak 120
5.3.3.3 Mode 3: Falling with a peak 120
5.3.3.4 Mode 4: Falling 121

5.3.4 Proteins in liver tissue following PHx show dynamic expression changes in wild-type mice 122

5.3.4.1 Proteins with similar expression dynamics in serum and tissue post-PHx in wild-type mice 122

5.3.4.1.1 Mode 3: Falling with a peak 123
5.3.4.1.2 Mode 5: Cyclic 125

5.3.4.2 Proteins with opposite expression in serum and tissue post-PHx in wild-type mice 125

5.3.4.2.1 Mode 3: Falling with a peak 127
5.3.4.2.2 Mode 4: Falling 127

5.3.4.3 Proteins with tissue dynamics post-PHx in wild-type mice and no expression change in serum 128

5.3.5 Different proteins regulate priming in Adn-/- mice 128

5.3.5.1 Proteins with similar expression dynamics in the serum of wild-type and Adn-/- mice may represent robust features of priming 132
5.3.5.2 Proteins with different expression dynamics in wild-type and Adn-/- mice 142

5.3.6 Proteins in liver tissue following PHx show dynamic expression changes in Adn-/- mice 148

5.3.6.1 Proteins with similar expression dynamics in serum and tissue post-PHx in Adn-/- mice 148
5.3.6.2 Proteins with opposite expression in serum and tissue post-PHx in Adn-/- mice 150
5.3.6.3 Proteins with dynamic expression changes in tissue but no serum changes post-PHx in Adn-/- mice 151

5.3.7 Adn knockout leads to different tissue regulation of the priming phase 152
5.3.8 Priming for liver regeneration in Adn-/- mice appears to be controlled by a different regulatory network structure 154

5.4 Discussion 158

6 A COMPUTATIONAL MODEL TO SIMULATE LIVER REGENERATION ACROSS PHENOTYPES 161

6.1 Introduction 161
6.2 Methods 168

6.2.1 Computational model development 168
6.2.2 Transforming published data on liver regeneration into fractional recovery of tissue mass 173

6.2.2.1 High fructose-induced steatosis (NASH) and Controls 173
6.2.2.2 Ethanol-induced steatosis (ASH) 174
6.2.2.3 Toxin-Induced Cirrhosis 174
6.2.2.4 Toxin-Induced Type 1 Diabetes 175
6.2.2.5 Mouse Liver Regeneration 176
6.2.2.6 Human Liver Regeneration 177

6.2.3 Sensitivity Analysis 177
6.2.4 Statistical Methods 177

6.3 Results 178

6.3.1 Model Implementation 178
6.3.2 Extended model predicts the importance of Kupffer cell-mediated signaling during the priming phase 179
6.3.3 Extended model with cell growth better accounts for rat liver regeneration profile 181
6.3.4 Exploring the state space of liver regeneration reveals distinct regeneration modes 183
6.3.5 Sensitivity analysis reveals that molecular and physiological regulation strongly affects dynamic mass recovery 196
6.3.6 Paired parameter analysis reveals control principles governing the network balances driving liver regeneration 199
6.3.7 Translating Among Species Using the Computational Model .. 206
6.3.8 Simulating regeneration in hundreds of human patients 218

6.3.9 Simulating surgical interventions to enhance regeneration in a subset of human patients 220
6.3.10 Predicting effects of chronic disease on liver repair following partial hepatectomy 221
6.3.11 Comparison of regeneration in multiple genotypes of Adn-/- mice 233

6.4 Discussion 236

7 EXTENDING THE COMPUTATIONAL MODEL TO INCLUDE NON-PARENCHYMAL CELL TRANSCRIPTIONAL PHENOTYPES 243

7.1 Introduction 243
7.2 Materials and Methods 244

7.2.1 Computational Model Description 244

7.2.1.1 Hepatocyte Equations 244
7.2.1.2 Tissue Equations 246
7.2.1.3 Kupffer Cell Equations 247
7.2.1.4 Hepatic Stellate Cell Equations 248

7.2.2 Parameter Estimation 249
7.2.3 Sensitivity Analysis 250

7.3 Results 251

7.3.1 A New Multiscale Cellular and Molecular Network Model of Liver Regeneration 251

7.3.1.1 Metabolic Demand 253
7.3.1.2 Hepatocytes 253
7.3.1.3 Kupffer Cells 255
7.3.1.4 Hepatic Stellate Cells 256
7.3.1.5 Tissue-scale Response 258

7.3.2 Dynamic Balance of Hepatic Stellate Cell States during Regeneration 259
7.3.3 Hepatocyte apoptosis rate bifurcates liver recovery and failure 260
7.3.4 Co-ordinated Response of Multiple Cell Types is Required for Effective Regeneration 263
7.3.5 Dynamic Tissue Microenvironment Cycles Underlie Regeneration Dynamics 264

7.3.6 Hepatic Stellate Cell State Balances Modulate Regeneration Dynamics 266
7.3.7 Discussion 272

8 TESTING MODEL PREDICTIONS IN ETHANOL-ADAPTED RATS 274

8.1 Introduction 274
8.2 Materials and Methods 278

8.2.1 Animal Use 278
8.2.2 Immunohistochemical Staining 278
8.2.3 Laser Capture Microdissection (LCM) 279
8.2.4 High-throughput quantitative PCR 280
8.2.5 Data Analysis and Statistical Methods 281

8.2.5.1 Data Normalization 281
8.2.5.2 Cell Type Specificity Analysis 282
8.2.5.3 Linear Discriminant Analysis 282
8.2.5.4 Silhouette Score Analysis 283
8.2.5.5 Minimum Spanning Tree Analysis 283
8.2.5.6 Topological Maps 284

8.3 Results 284

8.3.1 Hepatic Stellate Cell Isolation and Identification Reveals High Transcriptional Variability within a Cell Type 284
8.3.2 Hepatic Stellate Cells Function in Discernible Transcriptional States 289
8.3.3 HSC State Dynamics during Effective Regeneration 299
8.3.4 HSC State Dynamics during Ethanol-impaired Regeneration 301
8.3.5 Transcriptional variability following ethanol adaptation and resection 303
8.3.6 Independent dataset used to validate cell population balances 303
8.3.7 Transcriptional strength across conditions 314
8.3.8 Computational Modeling in Combination with Experimental Results Suggests Matrix Preconditioning and Dynamic Hepatic Stellate Cell Transition Insufficiency Contribute to Suppressed Liver Regeneration 316

8.4 Discussion 321

9 IMPLICATIONS FOR NON-PARENCHYMAL CELL NETWORKS IN TISSUE HOMEOSTASIS 325

9.1 Introduction 325
9.2 Materials and Methods 326

9.2.1 Model development 326
9.2.2 Parameter constraints 328

9.2.2.1 Literature-based constraints 328
9.2.2.2 Steady-state constraints 329

9.2.3 Model selection for robustness 330
9.2.4 Global and parametric sensitivity analyses 331

9.2.4.1 Global sensitivity analysis 331
9.2.4.2 Parametric sensitivity analysis 332

9.2.5 Non-parenchymal cell controllers 332
9.2.6 Model simulation 332

9.3 Results 332

9.3.1 Feedback is required to maintain a steady state 332
9.3.2 Different types of feedbacks result in different system dynamics 335

9.3.2.1 Capacity constraint OR implicit competition within hepatocyte populations (Model A) 335
9.3.2.2 Product inhibition of proliferation OR negative feedback of differentiated cells on “stem-cell-like” cells (Model B) 338
9.3.2.3 Product inhibition of cell transitions OR Axin2+ maintenance microenvironment signaling saturation (Model C) 339
9.3.2.4 Exogenous populations supplying Axin2+ populations or stem cell-led renewal (Model D) 341
9.3.2.5 Timing of recovery from an insult 342
9.3.2.6 Parameter selection 345

9.3.3 Combinations of feedback result in a system that is robust to multiple biological challenges/disturbances 345
9.3.4 Systemic properties of homeostatic renewal revealed through model analyses 351

9.3.4.1 Sensitivity analyses show largely independent behavior of cell states 351

9.3.4.2 Stability analysis shows a co-ordination between model responsiveness to disturbances and stability ... 353
9.3.4.3 Frequency analysis shows that high insult frequencies impair systemic homeostatic renewal ... 354

9.3.5 Model simulations capture behavior of induced hepatocyte senescence ... 362
9.3.6 Non-parenchymal cells act to enhance disturbance rejection ... 365

9.4 Discussion ... 377

10 CONCLUSIONS AND FUTURE WORK ... 380

10.1 Conclusions ... 380
10.2 Future Work ... 382

10.2.1 Testing model predictions ... 383
10.2.2 Simulating regeneration in humans ... 384
10.2.3 Clinical implementation of modeling ... 384
10.2.4 Drug targeting for regeneration and beyond ... 385

REFERENCES ... 387

Appendix

A MODEL PARAMETERS ... 420
B SEGMENTATION METHOD FOR CALCULATING CORRELATIONS FROM TIME-SERIES BIOLOGICAL DATASETS: MITIGATING THE EFFECTS OF TERMINAL SAMPLES, FEW TIME POINTS, AND LIMITED REPLICATES ... 430

B.1 Introduction ... 430
B.2 Materials and Methods ... 431

B.2.1 Standard Method to calculate correlation ... 431
B.2.2 Segmentation Method to calculate correlation ... 432
B.2.3 Definition of high correlation ... 433
B.2.4 Calculating Correlation from Standard Method and Segmentation Method ... 434

B.3 Results and Discussion ... 434

B.3.1 Application of Segmentation Method to a Simulated Dataset ... 435
B.3.2 Robustness of the Segmentation Method ... 440

B.4 Conclusion 445

C PRIMER SEQUENCES FOR HIGH-THROUGHPUT QPCR EXPERIMENTS 446
D MATLAB CODE FOR MATHEMATICAL MODELS DEVELOPED IN THIS THESIS 451

D.1 Cell Growth Model of Liver Regeneration 451
D.2 Non-parenchymal Cell Model of Liver Regeneration 460
D.3 Liver Homeostatic Renewal Model 474

E R CODE USED TO EVALUATE SINGLE HEPATIC STELLATE CELL DATA 483
F SAMPLE (TOY) SINGLE CELL DATA 490
G VERTEBRATE ANIMAL PLAN (F31) AND IACUC PROTOCOL 496

G.1 Vertebrate Animal Plan (F31) 496
G.2 IACUC Protocol 500

H LICENSING FOR PREVIOUSLY PUBLISHED ARTICLES INCLUDED IN THIS DISSERTATION 518

H.1 BMC Systems Biology 518
H.2 Journal of Physiology 520
H.3 Frontiers in Physiology 526

LIST OF TABLES

Table 1.1: Timing of liver regeneration can be divided into phases 3

Table 2.1 FDR cutoff pathway analysis for Pattern 1 21

Table 2.2 FDR cutoff pathway analysis for Pattern 5 23

Table 2.3 FDR cutoff pathway analysis for Pattern 7 24

Table 2.4 Primer Sequences 28

Table 2.5 Pattern analysis of NF-κB binding during the priming phase post-PHx. 32

Table 3.1: Modified parameter values 79

Table 4.1 Primer sequences 87

Table 6.1 Parameter changes to simulate regeneration in multiple species 209

Table 6.2 Summary of parameters used to simulate alternate hypotheses of how human liver regeneration differs from rat liver regeneration 213

Table 6.3 Patterns of molecular regulation (30 days) and mass recovery (14 days) that could differentiate hypotheses of mechanisms underlying liver regeneration in humans 218

Table 6.4 Parameter changes to simulate alternate regeneration conditions 223

Table 6.5 Summary of predicted disease effects on liver regeneration 224

Table 6.6 Hepatocyte-specific parameter changes to simulate alternate regeneration conditions 231

Table 8.1 Distribution of hepatic stellate cell states in each condition 300

Table 8.2 Matrix-associated features predicted in chronic ethanol use and corresponding parameter values 317

Table 9.1 Parameter values for each model considered in this study 328

Table 9.2 DOE Results – A low recovery score indicates an overall lower recovery volume and more robust performance 347

Table 9.3 Control system parameters 368

Table A.1 Model parameters for the Cell Growth Model of liver regeneration (Chapter 6) 420

Table A.2 Hepatocyte model parameters for the Non-Parenchymal Cell Model of liver regeneration (Chapter 7) 424

Table A.3 Kupffer cell model parameters for the Non-Parenchymal Cell Model of liver regeneration (Chapter 7) 426

Table A.4 Hepatic stellate cell model parameters for the Non-Parenchymal Cell Model of liver regeneration (Chapter 7) 428

Table B.1: Correlation estimates using the standard and segmentation methods (true correlation is 1) 441

Table B.2: Correlations calculated from missing data study 444

Table C.1 Primer sequences and RefSeq IDs of mRNA measured in Chapter 8 446

Table F.1 Sample single cell data for use with the script in Appendix E (Genes 1-6) 490

Table F.2 Sample single cell data for use with the script in Appendix E (Genes 7-12) 493

LIST OF FIGURES

Figure 1.1 Pathological features of progressing ALD shown through H&E staining. (A) Control rat liver (Liu et al, 2011). (A) Alcoholic steatosis in the rat liver shows lipid droplet accumulation and may be accompanied by hepatomegaly (Liu et al, 2011). (B) Alcoholic fibrosis in the mouse liver causes an increase in hepatocyte apoptosis and areas of increasing scar tissue deposition (Liu et al, 2015). (C) Alcoholic cirrhosis in the rat is characterized by "chicken-wire" scarring. Note: This image shows CCL4-induced cirrhosis as opposed to alcoholic cirrhosis (Bahk et al, 2011). Until recently, cirrhosis was thought to be unresolvable even if the underlying insult was removed. This figure was adapted from the references cited in this caption. 6

Figure 1.2 The effects of an 18-week ethanol feeding diet on liver pathology. (A) Liver sections of control rats. (B) Liver sections of rats fed an ethanol diet with 36% of calories from ethanol for 18 weeks. Arrow indicates fatty accumulation. This figure was adapted from (Ronis et al, 2011). 7

Figure 2.1 Quality control for NF-κB ChIP assay for measuring NF-κB binding post-PHx. (A) Sonication optimization for the ChIP procedure. (B) The NF-κB p65 antibody used is specific for NF-κB binding. (C) Representative PCR gel showing ChIP of NF-κB on the SOD2 gene from 0-6 hours post-PHx. (D) Representative PCR gel showing ChIP of NF-κB on the NOS2 gene from 0-6 hours post-PHx. (C) Representative PCR gel showing ChIP of NF-κB on the G0S2 gene from 0-6 hours post-PHx. (C) Representative PCR gel showing ChIP of NF-κB on the IGFBP1 gene from 0-6 hours post-PHx. ChIP = NF-κB antibody-treated, IGG = negative control, Sonicated = positive control. 16

Figure 2.2 Analysis of optimum FDR to maximize binding peaks identified and minimize false positives. Maximum FDR cutoff was varied from 0 to 0.2 in increments of 0.01. An FDR cutoff at 0.05 allows for identification of a large number of NF-κB binding peaks while minimizing the expected number of false positives. 18

Figure 2.3 Analysis of how FDR affects relative fraction of genes in each binding pattern. Selecting an FDR cutoff between 0.01 and 0.20 does not dramatically change the relative fractions of genes in binding patterns 2-6. Increasing the FDR causes a decrease in the fraction of genes bound in pattern 1 and an increase in the fraction of genes bound in patter 7; however, at an FDR cutoff near 0.05, the fractions of genes in patterns 1 and 7 are relatively stable. 20

Figure 2.4 Differentially expressed genes (Fold change cutoff = 2) at 4 hours and 12 hours post-PHx. 25

Figure 2.5 Scree plots of peak scores for NF-κB binding at 0h, 1h, and 6h post-PHx. At each time point, a cutoff value for peak score was chosen based on when a "knee" occurred in the scree plot and maintaining 500-1,000 NF-κB peaks. 27

Figure 2.6 Distance to transcription start site (TSS) at each time measured post-PHx. At 1 hour post-PHx, the peak distance to TSS appears to decrease with more NF-kB binding close to the regulated gene both upstream and downstream. 30

Figure 2.7 NF-κB binding patterns with associated pathways found using DAVID. (A) Immediate binding and unbinding (B) Transient Binding and unbinding (C) Delayed Binding and Unbinding (D) Constitutive Binding. Our analysis revealed that NF-κB binds to many genes involved in sensory perception of smell at baseline. Following PHx, however, these targets become unbound as NF-κB instead targets pathways previously related to be critical to liver regeneration. It is possible that genes involved in sensory perception of smell serve as a sink for NF-κB binding so that transient pulses to NF-κB binding do not start cascades of inflammation. 35

Figure 2.8 NF-κB binding regions for olfactory receptor genes compared to DNAse1 hyperactivity sites from whole-liver tissue in mice from the ENCODE project. 36

Figure 2.9 Switching mechanisms of NF-κB binding post-PHx. (A) NF-κB immediate response switch. (B) NF-κB transient response switch. (C) NF-κB delayed switch. (D) NF-κB constitutive binding. NF-κB was constitutively bound to genes responsible for cell cycle, cellular response to stress, and the JAK-STAT pathway. The regulation of these genes by NF-κB may be essential for tissue function. 39

Figure 2.10 Pattern-based motif analysis of NF-κB binding sites. Strongly bound sites in each binding pattern were matched to known transcription factor binding sites using the software DME and the TRANSFAC database. Potential co-regulators of NF-κB binding switches were identified for each binding pattern. 42

Figure 2.11 Motif analysis of NF-κB binding sites. The top binding motifs were matched to TRANSFAC to identify potential cofactors regulating gene expression with NF-κB at each time point (excluding those motifs involved in mainly DNA binding and polymerase activity). 44

Figure 2.12 Co-ordinated activation of AP-1 and ATF family transcription factors during liver regeneration. Our motif analysis suggested that AP-1 binding coincided with NF-κB binding to co-regulate expression of genes during the priming phase of liver regeneration. The AP-1 family of transcription factors were found to be strongly activated by 1 hour post-PHx in rats. This activation was maintained throughout the priming phase for all transcription factors except FOSB and JUNB. FOSB activity decreased following PHx, which JUNB activity transiently increased before returning to baseline levels. *p-value < 0.05, **p-value < 0.01. 47

Figure 2.13 ChIP qPCR validation. Binding patterns for selected genes were investigated using ChIP-qPCR. 48

Figure 2.14 ChIP qPCR validation of NF-κB targets following PHx. 49

Figure 2.15 NF-kB binding for the top 20 differentially expressed genes clustered according to NF-kB binding pattern (A) NF-kB binding at baseline, (B) NF-kB binding at 1 hour post-PHx, (C) NF-kB binding at 6 hours post-PHx. Black = Bound, Gray = Unbound. 51

Figure 3.1 Analysis of hepatocyte replication after PHx in WT and adiponectin KO mice. (A) Representative histological sections from mice at various times after PHx and injected with BrdU 2 hrs prior to sacrifice were stained using BrdU-specific antibodies. (B) The percentage of BrdU positive hepatocytes was calculated by quantifying BrdU positive nuclei and total nuclei from 5 representative fields at 20x magnification (n=4/group). (C) Western blot of representative liver samples probed with antibodies specific for cyclin D1, PCNA, Cyclin A and GAPDH. (D) Quantitation of western blots for cyclin D1, PCNA, Cyclin A (n=3/group). (E) Liver to body weight ratio. Data are presented as mean +/- SEM. NS: not significant, * P<0.05, *** P<0.01 adiponectin -/- significantly different from WT. 65

Figure 3.2 Identifying the key control factors through sensitivity analysis of a computational model of liver regeneration. (A) Schematic representation of the network model of liver regeneration following PHx incorporates contributions of non-parenchymal cells to catalyze hepatocyte replication. (B) Pulse changes to the metabolic demand parameter (M) caused delayed regeneration if administered early post-PHx, and enhanced regeneration if administered late post-PHx. (C) (Upper panel) The nominal profiles of IL-6, STAT3 and fractional recovery. (Lower Panel) Hour-long, 50% pulsatile decreases in IL-6 production rate (kIL6) caused a temporary decrease in the IL-6 levels, independent of when the pulsatile change was introduced (note the consistent blue diagonal). Such a temporary reduction in IL-6 led to a much longer and more pronounced decrease in STAT3 phosphorylation, with earlier IL-6 changes leading to longer STAT3 transients, and ultimately delayed regeneration. The earlier the pulsatile reduction in IL-6 and subsequent transient decrease in STAT3, the longer the regeneration deficit persisted. (D) Phase-based sensitivity analysis showed that the timing of alterations to the key controlling factors leads to a phase-dependent effect on overall regeneration. In general, changes to these key factors during the priming phase had opposite effects on regeneration as compared to the effect of changes during the replicating and termination phases. 67

Figure 3.3 Normalized sensitivity values of the top-ranked controlling factors. Overall regeneration was highly sensitive to both molecular and physiological parameters. More molecular parameters were identified as key controlling factors, but the alterations in physiological parameters k_{prol} and k_R produced the largest effects of all parametric changes. 69

Figure 3.4 Time-dependent effects of pulsatile changes to the key controlling parameters on molecular variables as well as overall regeneration. The effect of a 50% pulsatile increase in metabolic demand (M) on overall regeneration was dependent on when the pulse was administered. Early increases during the priming phase led to a transient decrease in the fractional recovery due to a temporary increase in cell death. Later increases in metabolic demand led to a higher overall regeneration, stimulated by increase in replication. Pulsatile increases in IL-6 production (k_{IL6}), growth factor production (k_{GF}), and pro-STAT3 levels led to increased overall regeneration, with differences in magnitude of effects based on when the pulse occurred. Increasing growth factor or IL-6 degradation, in contrast, decreased overall regeneration with a maximum effect occurring when the pulsatile change was introduced in the early phase following PHx..... 72

Figure 3.5 Time-dependent effects of transient increases in IL-6 production rate during different phases of liver regeneration. (A) Transient increases in IL-6 production rate (k_{IL6}) during the priming and replication phase. (B) Transiently increasing IL-6 production rate during the priming phase (0-6 hours) caused a transient increase in IL-6 levels followed by a persistent reduction in IL-6 levels. Transiently increasing IL-6 production rate during the replication phase (12-100 hours) caused a sustained increase in IL-6 levels. (C) Persistent reduction in IL-6 levels from increased production during priming caused a persistent decrease in hepatocyte replication rate and a blunted overall tissue recovery. Sustained increase in IL-6 levels caused a persistent increase in hepatocyte replication rate and an enhanced overall tissue recovery. 74

Figure 3.6 Cells entering the replicating phase too early as compared to the experimental measurements of Adn-/- hepatocyte entry into the cell cycle. (A) Hepatocyte replication was delayed early post-PHx and recovered by 60 hours post-PHx, but with replication levels higher than seen experimentally in Adn-/- mice. (B) This high replication was induced by increased GF signaling. 76

Figure 3.7 Regeneration profile renormalizing too late as compared to the experimental measurements of Adn-/- liver to body weight recovery. (A) The replication profile appeared to match experimental measures of Adn-/- hepatocyte cell cycle entry, but renormalization occurred well beyond 60 hours post-PHx due to the decreased priming response early post-PHx and the length of the cell cycle. (B) The decreased priming was caused by decreased IL-6 signaling decreasing STAT3 phosphorylation. 77

Figure 3.8 Regeneration profile with an initial delay and an overshoot. (A) These parameters induced a transient wave of apoptosis early post-PHx coupled with enhanced replication, which led to a delayed liver recovery but an increase in final liver recovery. (B) This profile was caused by a large increase in apoptosis (not shown), enhanced IL-6 signaling and STAT-3 phosphorylation, and large increases in GF signaling. 78

Figure 3.9 Modeling the dynamics of the Adn-/- regeneration phenotype. (A) Simulated profile for Adn-/- mice showed delayed onset of liver regeneration, followed by renormalized liver mass at approximately 60 hours post-PHx and enhanced recovery thereafter. This profile was mediated by delayed and suppressed priming as well as replication during the first 20 hours post-PHx and enhanced replication beyond 30 hours post-PHx. (B) The Adn-/- phenotypic changes were governed by decreased IL-6 signaling in the priming phase, causing decreased STAT3 phosphorylation, and increased GF signaling during peak hepatocyte replication. 80

Figure 4.1 Altered TNFα and IL-6 signaling and enhanced growth factor kinetics following PHx in the Adn-/- mice. (A) TNFα protein levels after PHx were measured in liver lysates by ELISA and normalized to total sample protein levels. (B) Serum IL-6 levels were analyzed by Quantibody® Multiplex ELISA Array. Each point represents an individual animal and horizontal bars represent mean IL-6 levels at each time point. (C) NF-κB DNA binding activity in liver nuclear extracts. (D) Western blot of representative liver samples probed with antibodies specific for phosphor-STAT3 (Tyr 705), STAT3 protein and GAPDH. (E) Quantitation of pSTAT3 normalized to total STAT3 protein (n=3/group). (F) SOCS3 transcripts were assessed by RT-PCR and normalized to WT control transcript levels. (G) Quantitation of Western blots of liver lysates for ANG-1. (H) Quantitation of Western blots of liver lysates for FGF-2. (I) Quantitation of Western blots of liver lysates for HGFα. Data are presented as mean +/- SEM. *: $p<0.05$, ***: $p<0.01$ compared with control of respective genotype; #:$p<0.05$, ###: $p<0.01$ Adn -/- different from WT at same time point (n=3/group). 89

Figure 4.2 Modeling the regeneration dynamics corresponding to the rosiglitazone-induced supraphysiological Adn phenotype. (A) The key controlling factors corresponding to the Adn-/- phenotype were altered in the opposite manner to simulate the effect of increase in Adn levels. Simulated profile for rosiglitazone-treated mice showed suppressed liver regeneration. Although rosiglitazone treatment initially caused a slight lead in liver recovery due to increased priming, ultimately reduced replication suppressed liver recovery from PHx. (B) These phenotypic changes were governed by sustained IL-6 signaling but decreased GF signaling throughout regeneration. 92

Figure 4.3 Effects of rosiglitazone treatment on hepatocyte replication after PHx in WT and Adn -/- mice. (A) Serum samples taken from tail blood of WT mice at various times were assessed for adiponectin by ELISA. (B) The percentage of BrdU positive hepatocytes was calculated from liver sections stained for BrdU and quantifying BrdU positive nuclei and total nuclei from 5 representative fields at 20x magnification (n=4/group). (C) Quantitation of Western blots for cyclin A (n=3/group). (D) Quantitation of Western blots for Cyclin D1 (n=3/group). (E) Western blot of representative liver samples probed with antibodies specific for FGF-2 and β-Actin. (Lower) Quantification of Western blots for FGF-2 (n=3/group). (F) Western blot of representative liver samples probed with antibodies specific for HGF-α and β-Actin. (Lower) Quantification of Western blots for HGF-α (n=3/group). Data are presented as mean +/- SEM. ***P<0.01* P<0.05 significantly different from WT veh treated. ### P<0.01 compared to vehicle treated Adn-/- 94

Figure 5.1 Effects of adiponectin knockout on protein expression following 70% PHx. (A) Experimental design. Wild-type and Adn-/- mice were subjected to 70% PHx and samples were taken throughout the priming phase. (B) Proteins measured in serum and tissue that show statistically discernable dynamic changes. (C) Differences in protein expression in the serum of wild-type and Adn-/- mice prior to PHx. Adn-/- mice expressed proteins (1) below the limit of detection, (2) at lower levels than wild-type mice, or (3) at higher levels than wild-type mice. 107

Figure 5.2 Proteins with trends towards differences in baseline expression between wild-type and Adn-/- mice. Not all of the differences in these protein levels are statistically discernable. All non-corrected p-values <= 0.30. 114

Figure 5.3 Proteins that may have different variances at baseline between genotypes. CXCL9 appears to be more tightly regulated in WT mice, while IGF1 and TNFRSF1B appear to be more tightly regulated in Adn-/- mice. P-values are indicated as uncorrected/corrected by the Bonferroni method. No discernable differences in variance between genotypes were found after p-value correction. 115

Figure 5.4 Modes of response for proteins following 70% partial hepatectomy. Other modes are possible, but the proteins measured in this study all follow these expression modes. 116

Figure 5.5 Heatmap showing WT serum response to resection organized into modes of expression. 117

Figure 5.6 Heatmap showing WT serum responses organized into modes including all proteins measured. Proteins are grouped within an expression mode if the ANOVA p-value was <= 0.30. 118

Figure 5.7 Several of the proteins measured in wild-type mice showed similar expression trends in animal tissue and serum. This similarity indicates that the liver is the main producer of these proteins following resection and transport into the tissue is relatively fast. 124

Figure 5.8 Several of the proteins measured in wild-type mice showed opposite expression trends in animal tissue and serum. This dissimilarity indicates that the liver may not be the main producer of these proteins following resection or that transport into the tissue is relatively slow. . 126

Figure 5.9 P-selectin showed cyclic dynamics post-PHx in wild-type mouse tissue, but no discernable dynamics in serum. 128

Figure 5.10 Heatmap showing Adn-/- serum response to resection organized into modes of expression (p <= 0.05) 129

Figure 5.11 Heatmap showing Adn-/- serum response to resection organized into WT modes of expression (p-value <= 0.05). 130

Figure 5.12 Heatmap showing the behavior of proteins in Adn-/- mice. Proteins were included in a group if the p value calculated using an ANOVA was <= 0.30. 131

Figure 5.13 Many of the proteins measured in wild-type and Adn-/- mice show similar expression trends in animal serum. 133

Figure 5.14 Many of the proteins measured in wild-type and Adn-/- mice show similar expression trends in animal serum. 134

Figure 5.15 Proteins with similar expression trends but altered timing in the serum of wild-type and Adn-/- mice. 135

Figure 5.16 Mode 1 behavior in Adn-/- mouse serum post-PHx, but no statistically discernable dynamics in wild-type mice. Nevertheless, the expression trends in wild-type animals are similar, tending to increase throughout the priming phase. 138

Figure 5.17 Several proteins show mode 1 behavior in wild-type mice, but no statistically discernable dynamics in Adn-/- mice. These proteins in Adn-/- mice, however, do show increasing trends throughout the priming phase. 142

Figure 5.18 Proteins increasing during the priming phase in Adn-/- mice that do not increase in wild-type mice (or may decrease slightly). 144

Figure 5.19 Adn knockout inhibits dynamic expression of some proteins. 146

Figure 5.20 Several of the proteins measured in Adn-/- mice show similar expression trends in animal tissue and serum. This similarity indicates that in And-/- mice the liver is the main producer of these proteins following resection and transport into the tissue is relatively fast. 150

Figure 5.21 One proteins measured in Adn-/- mice shows opposite expression trends in animal tissue and serum. This similarity indicates that in Adn-/- mice the liver is either not the main producer of these proteins following resection or transport into the tissue is relatively slow. 150

Figure 5.22 Several proteins measured in Adn-/- mice show dynamic expression trends in animal tissue. These dynamics are not reflected in the serum. 151

Figure 5.23 Adn knockout leads to different tissue regulation of the priming phase. 153

Figure 5.24 The differences in protein expression in wild-type and Adn-/- mice during the priming phase of regeneration may be caused by an altered regulatory network governing dynamic protein expression. The structure of the regulatory network can be represented using a clustered correlation heatmap among proteins. In this schematic, the lower triangular matrix represents correlations among proteins in the serum, the upper triangular matrix represents correlations among the proteins in the tissue, and on the diagonal of the matrix is a representation of the correlation between tissue and serum for each protein. Gray pixels represent NA values in the data. 156

Figure 5.25 The differences in protein expression in wild-type and Adn-/- mice during the priming phase of regeneration may be caused by an altered regulatory network governing dynamic protein expression. The structure of the regulatory network can be represented using a clustered correlation heatmap among proteins. These networks were calculated using the segmentation method detailed in Appendix B with pseudo-samples (see text for details). In this schematic, the lower triangular matrix represents correlations among proteins in the serum, the upper triangular matrix represents correlations among the proteins in the tissue, and on the diagonal of the matrix is a representation of the correlation between tissue and serum for each protein. 157

Figure 6.1 Computational models of liver regeneration. (A) Computational limitations require a trade-off between high-resolution (molecular or spatial) and the ability to predict whole-tissue function. (B) Agent-based models, such as that developed by (Hoehme et al., 2010) based on CellSys, allow for high spatial resolution, but often for only a section of tissue. (C) Models based on 'omics' data, such as Hepatonet1 developed by (Gille et al., 2010), provide a middle ground where there is high resolution of molecular events at the desired scale (transcriptome, proteome, metabolome) and the molecular regulation can be extrapolated to whole tissue. (D) Physiological models, such as that developed by (Furchtgott et al., 2009), predict the regeneration of the whole liver, but offer limited mechanistic insight into the molecular events. (E) Outputs from the physiological model can show cells in discrete physiological states as well as (F) molecular regulation governing those cell state transitions. Figure 1C was reproduced from (Gille et al., 2010). 163

Figure 6.2 Schematic representation of the changes occurring during liver regeneration following PHx. (A) Detailed schematic. (1) Following PHx, hepatocytes respond within 30 seconds of tissue damage. Early post-PHx, previous work has shown release of ATP, increases in WNT signaling, and ionic Calcium release from hepatocyte mitochondria. (2) These responses in hepatocytes are likely to be driven by an increase portal blood flow, an increase in portal pressure, and an increase in metabolic demand per cell (increased nutrient availability, increased toxin flux, and increased extra-hepatic signals including LPS). (3) Signals from the blood and from hepatocytes activate non-parenchymal cells to produce factors governing hepatocyte entry into the cell cycle (including priming). (B) Simplified schematic diagram. This schematic shows the relationships included in the computational model. Several important pathways are lumped or represented as physiological transitions rather than including truly mechanistic detail. This physiological approach allows for insight into control principles of regeneration governed by archetypal signaling pathways. The gray matrix-bound factor (MBF) signaling was added to the model to investigate the contribution to liver mass recovery of matrix-bound signaling, but because of a relatively small impact on the dynamic mass recovery was excluded from further analyses. 169

Figure 6.3 Relative levels of IE genes (Fold Change) and signals released from the ECM (Relative Amount) during the priming phase. Model parameters were scaled in such a way that priming signals from Kupffer cells and from initially matrix-bound factors had relatively equal contributions to hepatocyte priming. The peak of MBF signaling occurred at approximately 45 minutes post-PHx. 180

Figure 6.4 Comparison of simulated mass recovery with and without considering Matrix Bound Factors (MBF). (A) Including EBF signaling in the computational model did not significantly change the overall dynamic mass recovery profile. (B) Including EBF signaling impacted the onset timing of regeneration leading to a small offset between dynamic regeneration including and excluding EBF signaling. This small offset (~0.006 mass recovery fraction) remained throughout regeneration. 181

Figure 6.5 Comparison of experimental data of liver regeneration in rats from Tanoue et al. (2011) (Experimental data) to the models proposed by Furchgott et al. (2009) (No cell growth) and proposed in this work (Cell growth). The model proposed in this work is able to fully capture the dynamics of liver repair following 70% partial hepatectomy in rats. 182

Figure 6.6 Model-predicted modes of regeneration revealed through sampling model parameters (+/- 50% of nominal values). Varying model parameters simultaneously revealed distinct regeneration modes, including (A) delayed, (B) suppressed, (C) enhanced, (D) delayed and enhanced, (E) unresponsive, and (F) liver failure. The dashed line is the nominal profile; the gray areas indicate +/- 1 standard deviation. .. 184

Figure 6.7 Molecular regulation governing altered regeneration profiles. (A) Average mass recovery, (B) One representative instance of mass recovery, (C) Average molecular regulation for regeneration modes: (1) Delayed, (2) Suppressed, (3) Enhanced, (4) Delayed and Enhanced. Dashed line represents nominal profile, black line represents average (or [B] one instance of the) profile, gray area represents +/- 1 standard deviation. 185

Figure 6.8 Model-predicted molecular regulation profiles underlying delayed regeneration response. (A) Mass recovery of specific delayed cases of liver regeneration compared to nominal and (B) molecular regulation for each regeneration profile. Deficiencies in either priming signals or growth factor bioavailability can lead to delayed regeneration. Note that parameters related to hepatocyte response to these signals change in addition to parameters governing molecular regulation. Dashed line represents nominal profile, black line represents the profile corresponding to delayed regeneration. 187

Figure 6.9 Model-predicted molecular regulation profiles underlying suppressed regeneration response. (A) Mass recovery of specific suppressed cases of liver regeneration compared to nominal and (B) molecular regulation for each regeneration profile. Suppressed regeneration can be caused by deficient priming signals or deficient growth factor bioavailability. Dashed line represents nominal profile, black line represents the profile corresponding to suppressed regeneration. 189

Figure 6.10 Model-predicted molecular regulation profiles underlying enhanced regeneration response. (A) Mass recovery of specific enhanced cases of liver regeneration compared to nominal and (B) molecular regulation for each regeneration profile. Enhanced regeneration can be regulated by enhanced GF bioavalability or by enhanced hepatocyte response to the presence of growth factors. Dashed line represents nominal profile, black line represents the profile corresponding to enhanced regeneration. 191

Figure 6.11 Model-predicted molecular regulation profiles underlying delayed and enhanced regeneration response. (A) Mass recovery of specific delayed and enhanced cases of liver regeneration compared to nominal and (B) molecular regulation for each regeneration profile. One model-predicted cause of this profile is deficient priming signals coupled with enhanced growth factor bioavailability. Dashed line represents nominal profile, black line represents the profile corresponding to delayed and enhanced regeneration. 193

Figure 6.12 Model-predicted molecular regulation profiles underlying unresponsive regeneration response. (A) Mass recovery of specific unresponsive cases of liver regeneration compared to nominal and (B) molecular regulation for each regeneration profile. Both regeneration profiles and molecular regulation appear to be unresponsive in the profiles investigated. Dashed line represents nominal profile, black line represents the profile corresponding to unresponsive regeneration. 194

Figure 6.13 Model-predicted molecular regulation profiles underlying liver failure. (A) Mass recovery of specific liver cases of liver failure compared to nominal regeneration and (B) molecular regulation for each liver failure profile. As the liver fails, Kupffer cells and hepatic stellate cells attempt to rescue the liver by producing more pro-regenerative factors. Dashed line represents nominal profile, black line represents the profile corresponding to liver failure. 195

Figure 6.14 Dynamic local sensitivity analysis of the regeneration model with and without cell growth. (A) Maximum normalized sensitivities were calculated for each parameter. (B) Normalized local sensitivity of metabolic demand when not considering cell growth. Metabolic demand is inhibitory for the first 53 hrs post-PHx, likely through increases in cell apoptosis. After 53 hrs, metabolic demand enhances regeneration, likely through increased production of growth factors. (C) Normalized local sensitivities of metabolic load and growth rate reveal a dynamic competition between replication and growth. From 43-87 hrs post-PHx growth rate and metabolic demand both drive regeneration. During initiation and termination, however, imbalances between growth and metabolic load can inhibit regeneration. 197

Figure 6.15 Potential antagonism between pairs of parameters. We used a local sensitivity analysis to identify pairs of parameters that impact the levels of a single factor or are closely related but have opposing effects on overall mass recovery. In addition to metabolic demand and growth rate (Figure 6.14 C) this analysis identified (A) IL-6 production and degradation and (B) GF production and degradation as potentially antagonistic parameter pairs. 198

Figure 6.16 Heatmaps show the overall liver mass recovered is sensitive to combinatorial effects of (A) Metabolic load and hepatocyte growth rate, (B) IL-6 turnover rate, and (C) GF turnover rate. All parameter changes are displayed in Fold change [FC] over nominal parameter value. (A) The proper balance between regenerative drive and cell growth in response to stress is required for normal regeneration. (B) IL-6 and (C) GF production rates have large-scale effects on overall recovery, while degradation rates act as fine tuning. 200

Figure 6.17 Heatmap comparison of overall liver mass recovered for altered GF production and degradation rates. (A) Heatmap with rescaled color mapping showing a subtle effect of coarse-grained control of regeneration by GF production and fine-tuned control by GF degradation (legend below), (B) Mass recovery holding one parameter constant at 20 and varying the other, and (C) Mass recovery holding one parameter constant at 20 and varying the other between 0-20. All parameter changes are displayed in Fold change [FC] over nominal parameter value. The black line indicates when GF production rate fold change equals GF degradation rate fold change. Asymmetry around this line, as in (A), indicates a differential effect of GF production and degradation. 202

Figure 6.18 Effect of decreasing IL-6 production. (A) IL-6 signals through the JAK-STAT signaling pathway to prime hepatocytes for replication. (B) Reduced IL-6 production causes delayed regeneration, with delays increasing as regeneration progresses. (C) A slight decrease in IL-6 production (25% reduction in peak levels) amplifies as the signal propagates through the JAK-STAT cascade. Ultimately, this slight IL-6 decrease results in reduced STAT-3 phosphorylation (75% reduction in peak) and reduced priming (~10% reduction at peak). This reduced priming leads to delayed recovery and a slightly reduced overall mass recovery (~5%). 204

Figure 6.19 Effects of decreasing GF bioavailability. (A) Decreased GF production causes a delay in regeneration. (B) As GFs become less available, (C) fewer hepatocytes enter the cell cycle, decreasing peak of regenerating cells. The synchronicity of hepatocyte entry into the cell cycle, however, is affected only slightly. (D-E) To decrease the synchronicity of entry into the cell cycle, it is necessary to decrease the proliferation rate. 205

Figure 6.20 Cross-species comparison of (A) rat, (B) mouse, and (C) human (upper panel) mass recovery profiles with experimental liver regeneration data (Pomfret et al, 2003;Shu et al, 2009b;Tanoue et al, 2011) and (lower Panel) predicted fraction of replicating hepatocytes for each species. This model suggests that the key difference governing regeneration profiles between species is an altered balance between proliferative and replicative balance in hepatocytes. This species-specific balance alters the levels of GFs available during regeneration thereby altering the BrdU incorporation of hepatocytes post-PHx. Rats and mice have similar metabolic loads and growth rates causing similar BrdU incorporation with several slight differences. Rats have a slightly later peak BrdU than mice (30h vs. 28h) and a higher peak value (0.75 vs. 0.66). Mouse BrdU incorporation, however, continues longer than rat. Similarly, humans show a reduced peak replication response (note change of scale) but a lengthened regeneration period, leading to similar overall recovery. 208

Figure 6.21 Relationships between fitted parameters and body mass across species. (A) Metabolic demand shows a negative exponential relationship with body mass following the equation: $Metabolic\ Demand = 47.315 * Mass - 0.1825$ (R2 = 0.95). (B) Cell growth rate for humans was estimated as the average growth for mouse and rat because there is little difference in cultured hepatocyte growth rates between species. . 210

Figure 6.22 Alternate parameter changes that can reproduce experimental liver regeneration profiles in humans. Parameters were varied to fit experimental data of human mass recovery to test several possible hypotheses about how human liver regeneration differs from rat: the hypothesis that humans have a higher stress response than rats (blue, MSE=6.1x10-3), the hypothesis that humans store a greater quantity of growth factors in the ECM that is liberated early post-PHx and may have an altered ECM production/degradation balance (red, MSE=6.25x10-3), the hypothesis that human hepatocytes have a higher transition time between physiological states (green, MSE=0.25x10-3), the hypothesis that humans have a longer cell cycle, a higher apoptosis rate, a higher requiescence rate, and a higher transition rate between physiological states as was assumed by Periwal et al. (2014) (magenta, MSE=12.16x10-3), and the hypothesis that only the metabolic demand parameter changes (black, MSE=4.91x10-3). (A) Simulated mass recovery compared to experimental data (Pomfret et al, 2003). (B) Mass recovery over the first 30 days following resection. (C) Fraction of replicating cells (simulated BrdU incorporation) post-resection. (D) IL-6 levels post-resection. (E) GF levels post-resection. (F) ECM accumulation post-resection. It may be possible to differentiate between most of these hypotheses by measuring at 30 days post-resection (G) IL-6, (H) GF, and (I) ECM. To differentiate between the high transition time hypotheses (green) and the hypothesis presented by Periwal et al. (orange), it may also be necessary to measure mass recovery. Approximately two weeks post-resection showed the maximum difference between mass recovery between these two hypotheses. MSE = Mean Squared Error between experimental and simulated data. 215

Figure 6.23 Regenerative modes of simulated human patients. (A) Supressed. (B) Delayed. (C) Ehanced. (D) Delayed and Enhanced. (E) No response. (F) Liver failure. Dashed line represents nominal regeneration, solid line represents mean, gray area represents +/- one standard deviation. 219

Figure 6.24 Effects of transient increases in metabolic demand on (A) suppressed regeneration and (B) no response. Dashed line represents nominal profile, solid line represents altered profile, arrows represent metabolic demand increase times. 220

Figure 6.25 Model fit to disease regeneration profiles revealed altered non-parenchymal cell activity coupled with imbalances in the growth/replication propensity of hepatocytes was sufficient to explain disease-induced inhibition of regeneration. (A) Non-alcoholic steatohepatitis (Tanoue et al, 2011), (B) Alcoholic steatohepatitis (Yang et al, 1998b), (C) Cirrhosis (Kaibori et al, 1997), and (D) Diabetes (JOHNSTON et al, 1986). 222

Figure 6.26 Regeneration profiles for healthy livers and those with high fat, fructose-induced steatosis. (A) NASH causes an inhibited replication response following PHx. The majority of mass recovery is caused by cell growth rather than replication. (B) This regeneration profile is driven by a lack of inflammatory signaling, leading to reduced priming. Although GFs are available, the low priming means that few hepatocytes are available to enter the replication stage. (MSE=2.25×10^{-4})..... 225

Figure 6.27 Regeneration profiles for healthy livers and those with alcohol-induced steatosis. (A) Alcoholic steatosis causes suppressed liver regeneration, with little mass recovery. The slight increase in liver mass is caused predominantly by cell growth rather than replication. (B) This profile is driven by sustained inflammatory signaling, lack of growth factor bioavailability, and increased matrix deposition following wounding. (MSE=8.82×10^{-5})..... 226

Figure 6.28 Regeneration profiles for healthy livers and those with toxin-induced cirrhosis. (A) Fibrosis causes a delay in the initiation of regeneration (note change in time scale) but ultimately little change in overall mass recovery. Mass recovery is due mainly to hepatocyte replication rather than cell growth. (B) This profile is driven by a sustained inflammatory response, a lack of growth factor bioavailability, and impaired matrix deposition following wounding. (MSE=2.50×10^{-3}).... 227

Figure 6.29 Regeneration profiles for healthy livers and those with diabetes. (A) Diabetes causes enhanced priming but delayed proliferation and delayed mass recovery. (B) This profile is driven predominantly by sustained cytokine signaling and a lack of growth factor bioavailability. (MSE=4.05×10^{-4})..... 229

Figure 6.30 Simulations using hepatocyte-specific parameter alterations compared to disease regeneration profiles. Model fits to disease regeneration profiles reveals altered hepatocyte response to non-parenchymal cell signaling is sufficient to explain disease-induced inhibition of regeneration in (A) Non-alcoholic steatohepatitis (MSE=$1.96x10^{-2}$), (B) Alcoholic steatohepatitis (MSE=$1.89x10^{-2}$), and (C) Chirrhosis (MSE=$5.14x10^{-2}$), but not in (D) Diabetes (MSE=1.19). In all cases, the previous set of parameters (Table S2) gave lower MSE than the hepatocyte-specific parameter alterations (Table S3). MSE = Mean Squared Error between experimental and simulated data. 232

Figure 6.31 Cross-species validation of model utility can predict changes to organizational principles of liver function by differentiating liver regeneration modes in two strains of Adn-/- mice. (A) Mass recovery from Adn-/- C67BL/6J from Correnti, Cook et al. (2014) and (B) from Adn-/- 129S mice from Shu et al. (2009). (C) Predicted molecular profile for IL-6 and GF for both Adn-/- mouse strains and wild-type mice. 235

Figure 7.1 Comparison of model dynamics between this model and previous model during the first 25 hours post-resection (Chapter 6)..... 250

Figure 7.2 Cell network model of non-parenchymal cell activation contributing to liver regeneration. (A) Full network diagram showing cell states, transitions among states, and molecules promoting or inhibiting cell transitions. (B) Cell signaling models showing a schematic representation of molecular interactions occurring within each cell type considered. Solid lines represent direction signaling; dashed lines represent indirect production. (C) Simulated liver mass recovery profiles compared to experimental data from (Tanoue et al, 2011). (D) Simulated cytokine dynamics following resection. (E) Simulated dynamics of growth factors and collagens following resection. (F) Simulated profile of HSC state dynamics following resection. 253

Figure 7.3 Parameters from all cell types contribute to regeneration dynamics and time to failure. (A) Hepatocyte apoptosis rate correlates relatively strongly with time to liver failure, suggesting that this parameter has a large influence causing liver failure. (B) Changing hepatocyte apoptosis rate results in a bifurcation between liver recovery following resection and liver failure. (C) Removing hepatocyte apoptosis rate from the global sensitivity analysis shows that regeneration and time to liver failure are sensitive to changes in many parameters. (D) The 20 parameters with the highest combined sensitivity coefficients for regeneration among and time to liver failure. Of the top 20 most sensitive parameter, 8 are HSC-related parameters, 7 are hepatocyte-related parameters, and 5 are KC-related parameters. (E) Time to failure sensitivity coefficients for parameter values associated with each cell type. 67% of hepatocyte parameters show positive failure sensitivity (compared to 48% for KCs and 50% for HSCs). (F) Regeneration sensitivity coefficients for parameter values associated with each cell type. 60% of HSC parameters show negative regeneration sensitivity (compared to 45% for hepatocytes and 43% for KCs). 262

Figure 7.4 Several parameters related to hepatocyte apoptosis cause a separatrix-like behavior between liver regeneration and liver failure. (A) Apoptosis rate, (B) shape parameter, (C) scale parameter. 262

Figure 7.5 Phase planes behavior during successful liver regeneration. Dynamic tissue microenvironment influences and is shaped by cell state balances. Dots on the phase planes represent time = 0hr, 24hr, 48hr, 72hr, and 168hr following resection. 265

Figure 7.6 Model analyses show the impact of imbalances among multiple hepatic stellate cell transcriptional states on liver regeneration dynamics. (A) HSC behavior is constrained prior to 24 hr post-PHx even after increasing the baseline fraction of pro-regenerative HSCs. This behavior assumes the absence of other changes associated with changing baseline amounts. (B) Similar to the phase plane behavior, transition dynamics converge prior to 24 hr post-PHx. (C) Increasing the baseline amount of pro-regenerative HSCs has little effect on the dynamic regeneration profile. (D) HSC behavior is constrained prior to 24 hr post-PHx even after increasing the baseline fraction of anti-regenerative HSCs. This behavior assumes the absence of other changes associated with changing baseline amounts. (E) Similar to the phase plane behavior, transition dynamics converge prior to 24 hr post-PHx. (F) Increasing the baseline amount of anti-regenerative HSCs has little effect on the dynamic regeneration profile. (G) Increasing the quiescent to anti-regenerative transition rate leads to a dynamic change in HSC transcriptional state balances. (H) HSC transition dynamics change based on the balance of transition rates. (I) Increasing the quiescent to anti-regenerative transition rate causes a suppressed regeneration profile. This type of profile can be seen in diseased states..... 267

Figure 7.7 Effects of increasing initial fraction of pro-regen HSC on dynamic tissue microenvironment 269

Figure 7.8 Effects of increasing initial fraction of anti-regen HSC on dynamic tissue microenvironment 270

Figure 7.9 Effects of increasing the anti-regen HSC transition rate on tissue microenvironment 271

Figure 8.1 Isolation of single / pooled hepatic stellate cells and hepatocytes. (A) Representative images showing LCM isolation of single hepatic stellate cells. DAPI and Phalloidin staining were used to identify nuclei and cell boundaries. Co-localization of DAPI and Gfap was used to identify HSCs. (B) Single HSCs and hepatocytes were collected from the same tissue and tested for cell type marker genes using high throughput qPCR. Cells expressed high levels of marker genes in a cell-type specific manner. (C) Using PCA on expression levels of 34 genes measure in both hepatocytes and HSCs separated cell types. The variability within a cell type appeared to be higher than variability between cell types. (D) PCA scores shows the genes contributing to the PCA plot. (E) Different genes showed unique patterns when comparing cell types. TNFR1 showed different mean CT values but similar variability. (F) PDGFA showed similar mean CT values and similar variability. (G) ALDH1A1 showed different mean CT values and different variability. 286

Figure 8.2 Technical reproducibility of the experimental strategy within a Biomark array and across Biomark arrays. (A) One sample run twice on the same array. (B) One sample run twice on the same array. (C) One sample run on two different arrays. (D) One sample run on two different arrays. 287

Figure 8.3 Principal Component scores for PCs 1-6, used to discriminate between HSCs and hepatocytes. 289

Figure 8.4 Gene expression in single hepatic stellate cells reveals functional transcriptional states. (A) Manual clustering of functional HSC states reveals four states: Quiescent (low GF/low collagen), Pro-regenerative (high GF/low collagen), Anti-regenerative (low GF/high collagen), and mixed (high GF/high collagen). (B) Linear discriminant analysis shows separation of the four HSC states in two dimensions. (C) LDA shows further separation of the four HSC states in three dimensions. (D) Genes contributing to discrimination among functional states. (E) Minimum spanning tree representation of single HSCs shows relationships between individual cells based on gene expression. (F) Cyclic representation of HSC functional states shows the potential distribution of individual HSCs as they progress through the cycle. (G) Heatmap representation of gene expression values for individual HSCs. Cells are grouped based on functional state. Genes are grouped by hierarchical clustering with Pearson correlation. Gene annotations are colored based on functional annotations. Green = growth factors, gray = collagen-related genes, orange = Tgfb signaling, blue = matrix-modulating genes. 291

Figure 8.5 Linear discriminants for LD1, LD2, LD3, used to discriminate among HSC functional states 292

Figure 8.6 Significance of clustering results assessed by silhouette score. Our silhouette score falls well outside the range generated from randomizing our data 1,000 times. This gives an empirical p-value of less than 0.001. 293

Figure 8.7 Validation of single cell results using 10 cell pools of HSCs collected from the same animals. Pools of HSCs showed a stronger gene expression signal, but a higher variability than single cells. (A) Manual clustering of functional HSC states into four states: Quiescent (low GF/low collagen), Pro-regenerative (high GF/low collagen), Anti-regenerative (low GF/high collagen), and mixed (high GF/high collagen). (B) Linear discriminant analysis shows separation of the four HSC states in two dimensions. (C) LDA shows further separation of the four HSC states in three dimensions. (D) Genes contributing to discrimination among functional states. (E) Minimum spanning tree representation of single HSCs shows relationships between individual cells based on gene expression. (F) Significance of clustering results assessed by silhouette score. 294

Figure 8.8 Dendogram showing the definition of gene clusters using a height cutoff value of < 0.93. 296

Figure 8.9 Overrepresented functions (GO Terms) for each gene group identified in our single cell data compared to the background of all genes measured. * Indicates p-value < 0.05. 297

Figure 8.10 Topical map representation of hepatic stellate cells states shows the clustering of HSCs in (A) control animals at 0 hours and 24 hours post-PHx and (B) ethanol-fed animals at 0 hours and 24 hours post-PHx. 303

Figure 8.11 Kernel estimation of HSC states using HSC-enriched genes and 10 cell pools. (A) Kernel estimation. (B-C) Predicted levels of each HSC state during different conditions. (D-G) Comparison of predicted state balances with experimental data. Error bars are 95% confidence intervals. 306

Figure 8.12 New kernels from smaller set of genes. (A) Kernel estimation. (B-C) Predicted levels of each HSC state during different conditions. (D-G) Comparison of predicted state balances with experimental data. Error bars are 95% confidence intervals. 309

Figure 8.13 Regression technique applied to single HSCs. (A) Kernel for single HSCs compared to the kernel from pooled HSCs. (B) Predicted Levels in control rats. (C) Predicted levels in ethanol-fed rats. (D-G) Predicted levels compared to experimental data. Error bars are 95% confidence intervals. 311

Figure 8.14 Regression technique applied to single HSCs using the selected genes only. (A) Kernel for single HSCs compared to the kernel from pooled HSCs. (B) Predicted Levels in control rats. (C) Predicted levels in ethanol-fed rats. (D-G) Predicted levels compared to experimental data. Error bars are 95% confidence intervals. 313

Figure 8.15 Relative HSC transcriptional strength predicted using the NNLS regression approach. Error bars represent 95% confidence intervals. .. 315

Figure 8.16 Implications of HSC activation results and model predictions for chronic ethanol-treated rats. (A) Chronic ethanol use leads to increased levels of pro-inflammatory and anti-inflammatory cytokines following PHx. (B) Chronic ethanol appears to lead to a deficient pro-regenerative HSC response following PHx. (C) The effects of increased cytokine production, imbalanced HSC functional states, and changes to the tissue microenvironment combine to suppress regeneration following ethanol adaptation. The simulated regeneration profile of ethanol adapted rats is consistent with results from (Yang et al, 1998b). 318

Figure 8.17 Effects of chronic ethanol consumption on liver regeneration control and tissue microenvironment..... 319

Figure 8.18 Simulations lead to the prediction that there is more apoptosis of HSCs in the ethanol-fed rats than controls. 320

Figure 8.19 Potential hepatic stellate cell transition patterns. (A) Star-type transitions could allow any functional state to shift its transcriptional profile into any other functional state. (B) A cyclic transition pattern, like the cell cycle, could allow for distributions of cells aiding hepatocyte regeneration or homeostatic renewal. Getting “stuck” in one phase of the cycle could lead to cell exit into apoptosis or pre-fibrotic phenotypes. (C) A cell fate commitment pattern would allow cells to transition only one way. In such a pattern, quiescent cells would have to be continuously replenished. Perhaps hepatic stem cells (or oval cells) play a role in this replenishment. 321

Figure 9.1 Homeostatic renewal model. (A) Model schematic showing two populations of hepatocytes: Axin2+ and Axin2-. Each population can replicate at a specific rate and each has a specific apoptosis rate. Axin2+ cells are able to transition to Axin2- cells, but not the reverse. (B) Equations governing model behavior. (C) Steady-state behavior of the model shown using phase plane. There are multiple steady states but no stable attractor. Blue arrows represent the sign of the local derivative in the y-direction, red arrows represent the sign of the local derivative in the x-direction. (D) In response to a transient stress, like increased apoptosis rate, the system shifts to a new steady-state. (E) Phase-plane representation of model behavior in response to a transient apoptosis stress shows the transition to a new state. 335

Figure 9.2 Response to stressors (A) Response of Model A increased apoptosis (left column), increased proliferation (middle column), and initial imbalanced populations (right column). (B) Response of model B. (C) Response of Model C. (D) Response of model D. Points represent t = 0 days, 10, 40, and 60 days then every 30 days until 1 year, then points represent each subsequent year. Gray arrows represent the direction of motion on the phase plane. 337

Figure 9.3 A different specific form of the feedback on the transition rate (Model C) gives rise to similar systems behavior. We investigated how a Hill-type inhibition would affect system behavior. We show that Hill coefficient of (A) one, (B) two, or (C) three give rise to similar system behavior (D). In addition, this unstable steady state is similar to that seen using a simpler inhibition term (See Figure 9.2F). 340

Figure 9.4 Response to stressors (A) Response of Model A increased apoptosis (left column), increased proliferation (middle column), and initial imbalanced populations (right column). (B) Response of model B. (C) Response of Model C. (D) Response of model D. Points represent t = 0 days, 10, 40, and 60 days then every 30 days until 1 year, then points represent each subsequent year. Gray arrows represent the direction of motion on the phase plane. 343

Figure 9.5 Effect of carrying capacity on response to transient apoptosis challenges. As carrying capacity increases above the steady-state population balances, the system response to disturbances increases as well. Gray arrows represent the direction of motion on the phase plane. 344

Figure 9.6 Selection of the "Robust model" of homeostatic renewal for further analysis. (A) Robustness of system response to multiple transient disturbances and variance in the response in simulated patients with altered physiological parameters. The systems that responded with the smallest deviation (highest robustness) also show the smallest normalized variance in response to altered parameters. (B) ANOVA shows that feedbacks A, B, and C are significant as are their interactions. Feedback D and its interactions do not affect model output significantly. (C) Robust model (Model A+B+C) response to transiently increased and transiently decreased apoptosis. (D) Robust model response to transiently increased and transiently decreased proliferation. (E) Robust model response to initial population imbalances shows that multiple starting conditions converge on a steady-state. Points represent t = 0 days, 10, 40, and 60 days then every 30 days until 1 year, then points represent each subsequent year. Gray arrows represent the direction of motion on the phase plane. MRS is the Mean Recovery Score, which is the sum of the recovery volumes for all disturbances. 349

Figure 9.7 Model analyses of the robust model. (A) Parametric sensitivity analysis shows that model parameters tend to affect either Axin2+ steady-state populations or Axin2- steady-state populations. Carrying capacity and proliferation rate have the large effects on cell populations, as does the apoptosis rate of Axin2- cells. (B) Variance-based global sensitivity estimates corroborate the findings from the parametric sensitivity analysis, suggesting that population levels of each hepatocyte state are affected by their individual governing parameters. (C) The effect of changing Axin2- carrying capacity in the absence of other changes on overall liver mass. (D) Increasing the carrying capacities of Axin2+ and Axin2- hepatocytes can lead to an unstable system. 352

Figure 9.8 Visualizations of what frequencies mean with respect to one week. Each frequency is interpreted in the context of alcohol binges per week (leading to an increased apoptosis). 354

Figure 9.9 Simulating multiple Axin2+ apoptosis frequencies. At frequencies > 1.4 cycles/day (between binge drinking daily and every other day), the Axin2+ hepatocyte population begins to become unstable. 356

Figure 9.10 Simulating multiple Axin2- apoptosis frequencies. At frequencies > 2.0 cycles/day (between binge drinking daily), the Axin2- hepatocyte population begins to become unstable..... 357

Figure 9.11 Simulating multiple whole liver apoptosis frequencies. At frequencies > 2.0 cycles/day (binge drinking daily), the Axin2+ and Axin2- hepatocyte populations begin to become unstable. 358

Figure 9.12 Simulating multiple whole liver apoptosis events. Apoptotic events likely follow a step-like function rather than a sinusoidal function. At low frequencies, the liver has a chance to recover between apoptotic events. At high frequencies (f ~ 2.0 cycles/day and above), the hepatocyte populations are unable to recover between events and population levels become unstable. 359

Figure 9.13 Simulating multiple whole liver apoptosis events. For a given amount of damage per event, the frequency of the event determines the overall damage to the tissue. Low frequency events allow for nearly complete recovery between apoptotic events, while high frequency events to not allow for this recovery. 360

Figure 9.14 Simulating multiple whole liver apoptosis events. For a given frequency of damage (1.0 cycles per day in this figure), the damage per event changes homeostatic liver mass. The pattern of insult and recovery appears similar for all damage amounts. The stable populations of hepatocytes, however, become smaller with increasing damage amounts. 361

Figure 9.15 Comparison of the robust model response to disturbances with and without stem cell renewal. The addition of stem cell renewal does little to affect system behavior and response to transient individual disturbances. Points represent t = 0 days, 10, 40, and 60 days then every 30 days until 1 year, then points represent each subsequent year. Gray arrows represent the direction of motion on the phase plane. 363

Figure 9.16 Homeostatic renewal recovers liver mass when hepatocytes in the liver become senescent coupled with a large apoptotic event. This model uses the robust model + stem cell renewal. Researchers from Dr. Forbes' lab showed complete renewal in 90 days post-injury, which our model also shows. No damage is shown in black, removal of 40% of the hepatocytes is shown in blue. Our model predicts that stem cells become active even without an additional apoptotic challenge and that the timeframe of recovery is slightly longer. Points represent t = 0 days, 10, 40, and 60 days then every 30 days until 1 year, then points represent each subsequent year. Gray arrows represent the direction of motion on the phase plane. 364

Figure 9.17 Non-parenchymal cell control of hepatocyte homeostatic renewal. (A) The biological process underlying the control system representation. (B) A control systems representation of liver homeostatic renewal controlled by non-parenchymal cell networks. In this representation, apoptosis rate increases and decreases are a disturbance to normal homeostatic renewal. (C) Ability of the non-parenchymal cell network controller to mitigate the effects of a periodic apoptosis challenge. Controller action causes an attractor state with minimal deviation around the steady-state. In the absence of non-parenchymal cell control, hepatocyte populations fall into an attractor cycle below steady-state levels. 368

Figure 9.18 Non-parenchymal cell control of homeostatic renewal allows for disturbance rejection (faster recovery, smaller perturbations) compared to the case without external control. The control action of both controllers is similar for a transient increase in apoptosis, suggesting that the local non-parenchymal cell networks in the pericentral zone and in the bulk tissue respond following similar dynamics in response to an apoptotic challenge. 369

Figure 9.19 Non-parenchymal cell control can mitigate the effects of a sustained apoptosis challenge. 371

Figure 9.20 Changing controller parameters affects the early dynamics of chronic injury. 373

Figure 9.21 Controller function (A) Response to band-limited white noise (Apoptosis rate standard deviation = 10% of nominal). Non-parenchymal cell control can respond to random variation in apoptosis rate by causing larger fluxuations in Axin2+ populations. The non-parenchymal cell controller, however, maintains Axin2- populations closer to nominal than in the absence of a controller. (B) Response to band-limited white noise (Apoptosis rate standard deviation = 10% of nominal) using a bandpass filter of +/- 0.5% of the setpoint. (C) Simulating chronic apoptosis challenges in 100 patients. Model parameters were sampled from a normal distribution with mean at the nominal parameter value and standard deviation of 1% of nominal values. Simulating multiple patients shows that the controller can maintain tissue populations near nominal levels even during a chronic apoptotic insult. The main effect of altered parameters is a change in the dynamics of initial response to the apoptosis challenge. 376

Figure 9.22 Simulated homeostatic renewal in 100 patients. Model parameters were sampled from a normal distribution with mean at the nominal parameter value and standard deviation of 10% of nominal values. Simulating multiple patients shows that the controller can maintain tissue populations near nominal levels even during a chronic apoptotic insult. The large variability in patient parameters, however, leads to poor controllability in many cases. 377

Figure B.1 Procedure for calculating estimates of correlation based on (A) the standard method and (B) the segmentation method (with k=3 segments). Gene expression values are based on the –ΔΔCT method; 12 animals were used over a time series of 6 hours post stimulus, with 3 biological replicates at each time point. 433

Figure B.2 Correlation estimates between sine waves phase-shifted between 1-180˚ using the standard method and the segmentation method are equal in the absence of noise. 434

Figure B.3 (A) Gene expression with white noise introduced around the mean expression level, (B) two genes with a correlation = 1 prior to the introduction of noise, (C) correlation of 0, (D) correlation of -1, (E) scatterplot of correlation estimate comparing the standard method and segmentation method with 12 simulated animals and 3 segments, (F) the same correlation comparison with 120 simulated animals and 30 segments. 438

Figure B.4 Estimates of correlation for the standard method and segmentation method when (A-B) true correlation = 1, (C-D) true correlation = 0, and (E-F) true correlation = -1. 439

ABSTRACT

Liver resection is used in the clinic for treatment of hepatocellular carcinoma and for live liver transplant. In otherwise healthy patients following resection, the liver initiates a program of regeneration that involves multiple cell types interacting across multiple length and time scales. As early as 30 seconds after injury, signaling cascades become active within the liver. Dynamic molecular changes continue for approximately 1 week following injury, restoring liver mass to the pre-injury levels. The dynamics of several molecular mediators of this process has been investigated previously to identify transient activation of inflammatory molecules for a few hours and a sustained activation of growth factors over several days. Yet much remains to be understood as to how the regulation of multiple molecular factors is coordinated to control liver repair mechanisms. Additionally, cell-types within the liver can each take on multiple distinguishable phenotypes either contributing to or inhibiting repair. The contributions of these phenotypes to liver repair and disease progression are just beginning to be appreciated.

In contrast to regeneration in otherwise healthy patients, patients requiring resection or transplant likely have multiple comorbidities impairing regeneration. These comorbidities include chronic diseases and common pharmaceutical and recreational drug use (including alcohol abuse). Despite extensive study, the molecular mechanisms governing comorbidity-impaired liver regeneration remain incompletely

understood. As a result, there are no robust predictors of liver regenerative capacity in patients undergoing liver resection.

In light of these complexities, we have taken a systems biology approach to understanding liver regeneration in health and disease. We measured the dynamics of genome-wide transcription factor binding of an early, pro-inflammatory responder in liver regeneration (NF-κB) to identify broad features of the pro-inflammatory regeneration response in rat livers. We then investigated a broad range of cytokines, chemokines, and growth factors that respond to pro-inflammatory signals in several cases of successful regeneration to identify possible changes to the liver microenvironment during regeneration. These analyses implicated non-parenchymal cells as important mediators of the successful regeneration response (total mass recovery).

We therefore developed a computational model of liver regeneration that takes into account molecular regulation in hepatocytes contributing to regeneration and course-grained estimations of non-parenchymal cell activation. Using this model, we predicted experimental liver regeneration profiles across multiple species including mice, rats, and humans by tuning a single parameter empirically related to body mass. Additionally, we predicted the molecular mechanisms governing impaired liver regeneration in multiple chronic disease conditions impairing regeneration, including alcoholic steatohepatitis. Our results implicated non-parenchymal cells as important regulators of the dynamics of regeneration in addition to overall mass recovery.

We extended our computational model to synthesize the intrinsically multi-scale nature of liver regeneration by simulating connections between physiological-scale dynamics, transcriptional phenotypes of non-parenchymal cells, and molecular signaling networks. Model analysis showed that shifting balances between populations of non-parenchymal cell activation phenotypes was sufficient to alter regeneration dynamics and overall tissue recovery following partial hepatectomy. As a perturbation to regeneration phenotype, we simulated alcohol-mediated suppression of liver regeneration by fitting our model to experimental data of liver recovery following chronic alcohol consumption and partial hepatectomy. Based on the model simulations, we predict that chronic alcohol consumption acts at a cellular-scale by shifting Kupffer cells from an M1 phenotype to an M2 phenotype following partial hepatectomy and by shifting hepatic stellate cells from a pro-regenerative phenotype to an anti-proliferative phenotype. At a molecular-scale, these changes in cell phenotypes are paralleled by dynamic increases in anti-inflammatory cytokine production and high levels of the anti-regenerative molecules such as fibrous collagens and TGFβ.

We tested these predictions using high-throughput measurements following partial hepatectomy in ethanol-fed rats and controls. We used laser capture microdissection to collect individual hepatic stellate cells from the livers of chronic ethanol-fed animals and controls before and after hepatectomy. We then used a high-throughput gene expression platform to quantify mRNA levels of ~100 genes across these individual cells and used multivariate statistics to identify clusters of hepatic stellate cell transcriptional phenotypes. Our experimental results indicate that multiple

transcriptional phenotypes of hepatic stellate cells arise following partial hepatectomy and ethanol exposure, consistent with model predictions. Furthermore, our results suggest that one of the main effects of chronic ethanol consumption is to imbalance hepatic stellate cell populations prior to resection, leading to altered extracellular matrix composition, increased matrix stiffness, and decreased intercalation with pro-regenerative molecules.

We then used similar modeling techniques to simulate homeostatic renewal of hepatocytes in the non-regenerating liver. Our results point to the existence of strong feedbacks within hepatocyte populations governing homeostatic renewal and an external control of hepatocyte renewal by a non-parenchymal cell network that involves multiple cell types and matrix property modulation. Model simulations were able to capture recently observed behaviors of tissue renewal involving stem cells following induced senescence of hepatocytes.

Taken together, these results provide novel insights into how molecular regulation during liver regeneration influences multiple scales to regulate non-parenchymal cell transcriptional phenotype and overall tissue mass recovery.

Chapter 1

INTRODUCTION

1.1 Therapeutic Significance of Liver Regeneration

The liver is made up of multiple cell types interacting within a highly structured tissue architecture. It is one of the largest organs in the body and performs a diverse range of functions, including xenobiotic metabolism, glucose storage, bile production, and bilirubin removal. All of the blood leaving the stomach and intestines passes through the liver, making it the first line of defense for metabolizing toxic compounds such as ethanol, which can lead to damage to multiple organs. Because of the often toxic environment in which the liver is situated, the liver has an ability unique among mammalian organs to augment homeostatic tissue renewal with a coordinated regeneration response to tissue damage. In response to toxic or mechanical damage of up to 70-80% of its total mass, the liver can enter a program of hepatocyte hypertrophy and hyperplasia whereby the original mass of the liver is restored. This regenerative ability serves as a valuable tool for physicians in the clinic and researchers in the laboratory.

Liver regeneration following surgical resection can be used to treat several liver diseases (hepatocellular carcinoma, metastatic cancer, etc. (Doci et al, 1991;Ringe et al, 1991)), as well as to facilitate a live donor transplant, which normally stimulates regeneration of the remnant liver in the donor and the transplanted liver in the recipient (Tanemura et al, 2012). One of the major complications of liver resection is post-operative liver failure where the liver fails to return to necessary

functional capacity, which has been shown to occur in rates of as high as 30% of patients (Dan et al, 2012). Despite this relatively high rate of post-operative liver failure, death following resection appears to be fairly uncommon, occurring in approximately only 3% of patients (Jaeck et al, 2004). Despite decades of study, an increasingly thorough understanding of the mechanisms involved in regeneration, and identification of risk factors associated with an increased risk of post-operative liver failure, however, there remains a lack of pre-operative predictors of post-operative liver failure or death (Kauffmann & Fong, 2014). One reason for this lack of pre-operative predictors is a failure to integrate current knowledge about liver regeneration into a model framework that would allow for understanding what factors predispose a liver to regeneration or failure.

1.2 Features of Liver Regeneration

In the laboratory, liver regeneration also provides a useful metric to assess dynamic liver function. One of the most common methods to induce liver regeneration, the 70% partial hepatectomy (PHx), relies on resection of the left lateral and medial lobes of the liver in rats or mice (~70% of overall tissue mass). A surgical resection allows for a precise estimate of the timing of the initial liver damage and does not lead to any toxic or mechanical damage to the remaining portion of the liver, thus removing the effects of cell necrosis, neutrophil infiltration, etc. Following resection in lab animals, the liver initiates a coordinated response of multiple cell types to replace liver mass. This response can be loosely categorized into five phases of liver regeneration based on the events occurring over predictable time ranges: immediate response, priming, hepatocyte replication, non-parenchymal cell

replication, and termination. Table 1.1 shows a summary of the approximate timing of each phase and the events occurring within for rats.

Table 1.1: Timing of liver regeneration can be divided into phases

Timing of Response In Rats	**Regulatory Events**
Immediate Response Phase (< 30 min)	Hepatocytes release ATP Calcium signaling occurs WNT signaling occurs
Priming Phase (0 - 6 hrs)	LPS levels increase in the liver Non-parenchymal cells produce cytokines and chemokines NF-kB activated in hepatocytes and non-parenchymal cells C/EBP-β to C/EBP-α ratio increases JAK-STAT signaling pathway activated in hepatocytes Hepatocytes begin to show signs of G0 to G1 transition
Hepatocyte Replication Phase (12 - 48 hrs)	Non-parenchymal cells produce MMPs, cleaving matrix Growth factors (HGF, EGF, FGF, et al.) are liberated from cleaved matrix Additional growth factors are synthesized by non-parenchymal cells New, basement-membrane matrix is deposited to facilitate proliferation Hepatocytes synchronously enter the cell cycle
Non-Parenchymal Cell Replication Phase (48 - 72 hrs)	VEGF signaling increases Angiogenesis occurs Non-parenchymal cells enter the cell cycle
Termination Phase (72hrs - ~1 week)	Matrix accumulates back to baseline levels Non-parenchymal cell activation decreases C/EBP-β to C/EBP-α ratio decreases to baseline levels Hepatocytes exit the cell cycle and return to G0 Liver mass may overshoot baseline, followed by a wave of hepatocyte apoptosis

1.3 Effects of Chronic Diseases on Regeneration Capacity

Although liver regeneration is tightly coordinated in healthy animals and plays an important role treating liver diseases in patients, many chronic diseases also impair regeneration. Unfortunately, these regeneration-impairing diseases are common comorbidities associated with hepatocellular carcinoma and other diseases treatable by resection (Montalto et al, 2002). The end stage of chronic liver disease, cirrhosis, delays the initiation of regeneration and suppresses overall recovery in laboratory animals (Kaibori et al, 1997). In human patients, fibrosis and cirrhosis lead to higher risk of death following surgical resection (Poon & Fan, 2004). Even in the early stages of liver disease – heptosteatosis or fatty liver – the regenerative potential of the liver can be reduced greatly (DeAngelis et al, 2005). Surgeons, therefore, tend to abstain from transplanting livers with a significant degree of fat accumulation (McCormack et al, 2011). Although research has shown that chronic diseases can impair regeneration, even the supposedly healthy livers of some patients do not regenerate for unknown reasons, as evidenced by a small number of resection patients who die post-resection without any pre-operative complications (Virani et al, 2007). Because of this apparent stochasticity in regenerative capacity, surgeons considering resection for a patient have few clinically-proven pre-operative predictors of liver regeneration amount following resection. Some pre-resection metrics associated with morbidity following liver resection include male gender, previous cardiac surgery, and increased bilirubin (Virani et al, 2007). Post-resection, the "50-50" criteria has been proposed to predict liver failure and death following resection. This metric classifies patients at day 5 post-resection to have high predicted mortality if prothrombin time is less than 50% and if serum bilirubin is greater than 50 μmo/L. Even though this metric has a high specificity (98.5%) and high accuracy (97.7%), it suffers from a low selectivity

(69.6%) (Balzan et al, 2005). This metrics and others like it do not indicate how to prevent the liver from progressing towards failure post-resection, although they are useful for the early detection of emerging liver failure.

One potential chronic disease that can inhibit regeneration is alcoholic liver disease (ALD), which is caused by heavy drinking over a long period of time (O'shea et al, 2010). The early stage of the disease (alcoholic steatotosis) is characterized by an enlarged liver and accumulation of lipid droplets, and may be associated with worsening liver metabolic function (O'shea et al, 2010). A tissue biopsy can show steatosis (Figure 1.1A) but only a patient history of drinking in the absence of other explanations for liver damage can result in a differential diagnosis of alcoholic steatohepatitis. Later stages of the disease are characterized by increasing hepatocyte death, accumulation of scar tissue, and worsening liver function. These events start less severe in fibrosis (Figure 1.1B) but worsen in cirrhosis (Figure 1.1C). Patients progressing though the stages of ALD do not all reach cirrhosis. A large portion of patients (~60%) do not progress beyond alcoholic steatosis although they continue to drink for the rest of their lives. A smaller portion of patients progresses to alcoholic fibrosis (~40%). And a still smaller proportion of patients progresses all the way to cirrhosis (O'shea et al, 2010). In spite of this low progression rate, liver disease is still one of the leading causes of death in the US; liver disease was the 12th most common cause of death in the US in 2013 (Xu et al, 2016).

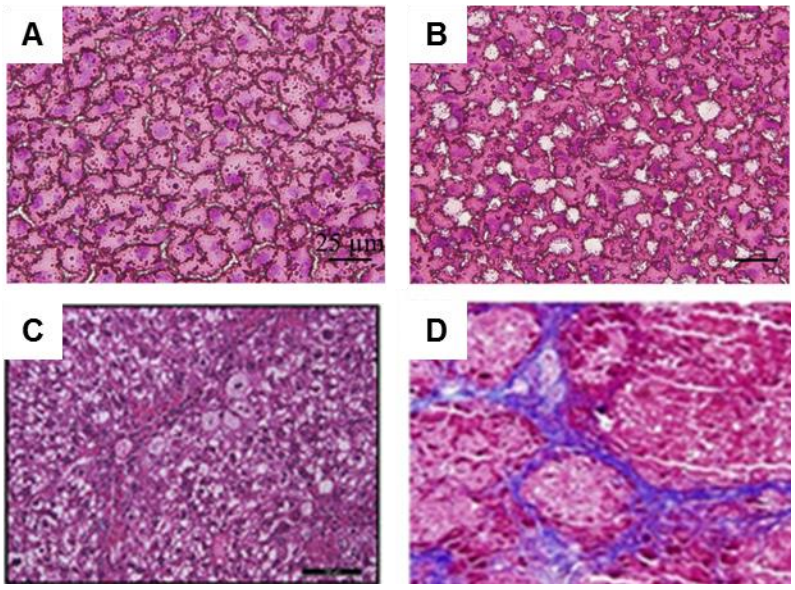

Figure 1.1 Pathological features of progressing ALD shown through H&E staining. (A) Control rat liver (Liu et al, 2011). (A) Alcoholic steatosis in the rat liver shows lipid droplet accumulation and may be accompanied by hepatomegaly (Liu et al, 2011). (B) Alcoholic fibrosis in the mouse liver causes an increase in hepatocyte apoptosis and areas of increasing scar tissue deposition (Liu et al, 2015). (C) Alcoholic cirrhosis in the rat is characterized by "chicken-wire" scarring. Note: This image shows CCL4-induced cirrhosis as opposed to alcoholic cirrhosis (Bahk et al, 2011). Until recently, cirrhosis was thought to be unresolvable even if the underlying insult was removed. This figure was adapted from the references cited in this caption.

Even at the early stages of ALD, prior to showing gross pathological features, liver regeneration is inhibited. In rats fed an ethanol diet with 36% of calories from ethanol for 5 weeks, regeneration is suppressed at 24 hrs and 48 hrs post-PHx (Yang et al, 1998b). This suppression occurs even though the diet is not maintained long enough for gross pathological features beyond macroscopic steatosis (fatty liver) to develop in the liver (Apte et al, 2004). Even a much longer amount of time on this diet (18 weeks) results in only mild steatosis in rats (Figure 1.2) (Ronis et al, 2011).

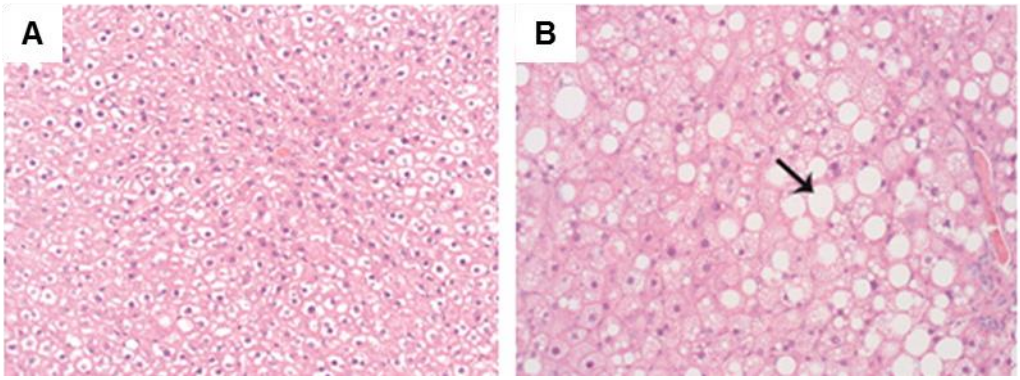

Figure 1.2 The effects of an 18-week ethanol feeding diet on liver pathology. (A) Liver sections of control rats. (B) Liver sections of rats fed an ethanol diet with 36% of calories from ethanol for 18 weeks. Arrow indicates fatty accumulation. This figure was adapted from (Ronis et al, 2011).

Some of the molecular and cellular events leading to suppressed regeneration due to ethanol-adaptation have been identified. For example, ethanol adaptation leads to an increased cytokine response post-PHx (Yang et al, 1998b), a change in binding patterns of the transcription factor NF-κB during the priming phase (Kuttippurathu et al, 2016a), and large changes to the expression levels of many genes during the course of regeneration (Kuttippurathu et al, 2016c). There remains, however, much that is unknown about how chronic ethanol abuse leads to suppressed regeneration. One reason is that despite clinical relevance and much study, there is still much to be learned about how molecular regulation and cellular interactions govern liver regeneration, how diseases suppress the liver's innate repair ability, and how to rescue livers adapted to chronic disease.

1.4 Thesis Overview

This thesis presents a combined computational modeling and high-throughput data analytics approach to identify how molecular and cellular coordination regulates

liver regeneration and how regeneration can be dysregulated by chronic disease, using ethanol adaptation as an example.

Chapter 2 describes our work investigating the molecular regulation of liver regeneration in laboratory rats.

Chapter 3 describes our work using an existing computational model of liver regeneration to predict the effects of a genetic knockout of the gene Adiponectin on regenerative capacity in mice.

Chapter 4 describes our experimental work investigating molecular regulation of liver regeneration in wild-type and Adiponectin knockout mice.

Chapter 5 describes our work using high-throughput ELISA to investigate the differences in regulation of priming between Adiponectin knockout mice and controls in an unbiased manner.

Chapter 6 describes our work extending the previously-published computational model of regeneration to fit experimental data and explore regeneration regulation in multiple disease states and species.

Chapter 7 describes our work developing a computational model based on our previous model extension to predict the effects of non-parenchymal cell transcriptional phenotypes on regeneration dynamics.

Chapter 8 describes our experimental testing of our model predictions in ethanol-fed and control rats.

Chapter 9 describes our work using computational models to investigate tissue homeostasis in the context of cell networks and population balances.

Chapter 10 describes our conclusion based on our research, the implications of the work described within this dissertation, and potential future work that could extend our findings.

Chapter 2

NF-κB BINDING DURING THE PRIMING PHASE OF LIVER REGENERATION IN RATS

This chapter was adapted from **Cook, D. J.**, Patra, B., Kuttippurathu, L., Hoek, J. B., & Vadigepalli, R. (2015). A novel, dynamic pattern-based analysis of NF-κB binding during the priming phase of liver regeneration reveals switch-like functional regulation of target genes. *Frontiers in physiology*, *6*. All experimental work featured in this chapter was performed by B. Patra.

2.1 Introduction

Liver resection followed by regeneration is used in the clinic for a variety of conditions, including treatment of hepatocellular carcinoma and live liver transplant. Despite its clinical relevance and decades of study, however, the molecular mechanisms governing liver regeneration following resection remain incompletely characterized. In the laboratory, 70% partial hepatectomy (PHx) of rodents has become a standard model to study liver resection and regulation. PHx provides an ideal model to study the liver's regenerative response because the regenerative stimulus is precisely defined and cell proliferation can be studied without the influence of parenchymal injury or excessive inflammatory cell infiltration.

Liver regeneration following partial resection typically follows a well-documented set of steps involving hepatocytes and non-parenchymal cells, details of which can be found in chapter 1, and occurs in three phases: priming, replication, and termination. Early in the priming phase, the liver initiates an activation of the innate

immune response, which is predominantly driven by cytokines derived from Kupffer cells but may be complimented by production of cytokines and other mediators by sinusoidal endothelial cells, hepatic stellate cells, parenchymal cells, and other resident cell types (Michalopoulos, 2007b;Taub, 2004c). Among the early intrahepatic intercellular signals detectable following PHx is an increase in pro-inflammatory cytokines, including TNF-α (Michalopoulos, 2007b). This early cytokine signaling induces a response in hepatocytes (and other hepatic cells) that includes NF-κB signaling and downstream transcription of NF-κB target genes (Juskeviciute et al, 2008). These NF-κB target genes have been implicated in priming hepatocytes to enter the cell cycle (Michalopoulos, 2007b). Previous studies of liver regeneration in rats have shown that an increase in NF-κB binding activity was detectable in whole-tissue extracts as early as 30 min following carbon tetrachloride (CCl_4) injection, peaked at approximately 1 hr post injection, and gradually decreased activity until beyond 48 hrs post injection, suggesting that NF-κB acts predominantly during the priming phase of liver regeneration (Salazar-Montes et al, 2006). Additionally, after 70% PHx in rats, NF-κB activation was evident within 15 minutes of surgery, peaked at 1 hour post-PHx, remained elevated at 2 hours post-PHx, and decreased to near baseline levels at 4 hours post-PHx before increasing again at 6 hours post-PHx, suggesting that NF-κB may play several roles during early priming, late priming, and early G1 phase of the cell cycle, possibly representing activation in different cell types in the liver (Juskeviciute et al, 2008).

When NF-κB signaling is disrupted, the regenerative ability of the liver is impaired. Although genetically deleting the p50 subunit of NF-κB caused no deficiencies in liver regeneration following CCl_4 injection, there was a compensation

of overall NF-κB activity by increased levels of the p65 subunit (DeAngelis et al, 2001). We speculate that following deletion of the p50 subunit, the p65 subunit may bind the same genes normally bound by the p50 subunit. Similarly, inactivation of the p65 subunit through a conditional knockout also did not impair liver regeneration (Ringelhan et al, 2012). In this case, NF-κB p50 may have compensated for the depleted p65 subunit. These results suggest that, although the NF-κB p65/p50 dimer is known to regulate immune response, there may be a compensatory effect if only one of the NF-κB p50 and p65 subunits is available during liver repair (Hayden & Ghosh, 2004). As these studies suggest, when all NF-κB signaling was suppressed by inducing IkBa (an inhibitor of NF-κB), hepatocyte proliferation following PHx was decreased resulting in impaired liver regeneration (Yang et al, 2005). The authors of this study suggested that the impaired regeneration was mediated primarily by decreased Kupffer cell activation and IL-6 signaling. These results underscore the importance of understanding the binding of each NF-κB isoform. Our present study focuses on identifying the dynamic binding targets of NF-κB p65 during liver regeneration.

Despite its important role governing liver regeneration, the targets of NF-κB during liver regeneration have not been adequately characterized. In this study we report a genome-wide analysis of NF-κB binding during the priming phase of liver regeneration. We used chromatin immunoprecipitation followed by microarray analysis (ChIP-chip) to identify how NF-κB dynamically binds to genes following PHx in rats. We then related this binding to previously published profiles of gene expression in hepatectomized rats to identify how the dynamic profiles of NF-κB binding relates to regulation of gene expression. Our study demonstrates that NF-κB

binding can be classified into dynamic binding switches. Furthermore, these switches appear to dynamically regulate functional pathways associated with liver regeneration. Therefore, NF-κB activation should be interpreted in the context of its dynamic functional binding during liver regeneration.

2.2 Methods

2.2.1 Animals

All animal studies were approved by the Institutional Animal Care and Use Committee (IACUC) at Thomas Jefferson University. Jefferson's IACUC is accredited by the Association for Assessment and Accreditation of Laboratory Animal Care and experiments were designed using the Guide for the Care and Use of Laboratory Animals.

Adult (8-10 week old) Sprague-Dawley rats were given ad-libitum access to food (Chow) and water. When their weight reached 275-350 g, they were anesthetized and subjected to 70% PHx by surgical removal of medial and left lateral lobes as per standard procedure (Higgins & Anderson, 1931;Juskeviciute et al, 2008). The medial and left lateral lobes were flash frozen using liquid nitrogen-cooled aluminum clamps to serve as within-animal, 0 hour controls. At 1 hour, 2 hours, 4 hours, and 6 hours post-PHx, rats were again anesthetized and the remnant liver tissue was excised and flash-frozen as before. Following excision of the remaining liver mass, rats were sacrificed by cervical dislocation. Liver tissue from 0h, 1h, 2h, 4h, and 6h post-PHx was subjected to chromatin immunoprecipitation. Immunoprecipitated samples (ChIP) from 0h, 1h, and 6h post-PHx were used to identify genome-wide NF-κB binding sites

using microarrays (ChIP-chip). Immunoprecipitated samples from 0h, 1h, 2h, 4h, and 6h post-PHx were used for validation and extension of ChIP-chip results using qPCR.

2.2.2 Chromatin Immunoprecipitation (ChIP)

Chromatin immunoprecipitation (ChIP) assays were performed using total liver tissue to map the *in vivo* distribution of NF-κB/DNA interactions using a Magna ChIP G Chromatin Immunoprecipitation kit (Merck Millipore) according to manufacturer's instructions. Approximately 50 µg minced liver tissue was fixed for 10 minutes with 1% formaldehyde, which crosslinks DNA and chromatin binding proteins to ensure co-immunoprecipitation. Glycine (1x in accordance with the EMD Millipore protocol) was then added to quench unreacted formaldehyde. Cells were lysed and chromatin was sheared by sonication to generate fragments of 200-1000 bp (40 min. of sonication using a 30s on, 30s off cycle). Fragments bound by NF-κB were immunoprecipitated using a ChIP-grade NF-κB antibody (Cat#ab7970, Rabbit polyclonal NF-κB p65 antibody and negative control IgG antibody from Abcam Inc, Cambridge, MA) in combination with Protein G conjugated solid support matrix magnetic beads enriched for the antibody of interest using electrophoresis on a 1% agarose gel. This NF-κB antibody has been employed extensively in previous studies to specifically detect NF-κB proteins in Western blots and immunohistochemistry assays, as well as for chromatin immunoprecipitation assays (Burdelya et al, 2013;Kasama et al, 2014;Luo et al, 2014). Negative controls in the absence of the primary antibody showed negligible signal intensity (Figure 2.1).

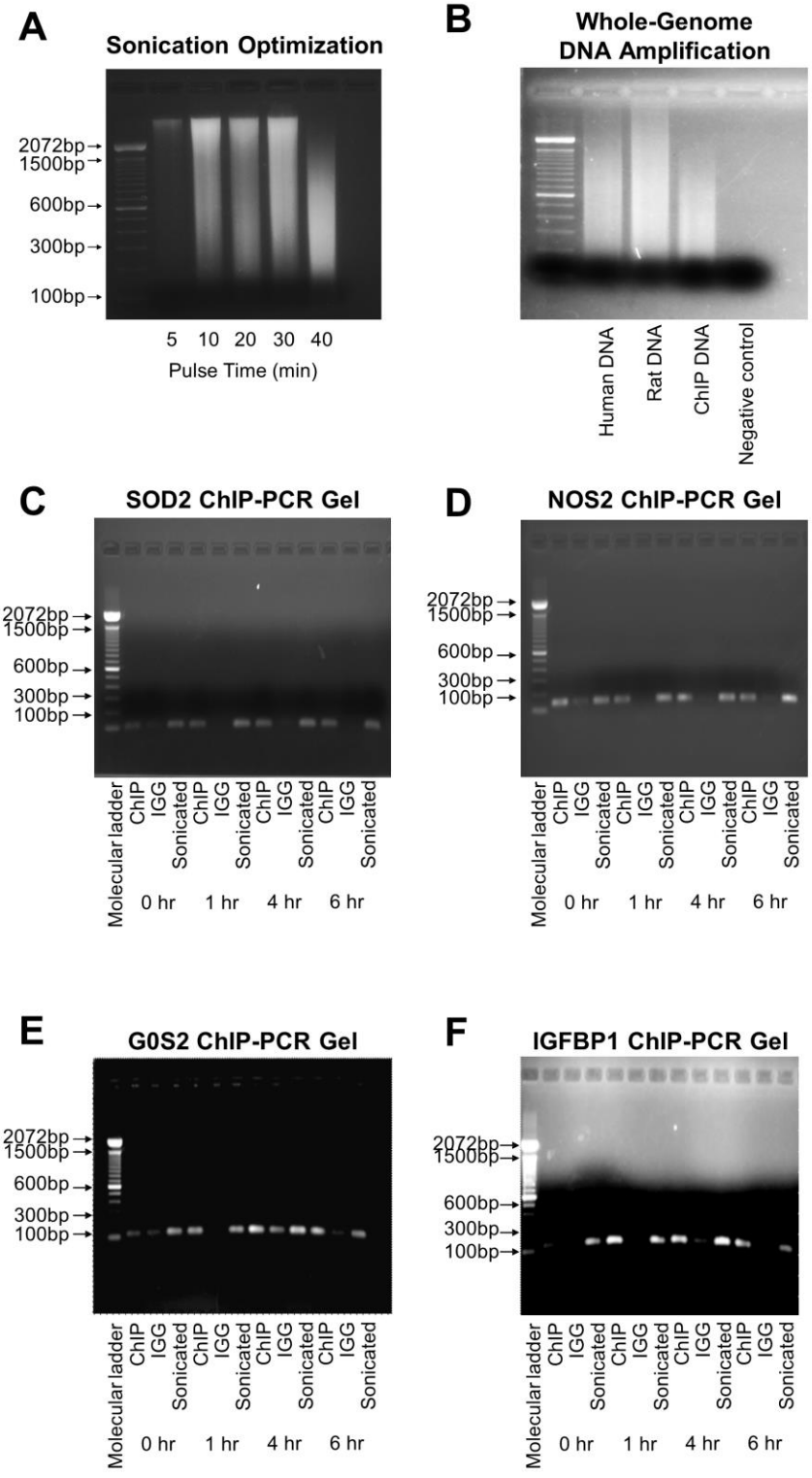
A
Sonication Optimization
2072bp
1500bp
600bp
300bp
100bp
5 10 20 30 40
Pulse Time (min)
B
Whole-Genome
DNA Amplification
Human DNA
Rat DNA
ChIP DNA
Negative control
C
SOD2 ChIP-PCR Gel
2072bp
1500bp
600bp
300bp
100bp
Molecular ladder
ChIP
IGG
Sonicated
0 hr
1 hr
4 hr
6 hr
D
NOS2 ChIP-PCR Gel
E
G0S2 ChIP-PCR Gel
F
IGFBP1 ChIP-PCR Gel

Figure 2.1 Quality control for NF-κB ChIP assay for measuring NF-κB binding post-PHx. (A) Sonication optimization for the ChIP procedure. (B) The NF-κB p65 antibody used is specific for NF-κB binding. (C) Representative PCR gel showing ChIP of NF-κB on the SOD2 gene from 0-6 hours post-PHx. (D) Representative PCR gel showing ChIP of NF-κB on the NOS2 gene from 0-6 hours post-PHx. (C) Representative PCR gel showing ChIP of NF-κB on the G0S2 gene from 0-6 hours post-PHx. (C) Representative PCR gel showing ChIP of NF-κB on the IGFBP1 gene from 0-6 hours post-PHx. ChIP = NF-κB antibody-treated, IGG = negative control, Sonicated = positive control.

2.2.3 Identification of NF-κB Binding Sites using Microarrays (ChIP-chip)

Purified ChIP DNA was amplified using the GenomePlex Complete Whole Genome Amplification (WGA) kit from Sigma that allows for nearly 500-fold amplification of genomic DNA using OmniPlex Library molecules flanked by universal priming sites. Genome-wide promoter enrichment was measured using the Roche Nimblegen Promoter array platform, which has 720,000 probes (Rat ChIP-chip 3x720K RefSeq Promoter Arrays - 3 identical arrays per glass slide with 72,000 probes per array, Roche NimbleGen, Inc., 504 South Rosa Road, Madison, WI). Experimental ChIP and total DNA samples are labeled using 9-mer primers that have Cy3 and Cy5 dyes attached and Klenow added. The labeled experimental ChIP and total DNA samples were co-hybridized to the array for 16 - 20 hours at 420ºC, washed, and scanned using an Agilent scanner (Agilent Technologies) following manufacturer instructions.

Array images were used for data extraction as paired files; genomic feature format files were then produced for analysis of scaled log2-ratio data. The intensity ratio of immunopreciptated to total DNA (not taken through immunoprecipitation steps) was calculated at each genomic position to identify regions where increased signal (i.e. DNA fragment enrichment) was observed relative to the control sample.

Peak regions identified as statistically significant binding sites were generated from the scaled log2-ratio data, and peaks were mapped to the nearest gene's transcription start site.

Roche NimbleGen arrays were used because their proprietary, light-mediated synthesis process produces high-density microarrays of long oligonucleotide probes (50-75mer). These long oligo arrays, when used in combination with high-stringency hybridization protocols, produce results of unparalleled sensitivity and specificity. In addition, because Roche NimbleGen performs ChIP-chip experiments using a two-color protocol, where control and test samples are co-hybridized to the same array, inter-array variation is eliminated. As a result, NimbleGen ChIP-chip service can readily detect enrichment as low as two-fold of the target binding site in a ChIP sample.

Data generated from these experiments as well as processed data used to draw the conclusions of this study were deposited in the Gene Expression Omnibus repository and are publically available at www.geo.ncbi.org.

2.2.4 Genome-wide Mapping and Peak Detection: Identification of Binding Sites

The possible binding regimes (peaks) that correspond to the binding targets were detected if 4 or more probes showed a signal above the cutoff value ranging from 90% to 15% using a 500bp sliding window. Cut-off values were set as a fraction of the hypothetical maximum signal (mean signal plus six standard deviations). An empirical false discovery rate (FDR) was calculated for each peak using a bootstrapping method, which randomized the probe signals 20 times. The calculated FDR is an approximation of the probability of a false positive. To minimize false positives while

maximizing NF-κB binding signal, an FDR cutoff of 0.05 was used for all analyses (See Figure 2.2). Any FDR cutoff higher than 0.05 would have led to an exponentially increased number of false positive NF-κB bound genes. Although steps were taken to limit false positives, some of these binding sites identified during peak detection might mediate higher-order genomic interactions and influence chromosome structural modifications.

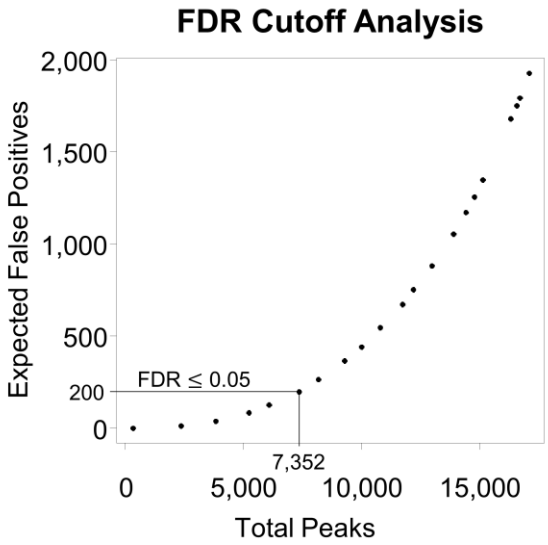

Figure 2.2 Analysis of optimum FDR to maximize binding peaks identified and minimize false positives. Maximum FDR cutoff was varied from 0 to 0.2 in increments of 0.01. An FDR cutoff at 0.05 allows for identification of a large number of NF-κB binding peaks while minimizing the expected number of false positives.

2.2.5 Peak Annotation

Peaks were annotated with candidate target genes with the assumption that the distance between a center of binding peak and the transcription start site (TSS) of the

gene is shorter than a threshold cutoff. We defined these "gene regions" as spanning from 5kb upstream of the TSS to 1.5 kb downstream of the end of transcription. The peak files were annotated with Ensembl version 5.0 (Rnor_5.0) transcript genes using a 5000 base pair cutoff distance from the TSS using the Chip Peak Anno Bioconductor package in R (Gentleman et al, 2004b;R Core Team, 2014;Zhu et al, 2010). The peaks were then annotated with detailed characteristic genomic features: peak region location, gene annotation of nearest transcript (intron, exon, intragenic, etc.), chromosome, start and end of genes, nearest transcripts and transcript boundaries, distance from TSS, RefSeq IDs, Entrez IDs, TSS, trophoblast-specific element (TSE) and average phastcon scores obtained.

2.2.6 Dynamic Pattern Analysis

We used a dynamic pattern-based strategy to analyze the dynamic NF-κB binding post-PHx. We first discretized NF-κB binding by identifying genes as bound (1) or unbound (0) at each time point post-PHx. To be identified as bound, NF-κB binding had to be seen in 2 out of 3 biological replicates at a time point (FDR $\leq$ 0.05). Additionally, we analyzed how our choice of FDR cutoff would influence our pattern-based analysis and found that choice of FDR cutoff has minimal effect on the fraction of NF-κB bound genes in each of several binding pattern (Figure 2.3).

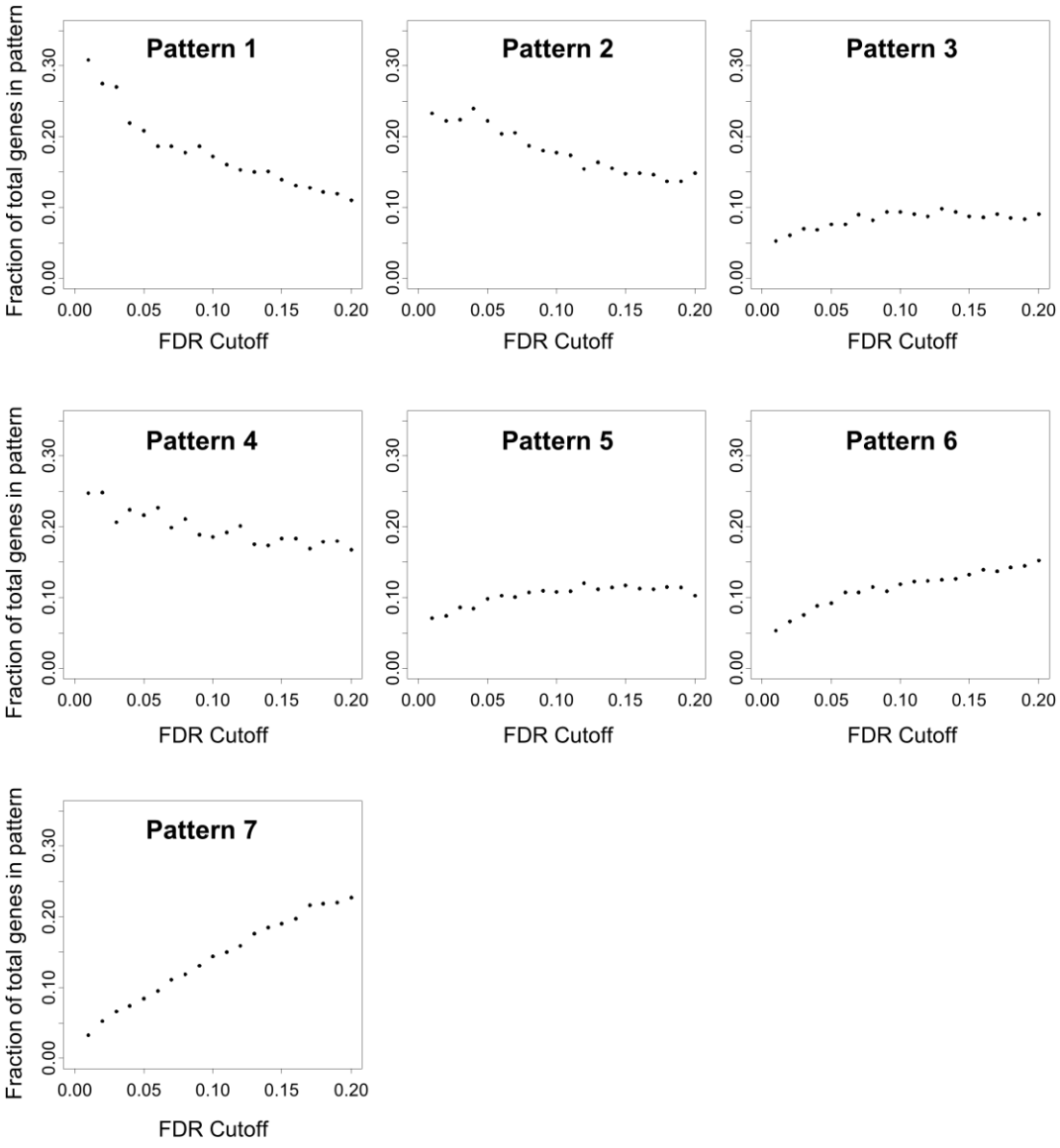

Figure 2.3 Analysis of how FDR affects relative fraction of genes in each binding pattern. Selecting an FDR cutoff between 0.01 and 0.20 does not dramatically change the relative fractions of genes in binding patterns 2-6. Increasing the FDR causes a decrease in the fraction of genes bound in pattern 1 and an increase in the fraction of genes bound in patter 7; however, at an FDR cutoff near 0.05, the fractions of genes in patterns 1 and 7 are relatively stable.

We found that setting the FDR cutoff too low appeared to remove useful pathways from the analysis, but setting the cutoff to high appeared to include pathways that may represent data from false positives (Tables 2.1-3). An FDR cutoff of 0.05 struck a balance between these extremes. Because discretized NF-κB binding has 2 distinct states (0, unbound; 1, bound) and we analyzed 3 time points, we generated 8 (2^3) dynamic binding patterns where NF-κB was identified as bound or unbound at each time: 000, 001, 010, 011, 100, 101, 110, 111. Each pattern was then described by both a binary string (i.e. 011) and its digital representation (i.e. Pattern 3). Because Pattern 0 contains no NF-κB bound genes, it was not considered in the subsequent analyses. Each gene bound by NF-κB was sorted into its binding pattern. Because the patterns are mutually exclusive, each binding pattern of each gene can match only one binding pattern.

Table 2.1 FDR cutoff pathway analysis for Pattern 1

FDR = 0.01	FDR = 0.02	FDR = 0.05	FDR = 0.10
Acute inflammatory response	Acute inflammatory response	Acute inflammatory response	Acute Inflammatory Response
Argenine and proline metabolism			
Carboxylic acid boisynthesic process			
Lipoprotein metabolic process	Lipoprotein metabolic process		
Mitochondrion	Mitochondrion	Mitochondrion	Mitochondrial Part
Negative regulation of apoptosis		Negative regulation of apoptosis	
Nucleosome			
Plasma			
Regulation of blood		Regulation of blood	

vessel size		vessel size	
Response to insulin stimulus	Response to insulin stimulus		
Ribosome	Ribosome	Ribosome	Ribosome
RNA Processing	RNA processing	RNA processing	
rRNA processing	rRNA processing	rRNA binding	
Triglyceride metabolic process			
Urea cycle	Urea cycle		
	Benzene and derivative metabolic process		
	Glucuronate metabolic processes		
	Peptidase inhibitor activity		
	Protein stabilization		
	Regulation of fibroblast proliferation		
	Ribosome assembly		
		Positive regulation of apoptosis	Induction of Apoptosis
		Positive regulation of protein kinase cascade	
		Response to xenobiotic stimulus	
			Androgen receptor binding
			Glucosamine metabolic process
			GPI anchor biosynthesis
			JmjC
			Negative regulation of protein binding

Table 2.2 FDR cutoff pathway analysis for Pattern 5

FDR = 0.01	FDR = 0.02	FDR = 0.05	FDR = 0.10
Fibrinogen complex	Fibrinogen complex		
Gluconeogenesis			
Liver	Liver		
Positive regulation of adaptive immune response			
Protein catabolic process			
	Carboxylic acid binding	Carboxylic acid binding	Carboxylic acid binding
	Inflammatory response	Inflammatory response	
	Response to ethanol	Retinol metabolism	
		Olfactory receptor activity	Olfactory receptor activity
		Pheromone receptor activity	Pheromone receptor activity
			GPCR
			Monocarboxylic acid binding
			Phenylalanine metabolism
			Protein complex assembly

Table 2.3 FDR cutoff pathway analysis for Pattern 7

FDR = 0.01	FDR = 0.02	FDR = 0.05	FDR = 0.10
Lung development			
	Acute inflammatory response	Acute inflammatory response	Acute inflammatory response
	Transcription factor complex		Transcription factor TFIIA complex
		Protein complex activity	Protein complex assembly
		Antimicrobial	Defense response to bacteria
		Liver	Liver
		Protein catabolic process	Protein catabolic process
		Regulation of JAK-STAT cascade	
			ATPase, AAA-type, core
			Negative regulation of apoptosis
			Negative regulation of DNA binding
			Sensory Perception of Smell
			UBL Conjugation

2.2.7 Integration with Expression Data

Because transcription factor binding does not cause immediate changes in gene expression level, we looked for previously published gene expression data from time points after 1 and 6 hours post-PHx. Illumina RNA-seq gene expression data for the liver following PHx was downloaded from GEO (Accession: GSE54673) (Edgar et al, 2002). Normalized average gene expression for 0h (baseline), 4h (following 1h NF-κB binding), and 12h (following 6h NF-κB binding) post-PHx was reported in reads per

million mapped reads (RPKM) (Naugler, 2014). Fold change over baseline was calculated for each time point by subtracting the log-transformed 0h expression value from the corresponding datum at 4h or 12h post-PHx. Genes were identified as differentially expressed if they had a fold-change $\geq$ 2 above or below baseline (Figure 2.4).

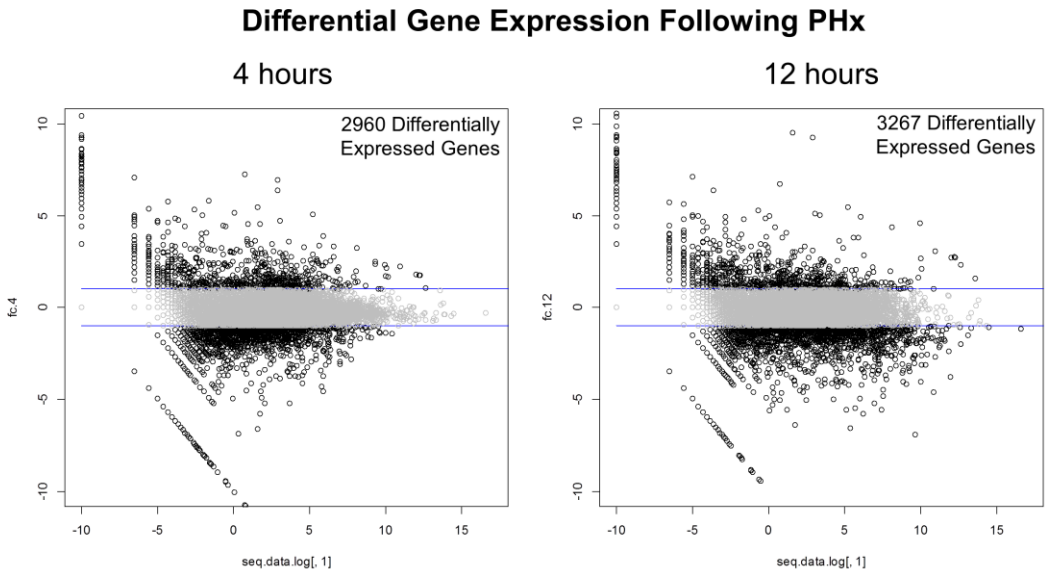

Figure 2.4 Differentially expressed genes (Fold change cutoff = 2) at 4 hours and 12 hours post-PHx.

Gene IDs from the expression data were converted to Refseq mRNA IDs using Clone/Gene ID Converter (Alibes et al, 2007). Each gene bound by NF-κB was then matched to a differentially expressed gene from the RNA-seq dataset using the RefSeq ID. Unless otherwise specified, non-differentially expressed genes were excluded from further analyses.

2.2.8 Pathway Analysis and Functional Association Identification

Functional associations between genes in each binding pattern were carried out using the online pathway analysis tool DAVID (Database for Annotation, Visualization and Integrated Discovery) (Huang et al, 2009). Because DAVID v6.7 provides a comprehensive set of functional annotation tools for investigators to understand biological meaning behind large list of genes, the DAVID software was used to identify enriched biological functions for each NF-κB binding pattern, particularly focused on gene ontology (GO) terms and KEGG pathways (Ashburner et al, 2000;Kanehisa & Goto, 2000;Kanehisa et al, 2014). A clustering p-value cutoff of 0.05 was used to filter the gene function list to only functions highly enriched in each pattern.

2.2.9 Motif Discovery

To find the binding sites enriched by NF-κB along with other transcription factors potentially associated with transcriptional regulation during liver regeneration, we used the de novo motif discovery program DME (Discriminating Motif Enumerator) using default parameters and a string length of 10 (Smith et al, 2005). DME is particularly well suited to our analysis because it is a de novo motif discovery program based on an enumerative algorithm that identifies optimal motifs from a discrete space of matrices with a specific lower bound on information content. It is therefore well suited for analyzing large datasets. This string length was chosen as 10 because it robustly identified NF-κB as a major binding motif in our data.

Peaks were filtered prior to using DME as follows. First, only peaks with an FDR $\leq$ 0.05 in at least 2 out of 3 biological replicates were considered in the analysis. Next, the peaks with the strongest peak scores were chosen for final analysis. Scree

plots of peak score were used to identify appropriate peak score cutoffs for each time point (Figure 2.5).

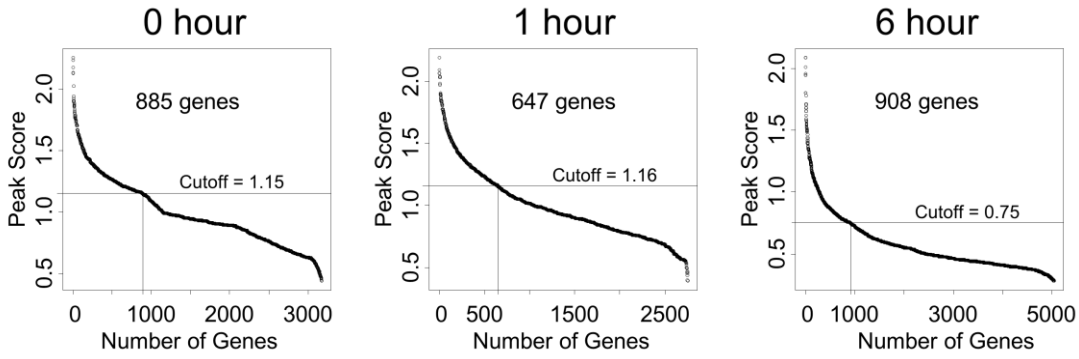

Figure 2.5 Scree plots of peak scores for NF-κB binding at 0h, 1h, and 6h post-PHx. At each time point, a cutoff value for peak score was chosen based on when a "knee" occurred in the scree plot and maintaining 500-1,000 NF-κB peaks.

Once de novo motifs were found, associated transcription factors were predicted by scanning the motifs against the TRANSFAC databases containing documented transcription factor binding sites using the clustering program STAMP with default parameters matching to TRANSFAC v11.3 (Mahony & Benos, 2007;Matys et al, 2006). Any motifs co-occurring with the NF-κB binding motif were considered to be potential co-regulators with NF-κB of a particular set of genes.

2.2.10 Quantitative PCR Validation of NF-κB Binding

Quantitative PCR primer sets for 21 genes across all 8 NF-κB binding patterns were designed using TRANSFAC, a Biobase software (Matys et al, 2006). Quantitative analysis of promoter binding was performed through real-time PCR on an

ABI Prism 7000 (Applied Biosystems, Foster City, CA) according to manufacturer's instructions and using iTaq SYBR Green super mix from Bio-rad (Bio-Rad Laboratories, Inc., 2000 Alfred Nobel Drive, Herles, CA 94547). Primer sequences can be found in Table 2.4.

Table 2.4 Primer Sequences

Gene Symbol	Foreword Sequence	Reverse Sequence
ALDH1A1	GTC TCG TGT GTG GGA CAT T	AAG GAC AGT GGC AAG GAG TG
ATF4	CTC TGC CTT GCT CTC CAA TTA	CCG GGG TAA TGA GCA GTA AA
BTG2	GAG CTC TGC TTG TGT CTG TCC	GCT CAG GGG AAA CAG AAC T
CEBPB	AGG AAA TCT TGG AGG GCT TC	CAG TGC TCC CTA TTC CCT CA
CYP4B1	TGT TAT TAC CTT TCC CGG TTT CCA AGC A	TTG GTC CTG CCA AGA CTG AAC CC
DSTN	TAG GGT GAC TCA TCT CAC TCA GCA	GCT GTG AAT GTC TAA ACT TGC ACT GAA GAG
FOXE1	ACT TCT TTG GAA GTC TGG AGG GCA	ACC TCG GTT TGC TTG GAG ACC TTT
G0S2	GGG CTT GTA AGA GTG CAT GAA GGT GAC A	TTT GCA GGC TAG GGT TGT GGA GTA CA
GDA	GCA CTC ATT AAT TGC CTG TAG TGC TTC	AGC AGA CCT GAA CAC CAG CTA ACA
IGFBP1	CGT CCT GTT GTG GTT TTG TG	CCT CCG CAC TAA GAA ACA TTG
JUNB	TAA GTC TTT GGC AGC TGT GTG GGA	TTG CTG GGT CTT CTT GGA AAC AGG CT
KLF3	GAG ATA GGG TCT TGA TAT GTA GCC CAG G	TTC TCC TGA GAA AGT GGC CC
KNG1	TGC TTT GAC CCT TAG TAA CCC GGA	TGT AGA CTC ACT CCC AGG ACA GTC A
MT1A	AGG CAT CCA GGT TGA GTC TG	GGC ATT AAC GGC TGG TTT TA
MT3	GCC GGG CTC CTA GTA	AGG CTC AAC AAG CAG

	CTT TT	AAA CAG
NOS2	GGA ACC ATG GGA TGA TGA GT	TAC ATG GCA TGG GAT TTT CC
SOD2	CCG GAA GAG GAC ACA GCT GAG ATC ATT GTA	TGA GGA AAG GTG GCT CTG ACG GTAT T
STAT3	ACC AAG ATA GAA CTC ACT GAT GGG C	TGA ACC CAG ATC TCT GGC ACT CAT GT
THBD	GCC TGT AGG TAA GCC CAT GA	CAG GAC CAC CAG CCT AAG AG
VIM	TTC TTT CTC AGC ACC CAA GG	GGA TCG AGC ACA GTC CTG TTA
ZPF36	TCA CGG GAC CAG CCC AGG AA	TGT GTG TAT GTG TGT GTG TGT GTG CG

2.3 RESULTS

2.3.1 NF-κB binding following partial hepatectomy

NF-κB is an important regulator and mediator of cytokine response to injury. We investigated how NF-κB binding responded to PHx by quantifying the number of genes bound by NF-κB at each time measured post-PHx. The genes bound at each time point included both genes unique to that time point and common among time points. We found that the total number of genes bound by NF-κB during the first six hours post-PHx was similar at each time point investigated, with 2518 genes bound by NF-κB at baseline (0 hr), 2440 genes bound at 1 hour post-PHx, and 2396 genes bound at 6 hours post-PHx (using an FDR cutoff ≤ 0.05), although, as the priming phase progressed, the numbers of genes bound by NF-κB decreased. Thus, although NF-κB has been shown to become activated quickly following PHx and maintain its activity until at least the end of the priming phase, the overall number of genes bound by NF-κB during the priming phase of liver regeneration remained similar in our

analysis. What changed, however, was the distance from the binding site to the transcription start site (TSS) of the nearest gene (Figure 2.6).

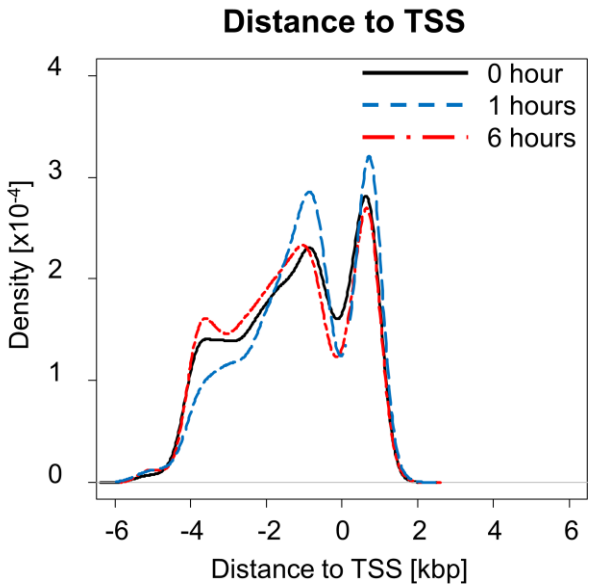

Figure 2.6 Distance to transcription start site (TSS) at each time measured post-PHx. At 1 hour post-PHx, the peak distance to TSS appears to decrease with more NF-kB binding close to the regulated gene both upstream and downstream.

At 0h and 6h post-PHx, NF-κB binding occurs with two peaks with similar frequency: one upstream of the TSS and one downstream. At 1h post-PHx, NF-κB binds to both upstream and downstream of the TSS but the downstream binding is clustered closer to the TSS than for 0h and 6h. Additionally, the upstream and downstream peaks appear higher at 1h than at 0h or 6h, indicating that NF-κB binds more genes close to their TSS at 1h (Figure 2.6). Transcription factors binding closer to the TSS of a gene have a stronger effect on regulation of gene expression (Cheng et

al, 2012;Cheng & Gerstein, 2012). Taken together, our data suggest that at 1 h following PHx NF-κB has a stronger effect on bound genes. This correlates with previous studies showing increased NF-κB activity at 1h post-PHx (Juskeviciute et al, 2008).

2.3.2 Dynamic Pattern Analysis of NF-κB binding

Activation of pro-inflammatory cytokines during the priming phase is a dynamic process involving multiple regulatory feedbacks. Therefore, we used a dynamic pattern-based strategy to analyze the binding of NF-κB to target genes following PHx. We first discretized NF-κB binding by identifying genes as bound (1) or unbound (0) at each time point post-PHx. To be identified as bound, NF-κB binding had to be seen in 2 out of 3 biological replicates at a time point (FDR $\leq$ 0.05). Because discretized NF-κB binding has 2 distinct states, we were then able to organize NF-κB binding into 7 dynamic binding patterns (Figure 2.7). Each pattern is described by both a binary string (i.e. 011) and its digital representation. Therefore, the binding pattern unbound by NF-κB at 0h and 1h but bound at 6h post-PHx (binary string 001) becomes pattern 1, the binary string 010 (0h unbound, 1h bound, 6h unbound) becomes pattern 2, and so on until binary string 111 becomes pattern 7 (Table 2.5).

The number of genes bound by NF-κB in each pattern (Table 2.5) showed that transient binding (Pattern 2: 010), immediate unbinding (Pattern 4: 100), and delayed binding (Pattern 1: 001) contained the highest number of genes bound by NF-κB. Therefore, the major dynamic effects of PHx on NF-κB during the priming phase appear to be a large unbinding event followed by a transient binding event and a delayed binding event at the end of the priming phase. This suggests that the bound NF-κB in the resting liver is not all bound in an active conformation.

Table 2.5 Pattern analysis of NF-κB binding during the priming phase post-PHx.

Digital Pattern	Binary Pattern	NF-κB Bound Genes	Differentially Expressed Genes
1	001	1067	154
2	010	1140	155
3	011	392	53
4	100	1108	155
5	101	502	71
6	110	473	55
7	111	435	190*

*Denotes total number of genes bound by NF-κB & measured in RNA-seq, not differentially expressed genes.

It should be noted that these binding sequences may represent a pool of previously available NF-κB that comes unbound from its normal location on the genome and dynamically induces transcription in two distinct sets of genes (one at 1 hour post-PHx and one at 6 hours post-PHx). All the other binding patterns contained approximately the same number of genes bound by NF-κB (Table 2.5, Digital patterns 3, 5, 6, and 7). These patterns of NF-κB binding may also considerably regulate early tissue response to PHx. There were also a considerable number of genes constitutively bound by NF-κB (Pattern 7: 111), suggesting that NF-κB binding following PHx continues to maintain functions occurring in non-stressed tissue in addition to dynamically switching binding locations.

2.3.3 Functional Pathways Represented by Genes Bound by NF-κB post-PHx

We first coupled NF-κB dynamic binding patterns into pairs of NF-κB binding switches (Figure 2.7, left panel). This allowed us to characterize NF-κB binding switches as an immediate response switch (Figure 2.7 A), a transient response switch (Figure 2.7 B), and a delayed response switch (Figure 2.7 C), with constitutive binding also occurring (Figure 2.7 D). We then investigated which functional pathways were bound and unbound by NF-κB during each switch using the DAVID software to identify functional clusters of genes (Huang et al, 2009). One unexpected result was that NF-κB binds to many genes within the functional category sensory perception of smell, specifically prior to PHx and in the "unbinding" (gray) patterns. Following PHx, NF-κB ceased binding to these genes to perform other functions. Overall, we found that NF-κB bound to 510 olfactory receptor genes; of these, 9 were differentially expressed following PHx (at a 2 fold-change cutoff). We investigated if the chromatin was accessible at these genes by comparing our NF-κB binding regions and associated gene region to whole-liver DNAse1 hypersensitivity regions in mouse livers found by the ENCODE project (Yue et al, 2014).

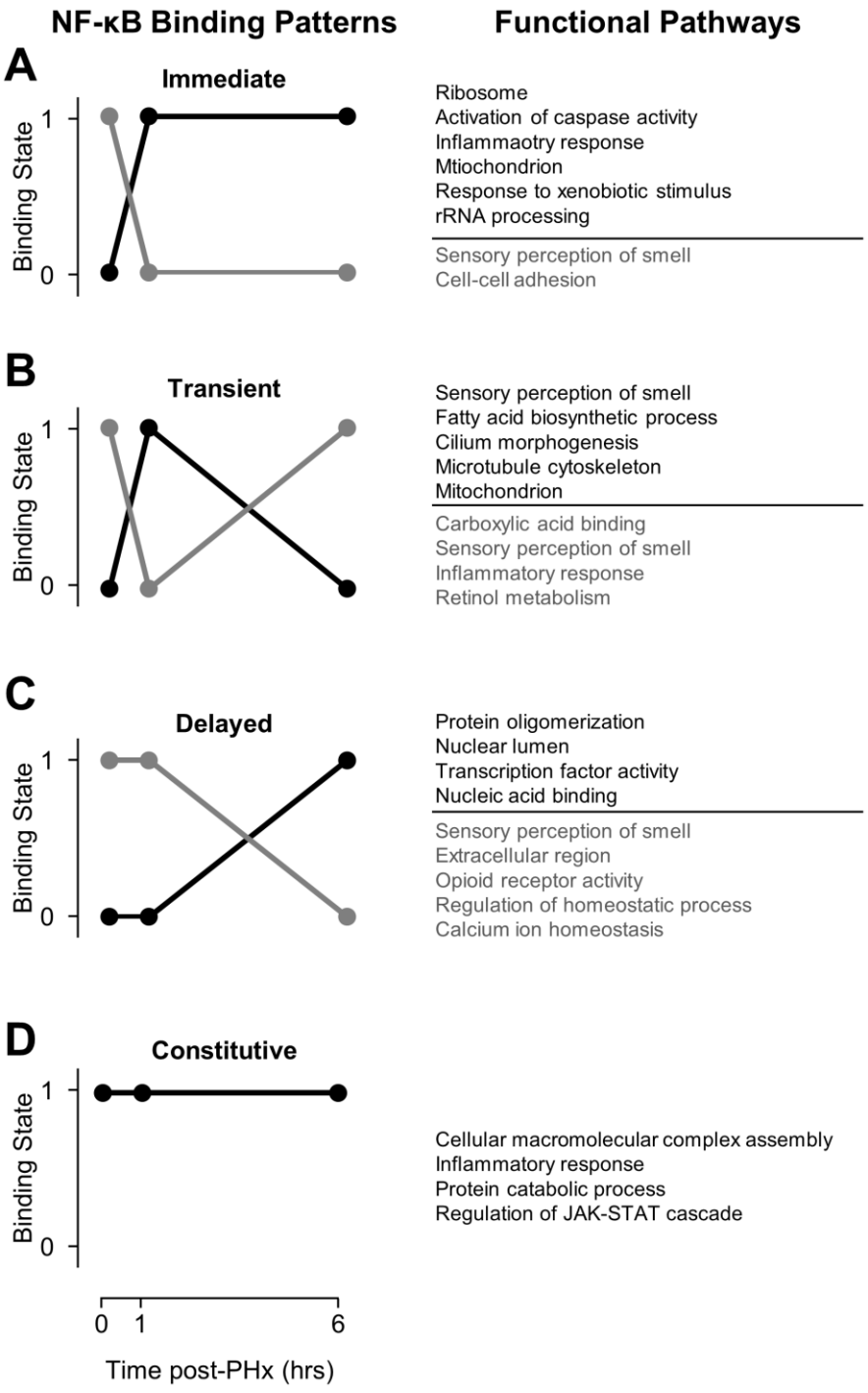
NF-κB Binding Patterns
Functional Pathways
A
Immediate
Binding State
1
0
Ribosome
Activation of caspase activity
Inflammaotry response
Mtiochondrion
Response to xenobiotic stimulus
rRNA processing
Sensory perception of smell
Cell-cell adhesion
B
Transient
Binding State
1
0
Sensory perception of smell
Fatty acid biosynthetic process
Cilium morphogenesis
Microtubule cytoskeleton
Mitochondrion
Carboxylic acid binding
Sensory perception of smell
Inflammatory response
Retinol metabolism
C
Delayed
Binding State
1
0
Protein oligomerization
Nuclear lumen
Transcription factor activity
Nucleic acid binding
Sensory perception of smell
Extracellular region
Opioid receptor activity
Regulation of homeostatic process
Calcium ion homeostasis
D
Constitutive
Binding State
1
0
0
1
6
Time post-PHx (hrs)
Cellular macromolecular complex assembly
Inflammatory response
Protein catabolic process
Regulation of JAK-STAT cascade

Figure 2.7 NF-κB binding patterns with associated pathways found using DAVID. (A) Immediate binding and unbinding (B) Transient Binding and unbinding (C) Delayed Binding and Unbinding (D) Constitutive Binding. Our analysis revealed that NF-κB binds to many genes involved in sensory perception of smell at baseline. Following PHx, however, these targets become unbound as NF-κB instead targets pathways previously related to be critical to liver regeneration. It is possible that genes involved in sensory perception of smell serve as a sink for NF-κB binding so that transient pulses to NF-κB binding do not start cascades of inflammation.

We found that the majority of these NF-κB binding sites had no DNAse1 hypersensitivity, with only 8 NF-κB binding sites robustly accessible across animal replicates (a subset of these genes are shown in Figure 2.8). Of these 8 genes, 6 had inaccessible gene regions (Figure 2.8 A), while 2 had open chromatin (DNAse1 hypersensitivity) at the beginning of the gene region (Figure 2.8 B and C). The accessible genes were not differentially expressed. We speculate that NF-κB binding sites for these sensory perception of smell genes may act as a buffer for NF-κB activation under normal conditions to prevent spurious hepatocyte priming but are made unavailable for NF-κB binding following a sustained challenge such as hepatectomy by mechanisms such as histone methylation or acetylation. Alternatively, recent work has shown functional olfactory receptors in the kidneys of mice which act as chemical sensors and can modulate glomerular filtration rate (Pluznick et al, 2009). It is possible that olfactory receptors in the liver may also act as chemical sensors to modify liver behavior. These results are difficult to interpret at present and require more detailed study.

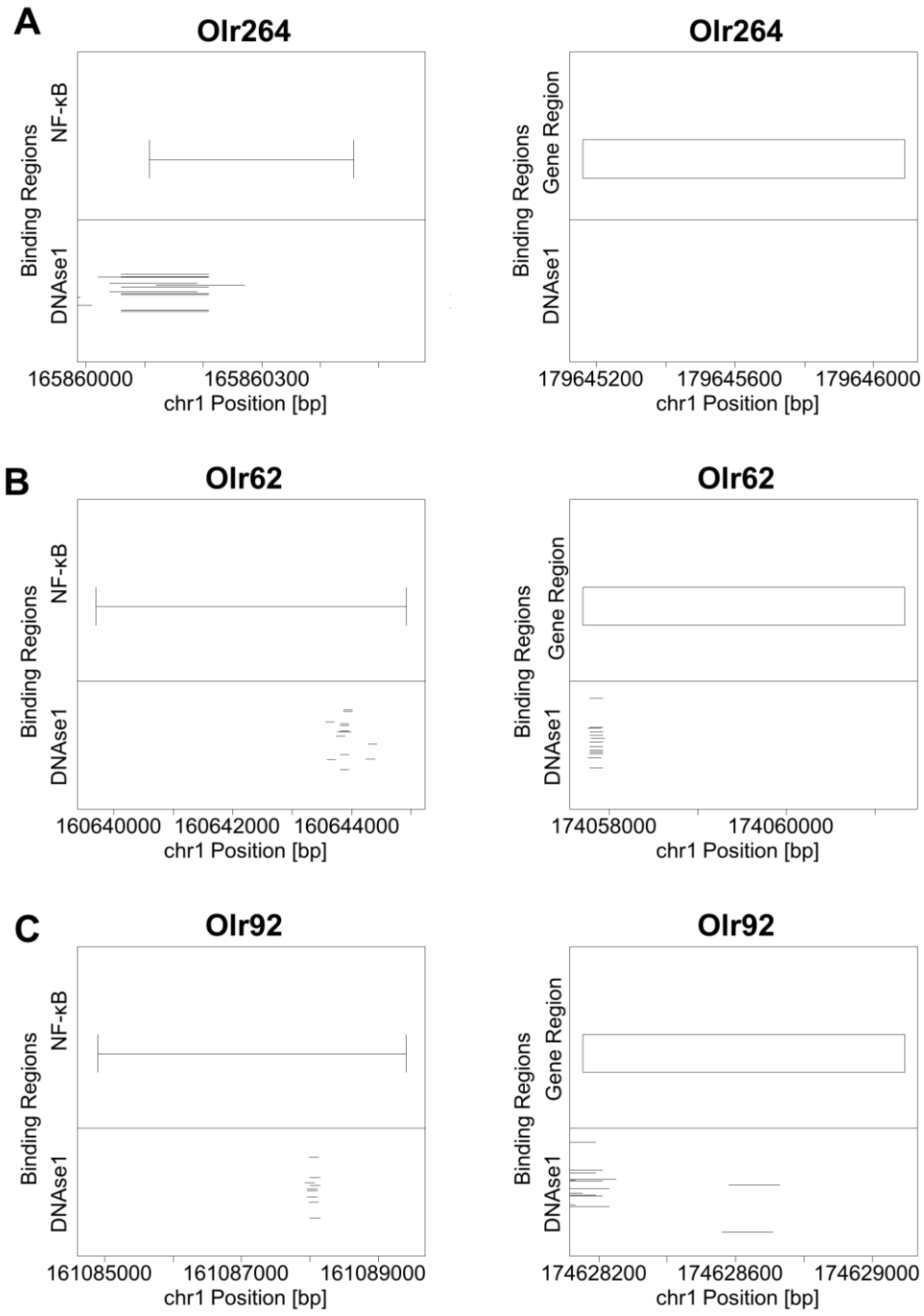

Figure 2.8 NF-κB binding regions for olfactory receptor genes compared to DNAse1 hyperactivity sites from whole-liver tissue in mice from the ENCODE project.

2.3.4 NF-κB Switches Co-ordinate Dynamic Tissue Function post-PHx

In light of the role of NF-κB in dynamically regulating tissue function post-PHx, we next investigated how NF-κB switches regulated gene expression. We first used the NF-κB switches to organize genes into binding patterns as before (Figure 2.9, left panel). We then identified gene expression levels of genes bound by NF-κB using a previously published RNA-seq gene expression data set of rat liver regeneration at 0h, 4h, and 12h post-PHx (Figure 2.9, center panel; Table 2.5). Genes were identified as differentially expressed with a fold-change value ≥ 2 (see Material and Methods for rationale). Differentially expressed genes corresponding to each NF-κB switch were then analyzed to identify functional clusters of genes using the DAVID software (Figure 2.9, right panel) (Huang et al, 2009). For constitutive NF-κB binding, all NF-κB bound genes were analyzed rather than only differentially expressed genes. This association of NF-κB binding with subsequent gene expression was somewhat tenuous because of the low sampling frequency and non-identical time points used between studies; however, this approach focused our analysis to NF-κB binding that appears to have a dynamic functional role in gene expression.

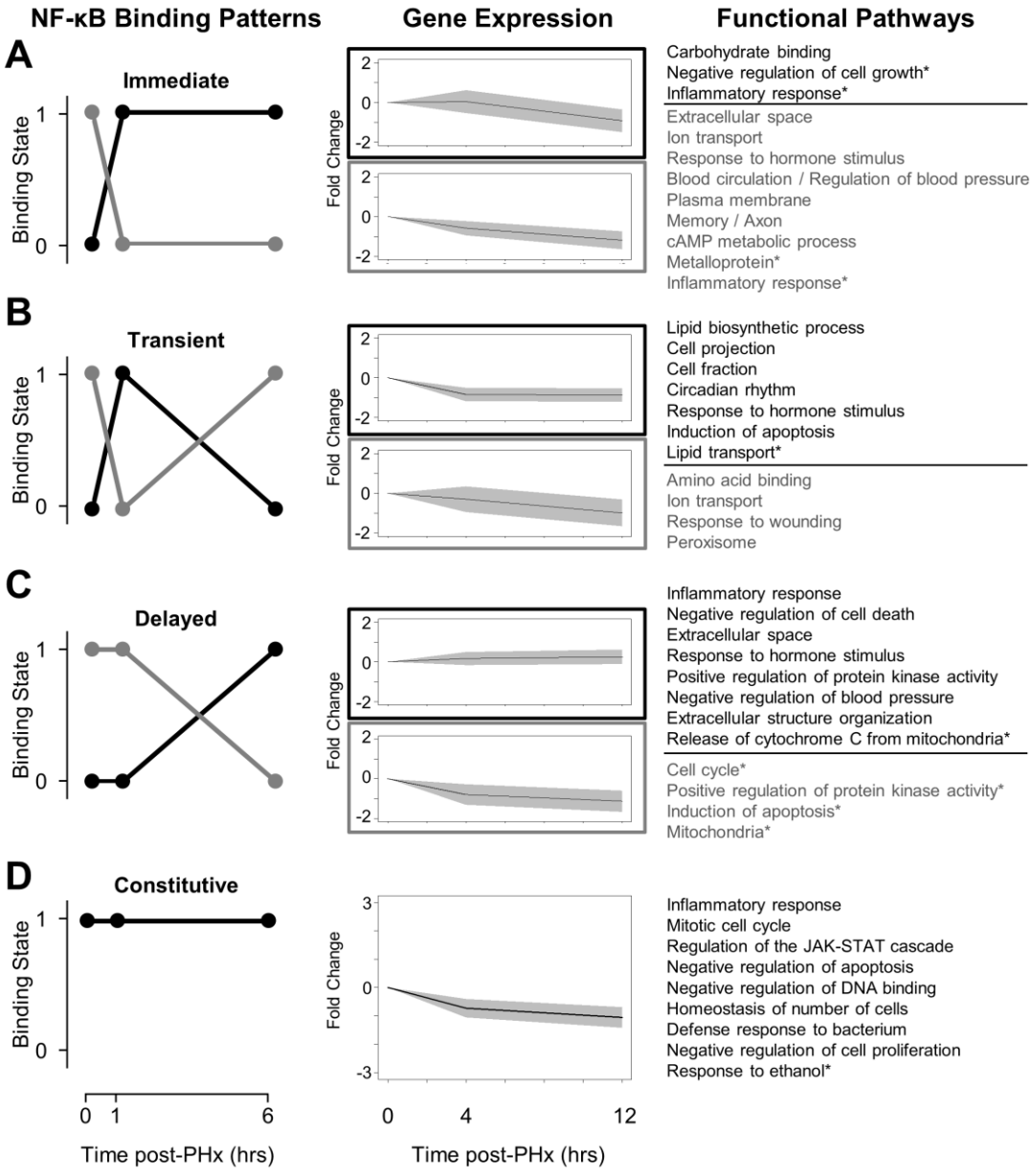

*Indicates functional pathway enrichment p-value > 0.05

Figure 2.9 Switching mechanisms of NF-κB binding post-PHx. (A) NF-κB immediate response switch. (B) NF-κB transient response switch. (C) NF-κB delayed switch. (D) NF-κB constitutive binding. NF-κB was constitutively bound to genes responsible for cell cycle, cellular response to stress, and the JAK-STAT pathway. The regulation of these genes by NF-κB may be essential for tissue function.

We found that although NF-κB binding follows switch-like behavior, gene expression patterns do not all follow the same switching behavior. In all switches analyzed, however, expression levels of those genes unbound by NF-κB tend to decrease while expression levels of those genes bound by NF-κB tend to increase (or decrease less) (Figure 2.9, Center panel). Several factors may contribute to a weak correlation between binding and gene expression. One factor is the time delay between measured NF-κB binding and measured gene expression. Although it has been well documented that transcription can have delayed effects on gene expression, 3 hours and 6 hours following binding events at 1 hour and 6 hours post-PHx may be too long for robust correlations between transcription factor binding and gene expression (McAdams & Arkin, 1997;Schmitt et al, 2004). Similarly, once transcribed, different mRNA may have different regulation, degradation rates, and half-lives. Additionally, NF-κB may coordinate with other transcription factors known to be active during liver regeneration to dynamically regulate gene expression.

We found that immediately post-PHx NF-κB stopped regulating genes associated with multiple pathways and instead began to regulate genes associated with only a few pathways, predominantly with the functions (GO Terms) negative regulation of cell growth and inflammatory response (Figure 2.9 A). This result suggests that immediately following PHx there may be a limit to NF-κB

bioavailability. The binding seen at 1 hour post-PHx occurs before there would be significantly increased production of NF-κB protein. This interpretation is consistent with mathematical models which can capture short-term dynamics of NF-κB signaling without considering additional NF-κB production (Lipniacki et al, 2004). Therefore, the available NF-κB may cease to regulate less essential functions like regulation of blood pressure and begin to regulate transcription of genes required to prime hepatocytes for replication. Additionally, the negative regulation of cell growth may ensure that all available metabolic energy goes towards cell replication rather than cell growth to meet functional demand (Shestopaloff, 2014).

Potentially using this same pool of available NF-κB, NF-κB transiently switched from regulating genes associated with amino acid binding, ion transport, and response to wounding, and began to regulate lipid biosynthetic processes, cell projection, circadian rhythm, and induction of apoptosis (Figure 2.9 B). This suggests that NF-κB transiently shifts from governing normal tissue functions (like amino acid binding and ion transport) to governing an additional response to tissue damage that may also modulate normal tissue functions (increasing binding to genes governing response to outside stimuli, circadian rhythm, and induction of apoptosis). The transient NF-κB switch also regulated functions associated predominantly with hepatic stellate cells. Specifically, NF-κB began to regulate lipid synthesis and transport as well as cell projections, potential components of modulating hepatic stellate cell activation. Because hepatic stellate cells are not thought to begin producing growth factors until approximately 12 hours post-PHx, this induced NF-κB binding may act as a pioneering signal stimulating a transcriptional cascade that will ensure that hepatic stellate cell activation occurs at the proper time post-PHx (Michalopoulos, 2007b).

After there has been sufficient time to begin producing additional NF-κB protein, NF-κB binding undergoes a delayed response switch (Figure 2.9 C). As opposed to the immediate response switch, the delayed switch turns off relatively few pathways and turns on multiple pathways. The pathways switched on included inflammatory response, positive regulation of protein kinase activity, negative regulation of apoptosis, and extracellular structure organization and suggest that by the end of the priming phase NF-κB begins to drive production of genes required for hepatocyte replication, including protein kinases. Additionally, NF-κB appears to switch its role from pro-apoptotic (transient) to anti-apoptotic (delayed). This switch may be an important regulator of liver failure after resection.

NF-κB also displayed constitutive binding to a select set of genes throughout the priming phase (Figure 2.9 D). These genes were normally bound by NF-κB and remained bound despite PHx, indicating that they may be essential for tissue function. They included genes in pathways canonically associated with NF-κB binding, including inflammatory response, regulation of the JAK-STAT signaling cascade, negative regulation of apoptosis, and the mitotic cell cycle. The constitutive binding to genes in these pathways indicates that these pathways, which are typically associated with a dynamic stress, may also be critical for normal tissue function.

2.3.5 NF-κB Binding Motif Analysis

NF-κB binding motif analysis revealed that NF-κB had multiple cofactors that may act to help regulate transcription following PHx (Figure 2.10).

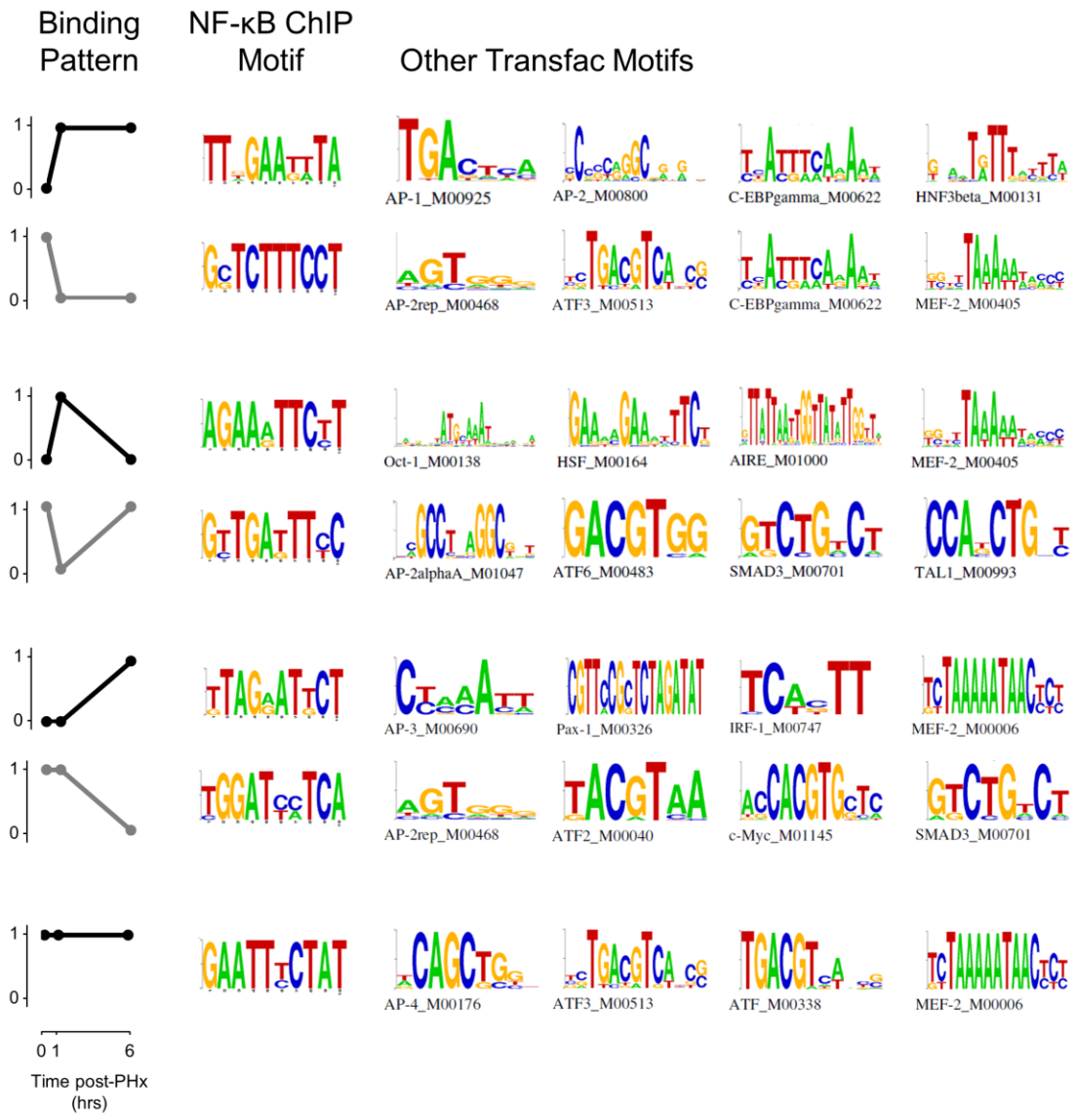

Figure 2.10 Pattern-based motif analysis of NF-κB binding sites. Strongly bound sites in each binding pattern were matched to known transcription factor binding sites using the software DME and the TRANSFAC database. Potential co-regulators of NF-κB binding switches were identified for each binding pattern.

We found several motifs associated with the immediate NF-κB switch in the AP-1 and ATF families. AP-2 in particular may be a cofactor helping to regulate genes within this switch. C/EBP-gamma was also associated with both the binding (black) and unbinding patterns (gray). The binding pattern (black) in the transient response switch was associated with transcription factors related to cellular response to stress (metabolic Oct-1 or heat HSF), immune response (AIRE, HSF) and the cell cycle (MEF-2). Whereas the transient unbinding pattern (gray) was associated with transcription factors related to immediate-early gene expression (AP-2a and ATF6) and those that may relate to transcriptional control of hepatic stellate cell activation (SMAD3 and TAL1). The delayed NF-κB switch was associated with many of these same transcription factors (AP-2, AP-3, ATF, ATF-4, SMAD3, and MEF-2) as well as several additional transcription factors involved in inflammation (IRF-1) and the cell cycle (c-Myc). Constitutive NF-κB binding was associated with similar transcription factors (AP-4, ATF, ATF-3, and MEF-2).

When analyzed at each time point instead of in each pattern, we found multiple transcription factors that may act in concert with NF-κB including IRF-1, IRF-2, IRF-7, ICSBP (IRF-8), HSF, and MEF-2 (Figure 2.11).

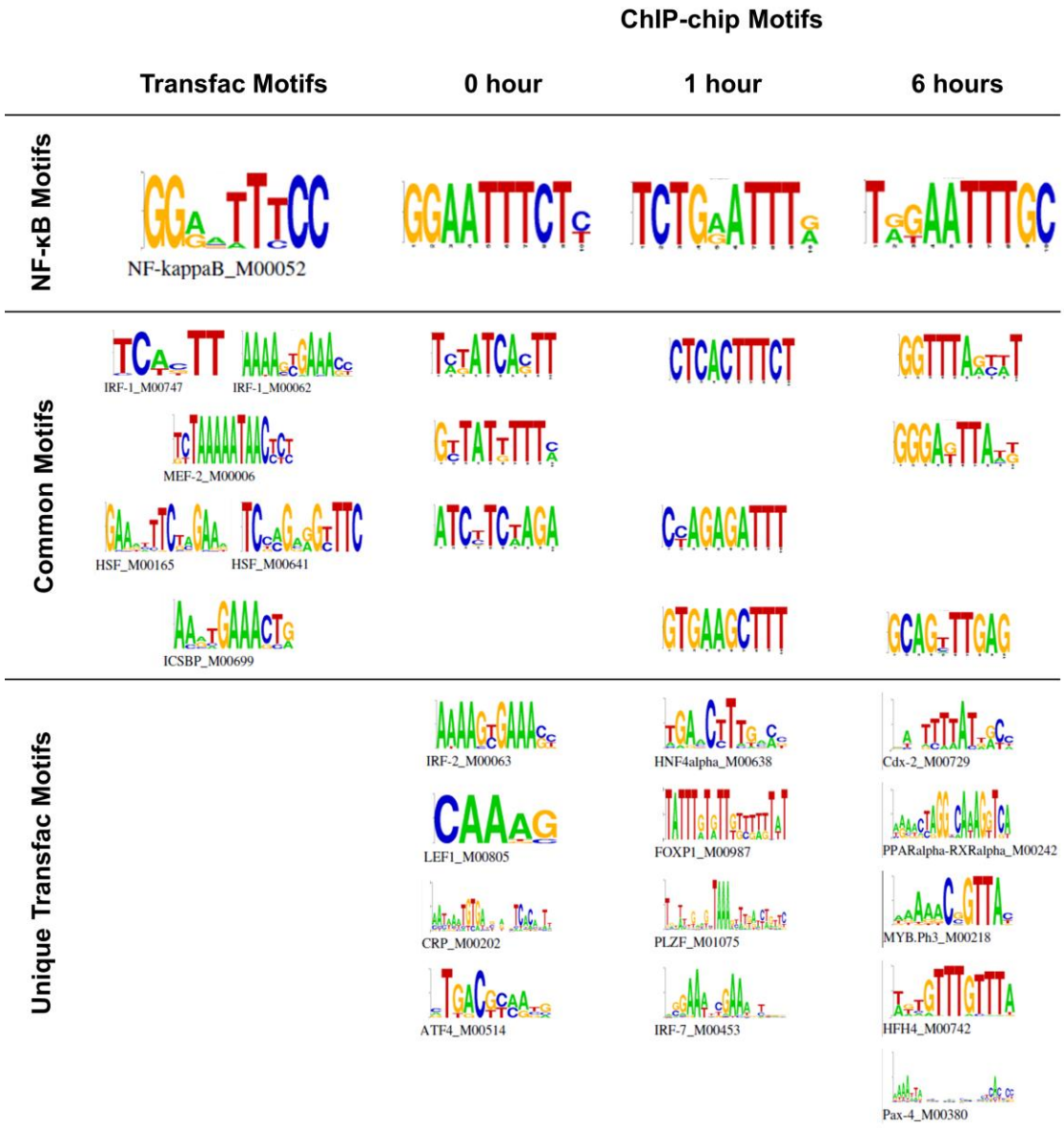

Figure 2.11 Motif analysis of NF-κB binding sites. The top binding motifs were matched to TRANSFAC to identify potential cofactors regulating gene expression with NF-κB at each time point (excluding those motifs involved in mainly DNA binding and polymerase activity).

The IRF family of transcription factors is predominantly involved in interferon regulation and may be induced as a response to pro-inflammatory signals. IRF-1 is involved in the NF-κB signaling pathway and response to IL-1α. IRF-2 is involved in regulation of transcription and may enhance the function of other IRF transcription factors. IRF-7 is involved in IFNβ and IFNγ production. ICSBP (also known as IRF-8) is involved in the granulocyte-macrophage colony stimulating factor signaling pathway and may indicate hepatocyte response to Kupffer cell activation. Similarly, HSF is typically involved in cellular response to heat stress but may also be active in cellular response to other forms of stress or local inflammation/tissue damage. MEF-2 is also involved in the cellular response to calcium changes and may bind as a cofactor to NF-κB to modulate NF-κB activity when calcium signaling increases, as it does following PHx (Diaz-Munoz et al, 1998).

In addition, we found several motifs to be selectively enriched at 6 hours post-PHx (Figure 2.11). These motifs included Cdx-2, HFH4, Pax-4, and PPARa. Cdx-2, HFH4, and Pax-4 are all involved in hepatocyte entry into the cell cycle. Cdx-2 is involved in positive regulation of cell proliferation, HFH4 is involved in cellular response to growth factor stimulus, and Pax-4 is involved in negative regulation of apoptosis. The selective enrichment of these cofactors at 6 hours post-PHx correlates with our results indicating that NF-κB may play a role preparing hepatocytes for entry into the cell cycle at the end of the priming phase. In contrast, PPARα binding as a cofactor to NF-κB may indicate that these factors work together to regulate correct timing of hepatic stellate cell activation post-PHx. PPARα is known to regulate fatty acid metabolism (which is increased during stellate cell activation) and may be a

therapeutic target to ameliorate alcoholic liver disease, which may proceed through activation of hepatic stellate cells (Friedman, 2008c;Nan et al, 2014).

2.3.6 AP-1 as a Co-regulator of NF-κB Bound Genes Following PHx

Our motif analysis found several motifs enriched in NF-κB binding sites belonging to the AP-1 and ATF transcription factor families. We therefore investigated the dynamics of AP-1 and ATF transcription factor family activities during the priming phase post-PHx. We found that the AP-1 family of transcription factors was strongly activated by 1hour post-PHx in rats and remained activated over the course of the priming phase (Figure 2.12 A). This behavior was true for AP-1 family all transcription factors measured except FOSB and JUNB. FOSB activity decreased following PHx, while JUNB activity showed little change (Figure 2.12 B). ATF family transcription factor activities were also increased above baseline throughout the priming phase. These results coupled with the potential co-regulatory binding sites identified with NF-κB indicate that, as expected, AP-1 and ATF family transcription factors coordinate with NF-κB in regulating the priming for liver regeneration.

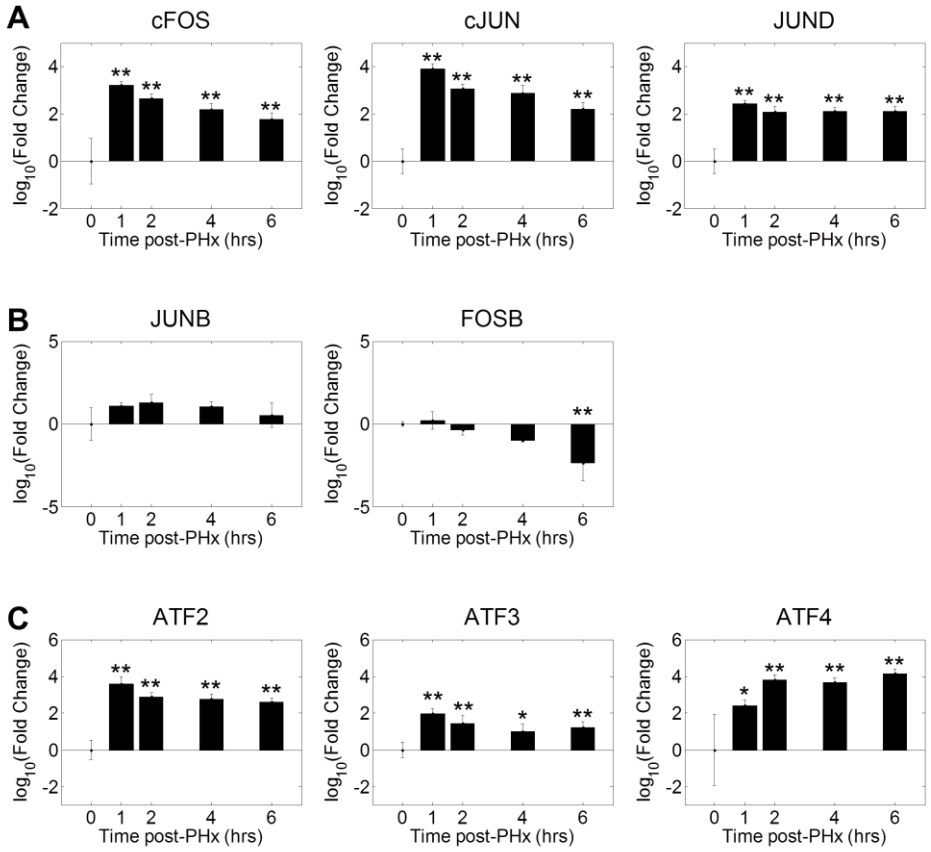

Figure 2.12 Co-ordinated activation of AP-1 and ATF family transcription factors during liver regeneration. Our motif analysis suggested that AP-1 binding coincided with NF-κB binding to co-regulate expression of genes during the priming phase of liver regeneration. The AP-1 family of transcription factors were found to be strongly activated by 1 hour post-PHx in rats. This activation was maintained throughout the priming phase for all transcription factors except FOSB and JUNB. FOSB activity decreased following PHx, which JUNB activity transiently increased before returning to baseline levels. *p-value < 0.05, **p-value < 0.01.

2.3.7 Validation of Selected NF-κB Binding Dynamics Using ChIP-qPCR

We tested a set of 21 of genes through the use of NF-κB ChIP followed by high-throughput qPCR (Figure 2.13, Figure 2.14) (Spurgeon et al, 2008). We found that NF-κB bound to the promoter regions of several of these genes with similar

dynamics as in the ChIP-chip analysis (Figure 2.13). The similar binding dynamics seen between platforms supports the results of our ChIP-chip analysis. We further validated our results for promoter enrichment at the Sod2, iNOS, G0S2, and IGFBP1 gene promoter regions using PCR followed by visualization in a 1% agarose gel (Figure 2.1).

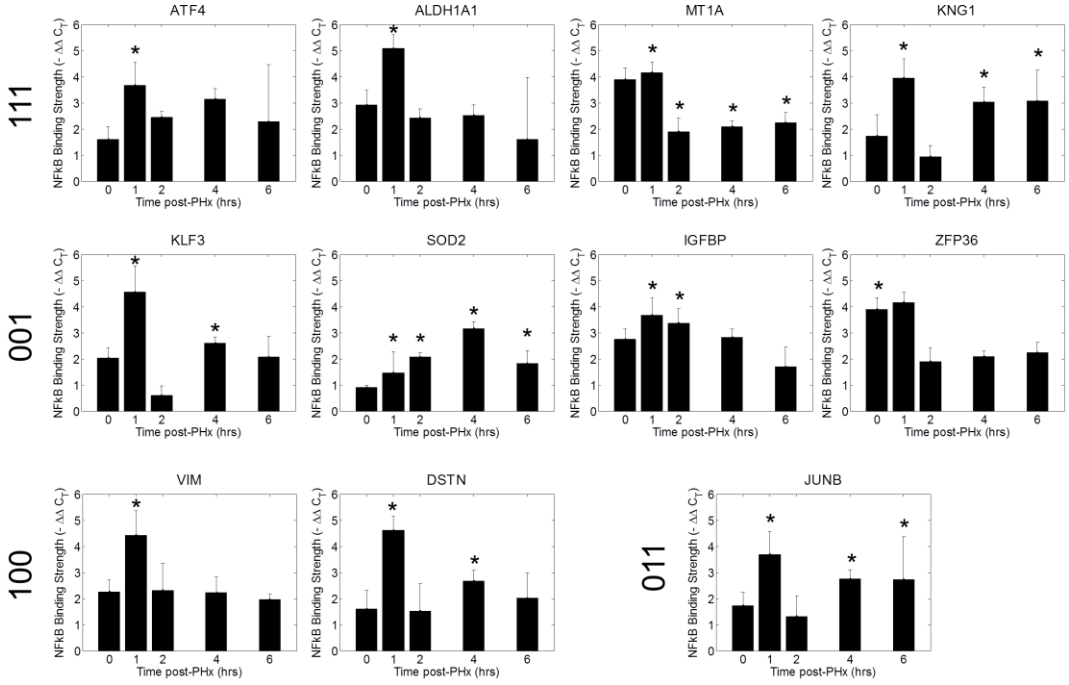

Figure 2.13 ChIP qPCR validation. Binding patterns for selected genes were investigated using ChIP-qPCR.

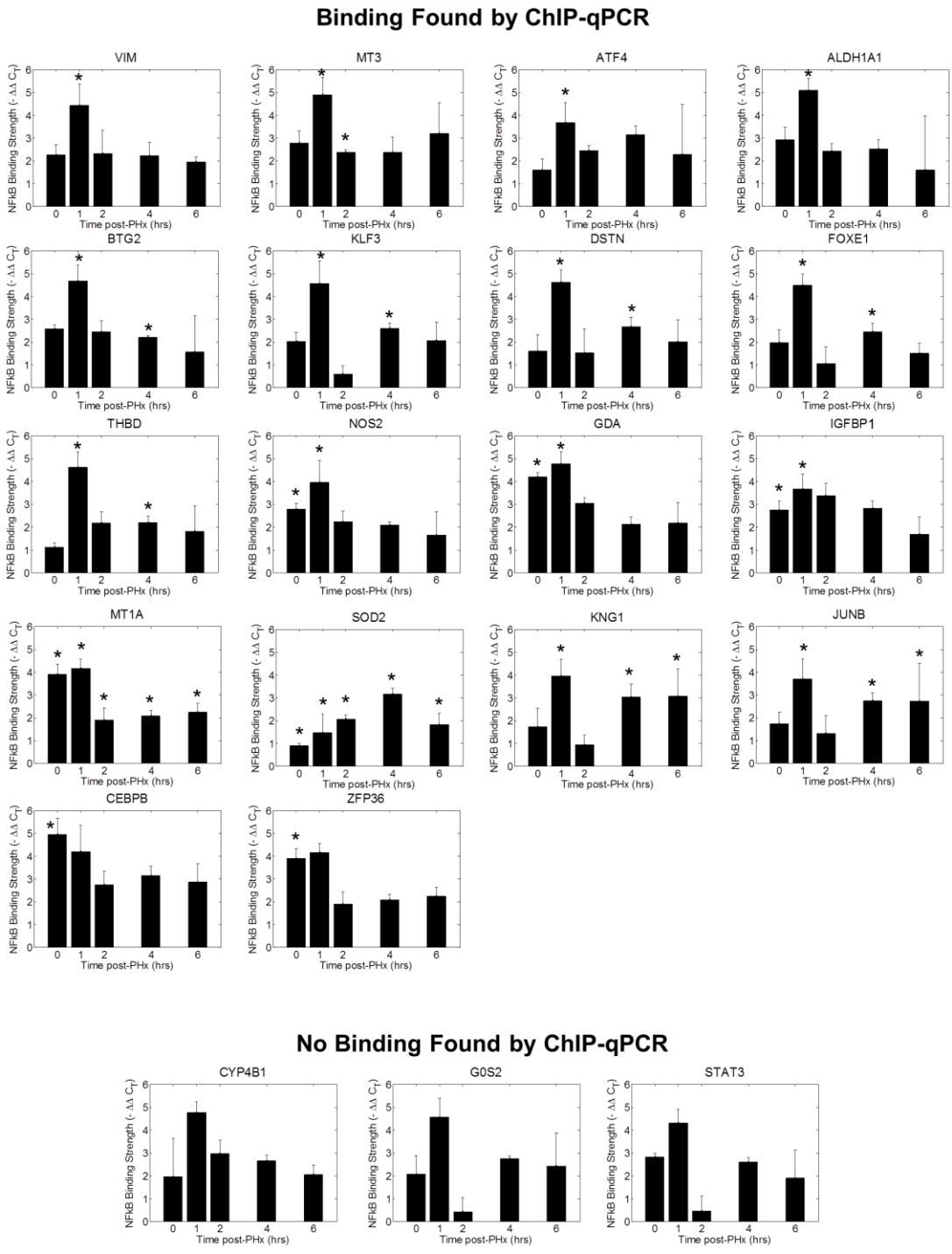

Figure 2.14 ChIP qPCR validation of NF-κB targets following PHx.

2.4 DISCUSSION

Our results indicate that the acute challenge of a partial hepatectomy causes NF-κB binding in the liver to operate as a dynamic switch regulating tissue function. The immediate, transient, and delayed NF-κB signaling profiles appear to serve different purposes in driving regeneration. Early post-PHx, NF-κB binding transitioned from governing many functions to governing mainly those functions necessary to set hepatocytes up for entry into the cell cycle. These functions were maintained throughout the priming phase. Transiently post-PHx, NF-κB binding transitioned away from binding genes involved in maintaining tissue function and toward binding genes involved in apoptosis, circadian rhythm, and hepatic stellate cell activation. The transient switch may therefore be involved in synchronizing healthy cells for entry into the cell cycle while inducing damaged cells to commit apoptosis. The transient switch may also ensure proper timing of hepatic stellate cell activation following PHx. As the priming phase ended, NF-κB began to regulate many genes setting up hepatocytes to enter the cell cycle. This switch may indicate a role for NF-κB contributing to hepatocyte entry into the cell cycle as regeneration progresses past the priming phase. Additionally, several genes involving mitochondrial function that are bound and unbound in this switch (including Atp5d, NDUFA10, ACSL5, and mfn1) may be important to govern the fraction of metabolic demand delegated to regeneration and that delegated to maintenance of tissue function as hepatocytes enter the cell cycle (Shestopaloff, 2014). The binding patterns of differentially expressed genes with the highest expression (top 20 genes) show dynamic regulation by NF-κB throughout the priming phase (Figure 2.15).

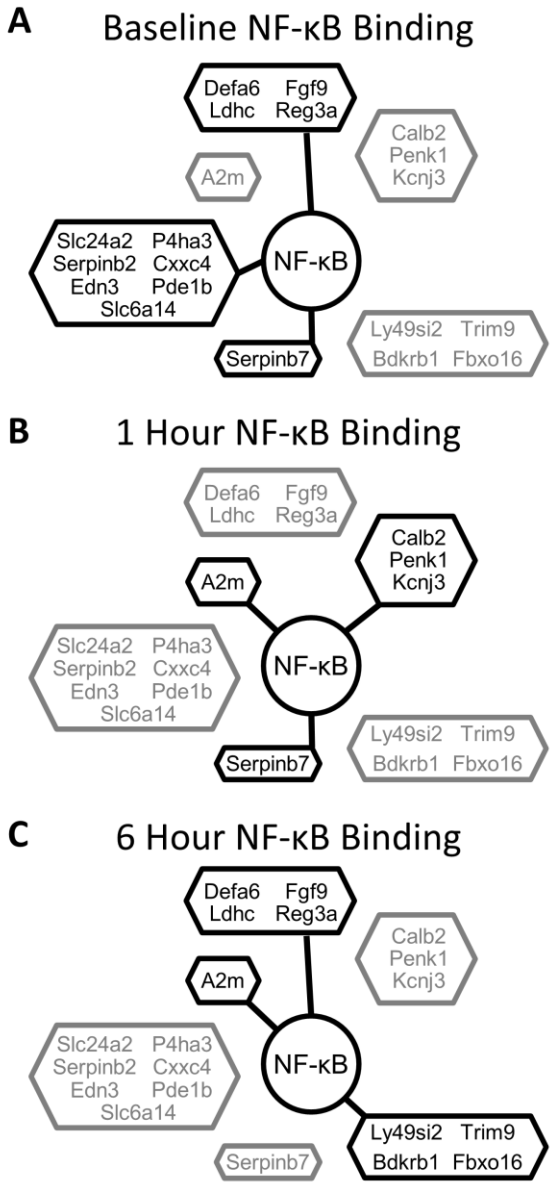

Figure 2.15 NF-kB binding for the top 20 differentially expressed genes clustered according to NF-kB binding pattern (A) NF-kB binding at baseline, (B) NF-kB binding at 1 hour post-PHx, (C) NF-kB binding at 6 hours post-PHx. Black = Bound, Gray = Unbound.

In addition to the NF-κB binding switches, we observed constitutive binding, where NF-κB was bound before PHx and remained bound throughout the priming phase. Because liver tissue function is maintained during regeneration, it is likely that these genes consist of an essential set of genes required for NF-κB contributions to normal liver function. The pathways constitutively governed by NF-κB suggest that NF-κB could be important for maintaining the balance of the innate immune system in the liver. The innate immune system must be balanced such that it can respond to pathogens or inflammation but not so active that chronic inflammation results. Another possibility is that, because the drivers for priming rely on processes in non-parenchymal cells (especially Kupffer cells), dynamics of NF-κB binding in the innate immune system may not be detectable in total tissue extracts. Alternatively, it is possible that some of the 'constitutively bound' genes still move to different binding sites closer to the TSS, or are otherwise activated, either through combinatorial binding with other factors, or through chromatin accessibility regulation.

These results may have implications beyond the field of liver regeneration for understanding carcinogenesis during inflammatory conditions. Barash et al. proposed that chronic inflammation can increase hepatocyte genomic instability and that these genomically unstable hepatocytes can become tumorigenic following liver resection (Barash et al, 2010). The results of our study show the binding response of NF-κB to liver resection in the first six hours post-resection. This NF-κB binding response can serve as a baseline from which to compare NF-κB response to resection during conditions of chronic inflammation caused by chronic liver diseases including alcohol use, obesity, hepatitis infection, or bile salt export pump deficiency (which causes inflammation and carcinogenesis in the absence of external, cancer-predisposing

factors) (Iannelli et al, 2014;Kudo et al, 2014;McGivern & Lemon, 2011;Sun & Karin, 2012). Such a comparison could provide insights into how NF-κB contributes to hepatocellular carcinoma genesis during regeneration under chronic inflammatory conditions. Further study of these areas will be necessary to determine the dynamic contribution of NF-κB to such carcinogenesis.

Our approach has several strengths and weaknesses that are important to consider when interpreting our results. ChIP-chip can be considered as a targeted approach for promoter regions of genes; whereas ChIP-seq (next generation sequencing) gives a much more global view of transcription factor binding which includes the promoter regions and other regions within genes (Ho et al, 2011). ChIP-chip's higher coverage of the promoter regions of genes also gives a higher sensitivity than ChIP-seq unless a high read count is used. Additionally, both techniques share the limitations of low resolution and lack of cell-type specificity. Neither technique can differentiate with a base-pair specificity the true NF-κB binding sites within the bound regions. Recent techniques, such as ChIP-exo, may allow for identification of NF-κB bound motifs on the bound regions (Rhee & Pugh, 2012). The signal from whole-liver ChIP approaches likely comes predominantly from hepatocytes with lower abundance non-parenchymal cells likely contributing a lesser signal. Cell isolation techniques, such as those used in the ENCODE project, may be used in the future to identify the contributions of different cell types in the liver to NF-κB binding during regeneration (Winter et al, 2013). Additionally, our novel, dynamic pattern-based analysis allowed for unique insights into the dynamic switching mechanisms of NF-κB binding during the priming phase of liver regeneration.

This genome-wide pattern counts analysis revealed several dynamic NF-κB switches which occur post-PHx. Using this technique, we were able to identify dynamics of NF-κB binding within multiple pathways during liver regeneration. Additionally, we were able to identify a subset of genes that may be critical for healthy tissue function. This analysis strategy has wide application when analyzing transcription factor binding and can be used in other contexts as well as to understand dynamic transcriptional regulation.

Chapter 3

PREDICTING MOLECULAR REGULATION OF LIVER REGENERATION IN ADIPONECTIN KNOCKOUT MICE USING AN EXISTING COMPUTATIONAL MODEL

This chapter was adapted from Correnti, J. M., **Cook, D.**, Aksamitiene, E., Swarup, A., Ogunnaike, B., Vadigepalli, R., & Hoek, J. B. (2015). Adiponectin fine-tuning of liver regeneration dynamics revealed through cellular network modelling. *The Journal of physiology*, *593*(2), 365-383. All experimental work featured in this chapter was performed by J.M. Correnti.

3.1 Introduction

Liver regeneration is a unique repair mechanism that allows a damaged liver to recover following traumatic or toxic injury or hepatic surgical procedures. This process is clinically important in liver mass recovery in both donor and recipient following live donor liver transplantation. After partial hepatectomy (PHx) normally quiescent hepatocytes are activated to reenter the cell cycle through a highly synchronized pro-proliferative response, which requires precise timing of cytokine and growth factor (GF) signals. This response is orchestrated through a dynamic pattern of activation and inhibition of a wide range of signaling processes coordinated across multiple cell types in the liver, including hepatocytes, Kupffer cells and hepatic stellate cells (Taub, 2004a). Kupffer cells are primary coordinators of the dynamic cytokine microenvironment following tissue damage (see chapter 2). Hepatic stellate cells produce growth factors critical to induce hepatocyte replication. Once lost tissue

mass is recovered, hepatic stellate cells also produce factors terminating regeneration (Taub, 2004a). In addition, signals from extra-hepatic tissues, including adipokines, play a role in modulating this coordinated cellular response. Because adipokines originate from outside the liver, treatment of hepatic surgery patients with adipokines is an attractive option to modulate liver regenerative ability following surgical intervention without the complications involved in modifying liver function directly.

One of the factors implicated in modulating both liver cytokine microenvironment and growth factor bioavailability is the serum adipokine adiponectin (Adn) (Yamauchi & Kadowaki, 2013). Adn is a 30 kD protein produced primarily by adipose tissue that circulates as low molecular weight (trimeric), middle molecular weight (hexameric), and high molecular weight oligomers (Turer & Scherer, 2012). Adn directly sensitizes the body to insulin, and Adn levels are low in patients with Type II diabetes (Kadowaki et al, 2006). It is thought to act in large part through two identified adiponectin cell surface receptors, adiponectin receptor (AdipoR) 1 and AdipoR2. Additionally, Adn has been shown to increase acute inflammation (Awazawa et al, 2011;Park et al, 2007) and is known to modulate balances of cytokines and growth factors critical to liver regeneration and repair. There is evidence that Adn also can act through direct binding and inhibition of growth factors. Taken together, these findings suggest Adn may have both pro- and anti-proliferative effects during liver regeneration (Kajimura et al, 2013;Landskroner-Eiger et al, 2009). Consistent with this hypothesis, previous studies suggested both reduced and increased Adn levels can impair regeneration. Adn -/- mice were reported to exhibit a delayed liver regeneration phenotype (Ezaki et al, 2009;Shu et al, 2009a), whereas treatment with the antidiabetic drug rosiglitazone, which is thought to act at

least in part by elevating serum Adn (Nawrocki et al, 2006;Yamauchi & Kadowaki, 2013), inhibits liver mass recovery (Turmelle et al, 2006). By contrast, rats with induced diabetes show a delayed initiation of hepatocyte replication after PHx, which is corrected by an increased replication from 36-72 hours post-surgery (Barra & Hall, 1977). We hypothesize that low Adn levels may have contributed to the regeneration dynamics observed in these diabetic animals.

The apparently conflicting actions through which Adn impacts liver regeneration points to nonlinear effects that are difficult to parse out with typical over/under-expression experimental analyses. In this study, we aim to develop a deeper understanding of the multifaceted impact of Adn on liver regeneration using an integrated computational modeling and experimental approach to characterize the molecular mechanisms underlying the Adn-mediated fine-tuning of liver regeneration dynamics.

Molecular mechanisms underlying liver regeneration are both redundant and complex, making prediction of effects of molecular or cellular manipulations difficult. For example, in studies using Cl_2MDP-liposomes to eliminate Kupffer cells from the liver, IL-6, TNFα, and HGF were all significantly decreased; however, mass recovery appeared to be only delayed but not blunted (Meijer et al, 2000a). Similarly, mice harboring a hepatocyte-specific deletion of *c-Met* were expected to show little or no regeneration following CCl_4 injection. These mice, however, showed similar kinetics and magnitude of proliferation following a single CCl_4 injection, indicating multiple compensatory mechanisms (Huh et al, 2004). After more extensive injury, the *c-Met* deficient mice did show lower recovery, but this was likely due to decreased cell motility rather than decreased proliferation.

Our computational modeling approach was designed to account for the net effect of such molecular redundancies and complex cellular interactions governing liver regeneration. We did not expect hepatocyte size increase to be a significant factor differentiating between regeneration in Adn-/- mice and control mice. We therefore use the computational model developed by Furchtgott et al. for the majority of this chapter (Furchtgott et al, 2009). Through model simulations and sensitivity analysis of the computational model of cellular interactions during liver regeneration, we investigate how changes to relative balances and timing of multiple regulatory mechanisms contribute to shaping the liver regeneration dynamics. Using this cellular interaction framework, the model acts as a bridge connecting the kinetics of molecular regulation to the regeneration dynamics.

We used Adn -/- mice to examine the kinetics of liver regeneration response after PHx through the priming and replicative phase and applied these experimental data to the computational model. We utilized the recently developed Pulsatile Sensitivity Analysis (PSA) to investigate which regulatory balances are critical for the effect of Adn on liver regeneration, and in what temporal intervals the specific changes to regulatory balances have the greatest impact on regeneration.

3.2 Materials and Methods

3.2.1 Animals

All animal studies were approved by the Institutional Animal Care and Use Committee (IACUC) at Thomas Jefferson University. Jefferson's IACUC is accredited by the Association for Assessment and Accreditation of Laboratory Animal

Care and experiments were designed using the Guide for the Care and Use of Laboratory Animals.

10-12 week old male Adn-/- mice (B6.129-*Adipoq*^{tm1Chan}), bred from mice kindly donated by Dr. Lawrence Chan, or C57BL/6J mice (Jackson Laboratories, Bar Harbor, Me) underwent partial hepatectomy based on surgical methods outlined by Mitchell and Willenbring (Mitchell & Willenbring, 2008). Briefly, animals were anesthetized by inhalation of 5% isoflurane in an induction chamber and anesthetic plane was confirmed by toe pinch. Anesthesia was maintained during surgery by continual inhalation of 2% isoflurane administered by nose cone. A midline incision was made followed by the sequential ligation and excision of the left-lateral and medial lobes of the liver. The abdominal cavity was rinsed with warm lactated Ringer's solution, the abdominal muscle layer was sutured and the skin was closed with wound clips. Following surgery, animals were given subcutaneous lactated Ringer's solution (1 mL/animal) and placed in a fresh cage under a heat lamp with ad libitum access to hydrogel (Contact ClearH_20, Portland, Me) and food. At specified times after PHx, animals were anesthetized with isoflurane as described for partial hepatectomy (induction and maintenance). While anesthetized, animals were weighed and sacrificed. The livers were either immediately (within 10 sec) freeze clamped using liquid nitrogen-cooled aluminum clamps as previously described (Crumm et al, 2008), preventing rapid post-mortem changes in cytokine or growth factor levels and protein phosphorylation, or the livers were fixed in 10 percent neutral buffered formalin (NBF) for assessment of BrdU labeling. For determination of liver to body weight ratios, the liver was dissected out and weighed prior to freeze clamping.

Blood was collected from the tail vein of live animals and from the vena cava under anesthesia at sacrifice. Collected blood was incubated at room temperature for 30 min, then centrifuged at 1500 rpm for 5 minutes. Serum was isolated and flash frozen for further analysis. In some cases, animals were given intraperitoneal injections of Bromodeoxyuridine (BrdU) solution (Sigma, St. Louis, Mo) (150 mg/kg) in sterile 0.9 percent saline two hours prior to sacrifice.

3.2.2 Histological analysis

Samples fixed in 10% NBF were paraffin-embedded, sectioned, and stained for hematoxylin and eosin by the Kimmel Cancer Center pathology core facility (Thomas Jefferson University) for analysis of hepatosteatosis. BrdU staining was performed using Impact DAB staining (Vector Laboratories, Burlingame, CA) according to manufacturer's instructions. For BrdU quantitation, five 20x fields were scored per animal.

3.2.3 Biochemical analysis

For Western blotting, tissue lysates were generated by homogenizing frozen tissue in RIPA buffer (Sigma) supplemented with phosphatase and protease inhibitor cocktails (Sigma). Protein was normalized using BCA Protein Assay Reagent (Pierce Biotechnology, Rockford, IL). 20 µg of protein was loaded onto an SDS-PAGE gel and Western blotting for cell cycle markers was performed as previously described (Crumm et al, 2008).

Data were compared using Student's t-test on raw data (BrdU incorporation and liver-to-body weight ratios) or log-transformed data (molecular measurements).

Paired statistics were used when appropriate. Data are presented as mean +/- standard error of the mean (SEM).

3.2.4 Computational modeling of liver regeneration

For a description of the computational model used in this study, see Chapter 4, Section 2.1 “Computational model development”, excluding cell growth and the original model derivation in (Furchtgott et al, 2009).

3.2.5 Sensitivity analyses for identifying key factors controlling regeneration phenotype

Parametric sensitivities were estimated based on a dynamic local sensitivity analysis (Zak et al, 2005), phase-based sensitivity (Gunawan & Doyle, 2007), and pulsatile sensitivity methodologies (Perumal & Gunawan, 2011). To calculate the dynamic local sensitivities (DLS), parameters were changed by +/- 10% and sensitivity was calculated as the change in overall liver recovery normalized to the number of cells at each time in the nominal regeneration profile divided by the percentage change in the parameter (20%), according to Equation 3.1.

$$DLS_{\mathrm{i}}(t) = \frac{\Delta N(t)/N(t)}{\Delta p_i/p_i} \tag{3.1}$$

where N(t) is the nominal fraction of hepatocytes at any given time, and ΔN(t) is the deviation from nominal caused by the parameter change.

Phase-based sensitivities (PBS) were calculated following the formulations of (Gunawan & Doyle, 2007;Perumal & Gunawan, 2011). Simulations were run with the value of a single parameter increased by 10% of its nominal value within one of the three phases of regeneration: the priming phase (0-6 hours post-PHx), the regeneration phase (12-100 hours post-PHx), and the termination phase (100-200 hours post-PHx).

The simulations were then run again with the same parameter decreased by 10% within the same phase. These two simulations were repeated for every parameter. Sensitivities were estimated as the change in overall liver faction recovered at 300 hours post-PHx normalized to the nominal regeneration profile divided by the percentage change in parameter value for the phase when the change occurs (20%), as shown in Equation 3.2.

$$PBS_i = \frac{\Delta N(t{=}300)/N(t{=}300)}{\Delta p_i/p_i} \tag{3.2}$$

Pulsatile sensitivities (PS) were calculated using an approach modified from (Perumal & Gunawan, 2011). In this modified approach, we altered each model parameter by + or – 10% of the corresponding nominal value at each hour following PHx for one hour, where τ represents the beginning of the time step where the parameter was changed. We estimated the pulsatile sensitivity at each time point after the pulsatile parametric change (at time τ) according to Equation 3.3.

$$PS_i(t,\tau) = \frac{\Delta N(t,\tau)/\mathrm{N(t,\tau)}}{\Delta p_{i,\tau}/p_{i,\tau}} \tag{3.3}$$

While this equation appears similar to that used to calculate DLS, the pulsatile sensitivity values (PS_i) take on nonzero values only after the time of the pulse change in the corresponding parameter value.

3.2.6 Parameter estimation to match Adn-/- regeneration phenotype

To estimate parameters characterizing the Adn-/- mice, Sobol sampling was used to search the parameter space of sensitive model parameters (Bratley & Fox, 1988). Each parameter was allowed to vary from its nominal value over approximately one order of magnitude (10x). Simulations were then run with each of ten thousand

parameter sets, and the resulting regeneration profiles were compared to the experimental Adn-/- mouse regeneration profile generated in this study. Parameter sets generating similar regeneration profiles were then analyzed for common molecular regulation governing tissue behavior. The search of the parameter space resulted in multiple parameter sets that could simulate regeneration profiles similar to that seen experimentally, but these multiple parameter sets contained similar parameters and caused similar molecular regulation. Therefore, parameter sets generating regeneration profiles similar to that observed in the experiments were further explored using a combination of manual manipulation and local optimization (*fminsearch* in Matlab). The parameter set resulting in the lowest mean squared error between simulation and experimental observations of liver regeneration in Adn-/- mice was reported as the parameter set for Adn-/- mice.

3.3 Results

3.3.1 Hepatocyte proliferation is delayed after PHx in Adn -/- mice

The dynamics of liver regeneration in Adn-/- and WT mice after PHx were assessed by BrdU pulse labeling and expression of cell cycle marker proteins between 24-54 hours post-PHx. BrdU incorporation increased in WT mice at 30 hours post-PHx relative to baseline levels. However, Adn-/- mice showed no increase at 30 hours (Figure 3.1 A and B). WT and Adn-/- mice showed similar levels of BrdU incorporation 36 hours post-PHx (Figure 3.1 A and B). Adn-/- mice incorporated significantly more BrdU at 42 hours post-PHx (Figure 3.1 A and B). By 54 hours post-PHx, WT and Adn-/- mice again showed no difference in BrdU incorporation. When compared to WT mice, Adn-/- mice also expressed significantly lower levels of G1-

phase cell cycle markers proliferating cell nuclear antigen (PCNA) and cyclin D1 at 24 hours post-PHx (Figure 3.1 C and D). Both PCNA and cyclin D1 levels were renormalized by 30 hours post-PHx and PCNA levels remained similar at all subsequent times (Figure 3.1 C and D). Similarly, Adn-/- mice expressed cyclin A, an important S phase cyclin, at lower levels than WT mice at 30 hours post-PHx; cyclin A levels were renormalized by 36 hours post-PHx and remained similar at 42 hours (Figure 3.1 C and D). Liver to body weight ratio was assessed as a measure of liver mass recovery. By 54 hours post PHx, both WT and Adn-/- mouse livers had approximately doubled in mass (Figure 3.1E). No significant difference was detected between WT and Adn-/- liver mass recovery at this time.

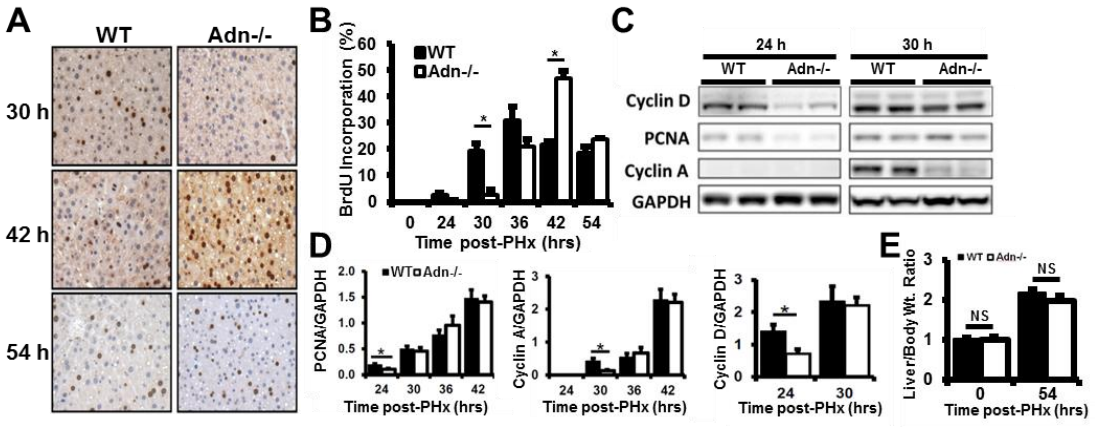

Figure 3.1 Analysis of hepatocyte replication after PHx in WT and adiponectin KO mice. (A) Representative histological sections from mice at various times after PHx and injected with BrdU 2 hrs prior to sacrifice were stained using BrdU-specific antibodies. (B) The percentage of BrdU positive hepatocytes was calculated by quantifying BrdU positive nuclei and total nuclei from 5 representative fields at 20x magnification (n=4/group). (C) Western blot of representative liver samples probed with antibodies specific for cyclin D1, PCNA, Cyclin A and GAPDH. (D) Quantitation of western blots for cyclin D1, PCNA, Cyclin A (n=3/group). (E) Liver to body weight ratio. Data are presented as mean +/- SEM. NS: not significant, * P<0.05, *** P<0.01 adiponectin -/- significantly different from WT.

Taken together, these results suggest that the onset of hepatocyte proliferation after PHx is delayed in Adn-/- relative to WT mice but that the cell cycle may be accelerated in Adn-/- mice to renormalize regeneration after a delayed cell-cycle onset. However, the dynamic changes to molecular balances underlying Adn fine-tuning control of liver regeneration remain unclear.

3.3.2 Pulsatile Sensitivity Analysis reveals critical time-windows of molecular effects on liver regeneration

We pursued a computational modeling approach to investigate which molecular balances are critical to alter regeneration dynamics and the time-windows

over which regenerating hepatocytes are responsive to these signals. We employed Pulsatile Sensitivity Analysis (Perumal & Gunawan, 2011) to analyze a recently developed computational model of liver regeneration (Furchtgott et al, 2009). The computational model simulates liver regeneration as a series of regulatory events initiated in non-parenchymal cells and influencing hepatocyte quiescence, priming and replication (Figure 3.2A). The initiation of regeneration is governed by a mismatch between "metabolic demand" (M) of the organism and the total number of hepatocytes (N) available to meet this demand. In this scheme, the "metabolic load" per hepatocyte (M/N) increases proportional to the mass of the liver removed, initiating non-parenchymal cell activation following PHx. Once activated, non-parenchymal cells respond to liver damage by early induction of IL-6 (representative of the inflammatory milieu observable post-PHx and its effect on hepatocytes), later production of GF (representative of the growth factor environment and effect post-PHx), and ECM remodeling (Figure 3.2A). These molecular signals induce hepatocytes to proceed from quiescence (Q) to a primed state (P), from the primed state to a replicating state (R) to recover lost liver tissue, and finally from primed and replicating states back to quiescence. This computational model uses representative molecular components to describe archetypical classes of signaling during liver regeneration. While the metabolic load parameter has no direct molecular correlate, it likely captures the effects of the molecular drivers of liver metabolism and mitochondrial activity such as AMPK activation or ATP levels or ATP/ADP ratio. Modulation of metabolic load by perturbing this metabolic demand parameter may therefore be considered to reflect a general metabolic challenge.

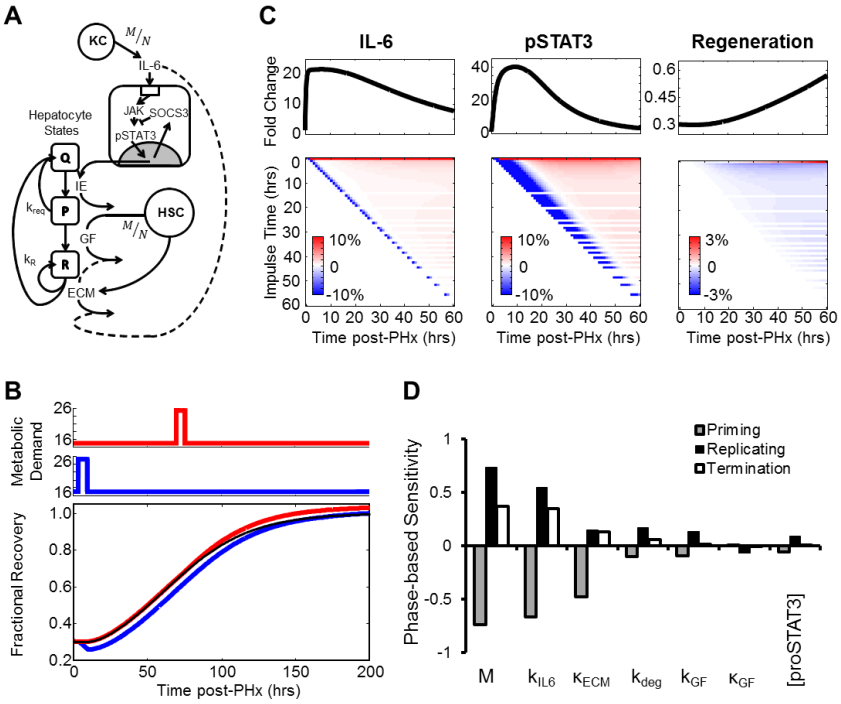

Figure 3.2 Identifying the key control factors through sensitivity analysis of a computational model of liver regeneration. (A) Schematic representation of the network model of liver regeneration following PHx incorporates contributions of non-parenchymal cells to catalyze hepatocyte replication. (B) Pulse changes to the metabolic demand parameter (M) caused delayed regeneration if administered early post-PHx, and enhanced regeneration if administered late post-PHx. (C) (Upper panel) The nominal profiles of IL-6, STAT3 and fractional recovery. (Lower Panel) Hour-long, 50% pulsatile decreases in IL-6 production rate (kIL6) caused a temporary decrease in the IL-6 levels, independent of when the pulsatile change was introduced (note the consistent blue diagonal). Such a temporary reduction in IL-6 led to a much longer and more pronounced decrease in STAT3 phosphorylation, with earlier IL-6 changes leading to longer STAT3 transients, and ultimately delayed regeneration. The earlier the pulsatile reduction in IL-6 and subsequent transient decrease in STAT3, the longer the regeneration deficit persisted. (D) Phase-based sensitivity analysis showed that the timing of alterations to the key controlling factors leads to a phase-dependent effect on overall regeneration. In general, changes to these key factors during the priming phase had opposite effects on regeneration as compared to the effect of changes during the replicating and termination phases.

We initially employed local parametric sensitivity analysis to identify the regulatory balances that control the dynamics of regeneration. We altered each model parameter to +/- 10% of the corresponding nominal value and calculated the normalized sensitivity at each time point according to:

$$S_i(t) = \frac{\left(\frac{\Delta N(t)}{N(t)}\right)}{\frac{\Delta p_i}{p_i}} \tag{3.4}$$

where N(t) is the nominal fraction of hepatocytes at any given time, and ΔN(t) is the deviation from nominal caused by the parameter change. This dynamic sensitivity metric considers how the time profile of liver regeneration responds to changes in the network parameters. We defined liver regeneration profile as "highly sensitive" to a given parameter if the maximum value of the corresponding normalized sensitivity coefficient had a magnitude greater than 0.15 at any time point. Our analysis identified 12 out of 32 parameters as significantly controlling the dynamics of liver regeneration. These included both molecular parameters -- metabolic load (M), IL-6 production rate (kIL6), concentration of monomeric STAT3 ([proSTAT3]), ECM degradation rate by MMPs (κdeg), ECM constitutive degradation rate (κECM), GF production rate (kGF), and GF degradation rate (κGF) -- and physiological parameters governing hepatocyte phenotypic state and apoptosis -- kP, kR, kprol, θap, and βap -- (Figure 3.3).

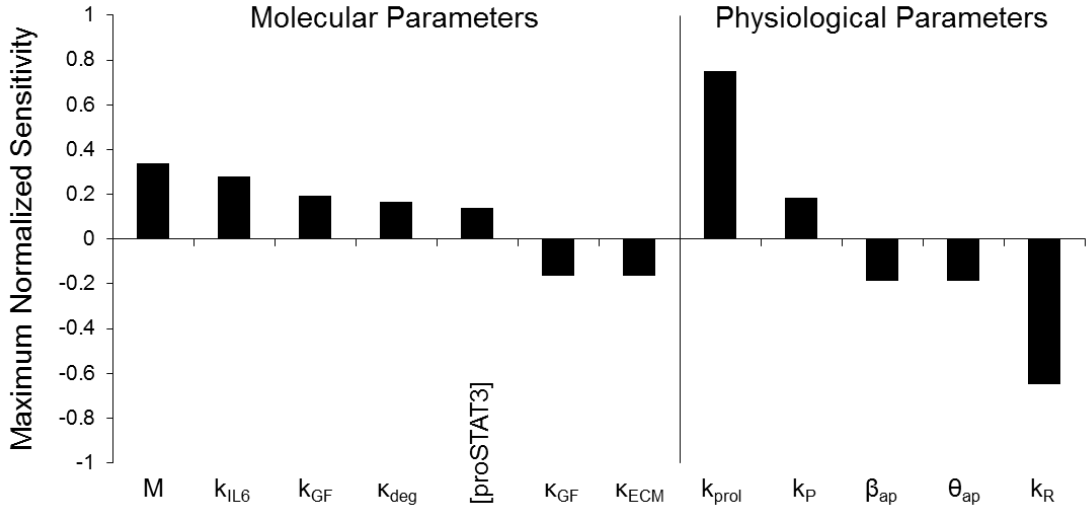

Figure 3.3 Normalized sensitivity values of the top-ranked controlling factors. Overall regeneration was highly sensitive to both molecular and physiological parameters. More molecular parameters were identified as key controlling factors, but the alterations in physiological parameters k_{prol} and k_R produced the largest effects of all parametric changes.

One consideration in the above sensitivity analysis is that the network parameters are altered as a step change throughout the regenerative response time. While the effect on the regeneration is dynamic, it is not possible to deconvolute the changes leading to instantaneous effects vs those altering response at later times. To address this issue, we employed a recently developed Impulse Sensitivity Analysis and modified the scheme to consider finite pulses of parameter changes in defined temporal intervals. In this modified approach, we altered each model parameter by + or – 10% of the corresponding nominal value at each hour following PHx for one hour. We estimated the pulsatile sensitivity at each time point after the pulsatile parametric change according to:

$$S_i'(t) = \frac{\left(\frac{\Delta N(t)}{N(t)}\right)}{\frac{\Delta p_i}{p_i}} \quad (3.5)$$

While this equation appears similar to equation 3.4, the pulsatile sensitivity values (S') take on nonzero values only after the time of the pulse change in the corresponding parameter value. The pulsatile sensitivity analysis revealed that magnitude and timing of changes to parameters were both key controlling factors in fine-tuning the regeneration profile. Among the parameters evaluated for their pulsatile sensitivity, the metabolic demand parameter showed a unique sensitivity profile. A short pulse or longer step increase in metabolic demand caused a decreased early regenerative response post-PHx, but led to an enhanced regeneration response at later times (Figure 3.2B and Figure 3.4).

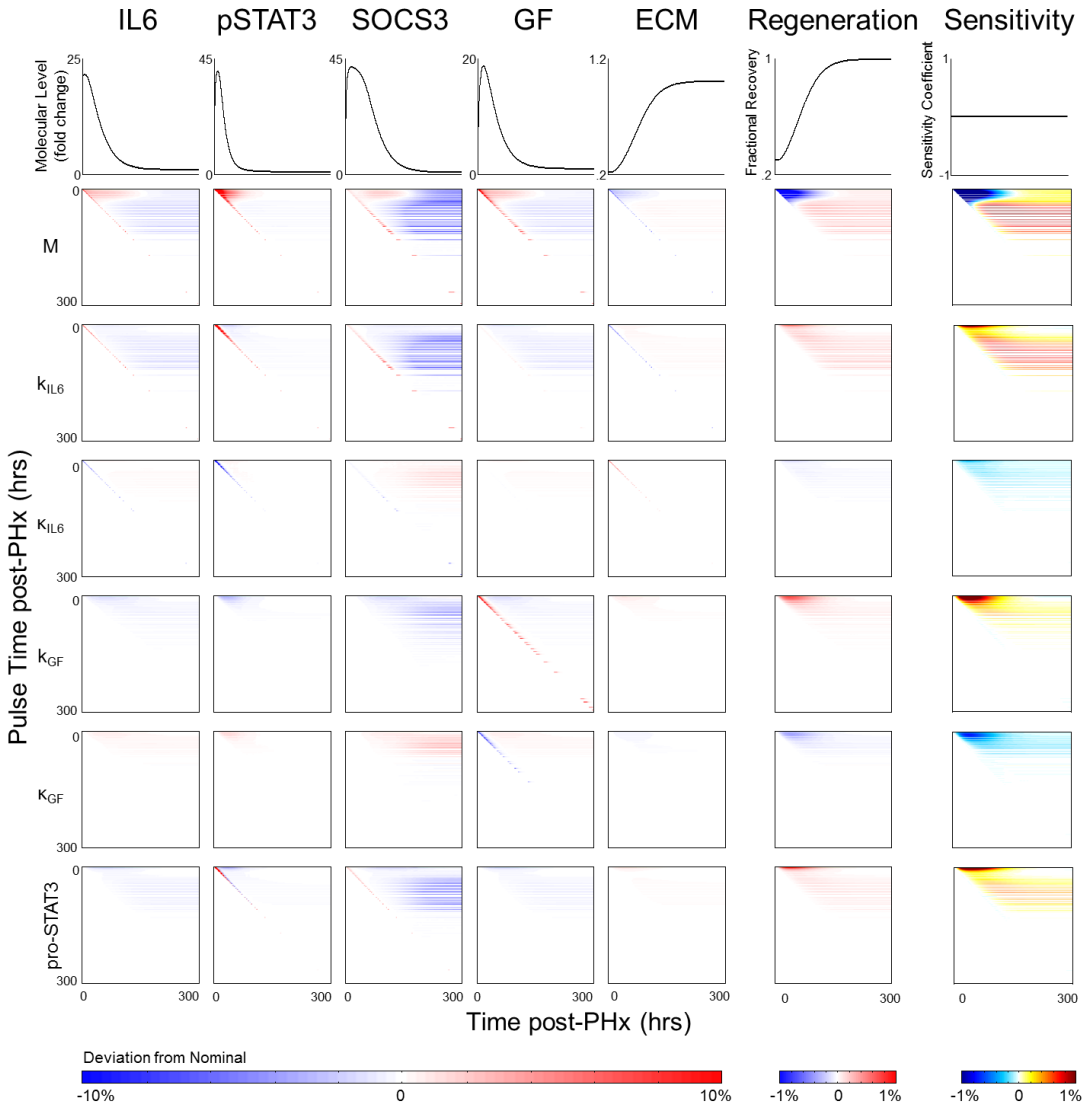
IL6
pSTAT3
SOCS3
GF
ECM
Regeneration
Sensitivity
Molecular Level (fold change)
Fractional Recovery
Sensitivity Coefficient
M
k_{IL6}
κ_{IL6}
k_{GF}
κ_{GF}
pro-STAT3
Pulse Time post-PHx (hrs)
Time post-PHx (hrs)
Deviation from Nominal
-10%
0
10%
-1%
0
1%

Figure 3.4 Time-dependent effects of pulsatile changes to the key controlling parameters on molecular variables as well as overall regeneration. The effect of a 50% pulsatile increase in metabolic demand (M) on overall regeneration was dependent on when the pulse was administered. Early increases during the priming phase led to a transient decrease in the fractional recovery due to a temporary increase in cell death. Later increases in metabolic demand led to a higher overall regeneration, stimulated by increase in replication. Pulsatile increases in IL-6 production (k_{IL6}), growth factor production (k_{GF}), and pro-STAT3 levels led to increased overall regeneration, with differences in magnitude of effects based on when the pulse occurred. Increasing growth factor or IL-6 degradation, in contrast, decreased overall regeneration with a maximum effect occurring when the pulsatile change was introduced in the early phase following PHx.

Such a time interval-dependent effect occurred through multiple processes affected by metabolic demand changes. Within the 0-50 hours post-hepatectomy period, additional increases in the metabolic demand led to a transient increase in hepatocyte apoptosis and delayed regeneration, but a renormalization (or moderately enhanced regeneration) caused by increased IL-6 signaling and hepatocyte priming. Additional increase of metabolic demand at later time intervals between 75-150 hours post-PHx caused increased GF signaling leading to enhanced liver regeneration. In contrast, a 50% impulse decrease in IL-6 production rate caused a transient decrease in IL-6 levels that was quickly renormalized (Figure 3.2C). Downstream STAT3 phosphorylation, however, showed a much larger magnitude decrease that persisted for several hours before renormalization. The time-window during which these changes consistently resulted in observable changes to regeneration profile were limited to the first 50 hours of regeneration (Figure 3.2C). In contrast, a 50% impulse increase in GF production rate caused a sustained increase in hepatocyte number when GF production was increased between 0-50 hours or at certain time points between 50-

127 hours post-PHx (Figure 3.4). These results suggest that fine-tuning signaling dynamics by modulating the timing and temporal balances of non-parenchymal cell activation can have significant functional consequences, with persistent impact on regeneration dynamics and tissue mass recovery.

While all of the molecular parameters apart from metabolic load showed similar pulsatile sensitivity profiles, the key subset identified as significant controlling factors by the parametric sensitivity analysis displayed a phase-dependent sensitivity (Figure 3.2D and Figure 3.4). For example, a transient increase in IL-6 production rate during the priming phase (0-6 hours) caused an early increase in IL-6 levels followed by a persistent decrease below nominal levels. This persistent decrease in IL-6 levels caused a persistently decreasing rate of hepatocyte replication and a blunted overall tissue recovery (Figure 3.5). In contrast, transiently increasing IL-6 production rate during the replication phase (12-100 hours) caused IL-6 levels to remain elevated above nominal levels. This persistent elevation caused a persistently increasing rate of hepatocyte replication and enhanced overall tissue recovery (Figure 3.5). This phase-dependent effect predicts that mistiming of enhanced factor production influences pro- or anti-regenerative effects. Therefore, our computational modeling and sensitivity analysis revealed the dynamic balances of initiation-related and replication-related factors that must be closely regulated to ensure the dynamics and magnitude of the normal liver regeneration profile.

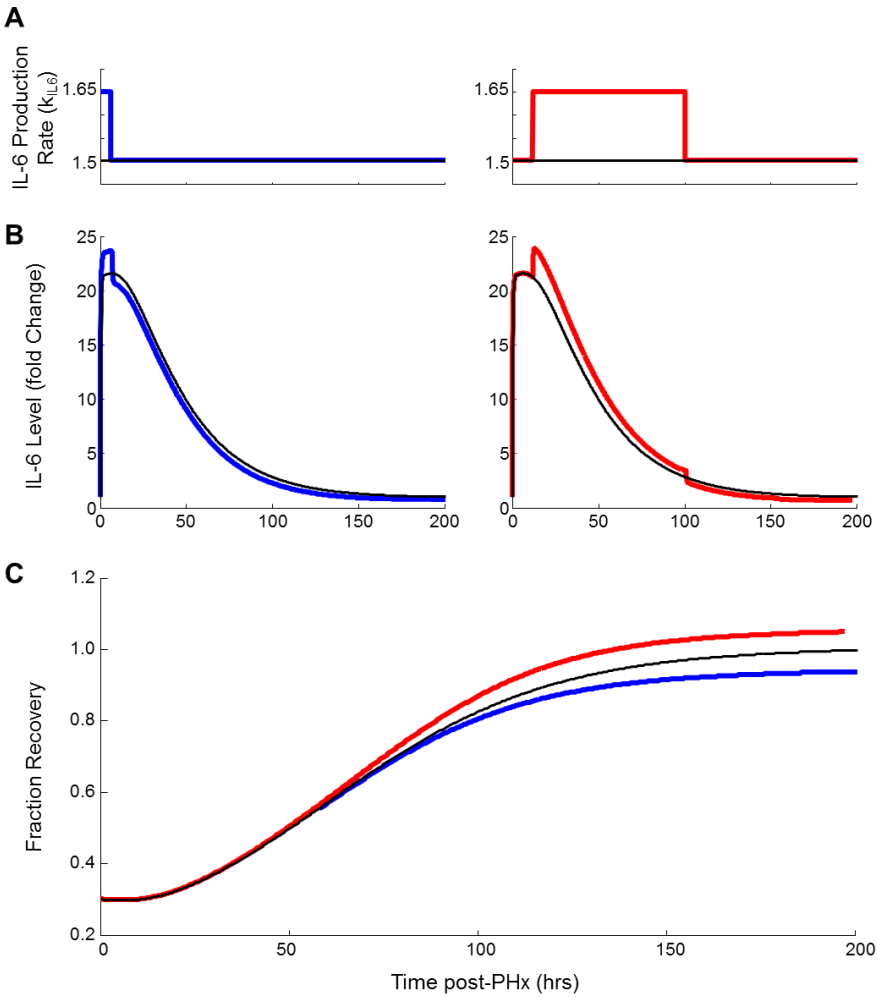

Figure 3.5 Time-dependent effects of transient increases in IL-6 production rate during different phases of liver regeneration. (A) Transient increases in IL-6 production rate (k_{IL6}) during the priming and replication phase. (B) Transiently increasing IL-6 production rate during the priming phase (0-6 hours) caused a transient increase in IL-6 levels followed by a persistent reduction in IL-6 levels. Transiently increasing IL-6 production rate during the replication phase (12-100 hours) caused a sustained increase in IL-6 levels. (C) Persistent reduction in IL-6 levels from increased production during priming caused a persistent decrease in hepatocyte replication rate and a blunted overall tissue recovery. Sustained increase in IL-6 levels caused a persistent increase in hepatocyte replication rate and an enhanced overall tissue recovery.

3.3.3 Computational modeling of the altered regenerative response in the Adn -/- mice reveals the key controlling molecular regulatory balances

We predicted the factors governing molecular control of the Adn-/- regeneration phenotype by considering simultaneous alterations to multiple molecular parameters identified as sensitive in the above analyses. Our Monte Carlo approach ensured efficient sampling coverage of the physiologically reasonable parameter space by using a Sobol sampling strategy to modify sensitive parameter values simultaneously (Bratley & Fox, 1988). We analyzed the simulation results for similar model parameter values that led to the Adn-/- regeneration phenotype. Our results revealed that the magnitude and timing of IL-6 signaling controlled the priming response of hepatocytes and therefore fine-tuned the timing of initiation of regeneration (Figures 3.6 – 3.8). Timing and magnitude of the GF peak controlled the hepatocyte entry into the replicating phase and therefore fine-tuned the overall tissue regeneration rate and magnitude (Figures 3.6 – 3.8).

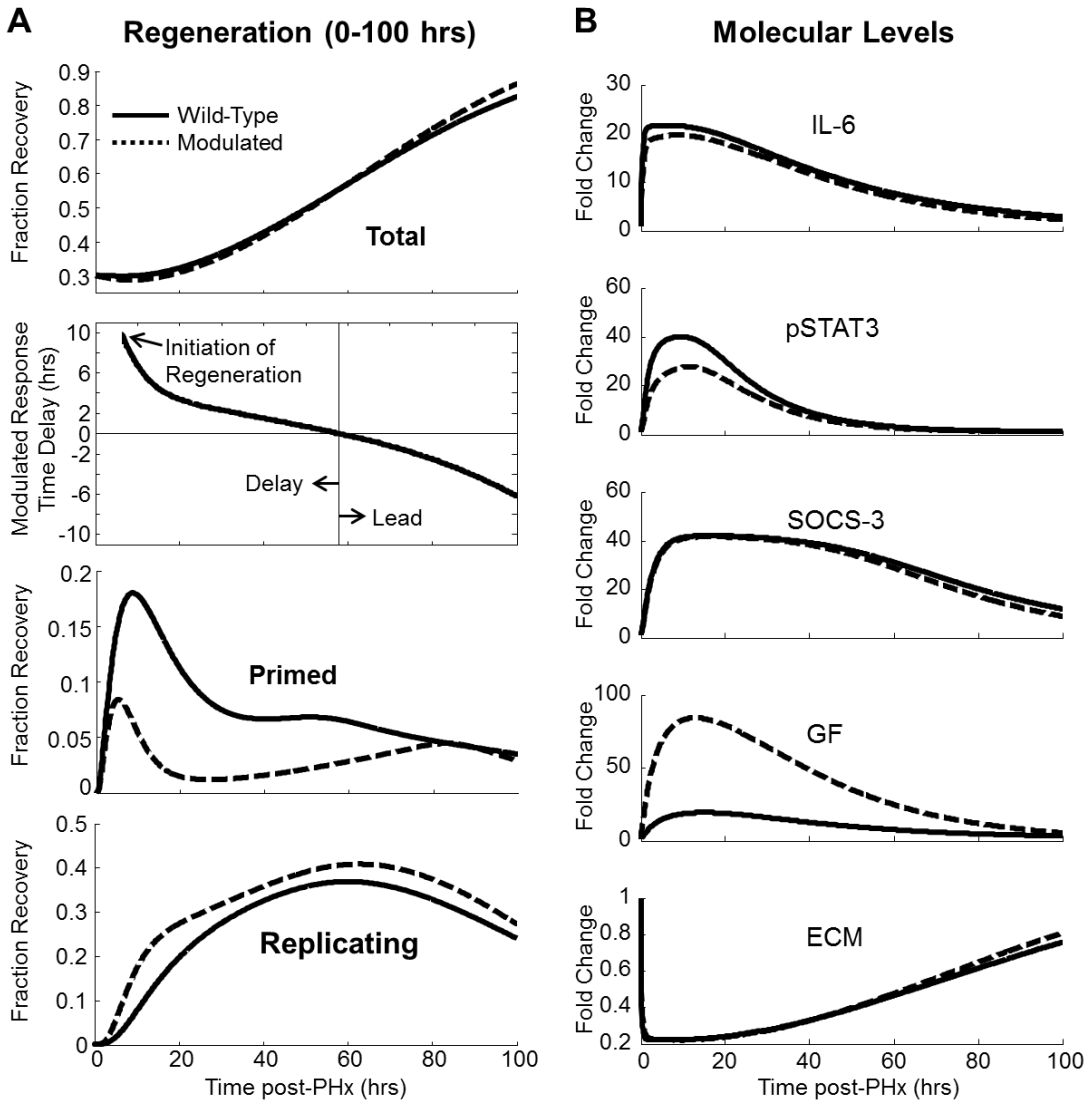

Figure 3.6 Cells entering the replicating phase too early as compared to the experimental measurements of Adn-/- hepatocyte entry into the cell cycle. (A) Hepatocyte replication was delayed early post-PHx and recovered by 60 hours post-PHx, but with replication levels higher than seen experimentally in Adn-/- mice. (B) This high replication was induced by increased GF signaling.

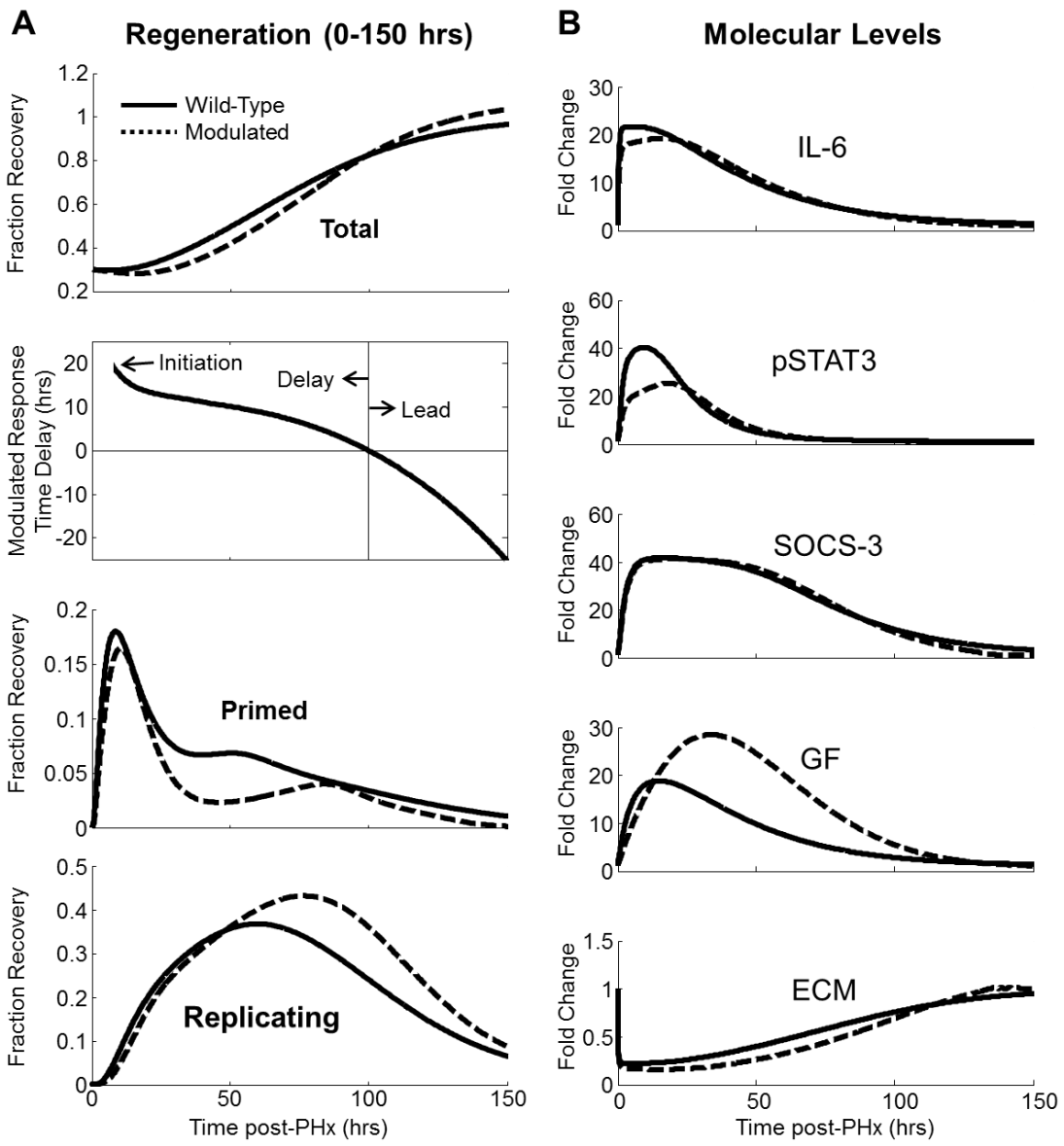

Figure 3.7 Regeneration profile renormalizing too late as compared to the experimental measurements of Adn-/- liver to body weight recovery. (A) The replication profile appeared to match experimental measures of Adn-/- hepatocyte cell cycle entry, but renormalization occurred well beyond 60 hours post-PHx due to the decreased priming response early post-PHx and the length of the cell cycle. (B) The decreased priming was caused by decreased IL-6 signaling decreasing STAT3 phosphorylation.

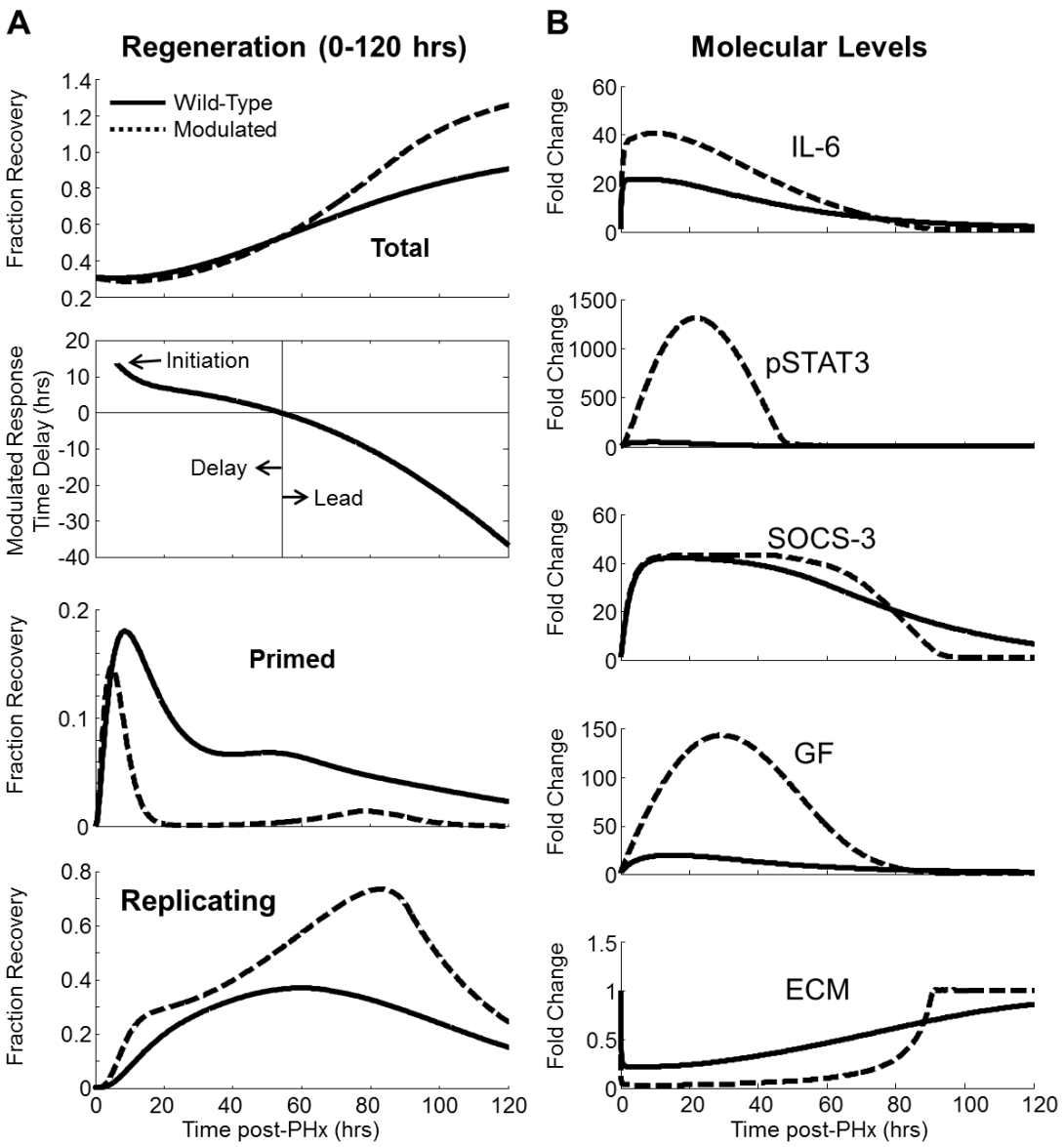

Figure 3.8 Regeneration profile with an initial delay and an overshoot. (A) These parameters induced a transient wave of apoptosis early post-PHx coupled with enhanced replication, which led to a delayed liver recovery but an increase in final liver recovery. (B) This profile was caused by a large increase in apoptosis (not shown), enhanced IL-6 signaling and STAT-3 phosphorylation, and large increases in GF signaling.

However, modulating these molecular parameters did not adequately account for the observed regeneration profile of Adn-/- mice. In all of the simulated scenarios, the hepatocytes entered the cell cycle either too early (Figure 3.6), renormalized too late (Figure 3.7), or showed a large increase in cell death in the early phase post-PHx coupled with a large overshoot in recovery (Figure 3.8). These regeneration profiles were inconsistent with the experimental observations in the Adn-/- mice. Because the length of the cell cycle was modeled as lasting approximately 30 hours, any molecular changes that allow renormalization of regeneration by 54 hours cause regeneration to increase earlier than was seen experimentally in the Adn-/- mice. To account for this difference, we increased the replication rate of hepatocytes in the Adn-/- condition. By increasing hepatocyte replication rate by 15%, the model captured the experimentally observed regenerative profile, including a delay in initiation of regeneration, similar replication by 36 hours post-PHx, and renormalization by 54 hours post-PHx (Figure 3.9A). Table 3.1 contains the key parameters and their modified values for which the model simulations exhibit an Adn-/- regeneration phenotype that is consistent with the experimental observations.

Table 3.1: Modified parameter values

Parameter	**Original Value**	**Adn-/- Value**
M	16.8	19.3365
k_{IL6}	1.5	0.7326
κ_{IL6}	0.9	0.0017
κ_{deg}	7	15.2973
κ_{ECM}	33	37
k_{GF}	0.113	0.04
κ_{GF}	0.23	0.05
k_{up}	0.06	0.0561
k_{prol}	0.02	0.023

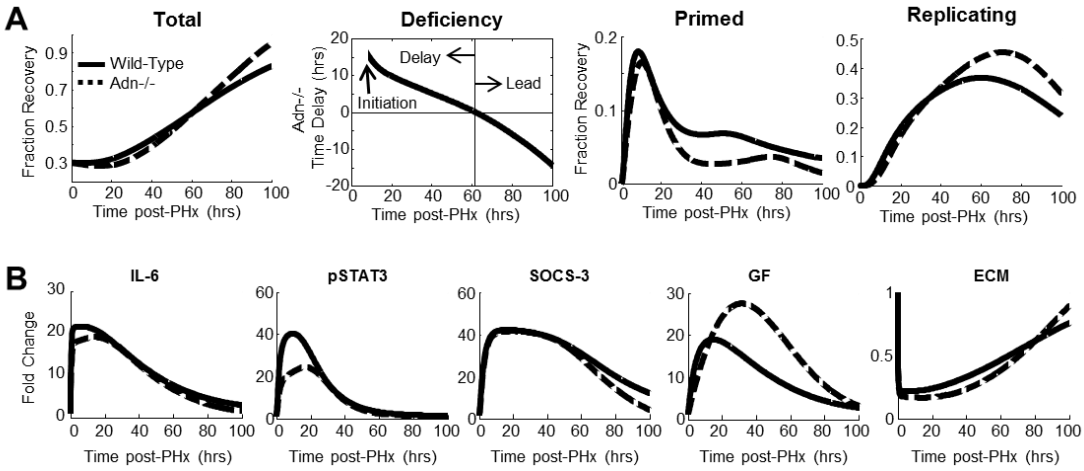

Figure 3.9 Modeling the dynamics of the Adn-/- regeneration phenotype. (A) Simulated profile for Adn-/- mice showed delayed onset of liver regeneration, followed by renormalized liver mass at approximately 60 hours post-PHx and enhanced recovery thereafter. This profile was mediated by delayed and suppressed priming as well as replication during the first 20 hours post-PHx and enhanced replication beyond 30 hours post-PHx. (B) The Adn-/- phenotypic changes were governed by decreased IL-6 signaling in the priming phase, causing decreased STAT3 phosphorylation, and increased GF signaling during peak hepatocyte replication.

Simulations with these parameters predicted that one of the key features driving the Adn-/- regeneration phenotype was a slightly decreased IL-6 level, detectable by 3 hours after PHx (Figure 3.9B). This moderate decrease (~2% decrease in peak levels) led to a simultaneous decrease in tyrosine phosphorylation of STAT3 by 3 hours post-PHx (Figure 3.9B). Despite this decrease, the levels of phosphorylated STAT3 (pSTAT3) remained at sufficient levels to induce production of Suppressor Of Cytokine Signaling-3 (SOCS-3) at levels nearly identical to that in the wild-type mice (Figure 3.9B). The combination of lower IL-6 and normal SOCS-3 synergistically inhibited STAT-3 phosphorylation (~25% decrease in peak levels) and thus its

activity, leading to the impaired priming response in simulated Adn-/- mice underlying the delayed regeneration. It should be emphasized that the IL-6 levels in the model are representative of the production of multiple inflammatory molecules, release, diffusion, receptor binding, and cellular response. Hence, the effects of changing the cytokine milieu post-PHx may be seen as relatively small changes in many inflammatory signaling levels instead of an isolated change in the IL-6 protein levels.

Our simulations pointed to an increase in the GF levels, detectable by 12 hours post-PHx and peaking at approximately 24 hours post-PHx as another key feature driving the Adn-/- regeneration profile (Figure 3.9B). This increased GF bioavailability stimulated the hepatocytes in the primed state to begin replication. Our analysis predicted that an increased number of replicating hepatocytes in Adn-/- mice, coupled with an increase in proliferation rate, can compensate for the initial delay in regeneration. Similar to the modeled changes in the IL-6 levels, increased GF levels in the simulated scenarios do not necessarily represent a single growth factor but rather reflect a strengthening of the growth factor milieu and their effects on hepatocyte replication. Based on the model predictions, we postulate that an increased bioavailability of growth factors associated with cell-cycle progression may also contribute to the enhanced cell-cycle rate seen in Adn-/- mice.

3.4 Discussion

The partial hepatectomy studies reported here demonstrate that Adn-/- mice have a delayed onset of hepatocyte proliferation compared to WT mice after PHx but show no difference in BrdU incorporation or liver mass recovery 54 hours after PHx. Our simulations using the computational model of liver regeneration suggest that the loss of Adn suppresses the processes associated with priming of the liver, at least in

part through a deregulation of STAT3 signaling. In our simulations of Adn-/- mice, however, cell-cycle kinetics eventually accelerate to normalize the regenerative response. Based on model simulations, we predict that this acceleration is likely due to sustained increases in critical pro-proliferative growth factors.

Chapter 4

TESTING MODEL PREDICTIONS IN ADIPONECTIN KNOCKOUT MICE AND CONTROLS

This chapter was adapted from Correnti, J. M., **Cook, D.**, Aksamitiene, E., Swarup, A., Ogunnaike, B., Vadigepalli, R., & Hoek, J. B. (2015). Adiponectin fine-tuning of liver regeneration dynamics revealed through cellular network modelling. *The Journal of physiology*, *593*(2), 365-383. Experimental work featured in this chapter was performed predominantly by J.M. Correnti with some experiments performed by E. Aksamitiene and A. Swarup.

4.1 Introduction

The utility of models lies in their ability to describe the physical world. As a descriptor of a real process, one way to validate a model is to compare model predictions with results from real-world processes. In chapter 3, we describe delayed but accelerating regeneration kinetics in Adn-/- mice and the use of a computational model of liver regeneration to predict the dysregulation underlying these dynamics. Based on model simulations, we predict that the regeneration dynamics in Adn-/- mice are due to (1) decreased cytokine signals transduced by hepatocytes during the priming phase of regeneration and (2) increased growth factor bioavailability at later times post-PHx. This chapter describes our experimental efforts testing these predictions.

4.2 Materials and Methods

4.2.1 Animals

All animal studies were approved by the Institutional Animal Care and Use Committee (IACUC) at Thomas Jefferson University. Jefferson's IACUC is accredited by the Association for Assessment and Accreditation of Laboratory Animal Care and experiments were designed using the Guide for the Care and Use of Laboratory Animals.

10-12 week old male Adn-/- mice (B6.129-*Adipoq*^{tm1Chan}), bred from mice kindly donated by Dr. Lawrence Chan, or C57BL/6J mice (Jackson Laboratories, Bar Harbor, Me) underwent partial hepatectomy based on surgical methods outlined by Mitchell and Willenbring (Mitchell & Willenbring, 2008). Briefly, animals were anesthetized by inhalation of 5% isoflurane in an induction chamber and anesthetic plane was confirmed by toe pinch. Anesthesia was maintained during surgery by continual inhalation of 2% isoflurane administered by nose cone. A midline incision was made followed by the sequential ligation and excision of the left-lateral and medial lobes of the liver. The abdominal cavity was rinsed with warm lactated Ringer's solution, the abdominal muscle layer was sutured and the skin was closed with wound clips. Following surgery, animals were given subcutaneous lactated Ringer's solution (1 mL/animal) and placed in a fresh cage under a heat lamp with ad libitum access to hydrogel (Contact ClearH_20, Portland, Me) and food. At specified times after PHx, animals were anesthetized with isoflurane as described for partial hepatectomy (induction and maintenance). While anesthetized, animals were weighed and sacrificed. The livers were either immediately (within 10 sec) freeze clamped using liquid nitrogen-cooled aluminum clamps as previously described (Crumm et al,

2008), preventing rapid post-mortem changes in cytokine or growth factor levels and protein phosphorylation, or the livers were fixed in 10 percent neutral buffered formalin (NBF) for assessment of BrdU labeling. For determination of liver to body weight ratios, the liver was dissected out and weighed prior to freeze clamping.

Blood was collected from the tail vein of live animals and from the vena cava under anesthesia at sacrifice. Collected blood was incubated at room temperature for 30 min, then centrifuged at 1500 rpm for 5 minutes. Serum was isolated and flash frozen for further analysis. In some cases, animals were given intraperitoneal injections of Bromodeoxyuridine (BrdU) solution (Sigma, St. Louis, Mo) (150 mg/kg) in sterile 0.9 percent saline two hours prior to sacrifice. For rosiglitazone treatment, animals were administered rosiglitazone (10 mg/kg, Cayman Chemical, Ann Arbor, MI) or vehicle (1:1 mixture of 1x phosphate buffered saline and polyethylene glycol, Sigma) by gavage twice daily beginning 2 days before surgery.

4.2.2 Biochemical analysis

For Western blotting, tissue lysates were generated by homogenizing frozen tissue in RIPA buffer (Sigma) supplemented with phosphatase and protease inhibitor cocktails (Sigma). Protein was normalized using BCA Protein Assay Reagent (Pierce Biotechnology, Rockford, IL). 20 µg of protein was loaded onto an SDS-PAGE gel and Western blotting for cell cycle markers and pSTAT3/STAT3 was performed as previously described (Crumm et al, 2008). Alternatively, for comparison of growth factor expression time-course, 50 µg of protein was resolved by LDS-PAGE, transferred onto nitrocellulose membrane using Multi-Strip Western blotting approach as described previously (Aksamitiene et al, 2007) and probed with mouse monoclonal antibodies against HGF (SBF5) (Thermo Fisher Scientific, Rockford, IL), FGF-2 (6)

(sc-136255, Santa Cruz Biotechnology, Dallas, TX), ANG I (C-1) (sc-74528, Santa Cruz Biot.), GAPDH (6C5) (EMD Millipore, Billerica, MA) or rabbit polyclonal antibodies against β-Actin (D6A8) (Cell Signaling, Danvers, MA). ELISA kits were used for measurement of adiponectin (B-Bridge International) and TNFα (eBioscience, San Diego, CA) according to manufacturer's instructions. Transcription factor binding activity was assessed from nuclear extracts prepared from frozen tissue using a nuclear extraction kit (Origene, Rockville, MD). NF-κB DNA binding activity in 100 µg of nuclear extract was measured using the NF-κB transcription factor assay kit (Cayman Chemical) according to manufacturer's instructions. Some samples were sent to Raybiotech for analysis of cytokine and chemokine levels using Quantibody® Multiplex ELISA Array (Raybiotech, Norcross, GA).

For RT-PCR analysis, RNA was extracted from frozen tissue using the RNeasy RNA extraction kit (Qiagen, Valencia, CA, USA). 2 µg of RNA was reverse transcribed with EasyScript Plus Reverse Transcriptase (Applied Biological Materials Inc.). cDNA was preamplified with TaqMan PreAmp Master Mix (Applied Biosystems, Foster City, CA, USA) and PCR reactions were performed using BioMark™ Dynamic Arrays (Fluidigm, South San Francisco, CA, USA). Primer sequences are shown in Table 4.1. CT values were calculated using Real-Time PCR Analysis software (Fluidigm) and normalized to the expression of housekeeping genes TBP and β2-microglobulin using the established -ΔΔCT method (Livak & Schmittgen, 2001a).

Data were compared using Student's t-test on raw data (BrdU incorporation and liver-to-body weight ratios) or log-transformed data (molecular measurements).

Paired statistics were used when appropriate. Data are presented as mean +/- standard error of the mean (SEM).

Table 4.1 Primer sequences

Primer	Foreword	Reverse
SOCS3	CTACGCATCCAGTGTGAGGG	TGAGTACACAGTCGAAGCGG
β2-Microglobulin	GTCGCTTCAGTCGTCAGCAT	TTTCAATGTGAGGCGGGTGG
TBP	CCCCTTGTACCCTTCACCAAT	GAAGCTGCGGTACAATTCCAG

4.3 Results

4.3.1 Biochemical analysis revealed an altered balance of cytokine and growth factor profiles in Adn-/- mice, consistent with computational model predictions

We analyzed biological correlates of the predicted control factors from the computational analysis. We focused on cytokine production and response during priming (0-6 hours post-PHx) and growth factor levels leading up to and during peak hepatocyte replication (6-42 hours post-PHx). We evaluated the changes in the inflammatory cytokines TNFα and IL-6 as well as several growth factors implicated in liver repair: hepatocyte growth factor (HGF), Angiogenin-1 (Ang-1), and fibroblast growth factor 2 (FGF-2 or bFGF). TNFα and IL-6 are the main inflammatory-type molecules identified as priming hepatocytes to enter the cell cycle. HGF is a potent mitogen and strongly contributes to hepatocyte entry into the cell cycle (Michalopoulos, 2007a;Taub, 2004a). Ang-1 contributes to regulation of angiogenesis in a variety of pathological conditions and has been shown to be involved in several

processes involved in liver recovery from hepatectomy, including wound healing and negative regulation of inflammation (Lee et al, 2014;Pan et al, 2012). In contrast to these two growth factors, FGF2 is not typically associated with liver repair, and genetic deletion does not impair regeneration post-PHx (Sturm et al, 2004). When FGF2 is deleted, however, VEGF increases post-PHx above that in WT mice, indicating that FGF2 may act synergistically with VEGF to maintain liver architecture, activate non-parenchymal cells, and induce hepatocyte replication.

Levels of TNFα protein, a driver of priming following PHx, were measured in liver tissue lysates. TNFα levels declined 1 hour after PHx in Adn-/- mice (Figure 4.1A). Both WT and Adn-/- mice showed reduced TNFα levels by 3 hours after PHx that remained reduced relative to baseline levels 6 hours after PHx (Figure 4.1A). No difference in liver TNFα levels was noted between WT and Adn-/- at 3 or 6 hours post-PHx (Figure 4.1A). Our data are consistent with membrane-bound TNFα present at baseline being cleaved and degraded following receptor activation. Serum IL-6 levels were significantly elevated relative to baseline levels at 3 and 6 hours after PHx in both WT and Adn-/- mice, with the peak observed levels occurring 3 hours after PHx (Figure 4.1B). No significant differences in IL-6 levels were noted between WT and Adn-/- mice (Figure 4.1B).

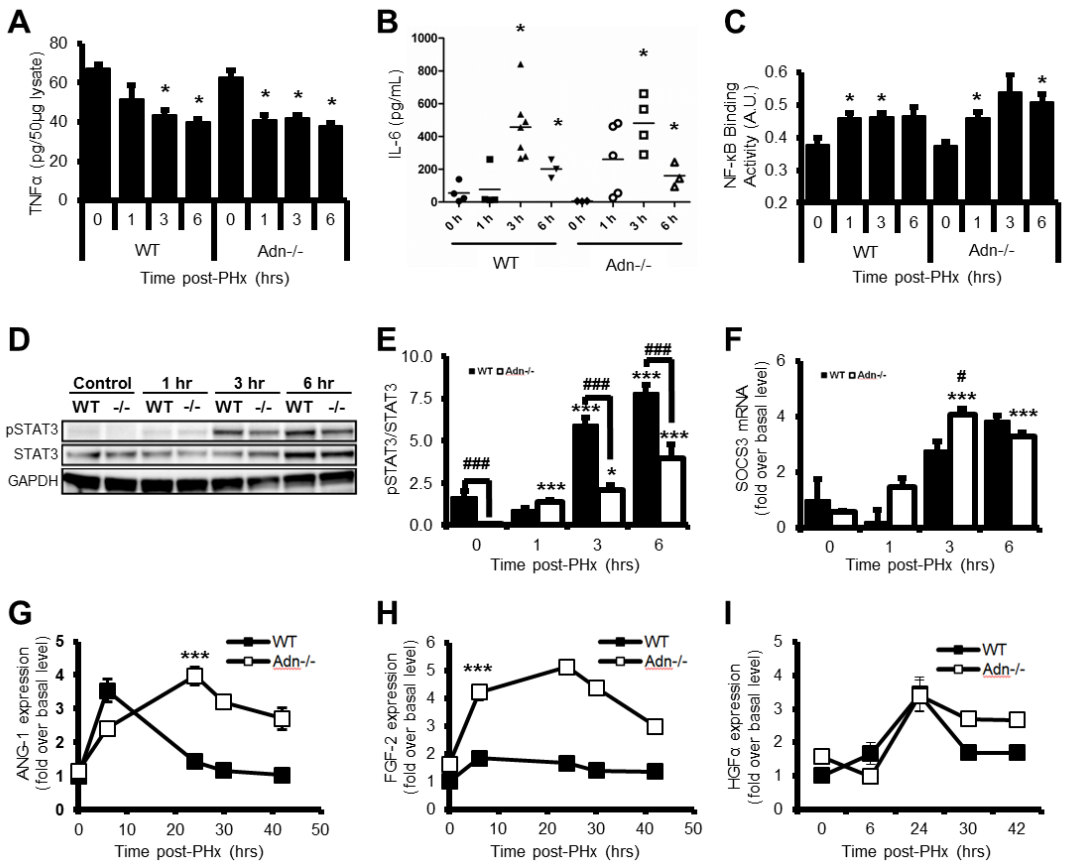

Figure 4.1 Altered TNFα and IL-6 signaling and enhanced growth factor kinetics following PHx in the Adn-/- mice. (A) TNFα protein levels after PHx were measured in liver lysates by ELISA and normalized to total sample protein levels. (B) Serum IL-6 levels were analyzed by Quantibody® Multiplex ELISA Array. Each point represents an individual animal and horizontal bars represent mean IL-6 levels at each time point. (C) NF-κB DNA binding activity in liver nuclear extracts. (D) Western blot of representative liver samples probed with antibodies specific for phosphor-STAT3 (Tyr 705), STAT3 protein and GAPDH. (E) Quantitation of pSTAT3 normalized to total STAT3 protein (n=3/group). (F) SOCS3 transcripts were assessed by RT-PCR and normalized to WT control transcript levels. (G) Quantitation of Western blots of liver lysates for ANG-1. (H) Quantitation of Western blots of liver lysates for FGF-2. (I) Quantitation of Western blots of liver lysates for HGFα. Data are presented as mean +/- SEM. *: $p<0.05$, ***: $p<0.01$ compared with control of respective genotype; #:$p<0.05$, ###: $p<0.01$ Adn -/- different from WT at same time point (n=3/group).

We assessed intracellular response to these cytokines by measuring NF-κB DNA binding and Tyrosine 705 phosphorylated STAT3 (pSTAT3), important mediators of TNFα and IL-6 action, respectively (Fausto et al, 2006). A significant increase in NF-κB DNA binding activity was observed 1 hour after PHx in both Adn-/- and WT mice (Figure 4.1C), simultaneous with the observed reduction in tissue levels of TNFα protein (Figure 4.1A). NF-κB activity remained elevated at 3 and 6 hours after PHx, with no significant differences in NF-κB DNA binding activity detected between WT and Adn-/- mice (Figure 4.1C). Although pSTAT3 levels at baseline were low in both genotypes, Adn-/- mice had significantly lower baseline pSTAT3 level than WT mice (Figure 4.1D and E). pSTAT3 levels increased relative to baseline levels in Adn-/- but not WT mice 1 hour after PHx (Figure 4.1D and E). Liver pSTAT3 was significantly elevated in WT mice relative to baseline at 3 and 6 hours after PHx (Figure 4.1D and E), coinciding with elevated serum IL-6 levels (Figure 4.1B). Despite similar IL-6 levels in WT and Adn-/- mice at 3 and 6 hours after PHx (Figure 4.1B), pSTAT3 was significantly lower in Adn-/- mice than WT mice at these times (Figure 4.1D and E), possibly leading to reduced hepatocyte priming.

To assess factors that could contribute to these reduced pSTAT3 levels, we analyzed transcript levels of SOCS-3, which codes for an inhibitor of STAT-3 phosphorylation (Fausto et al, 2006). At 3 hours after PHx, SOCS-3 transcripts in Adn-/- mice were elevated four-fold over baseline levels and were significantly higher than in WT mice (Figure 4.1F), coincident with reduced pSTAT3in Adn-/- mice. To test the model prediction of higher growth factor signaling in Adn-/- mice, we measured levels of multiple growth factors known to influence liver regeneration:

Ang-1, FGF-2, and HGF. We observed a transient elevation in Ang-1 levels in WT mice at 6 h, however Adn-/- mice showed significantly elevated and persistent Ang-1 levels at 24, 30 and 42 hours after PHx (Figure 4.1G). Adn-/- mice also showed FGF-2 levels higher than WT mice at all times examined after PHx (Figure 4.1H). Expression of HGF proceeded similarly in WT and Adn-/- mice up to 24 hours post-PHx. The increase in HGF levels persisted in Adn-/- mice, however, at both 30 and 42 hours post-PHx (Figure 4.1I), suggesting a sustained HGF signal in Adn-/- mice. Thus, our results show decreased STAT3 phosphorylation during the priming phase coupled with sustained elevation in several growth factors, consistent with our model predictions of their putative contributions to the altered Adn-/- regeneration phenotype. Increased levels of SOCS-3 may contribute to decreased STAT3 phosphorylation, which may induce lower hepatocyte priming. Additionally, elevated growth factors in Adn-/- mice coincident with accelerated cell cycle progression provide a potential mechanism underlying the observed acceleration of cell cycle progression in Adn-/- animals.

4.3.2 Computational analysis predicts that overexpression of adiponectin disrupts the regeneration by dysregulating the cytokine and growth factor profiles

We speculated that Adn-mediated fine-tuning of liver regeneration may be nonlinear, with increasing Adn levels leading to profoundly different effects than that of lowering Adn levels by the same degree. We explored this possibility using the computational model by simulating the putative effects of increased Adn levels during liver regeneration. We evaluated the effect of deviations to parameters in opposite direction to those required for matching the Adn-/- regeneration. This scenario approximated an increase of Adn to twice the normal physiological levels of serum

Adn prior to PHx. The resulting regeneration profile showed that increased Adn led to an initially accelerated regeneration (6-12 hours post-PHx) followed by a suppression of tissue mass recovery (Figure 4.2A).

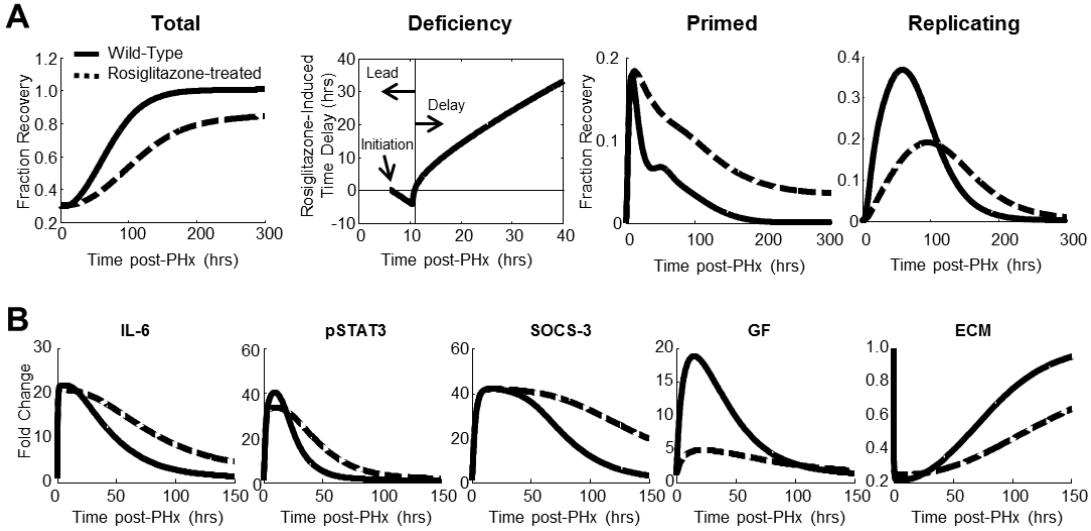

Figure 4.2 Modeling the regeneration dynamics corresponding to the rosiglitazone-induced supraphysiological Adn phenotype. (A) The key controlling factors corresponding to the Adn-/- phenotype were altered in the opposite manner to simulate the effect of increase in Adn levels. Simulated profile for rosiglitazone-treated mice showed suppressed liver regeneration. Although rosiglitazone treatment initially caused a slight lead in liver recovery due to increased priming, ultimately reduced replication suppressed liver recovery from PHx. (B) These phenotypic changes were governed by sustained IL-6 signaling but decreased GF signaling throughout regeneration.

The underlying molecular changes, however, were not merely the opposite of that of the Adn-/- scenario. Our simulation results revealed that increasing Adn levels will lead to a relatively minor decrease in IL-6 signaling and STAT-3 phosphorylation during the first 12 hours post-PHx, without significant effect on the hepatocyte

priming response during this time (Figure 4.2B). Increasing Adn levels also lengthened the priming response by sustaining IL-6 signaling and STAT-3 phosphorylation post-PHx, detectable by 48 hours post-PHx. In spite of this increased priming response, our simulations predicted that GF levels will be decreased at all times post-PHx counteracting any potentially beneficial effects of increased priming and leading to deficient regeneration in mice with increased Adn levels.

4.3.3 Rosiglitazone-induced super-physiological levels of adiponectin inhibited hepatocyte replication in WT but not Adn-/- mice

We tested the model predictions on the effects of elevation of Adn on hepatocyte replication after PHx by pharmacologically increasing serum Adn levels in WT and Adn-/- mice. We utilized rosiglitazone, an anti-diabetic drug known to elevate serum Adn levels (Nawrocki et al, 2006;Tao et al, 2010). Animals were administered rosiglitazone (10mg/kg) or vehicle by gavage twice a day during the two days preceding PHx. Blood samples were taken before treatment and at harvest, and livers were assessed for BrdU incorporation and cyclin A expression at the peak of S phase, 36 hours after PHx. Rosiglitazone treatment was associated with a 60 percent elevation in serum Adn in WT mice relative to controls both before surgery and at harvest (Figure 4.3A).

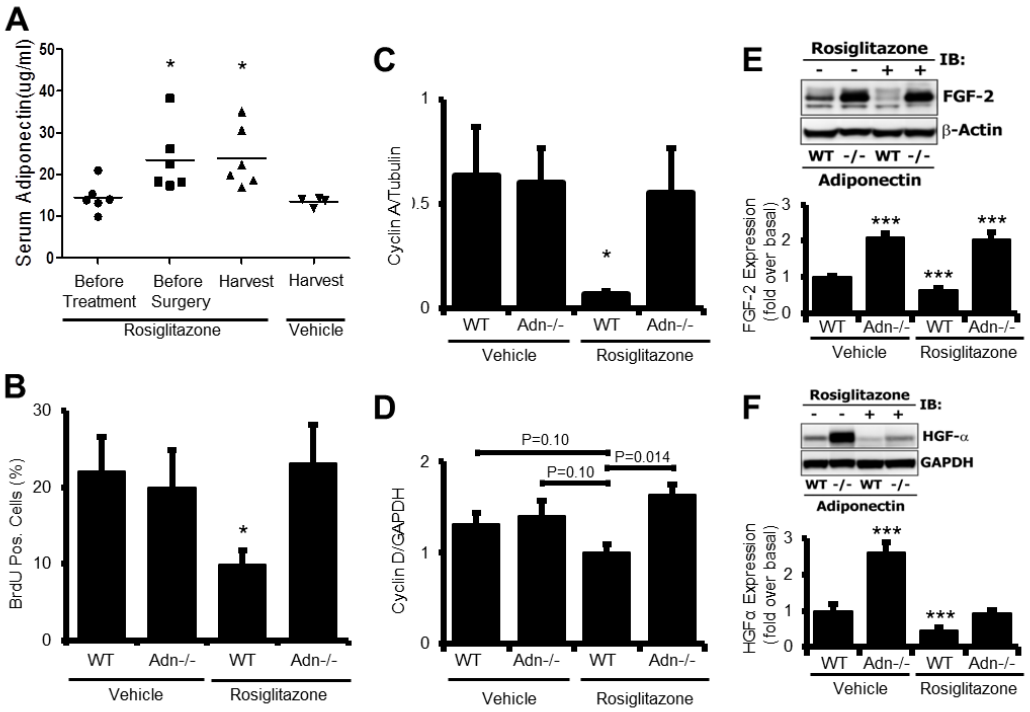

Figure 4.3 Effects of rosiglitazone treatment on hepatocyte replication after PHx in WT and Adn -/- mice. (A) Serum samples taken from tail blood of WT mice at various times were assessed for adiponectin by ELISA. (B) The percentage of BrdU positive hepatocytes was calculated from liver sections stained for BrdU and quantifying BrdU positive nuclei and total nuclei from 5 representative fields at 20x magnification (n=4/group). (C) Quantitation of Western blots for cyclin A (n=3/group). (D) Quantitation of Western blots for Cyclin D1 (n=3/group). (E) Western blot of representative liver samples probed with antibodies specific for FGF-2 and β-Actin. (Lower) Quantification of Western blots for FGF-2 (n=3/group). (F) Western blot of representative liver samples probed with antibodies specific for HGF-α and β-Actin. (Lower) Quantification of Western blots for HGF-α (n=3/group). Data are presented as mean +/- SEM. ***P<0.01* P<0.05 significantly different from WT veh treated. ### P<0.01 compared to vehicle treated Adn-/-.

No serum Adn was detected in Adn-/- mice at any time, which is consistent with previous studies of rosiglitazone effects in Adn-/- mice (Tao et al, 2010).

Rosiglitazone treatment was associated with significant reductions in both BrdU incorporation (Figure 4.3B) and cyclin A protein levels (Figure 4.3C) 36 hours after PHx in WT mice compared to vehicle-treated controls. Adn-/- mice showed no differences relative to vehicle-treated controls (Figure 4.3C and D). Cyclin D1 protein levels were also reduced in rosiglitazone-treated WT mice relative Adn-/- mice (Figure 4.3D).

We additionally investigated the effects of elevated Adn on growth factors at 36 hours post-PHx. Consistent with the model-based predictions, rosiglitazone treatment decreased both FGF-2 and HGF levels in WT animals at 36 hours post-PHx (Figure 4.3E and F). Adn-/- animals, however, showed a more complex response with no change to FGF-2 levels but a marked decrease in HGF levels (Figure 4.3E and F). This indicates that in addition to stimulating Adn to decrease HGF levels, rosiglitazone may both indirectly (through Adn) and directly inhibit HGF production. This is in direct conflict with a recent study reporting that rosiglitazone induces HGF production in vitro in isolated lung fibroblasts (Bogatkevich et al, 2012). Other studies, however, have found that rosiglitazone treatment in vitro inhibits HGF production by patient-derived primary effusion lymphoma cells (Bhatt et al, 2010). Together with our data, these studies indicate potential cell or tissue-type specific effects of rosiglitazone treatment on HGF production.

Our data show that rosiglitazone treatment elevates serum Adn levels in WT mice and, consistent with model-based predictions, inhibits PHx-induced GF bioavailability, cyclin A expression, and BrdU incorporation in WT mice. Rosiglitazone-treated Adn-/- mice, on the other hand, show no inhibition of cyclin A expression or BrdU incorportation but a differential GF response to PHx, with normal

levels FGF-2 and low levels of HGF (compared to untreated Adn-/- mice) at 36 hours post-PHx. These results suggest that elevated Adn inhibits hepatocyte proliferation through decreasing growth factor response to PHx but that rosiglitazone has one or more additional inhibitory effect on some growth factor levels that are independent of Adn.

4.4 Discussion

During hepatocyte priming, Adn-/- mice have similar serum IL-6 levels to WT mice; however, they have reduced pSTAT3, coupled with increased expression of the STAT3 inhibitor SOCS3. The computational model suggests that small deficiencies in IL-6 signaling transduction during the priming phase (modeled as ~2% decrease in IL-6 levels) in Adn-/- mice may be responsible for larger decreases in downstream STAT3 phosphorylation (up to ~25% decrease, based on the model). Two clear implications arise from these results. The first implication is that subtle, unobservable changes in upstream signaling may cause large, significant changes downstream. Therefore, it is important to consider systems-level interactions when unraveling complex disease phenotypes. The second implication is that interventions with relatively small effect on targeted upstream regulators may be effective at renormalizing the altered regeneration phenotypes.

Our data showing delayed onset of hepatocyte proliferation after PHx is consistent with previous reports involving Adn-/- mice (Ezaki et al, 2009;Shu et al, 2009a). In addition, Shu et al. also observed reduced STAT3 activation coordinate with SOCS3 upregulation at 24 and 48 hours after PHx in Adn-/- mice relative to WT. However, STAT3 phosphorylation at these times is much lower than STAT3

phosphorylation at 3 and 6 hours after PHx (Aoyama et al, 2009), and the functional importance of the later phosphorylation remains unclear.

Additionally, other signaling processes may contribute to the observed profile. Adn may also regulate changes in liver ceramide levels after hepatectomy (Correnti et al, 2014). TNFα is a potent activator of sphingomyelinase which hydrolyzes sphingomyelin to ceramide. Therefore, inflammatory signals early after PHx likely promote increases in cellular ceramide, which have been observed after PHx (Alessenko et al, 1999). We expect this effect to be enhanced in Adn-/- mice because of the absence of Adn receptor-dependent ceramidase activity (Holland et al, 2011). Increased ceramide levels have also recently been linked to elevated levels of the tyrosine phosphatase SHP-1 (Gopalan et al, 2013). Increased SHP-1, which can dephosphorylate STAT3, provides an additional potential mechanism for the abrogated STAT3 signaling observed in Adn-/- mice.

While hepatocytes are in the replicating stage of regeneration, Adn-/- mice have sustained higher levels of growth factors that are known drivers of regeneration as well as growth factors not typically associated with regeneration. HGF is one of only a few potent mitogens which can induce hepatocyte proliferation without the benefit of cofactors (Court et al, 2002). It is produced predominantly in hepatic stellate cells, can be bound to the ECM, and is released from ECM matrix metalloproteases produced by non-parenchymal cells. HGF signals through the c-Met receptor in hepatoctyes to stimulate regeneration (Michalopoulos, 2007a;Taub, 2004a). The sustained increase in HGF suggests hepatocytes from Adn-/- mice receive a more sustained growth signal, which may both promote cell cycle entry and contribute to the accelerated cell cycle progression in Adn-/- mice. Ang-1 is one of the highest

expressed genes in activated hepatic stellate cells *in vitro* and contributes to vascularization in tissues (Jiang et al, 2006a;Pan et al, 2012). Higher Ang-1 levels likely correspond to increased tissue remodeling in Adn-/- mice to maintain liver architecture during later periods of enhanced regeneration. In contrast to these two growth factors, FGF2 has been shown to have little effect during liver regeneration in wild-type animals. It is therefore not surprising that FGF2 levels were not altered after PHx in WT mice. In contrast, Adn-/- mice expressed elevated FGF2 following PHx, suggesting that Adn negatively regulates the FGF2 response. Also, an earlier report of an increase in VEGF after PHx in mice carrying a genetic deletion of FGF2 suggests that FGF2 can act similarly to VEGF to regulate liver structure and non-parenchymal cell activity. By measuring these three growth factors, we were able to characterize classical growth factor signaling to hepatocytes, remodeling growth factor signaling influencing non-parenchymal cell activity, and compensatory or additional growth factor signaling (Sturm et al, 2004). The sustained bioavailability of these growth factors in Adn-/- mice suggests that cells producing these growth factors (predominantly hepatic stellate cells) may be constitutively activated or activated to an alternate phenotype following PHx in the absence of Adn (Friedman, 2008a;Jiang et al, 2006a).

A recent study suggests that Adn may inhibit hepatic stellate cell activation and induce apoptosis by binding to AdipoR1 and AdipoR2, inducing activation of PPAR-α (Ding et al, 2005). It is possible that the absence of Adn removes this inhibition on stellate cell activation thus enabling stellate cell-produced factors to persist longer in the liver, including the growth factors FGF-2, Ang-1, and HGF. The altered dynamics of growth factor signaling during the first 20 hours post-PHx,

however, indicates that the modulatory effect of Adn on stellate cells is more complex than a simple activation/deactivation relationship.

Adn has also been shown to directly inhibit growth factor-mediated proliferation in part through direct binding of growth factors and inhibiting their association with their cognate receptors (Fayad et al, 2007;Wang et al, 2005). We observed significant decreases in serum Adn during the onset of S phase in WT mice, 30h post-PHx. While these decreases were modest, because serum Adn levels are tightly regulated, small decreases in Adn may have larger effects on sequestering GFs (Nawrocki et al, 2006). Although GFs were higher in Adn-/- mice, we noted no differences in cyclin D1 expression between genotypes at this time, suggesting the effect of elevated Adn is to block hepatocyte cell cycle after G1, potentially at the G1/S transition. We have investigated intracellular pathways classically activated by growth factors (ERK, JNK, Akt) but have found no differential regulation between WT and Adn-/- mice.

Rosiglitazone also modulates liver regeneration, likely in part through raising serum adiponectin. Rosiglitazone-treated mice show higher levels of serum adiponectin and opposite changes in the progression of regeneration to that observed in Adn-/- mice. Rosiglitazone-treated mice have lower growth factor levels and lower regeneration markers than WT mice. Our data show that deficient regeneration is associated with a significant elevation of serum adiponectin in WT mice and is abrogated in the Adn-/- mice, suggesting that adiponectin is required for this effect. This is also consistent with a growing body of literature demonstrating that adiponectin is required for the full beneficial effects of rosiglitazone treatment in diabetic patients (Combs et al, 2002;Hoo et al, 2007;Nawrocki et al, 2006;Tao et al,

2010). Rosiglitazone, however, may have an additional inhibitory effect on HGF production that is independent of Adn.

These results have further implications the systemic effects of rosiglitazone (and possibly other drugs of the glitazone class that act through increasing Adn levels). Rosiglitazone, which likely has tissue-specific effects, does not specifically target the liver. Previous studies have shown that rosiglitazone treatment increases risk of myocardial infarction and subsequent death from cardiovascular causes in humans (Nissen & Wolski, 2007), decreases the extent of lung injury in animals (Honiden & Gong, 2009), and may be protective in cancer (Monami et al, 2008), in addition to blunting liver repair as we have shown in the present study and has been shown previously (Turmelle et al, 2006). Additionally, our study suggests that Adn is required for the suppressive effect of rosiglitazone on liver regeneration. It is possible that the sustained inflammatory response to injury and reduced GF response that we observed may parallel the effect of rosiglitazone on other tissues as well, which may also be mediated by Adn.

Our integrated experimental and computational modeling demonstrates that Adn regulates liver regeneration through modulating multiple opposing hepatocyte signaling inputs from non-parenchymal cells governing the rate of progression through the cell cycle, cytokine signaling, and growth factor bioavailability. Adn likely fine-tunes the dynamics of regeneration by enhancing onset of hepatocyte proliferation during the priming phase by increasing STAT3 phosphorylation but suppressing overall liver regeneration through sequestration of GFs and decreasing GF persistence in the liver.

Chapter 5

AN UNBIASED COMPARISON OF MOLECULAR REGULATION OF PRIMING IN ADN-/- MICE AND CONTROLS

All experimental work featured in this chapter was performed by J.M. Correnti.

5.1 Introduction

As discussed in chapter 1, liver regeneration following surgical resection can be used to treat several liver diseases (hepatocellular carcinoma, metastatic cancer, etc. (Doci et al, 1991;Ringe et al, 1991)), as well as to facilitate a live donor transplant, which normally stimulates regeneration of the remnant liver in the donor and the transplanted liver in the recipient (Tanemura et al, 2012). Although liver regeneration is tightly coordinated in healthy animals and plays an important role treating liver diseases in patients, many chronic diseases also impair regeneration. Unfortunately, these regeneration-impairing diseases are common comorbidities associated with hepatocellular carcinoma and other diseases treatable by resection (Montalto et al, 2002).

One chronic disease associated with a worse resection outcome is fatty liver. A high fat diet (and subsequent fatty liver) leads to significant changes in transriptome-wide gene expression levels during regeneration in rats (Kuttippurathu et al, 2016). Through these changes, a fatty liver can reduce greatly the liver's regenerative potential (DeAngelis et al, 2005). Surgeons, therefore, tend to abstain from transplanting livers with a significant degree of fat accumulation (McCormack et al,

2011). The development of a fatty liver (especially non-alcoholic fatty liver) is associated with obesity, which is in turn associated with the balance between two adipokines linked to appetite: Adiponectin (Adn) and Leptin (Lep) (Fabbrini et al, 2010;Ryan et al, 2003). Adn stimulates appetite in the brain, whereas Lep suppresses appetite (Kubota et al, 2007;Minokoshi et al, 2004). This acute effect of Adn and Lep appears to reverse in obesity, which is associated with low Adn levels in the serum and high serum Lep levels (Ryan et al, 2003). On the other hand, deleting Lep in mice (so called *ob/ob* mice) results in obesity, likely due to the loss of appetite control by Lep (Lindstrom, 2007). Low Adn and high Lep levels in obesity, therefore, likely indicate a failure of the appetite control system rather than a reversal of the roles of Adn and Lep.

In addition to contributing to appetite and obesity, the balance of Adn and Lep affects systemic inflammation and function of multiple organs. In macrophages, Adn has been shown to suppress synthesis of the pro-inflammatory cytokines TNF-α and IFN-γ and to stimulate synthesis of the anti-inflammatory cytokine IL-10 (Tilg & Moschen, 2006). Lep, on the other hand, induces pro-inflammatory cytokine production by macrophages, including IL-6 and TNF- α. Lep has also been shown to modulate the adaptive immune response in mice by influencing proliferation rates of multiple types of T cells (Tilg & Moschen, 2006). Adn has been shown to be directly cardioprotective when administered prior to ischemia-reperfusion injury in the heart (Shibata et al, 2005). Similarly, Lep administered after ischemia-reperfusion injury in the heart is also cardioprotective (Smith et al, 2006). The liver is also affected by Adn and Lep. High serum levels of Adn are associated with a low incidence of fatty liver, and delivery of Adn to mice with fatty liver causes reduced hepatomegaly and

steatosis (Musso et al, 2005;Xu et al, 2003). Lep, meanwhile, has the capacity to activate hepatic stellate cells to produce extracellular matrix and can promote fibrosis (Saxena et al, 2002).

In chapters 3 and 4, we identify an important role for Adn in fine-tuning liver regeneration dynamics in response to liver resection using a combination of computational modeling and experimental investigation. We find that Adn-/- mice exhibit deficiencies in priming and a delayed onset of liver regeneration in response to liver resection (Correnti et al, 2015). Chapter 4 presents a targeted approach for investigating these deficient priming signals, measuring protein levels and mRNA levels involved in the IL6 signaling cascade through the JAK-STAT pathway, including the inhibitor SOCS3. We find that Adn-/- mice during the priming phase of regeneration have low levels of IL6 signaling in the serum, similar levels of SOCS3 transcript, and deficient STAT3 phosphorylation. We determine that this combination is sufficient to delay regeneration using our computational model-based approach. This delayed regeneration is renormalized at later times post-PHx due to enhanced growth factor signaling in Adn-/- mice (Correnti et al, 2015). Although our targeted approach to investigate molecular regulation of regeneration is useful, changes in cytokine, chemokine, and growth factor signaling are likely coordinated across many molecules due to changes in cell activation phenotype (for example M1 vs. M2 activated Kupffer cells). In this chapter, we take an unbiased approach to understand how the molecular regulation of priming differs in these two mouse genotypes through simultaneous measurement of a panel of cytokines, chemokines, and growth factors during the priming phase.

5.2 Materials and Methods

5.2.1 Animals

All animal studies were approved by the Institutional Animal Care and Use Committee (IACUC) at Thomas Jefferson University. Jefferson's IACUC is accredited by the Association for Assessment and Accreditation of Laboratory Animal Care and experiments were designed using the Guide for the Care and Use of Laboratory Animals.

PHx was carried out on Adn-/- and control mice as described in previous chapters (Chapter 3) and shown schematically (Figure 5.1A).

5.2.2 Biochemical analysis

Tissue lysates were generated by homogenizing frozen tissue in RIPA buffer (Sigma) supplemented with phosphatase and protease inhibitor cocktails (Sigma). Protein was normalized using BCA Protein Assay Reagent (Pierce Biotechnology, Rockford, IL). Samples were then sent to Raybiotech for analysis of cytokine and chemokine levels using Quantibody® Multiplex ELISA Array (Raybiotech, Norcross, GA).

5.2.3 Data normalization and batch correction

Tissue and serum samples were measured on multiple arrays in two batches. These batches were measured on two separate days and contained multiple overlapping samples. Data from each array was normalized using the standard curve provided by Raybiotech along with every array measured. We analyzed the data from overlapping samples measured in both batches, and found a significant batch effect. We therefore calculated the mean expression value of all proteins measured in all the

overlapping samples for each batch (giving a batch correction value for each batch) and subtracted this value from all expression values in each batch. The batch correction shifted the expression values for all samples, making the absolute expressions less useful. Therefore, protein expression values were converted to fold-change above wild-type baseline levels.

5.2.4 Multivariate data analysis

One-factor ANOVA (factor = time) with Tukey post-hoc testing was performed on log-transformed expression data to identify proteins with dynamic expression changes in either wild-type or Adn-/- mice. Traditionally, analysis of this type of data would be performed using a two-factor ANOVA (factors = time, genotype), and the results would be analyzed to find proteins whose expression was dependent on time, genotype, or a combination of both. We chose instead to use an approach considering the expression modes of proteins in each mouse genotype. Our approach organizes protein expression into distinct modes, then compares how proteins are regulated differently or similarly across genotypes based on these expression modes.

5.2.5 Correlation network analysis

Correlation networks were calculated for Adn-/- and wild-type mice using Pearson correlation on a per-animal basis, according to the following equation. Correlations were calculated separately for protein interactions in the tissue and protein interactions in the serum.

$$\rho_{XY} = \frac{cov(X,Y)}{\sigma_X \sigma_Y} \tag{5.1}$$

Where ρ_{XY} is the correlation between two random variables X and Y, cov(X,Y) is the covariance between these two variables, and σ_i is the standard deviation of the variable i = X or Y.

Additionally, pairwise correlation between pairs of proteins was calculated using the newly developed segmentation method for comparison of pseudo-time series data. For more information about the segmentation method, see Appendix B.

5.3 Results

5.3.1 Adn-/- mice dynamically regulate protein levels differently following resection than wild-type controls

We measured the levels of 80 cytokines, chemokines, and growth factors in the tissue and serum of Adn-/- mice and controls prior to liver resection and at 1hr, 3hrs, and 6hrs post-PHx. We find that Adn-/- mice and controls dynamically regulate approximately the same number of proteins post-PHx, but that only about half of these proteins are in common between the two genotypes (Figure 5.1B). This is true in both serum and tissue samples. We were interested to see that there are no proteins measured in wild-type mice that show dynamic expression changes in both the serum and tissue. Adn-/- mice, similarly, show only two proteins that have dynamic expression changes in the serum and tissue post-PHx. These results suggest that there may be a core priming response to resection in both genotypes and a genotype-specific contribution to priming that fine-tunes regeneration dynamics.

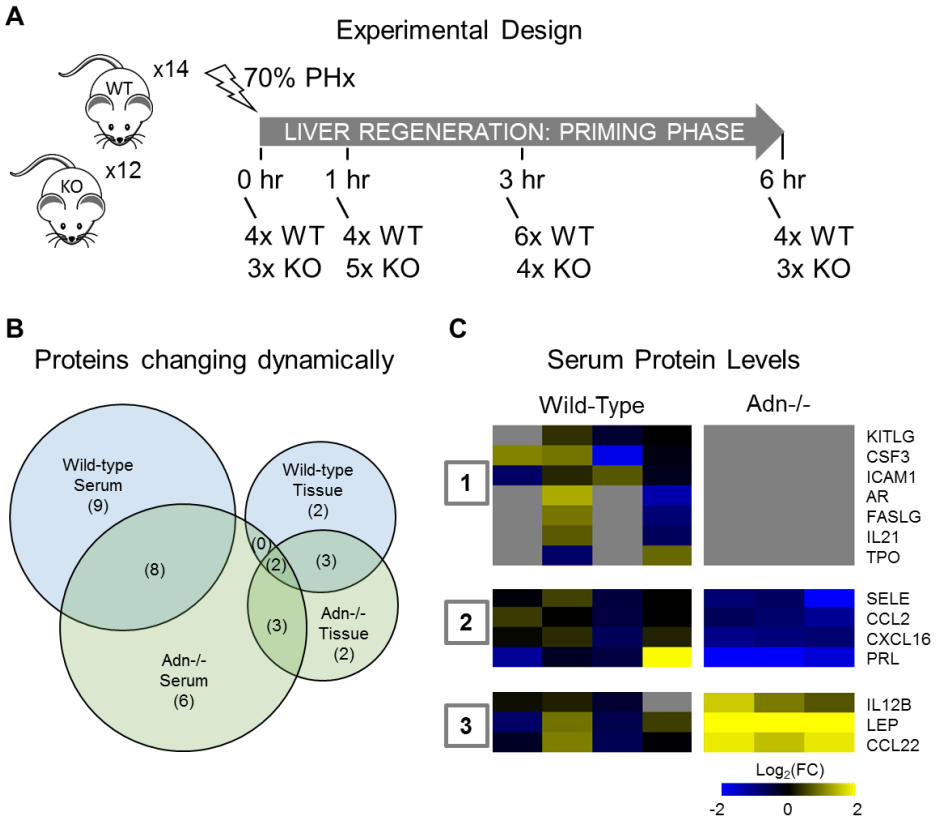

Figure 5.1 Effects of adiponectin knockout on protein expression following 70% PHx. (A) Experimental design. Wild-type and Adn-/- mice were subjected to 70% PHx and samples were taken throughout the priming phase. (B) Proteins measured in serum and tissue that show statistically discernable dynamic changes. (C) Differences in protein expression in the serum of wild-type and Adn-/- mice prior to PHx. Adn-/- mice expressed proteins (1) below the limit of detection, (2) at lower levels than wild-type mice, or (3) at higher levels than wild-type mice.

5.3.2 Adn knockout preconditions tissue microenvironment

5.3.2.1 Proteins highly down-regulated in Adn-/- mice may inhibit liver responsiveness to PHx

We find several proteins that are expressed in the serum of control animals, but are below the limit of detection in Adn-/- mice (Figure 5.1C, mode 1). Most of the proteins expressed below the limit of detection in Adn-/- mice relate to recruitment of non-resident cells to the liver (the notable exceptions are AR and FASLG). CSF3 (formerly GCSF) stimulates hematopoiesis thereby increasing the number of white blood cells and growth and differentiation of neutrophils (Kindt et al, 2007). Within the liver tissue, CSF3 has been shown to stimulate MMP9 production in hepatic stellate cells (Jiao et al, 2009). Therefore, CSF3 likely has a dual role in maintaining liver function: maintaining a population of neutrophils in the liver and promoting homeostatic matrix remodeling through mmp9 degradation of collagens. Similarly aiding in matrix remodeling, KITLG (formerly SCF) functions in the recruitment of mast cells, which have been shown to promote collagen deposition (Franceschini et al, 2006). As an extreme example of this collagen deposition, researchers have shown that KITLG overexpression contributes to fibrosis development, presumably through activation of resident hepatic stellate cells either directly or through mast cell recruitment and activation (Friedman, 2008c). Another protein involved in recruitment Interleukin-21 (IL21) enhances proliferation of and IFNG production by T cells and NK cells (Kindt et al, 2007). IFNG has been shown to inhibit hepatic stellate cell activation and promote Kupffer cell activation, potentially aiding in priming following liver resection (Paschos et al, 2010). Taken together, these protein deficiencies in Adn-/- mice suggest a homeostatic condition deficient in inflammatory cell recruitment that could be responsible for blunted priming in response to tissue damage.

Two recruitment proteins deficient in Adn-/- mice merit special mention: ICAM1 and TPO. ICAM1 is deficient in Adn-/- mice and involved in the recruitment of monocytes (Galkina & Ley, 2007). This has important implications for liver regeneration because research has shown that monocytes are recruited heavily following an acute carbon tetrachloride liver damage leading to a modified immune environment in the liver, which could influence regeneration dynamics (Cook et al, 2015;Karlmark et al, 2009). If such monocyte recruitment also occurs following resection, a homeostatic deficiency in ICAM1 could lead to a decreased population of recruited monocytes following resection and could help explain the deficient priming seen in this strain of Adn-/- mice (Correnti et al, 2015). Another protein important to wound healing and deficient in Adn-/- mice, thrombopoietin (TPO), stimulates platelet production leading to blood clotting and can aid in wound repair (Anitua et al, 2004;Tsai et al, 2016). In the field of liver regeneration, high preoperative levels of TPO are associated with an enhanced liver mass recovery in mice at 48 hours post-PHx (Murata et al, 2008). This effect could be caused in part through enhanced PDGF production by platelets and subsequently enhanced bioavailability to non-parenchymal cells. Other studies have found that pretreatment with TPO speeds liver recovery in rats through enhanced levels of HGF, likely through platelet to non-parenchymal cell interactions (Shimabukuro et al, 2009). Thus TPO deficiency could have detrimental effects on liver wound healing, non-parenchymal cell behavior post-PHx, and regeneration dynamics.

Other proteins deficient in Adn-/- mice include adrenergic receptor alpha (AR) and Fas ligand (FASLG). AR allows for norepinephrine signaling in the liver. Blockading AR prior to resection delays the peak of hepatocyte replication from 24

hours to 72 hours post-PHx. Additionally, hepatocytes are highly sensitive to the TGFB-inhibiting effects of norepinephrine at 12-16 hours post-PHx, indicating that AR production in the priming phase may be the event that predisposes hepatocytes to norepinephrine sensitivity (Michalopoulos, 1990). A lack of AR in the homeostatic liver could negatively affect hepatocyte priming post-PHx. In contrast to the other proteins deficient in Adn-/- mice during homeostasis, FASLG deficiency seems like it would be beneficial to liver regeneration. FASLG promotes cell death through apoptosis; therefore, lower levels of FASLG should lead a lower rate of apoptosis in Adn-/- mice livers. This potential decrease in apoptosis could be one reason why Adn-/- have been shown to have a higher propensity to develop liver cancer (Kamada et al, 2007;Sun & Lodish, 2010). Although within tumors derived from introducing either B16F10 melanoma cells or Lewis Lung Carcinoma cells, there appears to be no difference in apoptosis amount in Adn-/- mice (Sun & Lodish, 2010).

5.3.2.2 Proteins down-regulated in Adn-/- mice may cause impaired neutrophil and NKT cell recruitment

We also find proteins that are expressed in Adn-/- mice, but at consistently lower levels than controls (Figure 5.1C, mode 2). Similar to the proteins deficient in Adn-/- mice, several of the proteins down-regulated in Adn-/- mice are related to cell recruitment. CCL2 (formerly MCP1) can be produced by Kupffer cells and acts to recruit monocytes (Deshmane et al, 2009). Another chemoattractant protein down regulated in Adn-/- mice is CXCL16. This protein signals to recruit and enhance adhesion of CD8+ T cells and NK cells (Sahin et al, 2010). E-selectin (SELE) is also down-regulated in Adn-/- mice. SELE has been shown to recruit neurophils in chronic plus binge drinking and may contribute to pro-inflammatory cytokine expression in

response to resection (Bertola et al, 2013). The relationship between ADN and SELE, however, is not clear currently. Pioglitizone, which works by increasing ADN levels, inhibits the expression of SELE in vascular endothelial cells in response to TNFA (Nawa et al, 2000). Therefore, we would expect that removing ADN would lead to an increase in SELE. More research into the relationship between ADN and SELE is required to fully flush out their relationship.

Prolactin (PRL) is also down-regulated in Adn-/- mice and is unique among the proteins measured because it is not produced in the liver. Instead it is produced by other tissues, such as the pituitary glands (Simon-Holtorf et al, 2006). PRL is one of only a few identified direct hepatocyte mitogens. It acts to activate JAK2 leading to STAT5 production, inducing hepatocyte proliferation and increasing hepatocyte DNA replication rate in already replicating hepatocytes (Olazabal et al, 2009). Although it has been shown to enhance hepatocyte replication, there are several inconsistencies that make its role in liver regeneration unclear. It has been shown to suppress cytokine signaling in Kupffer cells, which could inhibit hepatocyte priming (Zhu et al, 1996). Additionally, post-PHx PRL has been shown to activate STAT3 but not STAT5, calling into question the pathways through which its mitogenic effects operate during recovery from PHx (Olazabal et al, 2009).

5.3.2.3 Proteins up-regulated in Adn-/- mice may modify non-parenchymal cell state balances

We find three proteins that are expressed at higher levels in Adn-/- mice than in controls in the homeostatic liver: interleukin 12b (IL12B, formerly IL12P40), chemokine ligand 22 (CCL22, formerly MDC), and leptin (LEP) (Figure 5.1C, mode 3). It is possible that the high expression levels of IL12B and CCL22 are

compensatory mechanisms to counteract the low expression levels of IL21 and CXCL16. Similar to IL21, IL12B induces IFNG production by T and NK cells (Kindt et al, 2007). IL21 is produced predominantly by B cells and CD4+ T cells, while IL12B has been shown to be produced in B cells, monocytes, macrophages, and neutrophils (Yeo et al, 2011). This difference in cellular production may be a result of Adn-/- mice having a lower number of infiltrated immune cells. Similar to CXCL16, CCL22 is chemotactic for dendritic cells and NK cells (Sahin et al, 2010). CCL22 overexpression may be responding to a lack of NK cell infiltration coupled with a low expression of CXCL16 to enhance NK cell recruitment. As a result of this alternate recruitment, the baseline immune cell composition of the liver may be different in Adn-/- mice than in wild-type mice. Also, CCL22 has been shown to have some anti-inflammatory effects, suggesting that, in addition to having an altered immune cell composition, the baseline immune environment of the Adn-/- liver is in a state less ready for priming in response to liver resection.

The altered LEP levels in Adn-/- mice may be due to altered regulation in adipocytes. Adipocytes are the primary producers of LEP (although it can also be produced by hepatic stellate cells in the liver) (Oh et al, 2007). LEP has been shown to help regulate body weight, modulate immune response, and influence the neuroendocrine response to fasting in human patients (Mantzoros et al, 2011). LEP is especially interesting to us because ADN and LEP have been shown to be inversely related in several diseases affecting liver function (Tsochatzis et al, 2006). In the liver, LEP stimulates STAT3 in hepatic stellate cells, activates hepatic stellate cells, and induces hepatic stellate cell production of alpha (I) collagen (Saxena et al, 2002). The baseline increase in LEP may therefore predispose Adn-/- livers to have baseline

increased hepatic stellate cell activation, localized extracellular matrix increased stiffness, and a predisposition to develop fibrosis. This increased LEP level due to adiponectin knockout may contribute to fibrosis development in multiple organs in Adn-/- mice, including liver, kidney, and heart (Fujita et al, 2008;Kamada et al, 2003;Ohashi et al, 2007).

Other proteins followed similar expression trends in the homeostatic livers of Adn-/- and wild-type mice (either up-regulated or down-regulated following adiponectin knockout), but none of the other protein differences were statistically discernable (p-value < 0.05) (Figure 5.2).

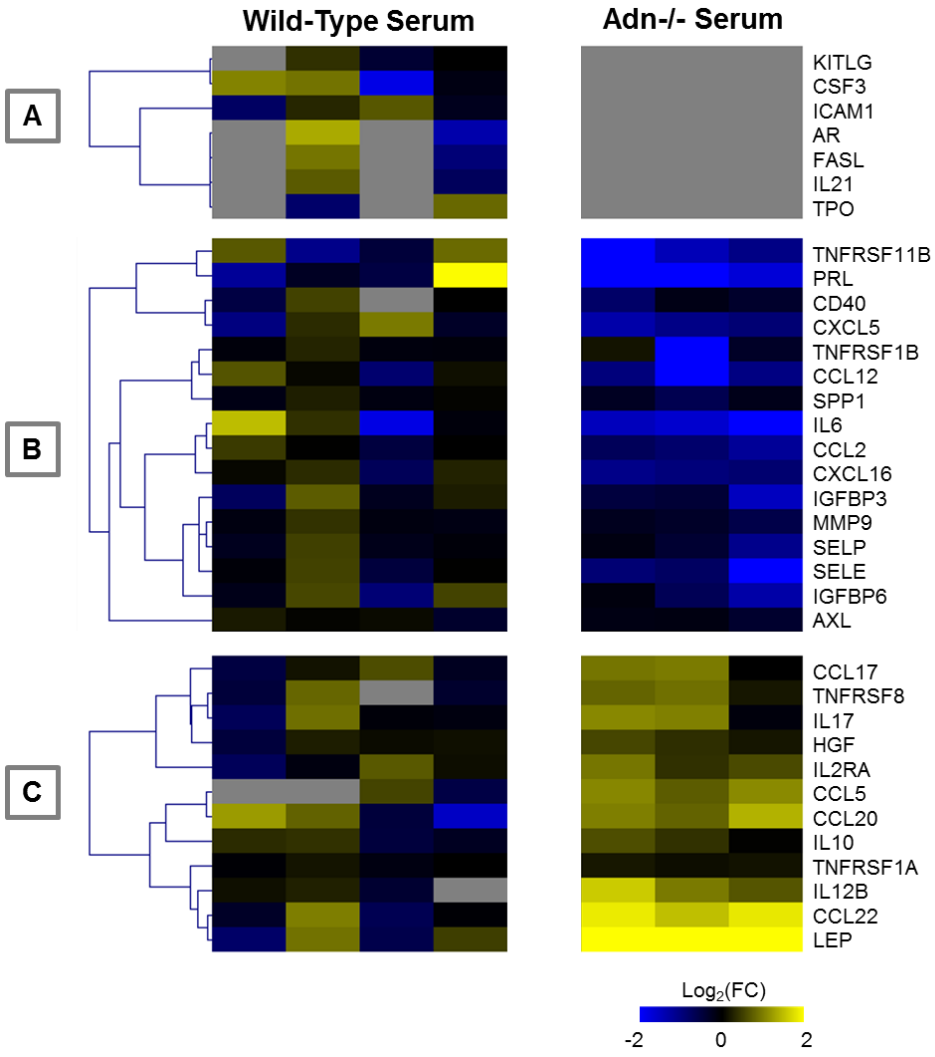

Figure 5.2 Proteins with trends towards differences in baseline expression between wild-type and Adn-/- mice. Not all of the differences in these protein levels are statistically discernable. All non-corrected p-values <= 0.30.

5.3.2.4 Protein variability in the homeostatic liver suggests constrained and deregulated control in Adn-/- mice

We measured protein levels in 3 Adn-/- mice and 4 controls prior to resection.

Three proteins show statistically discernable differences in expression variability

between genotypes: CXCL9 (formerly MIG), IGF1, and TNFRSF1B (formerly TNFR2) (Figure 5.3).

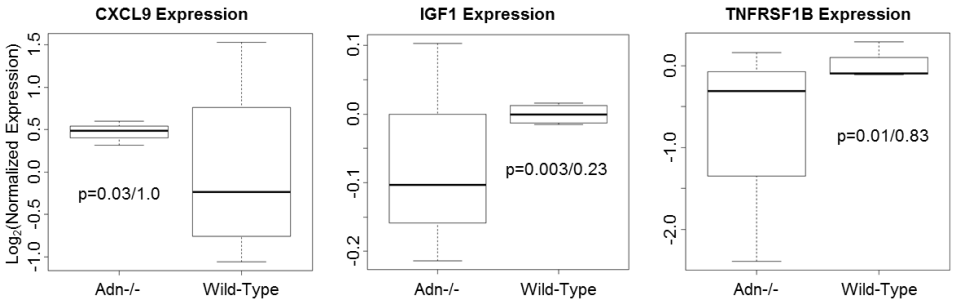

Figure 5.3 Proteins that may have different variances at baseline between genotypes. CXCL9 appears to be more tightly regulated in WT mice, while IGF1 and TNFRSF1B appear to be more tightly regulated in Adn-/- mice. P-values are indicated as uncorrected/corrected by the Bonferroni method. No discernable differences in variance between genotypes were found after p-value correction.

Of these, CXCL9 has higher variability in Adn-/- mice, while IGF1 and TNFRSF1B have higher variability in wild-type mice. Low variability in protein expression may indicate a strong regulatory constraint on protein production. None of the differences between Adn-/- and wild-type mice, however, are statistically discernable (p-value < 0.05) following correction for multiple tests.

5.3.3 Protein level responses following PHx are constrained into dynamic expression modes

We used hierarchical cluster to organize the expression levels of proteins in the liver post-PHx indo dynamic expression modes. Although many modes of expression

are possible, each protein measured in this study followed one of only six dynamic modes (Figure 5.4).

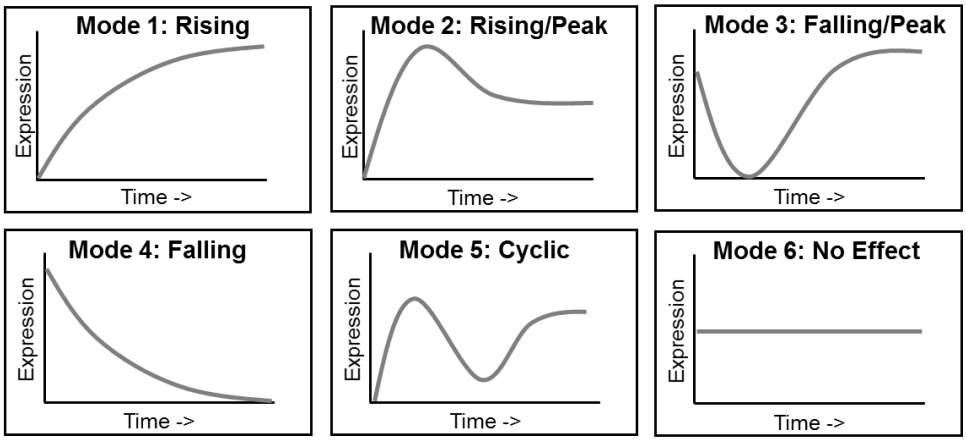

Figure 5.4 Modes of response for proteins following 70% partial hepatectomy. Other modes are possible, but the proteins measured in this study all follow these expression modes.

Most of the differentially expressed proteins in wild-type mice following resection behave consistent with Mode 1 (Rising), increasing throughout the priming phase (Figure 5.5). A smaller number behave consistent with Modes 2 and 3 (Rising or Falling with a peak). Only one protein, VEGF, behaves consistent with Mode 4 (Falling), decreasing throughout the priming phase.

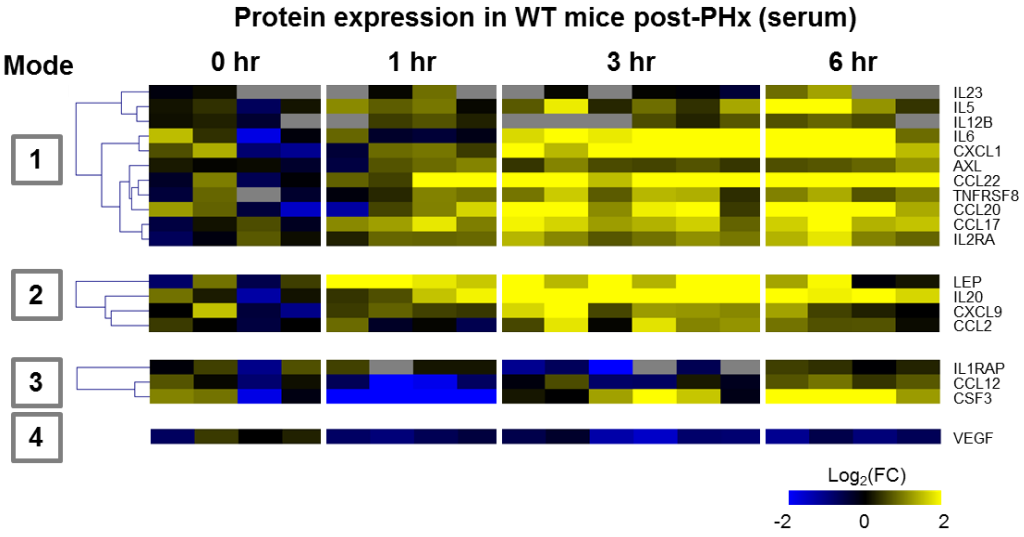

Figure 5.5 Heatmap showing WT serum response to resection organized into modes of expression.

More proteins show similar expression trends, but not all are statistically discernable (Figure 5.6).

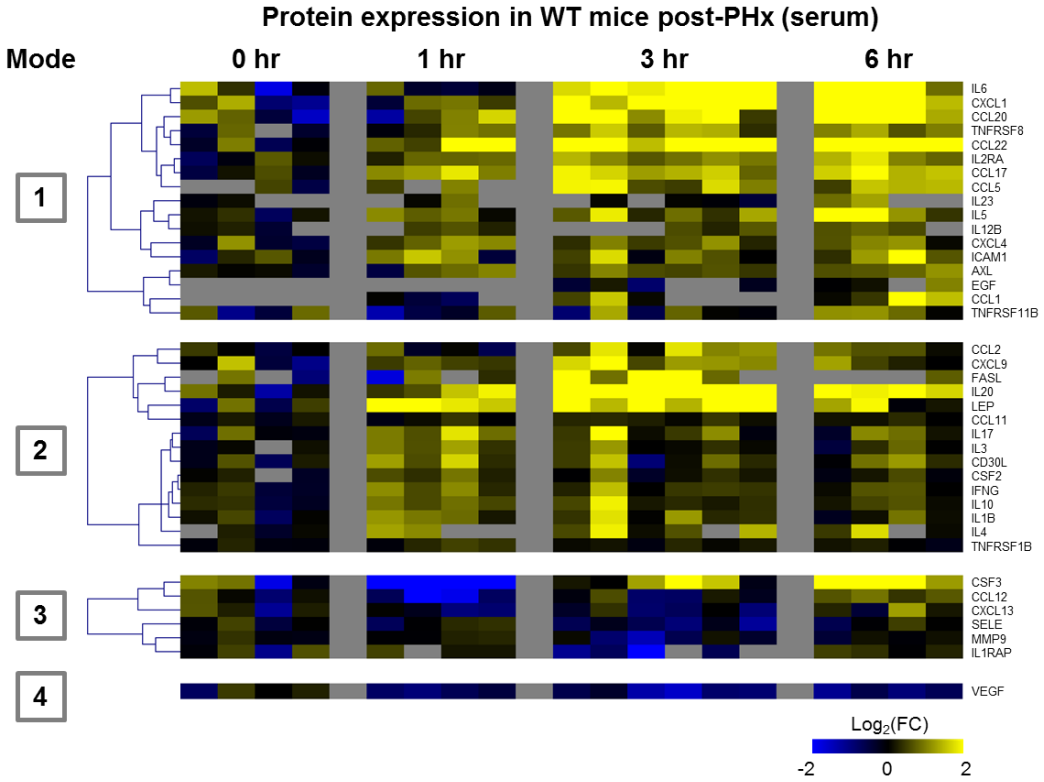

Figure 5.6 Heatmap showing WT serum responses organized into modes including all proteins measured. Proteins are grouped within an expression mode if the ANOVA p-value was <= 0.30.

5.3.3.1 Mode 1: Rising

The proteins that increase steadily during the priming phase post-PHx are related to two main functions: inflammation and immune cell recruitment (Figure 5.5, Mode 1). Among the pro-inflammatory proteins increasing during the priming phase is interleukin 6 (IL6). IL6 is perhaps the most studied cytokine in liver regeneration. It has been shown to be important for liver regeneration dynamics and overall recovery (Fausto et al, 2006). IL6 is thought to be produced primarily by Kupffer cells in the

liver post-PHx and primes hepatocytes to respond to growth factors by entering the cell cycle (Malik et al, 2002). It may also co-ordinate the behavior of other non-parenchymal cells during regeneration (See chapter 7). Several other interleukins (ILs) increase through the priming phase. IL23A has been shown to induce production of TNFA in Kupffer cells and to differentiate T cells to a state conducive to IL6 and TNFA production (Husted et al, 2006;Langrish et al, 2005). IL2RA is induced by IFNG and is the receptor for IL2, which has been shown to stimulate growth and differentiation of T cells, B cells, and NK cells (Kindt et al, 2007;Kmieć, 2001). IL12B has been shown to be produced by macrophages (and other cell types) and to induce IFNG production by T and NK cells (Kmieć, 2001). IL5, on the other hand, is antagonistic to IFNG (Reiman et al, 2006).

Several of the cytokines measured are related to development of fibrosis, likely through sustained inflammation. In addition to its other functions, IL5 may recruit eosinophils to the liver, potentially contributing to the development of fibrosis (Reiman et al, 2006). Similarly, CXCL1 (formerly KC) is a pro-inflammatory cytokine that has been shown to activate hepatic stellate cells and may contribute to fibrosis (Stefanovic et al, 2005). AXL is the receptor for GAS6 and induces macrophage inflammation and recruitment, eventually leading to fibrosis (Fourcot et al, 2011).

Proteins increasing during the priming phase also include proteins related to chemotaxis and attraction of circulating immune cells to the liver. CCL22 (formerly MDC) is chemotactic for dendritic and NK cells, MIP3A may be attractant to lymphocytes and may be involved in T-cell trafficking into the liver, and TARC is chemoattractant for monocytes, dendritic cells, B cells, and NK cells (Sahin et al,

2012). Taken together, this increase in proteins related to chemoattraction indicates that attracting circulating immune cells to the liver may be an important early step in liver regeneration.

Another protein that increases throughout the priming phase is TNFRSF8 (formerly CD30T). TNFRSF8 modifies immune responses but its exact function remains unclear (Fabrega et al, 2007). It has been shown that TNFRSF8 increases in patients prior to transplant rejection (including liver transplant rejection) and it is high in conditions associated with sustained liver inflammation, such as alcoholic liver disease (De Lazzari et al, 2002). What affect this has on priming the liver for regeneration, however, is unclear.

5.3.3.2 Mode 2: Rising with a peak

The levels of several proteins increase early post-PHx but then either level off or decrease to an intermediate level by the end of the priming phase (Figure 5.5, Mode 2). Among these are proteins that have been shown to induce hepatic stellate cell activation: LEP and CCL2. Also among these proteins are IL20, a promoter of angiogenesis, and CXCL9, an inhibitor of angiogenesis (Hsieh et al, 2006;Sahin et al, 2012). These proteins may be segregated spatially in the liver to promote angiogenesis only where it is required during regeneration.

5.3.3.3 Mode 3: Falling with a peak

We are interested to see that expression levels of CCL12 (formerly MCP5) fall during the priming phase, especially during the early hours post-PHx (Figure 5.5, Mode 3). CCL12 is involved in monocyte recruitment (Simpson et al, 2003). This decrease is in contrast to other monocyte recruiting proteins increasing throughout

priming (e.g. CCL17, formerly called TARC). Additionally, a pair of proteins related to MMP9 production by hepatic stellate cells fall early post-PHx before recovering somewhat. CSF3 (formerly GCSF) is most well-known for stimulating hematopoiesis and growth and differentiation of neutrophils (Kindt et al, 2007). It also functions in collaboration with HGF to stimulate MMP9 production in hepatic stellate cells, leading to matrix remodeling (Jiao et al, 2009). In contrast, IL1RAP (formerly IL1RA) has been shown to block MMP9 production in activated hepatic stellate cells (Lee et al, 2003). Taken together, these protein dynamics suggest that MMP9 production by hepatic stellate cells may be inhibited during the priming phase of regeneration. This is consistent with serum and tissue measures of MMP9 in wild-type mice, which show a trend towards decreasing levels during the priming phase, especially at 3hrs post-PHx; none of these MMP9 dynamics, however, are statistically discernable meaning that more studies are necessary to determine if there is an actual effect. Furthermore, alternate MMPs could compensate for any decreased matrix remodeling activity caused by decreases in MMP9.

5.3.3.4 Mode 4: Falling

VEGF levels decrease throughout the priming phase of regeneration (Figure 5.5, Mode 4). VEGF has been shown to be a potent inducer of angiogenesis (Corpechot et al, 2002). Therefore, this decrease suggests that angiogenesis does not occur during the priming phase. It is possible that the increase in blood volume traveling through the remnant liver induces the decrease in VEGF levels because there is an increased delivery of nutrients and oxygen and therefore no need for increased angiogenesis. As the liver begins to grow, VEGF will likely be induced at the leading edge of the tissue.

5.3.4 Proteins in liver tissue following PHx show dynamic expression changes in wild-type mice

5.3.4.1 Proteins with similar expression dynamics in serum and tissue post-PHx in wild-type mice

Upon inspection, many of the proteins measured showed similar dynamics in both serum and tissue; however, there are no proteins for which these dynamics are statistically discernable in both the tissue and serum. Therefore, this section will focus on proteins that showed statistically discernable dynamics in the tissue of wild-type mice post-PHx.

5.3.4.1.1 Mode 3: Falling with a peak

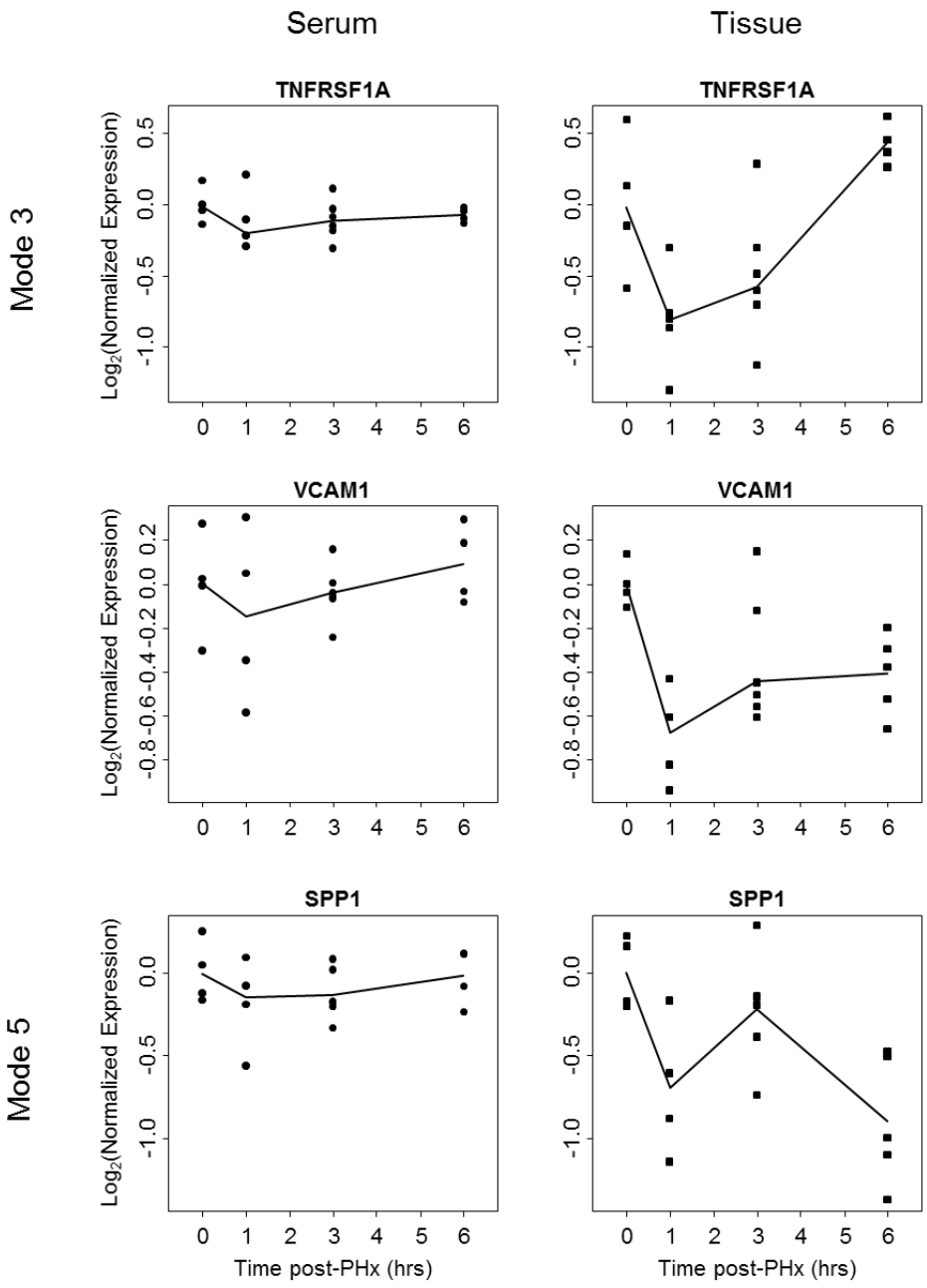

Figure 5.7 Several of the proteins measured in wild-type mice showed similar expression trends in animal tissue and serum. This similarity indicates that the liver is the main producer of these proteins following resection and transport into the tissue is relatively fast.

Two proteins measured in this study show behavior consistent with mode 3: TNFRSF1A (formerly TNFR1) and VCAM1 (Figure 5.7). TNFRSF1A is the main receptor for TNFA, and transduces the pro-inflammatory TNFA signal leading to STAT3 and NFKB activation (Kmieć, 2001). It has been implicated in Kupffer cell activation, hepatic stellate cell activation, and hepatocyte priming (Fausto et al, 2006;Tarrats et al, 2011). We expected TNFRSF1A levels to increase post-PHx in the tissue, especially at 1hr post-PHx, because 1hr post-PHx is the peak of TNFA levels in the tissue. TNFRSF1A decreasing post-PHx indicates that following traumatic damage, TNFA signaling may proceed through an alternate pathway. Alternatively, TNFRSF1A levels decreasing could indicate an increase in TNFRSF1A bound to TNFA and signaling actively, meaning that lower protein levels could indicate a higher biological activity at a given time. Levels of TNFRSF1A appear to return to baseline levels by the end of the priming phase. The same general trend is seen for TNFRSF1A in the serum, but the dynamics are not statistically discernable. VCAM1 is also important for pro-inflammatory response as a recruiter of monocytes (Kindt et al, 2007). Its decrease during the priming phase, especially at 1hr post-PHx, indicates that during the priming phase monocyte recruitment to the liver could be reduced or there could be other compensating recruitment proteins whose levels increase. There are no discernable dynamics for VCAM1 in the serum, but two animals did express low levels of VCAM1 in the serum at 1hr post-PHx.

5.3.4.1.2 Mode 5: Cyclic

SPP1 (formerly OPN) levels decrease in the tissue at 1hr post-PHx, increase back to baseline at 3hrs post-PHx, and again decrease by 6hrs post-PHx (Figure 5.7). A suggestion of this cyclic behavior can be seen in the serum levels of SPP1, but these dynamics are not statistically discernable. SPP1 is associated with hepatic stellate cell activation and has been shown to induce collagen deposition by hepatic stellate cells (Lee et al, 2004). It is produced in the liver by Kupffer cells and hepatic stellate cells predominantly (Kmieć, 2001). The dynamics of SPP1 suggest that hepatic stellate cell activation propensity is decreased during the priming phase of regeneration but that there could be some complex dynamics of hepatic stellate cell behavior even as early as 3hrs post-PHx. Decreasing hepatic stellate cell activation following traumatic liver injury could allow for hepatocyte renewal in the absence of TGFB prior to renewing the substrate with healthy matrix (COL4 rich basement membrane) or scar tissue (COL3 and COL6 rich fibrous matrix) depending on the extent of hepatocyte renewal and maintained tissue damage.

5.3.4.2 Proteins with opposite expression in serum and tissue post-PHx in wild-type mice

The proteins that show opposite expression trends in the serum and tissue of wild-type mice post-PHx likely have a more complex regulation than those that show the same dynamic behavior (Figure 5.8). These proteins could be regulated through selective secretion into the serum or organs other than the liver could contribute to the serum expression of these proteins.

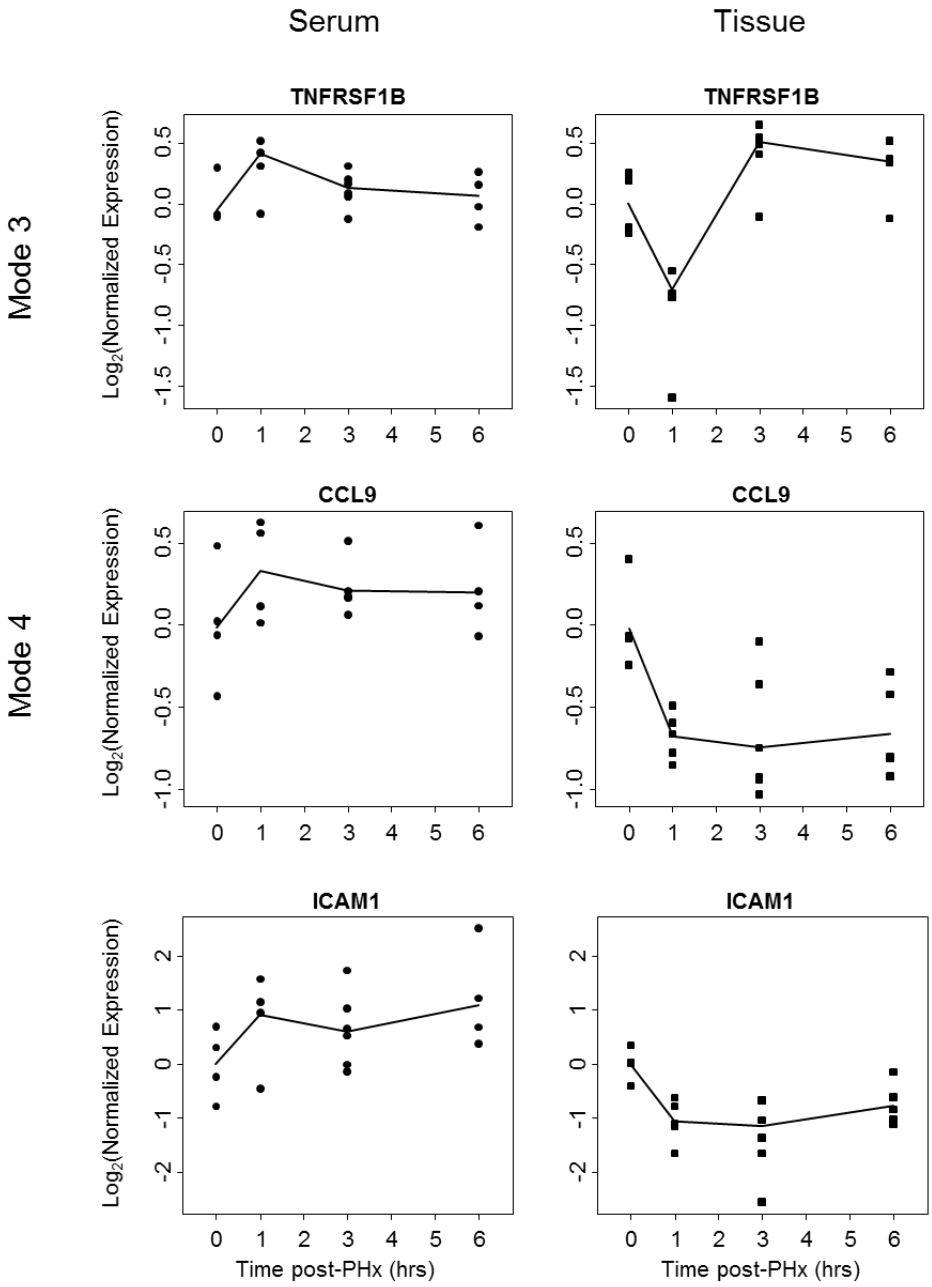

Figure 5.8 Several of the proteins measured in wild-type mice showed opposite expression trends in animal tissue and serum. This dissimilarity indicates that the liver may not be the main producer of these proteins following resection or that transport into the tissue is relatively slow.

5.3.4.2.1 Mode 3: Falling with a peak

Similar to TNFRSF1A levels, TNFRSF1B (formerly TNFR2) levels decrease at 1hr post-PHx before returning to baseline levels at 3hrs post-PHx and remaining at that level through the remainder of the priming phase. TNFRSF1B is an alternative receptor for TNFA. Although it has been shown to have similar effects as TNFRSF1A in some cases, in other cases it appears to be non-essential for TNFA signaling (Schümann et al, 2000;Tarrats et al, 2011). The decrease in TNFRSF1B levels at 1hr post-PHx could indicate a greater amount of TNFRSF1B bound in an active signaling complex. More work is required to confirm if this is occurring. We are interested to see a trend of increasing levels of TNFRSF1B in the serum of wild-type mice that is most pronounced at 1hr post-PHx, the opposite of the tissue expression dynamics. Although the serum dynamics are not statistically discernable, this result suggests there could be an alternate source of TNFRSF1B in the serum of wild-type mice post-PHx.

5.3.4.2.2 Mode 4: Falling

Levels of both ICAM1 and CCL9 (formerly MIP1G) decrease throughout the priming phase in the tissue of wild-type mice. Serum levels, however, appear to increase slightly during this same time (this increase is not statistically discernable; therefore, levels may not change in the serum). These proteins are both involved in recruiting cells to the liver; ICAM1 recruits monocytes while CCL9 recruits dendritic cells (Kindt et al, 2007;Zhao et al, 2003). The reduced levels of these proteins during the priming phase suggest that cell recruitment during the priming phase may be decreased compared to baseline.

5.3.4.3 Proteins with tissue dynamics post-PHx in wild-type mice and no expression change in serum

P-Selectin (SELP) shows a cyclic behavior in the tissue during the priming phase, but no discernable dynamics in the serum (Figure 5.9). SELP has been shown to be involved in tethering circulating immune cells to the liver tissue (Kindt et al, 2007). Levels decrease at 1hr and 6hrs post-PHx, which is consistent with other recruitment proteins decreasing early post-PHx as well (e.g. ICAM1, VCAM1, and CCL9). The transient increase at 3hrs post-PHx may indicate a transient recruitment of circulating immune cells. The lack of specific recruitment proteins correlated with SELP expression in the tissue, however, suggests a non-targeted recruitment of cells rather than a target approach to recruit a specific type of immune cell.

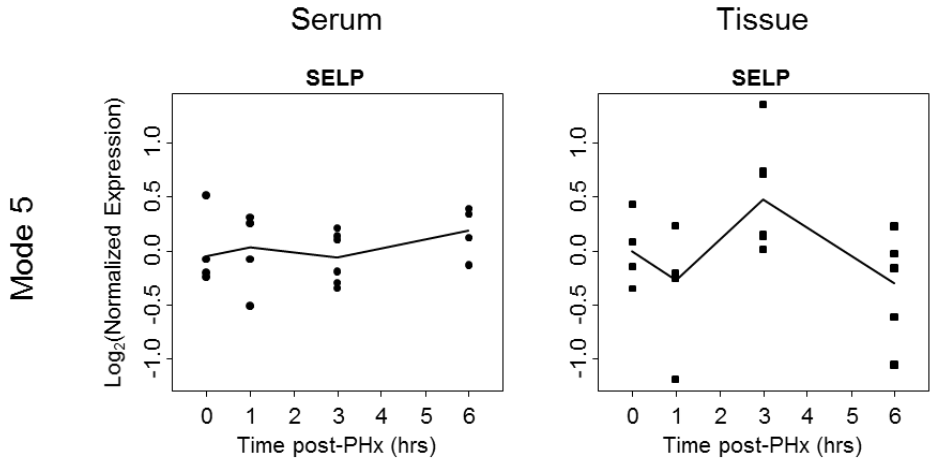

Figure 5.9 P-selectin showed cyclic dynamics post-PHx in wild-type mouse tissue, but no discernable dynamics in serum.

5.3.5 Different proteins regulate priming in Adn-/- mice

We measured levels of the same 80 proteins in the serum of Adn-/- mice during the priming phase of liver regeneration and found that proteins regulated

priming in Adn-/- mice are expressed following similar dynamic modes as in wild-type mice. The individual proteins behaving in these modes, however, is different between wild-type and Adn-/- mice (Figure 5.10).

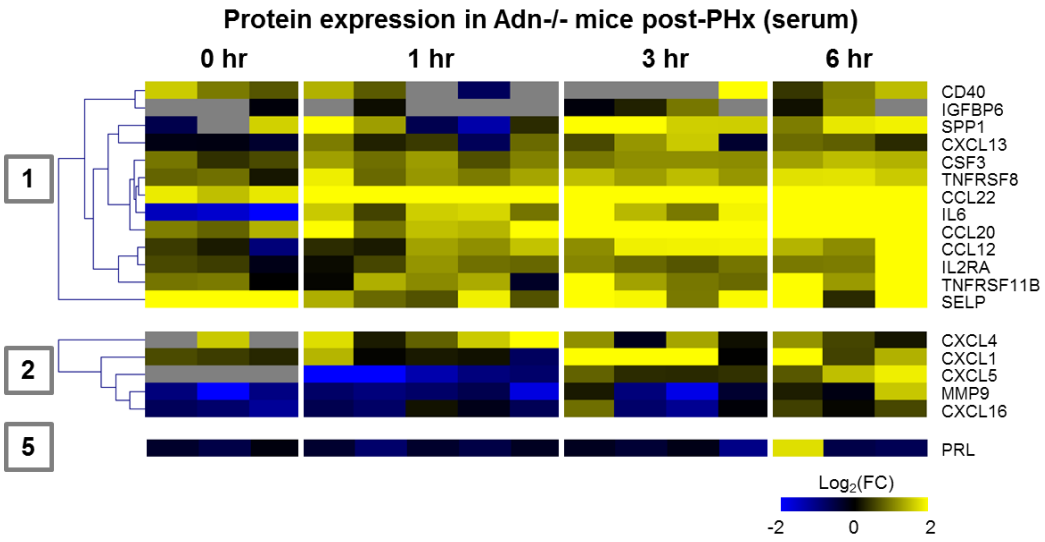

Figure 5.10 Heatmap showing Adn-/- serum response to resection organized into modes of expression ($p <= 0.05$)

For a visualization of how the wild-type expression modules behave in Adn-/- mice, see Figure 5.11.

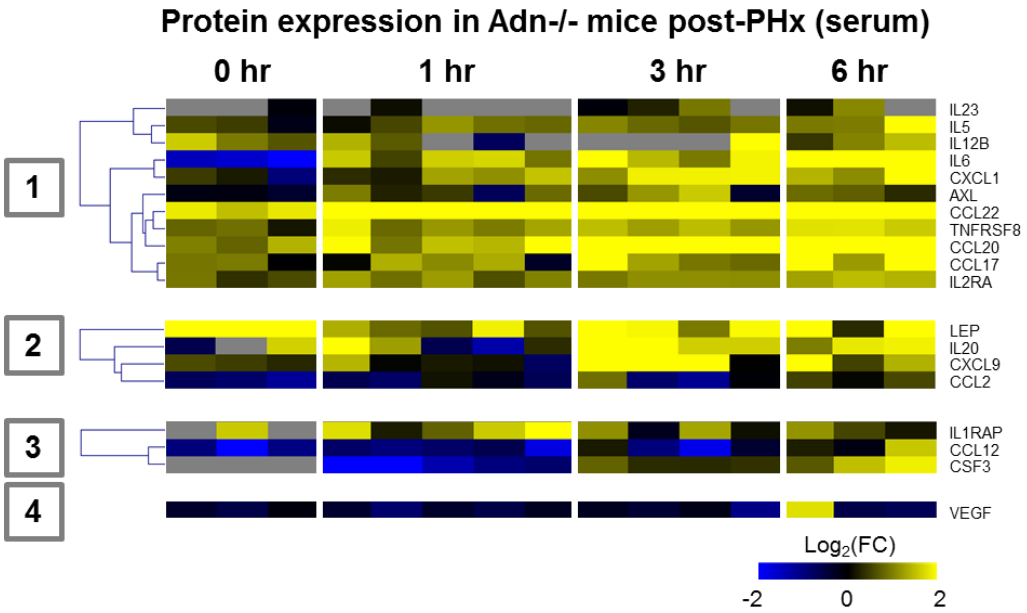

Figure 5.11 Heatmap showing Adn-/- serum response to resection organized into WT modes of expression (p-value <= 0.05).

For a visualization of dynamic protein expression in the serum of Adn-/- mice for proteins with possible dynamics (p-value < 0.30), see Figure 5.12.

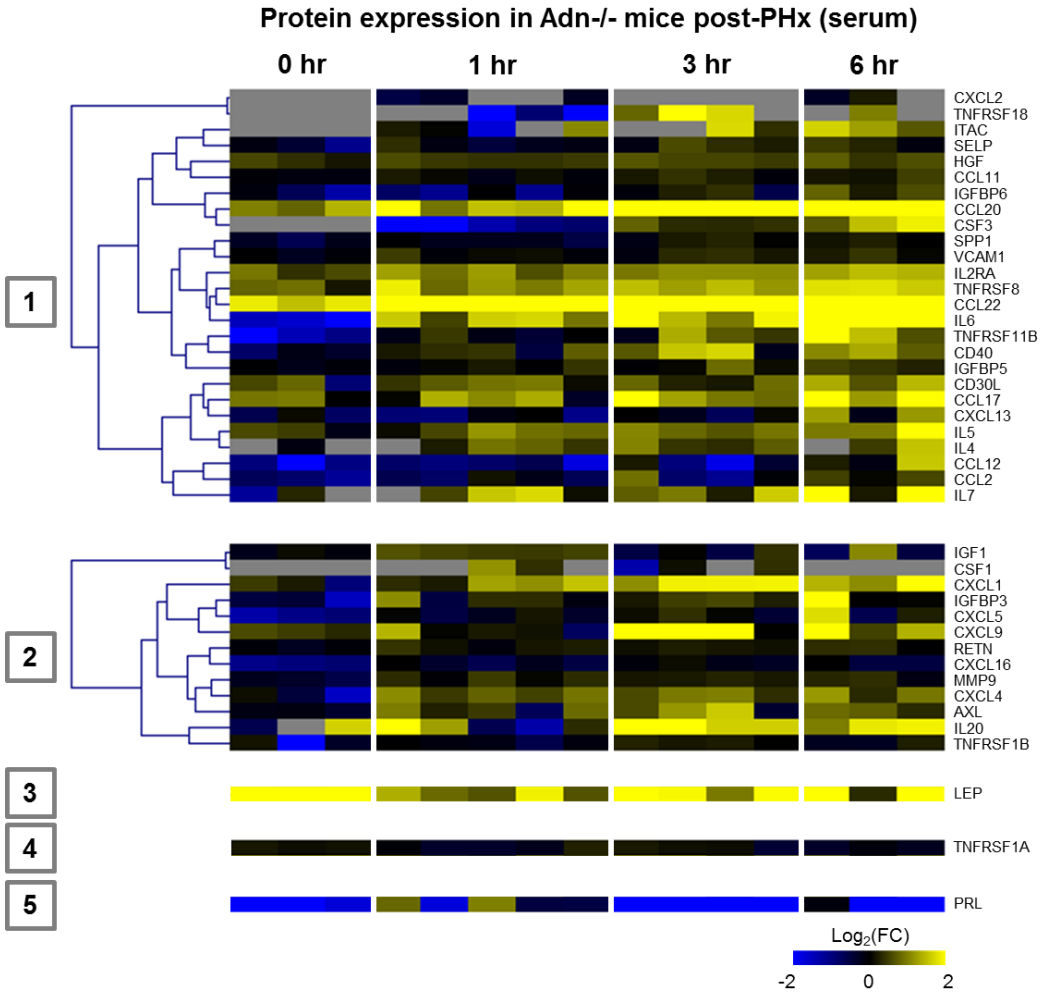

Figure 5.12 Heatmap showing the behavior of proteins in Adn-/- mice. Proteins were included in a group if the p value calculated using an ANOVA was <= 0.30.

5.3.5.1 Proteins with similar expression dynamics in the serum of wild-type and Adn-/- mice may represent robust features of priming

Several proteins display mode 1 behavior in both wild-type and Adn-/- mice (Figure 5.13). TNFRSF8 (formerly CD30T), IL2RA, CCL22 (formerly MDC), and CCL20 (formerly MIP3A) all increase throughout the priming phase. These proteins are related to recruitment of lymphocytes and T cells (CCL20) and dendritic and NK cells (CCL22). This module of protein expression may also be involved in cell activation (IL2RA) and modulating the tissue immune response (TNFRSF8).

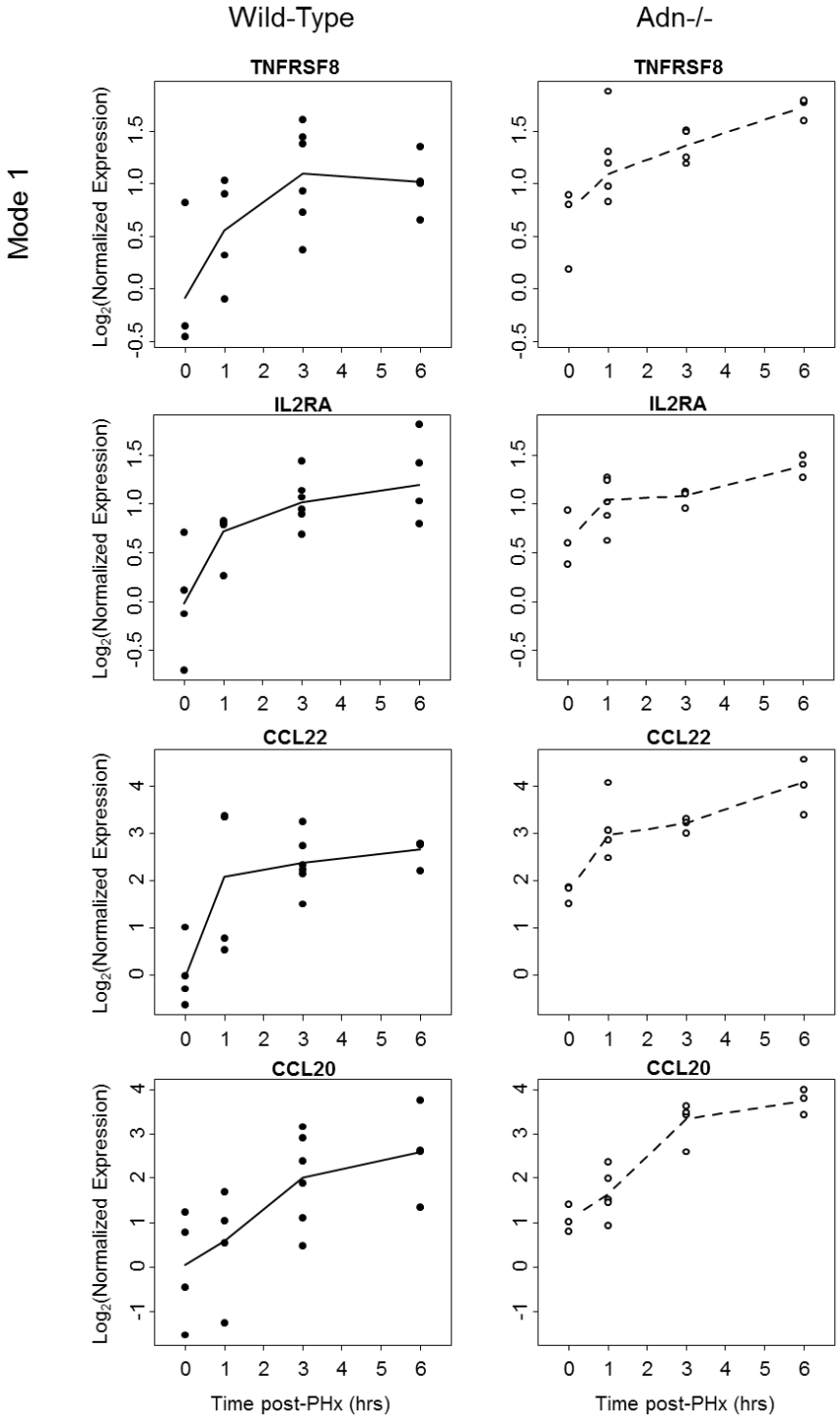

Figure 5.13 Many of the proteins measured in wild-type and Adn-/- mice show similar expression trends in animal serum.

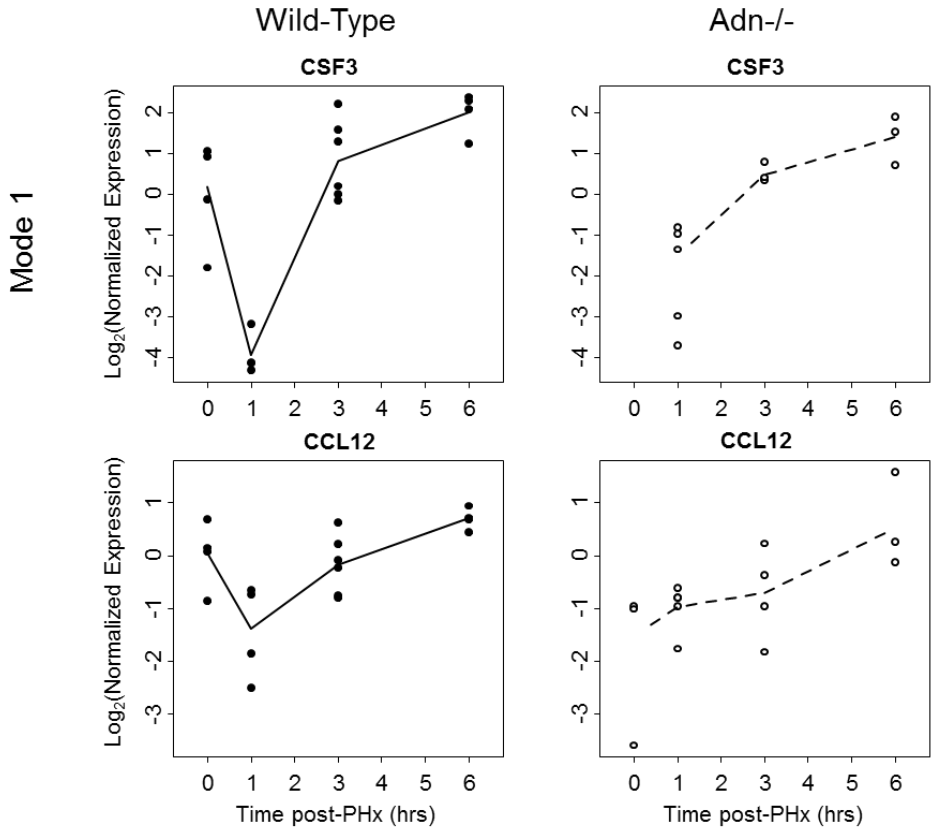

Figure 5.14 Many of the proteins measured in wild-type and Adn-/- mice show similar expression trends in animal serum.

Other proteins display mode 1 behavior following PHx (increasing steadily throughout priming) but show baseline differences between mouse genotypes (Figure 5.14). CSF3 (formerly GCSF) levels are high in wild-type mice at a baseline and below the limit of detection in Adn-/- mice. Similarly, CCL12 (formerly MCP5) levels are high in wild-type mice, but low in Adn-/- mice. Following PHx, levels of both proteins drop in wild-type mice and remain low in Adn-/- mice. These levels subsequently increase until 6hrs post-PHx. CSF3 aids in growth and differentiation of neutrophils and has been found to enhance MMP9 production by hepatic stellate cells,

while CCL12 has is involved in monocyte recruitment (Jiao et al, 2009;Kindt et al, 2007;Simpson et al, 2003). The baseline imbalance between genotypes likely indicates a difference in tissue microenvironment prior to PHx, with low inflammatory cell recruitment and low tissue remodeling. Following PHx, increasing levels of these proteins may result in increased neutrophil and monocyte infiltration and matrix remodeling as the priming phase progresses.

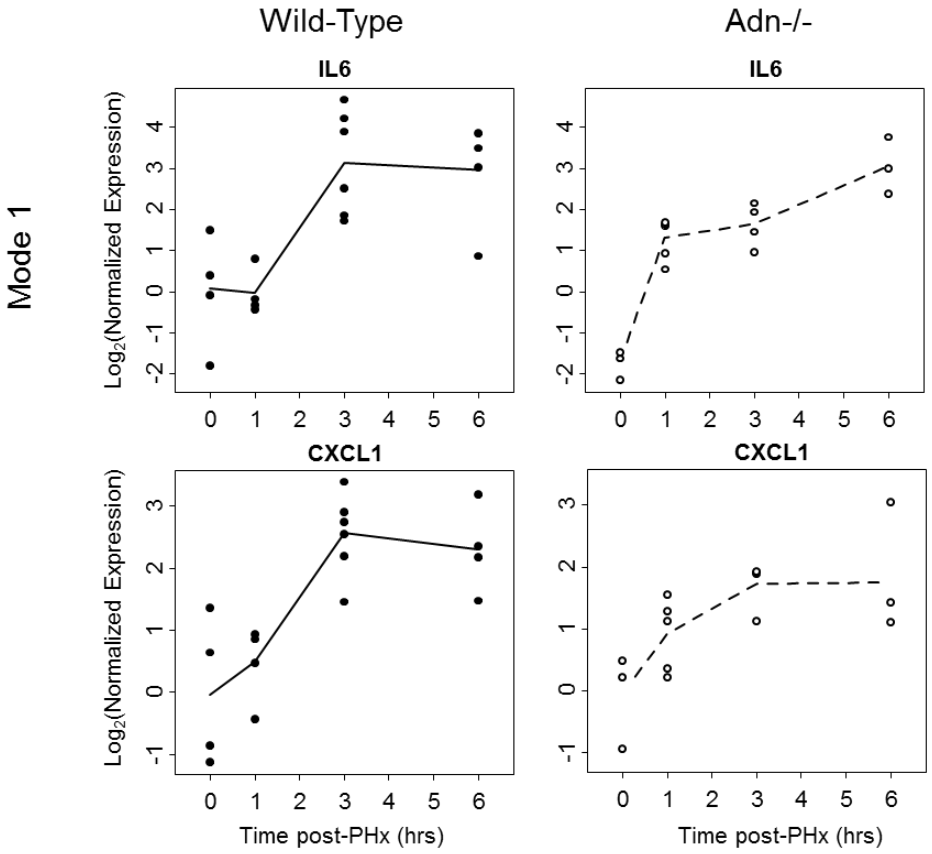

Figure 5.15 Proteins with similar expression trends but altered timing in the serum of wild-type and Adn-/- mice.

Two proteins related to a pro-inflammatory response increase early in the serum of Adn-/- mice when compared to wild-type mice: IL6 and CXCL1 (formerly KC) are increased at 1hr post-PHx in Adn-/- mice but not until 3hrs post-PHx in wild-type mice (Figure 5.15). Increasing levels of these pro-inflammatory proteins are thought to enhance liver regeneration, therefore earlier increases should enhance priming (Fausto et al, 2006;Malato et al, 2008). We have previously reported, however, how a slight decrease in IL6 levels at 3hrs post-PHx in Adn-/- compared to wild-type mice could lead to similar SOCS3 expression and an overall decrease in hepatocyte priming in Adn-/- mice (Correnti et al, 2015). It is possible that similar mechanisms affect CXCL1, impeding its effects enhancing priming.

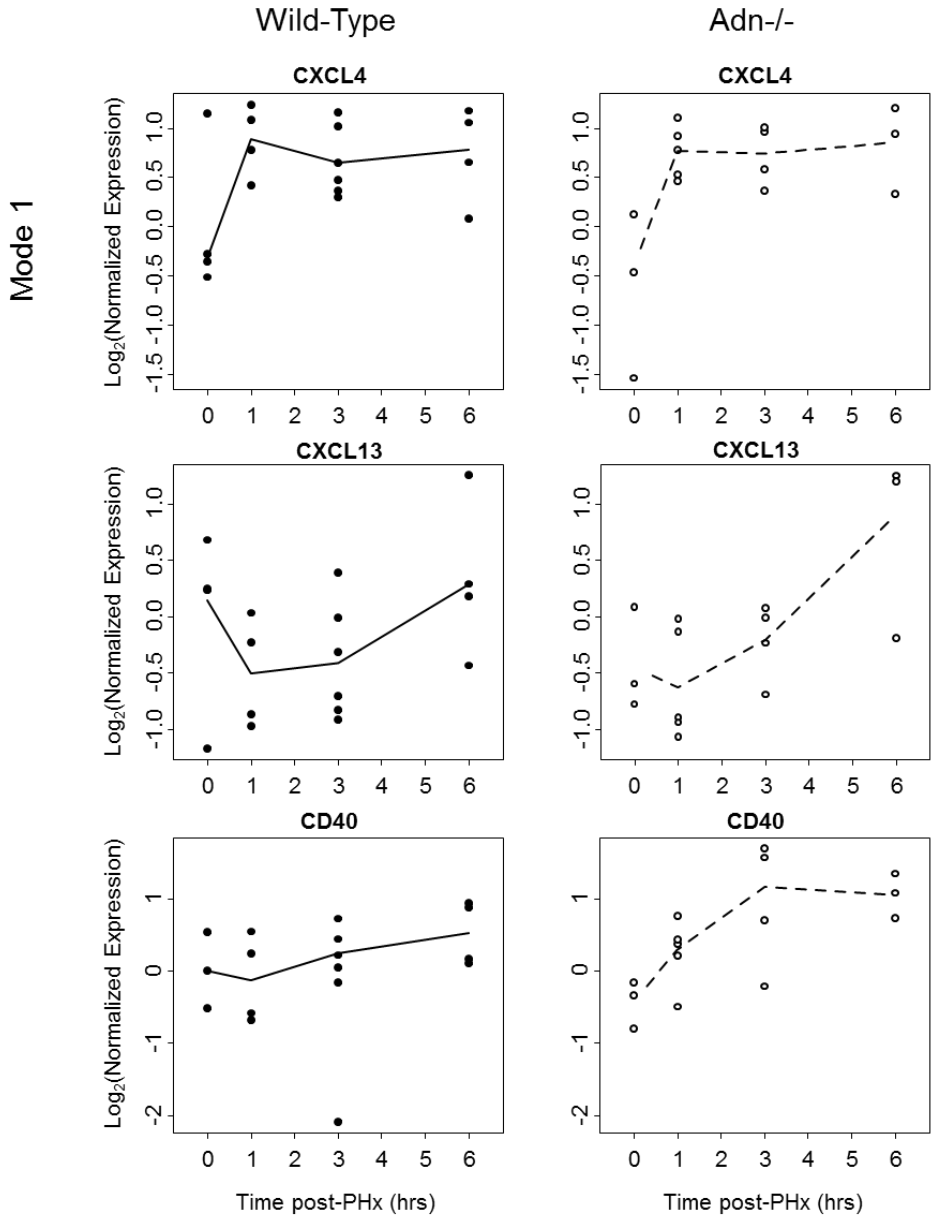
Wild-Type
Adn-/-
Mode 1
CXCL4
CXCL13
CD40
Log2(Normalized Expression)
Time post-PHx (hrs)

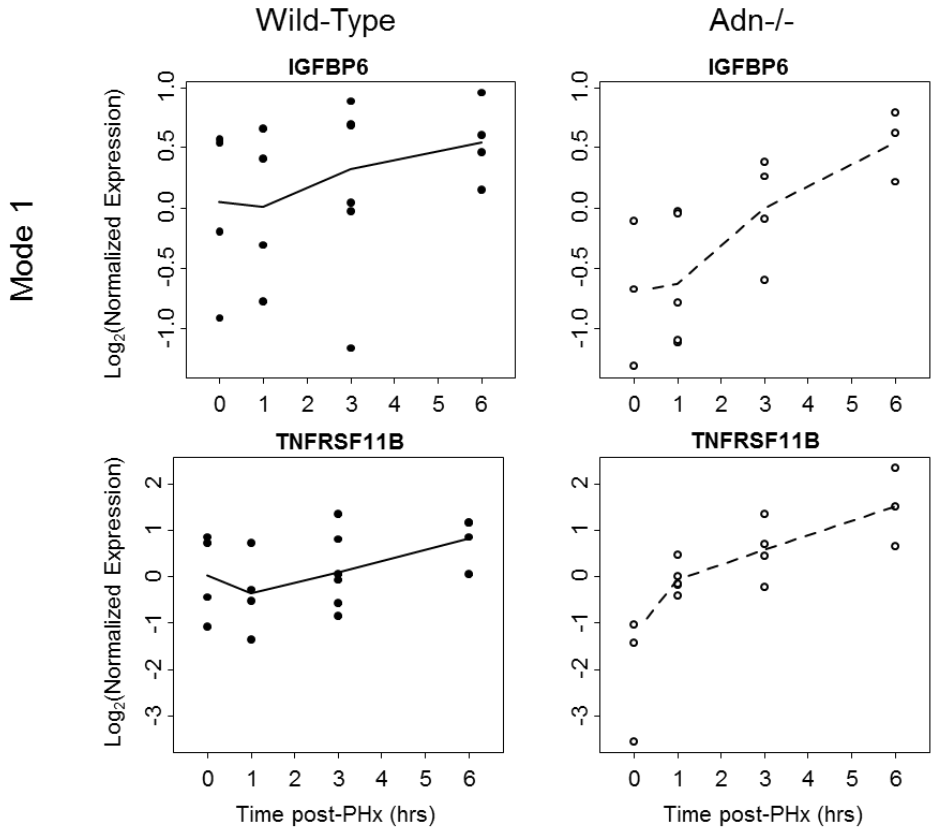

Figure 5.16 Mode 1 behavior in Adn-/- mouse serum post-PHx, but no statistically discernable dynamics in wild-type mice. Nevertheless, the expression trends in wild-type animals are similar, tending to increase throughout the priming phase.

Several proteins show mode 1 behavior in Adn-/- mouse serum post-PHx, but no statistically discernable dynamics in wild-type mice. Nevertheless, the expression trends in wild-type animals are similar, tending to increase throughout the priming phase (Figure 5.16). CXCL4 (formerly PF4), CXCL13 (formerly BLC), CD40, IGFBP6, and TNFRSF11B (formerly OPG) all fall into this group. It is possible that these proteins behave similarly between genotypes, but more power is required to confirm or refute this possibility. In Adn-/- mice, increasing levels of these proteins

may lead to increased stellate cell activation (CXCL4 and CD40), increased B cell recruitment (CXCL13), decreased hepatocyte apoptosis (TNFRSF11B), and decreased angiogenesis (IGFBP6) during the priming phase (Herr et al, 2007;Sahin et al, 2010;Sakai et al, 2012;Schwabe et al, 2001;Zaldivar et al, 2010;Zhang et al, 2012). We speculate that the hepatic stellate cell "activation" occurring during the priming phase in this case is a transition to a pro-regenerative state (See chapters 7 and 8). CD40 has been shown to induce hepatic stellate cell production of IL8 and MCP1, both aiding in regeneration, and CXCL4 has been shown to aid in hepatic stellate cell proliferation but not matrix deposition, indicating a transition to a non-matrix producing state (Schwabe et al, 2001;Zaldivar et al, 2010). This potential pro-regenerative stellate cell behavior during the priming phase could set up stellate cells to be able to produce high levels of growth factors later during regeneration (Correnti et al, 2015).

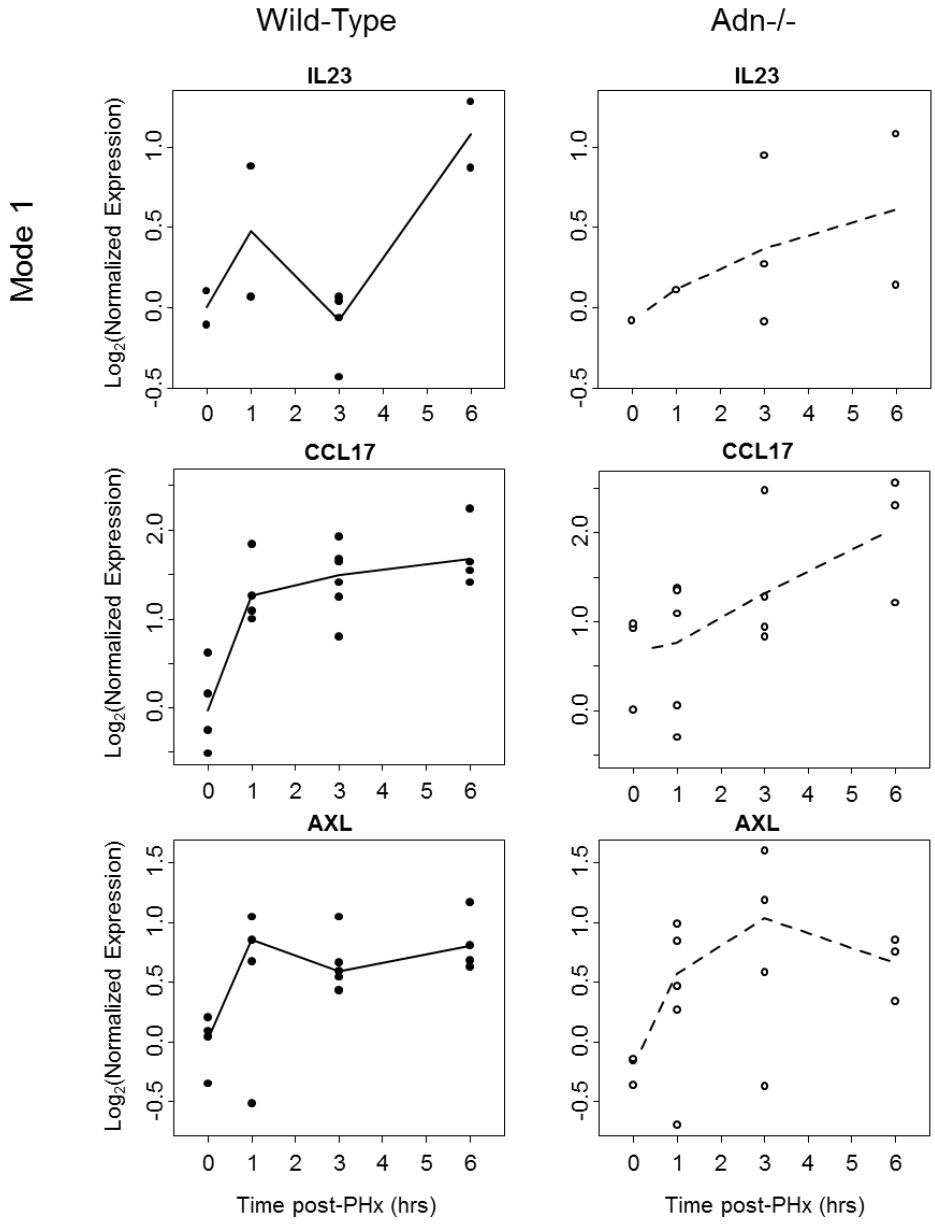
Wild-Type
Adn-/-
Mode 1
IL23
CCL17
AXL
Log2(Normalized Expression)
Time post-PHx (hrs)

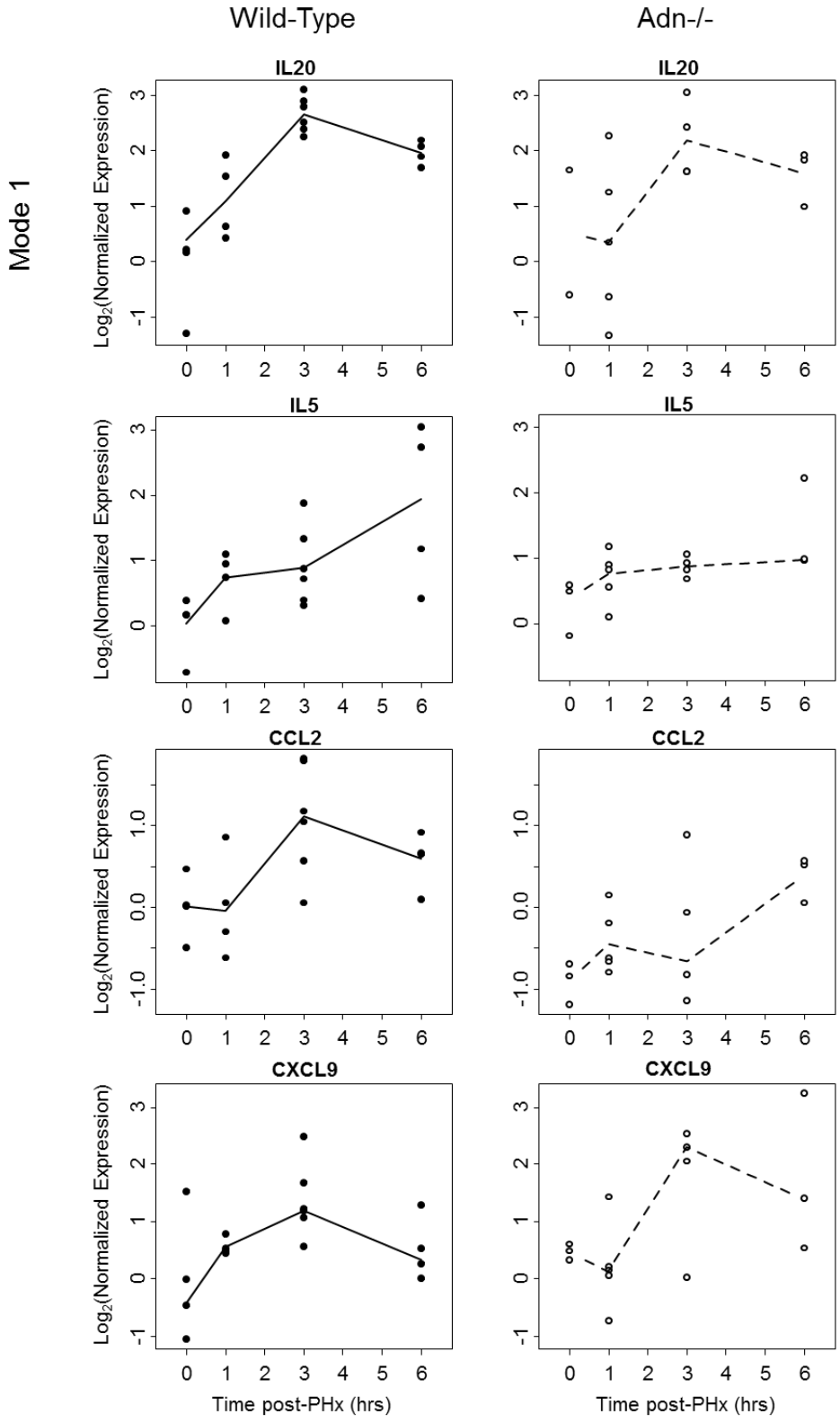
Wild-Type
Adn-/-
Mode 1
IL20
IL5
CCL2
CXCL9
Log2(Normalized Expression)
Time post-PHx (hrs)

Figure 5.17 Several proteins show mode 1 behavior in wild-type mice, but no statistically discernable dynamics in Adn-/- mice. These proteins in Adn-/- mice, however, do show increasing trends throughout the priming phase.

Additionally, several proteins show mode 1 behavior in wild-type mice, but no statistically discernable dynamics in Adn-/- mice (Figure 5.17). The proteins are IL23, TARC, AXL, IL20, IL5, CCL2 (formerly MCP1), and CXCL9 (formerly MIG). These proteins in Adn-/- mice, however, do show increasing trends throughout the priming phase. Further experiments with higher power are necessary to determine if any of these proteins in fact increase during the priming phase in Adn-/- mice.

5.3.5.2 Proteins with different expression dynamics in wild-type and Adn-/- mice

We find no proteins with statistically discernable dynamics in both wild-type and Adn-/- mouse serum that behave oppositely in the two genotypes. Several proteins appear to behave differently in Adn-/- mice, but further experiments with more power are needed to confirm or refute these potential differences.

Proteins increasing during the priming phase in Adn-/- mice that do not increase in wild-type mice (or may decrease slightly) are related to modulating stellate cell behavior (SPP1 [formerly OPN] and MMP9 [formerly PROMMP9]), hepatocyte proliferation (CXCL5 [formerly LIX] and PRL), and recruitment of circulating immune cells (CXCL16 and CXCL5) (Figure 5.18).

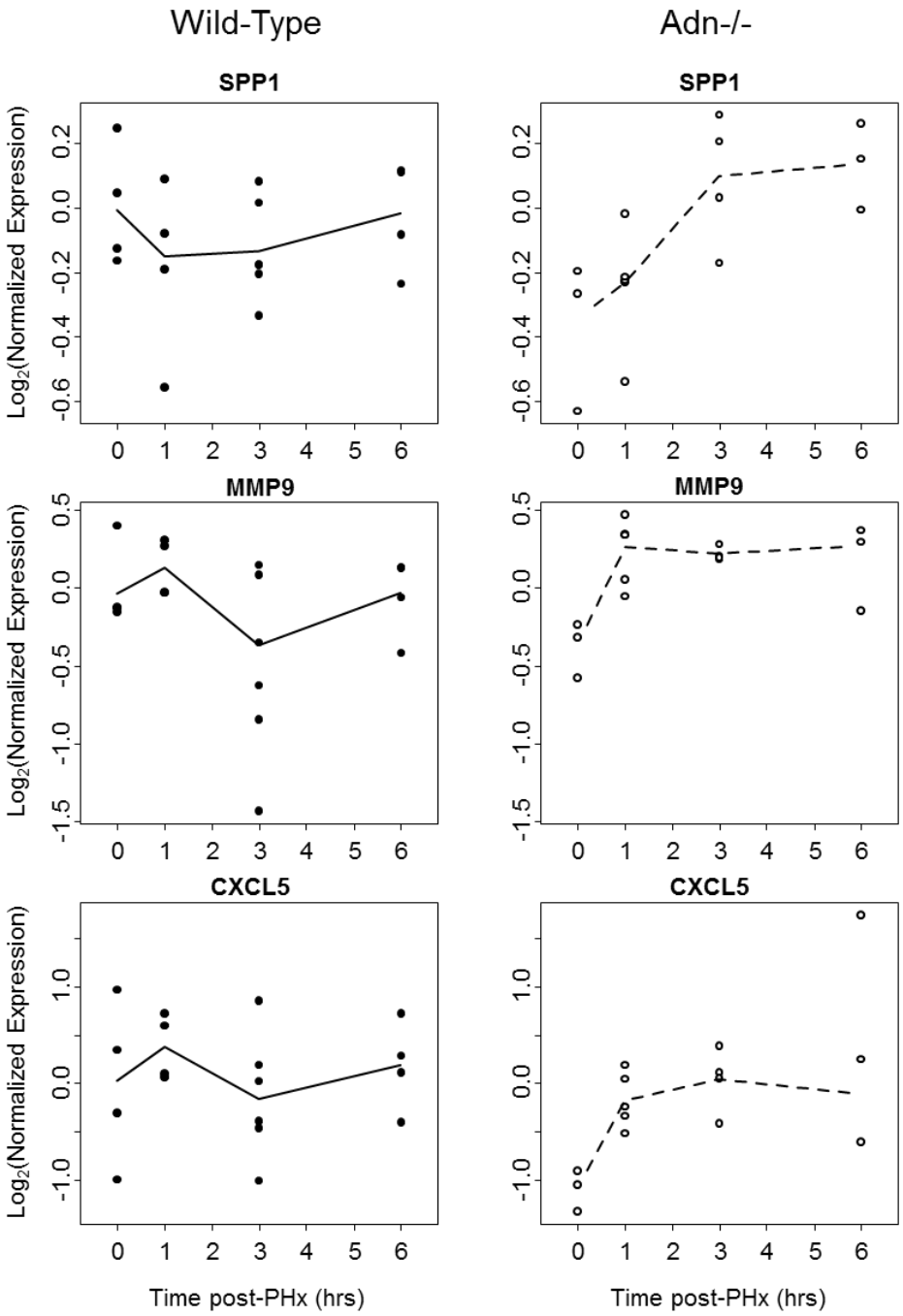
Wild-Type
Adn-/-
SPP1
SPP1
MMP9
MMP9
CXCL5
CXCL5
Log2(Normalized Expression)
Time post-PHx (hrs)
Time post-PHx (hrs)

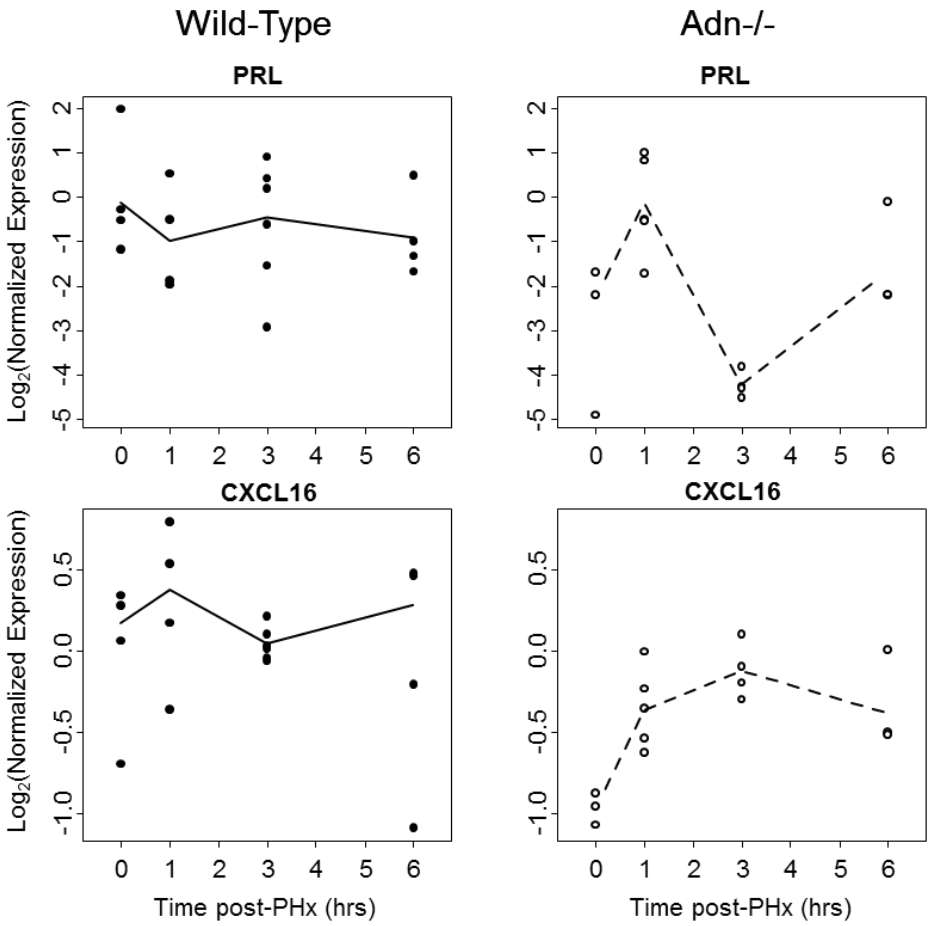

Figure 5.18 Proteins increasing during the priming phase in Adn-/- mice that do not increase in wild-type mice (or may decrease slightly).

SPP1 is associated with hepatic stellate cell activation, while MMP9 is produced by hepatic stellate cells and acts to cleave extracellular matrix – specifically collagen 4 and denatured collagens making up basement membrane (Hemmann et al, 2007). When increased together, they suggest a transition of hepatic stellate cells to a pro-regenerative state that is involved actively in remodeling the tissue matrix. Such a remodeling could contribute to the early release of growth factors and other pro-regenerative molecules stored in the extracellular matrix, enhancing liver regeneration

(Fausto et al, 2006;Michalopoulos, 1990). CXCL5 and PRL have both been shown to enhance hepatocyte proliferation in vitro and in vivo (Olazabal et al, 2009;Simpson et al, 2003). The increased expression of PRL over baseline levels in Adn-/- mice suggests the involvement of other tissues in enhancing hepatocyte proliferation following PHx in these animals. PRL is one of only a few known direct hepatocyte mitogens, and it may contribute to enhanced liver regeneration during pregnancy (GERSHBEIN, 1958). Therefore, we are interested to see that its levels dynamically change during priming in Adn-/- mice. It is possible that the altered immune response of Adn-/- mice to PHx leads to a whole-body response to enhance liver regeneration. What organ is the source of PRL and how it contributes to hepatocyte proliferation in Adn-/- mice, however, remain open questions. The increasing levels of CXCL5 and CXCL16 in Adn-/- mice indicate immune cell recruitment is occurring post-PHx in Adn-/- mice. This recruitment could be compensating for reduced immune cell recruitment prior to PHx (Figure 5.1C).

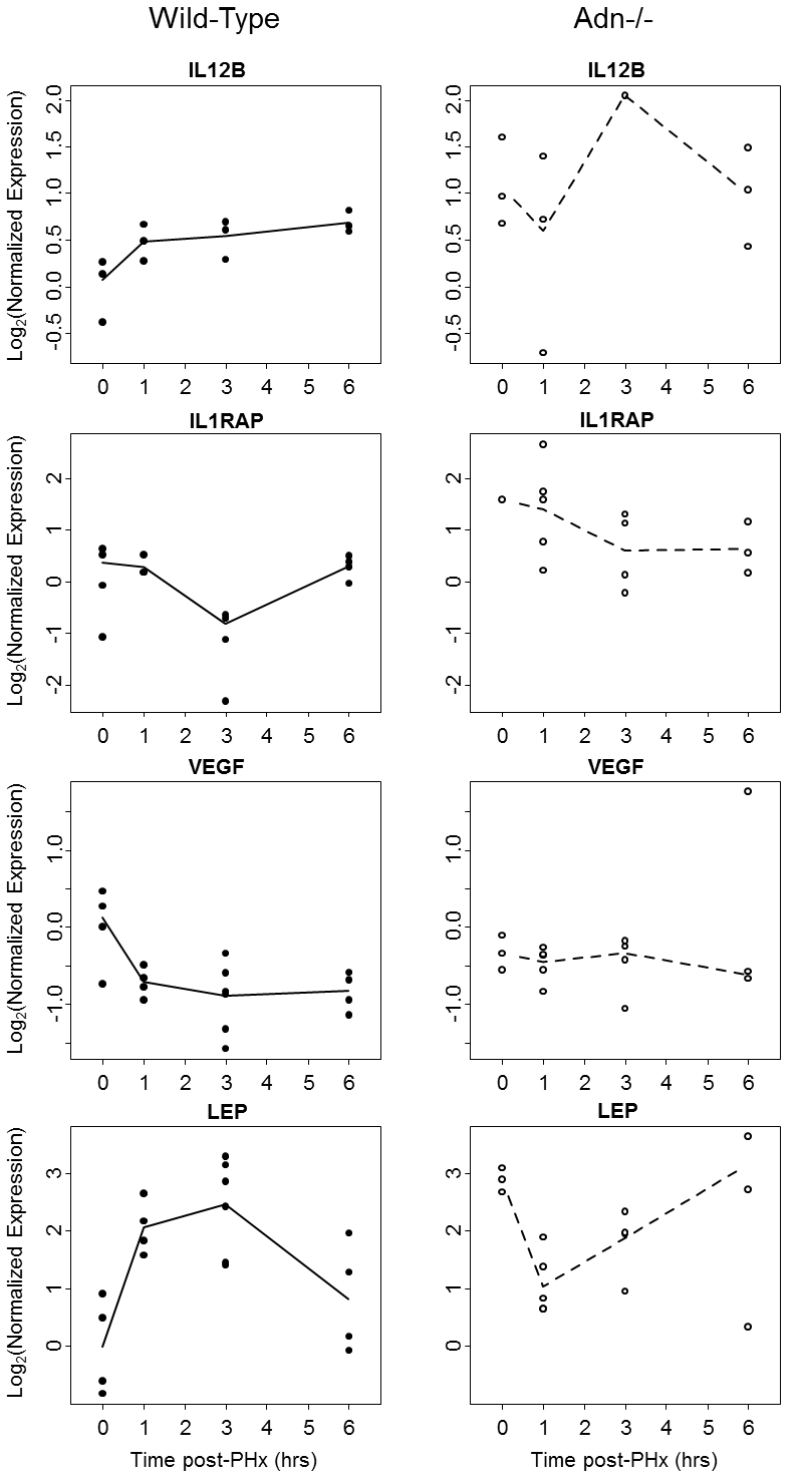

Figure 5.19 Adn knockout inhibits dynamic expression of some proteins.

Although Adn knockout appears to enhance expression of proteins aiding in regeneration, it also inhibits dynamic expression of others (Figure 5.19). Levels of IL12B (also known as IL12P40) increase throughout the priming phase in wild-type mice but do not change in Adn-/- mice. As it is produced predominantly by Kupffer cells in the liver, IL12B levels being low in Adn-/- mice may indicate a decreased Kupffer cell activation in response to PHx (Kmieć, 2001). IL1RAP (formerly IL1RA) levels are reduced in the serum of wild-type mice at 3hrs post-PHx; this decrease may not occur in Adn-/- mice or it may be a sustained decrease (more experiments with higher power are required to determine which). IL1RAP is involved in inflammation and may contribute to hepatocyte priming; therefore, low levels during the priming phase could inhibit priming (Kmieć, 2001). On the other hand, a reduced level of IL1RAP could lead to enhanced MMP9 production and matrix remodeling, aiding in regeneration (Lee et al, 2003). VEGFA (VEGF), a potent angiogenic growth factor, decreases in the serum of wild-type mice post-PHx but remains at the same levels in Adn-/- mice. This decrease could be due to resources being redirected towards regeneration processes, which would not happen in Adn-/- mice.

We were interested to compare the dynamics of LEP in the serum of wild-type and Adn-/- mice post-PHx. Although we find no statistically discernable dynamics in Adn-/- mice post-PHx, the expression trend is opposite that of wild-type mice. In wild-type mice, LEP levels start low then increase post-PHx, reach a peak at 3hrs post-PHx, then decrease to near nominal levels at 6hrs post-PHx. In contrast, LEP levels in Adn-/- mice start high then appear to decrease post-PHx before returning to nominal levels at 6hrs post-PHx. It is important to note that these dynamics in Adn-/- mice are not statistically discernable and more experiments are required to confirm or refute their

behavior. If, though, there is a difference in LEP expression dynamics in wild-type and Adn-/- mouse serum post-PHx, it is possible that altered regulation in adipocytes could be the cause. This potential altered LEP expression could lead to dynamic changes in hepatic stellate cell behavior in the liver post-PHx, as LEP has been shown to modulate hepatic stellate cell behavior (Saxena et al, 2002).

5.3.6 Proteins in liver tissue following PHx show dynamic expression changes in Adn-/- mice

In contrast to wild-type mice, several proteins measured in Adn-/- mice show statistically discernable dynamics in both serum and liver tissue post-PHx (Figures 5.20 and 5.21).

5.3.6.1 Proteins with similar expression dynamics in serum and tissue post-PHx in Adn-/- mice

Levels of SPP1 (formerly OPN) and SELP increase in the serum and tissue of Adn-/- mice post-PHx. Levels peak at 3hrs post-PHx and remain elevated at 6hrs post-PHx (Figure 5.20). Because tissue and serum levels behave so similarly, it is possible that the liver is the main producer of these proteins post-PHx in Adn-/- mice. Similarly, MMP9 increases at 1hr post-PHx and remains elevated for the rest of the priming phase in both serum and tissue of Adn-/- mice. MMP9, also, may be produced predominantly in the liver of these animals. In contrast, CXCL4 (formerly PF4) increases in the serum at 1hr post-PHx and in the tissue at 3hrs post-PHx in Adn-/- mice. It remains elevated in both for the duration of the priming phase. It is possible, therefore, that there may be an extrahepatic source of CXCL4 during liver regeneration in addition to tissue-produced CXCL4. More research is necessary to explore this possibility.

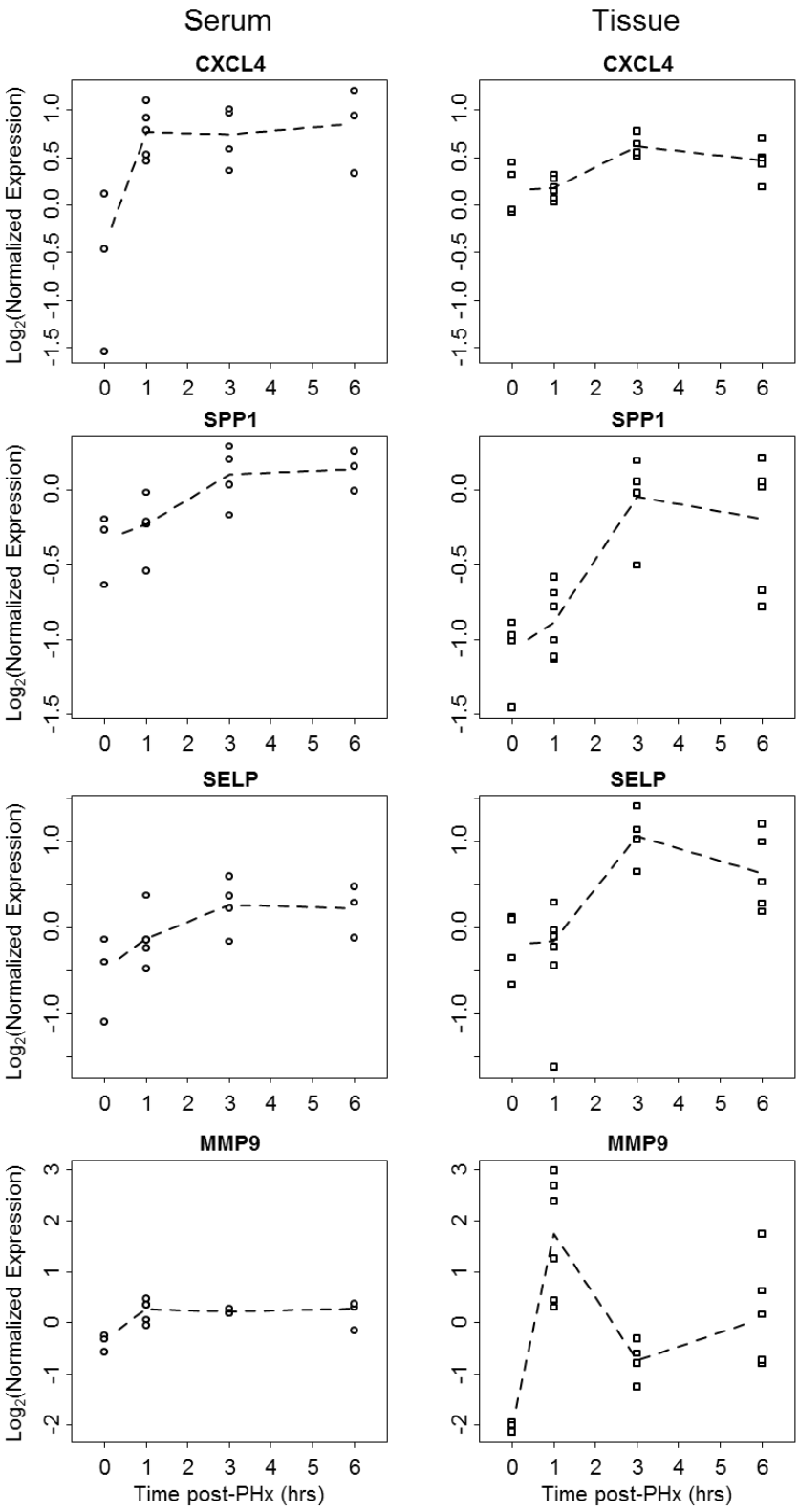
Serum
Tissue
CXCL4
SPP1
SELP
MMP9
Log2(Normalized Expression)
Time post-PHx (hrs)

Figure 5.20 Several of the proteins measured in Adn-/- mice show similar expression trends in animal tissue and serum. This similarity indicates that in And-/- mice the liver is the main producer of these proteins following resection and transport into the tissue is relatively fast.

5.3.6.2 Proteins with opposite expression in serum and tissue post-PHx in Adn-/- mice

CXCL16 increases in the serum of Adn-/- mice post-PHx but decreases in the liver tissue (Figure 5.21). Therefore, it is possible that the liver is not the predominant source of CXCL16 in the serum post-PHx in Adn-/- mice. This is consistent with serum concentration of CXCL16 in each animal being a factor of between ~1.2 to ~30 higher than tissue concentration, measured in pg/mL.

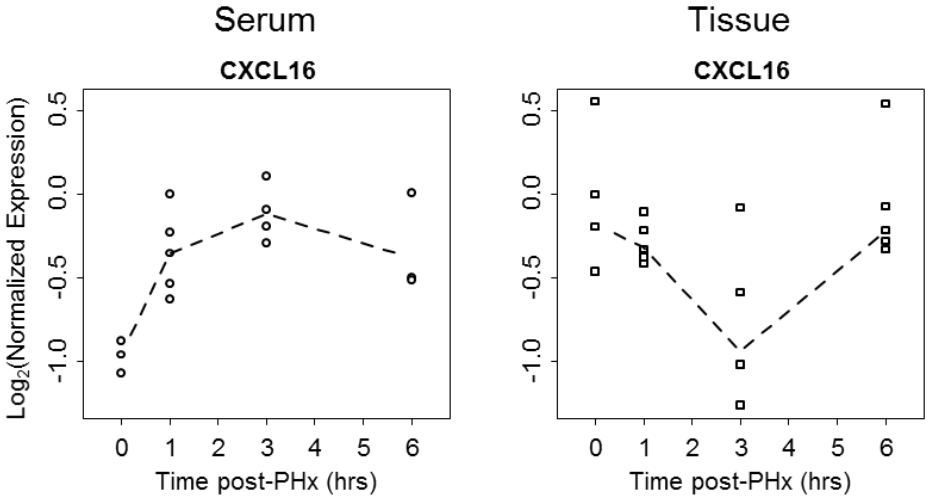

Figure 5.21 One proteins measured in Adn-/- mice shows opposite expression trends in animal tissue and serum. This similarity indicates that in Adn-/- mice the liver is either not the main producer of these proteins following resection or transport into the tissue is relatively slow.

5.3.6.3 Proteins with dynamic expression changes in tissue but no serum changes post-PHx in Adn-/- mice

Additionally, there are proteins with discernable dynamics in the liver of Adn-/- mice, but no discernable dynamics in the serum post-PHx (Figure 5.22).

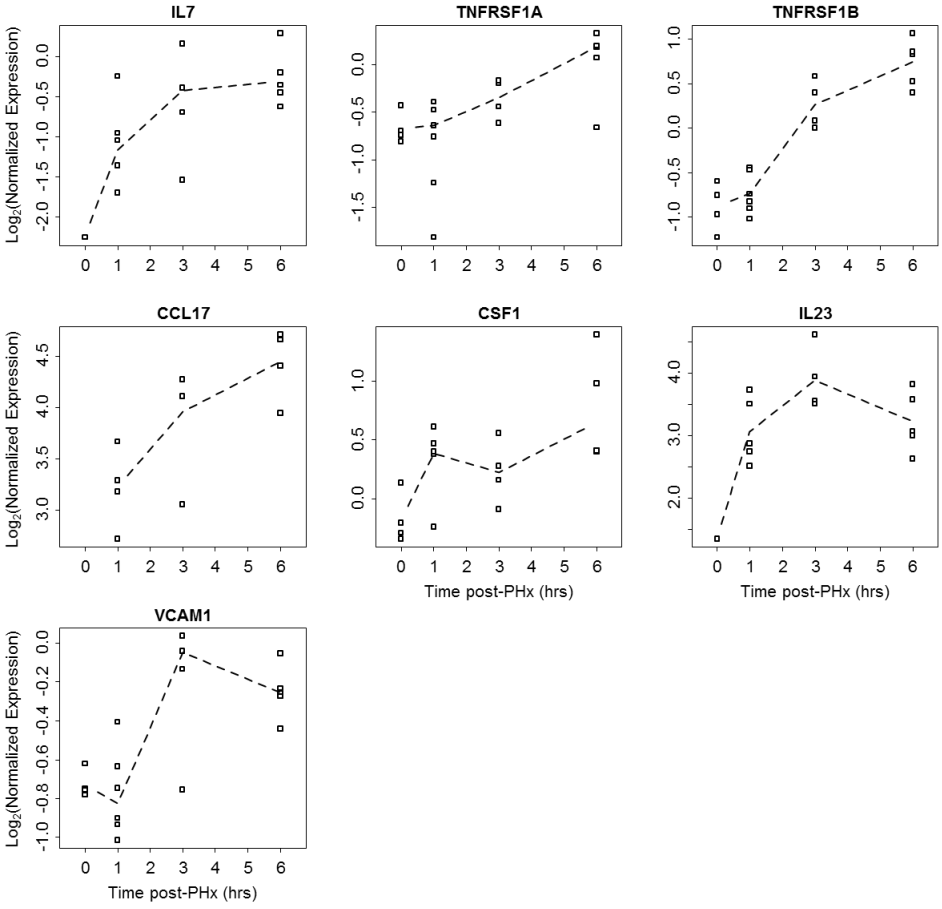

Figure 5.22 Several proteins measured in Adn-/- mice show dynamic expression trends in animal tissue. These dynamics are not reflected in the serum.

Although there are no discernable dynamics in the serum, the expression trends appear similar for all the following proteins in tissue and serum. IL7, TNFRSF1A

(formerly TNFR1), TNFRSF1B (formerly TNFR2), CCL17 (formerly TARC), and CSF1 (formerly MCSF) all increase throughout the priming phase, behaving in mode 1 in the tissue of Adn-/- mice. TNFRSF1A, however, decreases at 1hr post-PHx in some animals. IL23 and VCAM1 increase early post-PHx, but appear to peak prior to the end of the priming phase, behaving in mode 2. Taken together, these protein dynamics indicate an increased immune response (IL7, IL23, TNFRSF1A, and TNFRSF1B), an increased immune cell recruitment (CCL17 and VCAM1), and an increased angiogenesis ability (CSF1). Although, as discussed previously, high levels of the TNFA receptors TNFRSF1A and TNFRSF1B could be caused by a small amount of these receptors bound by TNFA and participating in active signaling.

5.3.7 Adn knockout leads to different tissue regulation of the priming phase

In the liver tissue of wild-type and Adn-/- mice post-PHx, levels of TNFRSF1A show the trend of decreasing at 1hr post-PHx, then increasing throughout the rest of the priming phase (Figure 5.23).

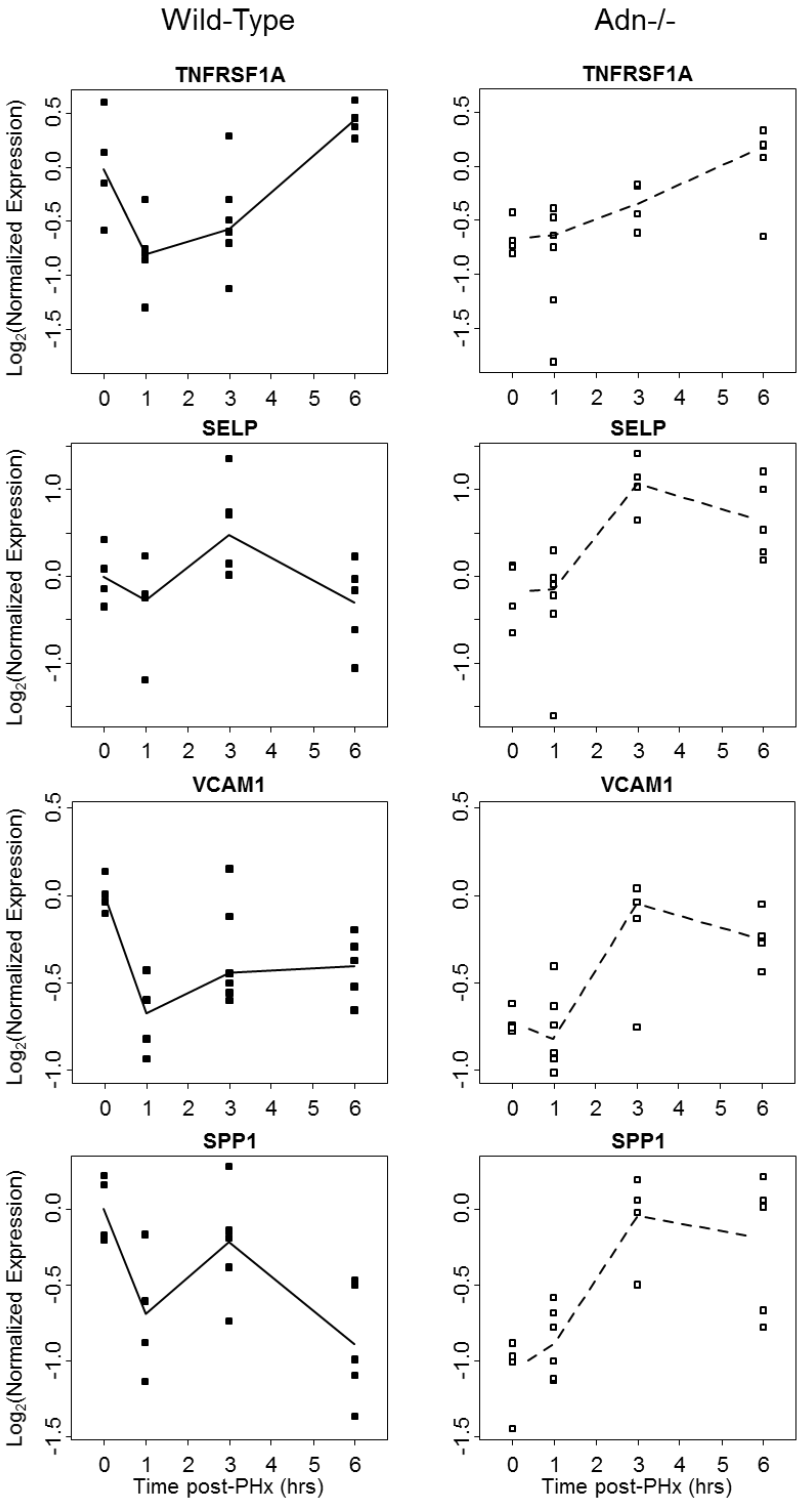

Figure 5.23 Adn knockout leads to different tissue regulation of the priming phase.

This is consistent with TNFRSF1A being bound in a signaling complex early post-PHx, contributing to Kupffer cell activation and hepatocyte priming (Fausto et al, 2006;Muppidi et al, 2004). SELP increases in the tissue of wild-type and Adn-/- mice at 3hrs post-PHx. It returns to baseline levels at 6hrs post-PHx in wild-type mice, but remains elevated in Adn-/- mice, indicating sustained immune cell recruitment in Adn-/- mice. VCAM1 and TNFRSF1B have baseline differences between genotypes, but their behavior is similar post-PHx. Both of these proteins are low at 1hr post-PHx but increase through the rest of the priming phase. SPP1 (formerly OPN), on the other hand, shows different dynamics in the tissue of wild-type and Adn-/- mice post-PHx, decreasing in wild-type mice and increasing in Adn-/- mice. It is possible that this increase in SPP1 in Adn-/- mice is one of the factors predisposing hepatic stellate cells to produce high levels of growth factors at later times during liver regeneration (Correnti et al, 2015).

5.3.8 Priming for liver regeneration in Adn-/- mice appears to be controlled by a different regulatory network structure

We used a heatmap to visualize the correlation network of protein expression in wild-type and Adn-/- mice during the priming phase of regeneration post-PHx (Figure 5.24). We calculated correlations for proteins within the serum (Figure 5.24, lower triangular matrix), within the tissue (Figure 5.24, upper triangular matrix), and between the tissue and serum for each protein (Figure 5.24, diagonal). Most, but not all tissue and serum samples come from the same animals. In some cases, the average of two tissue samples was used as a pseudo-tissue sample for calculating correlation. Similar correlation networks appear to be operating in tissue and serum; however, the correlations in the tissue are sparser than in the serum because the data from the tissue

had more missing expression values. Wild-type mice show several modules of correlated proteins likely corresponding to the modes of expression identified previously. Adn-/- mice, in contrast, show fewer proteins highly correlated within the same modules. Although the correlation network appears similar between species, the strength of correlations in Adn-/- mice appears weaker. This indicates that there could be regulatory mechanisms damping the regulatory network response to PHx in Adn-/- mice. One protein that could contribute to this effect is SOCS3, which we show in chapter 4 is up-regulated in Adn-/- mice during the priming phase of regeneration.

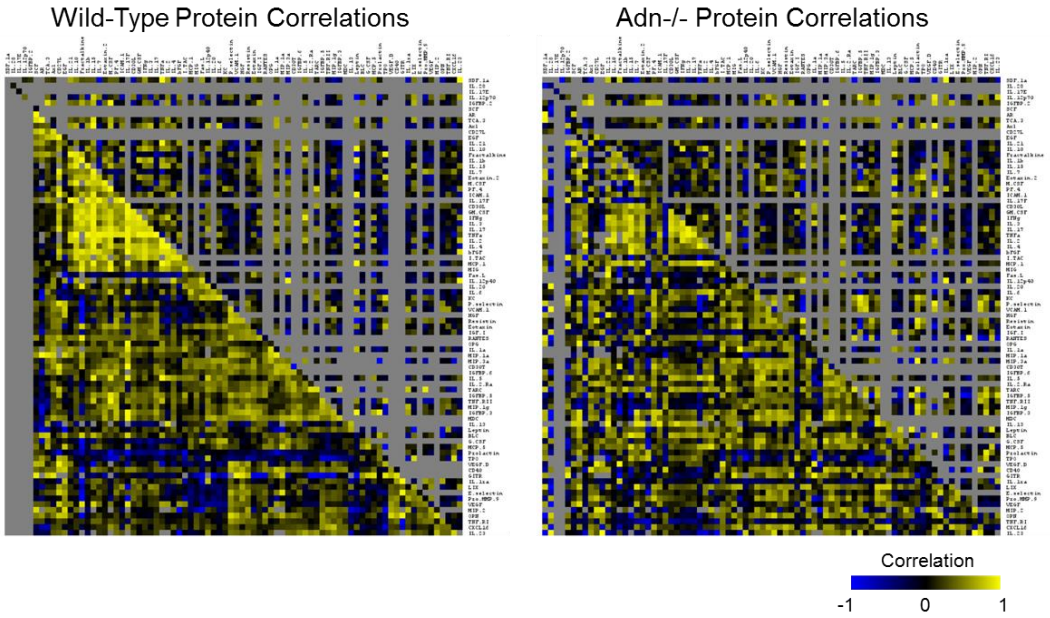

Figure 5.24 The differences in protein expression in wild-type and Adn-/- mice during the priming phase of regeneration may be caused by an altered regulatory network governing dynamic protein expression. The structure of the regulatory network can be represented using a clustered correlation heatmap among proteins. In this schematic, the lower triangular matrix represents correlations among proteins in the serum, the upper triangular matrix represents correlations among the proteins in the tissue, and on the diagonal of the matrix is a representation of the correlation between tissue and serum for each protein. Gray pixels represent NA values in the data.

We also calculated the correlation-based protein network in wild-type and Adn-/- mice using the segmentation method for calculating correlation from time-series, biological data (Figure 5.25), detailed in Appendix B. Using this method takes advantage of the time-series nature of the data to construct pseudo-longitudinal samples. Multiple correlation values are then calculated for each pair of proteins and averaged to estimate true correlation. In Appendix B, we show that this method is robust to missing data, technical and biological noise, and small sample sizes.

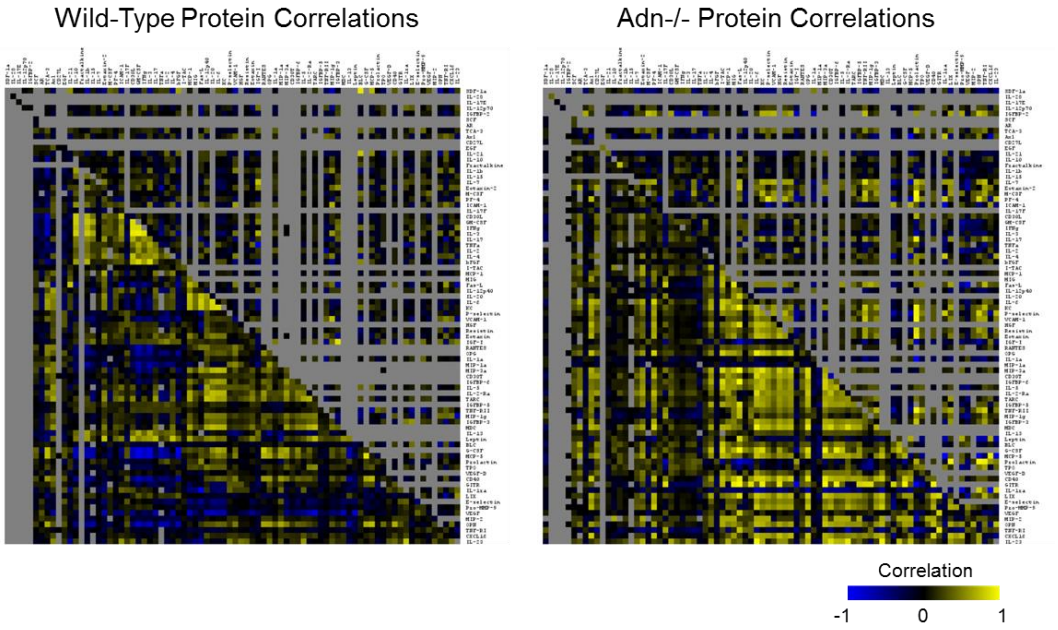

Figure 5.25 The differences in protein expression in wild-type and Adn-/- mice during the priming phase of regeneration may be caused by an altered regulatory network governing dynamic protein expression. The structure of the regulatory network can be represented using a clustered correlation heatmap among proteins. These networks were calculated using the segmentation method detailed in Appendix B with pseudo-samples (see text for details). In this schematic, the lower triangular matrix represents correlations among proteins in the serum, the upper triangular matrix represents correlations among the proteins in the tissue, and on the diagonal of the matrix is a representation of the correlation between tissue and serum for each protein.

The segmentation method for calculating correlation assumes explicitly that each biological replicate is indistinguishable from the others, i.e. the only source of variance among animal replicates is technical and biological noise. Other methods to calculate correlation from biological samples assume this relationship implicitly, but the segmentation method makes the assumption explicit. We therefore further employed this assumption to construct pseudo-samples from which to calculate

correlation. We measured proteins in the serum of three wild-type and three Adn-/- mice at baseline (0 hours post-PHx). We measured more animals during regeneration (4-6 animals per time point). We therefore used three animals from each time point for the segmentation method but "borrowed" protein measurements from the animals not included in the analysis when protein measurements from the included animals were missing (i.e. NA values).

The resulting correlation network using the segmentation is similar to the correlation network calculated using standard Pearson's correlation. There are, however, some differences. Using the segmentation method, we estimate that the relationships among the measured proteins are not as strong as estimated using the standard method. Furthermore, the segmentation-based results suggest that there is a strong negative relationship among many of the proteins estimated to be positive using the standard method (Figure 5.25, upper left quadrant). The loss of correlation estimated in Adn-/- mice (Figure 5.24, upper left quandrant) was even more pronounced using the segmentation method (Figure 5.25, upper left quadrant). The implications of these altered networks and which method accurately captures biological relationships in mice post-PHx remains to be determined.

5.4 Discussion

Using an unbiased approach to investigate cytokine, chemokine, and growth factor dynamics in wild-type and Adn-/- mice during liver regeneration, we find both baseline differences and dynamic differences in protein expression. Prior to resection, we find that Adn-/- mice express lower levels of proteins related to the recruitment of monocytes, neutrophils, and other immune cells. This finding helps to explain the

observation that Adn-/- mice are deficient in recruiting macrophages the site of melanoma and lung cancer tumors, promoting tumor growth (Sun & Lodish, 2010). It is possible that Adn-/- mice are also deficient in recruiting circulating immune cells during liver regeneration or following drug induced liver injury; more research, however, is needed to determine if this is the case.

The finding that Adn-/- mice express low levels of immune cell recruiting proteins is unexpected based on previous research. Levels of adiponectin and leptin in the serum are typically, but not always, inversely related in both health and disease (Chen et al, 2006;Haque et al, 2002;Matsubara et al, 2002;Silha et al, 2003;Vendrell et al, 2004). High leptin (and presumably low adiponectin) has shown to play a role in activation and chemotaxis of monocytes, neutrophils, and other immune cells (Fernandez-Riejos et al, 2010). Low leptin (and presumably high adiponectin) in *ob/ob* mice, on the other hand, has been shown to cause low neutrophil infiltration and high levels of ischemic-reperfusion injury in steatotic livers (Hasegawa et al, 2007). Our results showing that Adn-/- mice (low Adn, high Lep) express low levels of immune cell recruiting proteins suggests a more complex relationship between adiponectin and leptin and immune cell recruitment than previously thought.

During regeneration, we find several proteins that monotonically increase in both wild-type and Adn-/- mice. These include the pro-inflammatory proteins IL6, CCL20, and CCL22 and the receptor TNFRSF8. Wild-type and Adn-/- mice both express monotonically increasing levels of other pro-inflammatory cytokines during priming, which may act as redundant signals to activate the same or similar pathways to induce priming in hepatocytes. Adn-/- mice express increasing levels of SPP1 following PHx, which may indicate a role for hepatic stellate cells during priming in

these animals; there is no statistically discernable increase in SPP1 in wild-type animals, suggesting that any contribution of stellate cells during the priming phase is subtler. Wild-type and Adn-/- mice also express other proteins with different dynamics. We are especially interested to see that levels of PRL increase during the priming phase in Adn-/- mice. PRL has been shown to be a direct hepatocyte mitogen and could help to explain the accelerated regeneration that occurs in Adn-/- mice (Correnti et al, 2015;Olazabal et al, 2009). Taken together, our results suggest a different protein regulatory network governing regeneration in these two genotypes, leading to an altered priming response to resection due to Adn knockout.

Chapter 6

A COMPUTATIONAL MODEL TO SIMULATE LIVER REGENERATION ACROSS PHENOTYPES

Portions of this chapter were adapted from **Cook, D.**, Ogunnaike, B. A., & Vadigepalli, R. (2015). Systems analysis of non-parenchymal cell modulation of liver repair across multiple regeneration modes. *BMC systems biology*, *9*(1), 1. and **Cook D**, Vadigepalli R. Computational Modeling as an Approach to Study the Cellular and Driving Liver Regeneration. In: Liver Regeneration Basic Mechanisms, Relevant Models and Clinical Applications. 2015. p. 185–98.

6.1 Introduction

Liver regeneration involves a highly coordinated response to tissue damage involving multiple cell types (parenchymal, non-parenchymal, and extra-hepatic), multiple size scales (from molecular signaling at the atomic level to overall tissue function at the macro-scale), and multiple time scales (from nearly instantaneous release of ATP from hepatocytes following a partial hepatectomy to the weeks, months, or years it may take for humans to regrow lost liver mass following a resection). Understanding the complexity of the liver's regenerative response to tissue damage and being able to predict the outcome of resection would provide an invaluable tool to patients undergoing partial liver resection for hepatocellular carcinoma or live liver transplant. Computational modeling provides a framework to help understand the complex, multi-scale interactions (molecular, cellular, and organ to organ) governing the liver's innate regenerative ability. Computational modeling

enables researchers to collect and organize the available phenomenological as well as mechanistic knowledge, evaluate a wide range of scenarios in simulations that are experimentally intractable, predict the impact of altering particular underlying mechanisms on the cellular as well as the whole tissue response, and design experiments to test the model-predicted hypotheses on the key control mechanisms governing the overall physiological response.

Researchers in recent decades have made significant progress towards building computational representations of the regulatory events that are known to occur during liver regeneration. These models span a wide spectrum of detail incorporated into the model including spatial aspects, molecular processes and whole-tissue scale phenomena (Figure 6.1A). At one end of the spectrum, agent-based models allow for high spatial resolution, but often for only a section of tissue. At the other end, physiological models account for the regeneration of the whole liver, but offer limited molecular mechanistic insight into how these responses are orchestrated. Models based on the so-called ‘omics’ data provide a middle ground with high resolution of molecular events (e.g., transcriptome, proteome, metabolome) while empirically accounting for whole-tissue response. A broader challenge of connecting the ‘omics’-based modeling to tissue-scale and organ-scale physiology in a multi-scale framework remains unsolved.

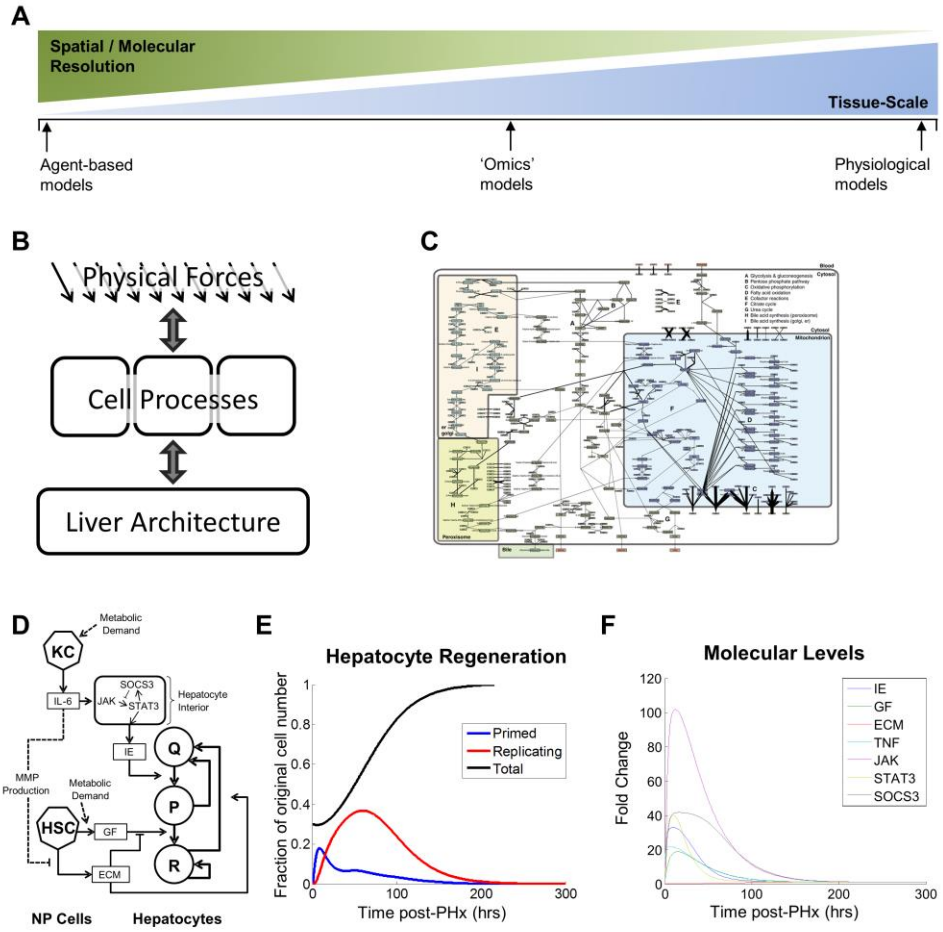

Figure 6.1 Computational models of liver regeneration. (A) Computational limitations require a trade-off between high-resolution (molecular or spatial) and the ability to predict whole-tissue function. (B) Agent-based models, such as that developed by (Hoehme et al., 2010) based on CellSys, allow for high spatial resolution, but often for only a section of tissue. (C) Models based on 'omics' data, such as Hepatonet1 developed by (Gille et al., 2010), provide a middle ground where there is high resolution of molecular events at the desired scale (transcriptome, proteome, metabolome) and the molecular regulation can be extrapolated to whole tissue. (D) Physiological models, such as that developed by (Furchtgott et al., 2009), predict the regeneration of the whole liver, but offer limited mechanistic insight into the molecular events. (E) Outputs from the physiological model can show cells in discrete physiological states as well as (F) molecular regulation governing those cell state transitions. Figure 1C was reproduced from (Gille et al., 2010).

A computational model recently published by the Drasdo lab took an agent-based modeling approach to simulating liver regeneration following carbon tetrachloride administration (Hoehme et al, 2010). This model integrated three disparate scales of data: liver lobule architecture, cell processes, and physical forces (Figure 6.1B). Liver architecture was reconstructed in 3-D from immunohistochemically stained confocal microscope images of livers. Liver architecture was considered as a fixed parameter as carbon tetrachloride does not drastically alter this aspect. Several cellular processes considered in the model were spatially distributed cell replication, necrosis following toxin administration, and hepatocyte-sinusoid contact area and orientation. The cell replication and necrosis were modeled as stochastic processes for each cell in the model, while hepatocyte-sinusoid orientation was simulated as a directed stochastic process with orientation biased towards an alignment along sinusoids. In addition, this model considered individual forces acting between cells. Each cell was modeled as a polarized, deformable sphere (with the bile canalicular structure oriented towards other hepatocytes and the basolateral membrane oriented towards the sinusoid). Physical forces, governed by cell adhesion, compression, and deformation were considered between cells. Model simulations predicted that hepatocytes must have a strong propensity for alignment along the sinusoid in order to capture the observed regeneration phenotype following chemical injury. Hoehme et al. (2010) speculated that endothelial cells that survive the toxic liver damage contribute to such an alignment propensity.

Omics" based modeling involves a more detailed account of molecular aspects. In this approach, high dimensional gene or protein expression data or metabolomics

data are used to train or inform a model structure and parameters. Often, these models are algebraic because they necessarily contain a large number of terms, not amenable for typical ordinary differential equation based dynamic modeling. An example of an 'omics' model of liver function is the HepatoNet model constructed by the Holzhutter lab (Gille et al, 2010). This model contains 2539 individual reactions and 777 metabolites to simulate the metabolic function of the liver (Figure 6.1C). The reactions were formulated into a stoichiometric matrix of fluxes and flux balance analysis was used to match the externally measure metabolites under an optimization objective of minimizing internal fluxes. The authors employed this model to investigate the robustness of the metabolic network active in hepatocytes by simulating single-enzyme knockouts. This model, though molecularly detailed, did not connect molecular regulation to the whole tissue function in the context of regeneration.

As an example at the other end of the modeling spectrum, the Periwal group developed a physiologically based model that simulates tissue-scale liver regeneration following partial hepatectomy (Furchtgott et al, 2009). This model includes the JAK-STAT signaling pathway induced by IL-6 and growth factors (GF) produced by non-parenchymal cells as drivers of regeneration and includes extracellular matrix (ECM) as a negative regulator of regeneration (Figure 6.1D). Hepatocytes were considered as existing in one of three physiological states: Quiescent (Q), Primed (P), or Replicating (R), with shifts between these states governed by factors produces by non-parenchymal cells, specifically Kupffer cells (KC) and hepatic stellate cells (HSC). This physiologically based model allowed the authors to connect the dynamic hepatocyte regeneration state (Figure 6.1E) to molecular regulation (Figure 6.1F). Using this model, Furchgott, Chow, and Periwal predicted that two smaller resections

can result in faster recovery than a single large resection and that decreasing metabolic load in the liver through fasting could lead to recovery following massive hepatectomy.

Other studies have also used computational modeling to explore liver function beyond the context of regeneration. For example, the Hunt lab used a game-theory model to explore the zonated liver metabolism of toxin clearance (Sheikh-Bahaei et al, 2009). Their model consisted of multiple agents that can either eliminate a toxin (using nutrients) or ignore the toxin. Each hepatocyte (agent) in the model learned rules for eliminating toxins through a reinforcement learning rule to optimize long-term toxin elimination. They found that, for certain classes of toxins with specific harm to nutrient cost ratios, the most efficient elimination strategy is a zonated approach. In contrast to utilizing an agent based approach, the Kuepfer lab developed a spatially-resolved model of the liver architecture coupled with a physiologically-based pharmacokinetic model to simulate blood flow and drug perfusion in the liver using partial differential equations (Schwen et al, 2014). This model was employed to assess and make predictions on how increasingly severe chronic liver disease would affect liver drug metabolism. In the context of liver fibrosis, the Vodovotz lab used an agent-based model to investigate the progression of and treatment for fibrosis (Dutta-Moscato et al, 2014). This model takes into account multiple cell types in the liver (hepatocytes, KCs, and HSCs) as well as multiple cell states (i.e. M1 and M2 polarization of KCs). Model simulations indicated that treating fibrotic livers with anti-TNF-α could lead to decreased collagen deposition. However, clinical treatment of patients with alcoholic steatohepatitis using anti-TNF-α have been poorly received

due to a suppressed immune system and increased likelihood of severe infections (Naveau et al, 2004).

In addition to the classes of models and examples summarized above, there exist several opportunities where the disparate models with varying level of detail can be combined or merged to more accurately represent liver function during regeneration (Figure 6.1A). For example, it is possible to combine the metabolomic modeling methods with the agent-based models by incorporating the detailed metabolic model into each hepatocyte component. This formulation may be able to capture the pericentral to periportal gradient of hepatocyte metabolism seen in the homeostatic liver and predict how this gradient may change in response to tissue resection. Alternatively, physiologically based models could be expanded to include data from transcriptomic or proteomic studies to account for a larger context of molecular mechanisms governing physiological changes. In such an extended multi-scale framework, the combined physiological-molecular modeling could be used to inform and prioritize where additional molecular details are required to iteratively expand the molecular detail, connecting the physiological scale phenomenology with molecular scale mechanisms.

In this chapter, we employ a physiologically based model to explore and understand the control principles governing liver regeneration. In contrast to ‘omics’ data analysis studies aimed at identifying global molecular changes in the liver during regeneration, the present approach employs a targeted approach to identify classes of molecular regulatory events that strongly contribute to liver regeneration or deficiencies in liver repair. We extended the cell phenotype based computational model of liver regeneration first proposed by (Furchtgott et al, 2009) to include both

cell growth and replication. We employ this extended model to investigate quantitatively how altering the molecular regulation of hepatocytes affects the liver's innate repair ability. Our extended model maintains the structure of the original model by combining classes of molecular signals with physiological observations of regeneration to capture dynamic regeneration phenotypes.

6.2 Methods

6.2.1 Computational model development

We used an extended computational model of liver regeneration (represented schematically in Figure 6.2) to investigate quantitatively how altering the molecular regulation of hepatocytes affects the liver's innate repair ability.

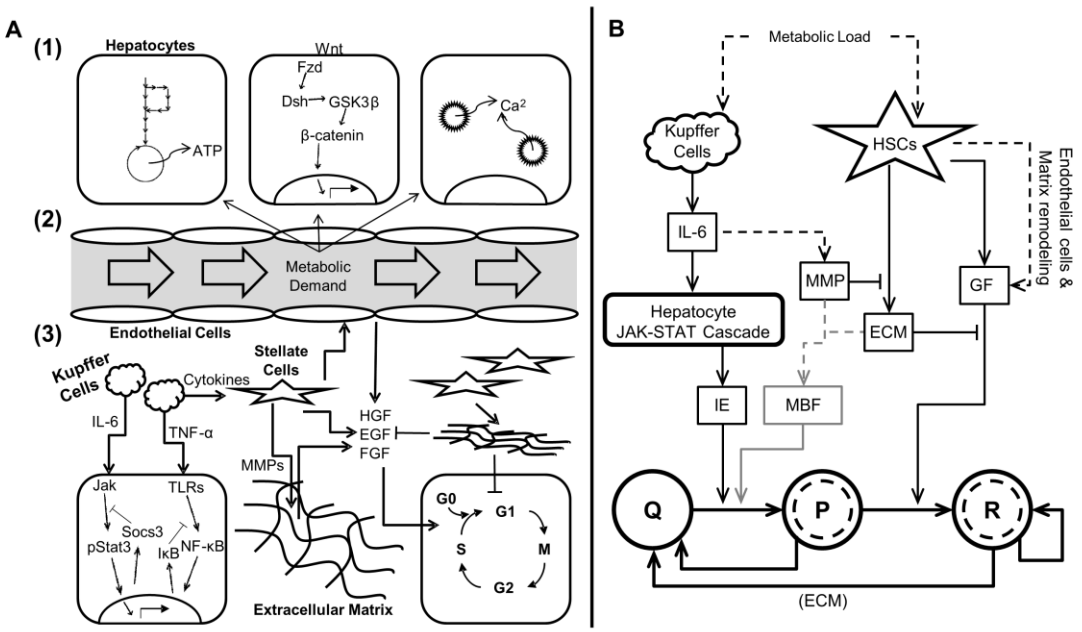

Figure 6.2 Schematic representation of the changes occurring during liver regeneration following PHx. (A) Detailed schematic. (1) Following PHx, hepatocytes respond within 30 seconds of tissue damage. Early post-PHx, previous work has shown release of ATP, increases in WNT signaling, and ionic Calcium release from hepatocyte mitochondria. (2) These responses in hepatocytes are likely to be driven by an increase portal blood flow, an increase in portal pressure, and an increase in metabolic demand per cell (increased nutrient availability, increased toxin flux, and increased extra-hepatic signals including LPS). (3) Signals from the blood and from hepatocytes activate non-parenchymal cells to produce factors governing hepatocyte entry into the cell cycle (including priming). (B) Simplified schematic diagram. This schematic shows the relationships included in the computational model. Several important pathways are lumped or represented as physiological transitions rather than including truly mechanistic detail. This physiological approach allows for insight into control principles of regeneration governed by archetypal signaling pathways. The gray matrix-bound factor (MBF) signaling was added to the model to investigate the contribution to liver mass recovery of matrix-bound signaling, but because of a relatively small impact on the dynamic mass recovery was excluded from further analyses.

A detailed explanation of initial model derivation and parameter estimation is available in (Furchtgott et al, 2009). Our extended model maintains the framework of the previously published initial model by allowing hepatocytes to exist in one of three states: Quiescent (Q), Primed (P), or Replicating (R). Factors produced by non-parenchymal cells in response to liver metabolic load (metabolic demand per cell or M/N) shift hepatocytes between states, according to the following equations.

$$\frac{d}{dt}Q = -k_{QP}([IE]-[IE_0])Q + k_{RQ}[ECM]R + k_{req}\sigma_{req}P - k_{ap}\sigma_{ap}Q \quad (6.1)$$

$$\frac{d}{dt}P = k_{QP}([IE]-[IE_0])Q - k_{PR}([GF]-[GF_0])P - k_{req}\sigma_{req}P - k_{ap}\sigma_{ap}Q \quad (6.2)$$

$$\frac{d}{dt}R = k_{PR}([GF]-[GF_0])P - k_{RQ}[ECM]R + k_{prol}R - k_{ap}\sigma_{ap}R \quad (6.3)$$

Where [IE] represents the concentration of immediate early genes expressed in response to STAT-3 transcriptional regulation and [ECM] represents the amount of extracellular matrix. σ_{ap} and σ_{req} are sigmoidal functions defined as:

$$\sigma_{ap} = 0.5 * \left(1 + \tanh\left(\frac{(\theta_{ap} - {}^{M}/_{N})}{\beta_{ap}}\right)\right) \quad (6.4)$$

$$\sigma_{req} = 0.5 * \left(1 + \tanh\left(\frac{(\theta_{req} - [GF])}{\beta_{req}}\right)\right) \quad (6.5)$$

The parameters β and θ in each of these equations are tuned so that when metabolic load is high, σ_{ap} is high; conversely, when [GF] is high, σ_{req} is low. Therefore, when cells are highly stressed (high metabolic load), apoptosis occurs at a high rate; when GFs are available, cells remain in the "Replicating" state.

The JAK-STAT signaling pathway, GF production, and ECM production are modeled as a combination of first order and Michealis-Menton kinetics, as shown in the following equations. For a schematic of the JAK-STAT signaling pathway, see Figure 6.4A.

$$\frac{d}{dt}[IL6] = k_{IL6}\frac{M}{N} - \frac{V_{JAK}[IL6]}{[IL6]+k_M^{JAK}} - \kappa_{\mathrm{IL6}}[IL6] + k_1 \quad (6.6)$$

$$\frac{d}{dt}[JAK] = \frac{V_{JAK}[IL6]}{[IL6]+k_M^{JAK}} - \kappa_{JAK}[JAK] + k_2 \quad (6.7)$$

$$\frac{d}{dt}[STAT3] = \frac{V_{ST3}[JAK][proSTAT3]^2}{[proSTAT3]^2+k_M^{ST3}(1+[SOCS3]/k_I^{SOCS3})} - \frac{V_{IE}[STAT3]}{[STAT3]+k_M^{IE}} - \frac{V_{SOCS3}[STAT3]}{[STAT3]+k_M^{SOCS3}} - \kappa_{ST3}[STAT3] + k_3 \quad (6.8)$$

$$\frac{d}{dt}[SOCS3] = \frac{V_{SOCS3}[STAT3]}{[STAT3]+k_M^{SOCS3}} - \kappa_{SOCS3}[SOCS3] + k_4 \quad (6.9)$$

$$\frac{d}{dt}[IE] = \frac{V_{IE}[STAT3]}{[STAT3]+k_M^{IE}} - \kappa_{IE}[IE] + k_5 \quad (6.10)$$

$$\frac{d}{dt}[GF] = k_{GF}\frac{M}{N} - k_{up}[GF][ECM] - \kappa_{GF}[GF] + k_7 \quad (6.11)$$

$$\frac{d}{dt}[ECM] = -k_{deg}[IL6][ECM] - \kappa_{ECM}[ECM] + k_6 \quad (6.12)$$

Where [proSTAT3] represents the concentration of monomeric STAT-3 available to dimerize following IL-6 signaling. It should be noted that in the original model our [IL-6] term representing cytokine signaling was called [TNF]. Cannonically, TNF signals through the NF-κB cascade, while IL-6 signals through the JAK-STAT cascade. As previously described in (Furchtgott et al, 2009) and in (Correnti et al, 2015), the [IL-6] variable should be considered a lumped variable representing the physiological impact of general cytokine signaling rather than an exact analogue to IL-6 protein levels. Therefore, we used the name [IL-6] for this variable with parameters derived from TNF.

The overall cell mass, N, was modified from the initial model to include cell growth of primed and replicating cells in response to metabolic load as follows:

$$N = Q + G(P + R) \quad (6.13)$$

Where G represents the relative cell mass, which is initially set to 1.

Additionally, when considering the contribution of matrix bound factors to the priming phase of regeneration (Figure 6.2B, gray portion), the following equations were added.

$$\frac{dMBF_{ECM}}{dt} = -k_{MBF}\left(\frac{1}{[ECM]} - [ECM]_0\right) + k_{up}[GF][ECM] \quad (6.14)$$

Where MBF_{ECM} represents the matrix-bound signals, which are released from the matrix when matrix is degraded at a rate of k_{MBF}. We assumed that these signaling factors, which could contain growth factors such as HGF and FGF, were replenished at a rate equivalent to growth factor uptake by the ECM.

$$\frac{dMBF_{Free}}{dt} = k_{MBF}\left(\frac{1}{[ECM]} - [ECM]_0\right) - \kappa_{MBF}[MBF_{Free}] \quad (6.15)$$

Where MBF_{Free} represents the signaling factors released from matrix and κ_{MBF} is the degradation rate of MBF_{Free} once they have been released.

These additional signals (specifically, MBF_{Free}) act to prime hepatocytes. We assumed that the transition rate from quiescent to primed was similar no matter whether MBF or IE gene signals were driving the transition. We therefore modified equations 6.1 and 6.2 as follows to take this additional signaling into account.

$$\frac{d}{dt}Q = -k_{QP}([IE] - [IE_0])Q - k_{QP}[S_{Free}]Q + k_{RQ}[ECM]R + k_{req}\sigma_{req}P - k_{ap}\sigma_{ap}Q \quad (6.1a)$$

$$\frac{d}{dt}P = k_{QP}([IE] - [IE_0])Q + k_{QP}[S_{Free}]Q - k_{PR}([GF] - [GF_0])P - k_{req}\sigma_{req}P - k_{ap}\sigma_{ap}Q \quad (6.2a)$$

All simulations were performed in Matlab (Mathworks, Natick, MA). Model equations were set up to prevent molecular levels from becoming negative; however, some parameter sets combined with the integration tolerances of ode15s led to GF levels becoming negative at longer simulation times (greater than 150 hours). These impossible GF levels did not significantly impact the regeneration profile because

most of the growth had concluded by the time GF became negative. Because of these numerical instabilities, however, GF levels were constrained to a minimum of 1.

6.2.2 Transforming published data on liver regeneration into fractional recovery of tissue mass

6.2.2.1 High fructose-induced steatosis (NASH) and Controls

In the study by Tanoue et al. (2011), male Sprague-Dawley rats (8 weeks old) were fed either a high fructose diet (total calories from 66% fructose, 11% fat, and 19% protein) or a control diet (chow with total calories from 10% fructose, 12% fat, and 19% protein) for a period of four weeks. Rats with high fructose-induced non-alcoholic steatohepatitis (NASH) showed high serum triglycerides, accumulation of hepatic fat, and more severe insulin resistance, indicating a disease state similar to human NASH. Following four weeks of their respective diets, rats were anesthetized with ether and a 70% partial hepatectomy was performed. Following resection, rats were fed a standard CE-2 diet. During recovery from resection, rats were sacrificed and their regenerating livers were removed and weighed. The data reported in this study were given in "liver regeneration rate", which is the percentage of liver mass recovered as normalized to the initial remnant liver mass immediately following hepatectomy, according to equation 6.16 (Tanoue et al, 2011).

$$Liver\ Regeneration\ Rate = 100\% \left\{ \frac{Final\ Weight - (Original\ Weight - Excised\ Weight)}{Original\ Weight} \right\} \quad (6.16)$$

Liver regeneration rate is the fractional mass recovery minus the remnant liver fractions; therefore, we added 30% to the reported liver regeneration rate to convert liver regeneration rate to fractional mass recovery.

6.2.2.2 Ethanol-induced steatosis (ASH)

In the study by Yang et al. (1998), Sprague-Dawley rats (125g body weight) were fed either a liquid ethanol diet (355 kcal ethanol, 115 kcal carbohydrates, 360kcal fat, and 180 kcal protein per liter) or a control diet (470 kcal carbohydrates, 360 kcal fat, and 180 kcal protein per liter) for a period of five weeks. After a five week adaptation to these diets, rats were anesthetized using ether and a 70% PHx was performed. Rats were sacrificed at 24 hours and 48 hours post-PHx, and liver weight was measured. The data presented by Yang et al. (1998) were given in percentage of initial weight at 24 and 48 hours post-hepatectomy (Yang et al, 1998b). We assumed that the initial % of initial liver weight was 30% because a 70% PHx was performed. Therefore, to convert from % initial liver weight to fractional recovery, we divided % initial liver weight by 100%. Although we imposed no further constraints on regeneration in rats with ASH, based on observations of ^{3}H-thymadine incorporation from previous studies, we surmise that it is unlikely that significant hepatocyte replication occurs beyond 48 hours post-hepatectomy in alcohol-fed rats (DUGUAY et al, 1982).

6.2.2.3 Toxin-Induced Cirrhosis

In the study by Kaibori et al. (1997), 6 week old male Sprague Dawley rats (150-200g body weight) were injected with thioacetamide (4% thioacetamide at 20mg/100g body weight) thrice weekly for 10 weeks. The rats were then kept for an additional 3 weeks to allow for thioacetamide washout. Cirrhosis was then confirmed by histology. Following development of cirrhosis, rats were anesthetized with ether and 45% partial hepatectomy was performed. Rats were sacrificed and their livers were excised and weighed at 1, 2, 3, 5, and 7 days post-PHx (Kaibori et al, 1997).

At the time of PHx, remnant cirrhotic livers from 10 additional rats were weighed as a measure of original remnant liver weight. Liver regeneration rate was calculated as follows:

$$Liver\ Regeneration\ Rate = \left(\frac{Remnant\ weight}{Original\ weight}\right) * 100\% \quad (6.17)$$

Therefore, the only conversion necessary to convert liver regeneration rate to fractional mass recovery was to divide by 100%.

6.2.2.4 Toxin-Induced Type 1 Diabetes

In the study by Johnston et al. (1986), diabetes was induced in male Wistar rats (200-300g body weight) by administering a single dose of streptozotocin (65mg/kg body weight) injected into the tail vein under light anesthesia (ether). Rats then received 0.28 M glucose to drink. Partial hepatectomy was performed five days following streptozotocin administration. During recovery, rats were sacrificed and dry liver weight was measured at 12, 24, and 48 hours post-resection. The data reported in this study were given in liver dry weight percent of total body weight.

To convert these data to fractional recovery, we first calculated the baseline liver dry weight to total body weight percent. From the 10 week-old organ weights of the Phenome project at the National BioResource Project for the Rat in Japan (www.anim.med.kyoto-u.ac.jp/nbr), we found that the average liver to body weight percent across rat strains (and specifically for the WST.F334-*Kmch*/Kyo strain) is approximately 3%. Johnston et al. (1986) states that water content in the livers of sham-operated rats was 64.9%. Thus, the following two equations were constructed to solve for initial dry liver to body weight percent.

$$\frac{(Dry\ Liver)+(Water)}{Body\ Weight} = 3\% \quad (6.18)$$

$$Dry\ Liver/_{25.1\%} = Water/_{64.9\%} \quad (6.19)$$

where *Dry Liver* and *Water* are the weights of the dry tissue and water content of the tissue. Equation 6.19, can be rearranged as follows.

$$Water = 2.586(Liver) \quad (6.20)$$

Thus, equation 6.18 can be solved for baseline dry liver to body weight percentage by inserting equation 6.20 into equation 6.18 to yield baseline dry liver to body weight percentage was 1.16% in the rats used in this study. A 70% PHx yields a starting dry liver to body weight percentage of 0.348% corresponding to a fractional recovery of 0.3. All data in this study were therefore scaled by a factor of 0.3/0.348% to convert the dry liver to body weight percentage to fractional recovery (JOHNSTON et al, 1986).

Previous studies have suggested that alloxan-induced diabetic rats showed a delay in regeneration but that diabetes did not suppress overall recovery (BARRA & HALL, 1977). We therefore constrained recovery at 300 hours post-PHx in diabetic rats to be the same as for wild-type rats.

6.2.2.5 Mouse Liver Regeneration

Male mice aged 8-12 weeks (129S1) were fed standard mouse chow *ad libitum*. Mice were anesthetized by pentobarbital and 70% PHx was performed. The data from Shu et al. (2009) for control mice were given in liver to body weight ratio (Shu et al, 2009b). To convert these data to fractional recovery, these data were scaled by 0.3 divided by initial value for liver-to-body weight ratio.

6.2.2.6 Human Liver Regeneration

The data presented by Periwal et al. (2014) were already given as the fraction of original liver volume, hence requiring no conversion (Periwal et al, 2014). Similarly, the data presented by Pomfret et al. (2003) were given in percent regeneration, which is defined as remnant volume divided by original volume (x100%) (Pomfret et al, 2003). No conversion was required for these data as well.

6.2.3 Sensitivity Analysis

Normalized sensitivity coefficients were estimated by changing each parameter (p_i) by +/- 10% of its nominal value and calculating sensitivity at each simulation time point according to equation 6.21.

$$S_{\mathrm{i}}(t) = \frac{\Delta Mass(t)/Mass(t)}{\Delta p_i/p_i} \tag{6.21}$$

Mass(t) represents the nominal mass fraction of hepatocytes at any given time, *t*, and *ΔMass(t)* is the deviation from nominal caused by the parameter change. The result is a dynamic parametric sensitivity, showing how the profile of liver regeneration responds to changes in parameters as a function of time.

6.2.4 Statistical Methods

We performed a log-likelihood ratio test to assess whether our extended model described the experimental data significantly better than the previous model. This test takes into account the number of parameters used in the model and the model error in fitting the experimental data. We assumed that the residuals from the fitted models followed a Gaussian distribution (i.e. there was no non-random pattern to the residuals) and used one degree of freedom, corresponding to the cell growth parameter we added to the model. In the case of this model comparison, the original model has 1

fewer parameters than the extended model, we therefore considered the extended model as the unrestricted model. For each model, the log-likelihood function was used to calculate the model fit to experimental data from Tanoue et al. (2011) in accordance with equation 6.22.

$$l(\mu, \sigma^2; x_1, x_2, \dots, x_n) = -\frac{n}{2}\ln(2\pi) - \frac{n}{2}\ln(\sigma^2) - \frac{1}{2\sigma^2}\sum_{j=1}^{n}(x_j - \mu)^2 \quad (6.22)$$

Where μ and σ^2 were estimated from the residuals for each model.

The ltestratio function in Matlab was used to compare the likelihood of the two models.

6.3 Results

6.3.1 Model Implementation

Our computational model extends the model previously published by Furchtgott, Chow, and Periwal by adding terms describing the contributions of cell growth and initially matrix-bound factors to liver regeneration following resection (Furchtgott et al, 2009). Our computational model consists of 11 ODEs (described in detail in the Methods section), 43 parameters (Appendix A), and 12 variables representing molecular levels and cell abundances (Appendix A). All variables representing molecular levels, except matrix bound factors (MBF), have an initial steady-state level of 1 and any change thereafter is a fold-change over baseline. Determination of MBF initial level is described in the following section. The initial level of quiescent hepatocytes is 1, while initial levels of primed and replicating hepatocytes are 0. All simulations were performed using Matlab (Mathworks, Natick, MA).

6.3.2 Extended model predicts the importance of Kupffer cell-mediated signaling during the priming phase

The importance of direct intercellular signaling leading to IE gene expression has been widely studied. Direct interventions to intercellular signaling have been shown to impact liver regeneration dynamics significantly (Meijer et al, 2000b). Whereas, the effects of matrix bound factors (MBF) are less well appreciated but appear to have a more subtle effect on regeneration dynamics (Zhou et al, 2015). Therefore, we reasoned that the effects of MBF are likely less than the effects of IE genes on driving regeneration. We tested model behavior if the effects of MBFs are just as important to regeneration as IE gene effects. Rather than match parameters for MBF signaling to a particular MBF (i.e. WNT) we tuned the model parameters initial MBF levels, production rate, and degradation rate such that the relative magnitude of the priming signal from initially MBF signaling and IE gene production were of the same order of magnitude during the timeframes when they were contributing to hepatocyte priming (Figure 6.3).

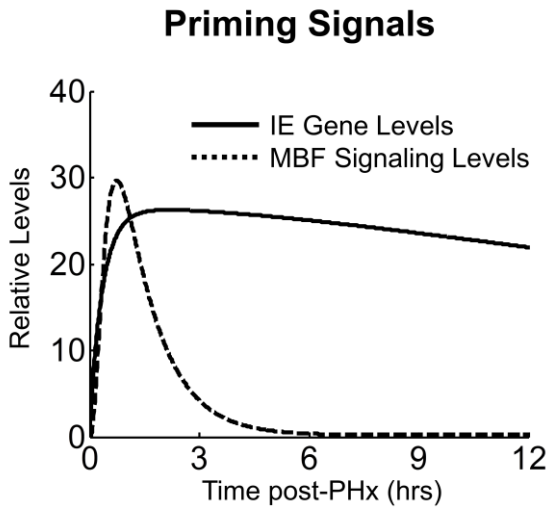

Figure 6.3 Relative levels of IE genes (Fold Change) and signals released from the ECM (Relative Amount) during the priming phase. Model parameters were scaled in such a way that priming signals from Kupffer cells and from initially matrix-bound factors had relatively equal contributions to hepatocyte priming. The peak of MBF signaling occurred at approximately 45 minutes post-PHx.

Appendix A contains the parameters that correspond to this phenotypic behavior. This parameter choice relies on the assumption that MBF signaling is as important as IE gene production to induce hepatocyte priming, and MBFs are depleted following the priming phase. Unbinding of MBF peaked approximately 45 minutes post-PHx and lasted over the duration of the priming phase (6 hours post-PHx), while IE gene levels peaked close to 3 hours post-PHx and remained high throughout the early stages of liver regeneration (>12 hours post-PHx). We found that including MBF signaling altered the dynamic mass recovery only slightly, leading to a sustained offset in mass recovery compared to the case without MBF signaling (Figure 6.4). The effect of MBF signaling in our model is slight most likely because the duration of MBF signaling is shorter than the duration of cytokine signaling. Because of the negligible

effect that MBF signaling had on liver regeneration dynamics, we excluded its contributions from the subsequent model analyses.

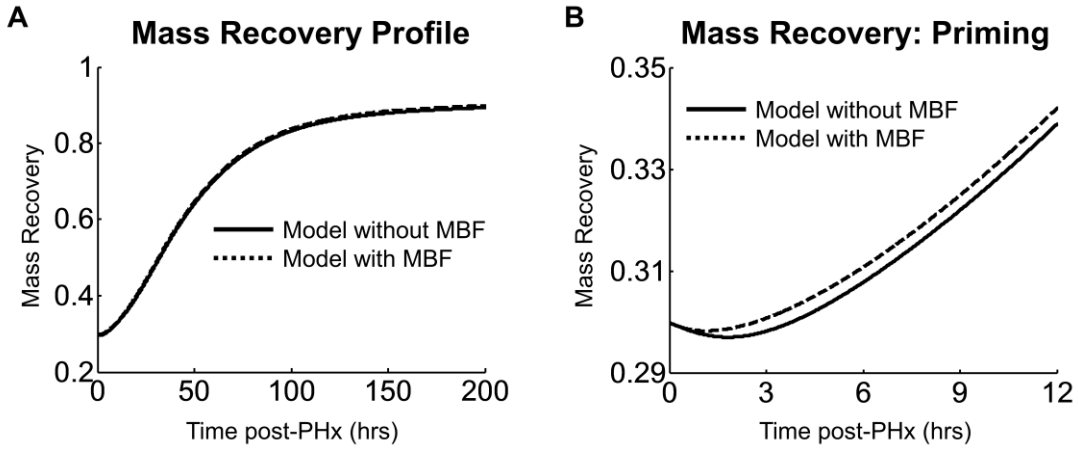

Figure 6.4 Comparison of simulated mass recovery with and without considering Matrix Bound Factors (MBF). (A) Including EBF signaling in the computational model did not significantly change the overall dynamic mass recovery profile. (B) Including EBF signaling impacted the onset timing of regeneration leading to a small offset between dynamic regeneration including and excluding EBF signaling. This small offset (~0.006 mass recovery fraction) remained throughout regeneration.

6.3.3 Extended model with cell growth better accounts for rat liver regeneration profile

Although the original model proposed by Furchgott, Chow, and Periwal (2009) captured the broad features of liver regeneration in rats, it considered relative hepatocyte number as a measure of tissue response rather than overall mass. Comparing this simulated number of hepatocytes to experimental data is difficult because the experimentally available measurement closest to cell number is relative tissue mass. When compared to relative tissue mass recovery, this model fails to match the mass recovery dynamics accurately: specifically, the model without cell growth

fails to capture the experimental observation that the rat liver doubles in mass by 24 hours post hepatectomy (Figure 6.5, “No cell growth” & “Experimental data”) (Furchtgott et al, 2009;Tanoue et al, 2011). Our extended model incorporating cell growth could better account for the dynamic profile of liver mass recovery in rats by more accurately simulating mass recovery dynamics (Figure 6.5, “Cell growth”).

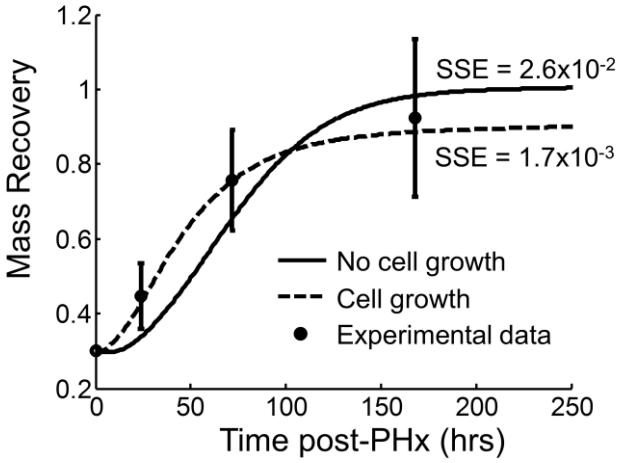

Figure 6.5 Comparison of experimental data of liver regeneration in rats from Tanoue et al. (2011) (Experimental data) to the models proposed by Furchgott et al. (2009) (No cell growth) and proposed in this work (Cell growth). The model proposed in this work is able to fully capture the dynamics of liver repair following 70% partial hepatectomy in rats.

We performed a log-likelihood ratio test to assess whether our extended model described the experimental data significantly better than the previous model. This test takes into account the number of parameters used in the model and the model error in fitting the experimental data. We assumed that the residuals from the fitted models

followed a Gaussian distribution (i.e. there was no non-random pattern to the residuals) and used one degree of freedom, corresponding to the cell growth parameter we added to the model. For further explanation of the test, see the Methods section. We found that the original model had a log-likelihood of 4.42, while our extended model had a log-likelihood of 9.64. The results of log-likelihood ratio test showed that our extended model was able to capture the experimental data more accurately than the previous model, with a p-value of 0.0012 ($G^2 = 10.53$). The ability to compare our simulated regeneration profiles to experimental mass recovery profiles allowed us to simulate experimentally observed cases of deficient liver regeneration and predict molecular and physiological deficiencies underlying these cases.

6.3.4 Exploring the state space of liver regeneration reveals distinct regeneration modes

We sampled the model's parameter space within a range of biologically reasonable parameter values using a Latin hypercube sampling method to sample each parameter uniformly from +/- 50% of its nominal value. We then simulated liver regeneration following 70% PHx using 150 parameter sets and classified the resulting regeneration dynamics. We found that liver regeneration is classifiable into several distinct modes of response to PHx: four regenerating modes (Figure 6.6A-D): delayed, suppressed, enhanced, and delayed and enhanced; and two non-regenerating modes (Figure 6.6E and F): unresponsive and liver failure.

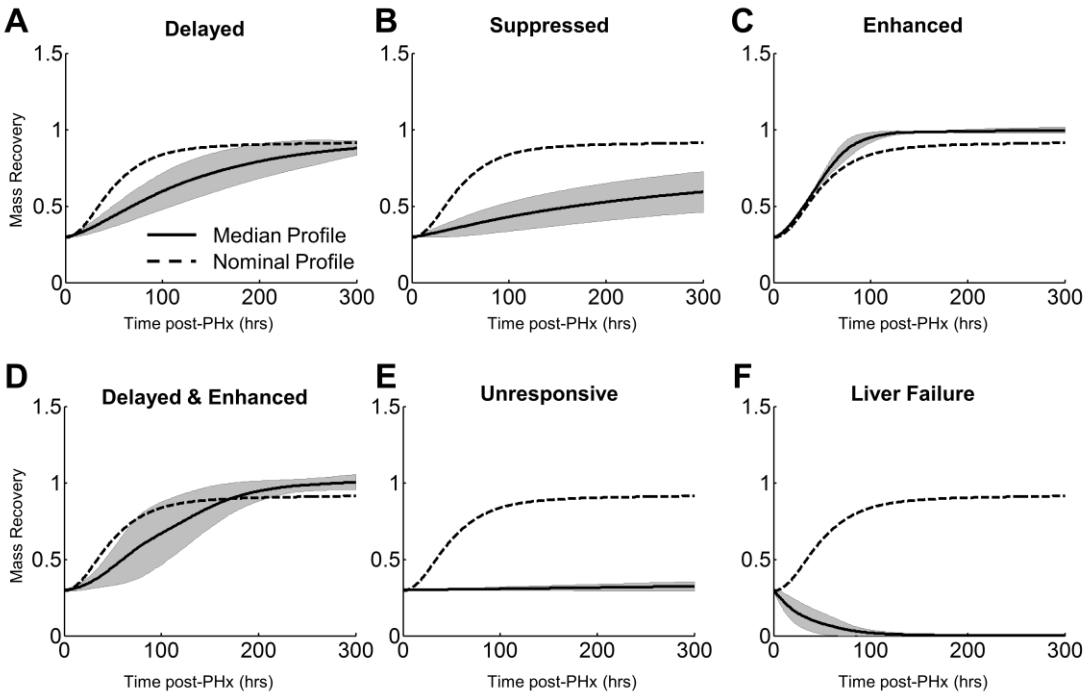

Figure 6.6 Model-predicted modes of regeneration revealed through sampling model parameters (+/- 50% of nominal values). Varying model parameters simultaneously revealed distinct regeneration modes, including (A) delayed, (B) suppressed, (C) enhanced, (D) delayed and enhanced, (E) unresponsive, and (F) liver failure. The dashed line is the nominal profile; the gray areas indicate +/- 1 standard deviation.

Next, we investigated the molecular regulation governing the distinct regeneration modes (Figure 6.7). We found that for most of the regeneration modes the variability in molecular regulation was high, often overlapping both the nominal regeneration case and zero levels (Figure 6.7C). These results show that there is no single molecular profile that gives rise to a particular regeneration mode and that imbalances in a combination of factors can have large effects on regeneration dynamics. Based on these results, we conclude that the balance and timing of multiple

factors acting in combination is critical in shaping the regeneration mode following resection.

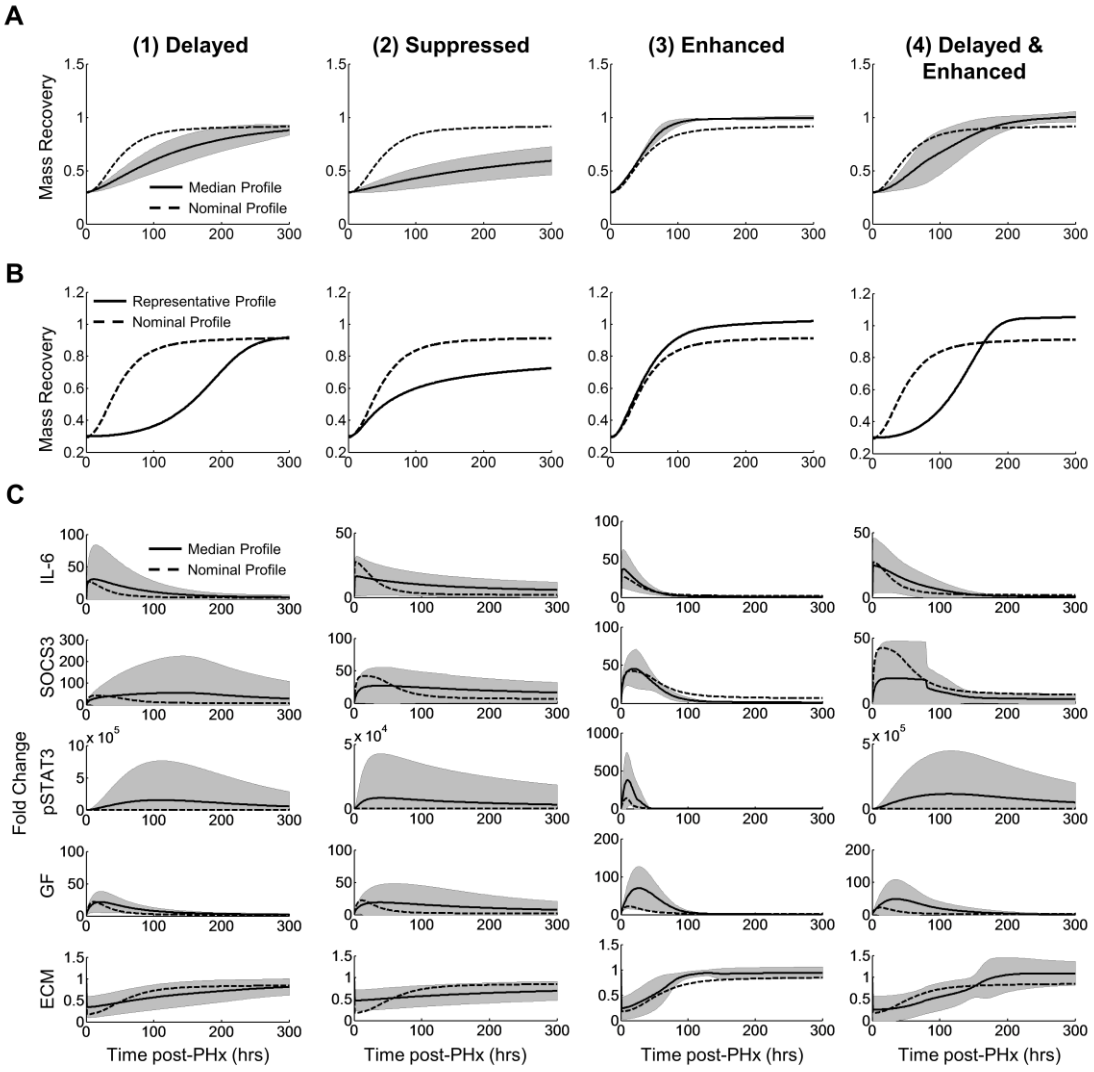

Figure 6.7 Molecular regulation governing altered regeneration profiles. (A) Average mass recovery, (B) One representative instance of mass recovery, (C) Average molecular regulation for regeneration modes: (1) Delayed, (2) Suppressed, (3) Enhanced, (4) Delayed and Enhanced. Dashed line represents nominal profile, black line represents average (or [B] one instance of the) profile, gray area represents +/- 1 standard deviation.

We further investigated specific molecular imbalances that could lead to instances of each altered regeneration modes. Each regeneration mode consists of many possible individual regeneration dynamics. The following figures show our simulations of some of these individual regeneration possibilities. Delayed regeneration can occur when there is enhanced priming but inhibited hepatocyte replication (Figure 6.8A, left panel), when there is delayed priming (Figure 6.8A, center panel), and when there is nominal priming but inhibited hepatocyte replication (Figure 6.8A, right panel). Enhanced priming and inhibited hepatocyte replication is associated with decreased IL6 signaling but increased STAT3 phosphorylation (Figure 6.8B, left panel), likely caused by extreme IL6 sensitivity. This regeneration profile also exhibits suppressed GF signaling and high ECM levels, leading to the suppressed mass recovery rate. GF levels, however, are maintained at levels slightly above nominal for a long time, allowing for eventual recovery to original liver mass. Delayed priming is associated with low levels of STAT3 phosphorylation (Figure 6.8B, center panel). Again, GF levels remain above nominal for the course of regeneration, allowing for complete mass recovery. We were interested to see that this specific profile also showed high levels of IL6, which could correspond to a liver consisting of hepatocytes with high inflammation resistance. Nominal priming but inhibited hepatocyte replication was associated with nominal levels of IL6, but low levels of STAT3 phosphorylation (Figure 6.8B, right panel). This recovery profile also exhibited high levels of GF signaling, likely meaning that the hepatocytes in this liver were resistant to GF signaling. This set of parameters could correspond to an aged liver (Bucher et al, 1964;BUCHER & GLINOS, 1950;Ono et al, 2011a).

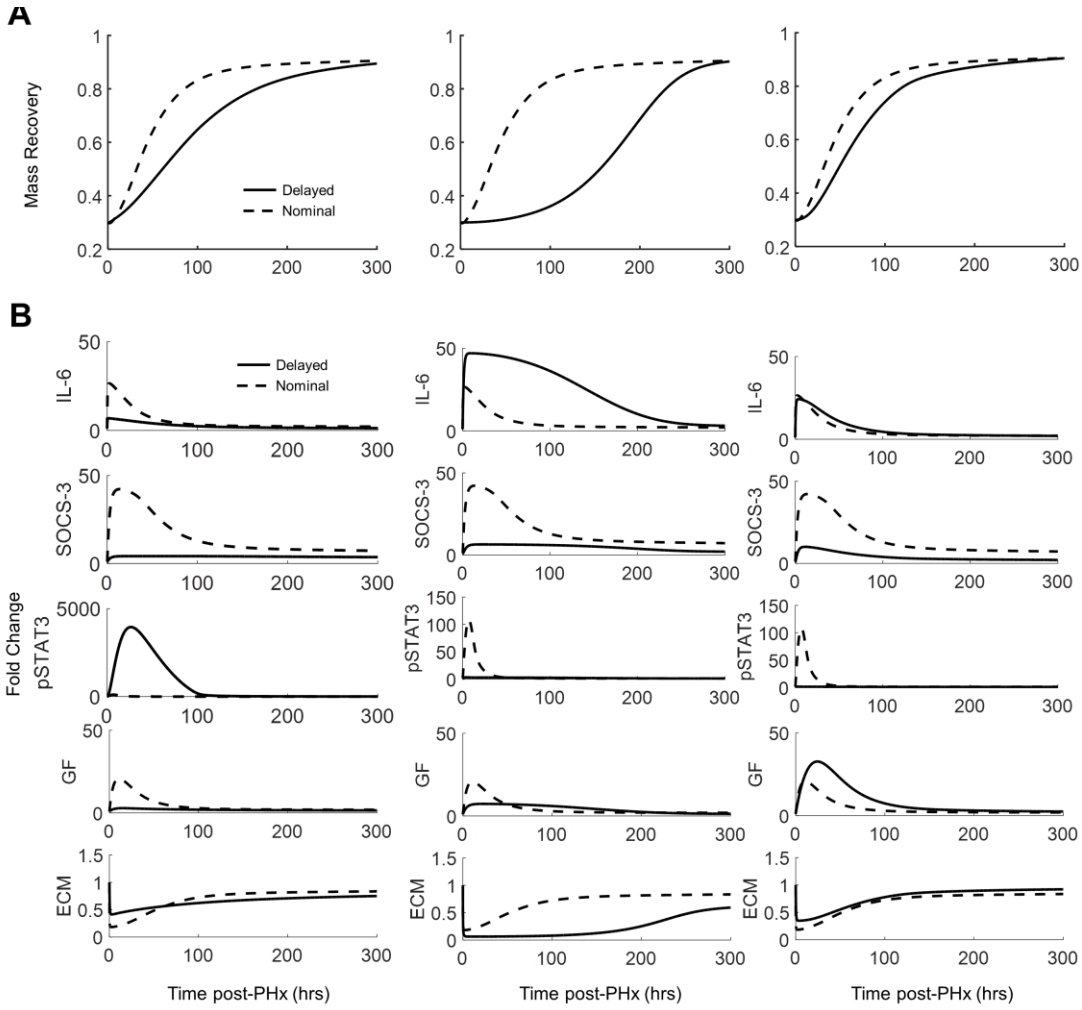

Figure 6.8 Model-predicted molecular regulation profiles underlying delayed regeneration response. (A) Mass recovery of specific delayed cases of liver regeneration compared to nominal and (B) molecular regulation for each regeneration profile. Deficiencies in either priming signals or growth factor bioavailability can lead to delayed regeneration. Note that parameters related to hepatocyte response to these signals change in addition to parameters governing molecular regulation. Dashed line represents nominal profile, black line represents the profile corresponding to delayed regeneration.

Suppressed regeneration can occur with normal priming and suppressed replication (Figure 6.9A, left panel), with delayed priming and suppressed regeneration (Figure 6.9A, center panel), and with delayed priming and early termination (Figure 6.9A, right panel). The profile with normal priming and suppressed regeneration is governed by nominal levels of IL6 signaling and STAT3 phosphorylation but low levels of GF signaling (Figure 6.9B, left panel). In this scenario, cells are primed but few go on to progress through the cell cycle. In contrast, the other two profiles both show deficient priming, as seen in low levels of STAT3 phosphorylation (Figure 6.9B, center and right panels). Both of these profiles also show increased GF levels that are sustained high for a long time. The problem in these regeneration scenarios is that there are few primed cells to respond to the GF signaling. The differences in regeneration dynamics in these two cases are likely caused by a different priming propensity in response to STAT3 downstream signaling and different cell cycle kinetics (simulated as changes in the hepatocyte proliferation rate).

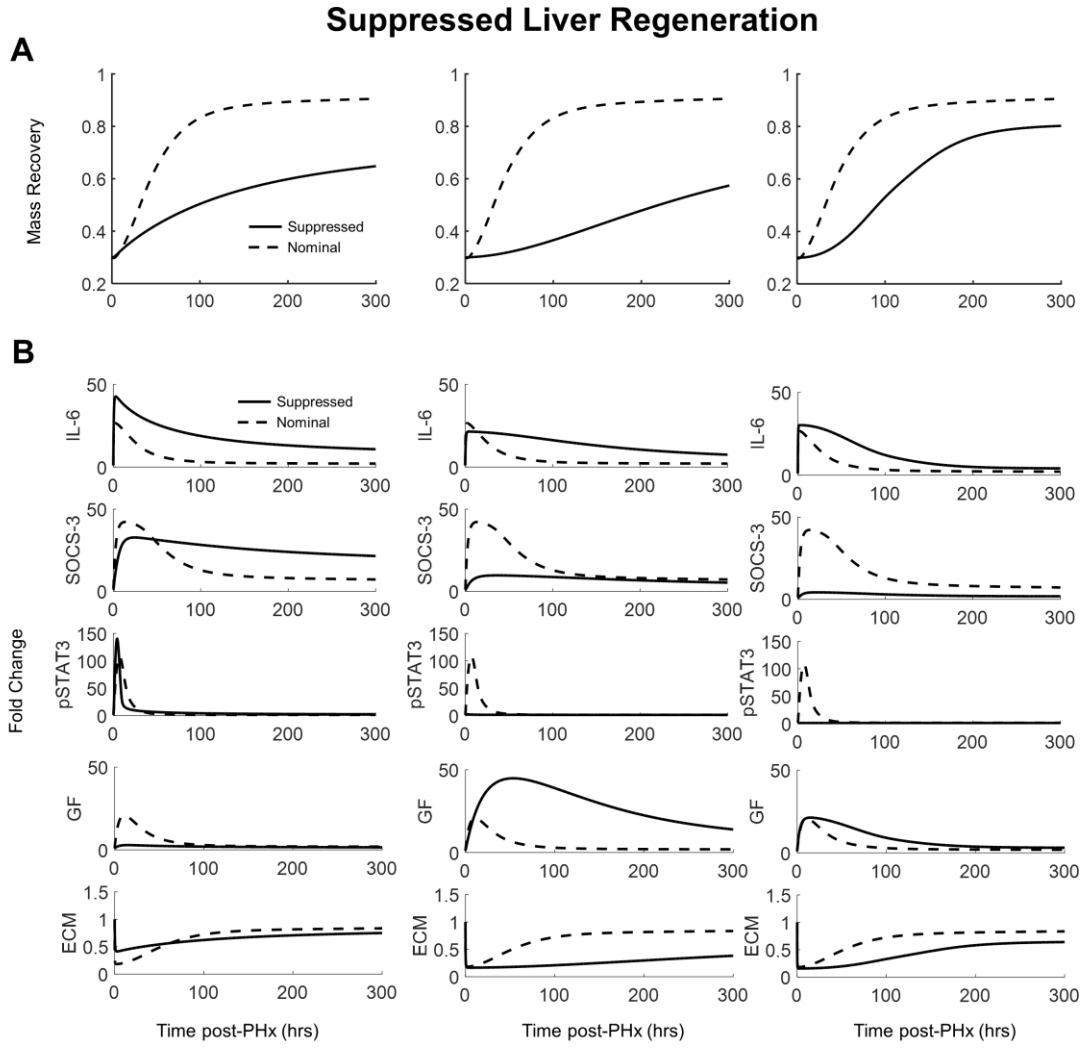

Figure 6.9 Model-predicted molecular regulation profiles underlying suppressed regeneration response. (A) Mass recovery of specific suppressed cases of liver regeneration compared to nominal and (B) molecular regulation for each regeneration profile. Suppressed regeneration can be caused by deficient priming signals or deficient growth factor bioavailability. Dashed line represents nominal profile, black line represents the profile corresponding to suppressed regeneration.

Some parameter sets lead to enhanced recovery following resection. This enhanced recovery is often associated with nominal priming followed by regeneration that exceeds the nominal recovery by increasing the rate of replication (Figure 6.10A, left panel), maintaining replication for longer (Figure 6.10A, center panel), or recoverying a high mass followed by a decrease in total mass prior to stabilizing (Figure 6.10A, right panel). Enhanced recovery due to increased recovery rate is associated with enhanced priming and enhanced GF signaling (Figure 6.10B, left panel). Enhanced recovery due to a maintained replication is associated with a decreased priming and nominal GF signaling (Figure 6.10B, center panel). This maintained replication is therefore likely caused by a reduced requiescence rate of replicating hepatocytes. Enhanced recovery with a mass decrease at the end of regeneration is associated with low priming and high GF signaling (Figure 6.10B, right panel). The mass loss is associated with a spike in ECM production; ECM itself, however, likely does not cause the mass decrease directly. The mass decrease is likely caused by a decreased in individual cell mass (the variable G), which could be caused by an ECM buildup reducing suddenly the numbers of primed and replicating cells.

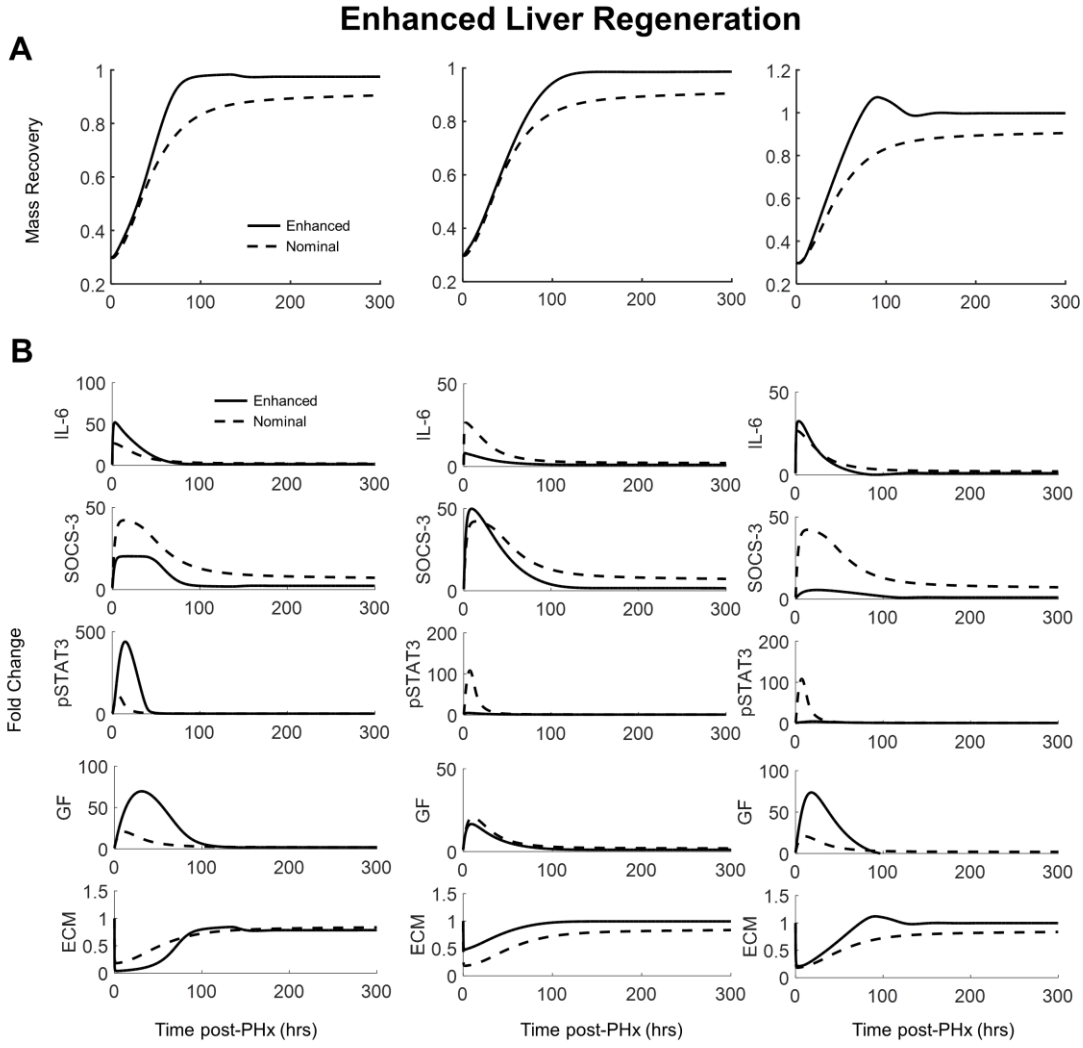

Figure 6.10 Model-predicted molecular regulation profiles underlying enhanced regeneration response. (A) Mass recovery of specific enhanced cases of liver regeneration compared to nominal and (B) molecular regulation for each regeneration profile. Enhanced regeneration can be regulated by enhanced GF bioavalability or by enhanced hepatocyte response to the presence of growth factors. Dashed line represents nominal profile, black line represents the profile corresponding to enhanced regeneration.

Some profiles were delayed initially, but later recovered and exhibited enhanced recovery. This recovery mode can be caused by a delay in priming and a later acceleration of hepatocyte replication (Figure 6.11A, left and right panels), which is similar to the type of regeneration profile we observed experimentally in Adn-/- mice (See Chapters 3 and 4) (Correnti et al, 2015). This recovery mode can also be caused by a low replication rate that is maintained throughout recovery (Figure 6.11A, center panel). All three of these profiles are associated with enhanced GF signaling, either at the same time as the nominal case but a higher magnitude (Figure 6.11B, center and right panels) or delayed from nominal (Figure 6.11B, left panel). The delayed regeneration profiles are both associated with impaired priming (Figure 6.11B, left and right panels). The low but sustained replication profile is associated with enhanced priming signals (likely leading to similar priming phases) but maintained high levels of ECM (Figure 6.11B, center panel). These high ECM levels likely impair hepatocyte transition to the replicating state, leading to the slow replication rate.

Certain parameter combinations led to no response following resection (Figure 6.12A) or complete liver failure (Figure 6.13A). The profiles following the unresponsive regeneration mode are characterized by a lack of priming response, GF response, and ECM restructuring (Figure 6.12B). Profiles following the liver failure mode are characterized by steadily increasing levels of IL6 and GF as non-parenchymal cells try to enable hepatocyte replication prior to liver failure (Figure 6.13B). The main parameters leading to liver failure are related to hepatocyte apoptosis rate.

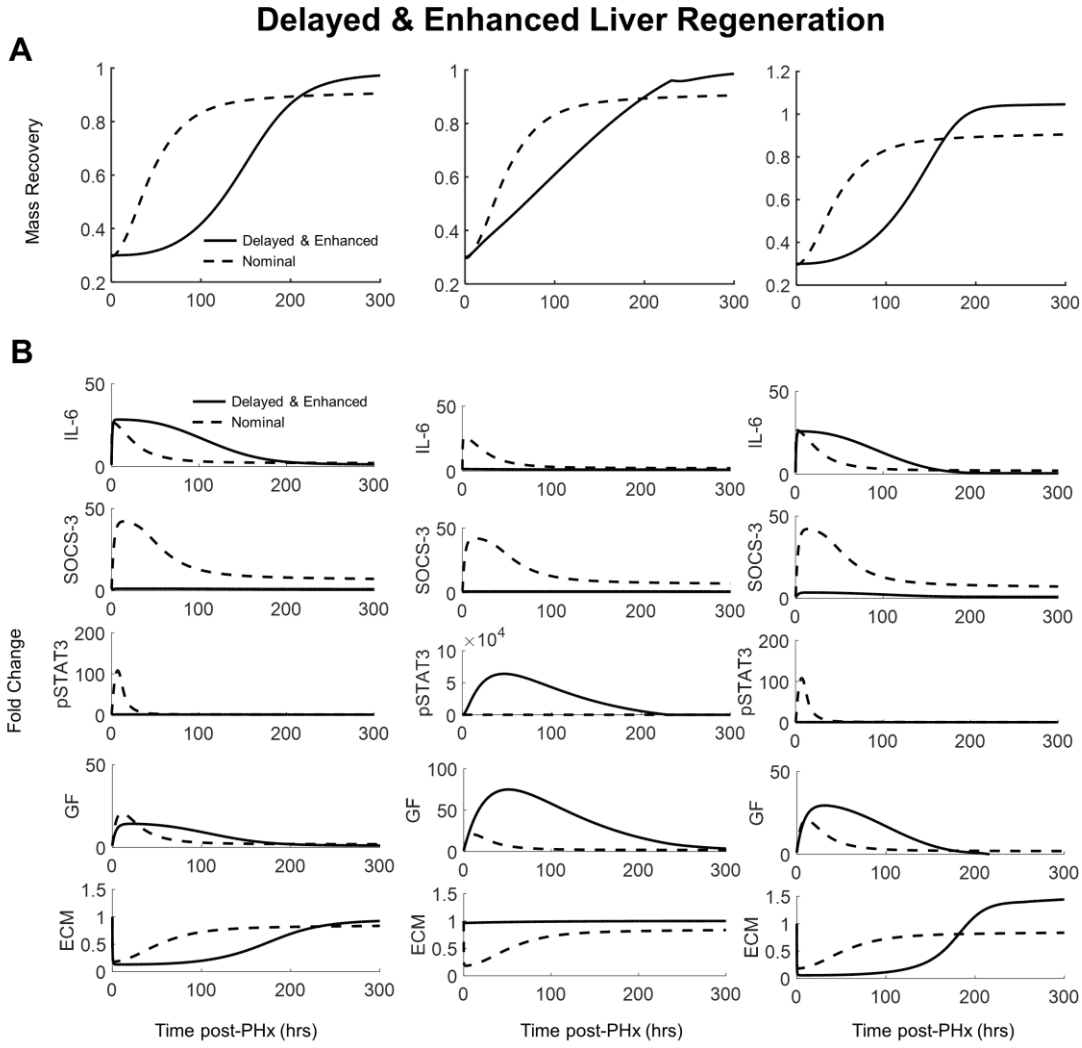

Figure 6.11 Model-predicted molecular regulation profiles underlying delayed and enhanced regeneration response. (A) Mass recovery of specific delayed and enhanced cases of liver regeneration compared to nominal and (B) molecular regulation for each regeneration profile. One model-predicted cause of this profile is deficient priming signals coupled with enhanced growth factor bioavailability. Dashed line represents nominal profile, black line represents the profile corresponding to delayed and enhanced regeneration.

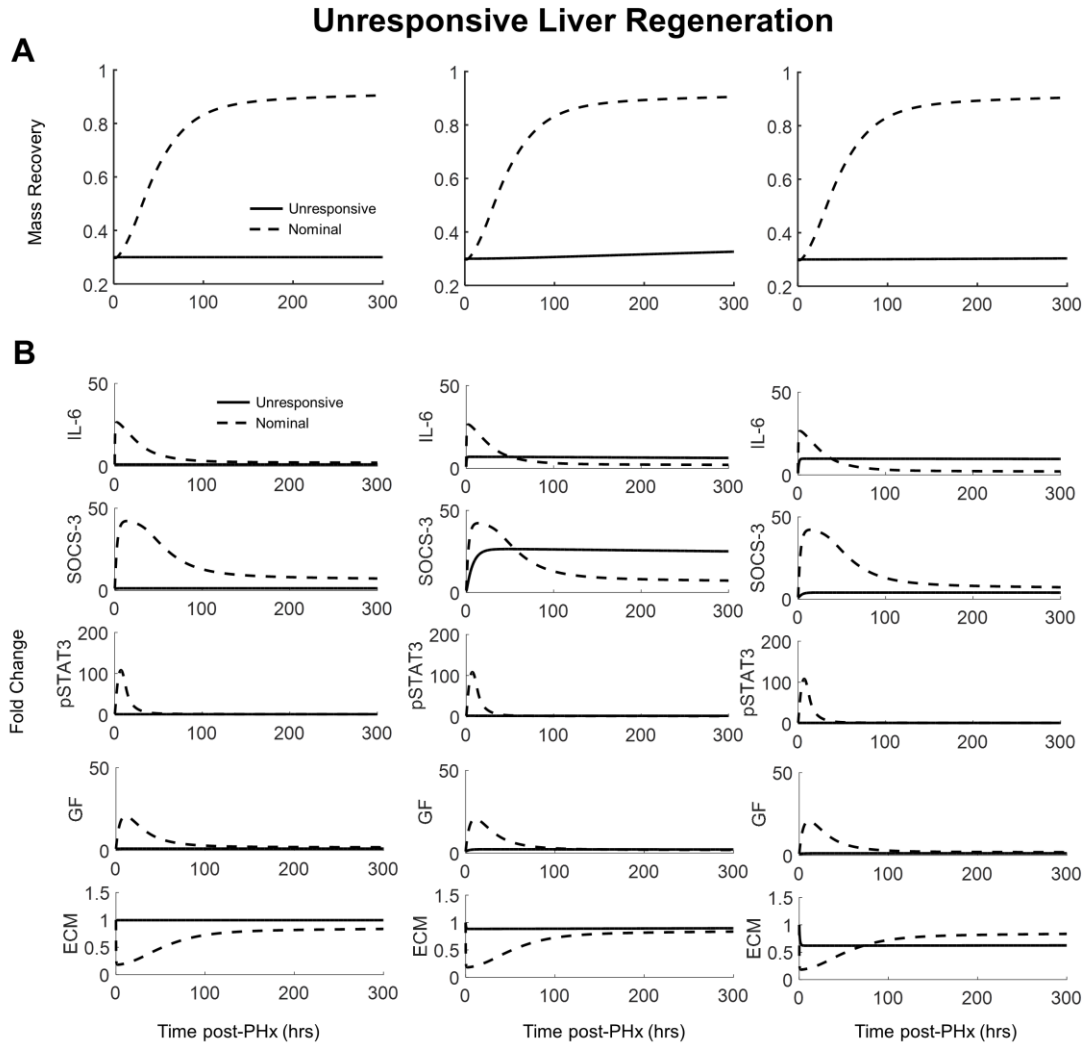

Figure 6.12 Model-predicted molecular regulation profiles underlying unresponsive regeneration response. (A) Mass recovery of specific unresponsive cases of liver regeneration compared to nominal and (B) molecular regulation for each regeneration profile. Both regeneration profiles and molecular regulation appear to be unresponsive in the profiles investigated. Dashed line represents nominal profile, black line represents the profile corresponding to unresponsive regeneration.

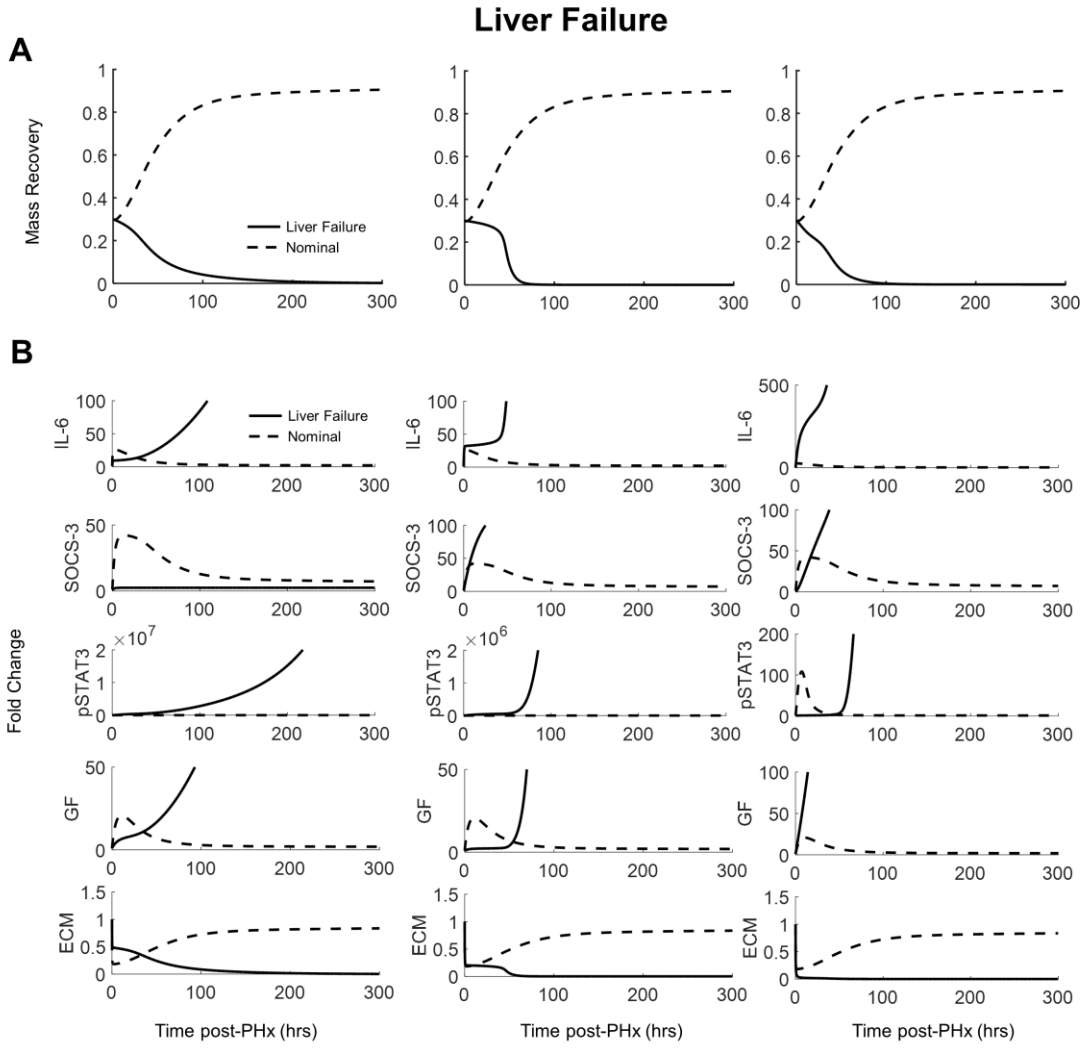

Figure 6.13 Model-predicted molecular regulation profiles underlying liver failure. (A) Mass recovery of specific liver cases of liver failure compared to nominal regeneration and (B) molecular regulation for each liver failure profile. As the liver fails, Kupffer cells and hepatic stellate cells attempt to rescue the liver by producing more pro-regenerative factors. Dashed line represents nominal profile, black line represents the profile corresponding to liver failure.

6.3.5 Sensitivity analysis reveals that molecular and physiological regulation strongly affects dynamic mass recovery

We performed a local parametric sensitivity analysis to identify additional factors and network balances significantly affecting the liver regeneration dynamics. We found that the addition of cell growth to the extended model did not have a strong effect on the maximum local sensitivity coefficients of model parameters (Figure 6.14A). The exception to this observation is the maximum sensitivity of the metabolic demand parameter (M), which changed from positive to negative with the addition of cell growth. Sensitivity values computed for both the original model and the extended model including cell growth revealed that both molecular and physiological parameters showed high sensitivity.

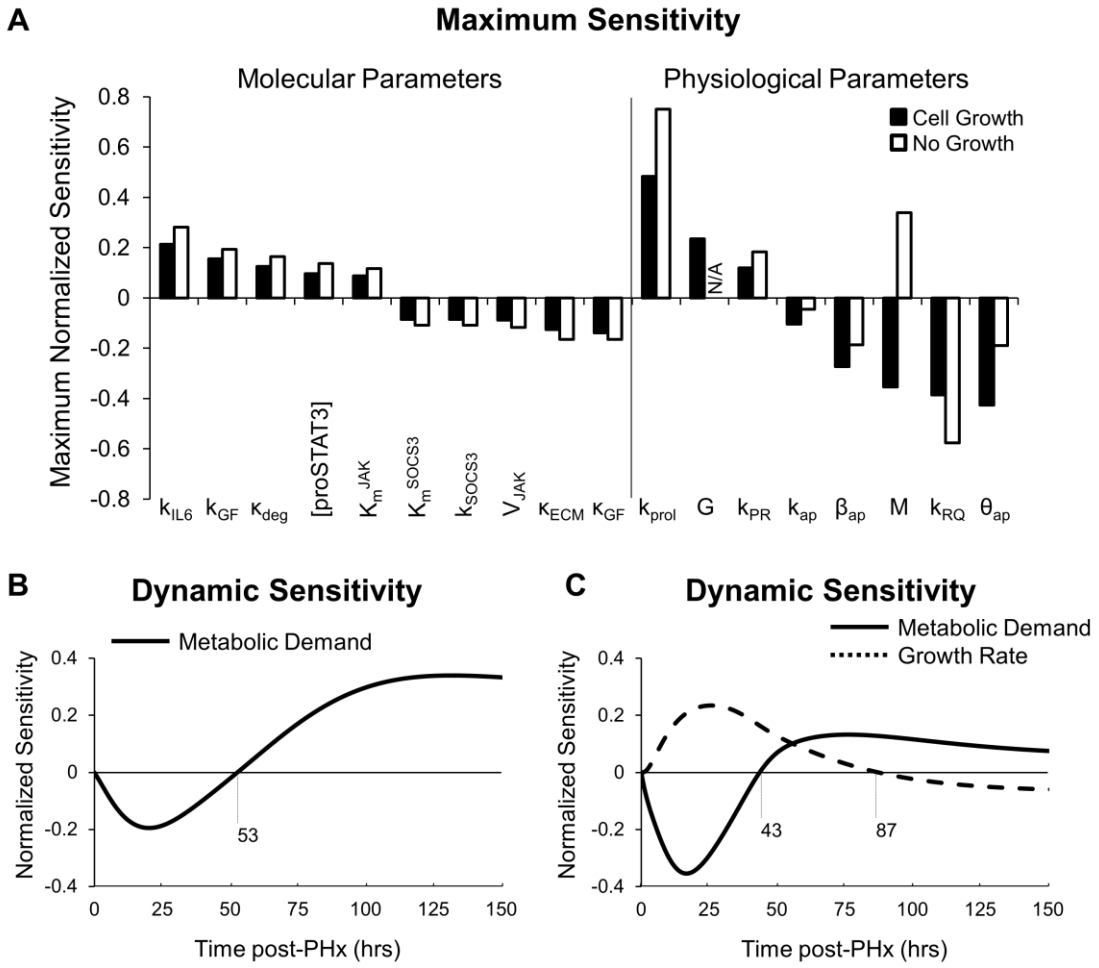

Figure 6.14 Dynamic local sensitivity analysis of the regeneration model with and without cell growth. (A) Maximum normalized sensitivities were calculated for each parameter. (B) Normalized local sensitivity of metabolic demand when not considering cell growth. Metabolic demand is inhibitory for the first 53 hrs post-PHx, likely through increases in cell apoptosis. After 53 hrs, metabolic demand enhances regeneration, likely through increased production of growth factors. (C) Normalized local sensitivities of metabolic load and growth rate reveal a dynamic competition between replication and growth. From 43-87 hrs post-PHx growth rate and metabolic demand both drive regeneration. During initiation and termination, however, imbalances between growth and metabolic load can inhibit regeneration.

The model's physiological parameters showed the highest absolute sensitivities, suggesting that such a lumped approach to studying tissue behavior may exclude detailed predictions about important biological processes. Model parameters related to production of factors from non-parenchymal cells as well as model parameters related to hepatocyte response to these factors showed high sensitivity, suggesting that parenchymal and non-parenchymal cell regulation are both important for governing liver regeneration. Specifically, we identified a potential antagonism between GF production rate (k_{GF}) and degradation rate (κ_{GF}) and between IL-6 production rate ($k_{IL\text{-}6}$) and IL-6 degradation rate ($\kappa_{IL\text{-}6}$) (Figure 6.15). Increasing the production rates of IL-6 and GF enhanced overall regeneration, while increasing degradation rates inhibited overall regeneration.

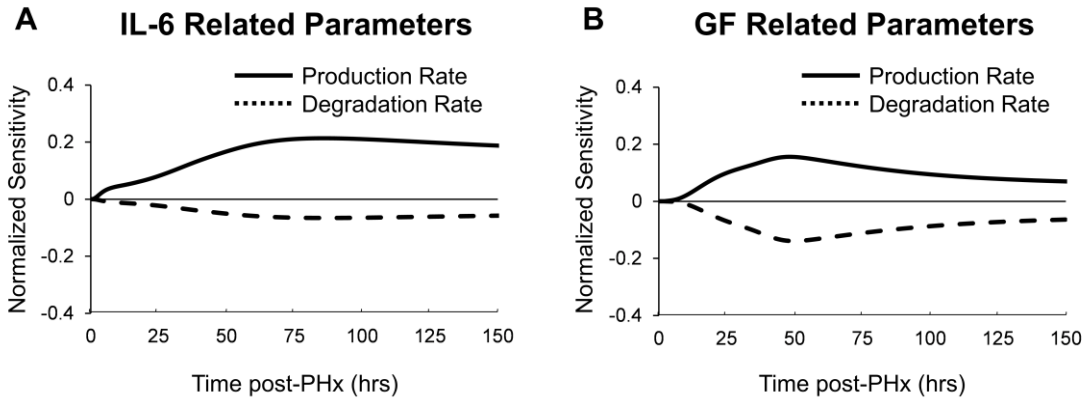

Figure 6.15 Potential antagonism between pairs of parameters. We used a local sensitivity analysis to identify pairs of parameters that impact the levels of a single factor or are closely related but have opposing effects on overall mass recovery. In addition to metabolic demand and growth rate (Figure 6.14 C) this analysis identified (A) IL-6 production and degradation and (B) GF production and degradation as potentially antagonistic parameter pairs.

We investigated how the inclusion of cell growth modified the dynamic sensitivity of the metabolic demand parameter (M). When cell growth is not considered, increased metabolic demand was inhibitory to liver recovery during the first 53 hours post-PHx, largely due to increased hepatocyte apoptosis (Figure 6.14B). After 53 hours, increased metabolic demand enhanced regeneration. With cell growth considered, the initial inhibitory effect of increasing metabolic demand lasted only for the first 43 hours post-PHx, after which it enhanced mass recovery but to a lower extent than the model without cell growth (Figure 6.14C). The inclusion of cell growth also allowed us to recognize a potential dynamic antagonism between metabolic demand and cell growth rate. Early post-PHx, hepatocyte growth was a positive contributor to liver regeneration, while metabolic demand negatively affected progression of regeneration. At this early time, metabolic demand acted in hepatocytes predominantly to induce apoptosis in damaged cells through high metabolic load, causing reduced liver mass. After approximately 43 hours post-PHx, high metabolic load induced high response in non-parenchymal cells causing increased priming and regeneration. From approximately 43 to 87 hours post-PHx, metabolic load and hepatocyte growth acted synergistically to promote liver regeneration. Near the termination stage of liver regeneration, however, hepatocyte growth inhibited liver regeneration by inducing hepatomegaly and decreasing the driving force for regeneration.

6.3.6 Paired parameter analysis reveals control principles governing the network balances driving liver regeneration

We investigated the organizational principles during liver regeneration by independently varying the pairs of antagonistic parameters identified from the

sensitivity analysis. We varied each parameter over an order of magnitude and simulated overall liver mass recovery (Figure 6.16).

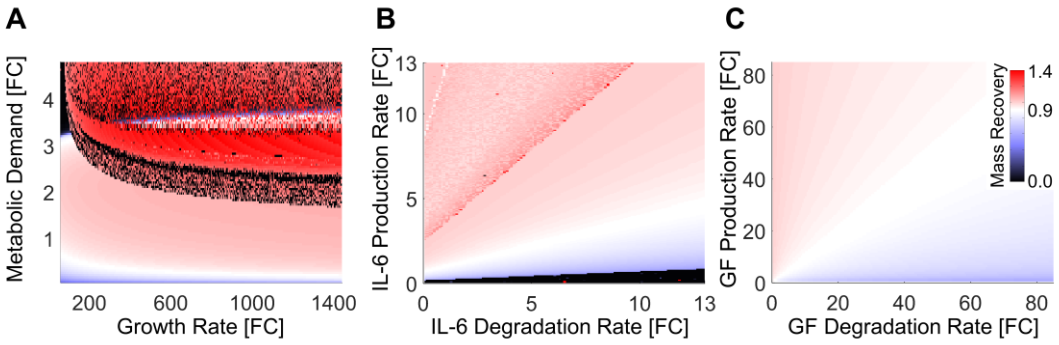

Figure 6.16 Heatmaps show the overall liver mass recovered is sensitive to combinatorial effects of (A) Metabolic load and hepatocyte growth rate, (B) IL-6 turnover rate, and (C) GF turnover rate. All parameter changes are displayed in Fold change [FC] over nominal parameter value. (A) The proper balance between regenerative drive and cell growth in response to stress is required for normal regeneration. (B) IL-6 and (C) GF production rates have large-scale effects on overall recovery, while degradation rates act as fine tuning.

We found that although increasing metabolic demand and hepatocyte growth rate had opposing effects during the beginning and end of liver mass recovery, simultaneously increasing these parameters tended to cause an increase in overall mass recovery (Figure 6.16A). When changed together, metabolic demand has a much stronger effect on overall mass recovery than cell growth rate, for metabolic demand parameter values lower than approximately 40 (or an approximate fold change of 2). When metabolic demand was high (> 2 fold change), regeneration is typically enhanced but certain growth rates coupled with these high metabolic demands could cause complete liver failure or govern the magnitude of the enhanced recovery. When

metabolic demand was high (> 3 fold change) and growth rate was low (< 0.05, or approximately 200 fold change), growth rate was not able to compensate for increased apoptosis caused by high metabolic demand and liver failure occurred. Based on the results near nominal parameter values for metabolic demand and cell growth rate, metabolic demand leading to cell replication appears to be a primary driver of liver repair following damage, while cell growth may be a secondary or compensatory driver.

When we investigated the relationship between IL-6 and GF production and degradation, we found that relatively slight increases to both IL-6 (Figure 6.16B) and GF (Figure 6.16C) production rate increased mass recovery, while degradation had to increase much more to cause an equivalent magnitude decrease in mass recovery. This antagonism was more pronounced in IL-6 balance, but was relatively subtle in GF balance. For further visualization of the effects of GF production and degradation balance, see Figure 6.17.

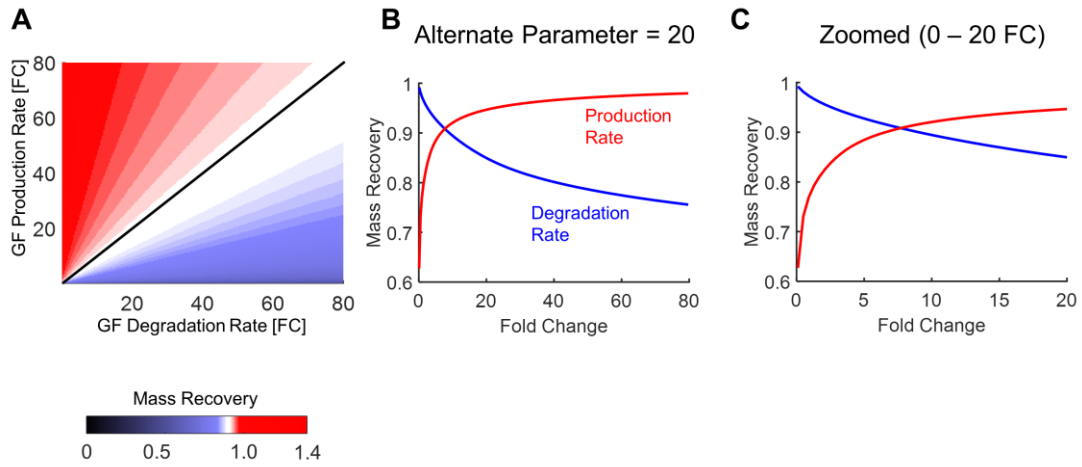

Figure 6.17 Heatmap comparison of overall liver mass recovered for altered GF production and degradation rates. (A) Heatmap with rescaled color mapping showing a subtle effect of coarse-grained control of regeneration by GF production and fine-tuned control by GF degradation (legend below), (B) Mass recovery holding one parameter constant at 20 and varying the other, and (C) Mass recovery holding one parameter constant at 20 and varying the other between 0-20. All parameter changes are displayed in Fold change [FC] over nominal parameter value. The black line indicates when GF production rate fold change equals GF degradation rate fold change. Asymmetry around this line, as in (A), indicates a differential effect of GF production and degradation.

These relationships reveal an organizational principle whereby production of molecules acts as a means of achieving coarse-grained control of molecular levels while degradation acts to achieve fine-tuned control. These results suggest that non-parenchymal cells may act predominantly as coarse-grained controllers of liver regeneration, while hepatocyte responsiveness and miRNA or other regulation may act to achieve fine-tuned control of liver regeneration.

We further investigated the mechanisms through which cytokines and growth factors affect regeneration dynamics. We found that the immediate inflammatory response to partial hepatectomy, represented in the model by IL-6 signaling (Figure

6.18A), controlled the timing of the regeneration response (Figure 6.18B) by controlling the magnitude of the priming response (Figure 6.18C). In simulations, a slight reduction in IL-6 production rate (causing an ~25% decrease in peak IL-6 levels) led to significantly decreased STAT-3 phosphorylation (~75% reduced) and a lower priming response (~10% reduced) caused by decreased IE gene signaling (Figure 6.18C). In addition, this decrease in IL-6 levels not only lowered the priming response (Figure 6.18C) but also slightly delayed the peak of priming, from 7 hours to 8 hours post-PHx. This early impaired priming response propagated through the time course of regeneration, lengthening the recovery for IL-6 signaling deficient cases (Figure 6.18B). This result indicates that relatively small upstream events can have a substantial effect on overall recovery. It is important to consider, however, that many biological processes (including inflammatory molecule production and secretion, receptor binding, competition with anti-inflammatory molecules and signaling pathways, and cellular responsiveness to inflammation) contribute to the simulated IL-6 signaling. Deficiencies in any steps within these processes could lead to the deficient priming indicated by the model simulation.

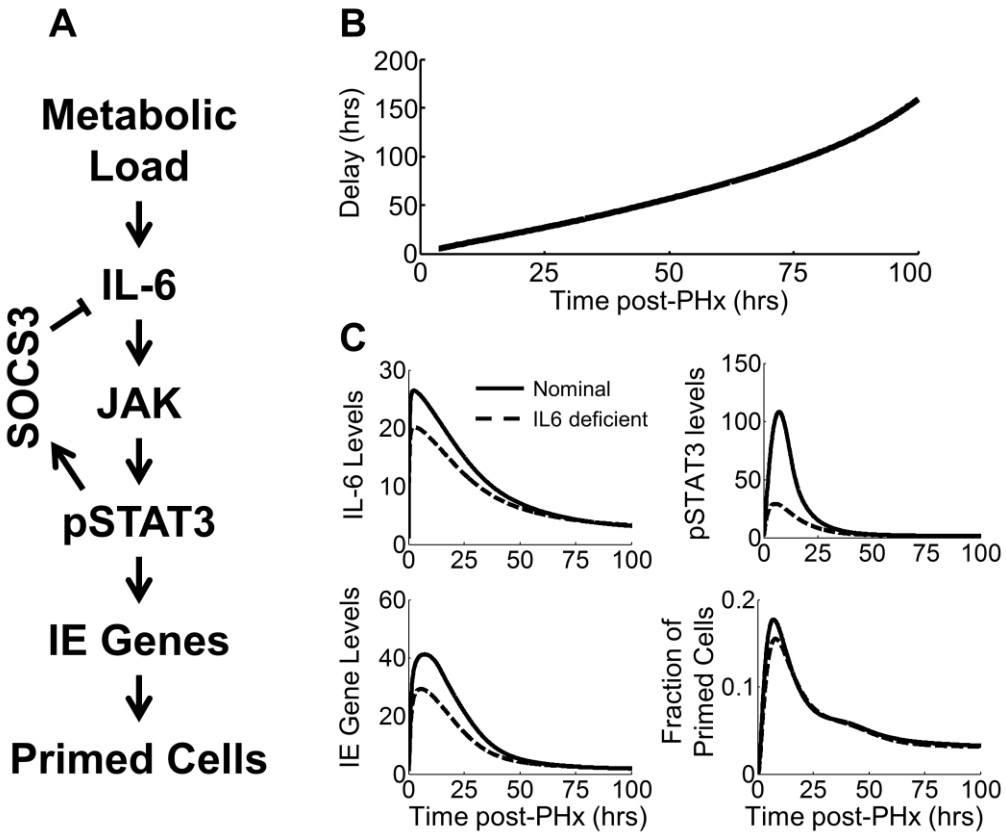

Figure 6.18 Effect of decreasing IL-6 production. (A) IL-6 signals through the JAK-STAT signaling pathway to prime hepatocytes for replication. (B) Reduced IL-6 production causes delayed regeneration, with delays increasing as regeneration progresses. (C) A slight decrease in IL-6 production (25% reduction in peak levels) amplifies as the signal propagates through the JAK-STAT cascade. Ultimately, this slight IL-6 decrease results in reduced STAT-3 phosphorylation (75% reduction in peak) and reduced priming (~10% reduction at peak). This reduced priming leads to delayed recovery and a slightly reduced overall mass recovery (~5%).

Growth factor bioavailability, in contrast, did not affect the priming phase but became important later in the regeneration process. Deficiencies in GF production led to a linearly increasing delay in liver mass recovery (Figure 6.19A). This delay

eventually led to a suppression of overall mass recovery. Low GFs mediated this suppression by reducing the fraction of hepatocytes in the replicating phase of the cell cycle (Figure 6.19B and C). Unlike inflammatory signaling, however, GF signaling deficiencies did not change the timing of peak regeneration. In order to shift the timing of peak regeneration, it was necessary to lengthen the duration of the cell cycle (Figure 6.19D). Decreasing the cell cycle progression rate coupled with a decrease in GF bioavailability not only decreased the magnitude of the cell cycle response, but also delayed the peak response by desynchronizing hepatocyte entry into the cell cycle (Figure 6.19E).

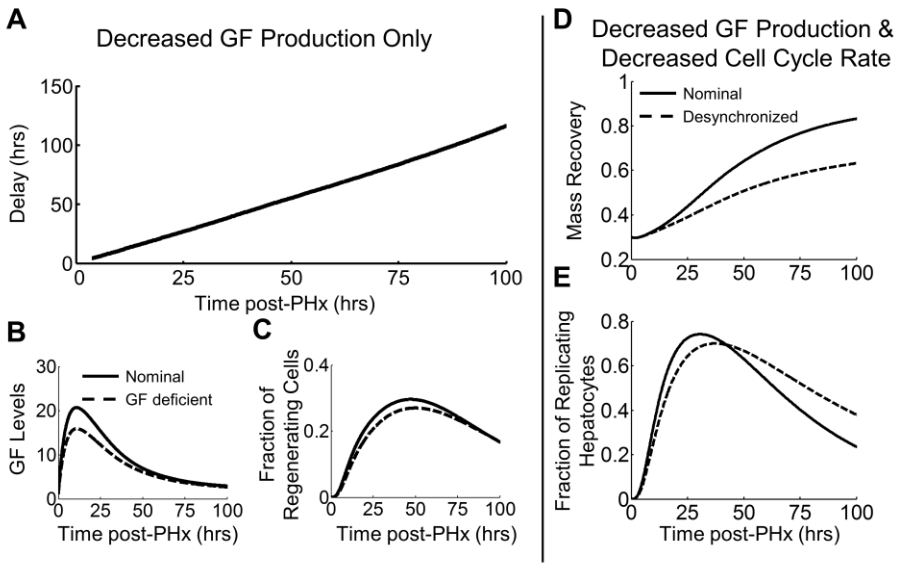

Figure 6.19 Effects of decreasing GF bioavailability. (A) Decreased GF production causes a delay in regeneration. (B) As GFs become less available, (C) fewer hepatocytes enter the cell cycle, decreasing peak of regenerating cells. The synchronicity of hepatocyte entry into the cell cycle, however, is affected only slightly. (D-E) To decrease the synchronicity of entry into the cell cycle, it is necessary to decrease the proliferation rate.

6.3.7 Translating Among Species Using the Computational Model

We tested whether translating among species can potentially be achieved simply by adjusting model parameters in the extended computational model. Prior to simulation, we sought to identify which parameters likely change among species. The cell cycle duration is known to be fairly consistent across mammalian species; therefore, we maintained this parameter at nominal levels (Alexiades & Cepko, 1996;Novak & Tyson, 2004;Singhania et al, 2011;ZETTERBERG & LARSSON, 1985). Similarly, the JAK-STAT pathway is understood to be ubiquitous in mammalian species. Therefore, we maintained JAK-STAT signaling pathway parameters constant across species. Additionally, while the physiological parameters used to approximate multiple pathways may indeed change between species, there is little reason to believe that the essential mechanisms of these pathways differ any more than the JAK-STAT signaling pathway does. Therefore we maintained the physiological parameters at nominal levels as well. This assumption of consistent pathway behavior across species does not take into account any differences in network dynamics caused by species-specific molecular dynamics, for example rat IL-6 half-life in rat macrophages compared to human IL-6 half-life in human macrophages.

We considered an approach where all molecular driving events were maintained constant between species, leaving the metabolic demand parameter and the cell growth rate parameter as the only ones available for modification. It has been shown that metabolic demand of an organism is proportional to the mass of the organism raised to an exponential power (estimated to be between 2/3 and 3/4); this is true for both plants and animals and appears to be an organizing principle of biology (Kolokotrones et al, 2010;Reich et al, 2006;White & Seymour, 2003). The metabolic demand parameter is a lumped parameter approximating extrinsic signals that occur in

parenchymal and non-parenchymal cells and intrinsic hepatocyte capacity to respond to these signals; however, a portion of these signals may be caused by increased nutrient and toxin flux. Therefore, this term represents, at least in part, a metabolic response to these fluxes, which may vary among species according to overall mass. Lumping extrinsic and intrinsic drivers of regeneration into one parameter makes it difficult to simulate experiments where hepatocytes from one species are transplanted into another, but such a technique is appropriate when considering each species individually (Weglarz & Sandgren, 2000). In addition to metabolic demand potentially changing across species, it is possible that cell growth rate may also differ across species. We were able to find no studies reporting grossly observable differences in cell growth rates, while several studies have suggested that the cell growth rate across species appeared to be fairly similar among mammalian species (TYSON, 1985;Wilk et al, 2014). These results led us to believe that cell growth rate likely changes among mammalian species, but that change is likely not orders of magnitude different. Therefore, we changed the cell growth rate and metabolic demand parameters across species in our model to simulate regeneration in multiple species.

We fit regeneration profiles of rats, mice, and humans by simultaneously changing only the hepatocyte growth rate and metabolic demand parameters and minimizing the sum of squared error between experimental data and simulation output. For rats and mice, the growth rates estimated using this least squares approach were fairly similar ($G = 3.5x10^{-4}$ and $9.7x10^{-4}$ mass equivalent doublings/minute, respectively). The optimum fit for humans, however, resulted in a much higher estimated growth rate ($G = 2.5x10^{-2}$ mass equivalent doublings/minute). This estimation is inconsistent with literature suggesting cell growth rate is fairly similar

among mammalian species (TYSON, 1985;Wilk et al, 2014). We therefore constrained human hepatocyte growth rate to the average of rat and mouse growth rates ($G = 6.6x10^{-4}$ mass equivalent doublings/minute) (Table 6.1) and changed only the metabolic demand parameter to fit human regeneration data.

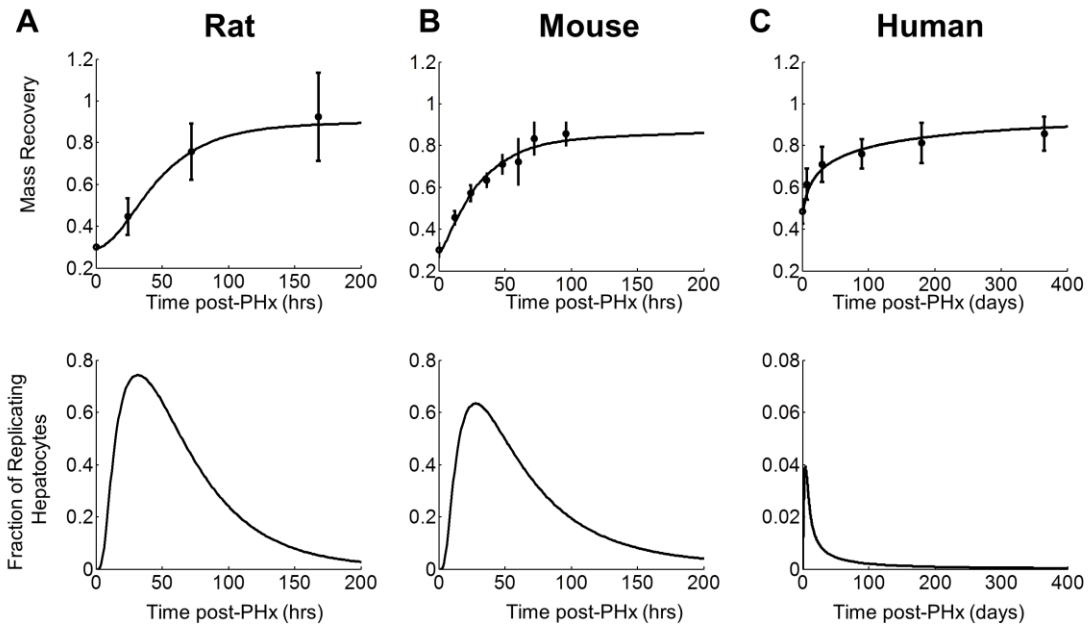

Figure 6.20 Cross-species comparison of (A) rat, (B) mouse, and (C) human (upper panel) mass recovery profiles with experimental liver regeneration data (Pomfret et al, 2003;Shu et al, 2009b;Tanoue et al, 2011) and (lower Panel) predicted fraction of replicating hepatocytes for each species. This model suggests that the key difference governing regeneration profiles between species is an altered balance between proliferative and replicative balance in hepatocytes. This species-specific balance alters the levels of GFs available during regeneration thereby altering the BrdU incorporation of hepatocytes post-PHx. Rats and mice have similar metabolic loads and growth rates causing similar BrdU incorporation with several slight differences. Rats have a slightly later peak BrdU than mice (30h vs. 28h) and a higher peak value (0.75 vs. 0.66). Mouse BrdU incorporation, however, continues longer than rat. Similarly, humans show a reduced peak replication response (note change of scale) but a lengthened regeneration period, leading to similar overall recovery.

Table 6.1 Parameter changes to simulate regeneration in multiple species

Parameter	Rat	Mouse	Human
M	20.8217	23.0294	5.8507
G	3.4742×10^{-4}	9.6607×10^{-4}	6.5675×10^{-4}

By modifying only hepatocyte growth rate and metabolic demand parameters, and appropriately scaling the apoptosis parameter θ_{ap}, we were able to fit regeneration profiles from rats, mice, and humans post-hepatectomy (Figure 6.20A-C) (Pomfret et al, 2003;Shu et al, 2009b;Tanoue et al, 2011). We scaled the apoptosis parameter θ_{ap} by multiplying θ_{ap} by the ratio of $M_{mouse/human}$ to M_{rat}. Both rats and mice regenerate to the initial level of liver mass within ~168 hours post-hepatectomy (7 days), while humans take nearly 100 days to recover mass fully. Both rats and mice had a robust response to partial hepatectomy, with an early spike in regenerating cells (peaking near 30 hours post-PHx). Rats appeared to have a slightly higher regeneration peak (Figure 6.20A), while mice appeared to sustain regeneration slightly longer than rats (Figure 6.20B). Although these results did not capture the shift in peak hepatocyte replication from 24 hours post-PHx in rats to 48 hours post-PHx in mice, fitting the mass recovery dynamics between these two rodent species underscore the similarity in regeneration response between them. Humans, on the other hand, showed lower peak regeneration but sustained regeneration across many months rather than days (Figure 6.20C).

After fitting the metabolic demand parameter to experimental data, we determined an empirical relationship for determining the metabolic demand parameter

from the organism body mass, Equation 6.23 (Figure 6.21). We used a power-law expression to describe the relationship between these terms because of the well-known power-law relationship between organism mass and metabolic function.

$$Metabolic\ Demand = 47.315 * Mass^{-0.1825} \quad (6.23)$$

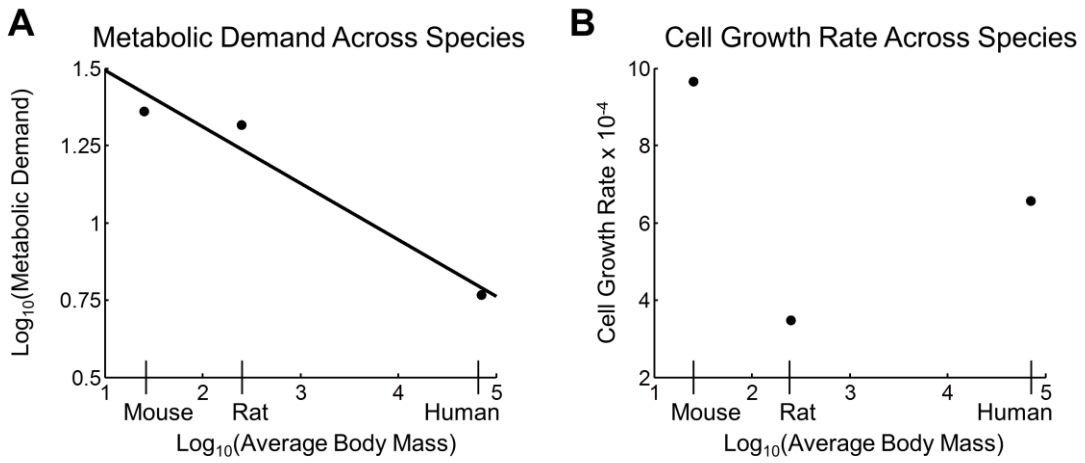

Figure 6.21 Relationships between fitted parameters and body mass across species. (A) Metabolic demand shows a negative exponential relationship with body mass following the equation: $Metabolic\ Demand = 47.315 * Mass^{-0.1825}$ (R2 = 0.95). (B) Cell growth rate for humans was estimated as the average growth for mouse and rat because there is little difference in cultured hepatocyte growth rates between species.

We have shown that it is possible that the difference in time necessary to regenerate fully is due predominantly to the differential functional demands of the liver across species. Rodents, which live in an environment more prone to infection and liver injury, may require a higher metabolic demand (a component of which is the nutrient delivery per cell) to maintain healthy liver function than humans, which live

in a relatively clean environment. Because blood flow and overall nutrient delivery does not change following PHx, a smaller number of cells are receiving a relatively increased nutrient delivery in all species. It is possible that post-PHx the relative increase in metabolic demand per cell—and therefore the driving force for regeneration—may be higher in rodents than in humans.

Liver mass recovery is a much longer process in humans than in rats, lasting months rather than weeks. While our assumptions allowed us to model liver regeneration in humans, other alternative hypotheses about the differences in liver regeneration between rats and humans remain possible. We therefore tested several alternate hypotheses that may be able to explain the differences in regeneration profiles between rats and humans. We tested the hypotheses that humans have an altered stress response compared to rats (Hyp 1); that humans have altered matrix remodeling dynamics and ECM-GF binding compared to rats (Hyp 2); that human hepatocytes have an altered transition time between physiological states (Hyp 3); and that human hepatocytes have a longer cell cycle, a higher apoptosis rate, a higher requiescence rate, and an altered transition rate between physiological states, as was assumed by Periwal et al. (2014) (Hyp 4) (Periwal et al, 2014). The study by Periwal et al. (2014) reduced the values of parameters controlling the hepatocyte cell cycle rate, apoptosis rate, and requiescence rate by a factor of 24, roughly the difference in lifespan between rats and humans. Additionally, they used clinical data to fit the three physiological parameters governing the rate of hepatocyte transition between states (k_P, k_R, and k_Q), reasoning that since these parameters abstract multiple signaling pathways and regulation, these parameters are most likely to be altered between species. Recent research from the Periwal lab, however, has agreed with our view that

cell growth and metabolic demand can be used to translate among species (Young & Periwal, 2015a). Table 6.2 contains the parameters used to test these hypotheses. We compared these hypotheses to our hypothesis that an altered metabolic demand can account for differences in liver regeneration dynamics between humans and rats (Hyp 5).

Table 6.2 Summary of parameters used to simulate alternate hypotheses of how human liver regeneration differs from rat liver regeneration

Hyp 1: Altered cytokine response	Hyp 2: Altered GF storage and ECM balance	Hyp 3: Altered state transition rate	Hyp 4: From Periwal et al. (2014)	Hyp 5: Reduced metabolic demand
$k_{IL6} = 0.1435$	$\kappa_{deg} = 4.955$	$k_{QP} = 1.4x10^{-3}$	$k_{QP} = 1.1x10^{-3}$	$M = 20.8217$
$\kappa_{IL6} = 0.4942$	$\kappa_{ECM} = 56.30$	$k_{PR} = 1.5x10^{-3}$	$k_{PR} = 2.6x10^{-3}$	$G = 3.474x10^{-4}$
$V_{JAK} = 1.364x10^{3}$	$k_{GF} = 3.288x10^{-3}$	$k_{RQ} = 70.9x10^{-3}$	$k_{RQ} = 135x10^{-3}$	
$K_m^{JAK} = 7.565x10^{3}$	$\kappa_{GF} = 2.139x10^{-3}$		$k_{req} = 4.17x10^{-3}$	
$\kappa_{JAK} = 0.0398$	$k_{up} = 0.1008$		$k_{ap} = 4.17x10^{-3}$	
$[STAT3] = 2.031$			$k_{prol} = 8.33x10^{-3}$	
$k_{STAT3} = 1.109x10^{3}$				
$K_m^{STAT} = 0.5178$				
$\kappa_{SOCS} = 0.1682$				
$K_I^{SOCS3} = 0.0569$				
$k_{IE} = 18.60$				
$K_m^{IE} = 88.13$				
$\kappa_{IE} = 1.148$				

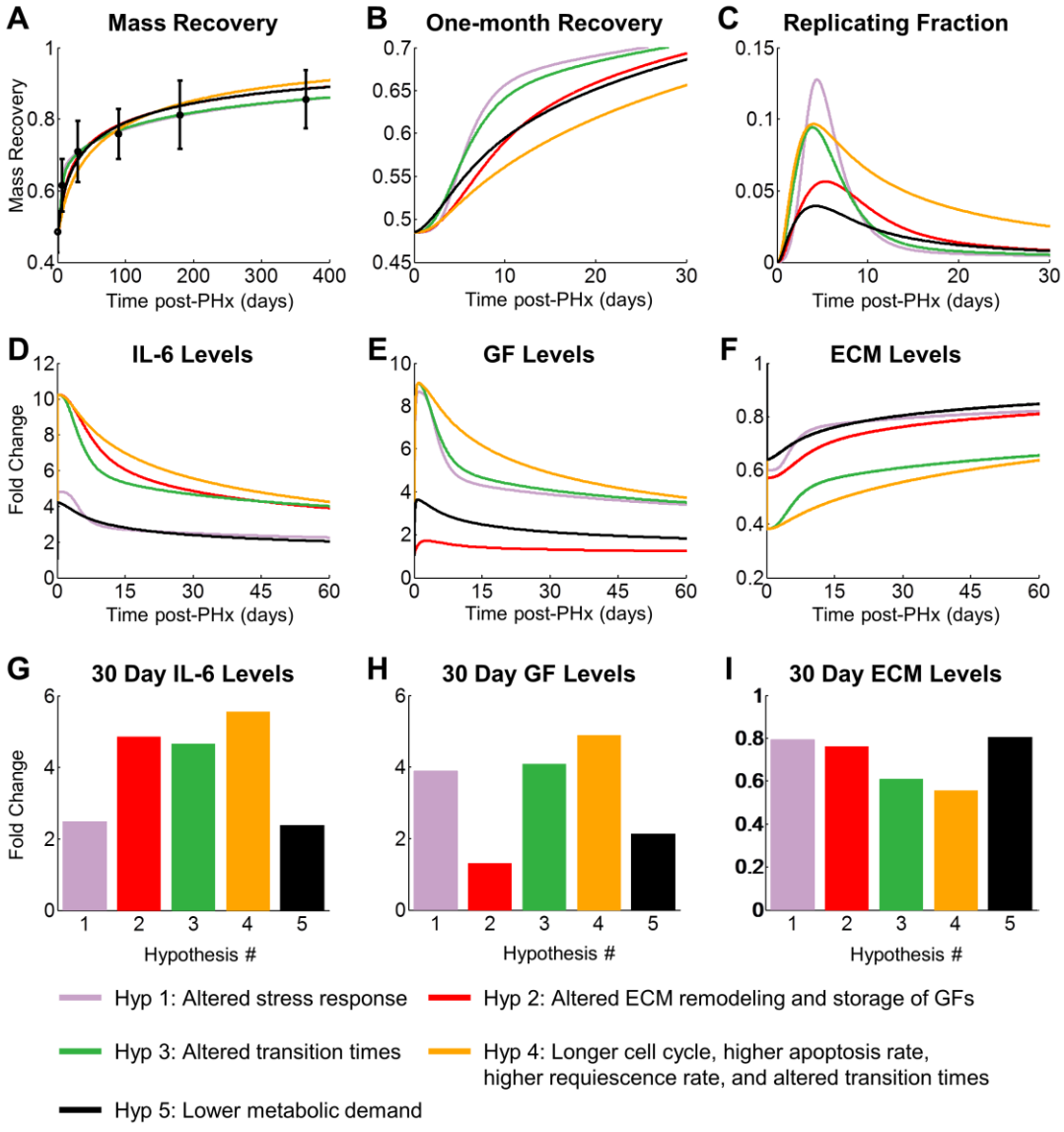
A
Mass Recovery
Mass Recovery
Time post-PHx (days)
B
One-month Recovery
Time post-PHx (days)
C
Replicating Fraction
Time post-PHx (days)
D
IL-6 Levels
Fold Change
Time post-PHx (days)
E
GF Levels
Time post-PHx (days)
F
ECM Levels
Time post-PHx (days)
G
30 Day IL-6 Levels
Fold Change
Hypothesis #
H
30 Day GF Levels
Hypothesis #
I
30 Day ECM Levels
Hypothesis #
Hyp 1: Altered stress response
Hyp 2: Altered ECM remodeling and storage of GFs
Hyp 3: Altered transition times
Hyp 4: Longer cell cycle, higher apoptosis rate, higher requiescence rate, and altered transition times
Hyp 5: Lower metabolic demand

Figure 6.22 Alternate parameter changes that can reproduce experimental liver regeneration profiles in humans. Parameters were varied to fit experimental data of human mass recovery to test several possible hypotheses about how human liver regeneration differs from rat: the hypothesis that humans have a higher stress response than rats (blue, MSE=6.1x10-3), the hypothesis that humans store a greater quantity of growth factors in the ECM that is liberated early post-PHx and may have an altered ECM production/degradation balance (red, MSE=6.25x10-3), the hypothesis that human hepatocytes have a higher transition time between physiological states (green, MSE=0.25x10-3), the hypothesis that humans have a longer cell cycle, a higher apoptosis rate, a higher requiescence rate, and a higher transition rate between physiological states as was assumed by Periwal et al. (2014) (magenta, MSE=12.16x10-3), and the hypothesis that only the metabolic demand parameter changes (black, MSE=4.91x10-3). (A) Simulated mass recovery compared to experimental data (Pomfret et al, 2003). (B) Mass recovery over the first 30 days following resection. (C) Fraction of replicating cells (simulated BrdU incorporation) post-resection. (D) IL-6 levels post-resection. (E) GF levels post-resection. (F) ECM accumulation post-resection. It may be possible to differentiate between most of these hypotheses by measuring at 30 days post-resection (G) IL-6, (H) GF, and (I) ECM. To differentiate between the high transition time hypotheses (green) and the hypothesis presented by Periwal et al. (orange), it may also be necessary to measure mass recovery. Approximately two weeks post-resection showed the maximum difference between mass recovery between these two hypotheses. MSE = Mean Squared Error between experimental and simulated data.

We found that all of the proposed hypotheses were able to explain human liver regeneration fairly well (Figure 6.22A). The early dynamics of regeneration, however, were able to differentiate between many of the hypotheses (Figure 6.22B and C). At two weeks post-PHx (14 days), the liver mass recovery should be able to differentiate between several of the hypotheses (Figure 6.22B). The biological variability in human liver mass recovery, however, may make this approach challenging. If liver biopsies are available, the fraction of replicating hepatocytes in these samples could be used to

identify which (if any) of these hypotheses is correct. Because biopsies of regenerating livers may not be beneficial to regeneration, it may be more clinically feasible to investigate cytokine and growth factor levels in the blood, assuming that they correlate to what is in the liver. Our model predicts that investigating cytokine levels (Figure 6.22D and G), growth factor levels (Figure 6.22E and H), and ECM accumulation (Figure 6.22F and I) at two weeks post-PHx will provide a surrogate for replication fraction to differentiate between hypotheses. The hypotheses that cell transition time differs between species (Hyp 3) and that cell transition time, replication rate, requiescence rate, and apoptosis rate differ between species (Hyp 4) gave similar predictions for molecular regulation at 30 days post-PHx; therefore, to differentiate between these hypotheses, it may be necessary to also investigate mass recovery or replicating fraction of cells. Furthermore, when measuring molecular levels in blood of patients, the fold changes may not match exactly the fold changes predicted to exist in the tissue from model simulations. What should allow for differentiation of hypotheses is the patterns of molecular regulation across multiple proteins.

We varied sets of model parameters to fit simulated regeneration dynamics to experimental human liver regeneration data to predict how human liver regeneration would have to differ from rat liver regeneration for these hypotheses to hold true. If the human cytokine response to PHx is entirely responsible for human to rat differences in regeneration dynamics (Hyp 1), then the production of pro-inflammatory cytokines should be suppressed in humans. Similarly, the hepatocyte response to these inflammatory cytokines should be suppressed as well. This would lead to decreased pro-inflammatory cytokine signaling (Figure 6.22 G – Hyp 1), causing low expression of MMPs and sustained high levels of ECM (Figure 6.22I –

Hyp 1). If ECM remodeling and GF signaling is entirely responsible for human to rat differences (Hyp 2), then GF production in humans should be slower than rats and human ECM should be more efficient in binding GF than rat ECM. This would lead to low levels of GF (Figure 6.22H – Hyp 2) and high levels of ECM (Figure 6.22I – Hyp 2). If the only difference between human and rat regeneration is hepatocyte transition time between physiological states (Hyp 3), then the transitions from Q to P and P to R promoting regeneration should be slower, while the transition from R to Q should be faster in humans than rats. If the assumptions made by Periwal et al. are true (Hyp 4), then the transition times should respond the same way. These longer transition times promoting regeneration lead to similar molecular profiles for these two cases, with high levels of cytokines and growth factors. Therefore, it becomes necessary to measure mass recovery to differentiate between these two hypotheses. The hypothesis that cell show altered transition times (Hyp 3) predicts a higher mass recovery at two weeks than the hypothesis proposed by Periwal et al. (Hyp 4). The difference in mass recovery at two weeks is caused by the assumption of a slower cell cycle, requiescence rate, and apoptosis rate by Periwal. et al. (Figure 6.22B – Hyp 4). Our hypothesis that lower metabolic demand is responsible for the differences between human and rat regeneration (Hyp 5) caused a lower overall response to PHx in human than in rats, but one that was sustained over a longer time period. This would lead to suppressed cytokine and GF signaling (Figures 6.22G and H – Hyp 5) as well as relatively high levels of ECM (Figure 6.22I – Hyp 5), because of low cytokine-induced MMP production. Patterns of molecular regulation that could differentiate hypotheses are summarized in Table 6.3. We recognize, however, that further experimental results in humans and further model refinement to include absolute molecular quantification and

factors not included in the current model may be required to differentiate fully between hypotheses.

Table 6.3 Patterns of molecular regulation (30 days) and mass recovery (14 days) that could differentiate hypotheses of mechanisms underlying liver regeneration in humans

Hypothesis	IL-6 / Inflammation	GF	ECM	Mass Recovery
(1) Altered Inflammation	Moderate	High	High	High
(2) Altered ECM remodeling and GF storage	High	Moderate	High	Moderate
(3) Altered transition times	High	High	Moderate	High
(4) Parameter changes assumed in Periwal et al. (2014)	High	High	Moderate	Low
(5) Lower metabolic demand	Moderate	Moderate	High	Moderate

6.3.8 Simulating regeneration in hundreds of human patients

Using hypothesis 5, that only metabolic demand differs among mammalian species, we simulated hundreds of human patients. We first sampled combinations of model parameters from their nominal values +/- 50% to identify how shifting balances of molecular and physiological regulators of regeneration influences regeneration dynamics. Each simulation with unique parameter values can be viewed as a virtual patient with a slightly different medical history and tissue physiology. We classified

liver regeneration in our virtual patients into distinct modes (Figure 6.23): suppressed, delayed, enhanced, delayed and enhanced, no response, and liver failure.

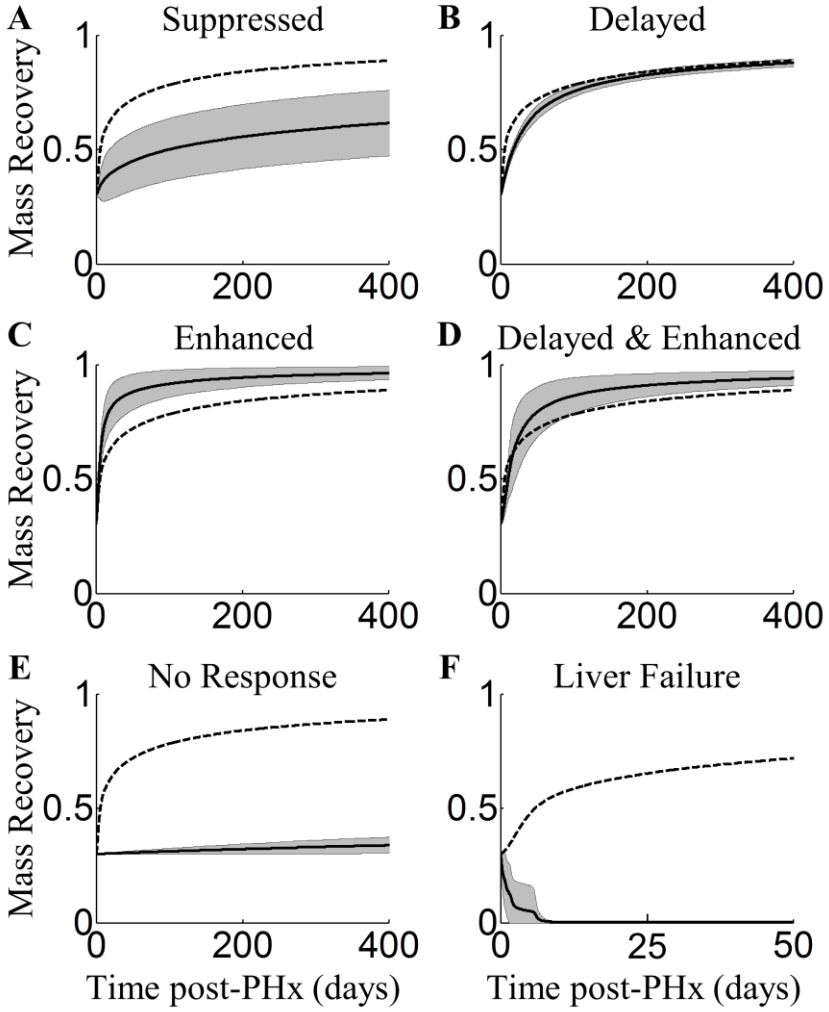

Figure 6.23 Regenerative modes of simulated human patients. (A) Supressed. (B) Delayed. (C) Ehanced. (D) Delayed and Enhanced. (E) No response. (F) Liver failure. Dashed line represents nominal regeneration, solid line represents mean, gray area represents +/- one standard deviation.

6.3.9 Simulating surgical interventions to enhance regeneration in a subset of human patients

Metabolic demand per cell can be modulated in the clinic by altering blood flow through the liver. Portal vein embolization (PVE) increases the blood flow through a section of the liver thereby increasing metabolic demand per cell. We therefore investigated whether a sustained perturbation to metabolic demand could act to rescue suppressed regeneration or unresponsive livers by doubling metabolic demand in the model at several times following resection (Figure 6.24). We found that increasing metabolic demand early post-resection caused increased apoptosis and organ failure, whereas increasing metabolic demand later was able to rescue suppressed regeneration by increasing growth factor bioavailability. This intervention had negligible effect on the no response mode, likely due to low baseline metabolic demand. Therefore, increasing blood flow through the liver after the first 100 days following resection (by methods such as PVE) may enhance recovery in patients with an otherwise suppressed regenerative response.

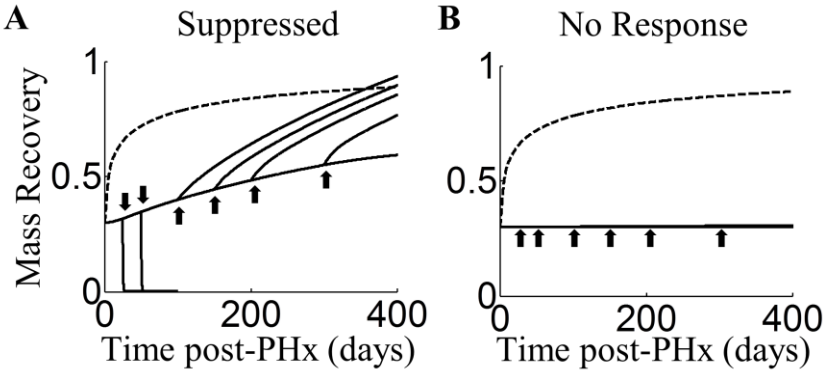

Figure 6.24 Effects of transient increases in metabolic demand on (A) suppressed regeneration and (B) no response. Dashed line represents nominal profile, solid line represents altered profile, arrows represent metabolic demand increase times.

6.3.10 Predicting effects of chronic disease on liver repair following partial hepatectomy

Just as non-alcoholic steatohepatitis (NASH), alcoholic steatohepatitis (ASH), cirrhosis, and diabetes affect liver function differently, each affects liver repair differently as well (Figure 6.25). Both non-alcoholic and alcoholic steatohepatitis suppress liver repair following partial hepatectomy as early as 48 hours post-surgery and lead to a sustained mass recovery deficit (Figure 6.25A and B). Toxin-induced cirrhosis also suppresses regeneration, causing a sustained offset from wild-type regeneration (Figure 6.25C). The simulated regeneration profile for diabetic rats suggests that the disease enhances early regeneration but delays full recovery (Figure 6.25D). These predictions are consistent with literature reporting that alloxan-induced diabetic rats show a delay in regeneration but no suppression of overall recovery (BARRA & HALL, 1977). In humans, studies have shown that diabetes results in a higher risk of post-operative liver failure and death in the first 90 days following liver resection, but when followed for longer than 6 months, diabetes causes no increase in the risk of complication or death, indicating that diabetes may impact the early stages of regeneration greater than the later stages (Allard et al, 2013;NAGASUE et al, 1993).

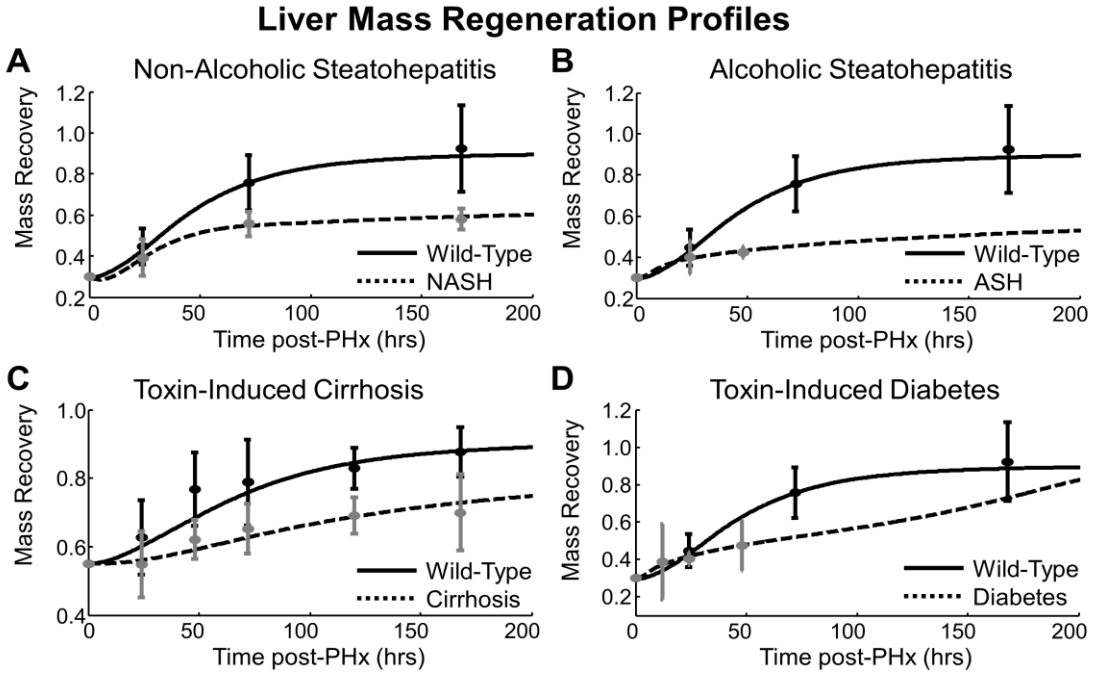

Figure 6.25 Model fit to disease regeneration profiles revealed altered non-parenchymal cell activity coupled with imbalances in the growth/replication propensity of hepatocytes was sufficient to explain disease-induced inhibition of regeneration. (A) Non-alcoholic steatohepatitis (Tanoue et al, 2011), (B) Alcoholic steatohepatitis (Yang et al, 1998b), (C) Cirrhosis (Kaibori et al, 1997), and (D) Diabetes (JOHNSTON et al, 1986).

We tested the hypothesis that alterations to non-parenchymal cell activation are sufficient to explain altered regeneration in these disease phenotypes. We found that despite the differences in repair dynamics, each of these regeneration phenotypes could be modeled by changing a relatively small number of parameters (9 out of 33), including metabolic load, hepatocyte growth rate, and parameters associated with non-parenchymal cells (Table 6.4). This result indicates that altered non-parenchymal cell activation is sufficient to explain altered regeneration in these disease phenotypes.

Table 6.4 Parameter changes to simulate alternate regeneration conditions

Parameter	NASH	ASH	Cirrhosis	Diabetes
M	23.1645	14.4017	18.0454	16.4539
G	$25x10^{-4}$	$14x10^{-4}$	$4.358x10^{-4}$	$8.92x10^{-4}$
k_{IL6}	0.3095	0.7900	2.1565	1.5892
κ_{IL6}	2.3633	0.2073	1.0430	0.03699
k_{deg}	1.7312	10.5646	0	6.4571
κ_{ECM}	9.5395	77.7923	83.5649	$1.8271x10^{-6}$
k_{GF}	0.0793	0.0002	0.0690	$1.7519x10^{-7}$
κ_{GF}	0.1679	0.1196	0.2456	0.5044
k_{up}	0.0075	0.0071	0.0027	0.1218

We investigated how these parameters change between disease conditions to predict of how diseases could impair regeneration by modulating non-parenchymal cell activation (Figures 6.26-6.29). A summary of our predictions of disease-impaired regeneration characteristics is available in Table 6.5.

Table 6.5 Summary of predicted disease effects on liver regeneration

Disease Model	Mass Recovery	Priming	Repli-cation	IL-6 Signaling	GF	ECM
(1) Non-alcoholic Steatohepatitis	Suppressed	Low	Low	Low	High	High
(2) Alcoholic Steatohepatitis	Suppressed	Sustained	Low	Sustained	Low	High
(3) Toxin-induced Cirrhosis	Suppressed	High	Low	High	Low	High
(4) Allotaxin-induced Diabetes	Delayed	High	Delay & low	Sustained	Low	Low

NASH inhibited regeneration mainly through impaired priming (Figure 6.26). NASH also caused an inhibited replication response following PHx, which was likely caused by low priming rather than GF deficiencies. Impaired priming and reduced replication caused a majority of mass recovery to occur through cell growth rather than replication.

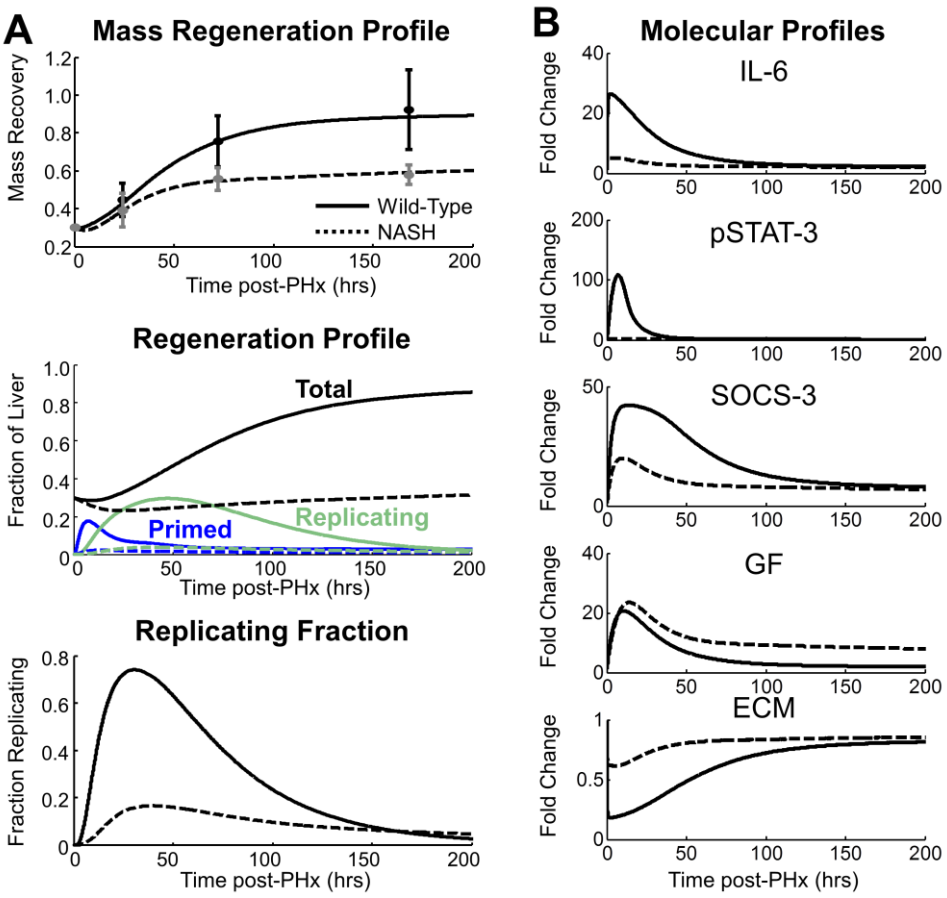

Figure 6.26 Regeneration profiles for healthy livers and those with high fat, fructose-induced steatosis. (A) NASH causes an inhibited replication response following PHx. The majority of mass recovery is caused by cell growth rather than replication. (B) This regeneration profile is driven by a lack of inflammatory signaling, leading to reduced priming. Although GFs are available, the low priming means that few hepatocytes are available to enter the replication stage. (MSE=2.25×10^{-4}).

Although its regeneration profile is similar to NASH's, ASH showed a robust priming response, but it inhibited regeneration mainly through deficiencies in GF bioavailability and ECM remodeling (Figure 6.27). The slight increase in liver mass was caused predominantly by cell growth rather than replication.

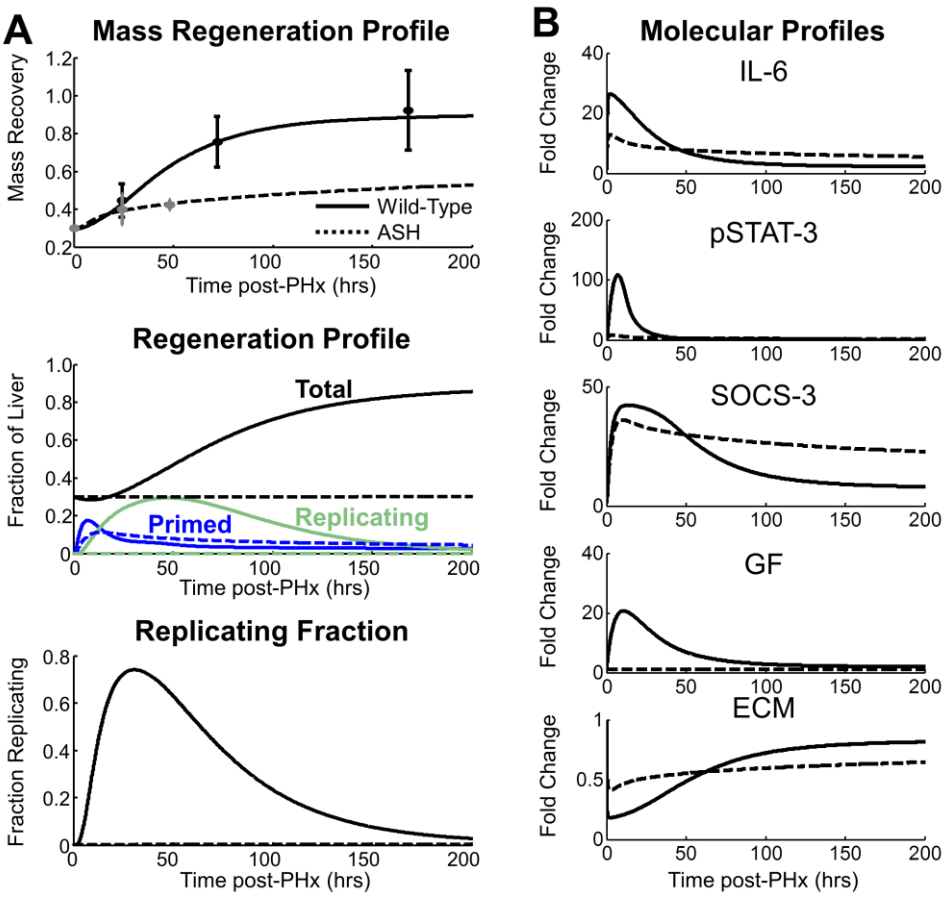

Figure 6.27 Regeneration profiles for healthy livers and those with alcohol-induced steatosis. (A) Alcoholic steatosis causes suppressed liver regeneration, with little mass recovery. The slight increase in liver mass is caused predominantly by cell growth rather than replication. (B) This profile is driven by sustained inflammatory signaling, lack of growth factor bioavailability, and increased matrix deposition following wounding. (MSE=8.82×10^{-5}).

Toxin-induced cirrhosis caused an enhanced priming response in hepatocytes but a reduced replication response (Figure 6.28). Reduced GF bioavailability coupled with high levels of ECM reduced the overall regenerative potential of cirrhotic livers.

In contrast to NASH and ASH, the mass recovery in cirrhosis was mainly due to cell replication rather than mass increase.

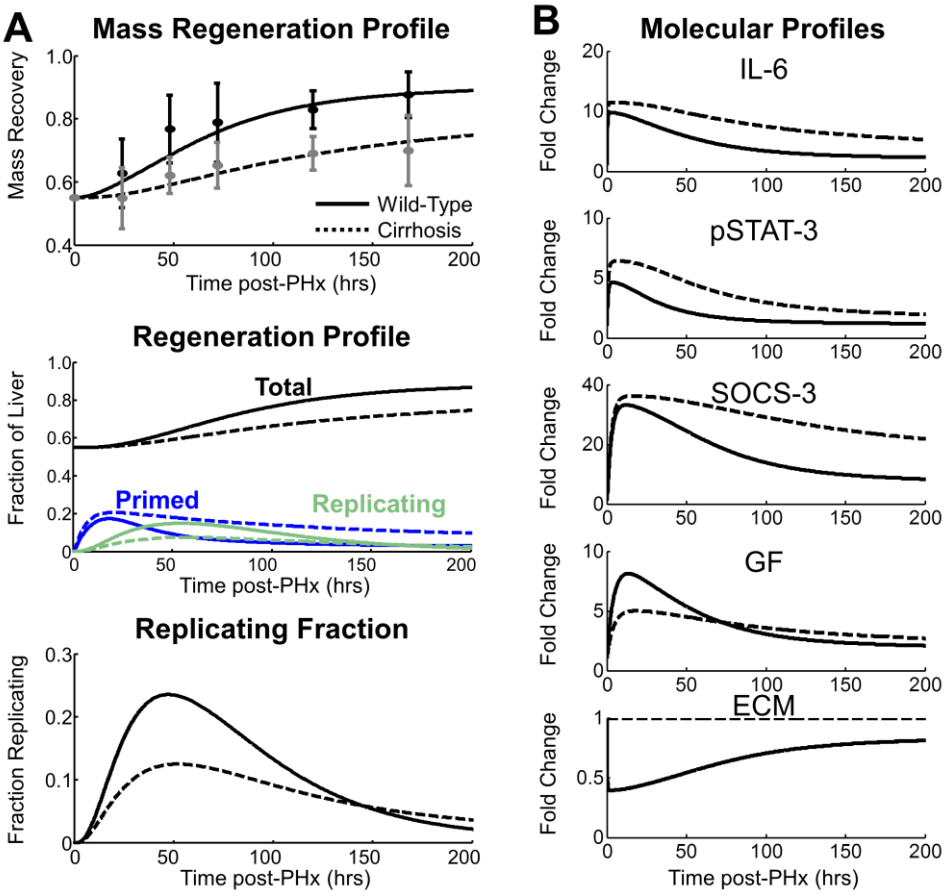

Figure 6.28 Regeneration profiles for healthy livers and those with toxin-induced cirrhosis. (A) Fibrosis causes a delay in the initiation of regeneration (note change in time scale) but ultimately little change in overall mass recovery. Mass recovery is due mainly to hepatocyte replication rather than cell growth. (B) This profile is driven by a sustained inflammatory response, a lack of growth factor bioavailability, and impaired matrix deposition following wounding. (MSE=2.50×10^{-3}).

Diabetes also inhibited regeneration through deficiencies in GF signaling (Figure 6.29). These GF deficiencies caused a delay in the initiation of replication. It is likely that the early enhanced mass recovery in diabetic rats may be due predominantly to hepatomegaly, while eventual mass recovery may be due to replication. Although the exact timing and magnitude of deficiencies in inflammation and GF signaling were not the same for all chronic disease states, all the chronic diseases simulated here showed deficiencies in both signaling pathways. This result suggests that many chronic diseases that affect the liver's repair ability do so in a combinatorial manner, altering the dynamics of inflammatory response and GF signaling.

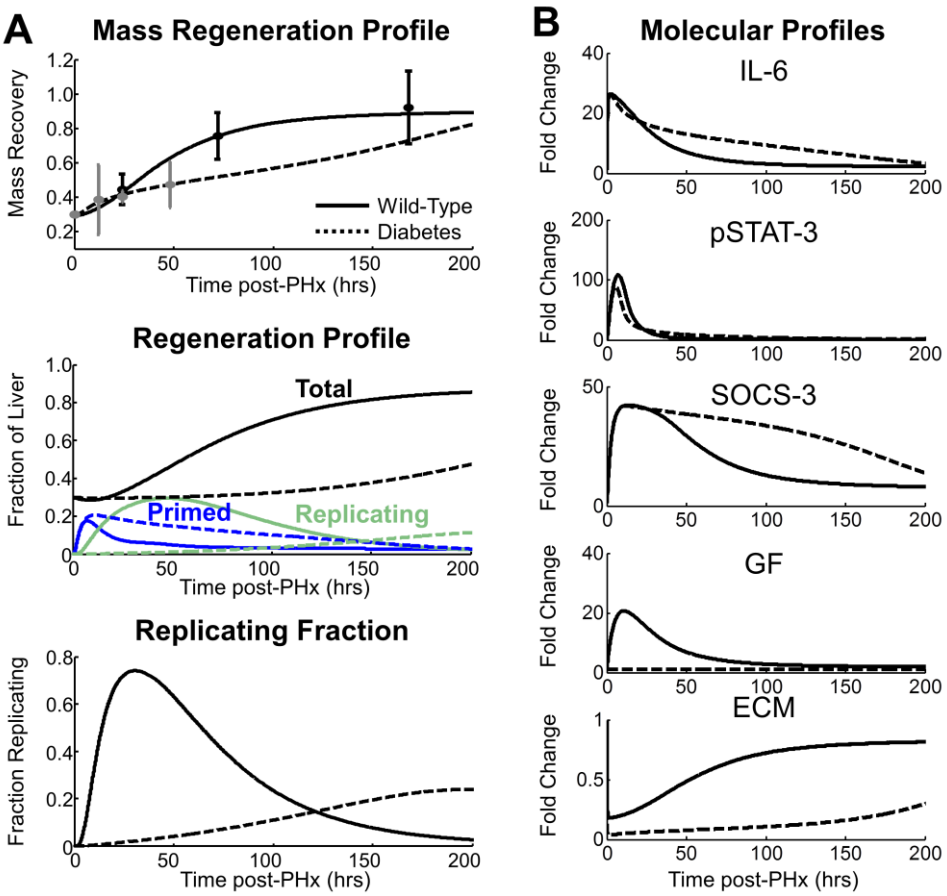

Figure 6.29 Regeneration profiles for healthy livers and those with diabetes. (A) Diabetes causes enhanced priming but delayed proliferation and delayed mass recovery. (B) This profile is driven predominantly by sustained cytokine signaling and a lack of growth factor bioavailability. (MSE=4.05×10^{-4}).

Adaptation to chronic diseases also appears to influence the liver's ability to recover a normal baseline function after an acute challenge. At long times post-PHx, NASH was characterized by sustained high levels of GF signaling, ASH was characterized by sustained high levels of IL-6 and reduced ECM accumulation, and diabetes was characterized by reduced ECM accumulation (Figures 6.26, 6.27, and

6.29). Cirrhosis, on the other hand, was characterized by all molecular levels returning to baseline (Figure 6.28). Our prediction of a sustained high inflammatory response in ASH simulations is consistent with previous reports of relatively high levels of inflammatory molecules found in the serum of patients with ASH (McClain et al, 2004). This result suggests that one of the fundamental mechanisms of disease progression between ASH and NASH may be a difference in inflammatory response of non-parenchymal cells.

Although our model simulations showed that altered non-parenchymal cell behavior is sufficient to cause impaired regeneration dynamics that are consistent with NASH, ASH, diabetes, and cirrhosis, parenchymal cells likely also contribute to impaired regeneration. We therefore tested whether alterations in hepatocyte response to non-parenchymal cells are sufficient to explain altered regeneration in these same disease phenotypes by changing parameters related to hepatocyte response to non-parenchymal cells (14 out of 33 parameters, Table 6.6).

Table 6.6 Hepatocyte-specific parameter changes to simulate alternate regeneration conditions

Parameter	NASH	ASH	Cirrhosis	Diabetes
V_{JAK}	$4.28x10^{4}$	$2.50x10^{4}$	$3.94x10^{3}$	$7.33x10^{4}$
K_M^{JAK}	$4.35x10^{0}$	0.99	609.5	$1.05x10^{4}$
κ_{JAK}	0.55	1.02	0.46	0.69
[STAT3]	2.54	4.00	4.18	1.67
V_{ST3}	723.5	443.4	790.7	3.5
K_M^{ST3}	0.35	0.45	0.56	$5.03x10^{-3}$
κ_{ST3}	0.04	0.14	$1.9x10^{-5}$	0.17
V_{SOCS3}	$3.14x10^{4}$	$2.14x10^{4}$	$2.26x10^{4}$	$1.53x10^{4}$
K_M^{SOCS3}	$3.21x10^{-4}$	$1.54x10^{-4}$	$11.55x10^{-4}$	$8.56x10^{-4}$
κ_{SOCS3}	$1.0x10^{-3}$	$2.5x10^{-10}$	0.67	0.12
K_I^{SOCS3}	0.015	0.010	0.007	0.004
V_{IE}	255.7	309.7	20.6	364.7
K_M^{IE}	43.2	28.5	28.6	0.53
κ_{IE}	6.8	6.9	8.2	1.8

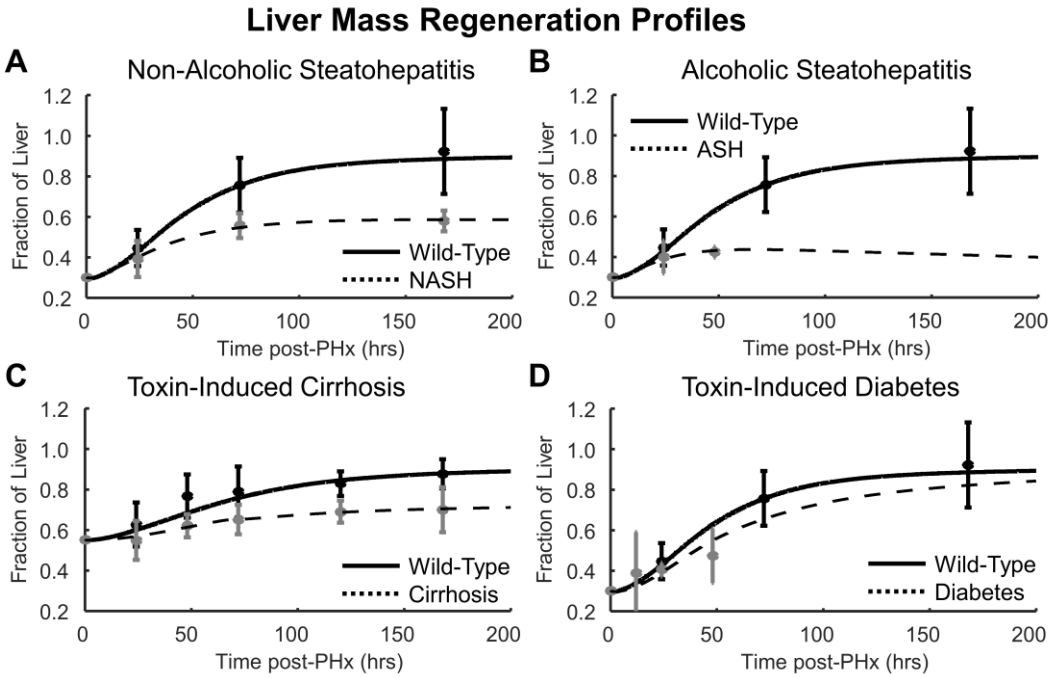

Figure 6.30 Simulations using hepatocyte-specific parameter alterations compared to disease regeneration profiles. Model fits to disease regeneration profiles reveals altered hepatocyte response to non-parenchymal cell signaling is sufficient to explain disease-induced inhibition of regeneration in (A) Non-alcoholic steatohepatitis (MSE=1.96×10^{-2}), (B) Alcoholic steatohepatitis (MSE=1.89×10^{-2}), and (C) Chirrhosis (MSE=5.14×10^{-2}), but not in (D) Diabetes (MSE=1.19). In all cases, the previous set of parameters (Table S2) gave lower MSE than the hepatocyte-specific parameter alterations (Table S3). MSE = Mean Squared Error between experimental and simulated data.

We found that for NASH, ASH, and cirrhosis, alterations in hepatocyte response to non-parenchymal cells was also sufficient to explain altered regeneration in these disease phenotypes (Figure 6.30A-C). Altering these hepatocyte response

parameters was insufficient to explain diabetes-impaired regeneration dynamics (Figure 6.30D). In all cases, the previous set of parameters (Table 6.4) gave lower mean squared error (MSE) than the hepatocyte-specific parameter alterations (Table 6.6). It was interesting to note that the parameter sets used to simulate NASH and ASH eventually resulted in liver failure, with hepatocyte numbers continuing to decrease as the simulation progressed. The results of these simulations, together with the simulations altering non-parenchymal cell behavior and experiments from literature, suggest that disease conditions likely alter the dynamic function of non-parenchymal cells and hepatocytes during liver regeneration. Therefore when investigating liver disease states and response to surgical interventions, a systems-based approach that explicitly accounts for cell-cell interactions is necessary to account for the underlying processes fully.

6.3.11 Comparison of regeneration in multiple genotypes of Adn-/- mice

This new model also has interesting implications for the study of regeneration in Adn-/- mice. We are not the first to study the effects of liver resection in Adn-/- mice. The results of our study (Chapter 4) appear to be in conflict with the results of a previous study (Shu et al, 2009b). We therefore attempt to use our computational model developed in this chapter to reconcile the divergent findings about liver regeneration dynamics in Adn-/- mice. The first strain of mice to be studied was an Adn-/- strain on the 129S background (Shu et al, 2009b). This strain was created by a replacement of a part of the second and third exons in Adn with a full length LacZ gene (Ren et al, 2005). When subjected to 70% liver resection, the Adn-/- 129S mice showed a suppressed regeneration at every time point measured. The second strain to be studies as a knockout of Adn on the C67BL/6J background (Strain: B6;129-

Adipoq^{tm1Chan}/J, The Jackson Laboratory, Bar Harbor, Maine). These Adn-/- C67BL/6J mice were created by replacing the second exon in Adn with a PGKneo cassette in embryonic stem cells derived from 129S mice. The embryonic stem cells were then injected into blastocyst and the resultant chimeric mice were then bred with C57BL/6J mice. These mutant mice were then back-crossed to maintain the Adn-/- on a C67BL/6J background. There are, however, some indications of an incomplete backcross, meaning that some background from the 129S mice could contaminate a true C67BL/6J genotype. In contrast to the suppressed regeneration displayed by the Adn-/- 129S mice, following 70% resection, Adn-/- C67BL/6J mice delayed initiation of regeneration but subsequently accelerated hepatoctye progression through the cell cycle (Correnti et al, 2015).

We evaluated whether our previously published computational model of liver regeneration could predict the molecular regulation underlying the different regeneration dynamics caused by differences in genetic background and gene knockout procedures. In Correnti, Cook et al. (2014), Adn-/- C67BL/6J mice showed an initial delay in regeneration, but a liver mass indistinguishable from wild-type mice at 54 hours post-PHx (Figure 6.31A). In contrast, Adn-/- 129S mice used by Shu et al. (2009) showed suppressed regeneration at all times post-PHx (Figure 6.31B).

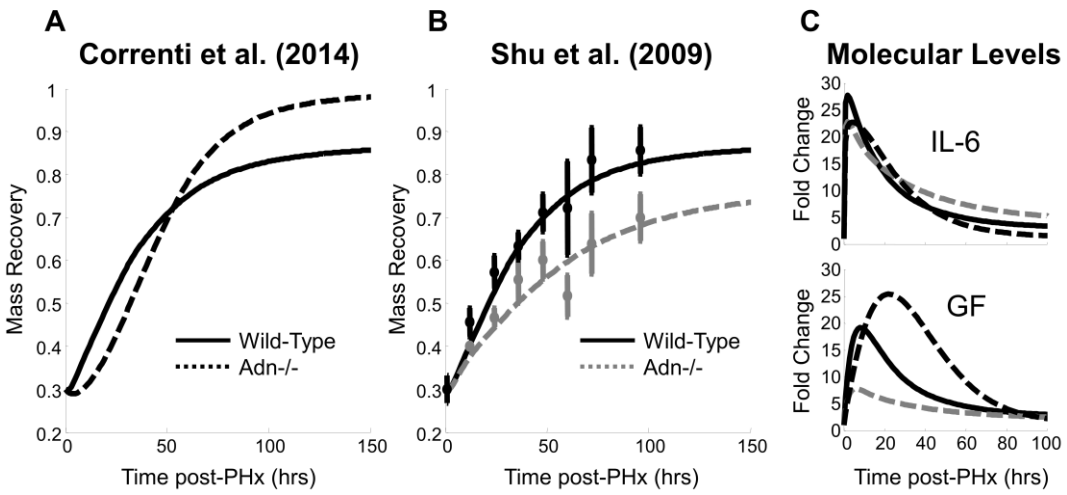

Figure 6.31 Cross-species validation of model utility can predict changes to organizational principles of liver function by differentiating liver regeneration modes in two strains of Adn-/- mice. (A) Mass recovery from Adn-/- C67BL/6J from Correnti, Cook et al. (2014) and (B) from Adn-/- 129S mice from Shu et al. (2009). (C) Predicted molecular profile for IL-6 and GF for both Adn-/- mouse strains and wild-type mice.

By altering computational model parameters, we predicted that the distinguishing factor discriminating between these two phenotypes was a difference in GF bioavailability (Figure 6.31C). Simulations of both genotypes showed an impaired inflammatory response leading to impaired priming early post-PHx (Figure 6.31C). We predicted, based on simulations, that the Adn-/- C67BL/6J mice compensated for this impaired priming by producing higher levels of growth factors than WT C67BL/6J mice at 24-48 hours post-PHx. We further predicted, however, that the Adn-/- 129S mice would have deficiencies in growth factor bioavailability at 12-36 hours post-PHx.

We have previously tested these predictions in Adn-/- C67BL/6J mice, where we showed inhibition of STAT-3 phosphorylation and sustained increases in HGF, FGF-2, and ANG1 in Adn-/- C67BL/6J mice following resection (See chapter 4). We predict that the levels of these same growth factors in the Adn-/- 129S mice following resection will be lower than in WT mice.

Whether or not GF bioavailability is indeed different at ~12-36 hours post-PHx between mouse strains, the results of studying GF levels in these two strains would have implications for how translatable knockout studies are across background strains, across species, and across knockout techniques. We would remain unsure whether the different response to resection was a result of strain differences or knockout techniques or whether there was another confounding factor, such as laboratory space or equipment or animal care. We believe, however, that this study is a useful first step towards an investigation of these issues.

6.4 Discussion

Our study provides an investigation into the organizational principles and molecular regulation underlying liver regeneration following resection across multiple species and disease states. Our study identified altered modes of regeneration and investigated disease states that cause regeneration to follow these altered modes. This study, however, only addresses surgical resection of the liver and has not been applied to drug-induced liver injury (DILI). Because similar archetypal processes also likely govern liver regeneration following DILI, it is possible that some of the results of our modeling study can be generalized to inform principles underlying regeneration following DILI as well. The altered regeneration dynamics following DILI indicate

that additional processes need to be added to the model to accurately capture the complete physiology (for example, clearance of injured or necrotic hepatocytes and immune cell infiltration).

This study investigated liver regeneration through a computational model involving archetypal signaling pathways that represent classes of molecular signaling. Therefore, the simulations in this study suggest relative balances and timing of molecular signals that may be deregulated in disease or altered across species.

Our study suggests several organizational principles of regeneration. Initiation of regeneration appears to be governed by the number of hepatocytes entering the priming phase, which in turn is largely driven by the inflammatory response (modeled as IL-6 signaling). The computational model simulations further suggest that IL-6 signaling activity is amplified at the level of STAT-3 phosphorylation, so that small changes in inflammatory response can cause large changes to STAT-3 phosphorylation and significantly alter the regeneration profile. The timing and magnitude of GF response appears critical to replication, with low or late GF response suppressing overall regeneration. Our results led us to predict that chronic diseases impair liver regeneration through a combination of deficient inflammatory signaling and growth factor bioavailability. We further predicted that these deficiencies are shared between non-parenchymal cell activation and hepatocyte responsiveness to extracellular stimuli.

Our approach allowed us to investigate several hypotheses about how regeneration differs between rats and humans. By maintaining molecular and phenomenological parameters constant across species and modifying metabolic load and hepatocyte growth rate, we were able to fit experimental regeneration profiles

across species. This approach has the benefit of conserving hepatocyte-related signaling pathways including the JAK-STAT signaling kinetics across species. These results revealed that regenerative capacity is likely related to animal mass, with larger species having fewer energetic resources to devote to regeneration. This explanation is consistent with identification of peak regeneration in pigs and dogs occurring later than in rats and mice (3 days post-PHx in pigs and dogs, as opposed to 1 day in rodents) (KAHN et al, 1988). Alternate hypotheses about differences between rat and human liver regeneration dynamics, however, offer different predictions about dynamic tissue behavior post-PHx. We predicted that tissue biopsies and scans taken at two weeks post resection or molecular measurements at one month post resection in humans could differentiate between these hypotheses.

Another factor governing the length of regeneration time is how rapidly hepatocytes are able to increase their functional mass to compensate for lost tissue. Large mass may not be beneficial to liver repair if much of the extra mass does not contribute to liver function; therefore, the mass regained in this simulation can be seen as functional mass increase that contributes to liver function. As opposed to the metabolic demand parameter, hepatocyte growth rate was not related to animal mass. Growth rate may therefore be governed by other factors, such as maximum glucose metabolic flux possible, mitochondrial activity and number of mitochondria, and the relative amount of nutrients available post PHx. By incorporating cell growth, the model proposed in this work was able to capture the rapid increase in tissue mass humans are capable of, up to 70% of liver mass restored by 30 days after 70% PHx (Pomfret et al, 2003). Experiments measuring growth rates of hepatocytes *in vitro* or further hepatectomy experiments performed using pigs or other species can be used to

test and refine the simple relationship proposed between metabolic demand and body mass.

According to our analysis, the number of parameters that need to be changed to translate across species is relatively small (a minimum of two). Furthermore, the minimum set of parameters changed were physiological parameters, M and G. This does not mean that there are no differences in molecular regulation across species; it does, however, suggest that the differences are the result of similar processes across species responding to species-specific physiology. This results in altered molecular and regeneration dynamics across species. In contrast, we changed multiple parameters, including parameters related to molecular signaling, to simulate disease effect on liver regeneration. Taken together, these results suggest that biological processes behaving normally can account for differences across species but cannot account for disease effects on regeneration phenotypes.

Although the model describes fairly well experimental data, the model description of the cell cycle does not contain specific phases of the cell cycle. The rate of cell proliferation in the model contains all the steps from exit from the G0 phase to a complete cell division. Therefore, this rate also includes any additional time taken for a quiescent hepatocyte to dedifferentiate, divide, and redifferentiate. Little is known about how long any dedifferentiation and redifferentiation takes or if the time needed for these processes varies across species. Therefore, the overall rate of cell proliferation may vary between species. Although we did not explicitly address this possibility in the current study, further studies could explore this as a potential contribution to the difference in peak hepatocyte replication times between rats and mice.

Parametric sensitivity analysis of the computational model revealed that regeneration is dynamically controlled and that not all factors respond the same across all times. This result coupled with the pulsatile sensitivity analysis recently performed on the original model proposed by Furchgott et al. (2009) indicates that treatments designed to improve regenerative ability during chronic disease or following liver transplant may need to be dynamic as well (Correnti et al, 2015). Extending the results of simulations of chronic disease states in rats to the human model may assist in scheduling treatments for patients suffering from chronic diseases post-transplantation to maximize regeneration. For example, during the first week (the apparent priming phase in humans) it might be necessary to renormalize hepatocyte response to inflammation signals while later treatments (replication phase) may need to increase growth factor levels.

Our model-based approach offers unique insights into the mechanisms of liver disease progression in the context of chronic disease; however, there are several limitations inherent to this approach. The first limitation is that only the JAK-STAT signaling pathway is explicitly considered in this model. Although this pathway has been shown to be critical for a normal repair phenotype, even a hepatocyte-specific STAT-3 knockout does not completely inhibit regeneration (Haga et al, 2005). In this genotype, signaling through ERK compensates for the lack of STAT-3. The importance of the liver's repair mechanism ensures that multiple compensatory signaling pathways are available to act (Taub, 2004c). Our model can be extended to include additional signaling pathways to account for compensatory signaling and cross-talk. We note, however, that the present simplification involving cell phenotype transitions sufficiently captures major features of the liver regeneration process. Such

simplified models have led to important insights into biological regulation in other contexts as well (Furchtgott et al, 2009;Kumar et al, 2004;Thakar et al, 2007).

Another limitation is that the current model takes into account only linear responses of non-parenchymal cells during liver repair. Many reviews highlight the important role of timing of non-parenchymal cell signaling during liver repair (Michalopoulos & DeFrances, 1997;Taub, 2004c). For instance, the critical contribution of non-parenchymal cells has been demonstrated using animals where Kupffer cells have been depleted, thereby significantly delaying regeneration following hepatectomy (Meijer et al, 2000b). The current simulations suggest that Kupffer cells are largely responsible for priming hepatocytes. Hepatic stellate cells appear to be the main regulator of hepatocyte regeneration, governing both proliferation through control of growth factor bioavailability and termination of regeneration through ECM production and degradation. Therefore, moving towards a more comprehensive computational model of liver repair in health and chronic disease requires inclusion of alternative regulatory mechanisms within hepatocytes, as well as the activation and signaling of non-parenchymal cells. To facilitate this integration, one could consider the existing models of macrophage or Kupffer cell activation and hepatic stellate cell activation. For instance, macrophage activation has been studied using a computational model of the cytokine-mediated pathways (Kuttippurathu et al, 2014;Marino et al, 2015). Specific to the liver, our group has recently developed a computational model of cytokine-mediated hepatic stellate cell activation that incorporates multiple pathways with cross-talk as well as microRNA mediated regulation (Kuttippurathu et al, 2014;Marino et al, 2015).

Our computational model was able to match liver regeneration profiles across multiple chronic disease models and across species. This modeling framework can act as a tool to translate results from rodent experiments to clinically actionable hypotheses in primates or humans. Our study suggests that liver regeneration is dynamically controlled by factors produced by non-parenchymal cells. Inflammatory signaling (predominantly from Kupffer cells) governs the priming response of hepatocytes, while growth factors (predominantly produced by hepatic stellate cells) govern hepatocyte entry into the cell cycle. The synchronicity of hepatocyte entry into the cell cycle is governed by both growth factor levels and timing as well as proliferation rate of hepatocytes. These findings underscore the importance of non-parenchymal cells to recovering the liver's repair ability from a diseased state. Therefore, future computational work should explicitly take contributions from non-parenchymal cells into account.

Chapter 7

EXTENDING THE COMPUTATIONAL MODEL TO INCLUDE NON-PARENCHYMAL CELL TRANSCRIPTIONAL PHENOTYPES

7.1 Introduction

Following resection, there is a coordinated response of liver cells (hepatocytes and non-parenchymal cells) that involves cell activation, intercellular signaling, hypertrophy, and hyperplasia, which have been well reviewed previously (Fausto, 2000;Michalopoulos, 2010;Taub, 2004c). Perhaps because such a coordinated response is required for effective regeneration, patients undergoing a liver resection exhibit a wide range of regeneration responses in the clinic, with some achieving effective regeneration and some failing to regenerate at all (Chenard-Neu et al, 1996). In lab animals, however, there is a much lower degree of variability in response to resection. Our approach is therefore to use a computational model to identify control principles and network properties governing regeneration, test these predictions at a lab-scale using rodents, then use our computational model to scale-up our results to humans, both in terms of liver size and subject variability. This type of approach has been previously successful in identifying phenotypically conserved principles of liver regeneration using a simplified model of liver regeneration (Cook et al, 2015).

There are multiple benefits for taking a systems-level computational modeling-centric approach to investigating liver regeneration. This systems perspective allows for integration of knowledge gained through experiments from multiple labs and even

across species. Computational modeling of this complex network allows for emergent behavior due to network properties. Investigating this emergent behavior allows for non-intuitive insights into liver regeneration. Additionally, and perhaps most importantly, cell network-based computational modeling allows for systematic investigation into the contributions of individual cell types to regeneration physiology.

7.2 Materials and Methods

7.2.1 Computational Model Description

Our computational model was extended from (Cook et al, 2015). The previous model included only a linear response of non-parenchymal cells to resection. Our extended model explores non-parenchymal cell behavior more fully. We maintained the original model architecture and hepatocyte equations. All simulations were performed in Matlab (Mathworks, Natick, MA).

7.2.1.1 Hepatocyte Equations

Our extended model maintains the framework of the previously published initial model by allowing hepatocytes to exist in one of three states: Quiescent (Q), Primed (P), or Replicating (R). Factors produced by non-parenchymal cells in response to liver metabolic load (metabolic demand per cell or M/N) shift hepatocytes between states, according to the following equations.

$$\frac{d}{dt}Q = -k_{QP}([IE]-[IE_0])Q + k_{RQ}[ECM]R + k_{req}\sigma_{req}P - k_{ap}\sigma_{ap}Q \quad (7.1)$$

$$\frac{d}{dt}P = k_{QP}([IE]-[IE_0])Q - k_{PR}([GF]-[GF_0])P - k_{req}\sigma_{req}P - k_{ap}\sigma_{ap}Q \quad (7.2)$$

$$\frac{d}{dt}R = k_{PR}([GF]-[GF_0])P - k_{RQ}[ECM]R + k_{prol}R - k_{ap}\sigma_{ap}R \quad (7.3)$$

Where [IE] represents the concentration of immediate early genes expressed in response to STAT-3 transcriptional regulation and [ECM] represents the amount of extracellular matrix. σ_{ap} and σ_{req} are sigmoidal functions defined as:

$$\sigma_{ap} = 0.5 * \left(1 + \tanh\left(\frac{(\theta_{ap} - {}^{M}/_{N})}{\beta_{ap}}\right)\right) \tag{7.4}$$

$$\sigma_{req} = 0.5 * \left(1 + \tanh\left(\frac{(\theta_{req} - [GF])}{\beta_{req}}\right)\right) \tag{7.5}$$

The parameters β and θ in each of these equations are tuned so that when metabolic load is high, σ_{ap} is high; conversely, when [GF] is high, σ_{req} is low. Therefore, when cells are highly stressed (high metabolic load), apoptosis occurs at a high rate; when GFs are available, cells remain in the "Replicating" state.

The JAK-STAT signaling pathway, GF production, and ECM production are modeled as a combination of first order and Michealis-Menton kinetics, as shown in the following equations.

$$\frac{d}{dt}[IL6] = k_{IL6}\frac{M}{N} - \frac{V_{JAK}[IL6]}{[IL6]+k_M^{JAK}} - \kappa_{IL6}[IL6] + k_1 \tag{7.6}$$

$$\frac{d}{dt}[JAK] = \frac{V_{JAK}[IL6]}{[IL6]+k_M^{JAK}} - \kappa_{JAK}[JAK] + k_2 \tag{7.7}$$

$$\frac{d}{dt}[STAT3] = \frac{V_{ST3}[JAK][proSTAT3]^2}{[proSTAT3]^2 + k_M^{ST3}(1 + [SOCS3]/k_I^{SOCS3})}$$

$$- \frac{V_{IE}[STAT3]}{[STAT3]+k_M^{IE}} - \frac{V_{SOCS3}[STAT3]}{[STAT3]+k_M^{SOCS3}} - \kappa_{ST3}[STAT3] + k_3 \tag{7.8}$$

$$\frac{d}{dt}[SOCS3] = \frac{V_{SOCS3}[STAT3]}{[STAT3]+k_M^{SOCS3}} - \kappa_{SOCS3}[SOCS3] + k_4 \tag{7.9}$$

$$\frac{d}{dt}[IE] = \frac{V_{IE}[STAT3]}{[STAT3]+k_M^{IE}} - \kappa_{IE}[IE] + k_5 \tag{7.10}$$

$$\frac{d}{dt}[GF] = k_{GF}\frac{M}{N} - k_{up}[GF][ECM] - \kappa_{GF}[GF] + k_7 \tag{7.11}$$

$$\frac{d}{dt}[ECM] = -k_{deg}[IL6][ECM] - \kappa_{ECM}[ECM] + k_6 \tag{7.12}$$

Where [proSTAT3] represents the concentration of monomeric STAT-3 available to dimerize following IL-6 signaling.

Hypoxia inducible factor (HIF-1α or HIF) is modeled as increasing when the liver mass increases faster than vascularization. HIF-1α then stimulates VEGF production within hepatocytes.

$$\frac{d}{dt}[HIF] = \frac{(N-N_0)}{HL} k_{HIF}(1 - \tanh(3 * Vascularization)) - \frac{V_{VEGF}[HIF]}{K_M^{VEGF} + [HIF]} - \kappa_{HIF}[HIF] + K_{SS}^{HIF} \quad (7.13)$$

Where HL is the tissue hypoxia load or tissue oxygen demand, k_{HIF} is the maximum HIF production rate, the 3 in the tanh function is a scaling term to ensure HIF production stops when the vascularization is appropriate for the organ mass, V_{VEGF} and K_M^{VEGF} are the michaelis-menton parameters for VEGF production from HIF, κ_{HIF} is the degredation rate of HIF, and K_{SS}^{HIF} is the steady state HIF production of the organ. VEGF production from HIF in hepatocytes is modeled according to michealis-menton kinetics.

$$\frac{d}{dt}[VEGF] = \frac{V_{VEGF}[HIF]}{K_M^{VEGF} + [HIF]} - \kappa_{VEGF}[VEGF] + K_{SS}^{VEGF} \quad (7.14)$$

Where κ_{VEGF} is the degradation rate of VEGF and K_{SS}^{VEGF} is the steady-state VEGF production.

7.2.1.2 Tissue Equations

The overall cell mass, N, includes hypertrophy and cell growth (hyperplasia) of primed and replicating cells in response to metabolic load as follows:

$$N = Q + G(P + R) \quad (7.15)$$

Where G represents the relative cell mass, which is initially set to 1.

Vascularization is promoted by increased levels of VEGF and proceeds through a phenotypic rate (k_{vas}).

$$\frac{d}{dt}[Vascularization] = k_{vas}([VEGF] - [VEGF_0]) \quad (7.16)$$

7.2.1.3 Kupffer Cell Equations

Kupffer cells were modeled to exist in one of three phenotypic states: Quiescent, Active, and Replicating. Kupffer cells become active initially due to physiological cues and early signaling events post-PHx, which we modeled using a lumped parameter (similar to the hepatocyte equations above). In addition to physiological signals, Kupffer cell states are governed by molecular parameters.

$$\frac{d}{dt}Q_{KC} = -k_{QA}\left[([TNF] - [TNF_0]) + \left(\frac{M}{N} - M\right)\right]Q_{KC} + k_{req}\sigma_{req}A - k_{ap}\sigma_{ap}Q \quad (7.17)$$

$$\frac{d}{dt}A_{KC} = k_{QA}\left[([TNF] - [TNF_0]) + \left(\frac{M}{N} - M\right)\right] + k_{RA}[ECM]R_{KC} - k_{req}\sigma_{req}A_{KC} - k_{AR}([VEGF] - [VEGF_0])A_{KC} - k_{ap}\sigma_{ap}A_{KC} \quad (7.18)$$

$$\frac{d}{dt}R_{KC} = k_{AR}([VEGF] - [VEGF_0])A_{KC} - k_{RA}[ECM]R_{KC} + k_{rep}R_{KC} - k_{ap}\sigma_{ap}R_{KC} \quad (7.19)$$

Where Q_{KC}, A_{KC}, and R_{KC} represent quiescent, activated, and replicating Kupffer cells, respectively. Requiescence, apoptosis, and replication are governed similar to hepatocytes with [VEGF] replacing [GF] in the sigmoidal requiescence function, see equation 5. Once activated, Kupffer cells secrete multiple molecules at different rates.

$$\frac{d}{dt}[TNF] = k_{TNF}A_{KC}\left(\frac{k_{TNF}^{Nom} + [IL10]}{[IL10]}\right) - \kappa_{TNF}[TNF] + K_{SS}^{TNF} \quad (7.20)$$

$$\frac{d}{dt}[IL6] = k_{IL6}A_{KC} - \kappa_{IL6}[IL6] + K_{SS}^{IL6} \quad (7.21)$$

$$\frac{d}{dt}[IL10] = k_{IL10}A_{KC} - \kappa_{IL10}[IL10] + K_{SS}^{IL10} \quad (7.22)$$

$$\frac{d}{dt}[TGF\beta] = k_{TGF}A_{KC} - \kappa_{TGF}[TGF\beta] + K_{SS}^{TGF} \quad (7.23)$$

Each protein is produced at a phenotypic rate k_{xx}, where xx is the species of interest. Each protein is degraded according for first order kinetics at a rate κ_{xx} and produced or degraded at a steady-state rate of K_{ss}^{xx}. In addition, the production of [TNF] is slowed by [IL-10] such that when [IL-10] is close to its initial value of 1, [TNF] is produced at a nominal rate according to k_{TNF}^{Nom}.

7.2.1.4 Hepatic Stellate Cell Equations

HSCs were simulated as existing in a quiescent state, two active states (pro-regenerative and anti-regenerative), and two replicating states (one from each activation state). Shifts between these states are catalyzed by molecular abundances, as shown in the equations below.

$$\frac{d}{dt}Q_{HSC} = -k_{Q\to PR}([IL6] - [IL6_0])Q_{HSC} + k_{PR\to Q}\sigma_{req}PR_A - k_{Q\to AR}([TGF\beta] - [TGF\beta_0])Q_{HSC} + k_{AR\to Q}\sigma_{req}AR_A - k_{ap}\sigma_{ap}Q_{HSC} \quad (7.24)$$

$$\frac{d}{dt}PR_A = k_{Q\to PR}([IL6] - [IL6_0])Q_{HSC} - k_{PR\to Q}\sigma_{req}PR_A + k_{PRR\to PR}[ECM]PR_R - k_{PR\to PRR}([PDGF] - [PDGF_0])PR_A - k_{ap}\sigma_{ap}PR_A \quad (7.25)$$

$$\frac{d}{dt}PR_R = k_{PR\to PRR}([PDGF] - [PDGF_0])PR_A - k_{PRR\to PR}[ECM]PR_R + k_{prol}PR_R - k_{ap}\sigma_{ap}PR_R \quad (7.26)$$

$$\frac{d}{dt}AR_A = k_{Q\to AR}([TGF\beta] - [TGF\beta_0])Q_{HSC} - k_{AR\to Q}\sigma_{req}AR_A + k_{ARR\to AR}[ECM]AR_R - k_{AR\to ARR}([PDGF] - [PDGF_0])AR_A - k_{ap}\sigma_{ap}AR_A \quad (7.27)$$

$$\frac{d}{dt}AR_R = k_{AR\to ARR}([PDGF] - [PDGF_0])AR_A - k_{ARR\to AR}[ECM]AR_R + k_{prol}AR_R - k_{ap}\sigma_{ap}AR_R \quad (7.28)$$

Where $k_{X\to XX}$ is the transition propensity from cell states X to cell state XX. Q is the quiescent state, AR_A is the anti-regenerative activation state, PR_A is the pro-

regenerative activation state, and AR_R and PR_R are the anti-regenerative replicating state and the pro-regenerative replicating state, respectively.

Once activated, HSCs produce pro-regenerative or anti-regenerative molecules depending on the activation state.

$$\frac{d}{dt}[HGF] = k_{HGF}\left(\frac{k_{HGF}^{nom}+[TGF\beta]}{[TGF\beta]}\right)PR_A - k_{up}[HGF][ECM] - \kappa_{HGF}[HGF] + K_{SS}^{HGF} \quad (29)$$

$$\frac{d}{dt}[TGF\beta] = k_{TGF}AR_A - \kappa_{TGF}[TGF\beta] + K_{SS}^{TGF} \quad (30)$$

$$\frac{d}{dt}[ECM] = k_{ECM}AR_A - \kappa_{deg}[TNF][ECM] - \kappa_{ECM}(ECM) + K_{SS}^{ECM} \quad (31)$$

Each protein is produced at a phenotypic rate k_{xx}, where xx is the species of interest. Each protein is degraded according for first order kinetics at a rate κ_{xx} and produced or degraded at a steady-state rate of K_{ss}^{xx}. In addition, the production of [HGF] is slowed by [TGFβ] such that when [TGFβ] is close to its initial value of 1, [HGF] is produced at a nominal rate according to k_{TNF}^{Nom}. Furthermore, [HGF] can be sequestered in the ECM with an uptake rate of k_{up}. This model does not allow explicitly for sequestered HGF to be re-released during regeneration.

7.2.2 Parameter Estimation

Where possible, parameters related to species found in the original model (Chapter 6) were tuned using a gain-matching technique. Parameters were selected so that the production of molecules included in the original model occurred with approximately the same dynamics during the first 10 hours post-PHx in both models and followed previously-studied dynamics (Figure 7.1).

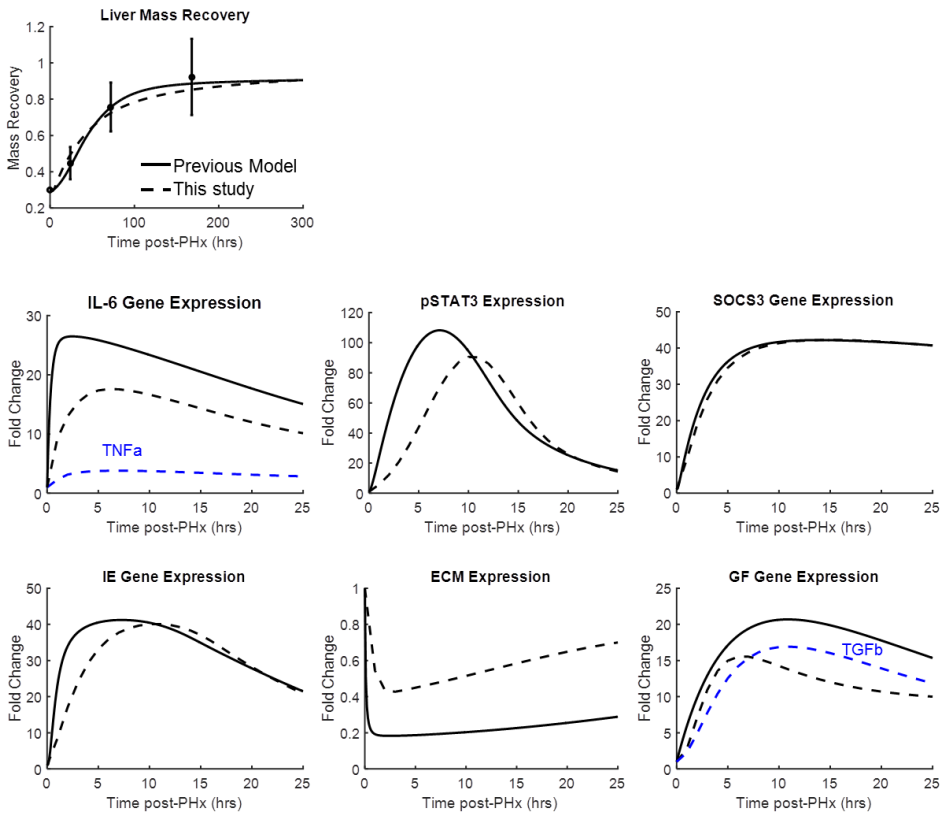

Figure 7.1 Comparison of model dynamics between this model and previous model during the first 25 hours post-resection (Chapter 6).

All other parameters were estimated using order of magnitude estimates so that the parameters were of the same magnitude as the parameters above. These remaining parameters were tuned manually to match experimentally observed molecular profiles or physiological observations during liver regeneration. A complete table of model parameter values used and physiological interpretations can be found in Appendix A.

7.2.3 Sensitivity Analysis

Global sensitivity coefficients were estimated by sampling the model's parameter space within 10% to 1,000% of each parameter's nominal value using a

Latin hypercube sampling method to sample each parameter uniformly over three orders of magnitude. We then simulated liver regeneration following 70% PHx using 150 parameter sets for the sensitivity analyses including kap and 1,500 parameter sets for the sensitivity analyses excluding kap. We calculated the overall mass recovery (N_i) for each case of liver regeneration and the time to liver failure (t_i) for each case of failed regeneration. We then calculated regeneration sensitivity coefficients and failure sensitivity coefficients for each parameter according to the partial rank correlation coefficient (PRCC) formulation using the "partialcorr" function in Matlab.

7.3 Results

7.3.1 A New Multiscale Cellular and Molecular Network Model of Liver Regeneration

We developed a computational model of liver regeneration that includes both hepatocyte hypertrophy and hyperplasia (Figure 7.2A and B) (Cook et al, 2015). Briefly, each cell type (hepatocytes, Kupffer cells, and HSCs) exists in discrete physiological states and factors they secrete initiate intracellular signaling cascades that lead to transitions among states for each cell type. These cells also respond to physiological perturbations by transitioning among states, increasing mass, or committing apoptosis. Each cell type was simulated to take on discrete states in response to regulation by distinct molecules, which we included in our model based on previous research identifying these molecules as important during liver regeneration or chronic ethanol abuse. The formalism for representing the physiological perturbations and Hepatocyte functional states were adapted from (Furchtgott et al, 2009). See the Materials and Methods section for details of the model and equations, and Appendix A for model parameters.

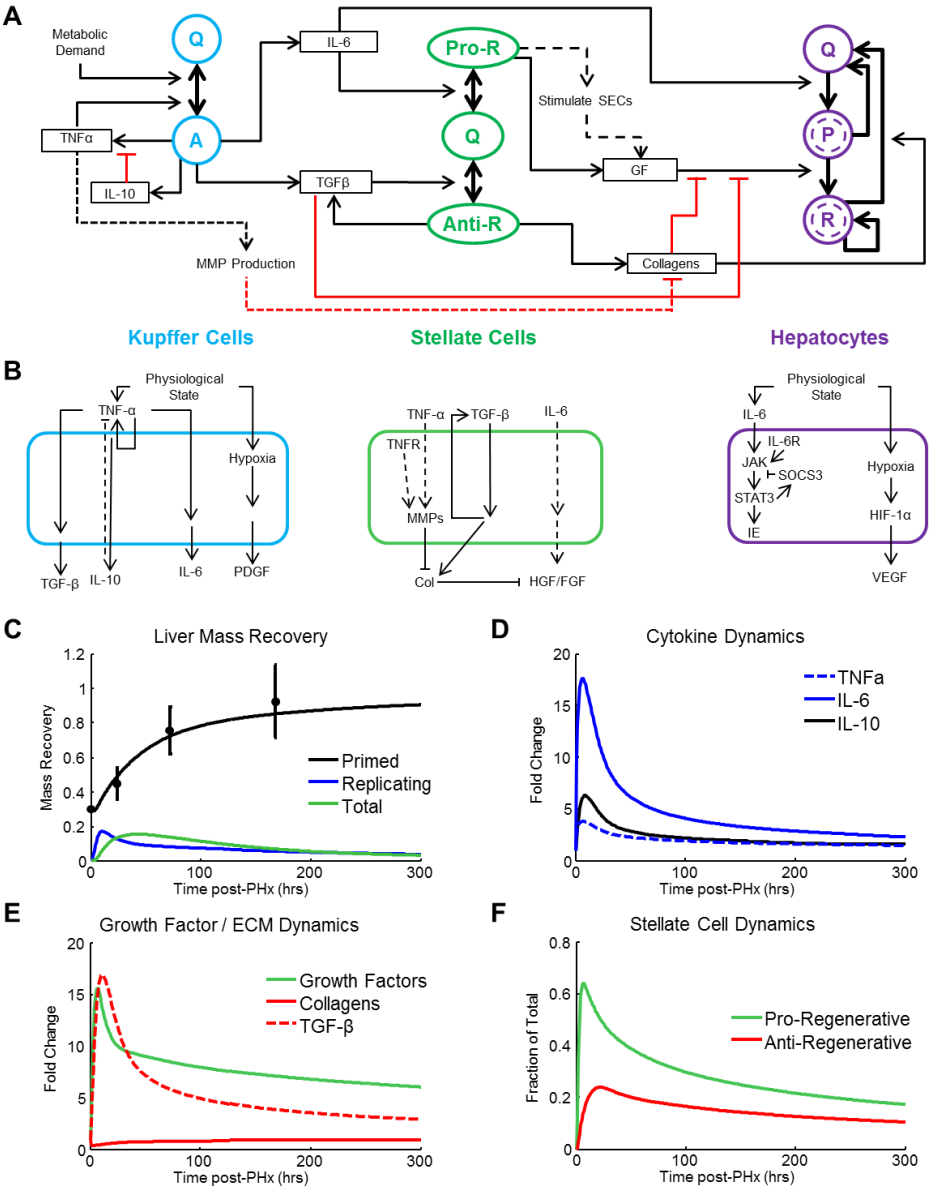
A
Metabolic Demand
Q
A
TNFα
IL-10
IL-6
TGFβ
Pro-R
Q
Anti-R
Stimulate SECs
GF
Collagens
MMP Production
Q
P
R
Kupffer Cells
Stellate Cells
Hepatocytes
B
Physiological State
TNF-α
Hypoxia
TGF-β
IL-10
IL-6
PDGF
TNF-α
TGF-β
IL-6
TNFR
MMPs
Col
HGF/FGF
Physiological State
IL-6
IL-6R
JAK
SOCS3
STAT3
IE
Hypoxia
HIF-1α
VEGF
C
Liver Mass Recovery
Mass Recovery
Primed
Replicating
Total
Time post-PHx (hrs)
D
Cytokine Dynamics
Fold Change
TNFa
IL-6
IL-10
Time post-PHx (hrs)
E
Growth Factor / ECM Dynamics
Fold Change
Growth Factors
Collagens
TGF-β
Time post-PHx (hrs)
F
Stellate Cell Dynamics
Fraction of Total
Pro-Regenerative
Anti-Regenerative
Time post-PHx (hrs)

Figure 7.2 Cell network model of non-parenchymal cell activation contributing to liver regeneration. (A) Full network diagram showing cell states, transitions among states, and molecules promoting or inhibiting cell transitions. (B) Cell signaling models showing a schematic representation of molecular interactions occurring within each cell type considered. Solid lines represent direction signaling; dashed lines represent indirect production. (C) Simulated liver mass recovery profiles compared to experimental data from (Tanoue et al, 2011). (D) Simulated cytokine dynamics following resection. (E) Simulated dynamics of growth factors and collagens following resection. (F) Simulated profile of HSC state dynamics following resection.

7.3.1.1 Metabolic Demand

Our model uses a lumped parameter, the metabolic demand (M), to represent the physiological state of the animal. The metabolic demand can be viewed as the normal stress put on a healthy liver to maintain physiological functions; it is likely related to a combination of external factors such as portal blood flow, portal pressure, nutrient availability, toxin flux (such as lipopolysaccharide) and intrinsic factors including hepatocyte metabolic capacity, functional history, and transcriptional state. In our model, the metabolic load (defined as metabolic demand per cell, or M/N, where N is the functional mass of the liver) increases following partial hepatectomy and is the driving force for liver regeneration.

7.3.1.2 Hepatocytes

The simulated hepatocyte state transition network in our model follows the framework presented by Cook, Ogunnaike, and Vadigepalli, which allows hepatocytes to exist as quiescent, primed, or replicating (Figure 7.2A) (Cook et al, 2015). IL-6 acting through the JAK-STAT signaling cascade initiates immediate early (IE) gene signals in hepatocytes that catalyze their transition from the quiescent state to the

primed state (Figure 7.2B, Hepatocytes). Primed hepatocytes can either return to quiescence, which occurs at a constitutive rate, or primed hepatocytes can enter the replicating state in response to sufficient levels of growth factors (GF) produced by non-parenchymal cells and liberated from the ECM. However, hepatocyte replication is inhibited by increased amounts of Transforming Growth Factor β (TGF-β) (Bissell et al, 1995). Replicating hepatocytes double their number approximately every 30 hours, and return to quiescence at a constitutive rate, which can be increased by ECM buildup. Hepatocytes in the primed and replicating states are also able to increase mass to respond to an increased metabolic demand driving liver regeneration. Such a framework allows a system representation where hepatocytes can respond to metabolic challenges through replication and through increasing functional capacity (mass) of each cell. This framework is also applicable in disease contexts, where replication may be impaired, providing a capability for hepatocytes to ameliorate damage to tissue in the absence of a regeneration response. Other models have been developed that include cell hyperplasia by representing primed and replicating hepatocytes with discrete size increases instead of allowing for a continuum of hyperplasia (Young & Periwal, 2015b). These models, however, have not yet been shown to be able to capture disease-specific dynamics of liver response to resection.

In addition, within this framework, hepatocytes are able to sense and respond to hypoxia (Liu et al, 2014). During liver regeneration, hepatocytes may begin hypoxic signaling when they have expanded into areas that are not yet vascularized fully (Maeno et al, 2005). In our model, the hypoxic signaling is considered as follows: hepatocytes responding to a low vascularization by inducing Hypoxia Inducible Factor

1α (HIF-1α), which induces hepatocytes production of VEGF and therefore NPC replication to replace lost tissue architecture (Copple et al, 2009).

7.3.1.3 Kupffer Cells

Kupffer cell activation during liver regeneration and in response to chronic and acute stresses has been studied extensively (Barnes et al, 2015;Melgar-Lesmes & Edelman, 2015;Sica et al, 2014;Wang et al, 2014;Yang et al, 1998a). Our model accounts for two functional states of Kupffer cells: quiescent and active (Figure 7.2A). In this scheme, active Kupffer cells can transition along a gradient of M1 to M2 activation in response to the autocrine feedback of the cytokines they produce. Activated Kupffer cells return to quiescence at a constitutive rate (Figure 7.2B). In our model, Kupffer cells are activated in response to an increased metabolic load; and once activated, they begin to produce cytokines associated with an M1 activation phenotype, high production rate of IL-6 and Tumor Necrosis Factor α (TNF-α), and low production rate of Interleukin 10 (IL-10) and TGF-β (Sica et al, 2014). TNF-α interacts with several receptors to mediate physiological response in Kupffer cells. TNF-α further increases numbers of activated Kupffer cells within a population by binding to TNF receptors (TNFRI and TNFRII) leading to NF-κB activation, transcription of NF-κB target genes (including IL-6, IL-10), immediate early (IE) gene expression, and Kupffer cell activation (Aggarwal, 2003;Chen & Goeddel, 2002). TNF-α also induces the production of AP-1 and its downstream targets, including osteopontin (OPN or SPP1), IL-10, and GM-CSF, which induce production of TGF-β in Kupffer cells (Bozinovski et al, 2002;Ogawa et al, 2005;Xing et al, 1997). We model the effects of these pathways by simulating activated Kupffer cells as constitutively expressing TNF-α, IL-6, IL-10, and TGF-β. Kupffer cell activation is

also modulated by negative feedback, most prominently by IL-10 impeding TNF-α production (Fiorentino et al, 1991). Our model includes a description of IL-10 antagonism of TNF-α production. Biologically, even high levels of IL-10 do not lead to complete inhibition of TNF-α production; therefore, our mathematical model considers a nominal amount of TNF-α production that occurs even at high levels of IL-10 (de Waal Malefyt et al, 1991).

Kupffer cells respond to other external factors in addition to activation signals. In response to poor vascularization, Kupffer cells produce HIF-1α, leading to production and secretion of PDGF (Copple et al, 2009). Activated Kupffer cells also respond to external VEGF, produced by hepatocytes. VEGF induces Kupffer cells to enter a replicating state, which results in a cell doubling in ~30 hours (Yang et al, 2004). Replicating Kupffer cells return to the activated state at a constitutive rate, which is increased by ECM buildup. These processes and state transitions are incorporated into the network model as detailed in the Materials and Methods.

7.3.1.4 Hepatic Stellate Cells

HSCs have been called the "protean, multifunctional, and enigmatic cells of the liver" (Friedman, 2008c), primarily because they contribute to liver function and disease through multiple mechanisms. In healthy livers, stellate cells contribute to ECM turnover, retinoid storage and transport, regulation of the tissue microenvironment through cytokine and growth factor production, and potentially to regulating blood flow through the liver. In liver fibrosis and cirrhosis, HSC activation causes increased buildup of fibrous ECM, which impairs hepatocyte replication (Issa et al, 2003). During development of hepatocellular carcinoma, HSCs may contribute to the tissue microenvironment promoting tumor growth and metastasis (Engelmann et

al, 2015). Although much work has focused on characterizing HSC activation into fibrotic or pro-fibrotic states, several studies have also found that HSCs contribute to liver regeneration through the production of growth factors that enhance regeneration, including HGF, EGF, and FGF (Li & Friedman, 1999;Reeves & Friedman, 2002). These disparate HSC functions led us to postulate the existence of two mutually exclusive HSC functional states: a pro-regenerative state, producing growth factors, and an anti-regenerative state, producing collagens and TGF-β (Figure 7.2A).

In our model, HSCs are considered as transitioning into distinct states in response to distinct external stimuli. IL-6 signals through the JAK-STAT signaling cascade to induce production of growth factors, such as HGF and FGF, and immediate early (IE) genes, which transition HSCs to a pro-regenerative phenotype. These interactions are represented in our model as a physiological transition between states (Figure 7.2B). Studies investigating contributions of NPCs to liver regeneration (Malik et al, 2002) have hinted at IL-6 induction of this pro-regenerative state. HSC transition to an anti-regenerative state, in contrast, occurs through TGF-β signaling via the SMAD2/3 pathway, considered in our model as a state transition (Figure 7.2B). The functional effects of this anti-regenerative state on the liver regeneration dynamics were matched to the known effects of pro-fibrotic HSC activation on hepatocyte proliferation and liver regeneration, which have been investigated rigorously *in vitro* and *in vivo* (De Minicis et al, 2007;Jiang et al, 2006b).

In our modelling framework, HSCs can enter a replicating phenotype from either the pro-regenerative or the anti-regenerative states in response to increased PDGF levels. Replicating HSCs transition from their replicating states back to their respective functional states (pro-regenerative or anti-regenerative) at a constitutive rate

and a matrix-dependent rate. These matrix-dependent rates are increased by ECM buildup, leading to a reduction in levels of HSCs replicating.

7.3.1.5 Tissue-scale Response

Maintenance of ECM and ECM-bound factors involves several cell types orchestrating the composition and properties of the ECM. Many cell types within the liver contribute to matrix degradation both through constitutive degradation and through active degradation using matrix metalloproteases (MMPs) (Haruyama et al, 2000;Malik et al, 2002;Sakaida et al, 2003;Wang & Keiser, 2000;Xu et al, 2005). Consequently, we modeled matrix degradation as a cell-independent process. Intrinsic matrix degradation was modeled as a constitutive rate of ECM removal, and extrinsic matrix degradation as TNF-α inducing MMP production, which increases ECM removal. The matrix itself is an active contributor to liver regeneration by sequestering and releasing growth factors at baseline and during the regeneration response. Our model includes matrix contribution to growth factor production by implicitly representing GF produced by HSCs as coming directly from these cells and from freed matrix-bound factors. Matrix sequestration of growth factors is included explicitly via a term that allows GF to be bound and sequestered by ECM.

Vascularization was modeled at the physiological scale by introducing a parameter representing the extent of vascularization within the tissue (i.e. the total volume of blood vessels and their distribution within the tissue). The amount of vascularization increases in response to the amount of VEGF produced by hepatocytes themselves responding to hypoxia. As vascularization increases, hypoxia decreases, causing VEGF levels to return to baseline. This feedback mechanism acts to maintain vascularization levels in the regenerating liver.

7.3.2 Dynamic Balance of Hepatic Stellate Cell States during Regeneration

Our computational model was able to match the dynamics of experimentally observed liver mass recovery following resection in rats (Figure 7.2C). Simulation results showed that the dynamic distribution of hepatocyte functional states matched the experimental observations. Priming peaked early post-PHx (within the first 12 hours) and was maintained at lower levels as regeneration progressed. This early priming peak is consistent with reports showing an approximate 16-hour delay between resection and DNA replication in rats (Fausto, 2001). Hepatocyte replication peaked at ~26 hours post-PHx, which agrees with the results of many studies showing that BrdU incorporation following 70% PHx in rats peaks at 24 hours post-PHx in young adult rats (Fausto, 2001). Our simulation results are also consistent with the observations on the tissue microenvironment following PHx: we show that TNF-α and IL-6 increase early post-PHx, with peaks at ~6 hours post-PHx (Figure 7.2D), corresponding closely with TNF-α and IL-6 peaks in the serum reported at 12 hours post-PHx in rats (Yang et al, 1998b). Also, we show that IL-10 increases early post-PHx but its peak is delayed until ~9 hours post-PHx, matching experimental observations that IL-10 increases following TNF-α and IL-6 and has a lower peak level than IL-6 (Figure 7.2D) (Yang et al, 1998b). Our simulation results also captured the reported dynamic behavior of GF (similar to rat HGF dynamics) and of TGF-β (similar to mouse TGF-β dynamics), with both increasing early post-PHx and decaying thereafter (Figure 7.2E) (Hayashi et al, 2012;Tomiya et al, 1998). The GF profile peaked prior to that of TGF-β and remained elevated longer, facilitating hepatocyte entry into the cell cycle. ECM degraded rapidly post-PHx, but had returned to nominal levels by the termination of regeneration, in accordance with results from previous studies investigating matrix dynamics during liver regeneration (Figure 7.2E)

(Rudolph et al, 1999). Our simulations predict the existence of an early transition of quiescent HSCs into both pro-regenerative and anti-regenerative states (Figure 7.2F). The levels of pro-regenerative HSCs peaked prior to the levels of anti-regenerative HSCs, and the balance of cell states favored the pro-regenerative state during the early stages of regeneration (0 – 100 hours post-PHx). The fraction of pro-regenerative HSCs decreases rapidly, while the fraction of anti-regenerative HSCs decreases more slowly. After ~100 hours post-PHx, the ratio of pro-regenerative and anti-regenerative HSCs tends to equalize, which may contribute to the slowing and eventual termination of regeneration (Figure 7.2C).

7.3.3 Hepatocyte apoptosis rate bifurcates liver recovery and failure

We performed global sensitivity analysis to investigate which parameters are important regulators of the regeneration dynamics. We sampled the model's parameter space within biologically reasonable parameter value limits using a Latin hypercube sampling method to sample each parameter uniformly from a uniform distribution with a range of three orders of magnitude around its nominal value (10x to 0.1x nominal value). We subsequently simulated liver regeneration following 70% PHx, corresponding to each of the 150 parameter sets. We found that the liver mass profiles could be broadly divided into regenerating and non-regenerating responses, and that there were more cases of the latter than the former. We therefore calculated the Pearson correlation between parameter values and regeneration amount or time to liver failure and found that hepatocyte apoptosis rate is strongly correlated with early liver failure (Figure 7.3A). We also found that a threshold value of the hepatocyte apoptosis rate (in this case, 2 times the nominal value) governs a bifurcating response between liver recovery and liver failure (Figure 7.3B).

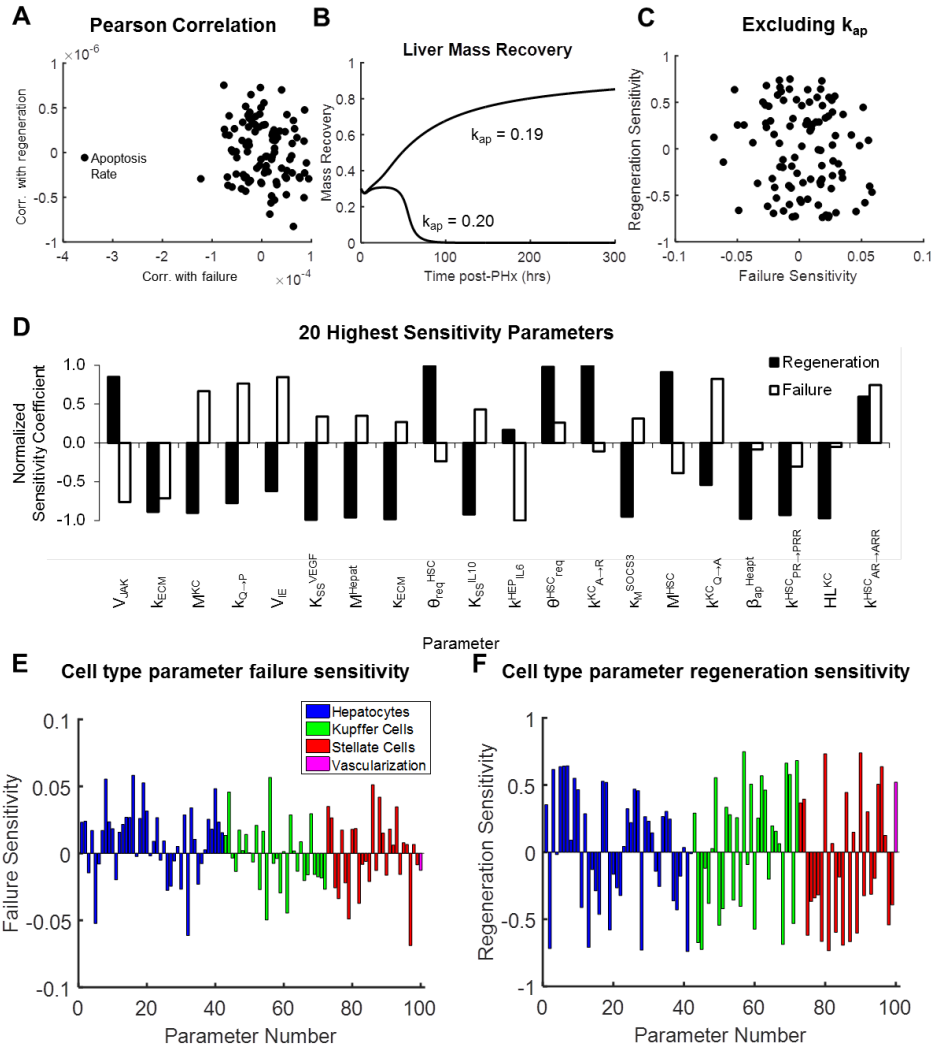
A
Pearson Correlation
Corr. with regeneration
Corr. with failure
Apoptosis Rate
B
Liver Mass Recovery
Mass Recovery
Time post-PHx (hrs)
k_ap = 0.19
k_ap = 0.20
C
Excluding k_ap
Regeneration Sensitivity
Failure Sensitivity
D
20 Highest Sensitivity Parameters
Normalized Sensitivity Coefficient
Regeneration
Failure
Parameter
E
Cell type parameter failure sensitivity
Hepatocytes
Kupffer Cells
Stellate Cells
Vascularization
Failure Sensitivity
Parameter Number
F
Cell type parameter regeneration sensitivity
Regeneration Sensitivity
Parameter Number

Figure 7.3 Parameters from all cell types contribute to regeneration dynamics and time to failure. (A) Hepatocyte apoptosis rate correlates relatively strongly with time to liver failure, suggesting that this parameter has a large influence causing liver failure. (B) Changing hepatocyte apoptosis rate results in a bifurcation between liver recovery following resection and liver failure. (C) Removing hepatocyte apoptosis rate from the global sensitivity analysis shows that regeneration and time to liver failure are sensitive to changes in many parameters. (D) The 20 parameters with the highest combined sensitivity coefficients for regeneration among and time to liver failure. Of the top 20 most sensitive parameter, 8 are HSC-related parameters, 7 are hepatocyte-related parameters, and 5 are KC-related parameters. (E) Time to failure sensitivity coefficients for parameter values associated with each cell type. 67% of hepatocyte parameters show positive failure sensitivity (compared to 48% for KCs and 50% for HSCs). (F) Regeneration sensitivity coefficients for parameter values associated with each cell type. 60% of HSC parameters show negative regeneration sensitivity (compared to 45% for hepatocytes and 43% for KCs).

We found similar bifurcations of liver mass profiles corresponding to the other parameters governing hepatocyte apoptosis (Figure 7.4).

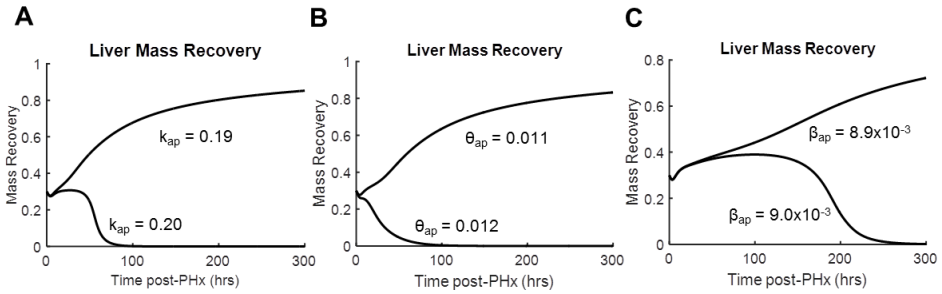

Figure 7.4 Several parameters related to hepatocyte apoptosis cause a separatrix-like behavior between liver regeneration and liver failure. (A) Apoptosis rate, (B) shape parameter, (C) scale parameter.

7.3.4 Co-ordinated Response of Multiple Cell Types is Required for Effective Regeneration

We then performed global sensitivity analysis using the partial rank correlation coefficient (PRCC) method (Marino et al, 2008). We simulated regeneration using 10,000 parameter sets varying all parameters except the hepatocyte apoptosis rate, because we have found that varying apoptosis rate has a disproportional effect on our analysis. Based on the results from global sensitivity analysis, we identified key parameters contributing to regeneration or liver failure (Figure 7.3C). We calculated the top 20 parameters contributing to liver regeneration or failure using a sum of squares distance metric to understand which parameters affect regeneration dynamics most strongly (Figure 7.3D). Parameters that contributed positively to regeneration, tended (mostly, but not always) to contribute negatively to liver failure. Although not in the top 20 highest sensitivity parameters, monomeric STAT-3 concentration showed a positive contribution to both regeneration and liver failure. This finding is consistent with previous experimental studies showing that acute inhibition of STAT-3 as well as long-term inflammation involving STAT-3 activation both suppress regeneration (Jin et al, 2006;Li et al, 2002).

We examined cell-type specific parameters to identify which cell types contribute the most to liver failure and regeneration. We found that hepatocyte and HSC parameters tended to have the highest sensitivity coefficients for the liver failure response, with 8 of the top 20 parameters associated with hepatocytes, and 8 of 20 associated with HSCs. This suggests that hepatocyte and HSC preconditioning prior to resection plays a significant role in determining whether a liver will regenerate or fail (Figure 7.3E). Among the most sensitive parameters affecting time to liver failure were steady-state production of Tgfb by HSCs (K_{SS}^{Tgfb}), concentration of monomeric

STAT3 ([STAT3]), IE gene activation rate (V_{IE}), and quiescent-to-primed transition rate ($k_{Q\rightarrow P}$). In addition, we found that there was no cell type whose parameters had a disproportionally large effect on regeneration dynamics, indicating that regeneration requires a coordinated regulation of all cell types in the liver (Figure 7.3F). Among the most sensitive parameters affecting liver regeneration were the hepatocyte parameters K_m^{JAK}, K_m^{SOCS3}, and β_{ap}; the Kupffer cell parameters $k^{KC}_{Q\text{-}A}$ and hypoxia load (HL^{KC}); the HSC parameters θ^{HSC}_{req}, k_{ECM}; κ_{ECM}, and κ_{deg}; and the physiological parameters representing metabolic demand (M) for all three cell types.

7.3.5 Dynamic Tissue Microenvironment Cycles Underlie Regeneration Dynamics

For successful regeneration cases, we investigated how HSC states and the tissue microenvironment respond to resection. We found that levels of pro-regenerative and anti-regenerative HSCs peak prior to or at 24 hours post-PHx, and decrease thereafter (Figure 7.5A). The phase-plane representation in Figure 7.5A allows us to visualize the coordinated behavior of the two cell states. The levels of cells in both states increase early post-PHx, with pro-regenerative levels peaking earlier than anti-regenerative levels. This corresponds with an earlier and higher magnitude peak transition rate in pro-regenerative cells (Figure 7.5B). Together, these cell states contribute to a successful regeneration response that matches the experimentally observed mass recovery dynamics following partial hepatectomy in rats (Figure 7.5C). The distribution of cell functional states affects the molecular state of the tissue microenvironment, which in turn regulates the transition between cell states. Figures 7.5D-I show the coordinated regulation of the tissue microenvironment following resection. Each pair of factors shows a cyclic response to resection, with

levels of these factors eventually returning to normal. The relationship of TGF-β to GFs, however, appears slightly more complex than the relationships between other pairs of factors (Figure 7.5G). Both TGF-β and GFs increase early following resection (< 24 hrs), but GF levels decrease more rapidly than TGF-β levels, causing a crossover in the phase plane. This crossover occurs ~72 hrs. post-PHx, and may correspond to the end of hepatocyte replication and the beginning of the termination of regeneration.

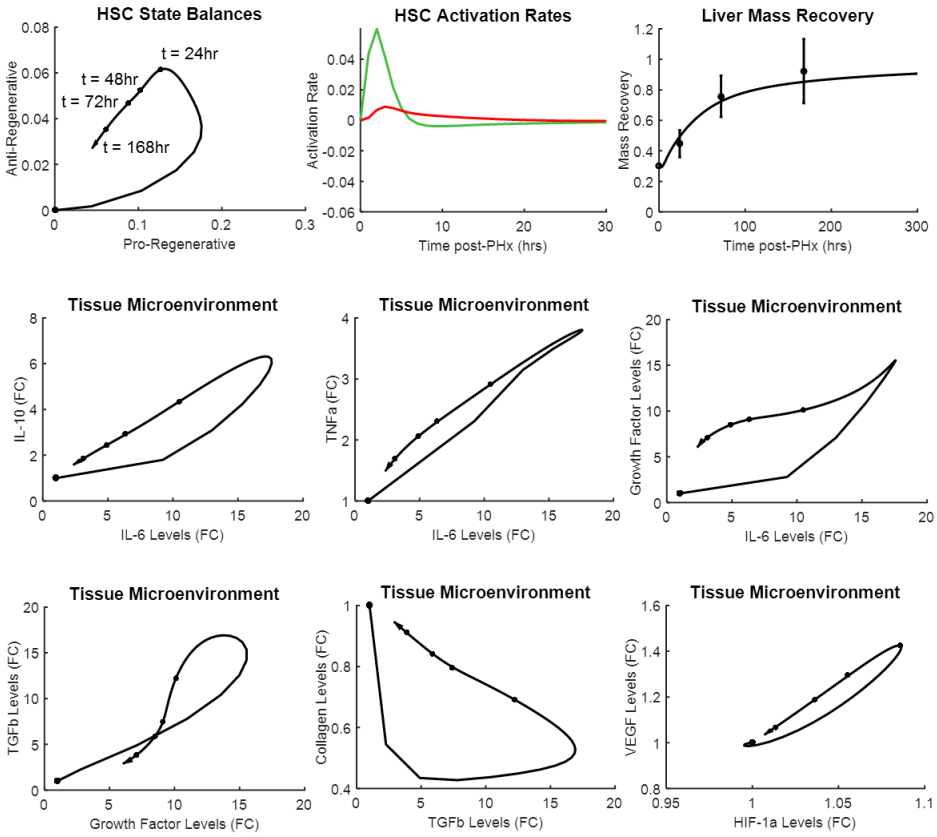

Figure 7.5 Phase planes behavior during successful liver regeneration. Dynamic tissue microenvironment influences and is shaped by cell state balances. Dots on the phase planes represent time = 0hr, 24hr, 48hr, 72hr, and 168hr following resection.

7.3.6 Hepatic Stellate Cell State Balances Modulate Regeneration Dynamics

We used our model to investigate how altering HSC dynamics could contribute to impaired liver regeneration. We sought to simulate enhanced liver regeneration through altering the baseline balance cells in the pro-regenerative and anti-regenerative HSC states.

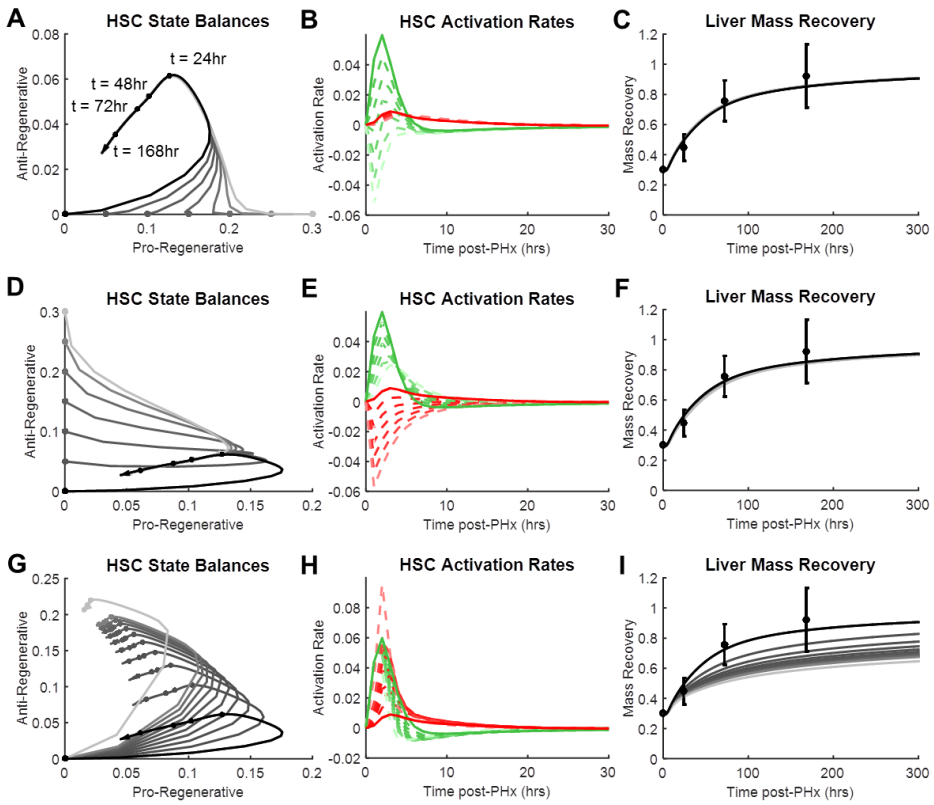

Figure 7.6 Model analyses show the impact of imbalances among multiple hepatic stellate cell transcriptional states on liver regeneration dynamics. (A) HSC behavior is constrained prior to 24 hr post-PHx even after increasing the baseline fraction of pro-regenerative HSCs. This behavior assumes the absence of other changes associated with changing baseline amounts. (B) Similar to the phase plane behavior, transition dynamics converge prior to 24 hr post-PHx. (C) Increasing the baseline amount of pro-regenerative HSCs has little effect on the dynamic regeneration profile. (D) HSC behavior is constrained prior to 24 hr post-PHx even after increasing the baseline fraction of anti-regenerative HSCs. This behavior assumes the absence of other changes associated with changing baseline amounts. (E) Similar to the phase plane behavior, transition dynamics converge prior to 24 hr post-PHx. (F) Increasing the baseline amount of anti-regenerative HSCs has little effect on the dynamic regeneration profile. (G) Increasing the quiescent to anti-regenerative transition rate leads to a dynamic change in HSC transcriptional state balances. (H) HSC transition dynamics change based on the balance of transition rates. (I) Increasing the quiescent to anti-regenerative transition rate causes a suppressed regeneration profile. This type of profile can be seen in diseased states.

We increased the baseline fraction of pro-regenerative HSCs while maintaining the baseline anti-regenerative fraction at zero. Our model predicted that increasing the pro-regenerative fraction of HSCs at baseline, in the absence of other changes, resulted in a rapid evolution of HSC state distribution to match the nominal case (Figure 7.6A), which was accomplished through dynamic changes to the pro-regenerative transition rates (Figure 7.6B), without yielding a noticeable effect on the mass recovery profile (Figure 7.6C). We then sought to simulate impaired regeneration through increasing the baseline amount of cells in the anti-regenerative phenotype, consistent with our experimental results in ethanol-fed rats. Similar to the previous case, changing the baseline level of anti-regenerative HSCs in the absence of other changes resulted in a constrained evolution of HSC state distribution prior to 24h

post-PHx to eventually follow the nominal trajectory, due to changes in both pro-regenerative and anti-regenerative transition rates (Figure 7.6D and E). As before, this baseline imbalance resulted in no discernible change the mass recovery profile (Figure 7.6F). The constrained HSC behavior in both cases was likely the result of similar Kupffer cell regulation. Regardless of initial HSC conditions, similar Kupffer cell signaling constrained HSC balances towards nominal case, leading to an effective regeneration response (Figures 7.7 and 7.8). Neither increasing the initial fraction of pro-regenerative HSCs nor increasing the initial fraction of anti-regenerative HSCs resulted in a significant change in liver mass recovery dynamics. It should be noted that this result should hold true only in the absence of other changes to the liver microenvironment caused by changing the initial balances of cells in each of these cell states.

In contrast, changing the balance of pro-regenerative and anti-regenerative transition propensities resulted in a shift in the behavior of HSC dynamics post-PHx (Figure 7.6G, Figure 7.9). By increasing the anti-regenerative transition propensity of HSCs, fewer HSCs transition to the pro-regenerative state and more transition to the anti-regenerative state. Furthermore, because of the positive feedback created by the production of TGF-β, HSCs tend to remain in the anti-regenerative state rather than return to quiescence. This leads to a slight decrease in the apparent pro-regenerative transition rate, likely caused by the reduced number of quiescent HSCs due to anti-regenerative transition rate increases (Figure 7.6H). This increase in anti-regenerative HSCs leads to a suppressed liver mass recovery post-PHx (Figure 7.6I).

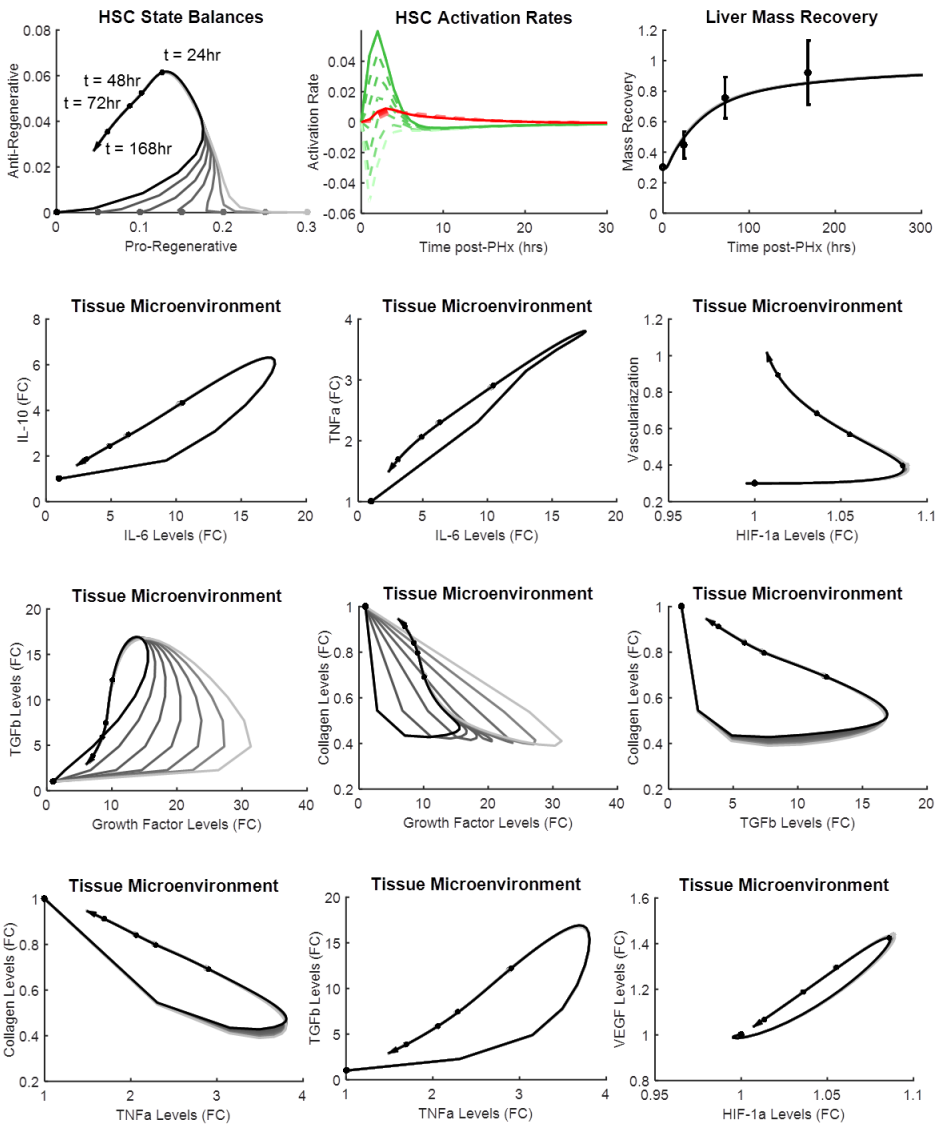

Figure 7.7 Effects of increasing initial fraction of pro-regen HSC on dynamic tissue microenvironment

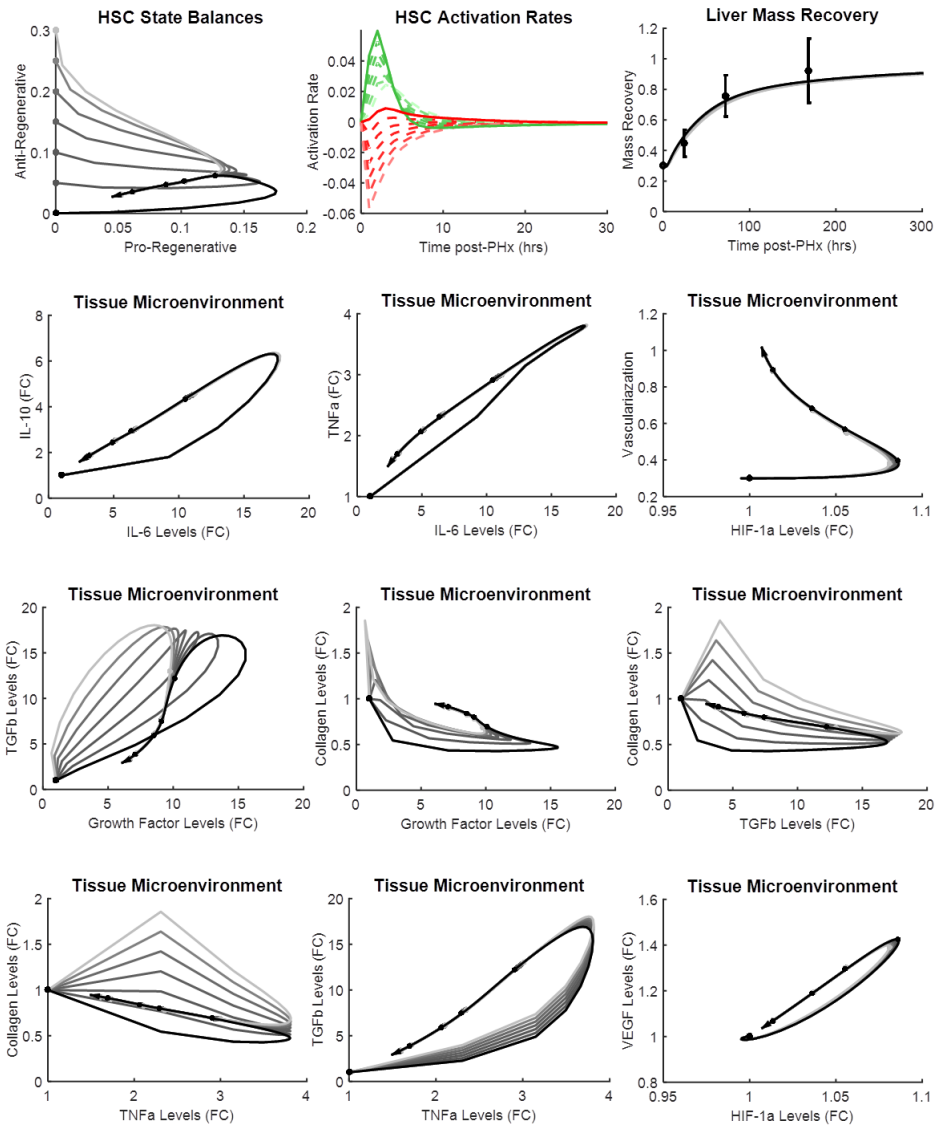

Figure 7.8 Effects of increasing initial fraction of anti-regen HSC on dynamic tissue microenvironment

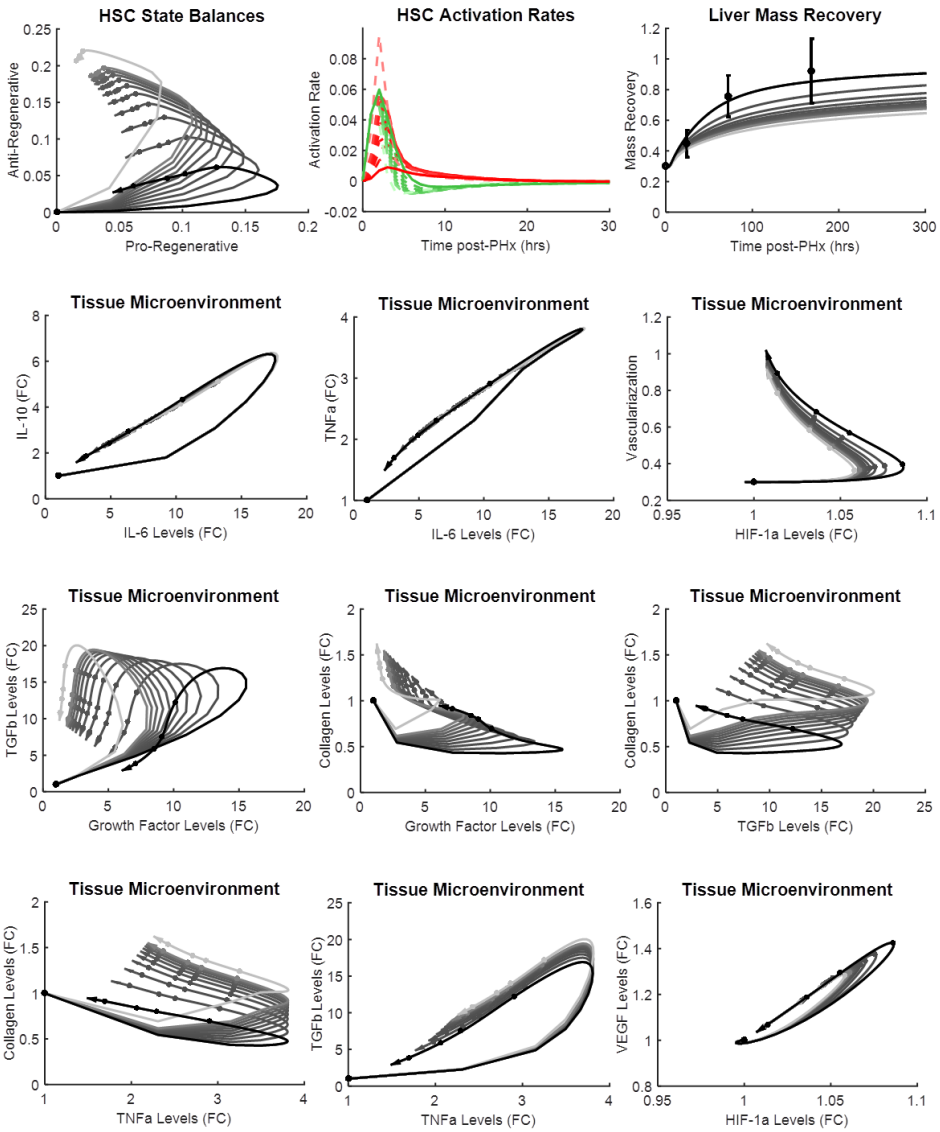

Figure 7.9 Effects of increasing the anti-regen HSC transition rate on tissue microenvironment

These results have implications for the study of multiple liver diseases that impair the liver's regenerative capacity. For example, both non-alcoholic steatohepatitis (NASH) and alcoholic steatohepatitis (ASH) are characterized by the accumulation of lipid droplets in the liver in humans and lead to the suppression of

liver mass recovery in the first 48 hours post-PHx in rats (Reddy & Rao, 2006;Tanoue et al, 2011;Yang et al, 1998a). It is possible that the lipid-rich microenvironment available to HSCs could modulate their ability to take on pro-regenerative or anti-regenerative states. Lipid-rich environments likely alter HSC metabolism and could suppress transition to a pro-regenerative state or enhance transition to an anti-regenerative state. Such an altered transition landscape could be one of the driving factors that induce progression of liver disease following a "second hit" in NASH or ASH. Similarly, the progression of fibrosis or cirrhosis may be exacerbated by HSCs' imbalanced transition propensities, potentially caused by metabolic imbalances or insufficiencies, by altered transcriptional regulation, by changes to tissue stiffness and tissue microenvironment, or by a combination of these and other factors.

7.3.7 Discussion

In this chapter, we present a new mathematical model for studying liver regeneration physiology as a distribution of cells in multiple functional states interacting in a dynamic network. Conventionally, it was thought that HSCs existed in one of two distinct states: quiescent and activated. Quiescent HSCs were known to assist in storage and transport of retinoids as well as in modulating the innate immune response (Hendriks et al, 1985;Paik et al, 2003;Paik et al, 2006). Activated HSCs alter gene and protein expression profiles, change morphology, and deposit fibrous collagens, causing scarring and worsening fibrosis and cirrhosis (Bataller & Brenner, 2005). In this chapter, we propose a framework involving three hepatic stellate cells functional states: quiescent, pro-regenerative, and anti-regenerative. Simulations using our computational model showed that the balance of these transcriptional states can affect regeneration dynamics. This is in agreement with experimental studies

suggesting that HSCs can enhance hepatocyte and HepG2 cell replication but that livers adapted to chronic diseases characterized by active HSCs (fibrosis and cirrhosis) exhibit impaired regeneration (Engelmann et al, 2015;Kaibori et al, 1997;Maher, 1993;Malik et al, 2002;Mullhaupt et al, 1994).

Chapter 8

TESTING MODEL PREDICTIONS IN ETHANOL-ADAPTED RATS

8.1 Introduction

Recent technological developments have enabled the study of transcriptional and proteomic profiles of single cells within a tissue at an unprecedented scale. Many cell types from diverse organs, developmental stages, and disease contexts have been profiled, revealing a high amount of heterogeneity in gene and protein expression (hereafter referred to as molecular variability) among single cells within a population. (For examples, see (Amir et al, 2013;Patel et al, 2014;Tang et al, 2010;Treutlein et al, 2014). Analysis of molecular variability at the single-cell scale has revealed that the coordinated expression of genes within single cells allows cells to be organized into multiple sub-phenotypes, with different sub-phenotypes likely arising in response to different cellular inputs (Park et al, 2015a;Park et al, 2014), spatial location in the tissue (Satija et al, 2015;Zeisel et al, 2015a), developmental stage (Bendall et al, 2014), and other intrinsic and extrinsic factors. The view now emerging is that during development, as well as in the biological function of a terminally differentiated tissue, cellular heterogeneity and the distribution of functional phenotypes are shaped by unique cellular inputs within an interacting network of cells constituting a tissue (Martinez-Jimenez & Odom, 2016). This cellular network interacts with physiological features important to tissue function (e.g., blood flow, extracellular matrix stiffness, and oxygen content), as well as the molecular cues within the tissue microenvironment (such as cytokine, paracrine, calcium, or electrical signals), to shape tissue and cellular

behavior. Put another way, the molecular state of each individual cell arises as a result of the cell's internal regulatory network interacting with unique physiological features of the local tissue microenvironment and with surrounding cells. The molecular states of individual cells do not appear to vary randomly; they can often be organized into cellular subtypes, which often still exhibit some amount of molecular variability. This cell-to-cell molecular variability has been proposed to enable effective tissue-scale response to perturbations in a manner that may not be possible in tissues comprised of cells that do not exhibit high molecular variability (Dueck et al, 2015).

Despite significant research efforts, it remains an open question how the variability intrinsic to molecular states of single cells translates to a tightly constrained tissue response to perturbations. For instance, neuroscience researchers have long grappled with this question when studying the electrical activity of brain circuits, which is unpredictable at the scale of individual ion channels and single neurons but is more coherent at the population level (Kreiman et al, 2000;Panzeri et al, 2001;Ramer et al, 2000). A prevailing view in neuroscience is that individual cellular variability is averaged out in cell populations, producing a net rate code of electrical activity that governs circuit function (Silberberg et al, 2004). Such a view of integrated cellular behavior is supported by studies of other cell types, which show that while NF-kB regulation oscillates over a wide range in single cells in response to stimulation, at the population level the response is damped, i.e., oscillates less and is therefore more homogenous (Paszek et al, 2010). In contrast to the view that molecular variability at the cell scale is integrated out at the tissue scale, emerging results point to the important contribution of heterogeneity in cellular subtypes in determining overall tissue function (Dueck et al, 2015;Skene & Grant, 2016). Recent studies have shown

that the variability observed in measurements of gene expression in single neurons allows for individual neurons to be clustered into multiple cellular functional states, where the gene expression patterns of each state are tuned on a gradient between the gene expression patterns of canonical archetypes (Park et al, 2014). One emerging view of the tissue scale physiological impact of single cell heterogeneity is that the balance among populations of cell functional states governs tissue function. These balances can be dynamic, changing in response to a physiological perturbation in order to contribute to overall tissue recovery.

While the tissue-scale response to a physiological perturbation is often well characterized or longitudinally observable, single cell-scale molecular regulation data are available often only at a few discrete times during recovery. Consequently, how to interpret the "snapshot" data of single cell transcriptional changes systematically for insights into the dynamics of overall tissue response to perturbations remains a challenge. To address this challenge, we collected and analyzed single cell data sets for distributions of functionally relevant phenotypes and evaluated the impact of shifts in these distributions on tissue function, using the computational model of the cellular networks underlying overall tissue response developed in chapter 7.

The role of non-parenchymal cells is becoming increasingly recognized as crucial to controlling the dynamics of liver regeneration (Malik et al, 2002). Depleting Kupffer cells from the liver has been shown to alter regeneration dynamics, with different studies reporting depletion delaying regeneration (Meijer et al., 2000) and enhancing regeneration (Rai et al., 1996). These opposite effects may be due to two different techniques used to deplete Kupffer cells, which targeted distinct Kupffer cell functional states. Delayed regeneration occurred following targeted depletion of both

M1 and M2 polarized Kupffer cells, while enhanced regeneration occurred following targeted depletion of just the M2 polarized Kupffer cells. Kupffer cell depletion affecting regeneration dynamics is likely due to the important role played by M1 polarized Kupffer cells during the priming phase, which includes secreting pro-inflammatory cytokines to prime hepatocytes for regeneration. Similar to Kupffer cells, endothelial cells have been shown to influence regeneration dynamics, although they do so through the production of hepatocyte growth factor (HGF) (DeLeve, 2013), Wnt2 (Ding et al, 2010), and angiopoietin 2 (Hu et al, 2014). Our own work using mathematical modeling to understand regeneration dynamics has identified hepatic stellate cells (HSCs) as key controllers of the regeneration dynamics (Cook et al, 2015;Correnti et al, 2015). While there is some recognition of HSCs as multifunctional cells with diverse contributions to liver homeostasis, repair, and disease etiology, the molecular and cellular dynamics of HSCs have largely been studied in the context of liver fibrosis, emphasizing a canonical view of HSCs as either quiescent (storing retinol) or activated (producing matrix) (Friedman, 2008b). Recent work challenges this two-state view by defining a new HSC state, termed the "inactive state", which is molecularly distinct from the quiescent state and whose response to activation signals is different from that of quiescent HSCs (Kisseleva et al, 2012). In the context of regeneration, several questions about HSC behavior remain: What are the identities of HSC functional states during liver regeneration? How do these HSC functional states and state transitions contribute to the dynamics of liver functional mass recovery? How is the balance of functional HSC states connected to defective overall tissue regenerative responses observed in disease cases? This chapter attempts to answer these questions.

8.2 Materials and Methods

8.2.1 Animal Use

All animal studies were approved by the Institutional Animal Care and Use Committee (IACUC) at Thomas Jefferson University. Jefferson's IACUC is accredited by the Association for Assessment and Accreditation of Laboratory Animal Care and experiments were designed using the Guide for the Care and Use of Laboratory Animals.

Adult (8-10 week old) Sprague-Dawley rats were subjected to a standard Leiber-DeCarli pair feeding protocol with 36% of calories provided by ethanol or carbohydrates (glucose). Following 5-7 weeks of ethanol feeding, rats were anesthetized and subjected to 70% PHx by surgical removal of medial and left lateral lobes as per standard procedure (Higgins & Anderson, 1931;Juskeviciute et al, 2008). The medial and left lateral lobes were quickly frozen in OCT blocks (TissueTek, QIAGEN, Valencia, CA) over a dry ice and methanol bath to serve as within-animal, 0 hour controls. At 24 hours post-PHx, rats were again anesthetized and the remnant liver tissue was excised and frozen as before. Following excision of the remaining liver mass, rats were sacrificed by cervical dislocation. Tissue was stored at -80°C until further use.

8.2.2 Immunohistochemical Staining

Frozen liver tissue in OCT blocks was sectioned 10 μm thick using a cryostat set at -20°C and thaw mounted on glass slides. Sliced tissue was stored at -80°C for up

to two weeks. Immunohistochemical staining was performed using a rapid staining protocol taking approximately 30 minutes to complete to preserve RNA integrity. Slides were first fixed in cold acetone and hydogen peroxide (Sigma-aldrich, St. Louis, MO, 50ml: 50µl) for 30 seconds, then blocked and permeabilized with PBS containing 2% BSA (Sigma–Aldrich, St. Louis, MO) for 1 minute. Afterwards, liver sections were incubated with the primary antibody anti-glial fibrillary acidic protein (Gfap) (ab4674, Abcam, Cambridge, MA), an HSC marker, for 4 minutes at room temperature. Then the slides were washed, and were incubated for 4 minutes at room temperature in the dark with the secondary antibody Cy3 anti-chicken 1/200 with DAPI 1/10,000, phalloidin 2.5/100, and PBS containing 2% BSA. Then slides were rinsed with PBS and dehydrated in graduated ethanol concentrations (70-100%) and in xylene for 5 min.

8.2.3 Laser Capture Microdissection (LCM)

The LCM process was performed using a PixCell system and CapSure Macro LCM caps (Arcturus Engineering, Mountain View, CA). Single cells or 10 cell pools of cells with positive staining (GFAP+) were lifted individually on caps. HSCs from the first 7 layers of hepatocytes around the portal or central vein were lifted and their position was annotated for future analyses. The annulus for the Laser was adjusted to the size of HSCs (approximately 10µm, HSCs were lifted and screened for quality as a whole cell on the cap after capture and only accepted if the cell target was fully lifted. During single cell sampling both the tissue and the corresponding cap were inspected for the removed cell body to ensure that the fluoresced HSC of interest is collected. Lysis buffer was added onto the single cell on the cap (5.5µl; Life Technologies,

Grand Island, NY) and cooled on ice before storage at -80°C. Hepatocytes, which stained negative for Gfap (Gfap-) and were discernable by size and morphology, were collected according to the same procedure.

8.2.4 High-throughput quantitative PCR

Our sample preparation calls for processing the single cells directly in a reverse transcriptase reaction rather than extracting RNA. Following reverse transcriptase reactions, cells were subjected to realtime PCR for targeted amplification and detection using primers designed to target specific genes using PrimerBlast (Ye et al, 2012). Official gene symbols (from the Nucleotide database of NCBI) were used to denote target genes throughout the manuscript. Refseq IDs are available in Appendix C. Where possible, primers were designed with intron-spanning PCR primers (Primer sequences can be found in Appendix C). The standard BioMark™ protocol was used to pre-amplify cDNA samples for 20 cycles using TaqMan® PreAmp Master Mix per the manufacturer's protocol (Applied Biosystems, Foster City, CA). qPCR reactions were performed using 96.96 BioMark™ Dynamic Arrays (Fluidigm®, South San Francisco, CA) enabling quantitative measurement of multiple mRNAs and samples under identical reaction conditions (Spurgeon et al. 2008). Each run consisted of 40 amplification cycles (15s at 95°C, 5s at 70°C, 60s at 60°C). Ct values were calculated by the Real-Time PCR Analysis Software (Fluidigm). Four 96.96 BioMark™ Arrays were used to measure gene expression across the ~300 single cell samples included. The same serial dilution sample set was included to verify reproducibility and test for technical variability.

8.2.5 Data Analysis and Statistical Methods

8.2.5.1 Data Normalization

Individual qRT-qPCR reactions were examined to ensure the quality of each qRT-PCR reaction. Each reaction was manually passed or failed based on the qualitative nature of the reaction curves obtained from the PCR. Any reaction below the limit of detection based on the CT-value of DNA suspension buffer undergoing qPCR procedure (no template control) was manually failed. Following this pass/fail analysis, samples having greater than 25% failed reactions and gene assays having greater than 80% failed reactions were excluded from the present analysis. This exclusion step further increases the quality and confidence in the data used for analysis. A total of 139 single cell samples (36 Ethanol 0h, 31 Ethanol 24h, 38 Control 0h, and 34 Control 24h) and 72 different gene assays were included in the present analysis.

Data was normalized using a modified $-\Delta\Delta C_T$ method (Livak & Schmittgen, 2001b). The median of the highest quality genes (pass in greater than 45% of samples) was used as a pseudo-housekeeping gene to account for differences in cell size, incomplete cell lifting, and BioMark™ Assay loading variation. We normalized the raw C_T values by subtracting them from the pseudo-housekeeping gene value on a per sample basis. We then removed any effects of relative expression levels across genes by median centering the expression value of each gene to give our normalized $-\Delta\Delta C_T$ value for each reaction.

8.2.5.2 Cell Type Specificity Analysis

Markers for four cell types were included in our qRT-PCR assays: Apoa4 for hepatocytes, Itgam for Kupffer cells, Pecam1 for endothelial cells, and Actb and Gfap for HSCs. Each individual hepatocyte or HSC captured expressed high levels of its marker gene(s) and low levels of marker genes for other cell types, often below the limit of detection (Figure 8.1B). We measured 42 gene assays in both hepatocytes and HSCs using two BioMark™ Arrays, one for each cell type. Batch effects were removed by normalizing the dilution curves for the overlapping gene assays to each other. This strategy worked because the same dilution series was used for both arrays. We then imputed missing data as the minimum value for each assay minus 1 CT (approximate limit of detection). This strategy of imputing missing values as equal to the limit of detection was used because in our data failed reactions were often caused by transcripts being expressed below the limit of detection rather than other causes of reaction failure. We then performed principal component analysis (PCA) on the collated raw CT values from these cells to identify using an unsupervised method if cell type was a major contributor to the variability in the data (Figure 8.1C). This analysis also allowed for us to identify genes that contribute significantly to the variability in the data (Figure 8.1D). Similar results were found when analyzing 10-cell pools of HSCs and individual hepatocytes from the same BioMark™ Array.

8.2.5.3 Linear Discriminant Analysis

High fidelity samples and assays were identified using a threshold of > 30% of assays working per sample, and > 10% of cells expressing each gene. Gene expression identified as below the limit of detection was called as "NA" in the original data, but

we imputed values below the limit of detection by assuming each non-expressed gene had a CT value of the maximum (for that gene) plus one, indicating that the gene is at least 1-fold below the limit of detection.

Linear discriminant analysis was then performed on these data using the 'MASS' package in the computing language R (Gentleman et al, 2004a;R Core Team, 2012;Venables & Ripley, 2002).

8.2.5.4 Silhouette Score Analysis

We calculated the silhouette score of the clusters identified in our linear discriminant analysis to quantify the separation of the identified clusters. We used the 'MASS' package in R for this calculation (Venables & Ripley, 2002). We then randomized our data 1,000 times and re-performed our linear discriminant analysis and silhouette score calculation. We calculated an empirical p-value for our silhouette score by finding the number of random scores equal to or greater than that calculated for our data.

8.2.5.5 Minimum Spanning Tree Analysis

We calculated minimum spanning trees to identify a possible progression of activation of single HSCs using Euclidian distance in the spantree function from the package 'Vegan' in R (Oksanen et al, 2013). Minimum spanning trees are a graphical approach that connects all nodes (single cells) in a data set that maintains a minimum weight between edges, where weight is a measure of unfavorable connections. Highly

correlated nodes are connected by edges, making this technique appropriate to hypothesize progression of a single cell through highly correlated nodes.

8.2.5.6 Topological Maps

Topological maps were produced from 2-dimensional kernel densities of all HSCs in the linear discriminant space using the R package MASS (Venables & Ripley, 2002).

8.3 Results

8.3.1 Hepatic Stellate Cell Isolation and Identification Reveals High Transcriptional Variability within a Cell Type

We set out to identify signatures of HSC states through their transcriptional regulation by collecting and analyzing a high-dimensional dataset of gene expression from single HSCs. We used laser capture microdissection (LCM) coupled with high-throughput qPCR (Biomark^{TM}) to isolate and transcriptionally characterize single HSCs from rat livers in each of four conditions: ethanol-fed rats prior to and and 24 hrs post 70% PHx and control fed rats to and 24 hours post 70% PHx (Figure 8.1A). We chose the time point 24 hours post-PHx, corresponding to the peak of hepatocyte replication in rats post-PHx (Fausto, 2001). To confirm cell-type specificity, we also isolated and transcriptionally characterized single hepatocytes from the same tissue. Using this novel approach, we were able to measure, with high reproducibility, ~100 gene assays in each of ~140 single HSCs (Figure 8.2). LCM made possible the capture of single HSCs and hepatocytes with low levels of contamination (Figure 8.1B) and a high degree of cell type specificity (Figure 8.1C).

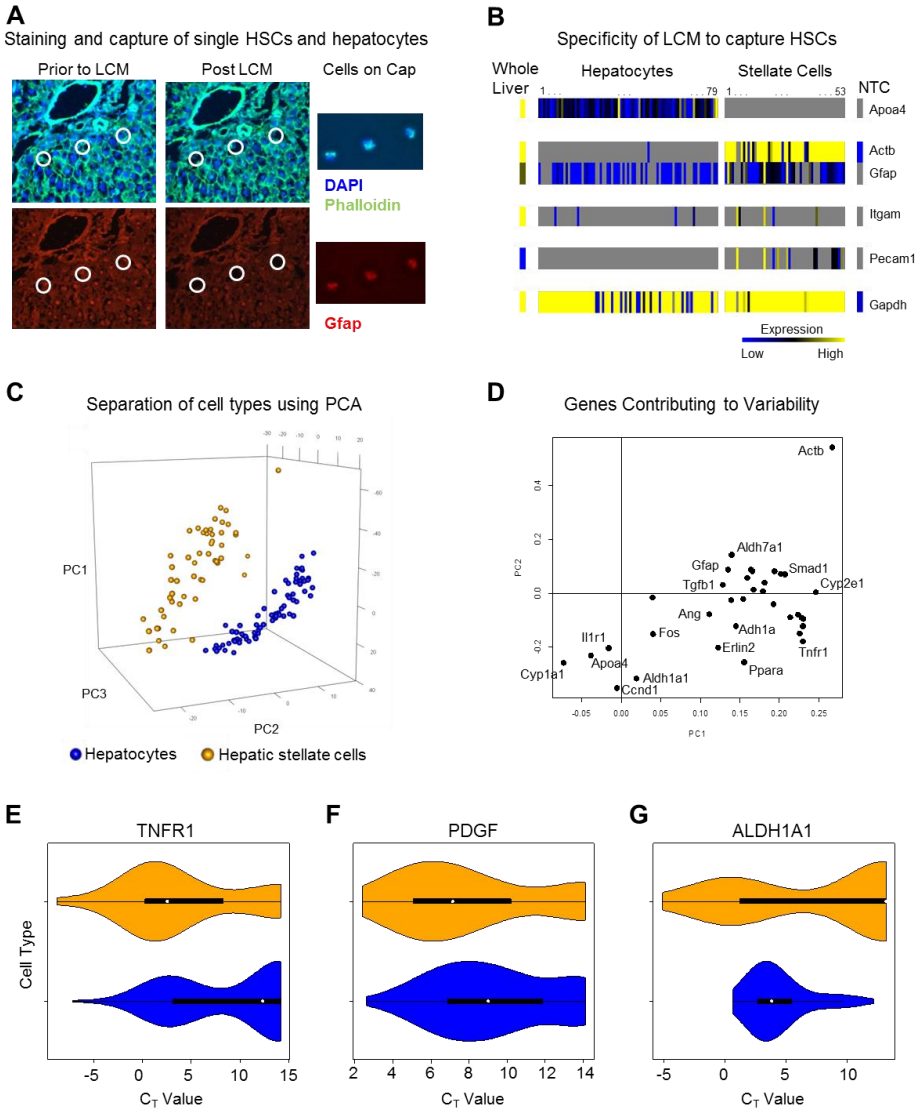
A
Staining and capture of single HSCs and hepatocytes
Prior to LCM
Post LCM
Cells on Cap
DAPI
Phalloidin
Gfap
B
Specificity of LCM to capture HSCs
Whole Liver
Hepatocytes
Stellate Cells
NTC
Apoa4
Actb
Gfap
Itgam
Pecam1
Gapdh
Expression
Low
High
C
Separation of cell types using PCA
PC1
PC2
PC3
Hepatocytes
Hepatic stellate cells
D
Genes Contributing to Variability
Actb
Aldh7a1
Gfap
Smad1
Tgfb1
Cyp2e1
Ang
Fos
Adh1a
Il1r1
Erlin2
Tnfr1
Apoa4
Cyp1a1
Aldh1a1
Ppara
Ccnd1
PC1
PC2
E
TNFR1
Cell Type
C_T Value
F
PDGF
C_T Value
G
ALDH1A1
C_T Value

Figure 8.1 Isolation of single / pooled hepatic stellate cells and hepatocytes. (A) Representative images showing LCM isolation of single hepatic stellate cells. DAPI and Phalloidin staining were used to identify nuclei and cell boundaries. Co-localization of DAPI and Gfap was used to identify HSCs. (B) Single HSCs and hepatocytes were collected from the same tissue and tested for cell type marker genes using high throughput qPCR. Cells expressed high levels of marker genes in a cell-type specific manner. (C) Using PCA on expression levels of 34 genes measure in both hepatocytes and HSCs separated cell types. The variability within a cell type appeared to be higher than variability between cell types. (D) PCA scores shows the genes contributing to the PCA plot. (E) Different genes showed unique patterns when comparing cell types. TNFR1 showed different mean CT values but similar variability. (F) PDGFA showed similar mean CT values and similar variability. (G) ALDH1A1 showed different mean CT values and different variability.

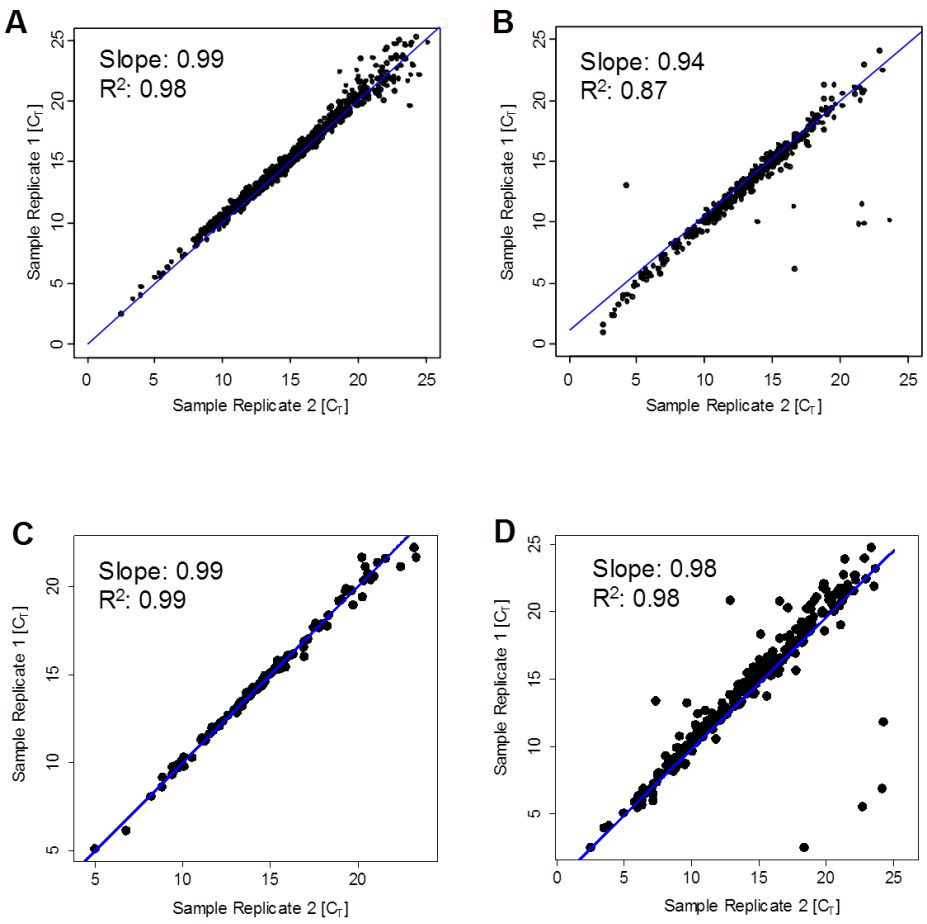

Figure 8.2 Technical reproducibility of the experimental strategy within a Biomark array and across Biomark arrays. (A) One sample run twice on the same array. (B) One sample run twice on the same array. (C) One sample run on two different arrays. (D) One sample run on two different arrays.

Principal component analysis (PCA) was used to identify variability between cell types and to quantify major sources of variability within the data (Figure 8.3). We found that, although there is clear separation between HSCs and hepatocytes, the variability within a cell type was of the same order of magnitude as the variability between cell types (Figure 8.1C). This surprising finding suggests that the variability of gene expression within a cell type may be as large as the differences in cell

behavior between cell types. Several of the major contributors to variability in gene expression within a cell type and between cell types are ethanol metabolism genes (Cyp1a1, Aldh1a1, Adh1a, Cyp2e1), genes associated with HSC activation (Actb, Smad1, Ppara), and growth factors (Ang, Pdgfa, TGFb1) (Figure 8.1D). The distributions of expression of certain single genes within a cell type were different between HSCs and hepatocytes. Some genes were expressed at different levels with similar distribution ranges (Figure 8.1E), some were expressed at similar values with similar distribution ranges (Figure 8.1F), and some were expressed at different levels with different distribution ranges (Figure 8.1G). These results point to a potential coordination of cellular behavior of different types within the liver that may be regulated, at least in part, through transcriptional regulation.

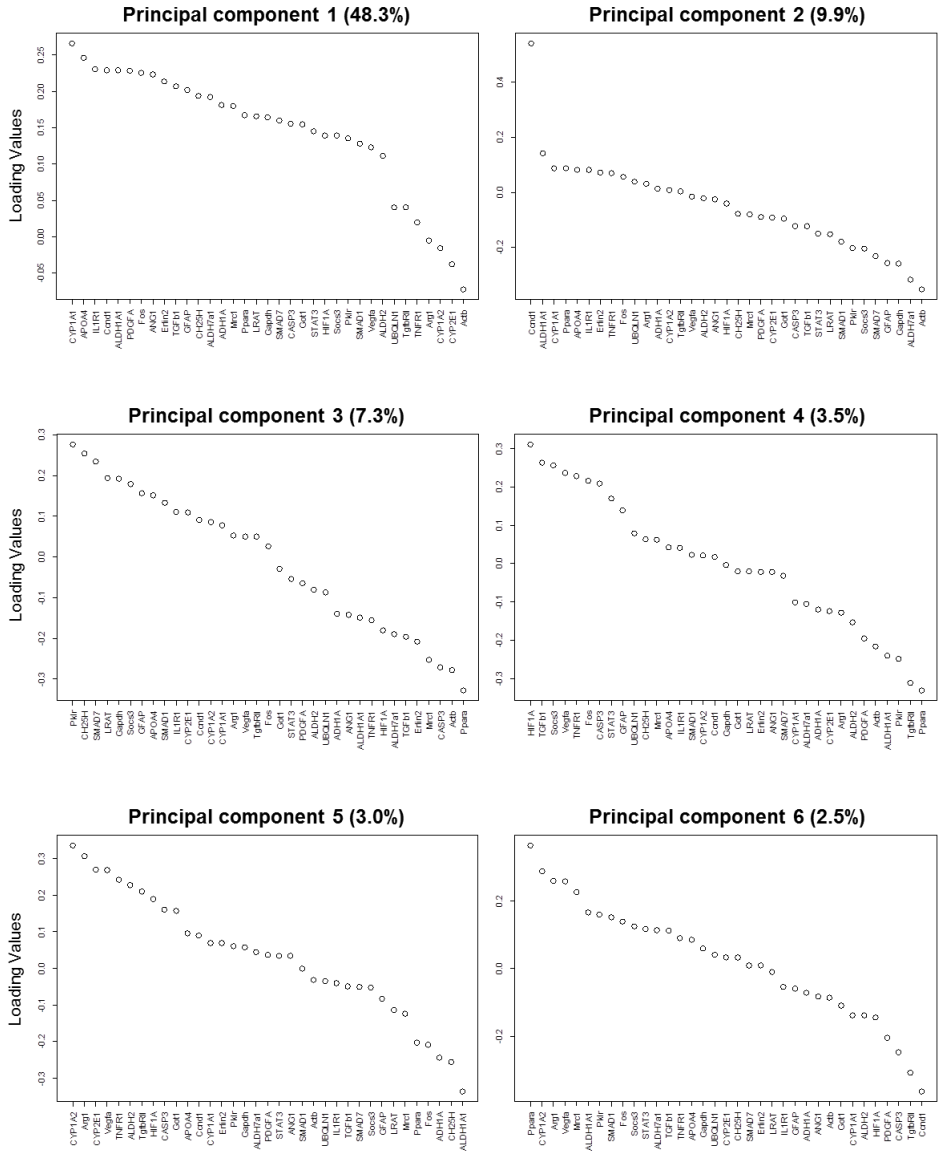

Figure 8.3 Principal Component scores for PCs 1-6, used to discriminate between HSCs and hepatocytes.

8.3.2 Hepatic Stellate Cells Function in Discernible Transcriptional States

We used a guided clustering technique to identify transcriptional states of HSCs across all conditions: ethanol-fed and control rats prior to and post-PHx.

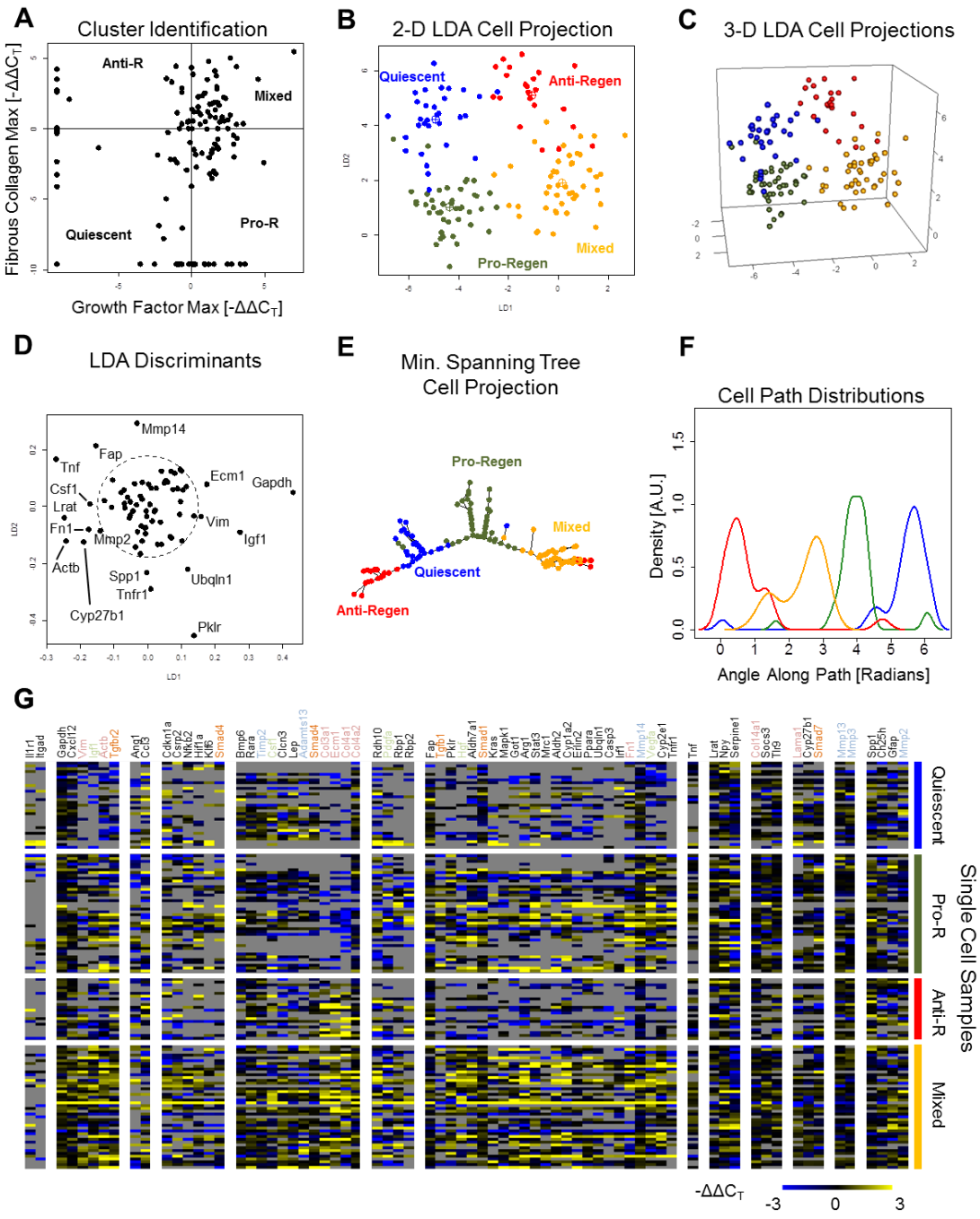
A
Cluster Identification
Anti-R
Mixed
Quiescent
Pro-R
Fibrous Collagen Max [-ΔΔC$_T$]
Growth Factor Max [-ΔΔC$_T$]
B
2-D LDA Cell Projection
Quiescent
Anti-Regen
Mixed
Pro-Regen
LD1
LD2
C
3-D LDA Cell Projections
D
LDA Discriminants
Mmp14
Fap
Tnf
Csf1
Lrat
Fn1
Actb
Mmp2
Ecm1
Gapdh
Vim
Igf1
Spp1
Ubqln1
Tnfrsf1
Cyp27b1
Pklr
E
Min. Spanning Tree
Cell Projection
Pro-Regen
Mixed
Quiescent
Anti-Regen
F
Cell Path Distributions
Density [A.U.]
Angle Along Path [Radians]
G
Quiescent
Pro-R
Anti-R
Mixed
Single Cell Samples
-ΔΔC$_T$
-3
0
3

Figure 8.4 Gene expression in single hepatic stellate cells reveals functional transcriptional states. (A) Manual clustering of functional HSC states reveals four states: Quiescent (low GF/low collagen), Pro-regenerative (high GF/low collagen), Anti-regenerative (low GF/high collagen), and mixed (high GF/high collagen). (B) Linear discriminant analysis shows separation of the four HSC states in two dimensions. (C) LDA shows further separation of the four HSC states in three dimensions. (D) Genes contributing to discrimination among functional states. (E) Minimum spanning tree representation of single HSCs shows relationships between individual cells based on gene expression. (F) Cyclic representation of HSC functional states shows the potential distribution of individual HSCs as they progress through the cycle. (G) Heatmap representation of gene expression values for individual HSCs. Cells are grouped based on functional state. Genes are grouped by hierarchical clustering with Pearson correlation. Gene annotations are colored based on functional annotations. Green = growth factors, gray = collagen-related genes, orange = Tgfb signaling, blue = matrix-modulating genes.

First, we categorized each cell based on the expression of fibrous collagen-related genes (Col3a1, Col14a1, and Ecm1) and growth factors (Hgf, Igf1, and Vegf) (Figure 8.4A). This allowed us to organize cells into four categories: GF high, collagen low (pro-regenerative); GF low, collagen high (anti-regenerative); GF high, collagen high (mixed); and GF low, collagen low (quiescent). Next, we calculated Pearson correlations of the expression of all genes in each sample to the centroid of gene expression of each sample category and reclassified samples with sufficiently high correlations (p-value ≤ 0.05) into the category to which they most closely correlated. We then used linear discriminant analysis to visualize the transcriptional behavior of each single cell and how they organized into states based on the expression level of all genes measured (Figure 8.4B and C). In addition to the genes used for classification, we identified several discriminant genes that may be useful as

biomarkers to differentiate among these states, including Actb, Mmp14, Mmp2, Igf1, Tnfr1 and Tgfbr2 (Figure 8.4D, Figure 8.5).

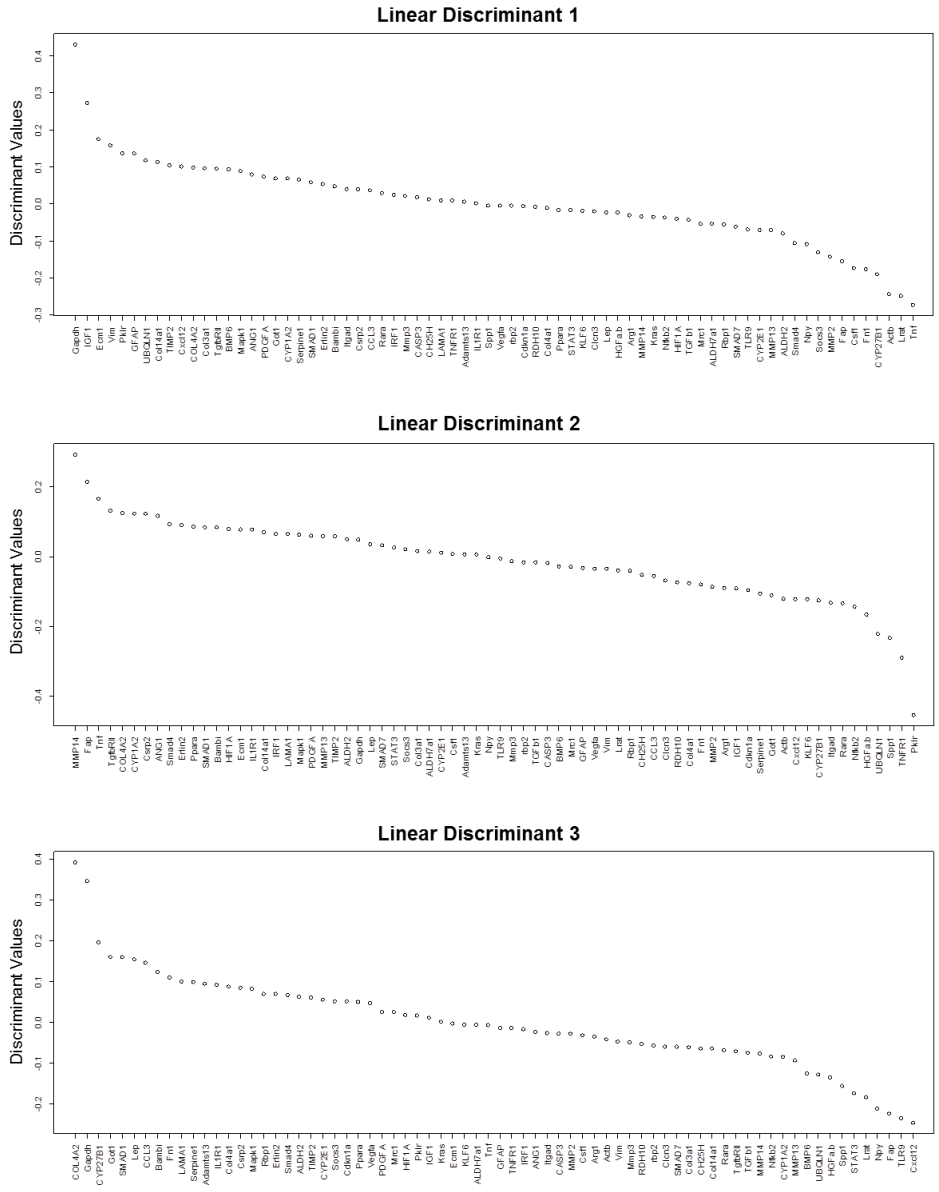

Figure 8.5 Linear discriminants for LD1, LD2, LD3, used to discriminate among HSC functional states

Next, to ensure that the separation we observed among HSC states was not an artifact of our data analysis technique, we randomized our data 1,000 times, re-performing our analysis on the randomized data, and calculating a silhouette score for each randomization. The silhouette score is a measure of the "betweeness" of clusters normalized by a commensurate measure of the "withiness" of clusters; therefore, a high silhouette score indicates clear separation among tightly packed clusters. The silhouette score from our data fell outside the distribution calculated from randomized data (Figure 8.6), giving an empirical p-value less than 0.001 meaning that the organization of the gene expression is important for identifying cell clusters. Such a relatively high silhouette score indicates that the cell states do not overlap significantly in the LD-space, suggesting that HSC states are governed by distinct transcriptional regulation.

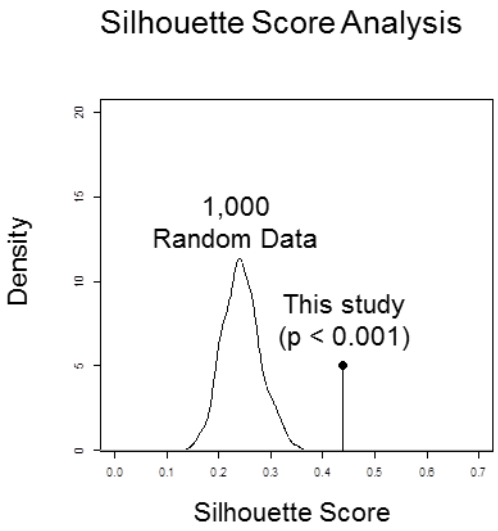

Figure 8.6 Significance of clustering results assessed by silhouette score. Our silhouette score falls well outside the range generated from randomizing our data 1,000 times. This gives an empirical p-value of less than 0.001.

We further validated these results using 10 cell pools of HSCs (Figure 8.7), which showed results similar to those using single cells.

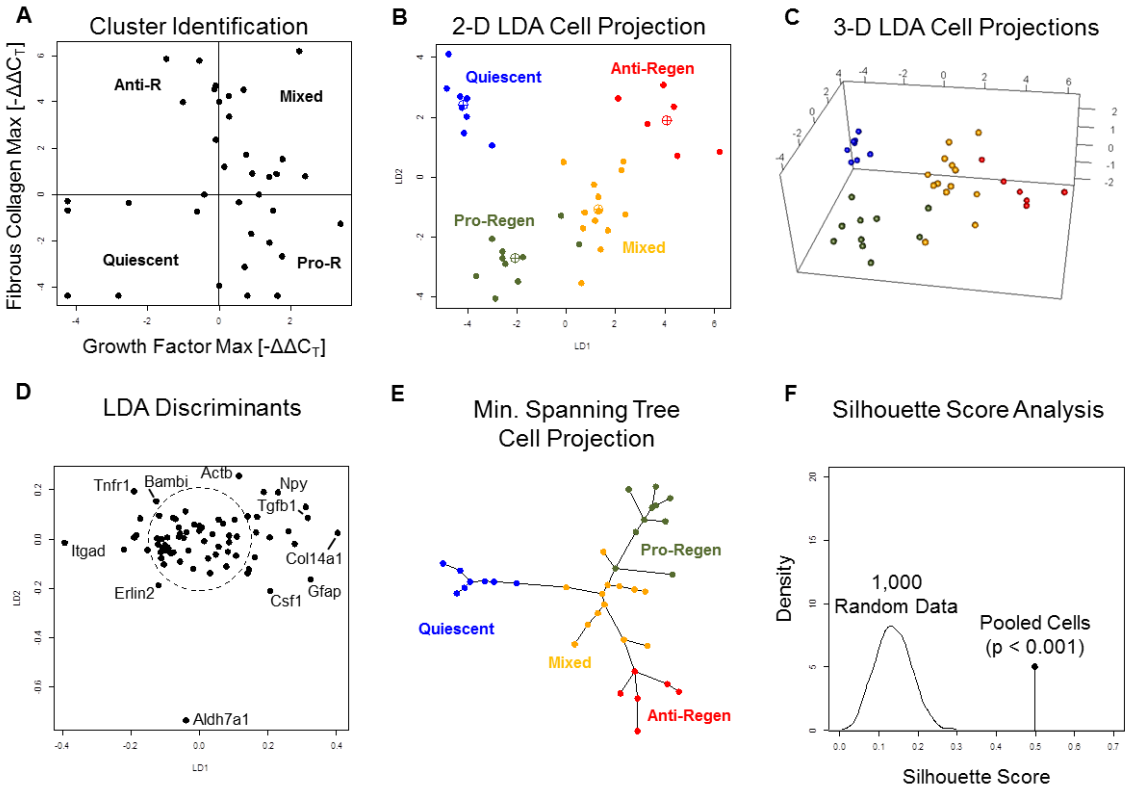

Figure 8.7 Validation of single cell results using 10 cell pools of HSCs collected from the same animals. Pools of HSCs showed a stronger gene expression signal, but a higher variability than single cells. (A) Manual clustering of functional HSC states into four states: Quiescent (low GF/low collagen), Pro-regenerative (high GF/low collagen), Anti-regenerative (low GF/high collagen), and mixed (high GF/high collagen). (B) Linear discriminant analysis shows separation of the four HSC states in two dimensions. (C) LDA shows further separation of the four HSC states in three dimensions. (D) Genes contributing to discrimination among functional states. (E) Minimum spanning tree representation of single HSCs shows relationships between individual cells based on gene expression. (F) Significance of clustering results assessed by silhouette score.

We sought to understand how an individual cell may transition across states by using a minimum spanning tree projection (Figure 8.4E). The minimum spanning tree projection connects each cell with its nearest neighbors according to an algorithm that minimizes the total connectivity of the network and prevents connection cycles. This type of projection may indicate how individual cells within a population could transition between states to minimize the transcriptional changes required to move from one state to another. The minimum spanning tree projection suggests a dynamic HSC transcriptional behavior shift whereby HSCs transition from a quiescent phenotype to either a pro-regenerative phenotype or an anti-regenerative phenotype. The connectivity of the spanning tree further suggests that pro-regenerative cells can transition to a mixed state then to an anti-regenerative state. It is possible that this activation trajectory culminates in a fully fibrotic "activated" phenotype, but cell tracing studies are needed to explore the trajectory within a single cell fully. It is also possible that, in contrast to a linear progression through states, HSC transitions occur in a cycle analogous to the cell cycle. If such a cycle is the case, the balance of HSCs may be represented as a distribution of states within a cycle (Figure 8.4F). Further work is needed to determine if either of these scenarios captures HSC state transitions.

We next investigated what modules of gene expression govern cell behavior within each state (Figure 8.4G). We grouped genes using hierarchical clustering based on Spearman rank correlation (Figure 8.8). We then colored genes according to their annotated and previously reported functions (Growth factors – light green, Tgfb signaling – light orange, collagens & matrix-related genes – light red, and matrix remodeling – light blue). In addition, we used DAVID to identify any functional annotations enriched within each group compared to all the genes we measured as an

unbiased approach to investigate gene module functions (Figure 8.9) (Huang et al, 2009).

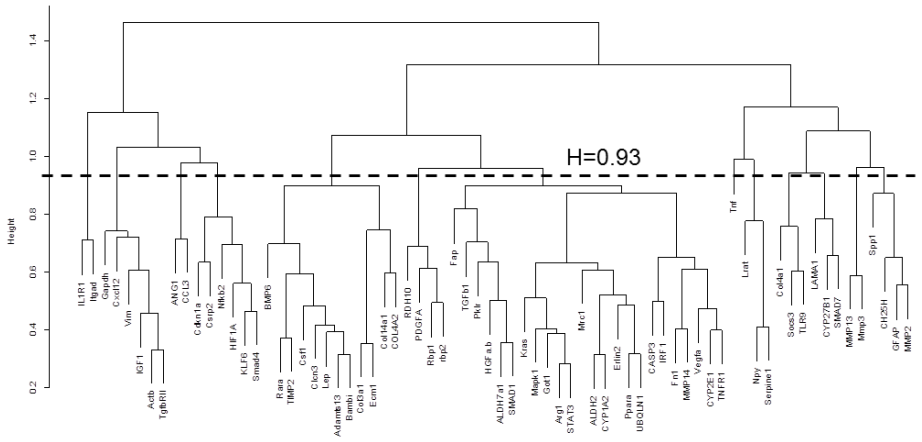

Figure 8.8 Dendogram showing the definition of gene clusters using a height cutoff value of < 0.93.

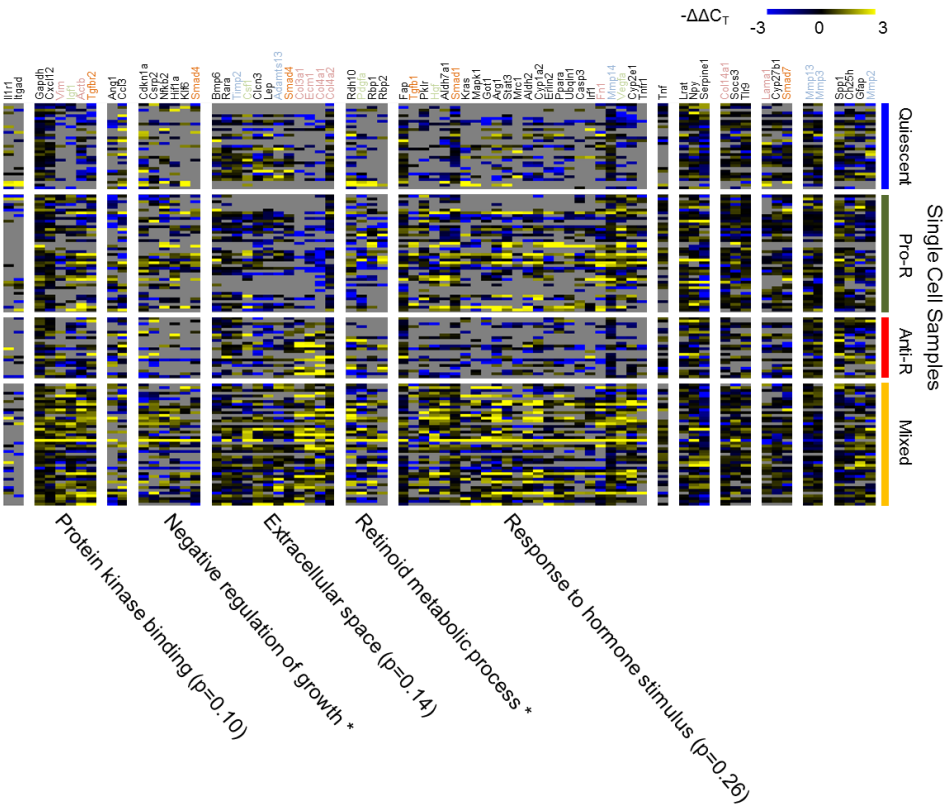

Figure 8.9 Overrepresented functions (GO Terms) for each gene group identified in our single cell data compared to the background of all genes measured. * Indicates p-value < 0.05.

We then grouped cells within each state by hierarchical clustering using Spearman rank correlation. We found that distinct HSC states tended to express distinct functional modules of genes. Quiescent HSCs tended to express high levels of the basement membrane gene Col4a2 and the matrix metalloprotease responsible for regulating Collagen-4 (Mmp2) and its regulator (Timp2), which has been shown to work with Mmp2 to degrade collagens. This suggests that quiescent HSCs play a more dynamic role in maintaining basement membrane architecture than previously

suspected in addition to their canonical role storing vitamin A. Pro-regenerative HSCs expressed genes aiding in regeneration, including the growth factors Igf1, Arg1, Vegfa, and Hgf. Cells within these clusters also expressed other genes, including Stat3, Socs3, and Tnfr1, suggesting that interleukins could be primary drivers of HSC transition to the pro-regenerative state from the quiescent state. Anti-regenerative HSCs were characterized by high expression levels of Col3a1, Col14a1, and Ecm1. Several of these cells also showed high expression of Mmp2, and Mmp3, suggesting that cells in the anti-regenerative state remodel existing matrix and deposit fibrous matrix. The anti-regenerative state cells also tended to express high levels of Spp1, which has been shown to activate HSCs to a pro-fibrotic state, suggesting a positive feedback from the anti-regenerative state to recruit more cells to this phenotype. Cells in the anti-regenerative state also tended to express high levels of the TGF-β receptors Tgfbr2 (as did pro-regenerative and mixed stellate cells), but not the ligand Tgfb, which is highest in pro-regenerative and mixed state stellate cells. This indicates that cells in this state may be sensitive to TGF-β signaling, but may not be the source of TGF-β in the tissue. The mixed phenotype expressed high levels of both the collagen deposition module and growth factor production modules. What separates this state from the anti-regenerative state is the high expression of genes related to TGF-β signaling, cytokine signaling, and retinol metabolism, including Rara and Rbp1. If cells must indeed transition through the mixed phenotype before becoming activated to a pro-fibrotic phenotype, then high levels of retinol metabolism-related genes indicate that this state may be where HSCs lose their lipid droplets and assume an activated morphology. Additionally, because several cells in the mixed and pro-regenerative states express Tgfb, there may be a coordination of anti-regenerative

HSCs and either mixed or pro-regenerative HSCs required for sustaining anti-regenerative HSC populations during chronic liver disease.

Understanding the additional molecular regulation underlying each state suggests additional annotations that may be appropriate to label the cell states. HSCs with high MMPs may be classified as quiescent or as matrix-modulating. HSCs with high GFs may be classified as pro-regenerative in the context of response to PHx or as cytokine-regulated HSCs or GF depositing HSCs in the context of normal tissue function. HSCs with high levels of collagens may be classified as anti-regenerative in the context of response to PHx, as TGF-β response primed HSCs in the context of normal tissue function, or as pre-fibrotic in the context of disease progression. HSCs that express high levels of GFs and collagens may be classified as a mixed phenotype in the context of regeneration or as a hyper-functional HSC or adaptive HSC in the context of normal liver function. These adaptive HSCs may produce high levels of multiple functional gene modules in order to be able to respond to external stimuli efficiently without having to produce additional transcripts.

8.3.3 HSC State Dynamics during Effective Regeneration

We next investigated how the balance of HSC states progresses during liver mass recovery (Table 8.1). We expected a high proportion of HSCs in the livers of control animals prior to resection to be in the quiescent state; however, what we found was that HSCs were distributed among all the possible states with a small fraction of cells in the quiescent state (11% of total cells). Control livers at baseline had a high proportion of cells in the mixed state (39%), a high proportion of cells in the pro-regenerative state (29%), and a slightly smaller proportion of cells in the anti-regenerative state (21%). Following resection, control livers showed a strong response

of pro-regenerative cells (38%) and maintained a large population of mixed cells (35%). Relatively few cells were found in the anti-regenerative state (6%). The balance of cells in the pro-regenerative and mixed states appeared to have shifted at 24 hours post-PHx compared to baseline; at 24 hours post-PHx the ratio of numbers of pro-regenerative cells to mixed cells is higher than at baseline. Following resection, it is possible that cells in the mixed state shift to the pro-regenerative state. This shift may correspond to lifting a "brake" on growth factor effectiveness, allowing for hepatocytes to progress through the cell cycle.

Table 8.1 Distribution of hepatic stellate cell states in each condition

State	Control 0h	Ethanol 0h	Control 24h	Ethanol 24h
Quiescent	0.11	0.31	0.21	0.29
Pro-Regen	0.29	0.17	0.38	0.39
Anti-Regen	0.21	0.33	0.06	0.00
Mixed	0.39	0.19	0.35	0.32
Total Cell Number	38	36	34	31

We postulate that the dynamic transition of HSCs between these states may correspond to phenotypic phases of liver regeneration characterized in the literature. In such a scheme, during the priming phase of regeneration (0 -12 hours post-PHx), HSCs would be predominantly in the pro-regenerative and quiescent states, making GFs available for hepatocyte entry into the cell cycle and remodeling basement matrix to allow for effective regeneration. During the replication phase (12-72 hours post-PHx), HSCs would be predominantly in the mixed state, continuing to produce GFs for hepatocyte replication but also actively producing additional scaffolding for new

hepatocytes to use for adherence. During the termination of regeneration (following ~96 hours post-PHx), HSCs would be predominantly in the anti-regenerative state, no longer producing GFs but still remodeling and producing matrix to allow for hepatocyte migration and mass increase as well as allowing for revascularization of the tissue. The hypothesis that at termination, HSCs exist primarily in the anti-regenerative state is consistent with studies showing that Tgfb and extracellular matrix can both inhibit hepatocyte proliferation. Whether Tgfb signaling (within hepatocytes or in a non-parenchymal cell network) or matrix deposition contribute to the termination of regeneration alone or in combination with other factors upregulated in the anti-regenerative state remains a topic of active research (Michalopoulos, 2013;Oe et al, 2004). Further experiments looking at the balances of HSC states during the termination phase is needed to confirm whether this rebalancing occurs during termination.

8.3.4 HSC State Dynamics during Ethanol-impaired Regeneration

We next investigated how hepatic stellate cell population balances shift in one particular disease condition that suppresses liver regeneration, chronic ethanol consumption. Following chronic adaptation to ethanol consumption, the regenerative ability of the liver is greatly reduced, leading to deficiencies in mass recovery that are apparent by 24 hours post-PHx and exaggerated by 48 hours post-PHx (Kuttippurathu et al, 2016b;Yang et al, 1998a). We investigated how chronic ethanol use alters the balance numbers of cells in different HSC states at baseline and at 24 hours post-PHx (Table 8.1). In contrast to control rats, ethanol-fed rats had a high proportion of cells in the anti-regenerative state (33%) prior to resection. This condition also showed a reduced fraction of cells in the pro-regenerative (17%) and mixed states (19%). This

result suggests that chronic ethanol use enhances HSC transition to the anti-regenerative state and inhibits other states. Such a cell state population balance after chronic adaptation to ethanol may result in a preconditioning of the ECM in such a way as to impair regeneration following resection.

Experimental results were not consistent with our model predictions on the distribution of HSC states post-PHx in ethanol group – specifically, analysis of single cell data showed that the proportion of anti-regenerative HSC state was not increased at 24h post-PHx in ethanol-fed rats. Instead, ethanol-fed rats showed a similar HSC response to resection as control rats, albeit with more quiescence (29% quiescent in ethanol-fed rats compared to 21% quiescent in control rats). Ethanol-fed rats also had high proportions of cells in the pro-regenerative state (39%) and mixed state (32%) and no cells in the anti-regenerative state (0%). These results indicate that HSCs may have a dynamic transition insufficiency following resection, resulting in a greater cell quiescence. At 24 hours post-PHx, the numbers of cells sampled show this dynamic insufficiency only subtly but analysis of other measurements, such as tissue-scale gene expression, may be able to shed further light on this behavior. The dynamic HSC insufficiency could be due to an altered transition propensity of HSCs from their baseline states or a dynamic insufficiency in intercellular signaling that contributes to suppressed transitions. The larger magnitude differences between ethanol and control HSC population balances at baseline than at 24 hours post-PHx indicates that chronic HSC imbalances may have more of an effect impairing regeneration than any dynamic insufficiencies.

8.3.5 Transcriptional variability following ethanol adaptation and resection

In addition to altered balances of HSC states caused by chronic ethanol intake followed by resection, we also investigated how the transcriptional state of HSCs may be constrained in different conditions (Figures 8.10A and B). Both ethanol-fed and control groups had similar within-state cellular variability prior to resection. The exact structure of this variability may not be the same following ethanol treatment, however. For example, the transcriptional space occupied by quiescent cells in control rats appears distinct from the transcriptional space occupied by quiescent cells in ethanol-fed rats at baseline. Following resection, there appeared to be similar variability in both treatments as prior to resection.

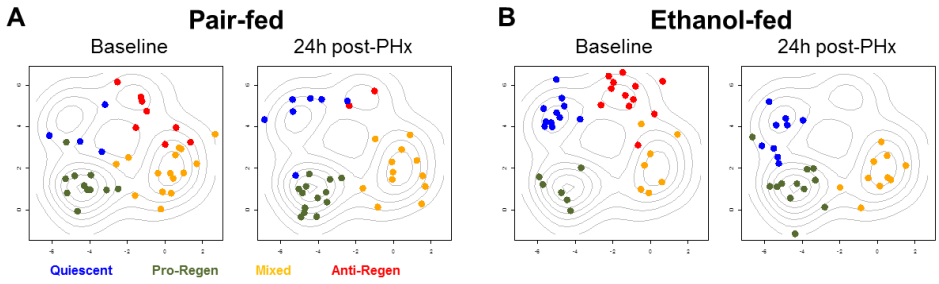

Figure 8.10 Topical map representation of hepatic stellate cells states shows the clustering of HSCs in (A) control animals at 0 hours and 24 hours post-PHx and (B) ethanol-fed animals at 0 hours and 24 hours post-PHx.

8.3.6 Independent dataset used to validate cell population balances

We were surprised that our results point to baseline imbalances among hepatic stellate cell states as the main contributor to impaired regeneration in ethanol-adapted rats. We therefore used an independently generated dataset to attempt to corroborate these findings. Previously, our lab generated microarray-based datasets describing

gene expression during liver regeneration in control rats and ethanol-fed rats post-PHx. The ethanol diet, animal housing conditions, and surgical procedure for PHx were identical in these animals and the ones used in our study. We used a non-negative least squares (NNLS) regression approach to identify different strengths of each HSC transcriptional state from the microarray data. Our NNLS approach begins by using data from 10-cell pools of HSCs to identify a kernel estimate of gene expression for each HSC transcriptional state. This kernel estimate is simply the median gene expression from all pools within each state. We then limit our kernel to genes that are expressed predominantly in HSCs (HSC-enriched genes) and were measured in both the high-throughput qPCR experiment and the microarray experiment. Using these genes, we then perform NNLS regression to estimate the contributions of each HSC transcriptional state to the microarray-based expression of HSC-enriched genes within the whole liver tissue, according to equations 8.1.

$$Y = \theta X + \epsilon \quad (8.1)$$

Where X is the kernel estimate for the HSC states, Y is the gene expression in each animal from the microarray data, and θ is the weighting vector describing the contribution of each cell population to whole-tissue expression.

The solution for this regression problem is the solution to a constrained least squares problem, constraining all θ to be non-negative, seen below in equation 8.2.

$$\theta_{CLS} = \theta + (X^T X)^{-1} L^T [L(X^T X)^{-1} L^T]^{-1} (v - L\theta) \quad (8.2)$$

In practice, this was implemented using the "nnls" package in R. Multiple rats were analyzed at each time point using microarrays, allowing construction of confidence intervals for the estimates of θ. Use of a NNLS regression approach is based on the assumption that each cell within a state adds linearly to the overall gene

expression signal from that state. Put another way, the assumption underlying NNLS is that measuring the gene expression from two cells then summing gives the same value as pooling the two cells, then measuring gene expression. This approach allows for the prediction of fractions of cells in each state and relative HSC transcriptional strength in each condition, by summing all θ within a given condition.

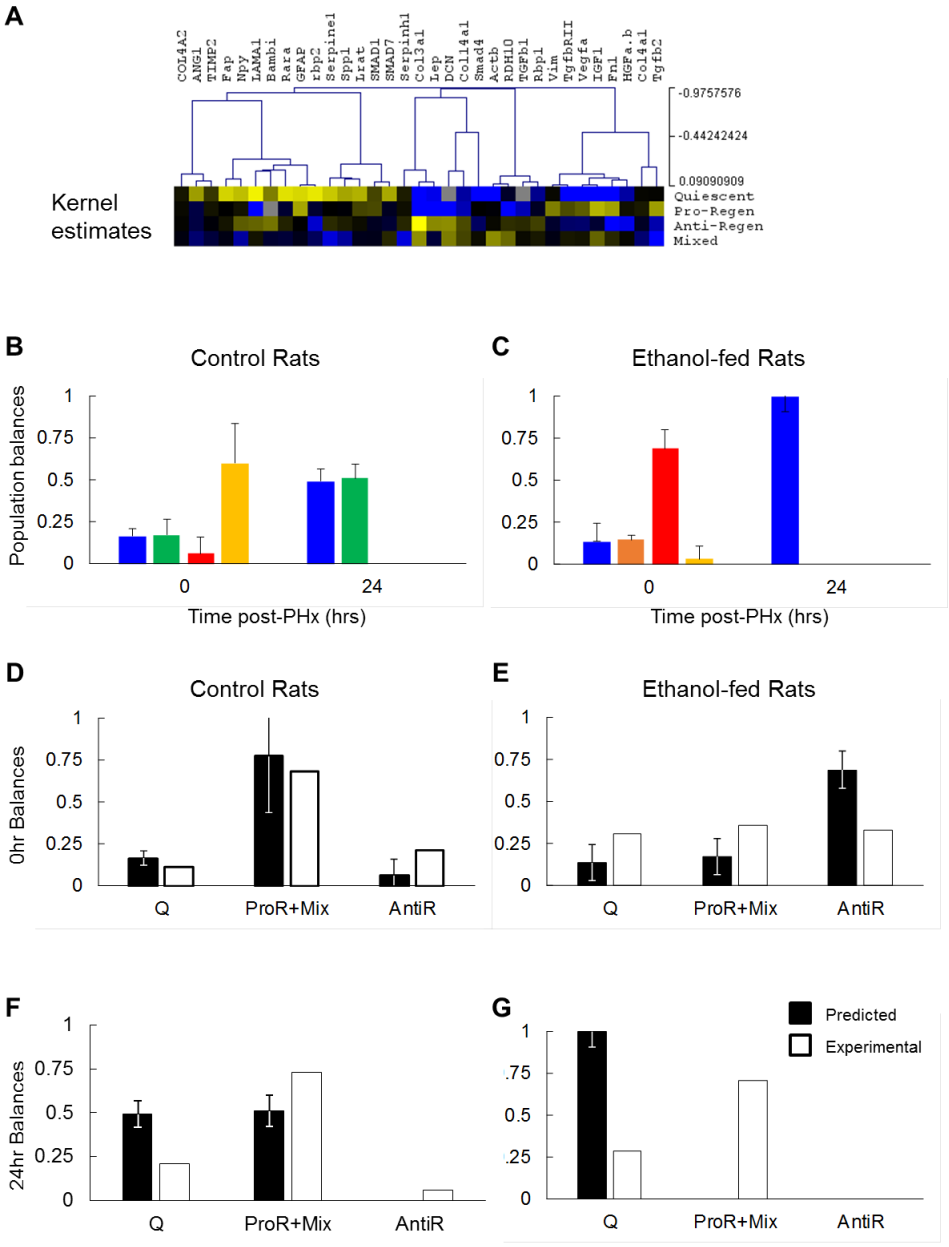

Figure 8.11 Kernel estimation of HSC states using HSC-enriched genes and 10 cell pools. (A) Kernel estimation. (B-C) Predicted levels of each HSC state during different conditions. (D-G) Comparison of predicted state balances with experimental data. Error bars are 95% confidence intervals.

We used this methodology to estimate kernels for each HSC transcriptional state based on the data from our 10 cell pools of HSCs (Figure 8.11A). The Quiescent HSC kernel is characterized by high levels of basement membrane-related genes (Col4a2, Lama1, Timp2), HSC marker genes (Gfap, Lrat, Npy), Tgfb signaling-related genes (Smad1, Smad7, Bambi), and retinol metabolism genes (Rara, Rbp2). The Pro-regenerative kernel is characterized by high levels of growth factors (Hgf, Igf1, Vegfa), but also high levels of several Tgfb-related genes (Tgfb2, Tgfbr2) and basement-membrane associated genes (Col4a1, Vim). The Anti-regenerative kernel is characterized by high levels of fibrotic matrix-associated genes (Col3a1, Col14a1), Dcn, and Lep. The Mixed kernel is shows high expression of genes in the Pro-regenerative and Anti-regenerative kernels, with some differences. Notably, Col4a1 is down-regulated in the Mixed kernel compared to the Pro-regenerative kernel, Lep is down-regulated in the Mixed kernel compared to the Anti-regenerative kernel, and Actb and Rdh10 are up-regulated in the Mixed kernel compared to all other kernels.

Using the NNLS regression technique, we predicted that most HSCs in control rats at baseline are in the mixed state (Figure 8.11B) and at 24 hours post-PHx these cells have all shifted to an even balance between the quiescent and pro-regenerative states. We predicted that ethanol adaptation leads to most HSCs at baseline exhibiting the anti-regenerative state (Figure 8.11C), shifting to all HSCs becoming quiescent at 24 hours post-PHx. We compared our predicted population balances to the balances calculated from the single HSCs sampled earlier. It should be noted that the limited number of genes used in the NNLS analysis does not allow for a clear distinction between the mixed and pro-regenerative states in the NNLS-based predictions, we therefore summed the cells in the pro-regenerative and mixed states from our

experimental data and from our NNLS-based predictions for comparison. Our predictions of cell balances match our experimental results for control rats at baseline (Figure 8.11D) and ethanol-fed rats at baseline (Figure 8.11E) fairly well. At 24 hours post-PHx, however, our predictions of cell balances overestimate the fraction of cells that are quiescent and underestimate the fraction of cells that are pro-regenerative and mixed (Figure 8.11F and G).

We therefore selected a subset of genes that would allow for our NNLS-based predictions to match experimental results. We selected HSC-enriched genes that were informative of HSC function (collagens, growth factors, and Tgfb receptors) and added HSC-enriched genes that caused a decreased error between predicted balances and fractions calculated from experiment. In this way, we found a subset of HSC-enriched genes that could be used to calculate HSC population kernels and estimate HSC population balances of from whole tissue measurements (Figure 8.12A).

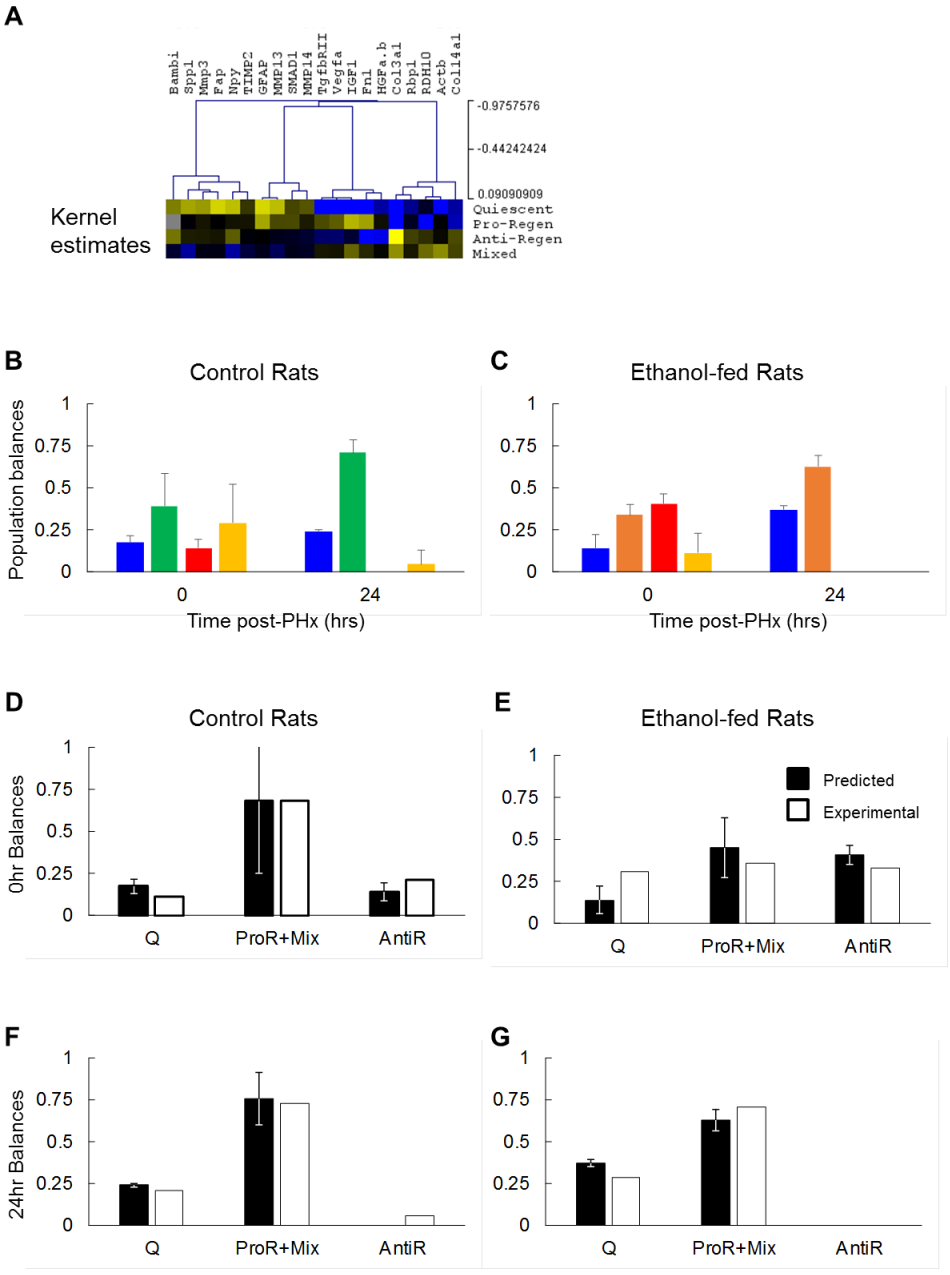

Figure 8.12 New kernels from smaller set of genes. (A) Kernel estimation. (B-C) Predicted levels of each HSC state during different conditions. (D-G) Comparison of predicted state balances with experimental data. Error bars are 95% confidence intervals.

Using the NNLS regression technique with the reduced kernels, we predicted that most HSCs in control rats at baseline are distributed among states (Figure 8.12B) and at 24 hours post-PHx these cells have all shifted to predominantly pro-regenerative. We predicted that ethanol adaptation leads to a higher fraction of HSCs at baseline exhibiting the anti-regenerative state and a lower fraction exhibiting the mixed state (Figure 8.12C). At 24 hours post-PHx, we predicted that the balances in ethanol-adapted rats matched control rats closely. As before, we compared our predicted population balances to the balances calculated from the single HSCs sampled earlier. Our new predictions match experimental measurements closely (Figure 8.12D-G).

We next sought to understand how our kernel estimates and predicted balances change if using data from single HSCs rather than pools of 10 HSCs. Using all HSC-enriched genes measured in both the high-throughput qPCR and microarray experiments, we found similar gene expression signatures for the HSC state kernels (Figure 8.13A). Although the trends of expression in the kernels is similar, the differences between kernels is more apparent using the 10 cell pools. It is possible that this is caused by the 10 cell pools picking up a stronger signal of gene expression than the single HSCs, resulting in more clear kernel signatures.

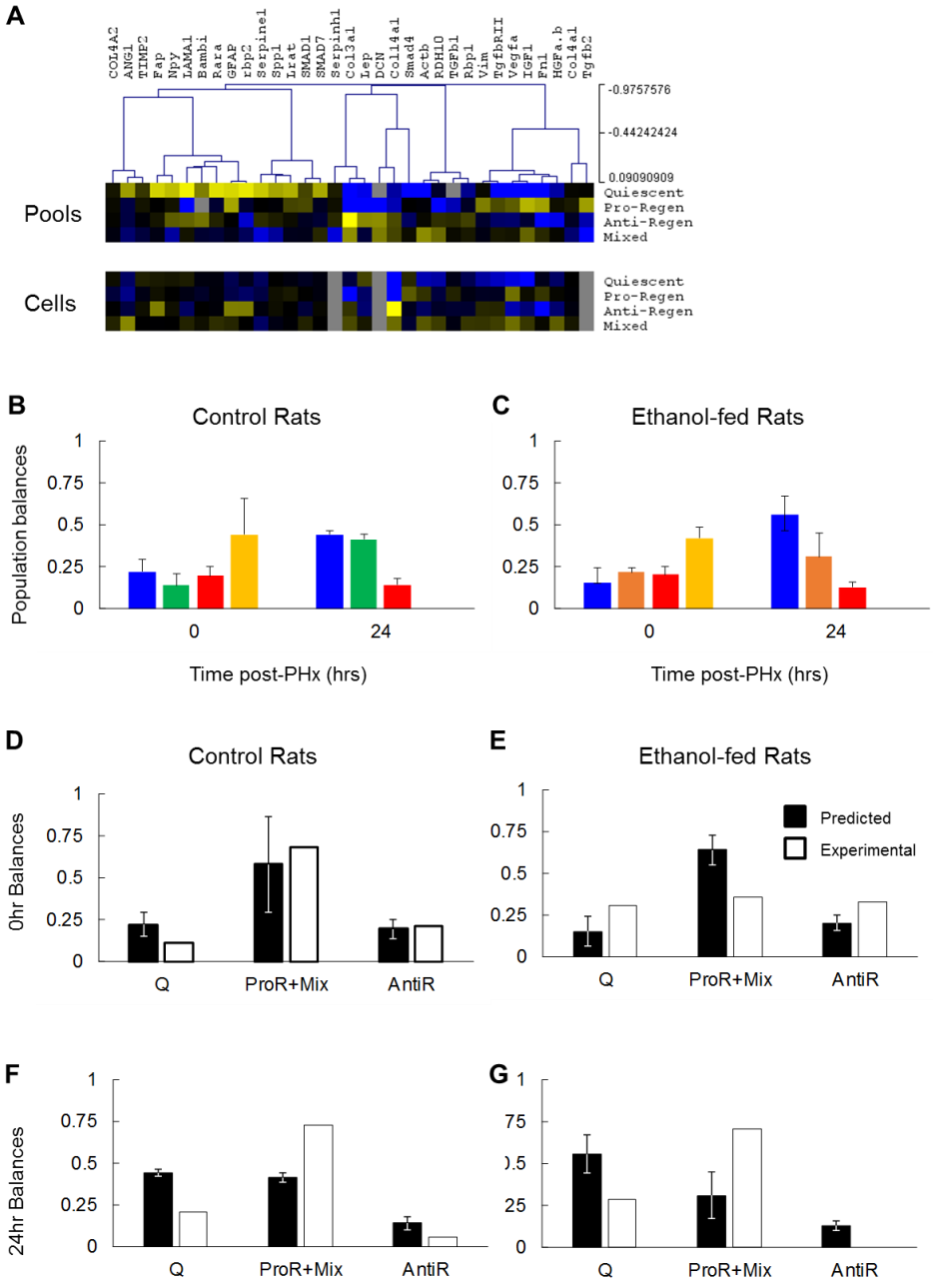

Figure 8.13 Regression technique applied to single HSCs. (A) Kernel for single HSCs compared to the kernel from pooled HSCs. (B) Predicted Levels in control rats. (C) Predicted levels in ethanol-fed rats. (D-G) Predicted levels compared to experimental data. Error bars are 95% confidence intervals.

Similar to our predictions using all HSC-enriched genes and 10 cell HSC pools, using single cells considering all HSC-enriched genes we predict that control rats at baseline exhibit all HSC transcriptional states but 24 hours post-PHx cells are evenly distributed between the quiescent and pro-regenerative states (Figure 8.13B). Using single cells leads us to predict that ethanol adapted rats have a similar distribution of states as control rats at baseline and a high fraction of quiescent cells at 24 hours post-PHx (Figure 8.13C). As with our predictions using 10 cell pools and all HSC-enriched genes, these predictions based on single cell kernels do a fairly good job predicting fractions of transcriptional states at baseline in control rats (Figure 8.13D), but do a poor job predicting all other conditions (Figure 8.13E-G).

We also tested whether the reduced kernel could lead to better predictions in single cells compared to all HSC-enriched genes. As with all HSC-enriched genes, the single cell-based kernel is similar to the 10 cell pool-based kernel, but the signal differences among the four kernels are not as strong in the single cell-based kernel as in the pool-based kernels (Figure 8.14A).

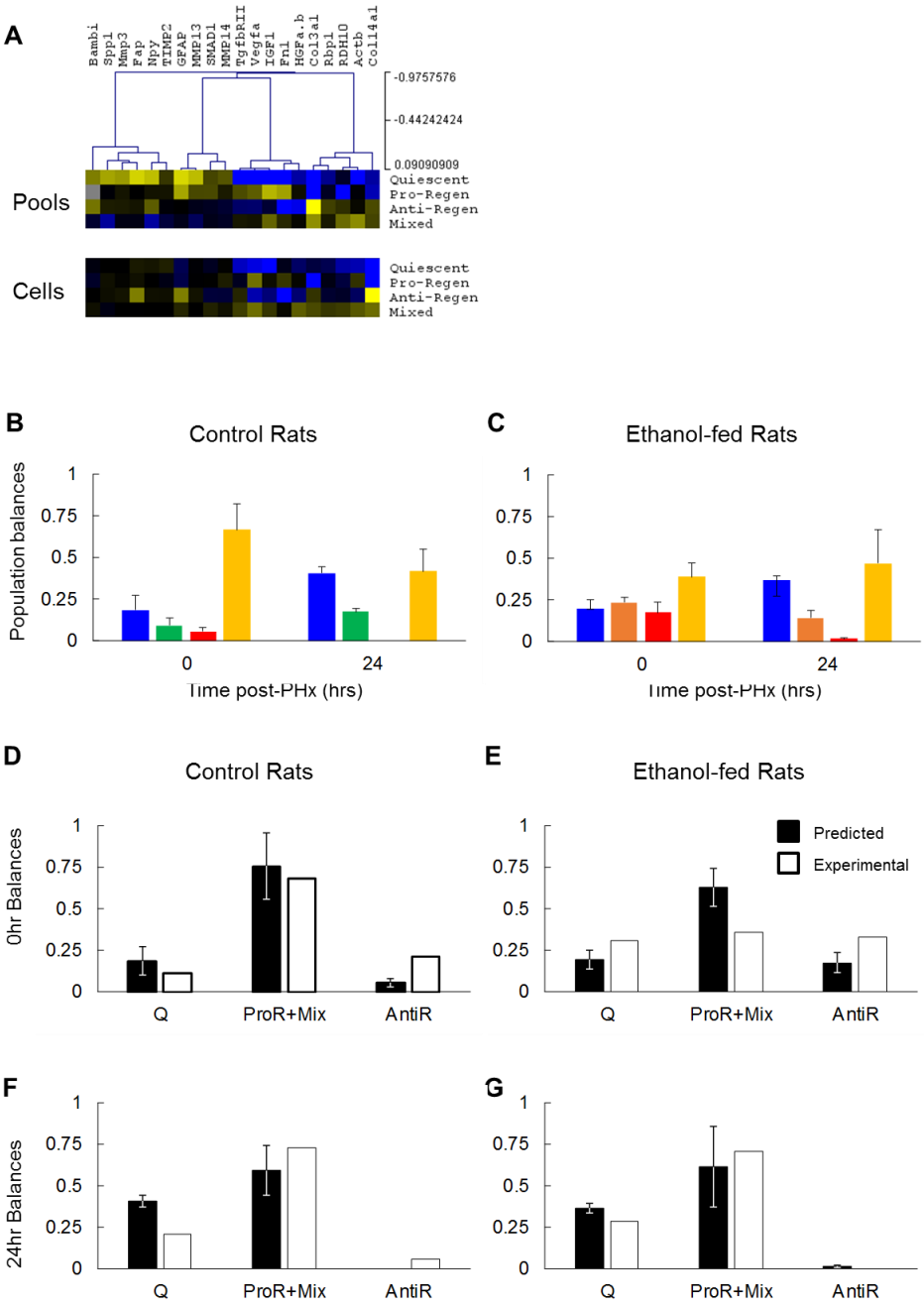

Figure 8.14 Regression technique applied to single HSCs using the selected genes only. (A) Kernel for single HSCs compared to the kernel from pooled HSCs. (B) Predicted Levels in control rats. (C) Predicted levels in ethanol-fed rats. (D-G) Predicted levels compared to experimental data. Error bars are 95% confidence intervals.

When considering this reduced kernel, we predict a high level of mixed cells at the baseline in control rats and cells distributed among the quiescent, pro-regenerative, and mixed states at 24 hours post-PHx (Figure 8.14B). In contrast, we predict a higher fraction of cells in the anti-regenerative state in ethanol-adapted rats at baseline (Figure 8.14C). We predict that this ethanol-adapted imbalance recovers by 24 hours post-PHx (Figure 8.14C). Comparison of these predictions with experimental results again yields fairly good agreement. Our method underestimates slightly the fraction of anti-regenerative HSCs at baseline in both diets (Figure 8.14D and E). We also overestimate the fraction of pro-regenerative and mixed HSCs in ethanol-adapted rats at baseline (Figure 8.14D). At 24 hours post-PHx, our method overestimates slightly the fraction of quiescent cells (Figure 8.14F and G). In general, though, our predicted results show the same trends comparing the baseline levels of ethanol-adapted and control rats at baseline as seen in our experimental work. Ethanol-adapted rats have a higher fraction of cells in the anti-regenerative state than control rats. This validation of our experimental results with an externally generated dataset increased our confidence that the results from our single cell experiment are representative of the true biology.

8.3.7 Transcriptional strength across conditions

Even though our predictions of HSC state balances using the microarray data match closely our cell state balances found experimentally, the finding that HSC balances are similar between ethanol-adapted and control rats at 24 hours post-PHx appears to contradict the previous interpretation of the microarray data (Kuttippurathu et al, 2016c). Previously, these data were interpreted to suggest an imbalance in pro-regenerative and anti-regenerative HSC states at 24 hours post-PHx in ethanol-adapted

rats. To reconcile these interpretations of the microarray data, we use a feature of the NNLS regression approach: NNLS allows for predicting fractions of HSCs in transcriptional states and overall transcriptional strength of HSCs in each condition. We used the reduced kernel from the 10 HSC pools and the single HSCs to calculate two estimates of the transcriptional strength of HSCs across all conditions, by summing the θs from each condition (Figure 8.15).

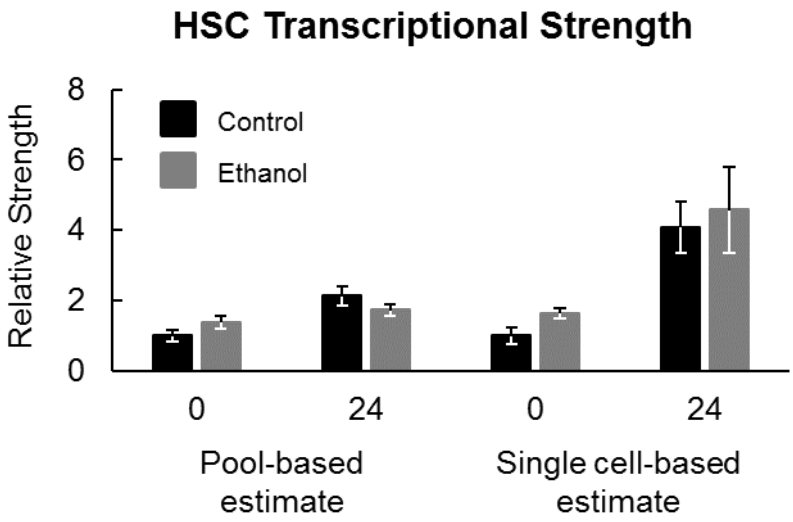

Figure 8.15 Relative HSC transcriptional strength predicted using the NNLS regression approach. Error bars represent 95% confidence intervals.

Both the pool-based estimation and the single cell-based estimation of relative HSC transcriptional strength indicate that there is a slightly higher HSC transcriptional strength in the ethanol-adapted state at baseline. At 24 hours post-PHx, the pool-based estimate suggests that ethanol-adapted rats have a slight deficiency in HSC transcriptional state transitions. This agrees with our experimental single-cell data,

which suggests that post-PHx, more HSCs in ethanol-adapted rats exhibit the quiescent state than in control rats. The single cell-based estimate, in contrast, shows no statistically discernable differences in the predicted HSC transcriptional strengths between conditions at 24 hours post-PHx. We should note that several of the genes interpreted from the microarray as relating to HSC activation are highest in the quiescent kernel (Spp1 and Serpine1). Their increase at 24 hours post-PHx in the microarray data therefore agrees with the interpretation from the single cell data that suggests a state transition insufficiency caused by ethanol adaptation.

8.3.8 Computational Modeling in Combination with Experimental Results Suggests Matrix Preconditioning and Dynamic Hepatic Stellate Cell Transition Insufficiency Contribute to Suppressed Liver Regeneration

Although our single cell gene expression analysis uncovered imbalances in HSCs states at the baseline as characterizing the disease versus control conditions, our simulations suggest that these differences are not sufficient to alter the response to resection (see Chapter 7). This indicates that the regeneration deficit in the ethanol group may be due to multiple hits that alter HSC behavior: the first hit to precondition the ECM by increasing the fraction of HSCs in the anti-regenerative state at the baseline chronic ethanol-adapted state, and the second hit is dynamically decreasing HSC functional state transitions post-resection. If the altered matrix composition in the ethanol-adapted state results in a stiffer or denser matrix, it is possible that growth factors and other matrix-bound factors are less able to intercalate into the matrix to be available to promote cell growth post-resection. Furthermore, such a dense matrix may slow degradation due to metalloproteases. Using our computational model, we investigated whether this matrix preconditioning and dynamic transition insufficiency were sufficient to explain ethanol-induced suppression of liver regeneration by

changing parameters consistent with our hypotheses (Parameter changes are shown in Table 8.2).

Table 8.2 Matrix-associated features predicted in chronic ethanol use and corresponding parameter values

Feature	**Control**	**Ethanol**	**Parameter**	**Value in Ethanol (% of nominal)**
ECM Density	Sparse	Dense	k_{ECM}	400%
ECM Composition	Enriched in basement membrane	Enriched in fibrous collagens	κ_{deg}	10%
Tissue Stiffness	Relatively low	Areas of high stiffness	$k_{Q\rightarrow PR}$ $k_{Q\rightarrow AR}$	65% 25%
Availability of Matrix-bound factors	High	Low	K_{up}	70%
Growth factor intercalation	High	Low	k_{up}	70%

We maintained parameters related to Kupffer cell activation constant from our previous simulations to maintain ethanol-induced increases in Kupffer cell activation post-PHx, resulting in high levels of IL-6 and IL-10 (Figure 8.16A). We then altered parameters related to matrix deposition, matrix metalloprotease function, and HSC transition propensity in accordance with our experimental results (Table 8.2, Figure 8.17). We also reduced the value of the parameter governing JAK activation rate in hepatocytes in response to IL-6 because studies have shown that ethanol-adapted

hepatocytes have a deficient STAT3-pathway response to cytokine signaling (Chen et al, 1997;Horiguchi et al, 2007).

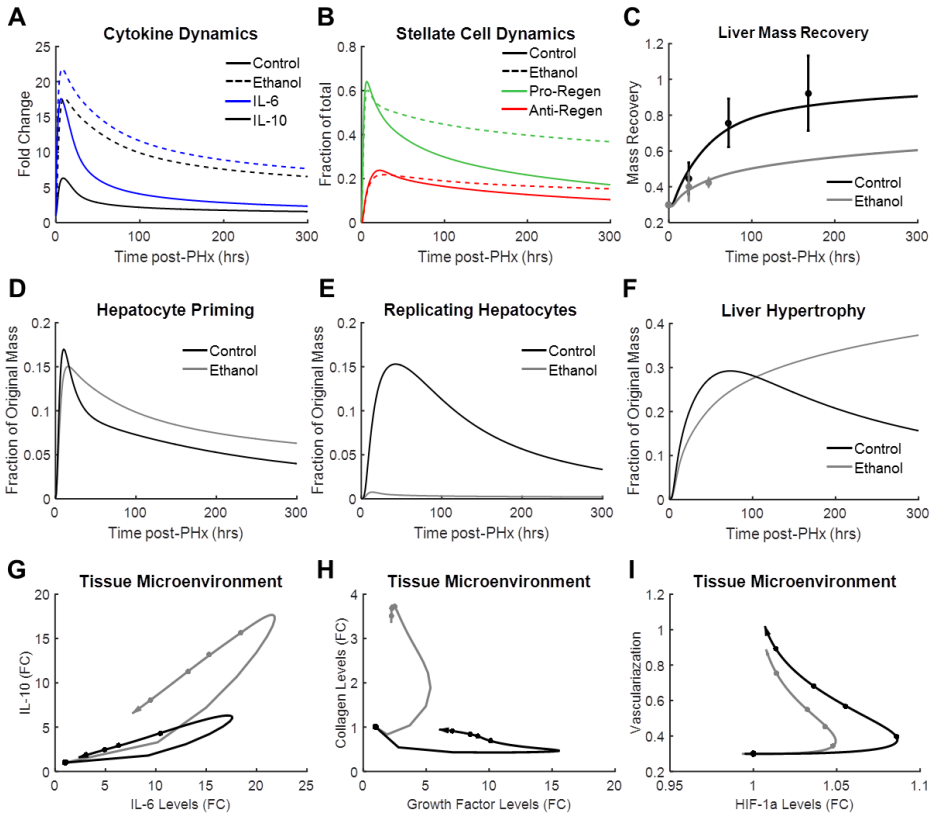

Figure 8.16 Implications of HSC activation results and model predictions for chronic ethanol-treated rats. (A) Chronic ethanol use leads to increased levels of pro-inflammatory and anti-inflammatory cytokines following PHx. (B) Chronic ethanol appears to lead to a deficient pro-regenerative HSC response following PHx. (C) The effects of increased cytokine production, imbalanced HSC functional states, and changes to the tissue microenvironment combine to suppress regeneration following ethanol adaptation. The simulated regeneration profile of ethanol adapted rats is consistent with results from (Yang et al, 1998b).

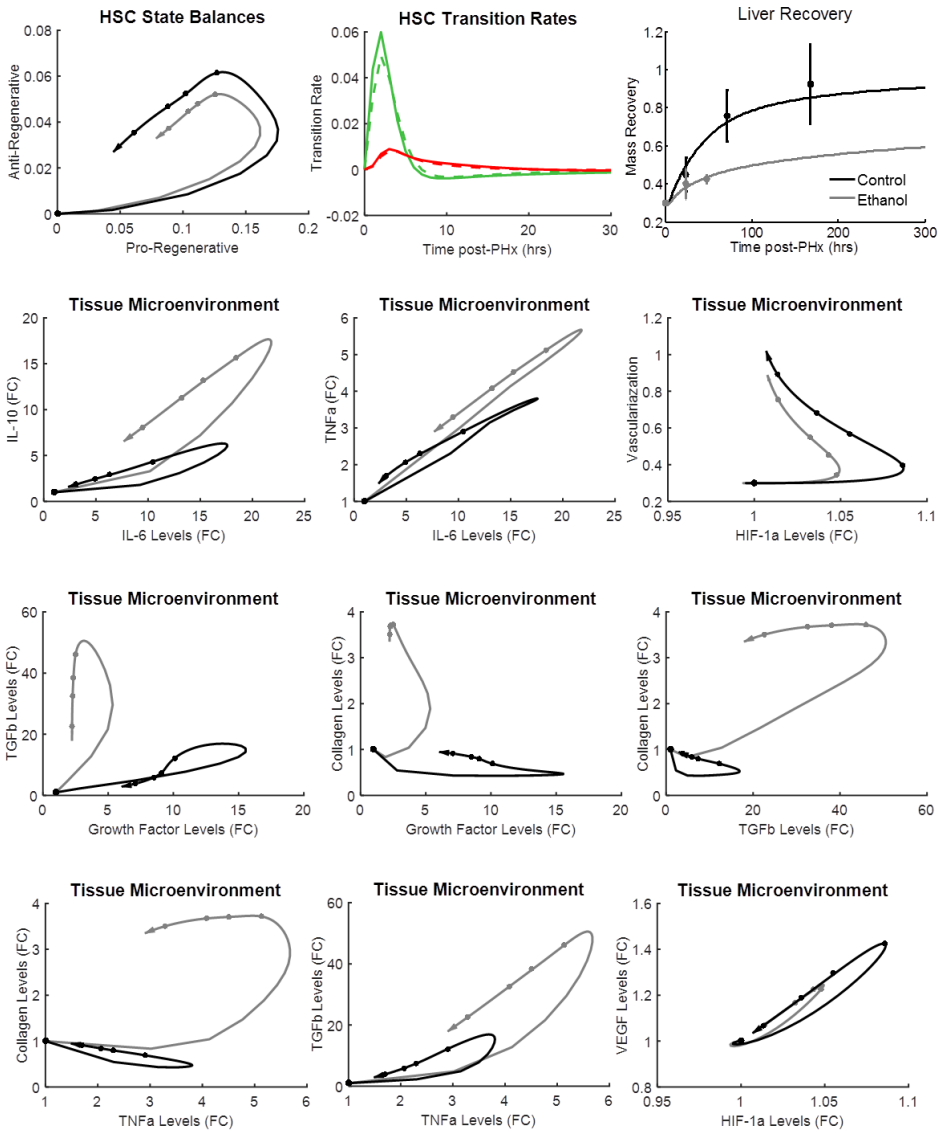

Figure 8.17 Effects of chronic ethanol consumption on liver regeneration control and tissue microenvironment.

Tuning these parameters allowed us to match our experimental observations that HSC population levels were dynamically insufficient post-PHx, (Figure 8.16B). Based on simulation results, one reason for this dynamic insufficiency may be increased HSC apoptosis in ethanol-adapted rats (Figure 8.18).

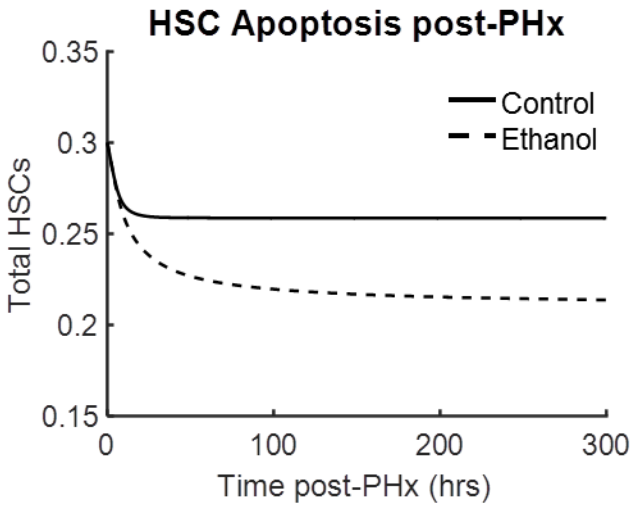

Figure 8.18 Simulations lead to the prediction that there is more apoptosis of HSCs in the ethanol-fed rats than controls.

These simulations then matched to experimentally observed mass recovery data following 70% PHx in rats (Figure 8.16C) (Yang et al, 1998a). Our simulations captured experimental observations that chronic ethanol use suppresses hepatocyte priming (Figure 8.16D), impairs hepatocyte replication post-PHx (Figure 8.16E), and results in hepatomegaly (Figure 8.16F) (Chen et al, 1997;Israel et al, 1979;Yang et al, 1998a). Model simulations suggest, however, that hepatocyte size increases early in control rats in response to PHx but that the hepatomegaly caused by ethanol adaptation is a delayed response to PHx. Altered cell network behavior in ethanol-adapted animal simulations led to dramatic differences in tissue microenvironment (Figure 8.16G, H & Figure 8.17) but little difference in final amount of tissue vascularization (Figure 8.16I), suggesting that chronic ethanol consumption does not impair revascularization of the liver.

8.4 Discussion

Our study has shown that HSCs can exhibit transcriptional behavior that appears to correlate with the cellular functional state. What is less clear is the path of progression of HSCs through these functional states. One possibility is that HSCs could exist in a "transcriptional continuum" where cells can transition between any two states in response to internal and external stimuli (Figure 8.19A). Alternatively, HSCs could progress through a series of states beginning at quiescent state and moving towards an anti-regenerative state (Figure 8.19B).

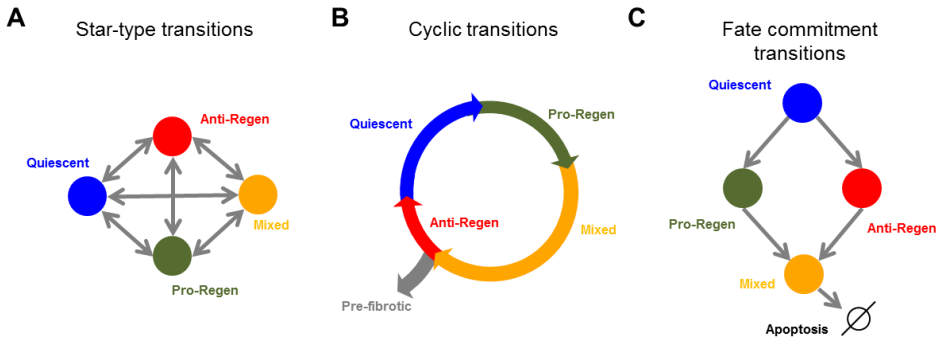

Figure 8.19 Potential hepatic stellate cell transition patterns. (A) Star-type transitions could allow any functional state to shift its transcriptional profile into any other functional state. (B) A cyclic transition pattern, like the cell cycle, could allow for distributions of cells aiding hepatocyte regeneration or homeostatic renewal. Getting "stuck" in one phase of the cycle could lead to cell exit into apoptosis or pre-fibrotic phenotypes. (C) A cell fate commitment pattern would allow cells to transition only one way. In such a pattern, quiescent cells would have to be continuously replenished. Perhaps hepatic stem cells (or oval cells) play a role in this replenishment.

In such a scheme, progression to the anti-regenerative state requires transcriptional regulation into the pro-regenerative and mixed states before reaching

the anti-regenerative state. Regeneration could be enhanced by maintaining cells in the pro-regenerative intermediate states for a longer period of time or impaired by speeding the progression through these states. Furthermore, such a progression may correspond to the physiological stages of regeneration, which may mean that such an ordered progression does not necessarily hold true for disease contexts that yield diminished regeneration. It is also possible that HSCs could progress through committed fate transitions from a quiescent phenotype to a mixed phenotype (Figure 8.19C). In this scheme, the only way to rebalance the distribution of HSC states is though cell death of terminally differentiated HSCs. Further investigation, however, is needed to identify which, if any, of these hypotheses are correct. As an additional consideration, the effects of tissue microenvironment, including tissue stiffness, may also be important to determine how cells can transition between states.

Several opportunities exist for extending our current study. We considered a select set of transcripts to define HSC functional states. Future studies could benefit from a more comprehensive transcriptomic characterization of single HSCs, for example, using single cell RNAseq. It should be noted, however, that even when considering transcriptomic data, only a fraction of the transcripts (a few tens to hundreds, depending on the context) contribute to separation of functional states, as evidenced by typical factorization analysis of these data sets using strategies such as Principal Component Analysis, Multi-dimensional Scaling, and Stochastic Embedding (Patel et al, 2014;Tang et al, 2010;Treutlein et al, 2014;Zeisel et al, 2015b). The identity of functional states depends on the subset of the transcriptome that is considered as relevant to a specific context under study. For example, fractionation of cell states based on metabolic pathways may yield a different hierarchy of cell states

than fractionation based on transcription factors, cell surface receptors, signaling pathway components, or a combination thereof. Our analysis of cellular functional states based on select set of approximately 100 transcripts could be considered as parallel to single cell cytometry studies of select (~20-100) proteins using the CyTOF approach that have uncovered new insights into the cellular hierarchy of multiple cell types, including immune cells and stem cells (Han et al, 2015;Qiu et al, 2011;Yao et al, 2014).

Another opportunity is to extend the computational model to incorporate our novel experimental data describing single HSC gene expression. The model includes only three HSC states, excluding the mixed HSC state identified as a major contributor to HSC population balances. Accounting for this additional state, however, may require a more thorough understanding of how HSCs transition across these states. To this end, future investigations need to develop temporally informative data, for example through cell lineage tracing techniques, to identify the dynamics governing progression of individual HSCs through different states. Additionally, we considered hepatocyte replication following resection as a uniform property of all hepatocytes, although recent studies have begun to appreciate the contributions of liver "stem cell-like" cells contributing to regeneration (Wang et al, 2015a;Yimlamai et al, 2014). Our combined single-cell based transcriptional analysis and computational modeling approach could be a powerful tool to investigate the contributions of these "stem cell-like" hepatocytes as well as additional hepatocyte transcriptional states to liver regeneration and dynamic liver function. Further extensions of our approach could be used to study the relationship between spatial heterogeneity in the liver and regeneration. Using our approach, we collected single cells from portal and central

regions of multiple liver lobes and record exact spatial information about each cell. Coupling such data with a spatially resolved cell network model would allow for in-depth investigation into how spatial heterogeneity affects regeneration and vice versa.

Finally, our study has several implications for studying the mechanisms driving chronic liver diseases such as fibrosis, cancer, and others. Our results demonstrate that the dynamic liver function is governed by multiple levels of physiological controls: molecular, intracellular, and inter-cellular networks. Molecular control of liver function has been widely studied, but has yet to progress to promising therapies for severe liver disease (Jain et al, 2015;Zhu et al, 2015). Previous studies have focused on the effects of canonical cell types interacting or the effects of other organs, such as adipose tissue, on liver function (Chiang et al, 2011;Engelmann et al, 2015). Our work takes a different approach, using a data-driven understanding of cell functional states to gain insights into how the dynamic distributions of cells in various functional states contribute to overall tissue function. This study presents the first steps towards understanding the contributions of cell states and interactions among many types of cells in multiple states to tissue function. It is possible that modifying the population balances of cells in different states may be an effective strategy to influence disease progression and remission. This novel concept of cell state population imbalances contributing to disease progression suggests a new way to think about treating chronic diseases. Disease regression may be achievable through inhibiting certain cell states and enhancing others rather than targeting specific molecular pathways.

Chapter 9

IMPLICATIONS FOR NON-PARENCHYMAL CELL NETWORKS IN TISSUE HOMEOSTASIS

9.1 Introduction

Day to day tissue renewal is accomplished through a program of homeostatic renewal involving adult cells, stem cells, and increasingly recognized subpopulations of cells that display characteristics of both stem cells and adult cells, so called "stem-cell-like" cells. Cell turnover rates in the body can vary from days to years. Certain tissues, like the intestinal epithelium, have a high turnover rate (average lifespan ~ 5 days), while some tissues, like the intercostal skeletal muscle, have a much slower turnover rate (average lifespan ~ 30 years) (Spalding et al, 2005). The majority of this replacement occurs through homeostatic renewal. In humans, only one organ, the liver, is able to regenerate lost mass through other means (Michalopoulos, 2013). Despite the ubiquitous presence of homeostatic renewal in biology and decades of study, researchers are still investigating the mechanisms underlying homeostatic renewal and how different cell populations interact with tissue microenvironments to govern the renewal process.

One interesting organ in which to study homeostatic renewal is the liver. The liver is one of the main detoxifying organs of the body and is therefore exposed to potential toxins. This sometimes toxic environment requires a robust homeostatic renewal process. Facilitating a robust homeostatic renewal, the liver contains multiple stages of developed cells contributing to renewal, including stem cells (or oval cells),

"stem-cell-like" cells, and fully differentiated parenchymal cells (mature hepatocytes) (Fausto & Campbell, 2003;Miyajima et al, 2014;Wang et al, 2015b). Additionally, a large body of literature exists investigating regeneration following mechanical or toxic damage in the liver, reviewed in (Michalopoulos, 2013;Taub, 2004b). Studies on regeneration have shed light onto how hepatocytes progress through the cell cycle (Loyer et al, 1994), how and when stem cells contribute to regeneration (Wang et al, 2003), and how the tissue microenvironment can inhibit regeneration as in the case of liver fibrosis (Friedman, 2008b). Recently, our lab used a combined mathematical modeling and single-cell based gene expression approach to investigate how the balance of non-parenchymal cells governs regeneration (for details, see Chapters 7 and 8). We find that imbalances among different subpopulations of hepatic stellate cells impair the liver's regenerative ability. These imbalances are most striking in the liver after chronic ethanol use but before resection, suggesting that it is long-term, baseline imbalances that impair regeneration. We therefore wonder whether imbalances in cell populations could have an effect on homeostatic renewal in the liver. We seek to explore this question using a mathematical modelling approach.

9.2 Materials and Methods

9.2.1 Model development

We developed a new mathematical model of liver homeostatic renewal that takes into account two recently described populations of hepatocytes: Axin2+ (H^{A2+}) and Axin2- (H^{A2-}) hepatocytes (Wang et al, 2015b). Hepatocytes renew predominantly by replication of Wnt-responsive Axin2+ "stem-cell-like" hepatocytes, which have been shown to cluster pericentrally and respond to factors produced by pericentral

endothelial cells (i.e. WNT-2a). As Axin2+ hepatocytes renew, some of the daughter cells migrate from the pericentral region and lose Wnt responsiveness, becoming Axin2- cells. These Axin2- hepatocytes subsequently terminally differentiate to become mature hepatocytes and populate the remainder of the liver. It remains an open topic of research whether stem cells participate in homeostatic renewal and to what extent (Kopp et al, 2016).

We used an ODE-based approach to describing the dynamics of Axin2+ and Axin2- hepatocyte populations during homeostatic renewal. Although cell replication and apoptosis is an intrinsically stochastic process at the level of individual cells, at the population level these processes can be represented using deterministic modeling. Multiple studies have used this approach previously to simulate cell growth *in vitro* and *in vivo* (Baranyi & Roberts, 1994;Johnston et al, 2007;Lovrics et al, 2006).

In our modeling scheme, each population of hepatocytes maintains a proliferation rate (k_{prol}) and an apoptosis rate (k_{ap}). Additionally, we simulated Axin2+ hepatocytes as constitutively transforming to Axin2- hepatocytes according to a transition rate (k_T). This gives rise to the differential equations below.

$$\frac{dH^{A2+}}{dt} = [H^{A2+}]k_{prol}^{A2+} - [H^{A2+}]k_{ap}^{A2+} - [H^{A2+}](k_T) \quad (9.1)$$

$$\frac{dH^{A2-}}{dt} = [H^{A2+}](k_T) + [H^{A2-}]k_{prol}^{A2-} - [H^{A2-}]k_{ap}^{A2-} \quad (9.2)$$

We also included an exploration of potential feedback mechanisms that could be at work during homeostatic renewal. Biological justification for each feedback explored and equations describing each can be found in the Results section.

9.2.2 Parameter constraints

9.2.2.1 Literature-based constraints

Table 9.1 Parameter values for each model considered in this study

Parameter	0	A	B	C	D	Robust
k^{+}_{prol}	0.071429	0.214258	0.071429	0.071429	0.071429	0.214258
K^{+}_{cap}	--	0.075	--	--	--	0.075
K^{-}_{cap}	--	1.425	--	--	--	1.425
k^{-}_{prol}	0.035714	0.107129	0.035714	0.035714	0.035714	0.107129
k^{+}_{ap}	0.0375	0.0375	0.0375	0.0375	0.0375	0.044629
k^{-}_{ap}	0.0375	0.0375	0.0375	0.0375	0.0375	0.044629
k_T	0.033887	0.033887	0.033984	0.033887	0.034277	0.169629
k_P^{env}	--	--	0.14502	1	--	0.434961
k_T^{env}	--	--	--	0.95	--	0.95
k_A	--	--	0.1	--	--	0.1
C1	--	--	--	--	100	--
C2	--	--	--	--	8	--
k_{Renew}	--	--	--	--	8	--

All parameters values used in this study are listed in Table 9.1. Several of the parameters used in our model have direct biological correlates and have been measured experimentally. From the study by Wang et al., it has been estimated that Axin2+ hepatocytes replication takes approximately 14 days, giving an observed proliferation rate (k_{prol}^{A2+}) of 1/14 doublings/day (Stanger, 2015). Similarly, Axin2- cells were estimated to double every 28 days, giving an observed proliferation rate of 1/28 doublings/day (Stanger, 2015). These estimates appear to agree with previous

studies showing that the average lifespan of a hepatocyte in mice is between approximately 200 and 400 days (Malato et al, 2011).

Total apoptosis rate must balance with total proliferation rate to ensure the liver maintains homeostatic mass. Also, there is no study suggesting a differential homeostatic apoptosis rate due to liver zonation. Therefore, we simulated the homeostatic apoptosis rate for both Axin2+ hepatocytes and Axin2- hepatocytes are equal. Apoptosis rate was calculated to ensure a steady-state tissue mass.

One of the feedback mechanisms we consider is a cell competition constraint using the logistic equation, which includes carrying capacity for each population (K_{cap}^{A2+} and K_{cap}^{A2-}) (See Equations 1 and 2). In these equations, the carrying capacities were estimated to be 1.5x the steady-state value of the tissue. We chose 1.5x because infiltration of greater than 50% of hepatocytes by fat occurs rarely, occurring in only 33% of morbidly obese patients (Fris, 2004). We also explored the effect of changing the carrying capacities on model behavior.

Another feedback mechanism we consider is replacement of Axin2+ hepatocytes by a population of stem cells. Studies have shown no major contribution of stem cells to homeostatic renewal in the liver, we therefore chose parameters that would make the effect of stem cells zero at steady-state, but increase exponentially if liver mass decreases (See equation 9.13 and Table 9.1).

9.2.2.2 Steady-state constraints

The other model parameters were estimated similar to how we estimated apoptosis rate. Values were constrained so that $d/dt(H^{A2+})$ and $d/dt(H^{A2-})$ equaled zero, corresponding to steady-state. We simulated multiple possible models exhibiting all

feedback combinations and, in most cases, there was only one set of parameters that satisfied the steady-state constraints. When multiple parameter sets were possible, we chose the parameter set that maintained parameter values close to the other possible models.

9.2.3 Model selection for robustness

We used a systematic design of experiments-based (DOE) approach to investigate the system behavior under all possible combinations of feedback configurations, specifically characterizing system recovery in response to a wide variety of disturbances. We considered each feedback to be a factor with one of two levels: 1 (present) or 0 (absent). We considered four possible feedbacks, resulting in a 2^4 full factorial design. We then simulated a transient (30 day) increase in apoptosis, decrease in apoptosis, increase in proliferation, and decrease in proliferation and measured the system response. The metric we used to evaluate model response to multiple individual disturbances is given in equations 9.16 and 9.17 in the Results section. We also varied parameter values to simulate how robust the model is to slight deviations in parameters corresponding to potentially different regulation of homeostatic renewal in different patients. We created 9 additional parameter sets by sampling each parameter from a normal distribution with a mean at the parameter's nominal value and a standard deviation of 1% of the nominal value. We then re-performed the full 2^4 DOE for each parameter set. We used an ANOVA approach to identify feedbacks that contributed significantly to model response to transient disturbances.

9.2.4 Global and parametric sensitivity analyses

9.2.4.1 Global sensitivity analysis

The Sobol method for calculating was used to estimate sensitivity of model output to parametric changes based on output variance. A detailed description of Sobol sensitivity can be found in (Bilal, 2014;Sobol, 2001). Briefly, the total effect index (TEI) was calculated for each parameter by sampling 1,000 parameter sets from a normal distribution for each parameter with a mean value of the nominal parameter value and a standard deviation of 10% of its nominal value. We then simulated homeostatic renewal with each parameter set and recorded the resulting change in steady state levels of Axin2+ cells, Axin2- cells, and overall liver mass. A complimentary parameter set was generated for each parameter maintaining that parameter constant at the nominal level while all others varied. The sensitivity was then calculated according to equation 9.3.

$$S_T(i) = 1 - \frac{Var_{p_{\sim i}}\left(E_{p_i}(Mass|p_{\sim i})\right)}{Var(Mass)} \quad (9.3)$$

Where $S_T(i)$ is the TEI for each parameter, *Mass* represents the nominal mass fraction of Axin2+ cells, Axin2- cells, or total liver mass at the new steady state, p represents each parameter, and $p_{\sim i}$ respresents all parameters except p_i. Thus, the total sensitivity index can be viewed as the variance in model behavior caused all other parameters except i varying subtracted from the total variance caused by all parameters changing normalized to the total variance.

9.2.4.2 Parametric sensitivity analysis

Normalized sensitivity coefficients were estimated by changing each parameter (p_i) by +/- 10% of its nominal value and calculating sensitivity at each simulation time point according to equation 9.4.

$$S_{\mathrm{i}} = \frac{\Delta Mass/Mass}{\Delta p_i/p_i} \tag{9.4}$$

Mass represents the nominal mass fraction of either Axin2+ or Axin2- hepatocytes at the new steady state and *ΔMass* is the deviation from nominal caused by the parameter change. The result is a parametric sensitivity, showing how the steady state of Axin2+ or Axin2- cells changes in response to a parameter change.

9.2.5 Non-parenchymal cell controllers

Non-parenchymal cell controllers were modelled as PI controllers with set points equal to the nominal Axin2+ or Axin2- populations. Controllers were tuned using the automatic tuning function in Simulink.

9.2.6 Model simulation

All simulations were carried out using Matlab and Simulink (Mathworks, Natick, MA).

9.3 Results

9.3.1 Feedback is required to maintain a steady state

We first tested the behavior of our model in the absence of feedback (Figure 9.1). In this scheme both Axin2+ and Axin2- hepatocytes can proliferate, and each has a constitutive apoptosis rate (Figure 9.1A and B). In addition, Axin2+ hepatocytes can

transform or differentiate to Axin2- hepatocytes. We used a phase-plane approach to investigate model behavior at steady-state and find that, in the absence of feedback, the initial condition is an unstable steady-state (Figure 9.1C). The system is unable to respond to a challenge and maintain homeostatic liver mass. For example, a transient apoptosis challenge results in a permanent decrease in the populations of both Axin2+ and Axin2- hepatocytes (Figure 9.1D and E). Therefore, feedback is required to maintain steady state.

A Model Schematic

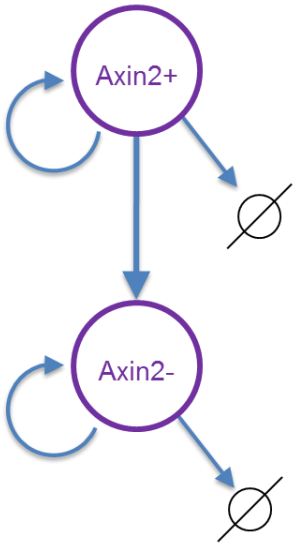

B Model Equations

$$dH^{A2+}/_{dt} = [H^{A2+}]\left(k_{prol}^{A2+} - k_{ap}^{A2+}\right) - [H^{A2+}](k_T k_P)$$

$$dH^{A2-}/_{dt} = [H^{A2+}](k_T k_P) + [H^{A2-}]\left(k_{prol}^{A2-} - k_{ap}^{A2-}\right)$$

C Steady-State Behavior Analysis

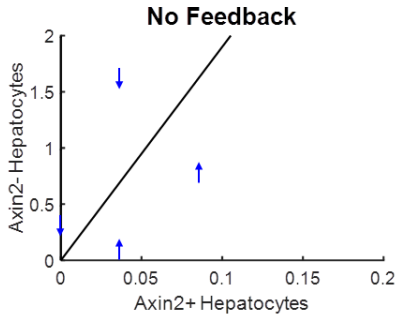

D Response to Transient Stress

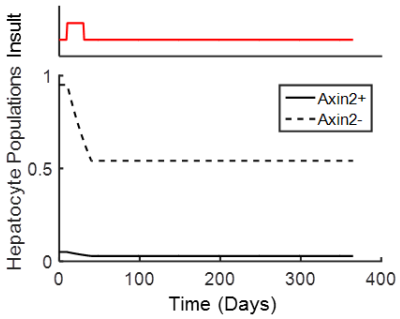

E Population Balance Response

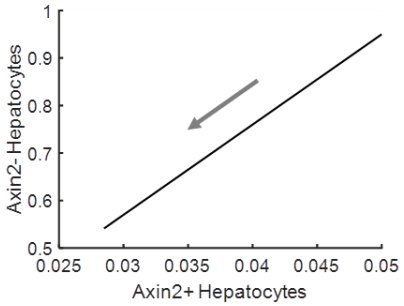

Figure 9.1 Homeostatic renewal model. (A) Model schematic showing two populations of hepatocytes: Axin2+ and Axin2-. Each population can replicate at a specific rate and each has a specific apoptosis rate. Axin2+ cells are able to transition to Axin2- cells, but not the reverse. (B) Equations governing model behavior. (C) Steady-state behavior of the model shown using phase plane. There are multiple steady states but no stable attractor. Blue arrows represent the sign of the local derivative in the y-direction, red arrows represent the sign of the local derivative in the x-direction. (D) In response to a transient stress, like increased apoptosis rate, the system shifts to a new steady-state. (E) Phase-plane representation of model behavior in response to a transient apoptosis stress shows the transition to a new state.

9.3.2 Different types of feedbacks result in different system dynamics

We investigated four potential feedback mechanisms that could confer stability to the system. We chose to investigate feedbacks that simulated different classes of biological processes rather than multiple types of feedback within a biological class (i.e. Michaelis-menton type feedback on cell proliferation vs. Hill-type feedback).

9.3.2.1 Capacity constraint OR implicit competition within hepatocyte populations (Model A)

In this scheme, hepatocytes within a subpopulation compete for limited resources, potentially including nutrients, space, or cofactors. Such competition for limited resources can be simulated using the logistic growth equation (Equations 9.5 and 9.6).

$$\frac{dH^{A2+}}{dt} = [H^{A2+}]k_{prol}^{A2+}\left(1 - \frac{[H^{A2+}]}{K_{cap}^{A2+}}\right) - [H^{A2+}]k_{ap}^{A2+} - [H^{A2+}](k_T) \quad (9.5)$$

$$\frac{dH^{A2-}}{dt} = [H^{A2+}](k_T) + [H^{A2-}]k_{prol}^{A2-}\left(1 - \frac{[H^{A2-}]}{K_{cap}^{A2-}}\right) - [H^{A2-}]k_{ap}^{A2-} \quad (9.6)$$

Where K_{cap}^{A2+} and K_{cap}^{A2-} are the carrying capacities for Axin2+ and Axin2- hepatocytes, respectively. Steady-state analysis of this model shows that there are three potential steady-states (1) the trivial state where all hepatocytes have died, (2) the initial condition steady state, and (3) a steady state where all Axin2+ hepatocytes have died, but Axin2- hepatocytes are able to repopulate the liver at a lower mass (Figure 9.2A).

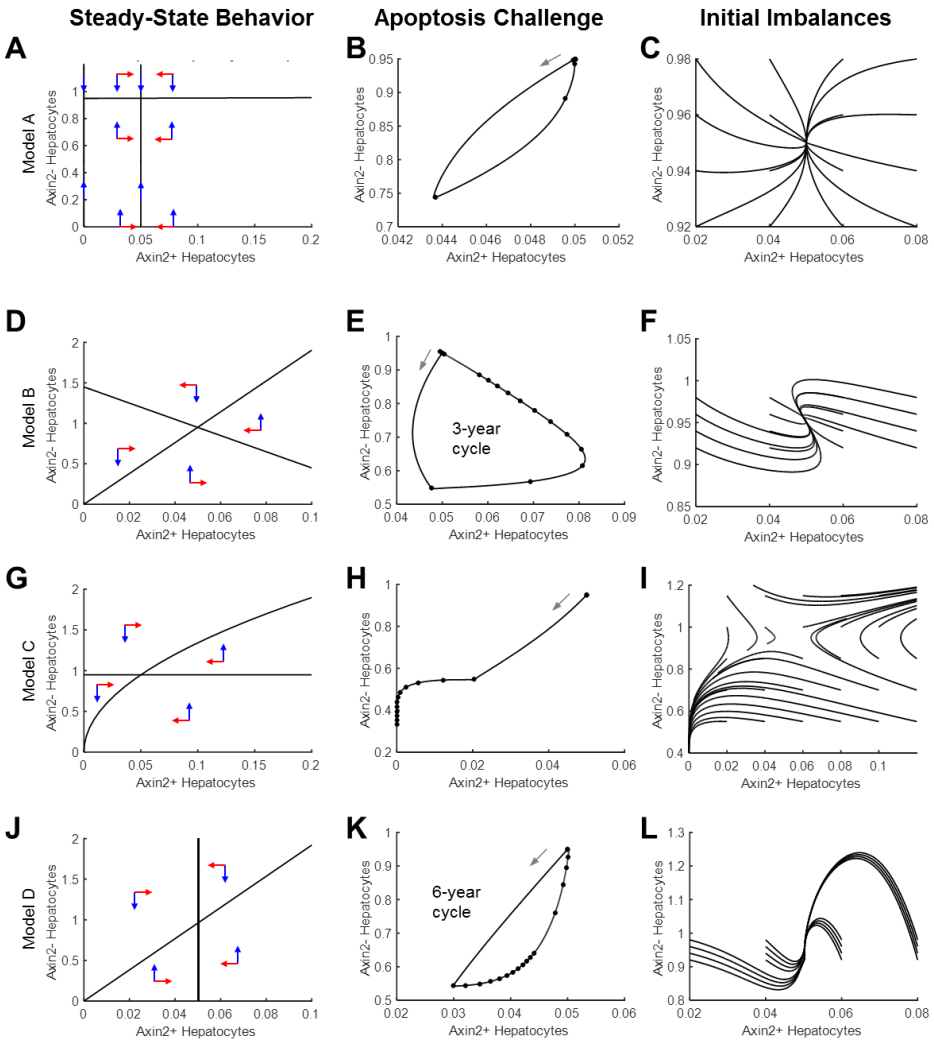

Figure 9.2 Response to stressors (A) Response of Model A increased apoptosis (left column), increased proliferation (middle column), and initial imbalanced populations (right column). (B) Response of model B. (C) Response of Model C. (D) Response of model D. Points represent t = 0 days, 10, 40, and 60 days then every 30 days until 1 year, then points represent each subsequent year. Gray arrows represent the direction of motion on the phase plane.

This third steady state may correspond to homeostatic renewal in patients who have had a liver transplant and now suffer from small-for-size syndrome, such as

recipients from older liver donors (Ono et al, 2011b). If pericentrally clustered Axin2+ hepatocytes are lost during the transplant, it might be possible that liver zonation would be dysregulated as well. In such patients we might expect to see impaired metabolic functions consistent with imbalances in liver zonation. A transient apoptotic challenge to this model results in relatively small hepatocyte loss and recovery in approximately 50 days after the challenge ends (Figure 9.2B). In healthy subjects, the initial condition is a stable steady-state (Figure 9.2C).

9.3.2.2 Product inhibition of proliferation OR negative feedback of differentiated cells on "stem-cell-like" cells (Model B)

In this scheme, proliferation of Axin2+ hepatocytes slows down as liver mass increases according to equations 9.7 and 9.8.

$$\frac{dH^{A2+}}{dt} = [H^{A2+}]k_{prol}^{A2+}\left(\frac{k_{env}^{P}}{[H^{A2+}]+k_A[H^{A2-}]}\right) - [H^{A2+}]k_{ap}^{A2+} - [H^{A2+}](k_T) \quad (9.7)$$

$$\frac{dH^{A2-}}{dt} = [H^{A2+}](k_T) + [H^{A2-}]k_{prol}^{A2-} - [H^{A2-}]k_{ap}^{A2-} \quad (9.8)$$

Where k^{P}_{env} is the microenvironment effect on proliferation parameter, which tells the relative effect of the microenvironment on Axin2+ cell proliferation compared to the effect of cell populations. k_A is the area parameter, which tells the relative contribution of H^{A2-} cells to impaired Axin2+ proliferation compared to H^{A2+} cells. The value of k_A was set to 0.1 because we reasoned that H^{A2+} cells have a larger proportional feedback on their own proliferation than H^{A2-} cells.

Model B has only one steady state, which is at the initial condition (Figure 9.2D). A transient apoptotic event leads to a relatively high hepatocyte loss that takes approximately 3 years to fully recover (Figure 9.2E). This steady state is stable, and starting with any population imbalance will result in a return to balanced levels

(Figure 9.2F). Axin2+ hepatocyte renewal occurs prior to Axin2- renewal, and in some cases there is an overshoot of Axin2+ populations above the steady-state.

9.3.2.3 Product inhibition of cell transitions OR Axin2+ maintenance microenvironment signaling saturation (Model C)

This scheme corresponds to the case where a signal from the microenvironment or lack of signal induces transition of hepatocytes from an Axin2+ state to an Axin2- state. Here as Axin2- cell populations build up, the transition signal (k^T_{env}) is diluted and the observed transition rate decreases according to equations 9.9 and 9.10.

$$\frac{dH^{A2+}}{dt} = [H^{A2+}]k_{prol}^{A2+} - [H^{A2+}]k_{ap}^{A2+} - [H^{A2+}](k_T)\left(\frac{k_{env}^T}{[H^{A2-}]}\right) \quad (9.9)$$

$$\frac{dH^{A2-}}{dt} = [H^{A2+}](k_T)\left(\frac{k_{env}^T}{[H^{A2-}]}\right) + [H^{A2-}]k_{prol}^{A2-} - [H^{A2-}]k_{ap}^{A2-} \quad (9.10)$$

We evaluated this model for stability and find that there is a single steady-state at the initial condition (Figure 9.2G) but it is an unstable steady-state (Figure 9.2H and I). We explored whether this instability is the result of the specific functional form used by re-performing the stability analysis using Hill-type inhibition with Hill coefficients between 1 and 3. We find that the instability remains regardless of the functional form of the feedback (Figure 9.3). Therefore, it is unlikely that product inhibition of cell transitions alone governs liver homeostatic renewal.

Model Equations

$$dH^{A2+}/_{dt} = [H^{A2+}](k_{prol}^{A2+} - k_{ap}^{A2+}) - [H^{A2+}](k_T)\left(\frac{{k_{env}^T}^n}{{k_{env}^T}^n + [H^{A2-}]^n}\right)$$

$$dH^{A2-}/_{dt} = [H^{A2+}](k_T)\left(\frac{{k_{env}^T}^n}{{k_{env}^T}^n + [H^{A2-}]^n}\right) + [H^{A2-}](k_{prol}^{A2-} - k_{ap}^{A2-})$$

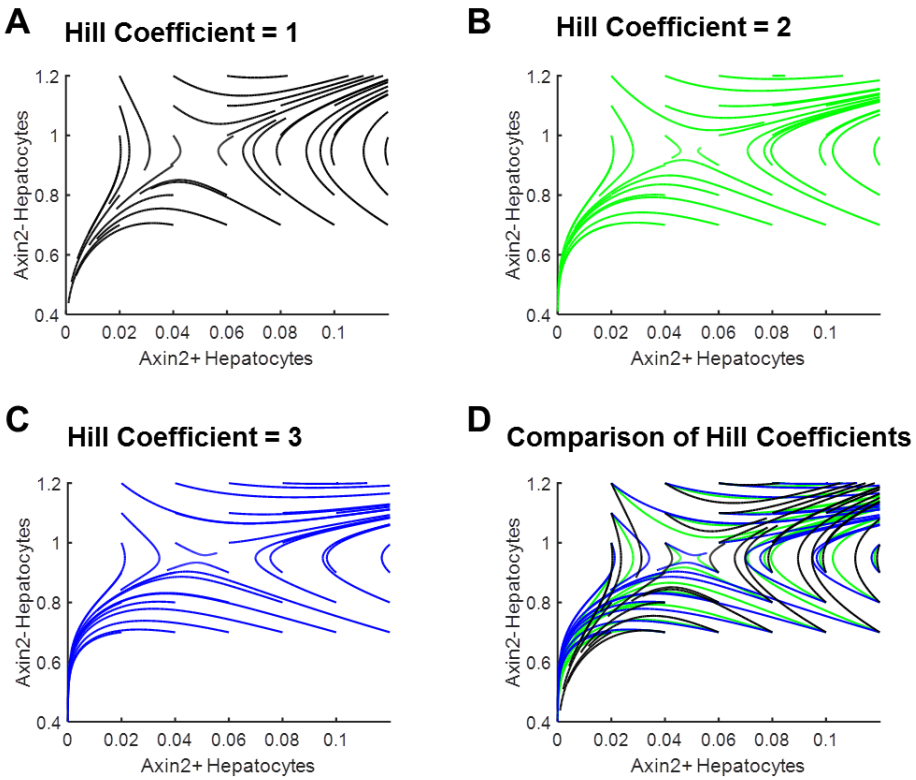

Figure 9.3 A different specific form of the feedback on the transition rate (Model C) gives rise to similar systems behavior. We investigated how a Hill-type inhibition would affect system behavior. We show that Hill coefficient of (A) one, (B) two, or (C) three give rise to similar system behavior (D). In addition, this unstable steady state is similar to that seen using a simpler inhibition term (See Figure 9.2F).

9.3.2.4 Exogenous populations supplying Axin2+ populations or stem cell-led renewal (Model D)

The most widely studied process in homeostatic renewal in multiple organs is stem cell-led renewal, although some organs like the pancreas renew by self-duplication rather than by stem cell differentiation (Dor et al, 2004;Poss, 2010;Ritsma et al, 2014). In the liver it is widely recognized that self-duplication governs homeostatic renewal; however, there may still be a role for stem cell renewal (Kopp et al, 2016;Miyajima et al, 2014). We simulated the effect of an exogenous populations of cells supplying the Axin2+ hepatocyte population using an inverse exponential function, Equations 9.11-13.

$$\frac{dH^{A2+}}{dt} = [H^{A2+}]k_{prol}^{A2+} - [H^{A2+}]k_{ap}^{A2+} - [H^{A2+}](k_T) + f([H^{A2+}]) \quad (9.11)$$

$$\frac{dH^{A2-}}{dt} = [H^{A2+}](k_T) + [H^{A2-}]k_{prol}^{A2-} - [H^{A2-}]k_{ap}^{A2-} \quad (9.12)$$

$$f([H^{A2+}]) = k_{Renew}\left(\frac{1}{1+\exp(C_1*[H^{A2+}]+C_2)}\right) \quad (9.13)$$

Where the parameters for the exponential function were chosen so that at steady-state there is no contribution of the exogenous populations to Axin2+ cells but there is an exponentially increasing contribution of the exogenous cells to renewal when Axin2+ populations fall below a certain threshold (in our model this threshold is ~4% of liver mass).

It should be noted that the exogenous population does not have to refer only to stem cells. Research from Dr. Forbes' lab as well as from other labs has shown that stem cells can be an important contributor of cell renewal, but they are far from the only one (Fausto & Campbell, 2003). Research suggests that other exogenous cell types may contribute to liver renewal, including hybrid hepatocytes (Baldo et al, 2010;Font-Burgada et al, 2015;Thorgeirsson & Grisham, 2006), transformation of

biliary cells into hepatocytes and vice versa (Michalopoulos et al, 2005;Yanger et al, 2013), and mesenchymal to epithelial transition of hepatic stellate cells into hepatocytes (Choi & Diehl, 2009;Yang et al, 2008). Any of these mechanisms could contribute to the effect of an exogenous cell population on homeostatic renewal.

We find that this model also displays a stable steady-state at the initial condition (Figure 9.2J). Following an apoptotic challenge, the liver is able to recover but recovery takes a relatively long time (Figure 9.2K). When deviations from the steady-state were small, there is an asymmetric dynamic response to return to steady-state (Figure 9.2L). When deviations became larger, however, the system responds asymmetrically with low Axin2+ cell populations recovering in a more direct manner than high Axin2+ cell populations.

9.3.2.5 Timing of recovery from an insult

In addition to showing different behavior trajectories on a phase plane, each individual feedback results in different recovery time following an insult. Model A recovers from a transient insult the most quickly (< 1 year to recover from 30 days of increased apoptosis or proliferation), followed by model B (3 years to recover from each), then model D (6 years to recovery from increased apoptosis and 15 years to recover from increased proliferation) (Figure 9.4). Model C does not recover from either challenge.

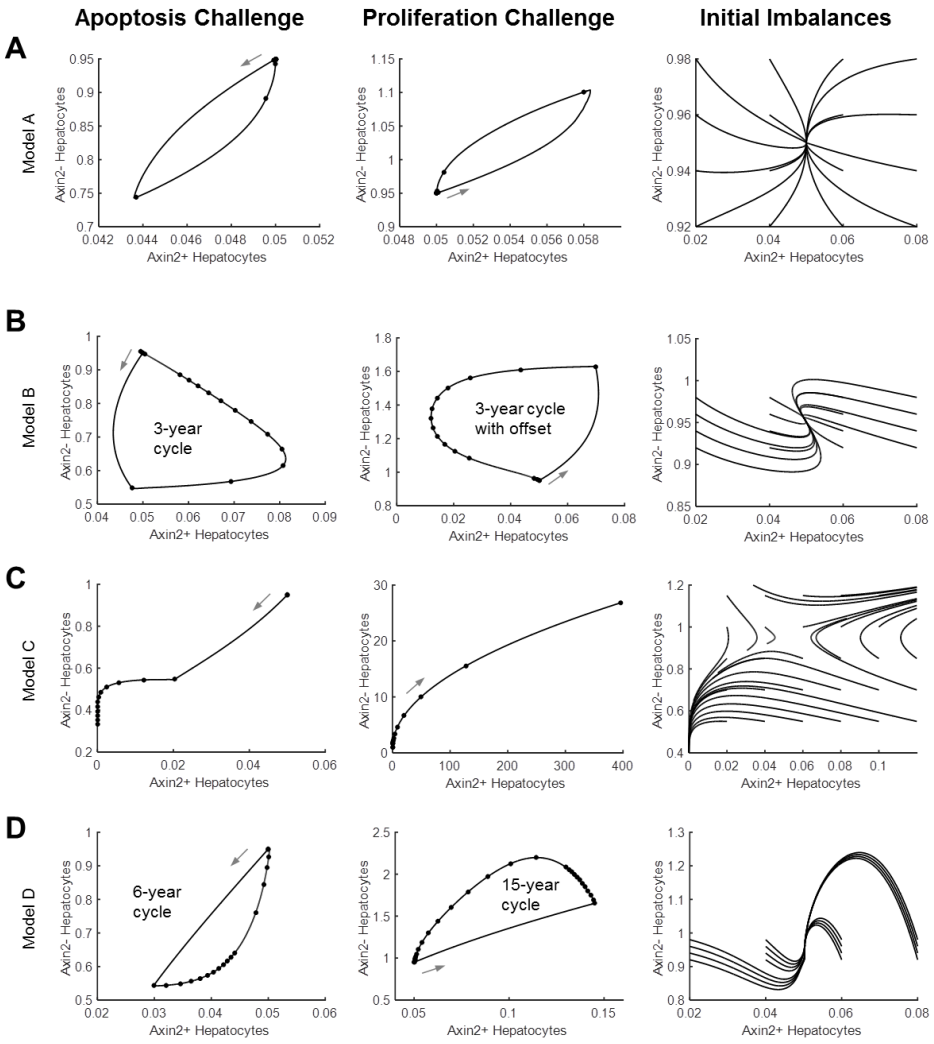

Figure 9.4 Response to stressors (A) Response of Model A increased apoptosis (left column), increased proliferation (middle column), and initial imbalanced populations (right column). (B) Response of model B. (C) Response of Model C. (D) Response of model D. Points represent t = 0 days, 10, 40, and 60 days then every 30 days until 1 year, then points represent each subsequent year. Gray arrows represent the direction of motion on the phase plane.

We further find that, for model A, the distance between the carrying capacity of each population and the steady-state values influences the magnitude of the

response to disturbance. When the deviation between carrying capacity and steady-state value is large, the response to disturbance is large as well. In contrast, when steady-state cell populations are already close to the carrying capacity, there is a smaller response to insult (Figure 9.5).

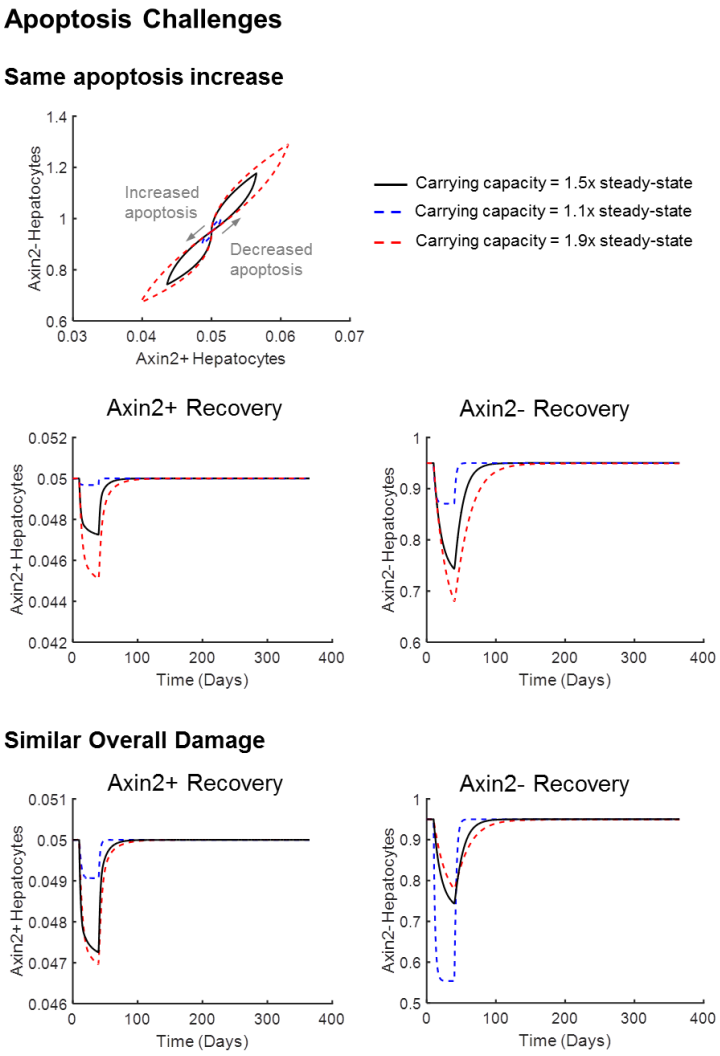

Figure 9.5 Effect of carrying capacity on response to transient apoptosis challenges. As carrying capacity increases above the steady-state population balances, the system response to disturbances increases as well. Gray arrows represent the direction of motion on the phase plane.

9.3.2.6 Parameter selection

For each of these models, parameters had to be constrained to slightly different values to allow for a steady state at the initial conditions. All model parameter values can be found in Table 9.1.

9.3.3 Combinations of feedback result in a system that is robust to multiple biological challenges/disturbances

From an evolutionary point of view, having a system able to respond to many challenges (optimized for robustness) is more favorable than having an efficient system that is not able to respond to challenges well (optimized for efficiency). In biology, there are many systems that appear to be optimized for robustness including protein coding (Goymer, 2007), DNA repair (Friedberg et al, 2005), and even whole transcriptional systems (Laranjeiro & Whitmore, 2014). We reason that the homeostatic renewal process in the liver would be optimized for robustness to disturbances, allowing the liver to maintain a steady mass even in the face of a toxic challenge. We therefore investigated which combination of feedbacks shows the most robust recovery following multiple types of challenges. We call the resulting model the "robust model" and use it for subsequent analyses.

We used a systematic design of experiment-based (DOE) approach to explore all possible combinations of model feedbacks to find the robust model. We used a 2^4 full factorial design where each feedback was a factor with two levels: on (1) or off (0). We then simulated a transient (30 day) increase in apoptosis, decrease in apoptosis, increase in proliferation, and decrease in proliferation and measured the

system response. The metric we used to evaluate model response to multiple individual disturbances is given in equations 9.14 and 9.15. Results of the DOE simulations are shown in Table 9.2.

$$Recovery\ Volume = \sum_{i=1}^{disturbances} \int dH^{A2+} * \int dH^{A2-} * \int dt \tag{9.14}$$

$$Robustness = \frac{1}{Recovery\ Volume} \tag{9.15}$$

Where there are four disturbances, and the recovery volume for each disturbance is the hypercube of deviation in the H^{A2+} and H^{A2-} space multiplied by recovery time.

Table 9.2 DOE Results – A low recovery score indicates an overall lower recovery volume and more robust performance

Design of Experiment Results [$\log_{10}$(Recovery Volume)]

Std Order	Model A	B	C	D	Increased Apoptosis	Decreased Apoptosis	Increased Proliferation	Decreased Proliferation	Total Recovery Volume
1	0	0	0	0	4.98	5.70	6.41	5.37	6.53
2	1	0	0	0	1.93	1.30	1.01	2.51	2.64
3	0	1	0	0	5.70	5.99	5.98	5.74	6.48
4	1	1	0	0	1.74	1.12	0.89	2.32	2.45
5	0	0	1	0	5.75	79.25	80.01	5.75	80.08
6	1	0	1	0	2.08	1.41	1.07	2.59	2.74
7	0	1	1	0	5.22	5.89	5.86	5.38	6.28
8	1	1	1	0	1.74	1.18	0.94	2.36	2.48
9	0	0	0	1	6.64	7.96	5.54	6.75	8.01
10	1	0	0	1	1.86	1.22	1.02	2.47	2.60
11	0	1	0	1	5.74	6.22	6.19	5.78	6.64
12	1	1	0	1	1.62	1.07	0.83	2.27	2.39
13	0	0	1	1	5.18	79.25	79.96	5.18	80.04
14	1	0	1	1	2.04	1.36	1.08	2.56	2.70
15	0	1	1	1	5.19	5.89	5.88	5.32	6.28
16	1	1	1	1	1.63	1.11	0.91	2.31	2.43

In addition to performing the DOE using nominal parameter values, we also varied parameter values to simulate how robust the model is to slight deviations in parameters corresponding to potentially different regulation of homeostatic renewal in different patients. We created 9 additional parameter sets by sampling each parameter from a normal distribution with a mean at the parameter's nominal value and a standard deviation of 1% of the nominal value. We then re-performed the full 2^4 DOE for each parameter set. This approach allows us to find a model that is robust to

physiological and parametric disturbances. It also allows us to use ANOVA to analyze which feedback mechanisms affect model behavior significantly.

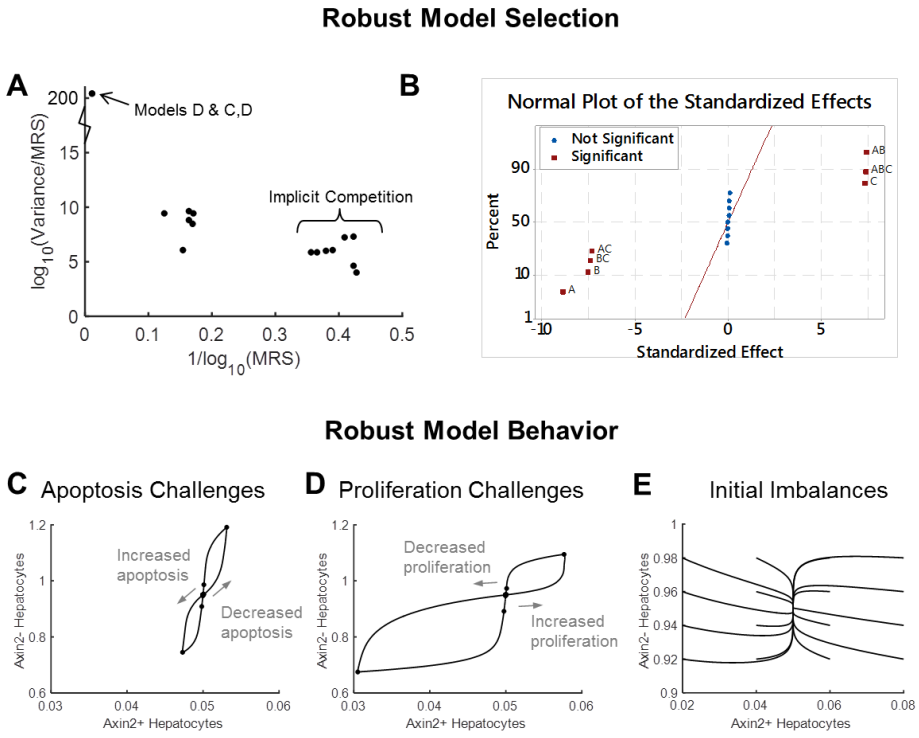

Figure 9.6 Selection of the "Robust model" of homeostatic renewal for further analysis. (A) Robustness of system response to multiple transient disturbances and variance in the response in simulated patients with altered physiological parameters. The systems that responded with the smallest deviation (highest robustness) also show the smallest normalized variance in response to altered parameters. (B) ANOVA shows that feedbacks A, B, and C are significant as are their interactions. Feedback D and its interactions do not affect model output significantly. (C) Robust model (Model A+B+C) response to transiently increased and transiently decreased apoptosis. (D) Robust model response to transiently increased and transiently decreased proliferation. (E) Robust model response to initial population imbalances shows that multiple starting conditions converge on a steady-state. Points represent t = 0 days, 10, 40, and 60 days then every 30 days until 1 year, then points represent each subsequent year. Gray arrows represent the direction of motion on the phase plane. MRS is the Mean Recovery Score, which is the sum of the recovery volumes for all disturbances.

We find that the combination models that included implicit competition (Model A) are able to recover from physiological disturbances with the most robustness and lowest variance caused by parametric changes (Figure 9.6A). Our ANOVA results show that all combinations of feedbacks A (implicit competition), B (product inhibition of proliferation), and C (product inhibition of transitions) are significant but feedback D (exogenous populations) is not significant (Figure 9.6B). We therefore include in our robust model all feedbacks except feedback from exogenous populations, according to equations 9.16 and 9.17.

$$\frac{dH^{A2+}}{dt} = [H^{A2+}]k_{prol}^{A2+}\left(1 - \frac{[H^{A2+}]}{K_{cap}^{A2+}}\right)\left(\frac{k_{env}^{P}}{[H^{A2+}]+k_A[H^{A2-}]}\right) - [H^{A2+}]k_{ap}^{A2+} - [H^{A2+}](k_T)\left(\frac{k_{env}^{T}}{[H^{A2-}]}\right) \quad (9.16)$$

$$\frac{dH^{A2-}}{dt} = [H^{A2+}](k_T)\left(\frac{k_{env}^{T}}{[H^{A2-}]}\right) + [H^{A2-}]k_{prol}^{A2-}\left(1 - \frac{[H^{A2-}]}{K_{cap}^{A2-}}\right) - [H^{A2-}]k_{ap}^{A2-} \quad (9.17)$$

We were interested to see that the effect of product inhibition of cell transitions (Model C) by itself is to decrease model robustness but that it acts synergistically with implicit competition (Model A) and product inhibition of proliferation (Model B) to enhance model robustness to physiological disturbances. Implicit competition (Model A) and product inhibition of proliferation (Model B) show the opposite effect, where they each individually enhance robustness but their interaction term decreases robustness (Figure 9.6B).

We simulated the response of the robust model to apoptosis challenges (Figure 9.6C), proliferation challenges (Figure 9.6D), and imbalanced initial conditions (Figure 9.6E). We find that the robust model is able to recover from transient apoptosis and proliferation challenges with relatively small deviations in cell numbers

compared to individual feedbacks. Additionally, most of the recovery occurs in the first 20 days following the end of the challenge.

9.3.4 Systemic properties of homeostatic renewal revealed through model analyses

9.3.4.1 Sensitivity analyses show largely independent behavior of cell states

We investigated the parametric sensitivity of the model to changes in parameter values around the steady state. We find that each parameter showed a largely independent effect on each of the cell states (Figure 9.7A). The highest positive sensitivities are carrying capacity and proliferation rate for each cell type, but each parameter set seems to affect mainly its own cell type. This observation holds for the total effect index (TEI) calculated using a variance-based global sensitivity approach (Figure 9.7B). Additionally, the parametric sensitivity analysis shows that several of the model parameters have the same sensitivity values, suggesting that these parameters can be combined to allow for model reduction. We do not combine these parameters, however, because the physical meaning of the microenvironment parameters (k^T_{env} and k^P_{env}) makes them useful as control parameters. We also calculated the TEI for each parameter and find that steady state liver mass is most sensitive to cell population carrying capacities ($K_{Cap}{}^{A2+}$ and $K_{Cap}{}^{A2-}$) and apoptosis rate of Axin2- cells ($k_{ap}{}^{A2-}$). The parameter with the highest sensitivity is Axin2+ carrying capacity ($K_{Cap}{}^{A2+}$) followed by apoptosis rate of Axin2- cells ($k_{ap}{}^{A2-}$). Changing any of these parameters, for example $K_{Cap}{}^{A2-}$, results in changes to hepatocyte population balances before any insults and after recovery from a transient insult (Figure 9.7C). Our results suggest that overall liver mass can be viewed as being governed by a

balance between maintenance of “stem-cell-like” hepatocyte population and mature hepatocyte apoptosis.

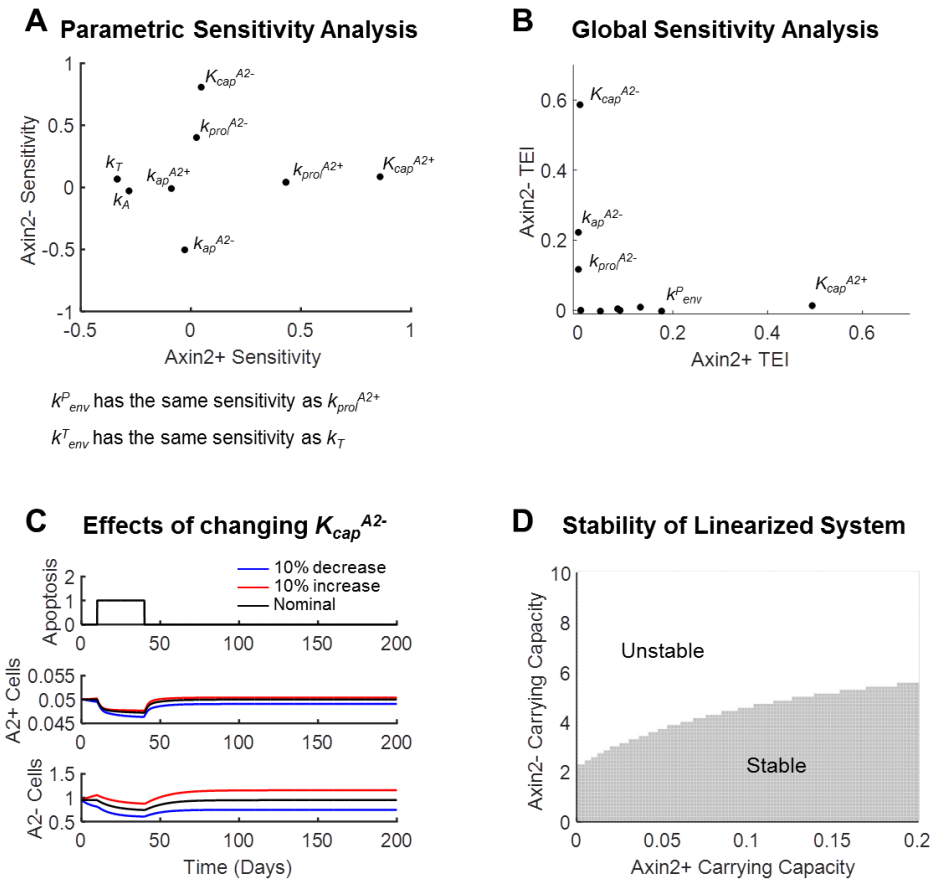

Figure 9.7 Model analyses of the robust model. (A) Parametric sensitivity analysis shows that model parameters tend to affect either Axin2+ steady-state populations or Axin2- steady-state populations. Carrying capacity and proliferation rate have the large effects on cell populations, as does the apoptosis rate of Axin2- cells. (B) Variance-based global sensitivity estimates corroborate the findings from the parametric sensitivity analysis, suggesting that population levels of each hepatocyte state are affected by their individual governing parameters. (C) The effect of changing Axin2- carrying capacity in the absence of other changes on overall liver mass. (D) Increasing the carrying capacities of Axin2+ and Axin2- hepatocytes can lead to an unstable system.

9.3.4.2 Stability analysis shows a co-ordination between model responsiveness to disturbances and stability

We next linearized the model to estimate model stability. The individual equations making up the Jacobian are shown below (Equations 9.18-21).

$$\frac{d}{dH^+}\left(\frac{dH^+}{dt}\right) = \frac{k_{prol}^{S}[WNT]\left(1-\frac{H_0^S}{K_{Cap}^S}\right)}{H_0^S+k_A H_0^m} - \frac{H_0^S k_{prol}^{S}[WNT]\left(1-\frac{H_0^S}{K_{Cap}^S}\right)}{\left(H_0^S+k_A H_0^m\right)^2} - \frac{H_0^S k_{prol}^{S}[WNT]\left(1-\frac{H_0^S}{K_{Cap}^S}\right)}{K_{Cap}^S\left(H_0^S+k_A H_0^m\right)} - \mathrm{k_{ap}^{s}} - \frac{\mathrm{k_T}}{[\mathrm{WNT}]\mathrm{k_A H_0^m}} \quad (9.18)$$

$$\frac{d}{dH^-}\left(\frac{dH^+}{dt}\right) = \frac{H_0^S k_T}{[WNT]H_0^{m2}} - \frac{[WNT]H_0^S k_{prol}^{S}\left(1-\frac{H_0^S}{K_{cap}^S}\right)k_A}{\left(H_0^S-k_A H_0^m\right)^2} \quad (9.19)$$

$$\frac{d}{dH^+}\left(\frac{dH^-}{dt}\right) = \left(\frac{1}{[WNT]}\right)\left(\frac{k_T}{H_0^m}\right) \quad (9.20)$$

$$\frac{d}{dH^-}\left(\frac{dH^-}{dt}\right) = k_{prol}^{m} - k_{ap}^{m} - \frac{2k_{prol}^{m}}{K_{cap}^{m}}H_0^m - \frac{k_T H_0^S}{[WNT]H_0^{m2}} \quad (9.21)$$

Where H_0^{A2+} and H_0^{A2-} are the steady-state values of Axin2+ and Axin2- hepatocytes.

We then varied pairs of parameters and calculated the eigenvalues of the resultant Jacobian to identify parametric changes that result in unstable model behavior. We find that the only two model parameters able to induce instability in the model are the carrying capacities of Axin2+ and Axin2- cells (K_{cap}^{A2+} and K_{cap}^{A2-}). The system is stable for small carrying capacities, but unstable when the carrying capacities increase (Figure 9.7D). We are interested to see a co-ordination between model stability and responsiveness. As carrying capacities increase, the system responds to disturbances with a slower recovery rate (Figure 9.5) and across a certain threshold of carrying capacities the model becomes unstable (Figure 9.7D). This

behavior suggests a co-ordination between aggressiveness of response and stability of the system.

9.3.4.3 Frequency analysis shows that high insult frequencies impair systemic homeostatic renewal

We next simulated how a chronic insult would affect homeostatic renewal. We simulated apoptosis rate as a sinusoidal input at increasing frequencies and investigated the resulting behavior of Axin2+ and Axin2- hepatocytes. Figure 9.8 shows a representation the behavior of apoptosis rate over the course of one week at different frequencies.

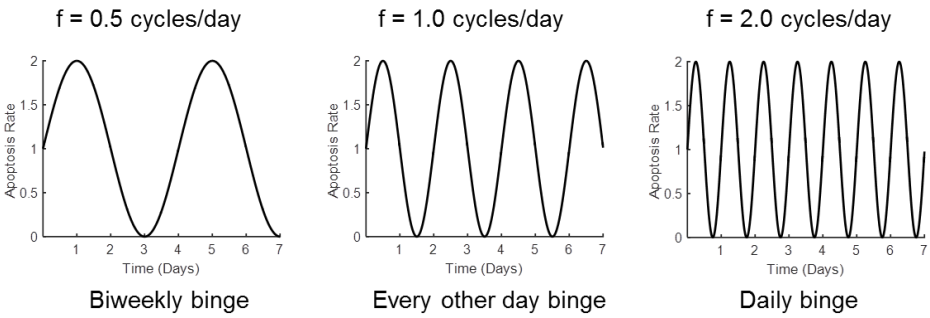

Figure 9.8 Visualizations of what frequencies mean with respect to one week. Each frequency is interpreted in the context of alcohol binges per week (leading to an increased apoptosis).

These frequencies can then be interpreted in the context of a common toxin introduced into the liver: alcohol. For example, a frequency of f = 2.0 cycles/day corresponds to a daily alcohol binge leading to a peak in apoptosis once per day (Figure 9.8). We investigated model response when Axin2+ hepatocytes are selectively targeted (Figure 9.9), when Axin2- hepatocytes are selectively targeted

(Figure 9.10), and when apoptosis rate of both cell populations change (Figure 9.11). In all cases, the system response to apoptosis challenges begins to become unstable at a frequency around 2.0 cycles/day (or a daily binge).

Toxic challenges likely do not cause a sinusoidal change to apoptosis but rather a transient increase in apoptosis rate while the toxin is active. We therefore simulated different frequencies of insult using step functions (Figure 9.12). We find that the system often falls into an attractor cycle that deviates from the steady-state following this type of insult. Furthermore, as the insult frequency increases, the system is less and less able to maintain a stable attractor state. It is possible that such a sustained deviation from healthy balances could contribute to disease progression in the face of steady insults, but more research is needed to explore this possibility.

The previous analysis shows the effect of changing the frequency of insult when total insult remained constant. Chronic diseases may result in a given insult magnitude at varying frequencies. Such an insult pattern would increase total damage at high frequencies. We investigated this type of insult and find that low frequency apoptotic events allow for system recovery, while higher frequencies do not allow for this recovery and result in attractor states below nominal levels (Figure 9.13). We also investigated the effects of changing the magnitude of damage per apoptotic event for a given frequency (Figure 9.14). We find that the qualitative phase behavior of the system is governed by the frequency of insult but that the magnitude of that response is based on the magnitude of insult.

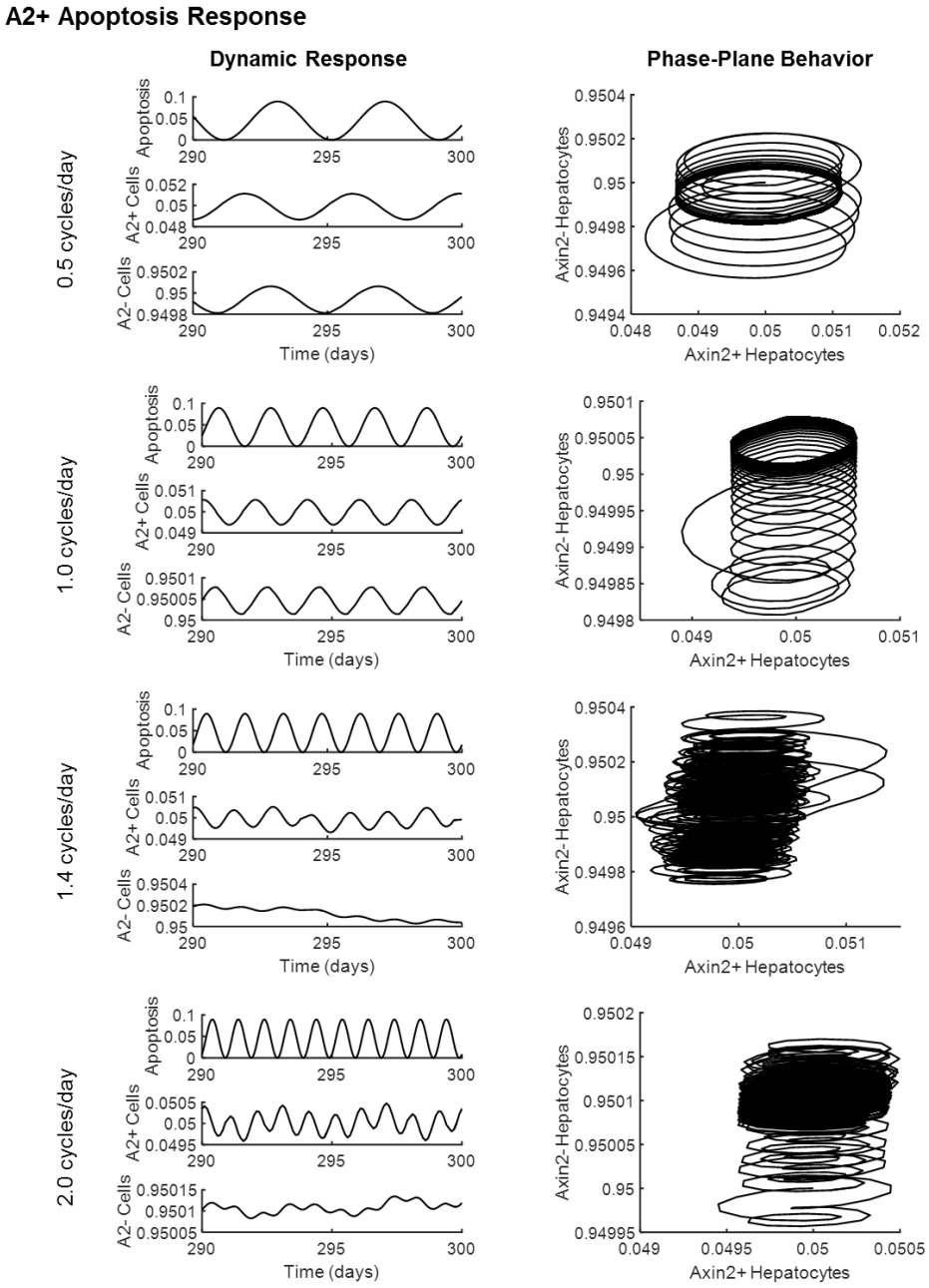

Figure 9.9 Simulating multiple Axin2+ apoptosis frequencies. At frequencies > 1.4 cycles/day (between binge drinking daily and every other day), the Axin2+ hepatocyte population begins to become unstable.

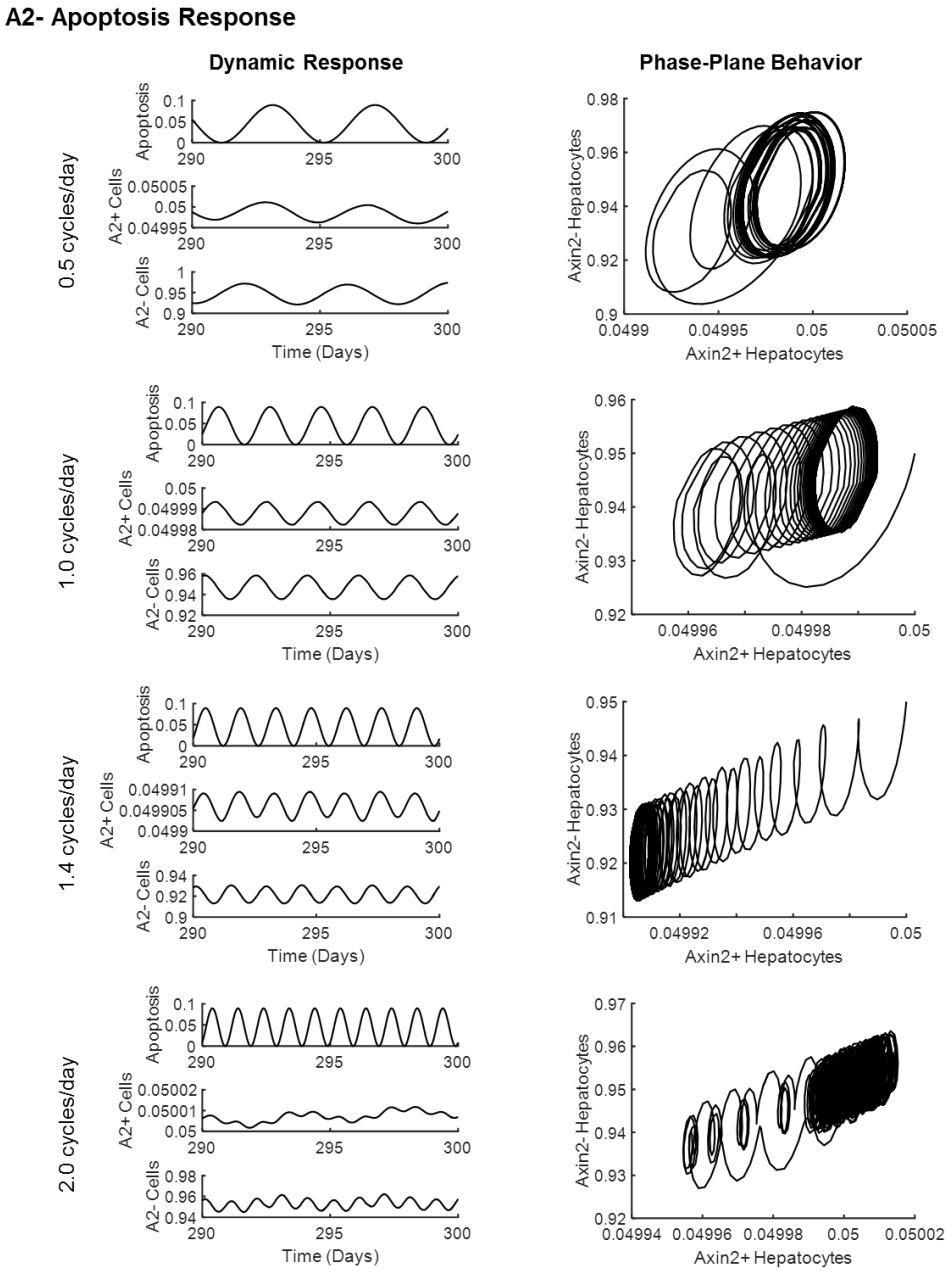

Figure 9.10 Simulating multiple Axin2- apoptosis frequencies. At frequencies > 2.0 cycles/day (between binge drinking daily), the Axin2- hepatocyte population begins to become unstable.

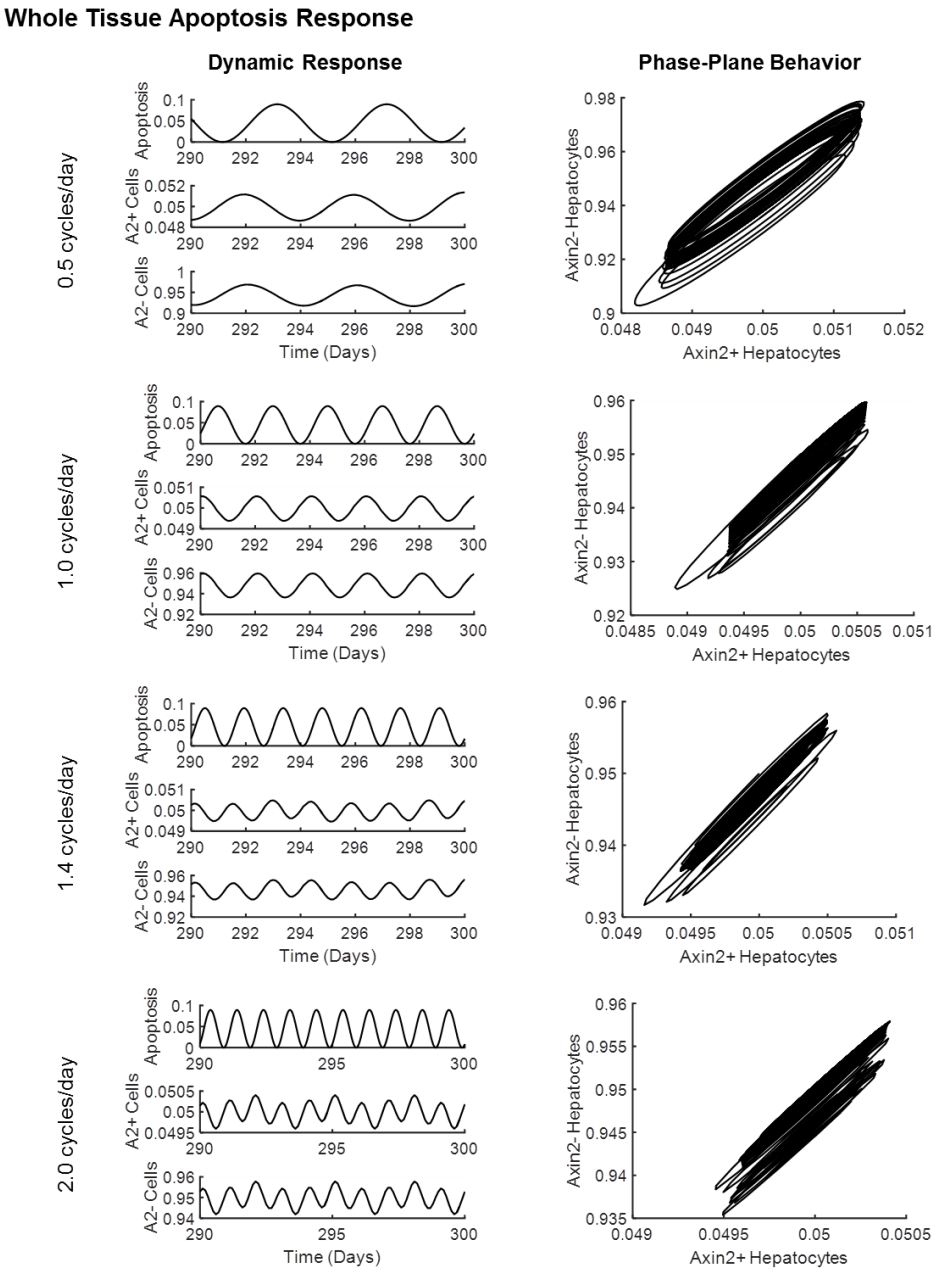

Figure 9.11 Simulating multiple whole liver apoptosis frequencies. At frequencies > 2.0 cycles/day (binge drinking daily), the Axin2+ and Axin2- hepatocyte populations begin to become unstable.

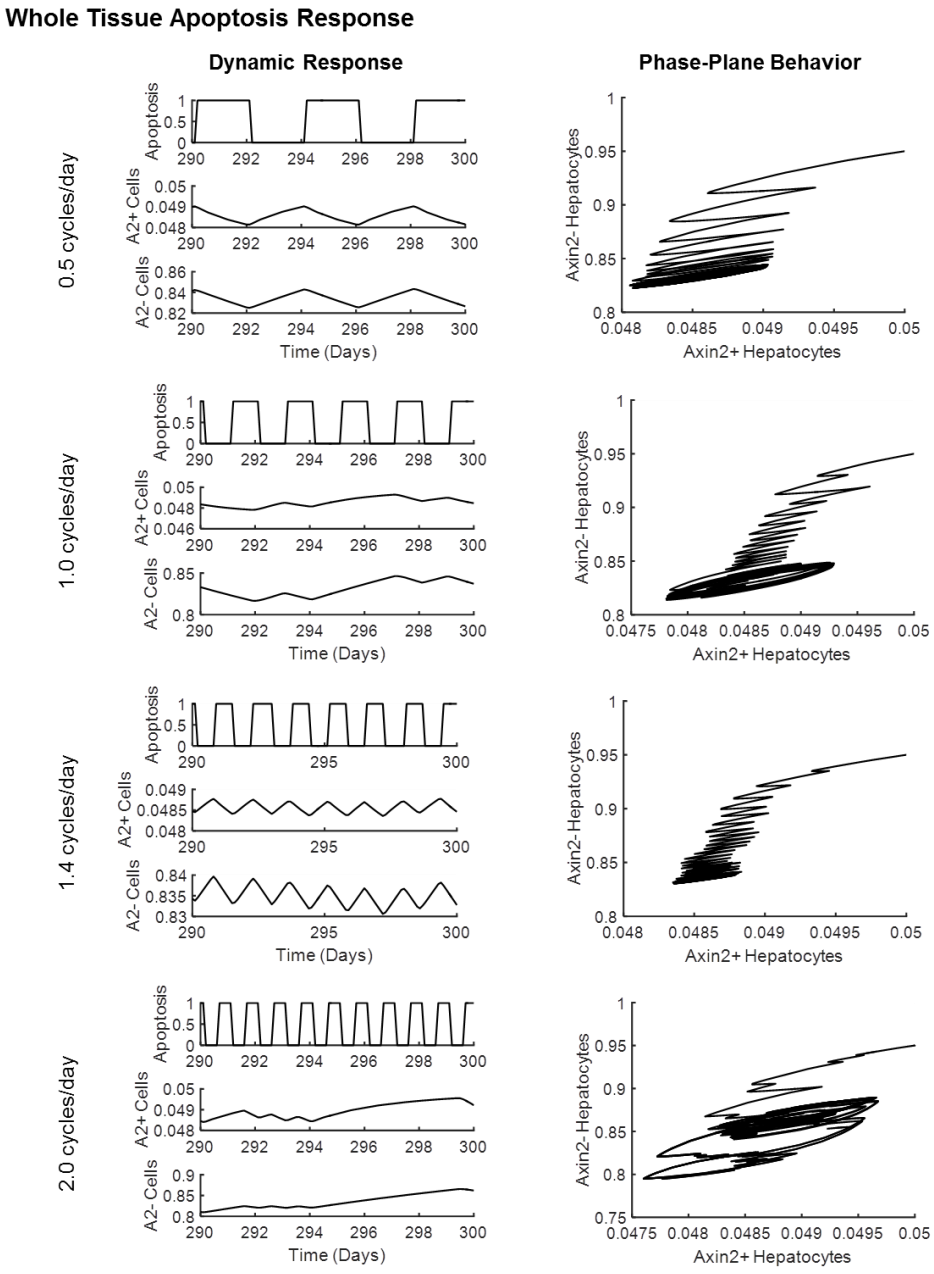

Figure 9.12 Simulating multiple whole liver apoptosis events. Apoptotic events likely follow a step-like function rather than a sinusoidal function. At low frequencies, the liver has a chance to recover between apoptotic events. At high frequencies (f ~ 2.0 cycles/day and above), the hepatocyte populations are unable to recover between events and population levels become unstable.

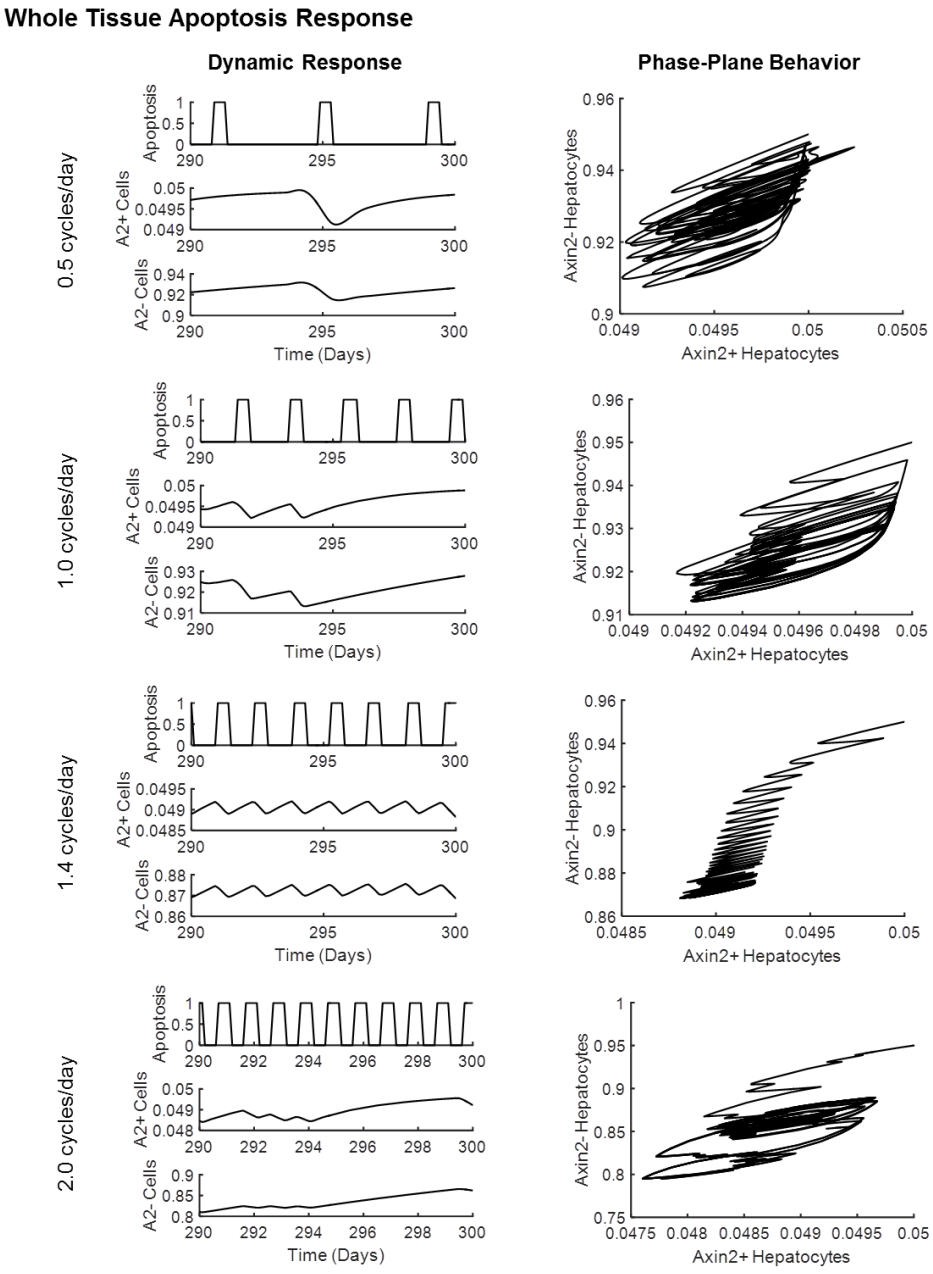

Figure 9.13 Simulating multiple whole liver apoptosis events. For a given amount of damage per event, the frequency of the event determines the overall damage to the tissue. Low frequency events allow for nearly complete recovery between apoptotic events, while high frequency events to not allow for this recovery.

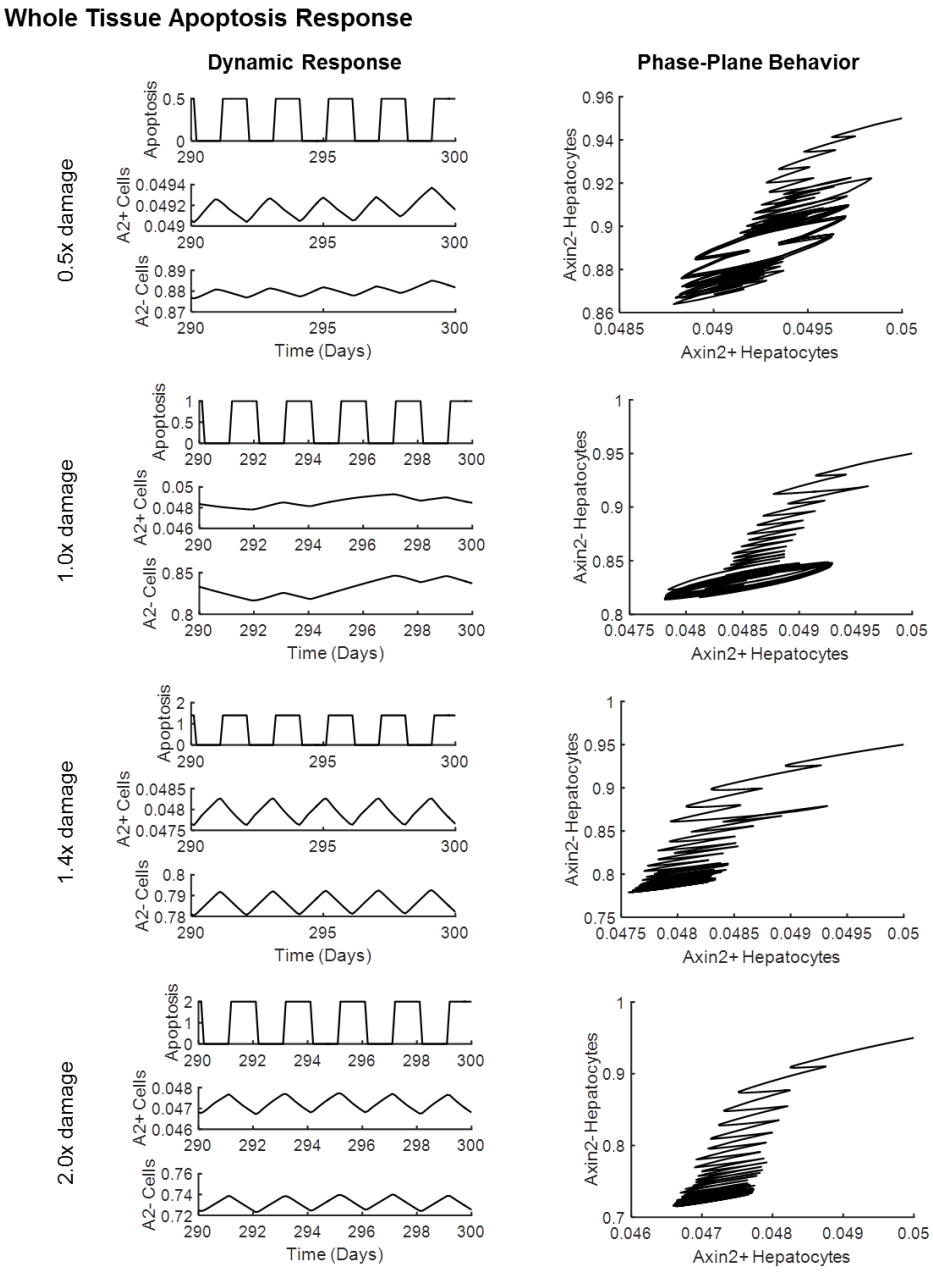

Figure 9.14 Simulating multiple whole liver apoptosis events. For a given frequency of damage (1.0 cycles per day in this figure), the damage per event changes homeostatic liver mass. The pattern of insult and recovery appears similar for all damage amounts. The stable populations of hepatocytes, however, become smaller with increasing damage amounts.

9.3.5 Model simulations capture behavior of induced hepatocyte senescence

Having developed a model of homeostatic renewal that is robust to individual, transient disturbances, we next investigated whether our model could capture experimentally observed behavior of liver homeostatic renewal. Under normal conditions, it has been shown that stem cells are not required for homeostatic renewal. Recent research from Dr. Forbes' lab, however, showed that stem cells are able to repopulate the liver when senescence is induced in hepatocytes (Wang et al, 2015b). In this study, hepatocyte senescence was induced using βNF. This treatment left approximately 99% of the hepatocytes in the liver unable to replicate, presumably both Axin2+ and Axin2- hepatocytes were affected. The livers were then dosed with βNF, to induce liver damage and subsequent regeneration. The livers of these mice had recovered their original mass by 90 days after toxin dosing. Cell lineage tracing was able to show that the new hepatocytes originated from stem cells.

We modified our model to be able to investigate the case of induced hepatocyte senescence. Our previous model analyses showed that, under normal conditions, stem cell proliferation does not have a significant effect on homeostatic renewal. We investigated the model response to challenges including and excluding stem cell renewal to ensure that model behavior is not significantly affected by including this term (Figure 9.15). As we expected, the inclusion of stem cell renewal does not cause changes to model response behavior or timing. We also included two additional populations of hepatocytes in our model senescent Axin2+ hepatocytes and senescent Axin2- hepatocytes. Senescent hepatocytes do not replicate, but senescent Axin2+ hepatocytes can still transition to senescent Axin2- hepatocytes. Model equations for the modified model are given below (Equations 9.22-25).

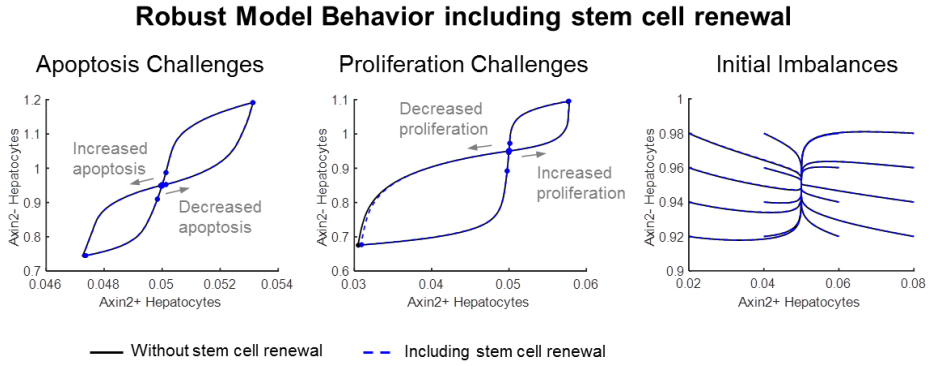

Figure 9.15 Comparison of the robust model response to disturbances with and without stem cell renewal. The addition of stem cell renewal does little to affect system behavior and response to transient individual disturbances. Points represent t = 0 days, 10, 40, and 60 days then every 30 days until 1 year, then points represent each subsequent year. Gray arrows represent the direction of motion on the phase plane.

$$\frac{dH^{A2+}}{dt} = [H^{A2+}]k_{prol}^{A2+}\left(1 - \frac{[H_{Tot}^{A2+}]}{K_{cap}^{A2+}}\right)\left(\frac{k_{env}^{P}}{[H_{Tot}^{A2+}]+k_A[H_{Tot}^{A2-}]}\right) - [H^{A2+}]k_{ap}^{A2+} - [H^{A2+}](k_T)\left(\frac{k_{env}^{T}}{[H_{Tot}^{A2-}]}\right) + +f([H_{Tot}^{A2+}]) \quad (9.22)$$

$$\frac{dH^{A2-}}{dt} = [H^{A2+}](k_T)\left(\frac{k_{env}^{T}}{[H_{Tot}^{A2-}]}\right) + [H^{A2-}]k_{prol}^{A2-}\left(1 - \frac{[H_{Tot}^{A2-}]}{K_{cap}^{A2-}}\right) - [H^{A2-}]k_{ap}^{A2-} \quad (9.23)$$

$$f([H_{Tot}^{A2+}]) = k_{Renew}\left(\frac{1}{1+\exp(C_1*[H_{Tot}^{A2+}]+C_2)}\right) \quad (9.24)$$

$$\frac{dH^{S}}{dt} = k_{ap}^{A2-}[H^{S}] \quad (9.25)$$

Where H^S are senescent hepatocytes, H_{Tot}^{A2+} is the sum of senescent and non-senescent Axin2+ hepatocytes ($[H^{A2+}]$ + 0.05x $[H^S]$), and H_{Tot}^{A2-} is the sum of senescent and non-senescent Axin2- hepatocytes ($[H^{A2-}]$ + 0.95x $[H^S]$). Both Axin2+ and Axin2- apoptosis rates are equal in our model, so we arbitrarily chose k_{ap}^{A2-} to use for senescent hepatocyte apoptosis rate in the following simulations.

Using this framework, we simulated homeostatic renewal following induced hepatocyte senescence in the absence of other insults and following a toxic injury to 40% of the liver (Figure 9.16).

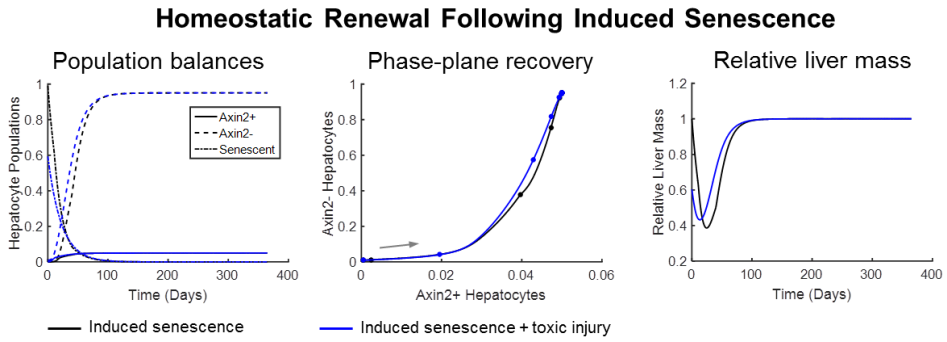

Figure 9.16 Homeostatic renewal recovers liver mass when hepatocytes in the liver become senescent coupled with a large apoptotic event. This model uses the robust model + stem cell renewal. Researchers from Dr. Forbes' lab showed complete renewal in 90 days post-injury, which our model also shows. No damage is shown in black, removal of 40% of the hepatocytes is shown in blue. Our model predicts that stem cells become active even without an additional apoptotic challenge and that the timeframe of recovery is slightly longer. Points represent t = 0 days, 10, 40, and 60 days then every 30 days until 1 year, then points represent each subsequent year. Gray arrows represent the direction of motion on the phase plane.

We find that constitutive apoptosis alone is enough to trigger stem cell renewal into Axin2+ hepatocytes followed by a repopulation of hepatocytes with non-senescent cells (Figure 9.16A, black lines). When no additional insult occurs, the liver fully recovers its replicating cells in approximately 120 days (Figure 9.16A, black lines), with Axin2+ hepatocytes beginning to recover more quickly followed by Axin2- hepatocytes (Figure 9.16B, black line). Our model simulations predict that a

significant amount of liver mass will be lost, however, prior to stem cells being able to repopulate enough replicating cells to overcome constitutive apoptosis (Figure 9.16C, black lines). When the additional insult of a 40% toxic shock is added to induce senescence, the liver responds in much the same way. Repopulation of the liver with replicating cells, however, begins more rapidly (Figure 9.16A, blue lines). Although the phase trajectory of recovery is similar between the two cases, adding an additional insult appears to speed recovery (Figure 9.16B, blue line). Simulations suggest that adding the additional insult decreases the maximum liver mass lost (45% remaining as opposed to 39%) and speed recovery time (90 days as opposed to 120 days) (Figure 9.16C, blue line). This simulated recovery time following dual insults matches the previously reported recovery time (Wang et al, 2015b).

9.3.6 Non-parenchymal cells act to enhance disturbance rejection

Our previous work investigating balances of hepatic stellate cell population balances in health and disease suggests that non-parenchymal cells contribute to the effects of chronic diseases though tuning the properties of the extracellular matrix and the molecular milieu of the microenvironment accessible to hepatocytes (for details, see Chapters 7 and 8). It is possible that such balances of non-parenchymal cells modulate not only regeneration but also homeostatic renewal. We postulate that such tuning of the liver's microenvironment could also contribute to the progression of chronic diseases. The structure of our homeostatic renewal model suggests two places where the non-parenchymal cell network could modulate homeostatic renewal dynamics (Figure 9.17A). The first is by modifying the tissue microenvironment local to the central vein. The effect of the pericentrally located non-parenchymal cell

network could be to modify the behavior of pericentral sinusoidal endothelial cells, leading to altered secretion of factors promoting Axin2+ cell renewal (WNT-2a and others).

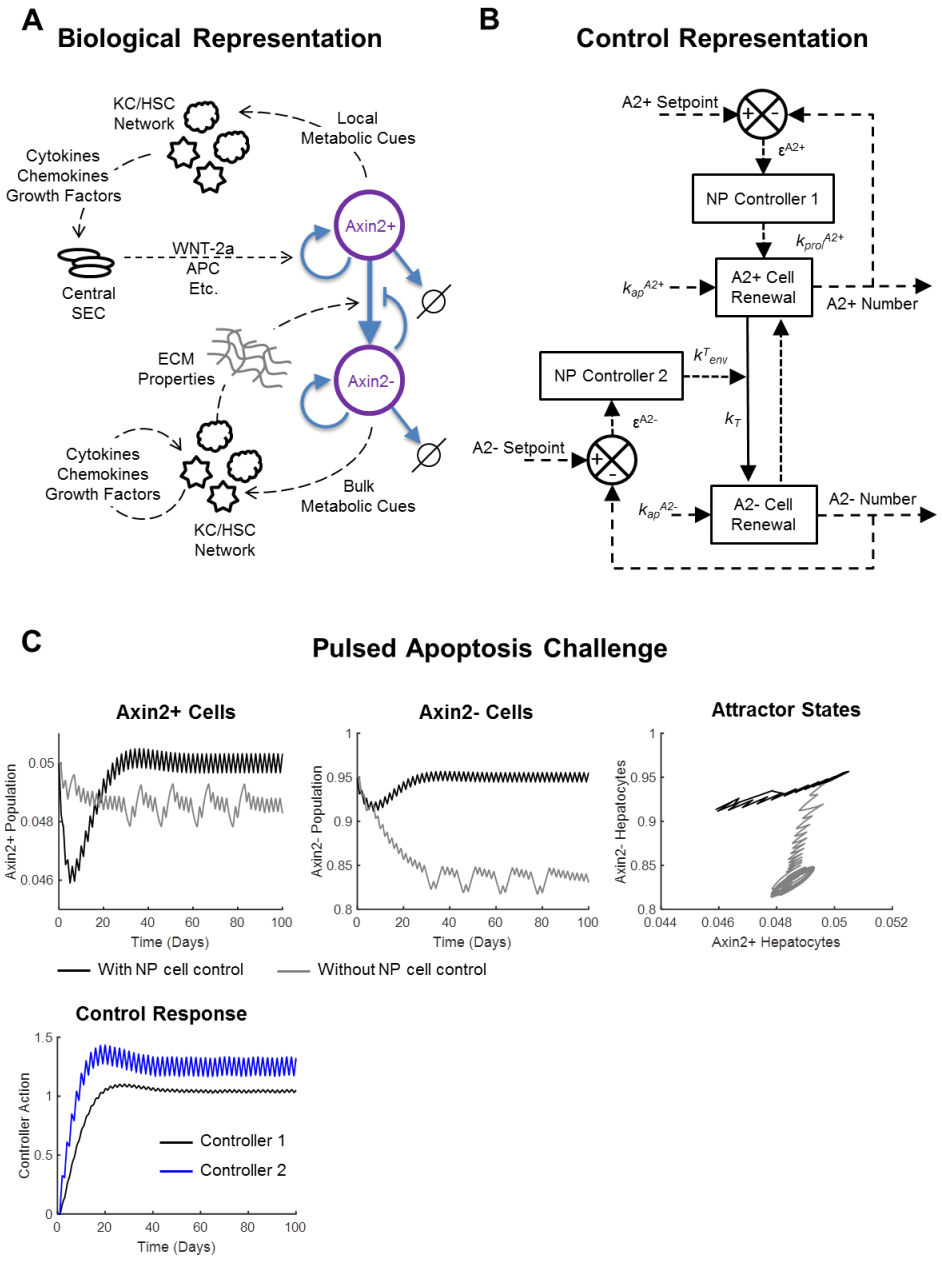
A
Biological Representation
KC/HSC Network
Local Metabolic Cues
Cytokines Chemokines Growth Factors
WNT-2a APC Etc.
Central SEC
Axin2+
Axin2-
ECM Properties
Cytokines Chemokines Growth Factors
Bulk Metabolic Cues
KC/HSC Network
B
Control Representation
A2+ Setpoint
NP Controller 1
A2+ Cell Renewal
A2+ Number
NP Controller 2
A2- Setpoint
A2- Cell Renewal
A2- Number
C
Pulsed Apoptosis Challenge
Axin2+ Cells
Axin2+ Population
Time (Days)
Axin2- Cells
Axin2- Population
Time (Days)
Attractor States
Axin2- Hepatocytes
Axin2+ Hepatocytes
With NP cell control
Without NP cell control
Control Response
Controller Action
Time (Days)
Controller 1
Controller 2

Figure 9.17 Non-parenchymal cell control of hepatocyte homeostatic renewal. (A) The biological process underlying the control system representation. (B) A control systems representation of liver homeostatic renewal controlled by non-parenchymal cell networks. In this representation, apoptosis rate increases and decreases are a disturbance to normal homeostatic renewal. (C) Ability of the non-parenchymal cell network controller to mitigate the effects of a periodic apoptosis challenge. Controller action causes an attractor state with minimal deviation around the steady-state. In the absence of non-parenchymal cell control, hepatocyte populations fall into an attractor cycle below steady-state levels.

The second way a non-parenchymal cell network could modulate homeostatic renewal is through changing the bulk properties of the liver's extracellular matrix thereby changing the transition rate of Axin2+ hepatocytes to Axin2- hepatocytes through altering the molecular diffusion of pro-transition and anti-transition molecules through the tissue. Non-parenchymal cell modulation of the tissue microenvironment adds an additional layer of control to the system such that the system has intrinsic stability plus external control to maintain tissue functional mass. A control system representation of this scheme is shown in Figure 9.17B. PI controllers were used to represent the NP cell networks. Tuned controller parameters are given in Table 9.3.

Table 9.3 Control system parameters

Controller	P	I	N
Central SEC	37.5	20.8	100
KC/HSC	15.9	2.5	100

Adding non-parenchymal cell control to the system allows for smaller overall deviation from steady state when homeostatic renewal is disturbed. Transient disturbances result in a deviation from nominal values at both the start and end of the

disturbance because the microenvironment has to return to normal following the end of the disturbance (Figure 9.18). The amount of deviation caused to Axin2+ cells is similar with and without non-parenchymal cell control. In contrast the deviation caused to Axin2- cells (which make up the bulk of the liver) is much lower when including non-parenchymal cell control in the model.

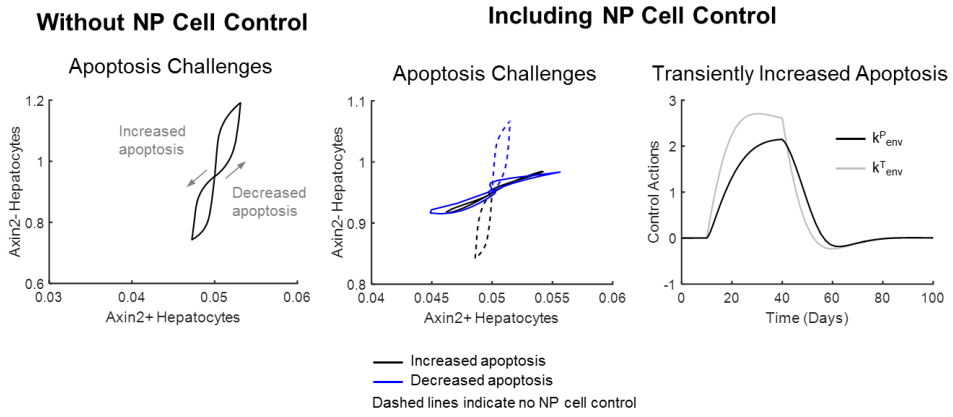

Figure 9.18 Non-parenchymal cell control of homeostatic renewal allows for disturbance rejection (faster recovery, smaller perturbations) compared to the case without external control. The control action of both controllers is similar for a transient increase in apoptosis, suggesting that the local non-parenchymal cell networks in the pericentral zone and in the bulk tissue respond following similar dynamics in response to an apoptotic challenge.

During a periodic pulsatile increase in apoptosis rate in the absence of non-parenchymal cell control, both Axin2+ and Axin2- hepatocyte populations oscillate within a limit cycle well below the healthy steady-state value (Figure 9.17C, gray lines). When non-parenchymal cell control is available to modulate renewal dynamics, however, there is a transient decrease in cell population numbers that recover after

approximately 30 days. Following this transient decrease, cell populations oscillate in a limit cycle near the steady state (Figure 9.17C, gray lines). The control action necessary to drive the system to this limit cycle is an early increase in control parameter values, then an oscillation around the higher values (Figure 9.17C). In this simulation, apoptotic events occur at a frequency of 1.0 events/day, with each event lasting ½ day. The controller response also has a frequency of approximately one cycle per day. For the controller governing k^P_{env}, this is not an unreasonable frequency because cytokine profiles can change much more rapidly than daily. For the controller governing k^T_{env}, this is also not an unreasonable frequency. Transition between Axin2+ and Axin2- cells is likely governed by a gradient of WNT-2a responsiveness. This WNT-2a responsiveness may be due to WNT-2a amounts produced by central endothelial cells, diffusivity of WNTs governed by matrix stiffness and density and pressure gradients, and motility of hepatocytes across sinusoids that could also be governed by matrix cues. While it may be difficult to imagine matrix properties changing within the span of one day, it is not outside the realm of possibility that factors controlling diffusivity and cell motility could change this quickly.

Another time when non-parenchymal control becomes important is during a sustained challenge. Without non-parenchymal cell control, both Axin2+ and Axin2- hepatocytes reach a new steady state resulting in lower total liver mass (Figure 9.19, dashed lines). In contrast when non-parenchymal cell control is present, there is an initial deviation from steady state that rapidly renormalizes (Figure 9.19, solid lines). This renormalization is achieved by non-parenchymal cells modifying the microenvironment to first facilitate cell transitions and then to induce Axin2+ hepatocyte proliferation (Figure 9.19, Controller Action). These changes allow for

long-term response to a sustained insult, such as a chronic infection, but they also modify the structure of the tissue microenvironment, which could lead to diseases such as fibrosis and cirrhosis.

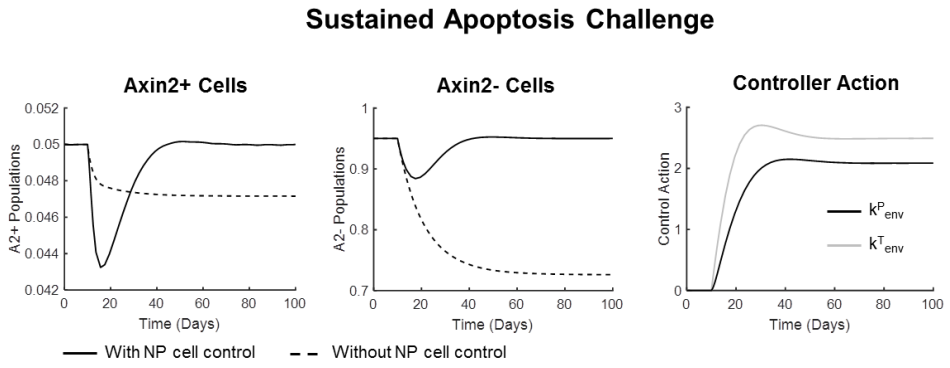

Figure 9.19 Non-parenchymal cell control can mitigate the effects of a sustained apoptosis challenge.

Chronic disease states do not only result from sustained challenges to the liver, they also alter non-parenchymal cell responses to disturbances. Our own lab has shown that the chronic insult of ethanol adaptation leads to an altered hepatic stellate cell response to resection (See Chapter 8). One way to capture such changes to the non-parenchymal cell network is to change the controller parameters describing the non-parenchymal control system (Figure 9.20). Changing parameters involved in the k^P_{env} controller has a large effect on Axin2+ response to periodic apoptosis challenges, but little effect on Axin2- populations. Such parameter changes could describe the early stages of chronic liver disease where the populations around the central vein receiving the highest dose of toxins (such as ethanol) begin to be affected but bulk liver function is not disturbed. In contrast, changing parameters involved in the k^T_{env}

controller affects both Axin2+ and Axin2- cells. Changes to this controller might be reflective of later disease states, when all areas of the liver are affected equally.

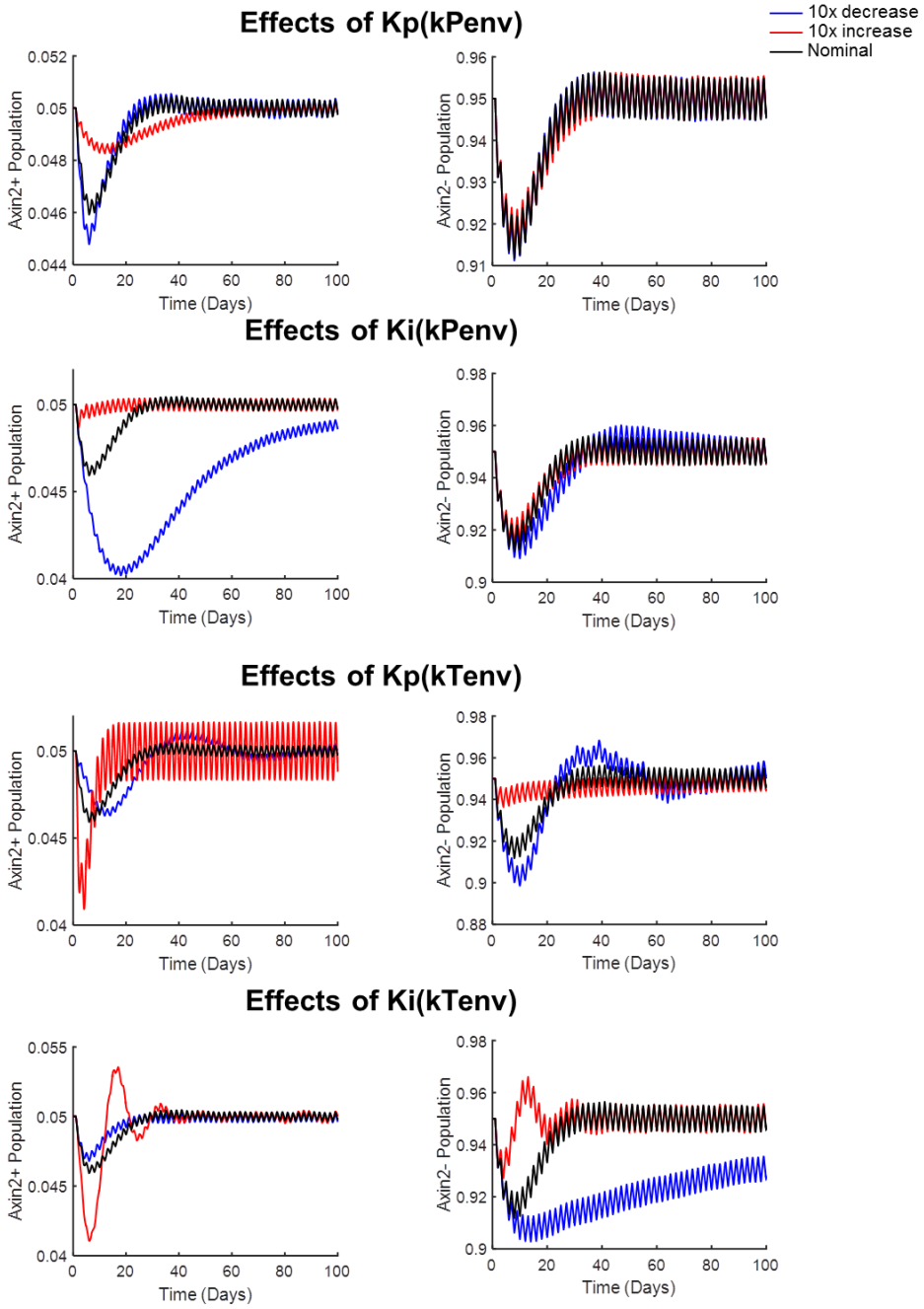

Figure 9.20 Changing controller parameters affects the early dynamics of chronic injury.

We tested how non-parenchymal cell control would work in a variety of situations. Cell apoptosis is an intrinsically stochastic process. We therefore tested how our non-parenchymal cell controllers responded to white noise added to cell apoptosis rates. We find that the addition of a controller makes the system response to white noise worse than the system response without a controller (Figure 9.21A). This is because feedback control amplifies white noise. We therefore implemented a 1% band gap around the steady-state and retested the controller. We find that in this case, the controller does not amplify the white noise (Figure 9.21B). In this scenario, the band gap represents an activation threshold that is often seen in biological systems (Félix & Barkoulas, 2015).

A

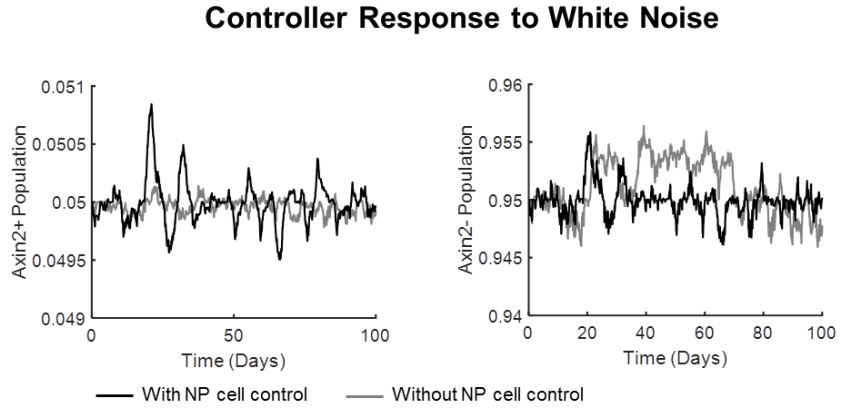
Controller Response to White Noise
Axin2+ Population
0.051
0.0505
0.05
0.0495
0.049
0
50
100
Time (Days)
Axin2- Population
0.96
0.955
0.95
0.945
0.94
0
20
40
60
80
100
Time (Days)
With NP cell control
Without NP cell control

B

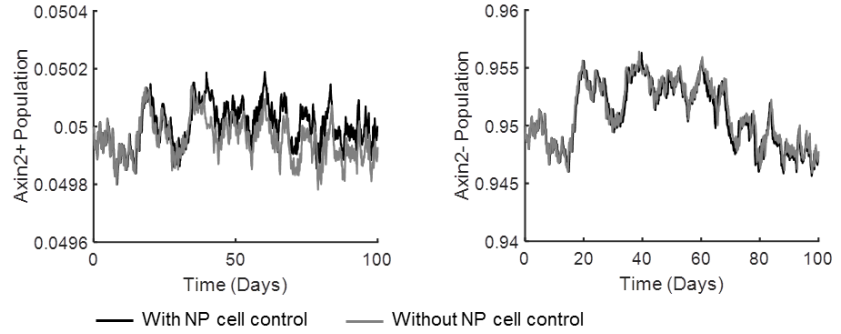
Controller Response to White Noise with Filter
Axin2+ Population
0.0504
0.0502
0.05
0.0498
0.0496
0
50
100
Time (Days)
Axin2- Population
0.96
0.955
0.95
0.945
0.94
0
20
40
60
80
100
Time (Days)
With NP cell control
Without NP cell control

C

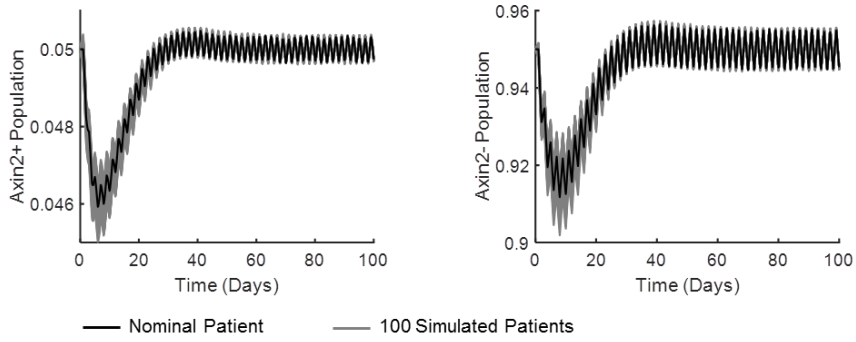
Simulating Chronic Apoptosis in 100 Patients
Axin2+ Population
0.05
0.048
0.046
0
20
40
60
80
100
Time (Days)
Axin2- Population
0.96
0.94
0.92
0.9
0
20
40
60
80
100
Time (Days)
Nominal Patient
100 Simulated Patients

Figure 9.21 Controller function (A) Response to band-limited white noise (Apoptosis rate standard deviation = 10% of nominal). Non-parenchymal cell control can respond to random variation in apoptosis rate by causing larger fluxuations in Axin2+ populations. The non-parenchymal cell controller, however, maintains Axin2- populations closer to nominal than in the absence of a controller. (B) Response to band-limited white noise (Apoptosis rate standard deviation = 10% of nominal) using a bandpass filter of +/- 0.5% of the setpoint. (C) Simulating chronic apoptosis challenges in 100 patients. Model parameters were sampled from a normal distribution with mean at the nominal parameter value and standard deviation of 1% of nominal values. Simulating multiple patients shows that the controller can maintain tissue populations near nominal levels even during a chronic apoptotic insult. The main effect of altered parameters is a change in the dynamics of initial response to the apoptosis challenge.

We next tested how our non-parenchymal cell controller is able to maintain hepatocyte populations across 100 simulated patients. We simulated liver homeostatic renewal in 100 unique patients by sampling parameters from a normal distribution for each parameter with mean of the nominal parameter value and standard deviation of 1% of the nominal parameter value. We sampled every parameter in each patient, so each of the 100 patients had a unique parameter set governing homeostatic renewal. We then subjected each patient to a pulsatile apoptotic challenge. We find that the non-parenchymal cell controllers are able to maintain hepatocyte populations within a limit cycle around the required steady-state level (Figure 9.21C). We are interested to see that, although there is wide variability in maximum liver damage, all patients eventually reach the same limit cycle. When the variability is increased substantially (10% vs. 1%), however, different modes of response are seen (Figure 9.22). This indicates that if tissue parameters vary substantially among patients, a single tuning of the non-parenchymal cell based control system is unlikely.

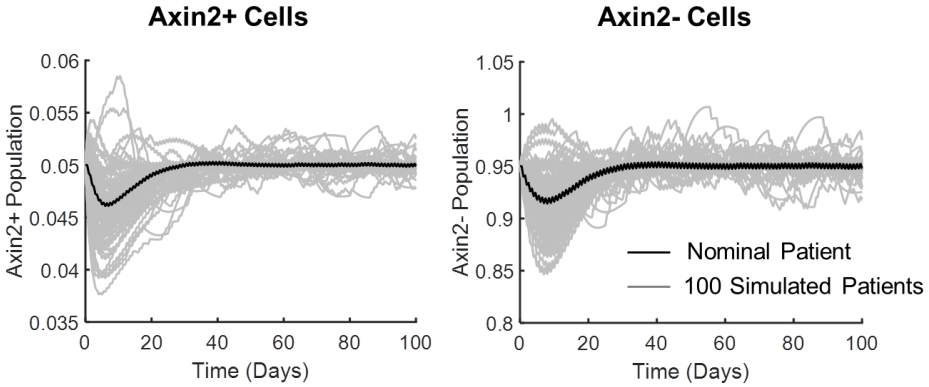

Figure 9.22 Simulated homeostatic renewal in 100 patients. Model parameters were sampled from a normal distribution with mean at the nominal parameter value and standard deviation of 10% of nominal values. Simulating multiple patients shows that the controller can maintain tissue populations near nominal levels even during a chronic apoptotic insult. The large variability in patient parameters, however, leads to poor controllability in many cases.

9.4 Discussion

Our findings suggest that multiple feedback mechanisms are active during tissue homeostatic renewal. Simulations of our mathematical model in the absence of feedback show that no feedbacks lead to a tissue with no steady-state and no ability to respond to disturbances. In contrast, simulations with multiple types of feedback result in a tissue that is able to respond robustly to several different disturbances, both transient and periodic. Intrinsic stability caused by multiple feedbacks on hepatocytes, however, is not enough to handle a sustained disturbance to homeostatic renewal, such as increased apoptosis caused by a sustained viral infection. In addition to intrinsic stability, there must be an external control that maintains hepatocyte populations in

such a condition. We propose that control of the extracellular microenvironment by a network of non-parenchymal cells could act as such a control circuit.

Our model is able to capture the experimentally observed behavior of the liver following induced hepatocyte senescence. Following induced senescence and toxic damage to a large portion of the liver, the liver is able to recover its original hepatocyte populations and overall mass in approximately 90 days. Although all of the replicating hepatocytes come from stem cells, based on model simulations, we predict that only Axin2+ cells are generated directly from stem cells. Replicating Axin2- cells are generated by transition from Axin2+ cells. We also predict that induced senescence without any additional damage will result in stem cell activation and differentiation, but that the time to repopulate the liver with replicating cells will be longer, on the order of 120 days.

Our model implicates control of homeostatic renewal by non-parenchymal cells as an important contributor to maintaining liver mass during chronic challenges. Many liver diseases are chronic issues and may affect the behavior of the non-parenchymal cell network. This can be seen by the number of liver diseases that result in fibrosis and cirrhosis if left untreated (Seki & Brenner, 2015). Work from our own lab and from others' on chronic alcoholism has shown that chronic alcoholism shifts the balances of non-parenchymal cell populations; for our work, see Chapters 7 and 8 (Saha et al, 2015). Future studies could investigate extracellular matrix properties during chronic insults and how these properties could influence non-parenchymal cell balances. Additionally, our study used only the automatic controller tuning in Matlab. A more robust control strategy could better control cell populations and may be a more realistic representation of the underlying biology.

Our study takes the first steps towards generating an integrated view of liver homeostatic renewal in the context of intercellular networks. Maintaining balances among cellular populations appears to be critical to maintain a healthy homeostatic renewal process. It is likely that interactions between parenchymal and non-parenchymal cells, interactions among each cell type, and interaction with the extracellular matrix are important for governing homeostatic renewal. Additionally, non-parenchymal cell control of the tissue microenvironment is likely spatial in nature leading to unique control actions depending on the needs of the tissue within a local neighborhood.

Chapter 10

CONCLUSIONS AND FUTURE WORK

10.1 Conclusions

Taken as a whole, the work presented in this dissertation suggests an integrated way to understand biological regulation of dynamic tissue function. Traditionally, tissue regulation has been seen as a multi-scale process, where molecular, electrical, and mechanical signals act through a network of parenchymal and non-parenchymal cells to govern tissue function. Our work suggests an additional level of complexity, where molecular, electrical, and mechanical signals are interpreted by cells in distinguishable transcriptional states prior to their integration into the cell network. The inclusion of cell state in understanding tissue dynamic behavior is important because each transcriptional state has a different transcriptional starting point, potentially leading to different responses to the same signal. The variability inherent within the transcriptional states and the relative balances among states could both contribute to the apparent "context specificity" that is often seen in biological response to a certain factor. For example, adiponectin has been shown to be anti-inflammatory in the liver, but its loss leads to a decreased pro-inflammatory response during the priming phase of liver regeneration (Correnti et al, 2015;Park et al, 2015b).

Our work also suggests a more complex regulation of dynamic liver function than previously suspected. Although the non-parenchymal cell network modulating liver regeneration has been studied previously, this work is the first to our knowledge to suggest a high amount of heterogeneity in non-parenchymal cell transcriptional

behavior (Malik et al, 2002). Our studies of transcriptional regulation in single hepatic stellate cells in the homeostatic liver and during regeneration suggest that the balance among distinguishable cell functional states governs tissue dynamics. Even within a functional state, however, there is a surprising amount of transcriptional variability. This variability likely arises from each individual cell inhabiting a unique microenvironment with a unique history of signaling (Park et al, 2014). What this variability means for tissue function is not yet fully clear. One possible reason for this variability is to make a population of stellate cells less susceptible to a virus or apoptosis event by making each cell as unique as possible while still carrying out a desired function.

Additionally, our work has shown a previously unidentified pro-regenerative hepatic cell state that appears to enhance liver regeneration. Previous studies have shown that growth factors enhance liver regeneration and suggest that sinusoidal endothelial cells are a major source of these growth factors (Kaibori et al, 1997). Our work suggests that hepatic stellate cells produce growth factors directly during regeneration and contribute to growth factor diffusion by modifying matrix properties. Furthermore, our studies suggest that imbalances in hepatic stellate cell functional states is a major contributor to impaired regeneration in disease conditions.

Finally, our work suggests computational modeling of cell states as an efficient method to integrate knowledge about single-cell based cell transcriptional states with cell networks to understand dynamic tissue function. We have demonstrated this technique in the context of liver regeneration (Chapters 7 and 8) and liver homeostatic renewal (Chapter 9).

10.2 Future Work

The work presented in this thesis gives a fresh understanding of the network contributions to dynamic liver function. There remains much work that could be done to further increase our understanding. As with any experimental work, more data could be collected. More hepatic stellate cells could be sampled to improve our understanding of the variability in gene expression among cell states. More cell types within the liver could be isolated to give a better understanding of the cell-to-cell communication that could result in coupled cell states. More time points during regeneration could be sampled to give a more detailed understanding of the dynamics of population balances during regeneration. Furthermore, our studies have focused on only a subset of functionally relevant genes. Future work could use genome-wide transcriptional profiling (using for example single cell RNA seq) to better understand the genome-wide regulation of each cell state and perhaps discover additional cell states. On the mathematical modeling side, there are many improvements that could be made to the models presented in this thesis. Our models use cell state transitions and archetypal signaling cascades to approximate complex, dynamic molecular signaling events leading to state transitions. More complexity could be added to the model, both in terms of molecular signaling (intercellular and intracellular) and in terms of cell states. Our model currently does not consider all the stellate cell states we found experimentally, and it is likely that all cell types in the liver also exhibit multiple transcriptional states. Finally, much more exact estimates for model parameters could be found to more closely mirror biology.

Rather than focus on how to improve or continue to refine the work presented in this thesis, however, this section will focus on how the results obtained during the development of this thesis can be used to extend research efforts.

10.2.1 Testing model predictions

Our computational modeling work has allowed us to make several predictions that can be tested experimentally. Based on simulations conducted using our cell-growth model of liver regeneration, we predict that different Adn-/- mouse genotypes produce growth factors differently in response to PHx (Chapter 6). We propose testing growth factor levels (specifically HGF, FGF2, and ANG1) in the genotype used by Shu et al. at 24-48 hours post-PHx to determine if this prediction is accurate. If it is accurate, it implies that the effect of knocking out a gene is dependent on the background genotype of the mouse, the method of knockout, or other as-yet unidentified factors.

Based on simulations conducted using our non-parenchymal cell network model of liver regeneration, we make several predictions about the effects of chronic ethanol adaptation on liver tissue properties. We predict that chronic ethanol adaptation leads to baseline imbalances in stellate cell states thereby changing the properties of the ECM in such a way that it inhibits regeneration. We predict that localized areas of ECM become populated by different collagen balances, stiffer, more crosslinked or denser, and less decorated by pro-regenerative molecules and growth factors. Several experiments could test these predictions. One such experiment would be to measure tissue elasticity using shear wave elasticity imaging ultrasound in ethanol-adapted animals and controls. This type of experiment could give information about the local tissue stiffness in ethanol-adapted livers. Another experiment to test these predictions would be to measure the levels of many collagen types in the livers of ethanol-adapted and control animals. Such measurements could be collected using techniques such as HPLC-MS/MS (Pataridis et al, 2008). We also predict that ethanol-adaptation leads to deficient stellate cell state transitions in response to a

second stressor (like PHx). This prediction could be tested by subjecting ethanol-adapted laboratory animals to several different stresses, such as acetaminophen administration, LPS injection, or TGFB induction and measuring HSC response using the methods described in this thesis.

Based on simulations using our model of liver homeostatic renewal, we predict that chronic ethanol abuse leads to an adaptation of the liver resulting in increased Axin2+ hepatocyte proliferation and an increased transition rate of Axin2+ hepatocytes to Axin2- hepatocytes. Fate tracing studies like those performed by Wang et al. could be used to test these predictions (Wang et al, 2015b).

10.2.2 Simulating regeneration in humans

One feature of our model is that instead of predicting regeneration outcome as a binary event (success or failure), our model is able to capture multiple modes of regeneration. Such variability in overall recovery following resection is a feature of liver resection in human patients. Future work could use time-rich data from human liver regeneration to estimate model parameters for patients exhibiting different modes of regeneration. Parameter features common to many patients within each mode could then be used to identify systemic issues leading to deficient regeneration or features leading to enhanced regeneration.

10.2.3 Clinical implementation of modeling

One important consideration of modeling human liver regeneration is that we want a predictive model, not only a descriptive model. Therefore, future work could be done to take parameter features related to deficient regeneration modes and relate them to clinically measurable physiology or biological assays. For example, changes

in the metabolic demand parameter in the model can have dramatic effects on regeneration capacity; therefore, an assay or test relating liver function and regeneration-specific metabolic demand could be informative for modeling regeneration prior to a resection surgery. Some tests like this could include a glucose challenge or hypoxic stress measured by HIF1A levels in the liver following a stress test. Not only will tests or assays need to be developed that will be informative of model parameters, but results from these assays need to be related to model parameters in a quantitative, semi-quantitative, or empirical way. If a patient-specific model can be developed, it could serve as a resource for physicians when they are deciding how much of a liver to resect for surgeries such as live liver transplant or cancer removal.

10.2.4 Drug targeting for regeneration and beyond

Our single cell experiments characterizing the transcriptional states of hepatic stellate cells suggest that each stellate cell transcriptional state is governed by modules of co-expressed genes. Furthermore, our computational modeling suggests that the dynamic balance among states is an important regulator of tissue function. Therefore, it should be possible to modulate tissue function by rebalancing among cell transcriptional states. The implication of these findings is that drugs targeting a single pathway or molecule may not be the only way to design drugs. Our results suggest that designing drugs that target modules of co-expressed genes that are over-expressed in one or more transcriptional states could be a method to change tissue behavior. In the context of the work included in this thesis, one such intervention could be to treat ethanol-adapted rats with miRNAs that specifically target the genes up-regulated in the anti-regenerative stellate cell state to attempt to renormalize regeneration capacity

post-PHx. This strategy could be applied further to many organ systems and disease conditions and provides an alternative strategy for targeted drug design.

REFERENCES

Aggarwal BB (2003) Signalling pathways of the TNF superfamily: a double-edged sword. *Nature Reviews Immunology* **3:**745-756

Alessenko AV, Platonova LV, Sakevarashvili GR, Khrenov AV, Shingarova LN, Shono NI, Galperin EI (1999) Role of endogenous TNF-alpha and sphingosine in induced DNA synthesis in regenerating rat liver after partial hepatectomy. *Biochemistry (Mosc)* **64:**890-895. doi: BCM64081060 [pii]

Alexiades M, Cepko C (1996) Quantitative analysis of proliferation and cell cycle length during development of the rat retina. *Developmental Dynamics* **205:**293-307. doi: 10.1002/(SICI)1097-0177(199603)205:3<293::AID-AJA9>3.0.CO;2-D

Alibes A, Yankilevich P, Canada A, Diaz-Uriarte R (2007) IDconverter and IDClight: Conversion and annotation of gene and protein IDs. *BMC Bioinformatics* **8:**9. doi: 10.1186/1471-2105-8-9

Allard M, Adam R, Bucur P, Termos S, Cunha AS, Bismuth H, Castaing D, Vibert E (2013) Posthepatectomy Portal Vein Pressure Predicts Liver Failure and Mortality after Major Liver Resection on Noncirrhotic Liver. *Ann Surg* **258:**822-830. doi: 10.1097/SLA.0b013e3182a64b38

Amir ED, Davis KL, Tadmor MD, Simonds EF, Levine JH, Bendall SC, Shenfeld DK, Krishnaswamy S, Nolan GP, Pe'er D (2013) viSNE enables visualization of high dimensional single-cell data and reveals phenotypic heterogeneity of leukemia. *Nat Biotechnol* **31:**545-552

Anitua E, Andia I, Ardanza B, Nurden P, Nurden AT (2004) Autologous platelets as a source of proteins for healing and tissue regeneration. *THROMBOSIS AND HAEMOSTASIS-STUTTGART-* **91:**4-15

Aoyama T, Ikejima K, Kon K, Okumura K, Arai K, Watanabe S (2009) Pioglitazone promotes survival and prevents hepatic regeneration failure after partial hepatectomy in obese and diabetic KK-Ay mice. *Hepatology* **49:**1636-1644

Apte UM, McRee R, Ramaiah SK (2004) Hepatocyte proliferation is the possible mechanism for the transient decrease in liver injury during steatosis stage of alcoholic liver disease. *Toxicol Pathol* **32:**567-576

Ashburner M, Ball C, Blake J, Botstein D, Butler H, Cherry J, Davis A, Dolinski K, Dwight S, Eppig J, Harris M, Hill D, Issel-Tarver L, Kasarskis A, Lewis S, Matese J, Richardson J, Ringwald M, Rubin G, Sherlock G, Gene Ontology Consortium (2000) Gene Ontology: tool for the unification of biology. *Nat Genet* **25:**25-29

Awazawa M, Ueki K, Inabe K, Yamauchi T, Kubota N, Kaneko K, Kobayashi M, Iwane A, Sasako T, Okazaki Y (2011) Adiponectin enhances insulin sensitivity by increasing hepatic IRS-2 expression via a macrophage-derived IL-6-dependent pathway. *Cell metabolism* **13:**401-412

Bahk JY, Han H, Jung JH, Piao Z (2011) *Treatment of the end stage liver cirrhosis by human umbilical cord blood stem cells: Preliminary results*. INTECH Open Access Publisher

Baldo G, Giugliani R, Uribe C, Belardinelli MC, Duarte MES, Meurer L, da Silveira TR, Matte U (2010) Bone marrow mononuclear cell transplantation improves survival and induces hepatocyte proliferation in rats after CCl4 acute liver damage. *Dig Dis Sci* **55:**3384-3392

Balzan S, Belghiti J, Farges O, Ogata S, Sauvanet A, Delefosse D, Durand F (2005) The "50-50 criteria" on postoperative day 5: an accurate predictor of liver failure and death after hepatectomy. *Ann Surg* **242:**824-829

Baranyi J, Roberts TA (1994) A dynamic approach to predicting bacterial growth in food. *Int J Food Microbiol* **23:**277-294

Barash H, R Gross E, Edrei Y, Ella E, Israel A, Cohen I, Corchia N, Ben-Moshe T, Pappo O, Pikarsky E, Goldenberg D, Shiloh Y, Galun E, Abramovitch R (2010) Accelerated carcinogenesis following liver regeneration is associated with chronic inflammation-induced double-strand DNA breaks. *Proc Natl Acad Sci U S A* **107:**2207-2212. doi: 10.1073/pnas.0908867107 [doi]

Barnes MA, McMullen MR, Roychowdhury S, Madhun NZ, Niese K, Olman MA, Stavitsky AB, Bucala R, Nagy LE (2015) Macrophage migration inhibitory factor is required for recruitment of scar-associated macrophages during liver fibrosis. *J Leukoc Biol* **97:**161-169. doi: 10.1189/jlb.3A0614-280R [doi]

Barra R, Hall JC (1977) Liver regeneration in normal and alloxan-induced diabetic rats. *J Exp Zool* **201:**93-99

BARRA R, HALL J (1977) Liver-Regeneration in Normal and Alloxan-Induced Diabetic Rats. *J Exp Zool* **201:**93-&. doi: 10.1002/jez.1402010111

Bataller R, Brenner DA (2005) Liver fibrosis. *J Clin Invest* **115:**209-218. doi: 10.1172/JCI24282 [doi]

Bendall SC, Davis KL, Amir ED, Tadmor MD, Simonds EF, Chen TJ, Shenfeld DK, Nolan GP, Pe'er D (2014) Single-cell trajectory detection uncovers progression and regulatory coordination in human B cell development. *Cell* **157:**714-725

Bertola A, Park O, Gao B (2013) Chronic plus binge ethanol feeding synergistically induces neutrophil infiltration and liver injury in mice: a critical role for E-selectin. *Hepatology* **58:**1814-1823

Bhatt AP, Bhende PM, Sin SH, Roy D, Dittmer DP, Damania B (2010) Dual inhibition of PI3K and mTOR inhibits autocrine and paracrine proliferative loops in PI3K/Akt/mTOR-addicted lymphomas. *Blood* **115:**4455-4463. doi: 10.1182/blood-2009-10-251082 [doi]

Bilal N (2014) Implementation of Sobol's method of global sensitivity analysis to a compressor simulation model.

Bissell DM, Wang SS, Jarnagin WR, Roll FJ (1995) Cell-specific expression of transforming growth factor-beta in rat liver. Evidence for autocrine regulation of hepatocyte proliferation. *J Clin Invest* **96:**447-455. doi: 10.1172/JCI118055 [doi]

Bogatkevich GS, Highland KB, Akter T, Silver RM (2012) The PPARgamma Agonist Rosiglitazone Is Antifibrotic for Scleroderma Lung Fibroblasts: Mechanisms of Action and Differential Racial Effects. *Pulm Med* **2012:**545172. doi: 10.1155/2012/545172 [doi]

Bonett DG, Wright TA (2000) Sample size requirements for estimating Pearson, Kendall and Spearman correlations. *Psychometrika* **65:**23-28

Bozinovski S, Jones JE, Vlahos R, Hamilton JA, Anderson GP (2002) Granulocyte/macrophage-colony-stimulating factor (GM-CSF) regulates lung innate immunity to lipopolysaccharide through Akt/Erk activation of NFkappa B and AP-1 in vivo. *J Biol Chem* **277:**42808-42814. doi: 10.1074/jbc.M207840200 [doi]

Bratley P, Fox BL (1988) Algorithm 659: Implementing Sobol's quasirandom sequence generator. *ACM Transactions on Mathematical Software (TOMS)* **14:**88-100

Bucher NL, Swaffield MN, DiTroia JF (1964) The influence of age upon the incorporation of thymidine-2-C14 into the DNA of regenerating rat liver. *Cancer Res* **24:**509-512

BUCHER NL, GLINOS AD (1950) The effect of age on regeneration of rat liver. *Cancer Res* **10:**324-332

Burdelya LG, Brackett CM, Kojouharov B, Gitlin II, Leonova KI, Gleiberman AS, Aygun-Sunar S, Veith J, Johnson C, Haderski GJ, Stanhope-Baker P, Allamaneni S, Skitzki J, Zeng M, Martsen E, Medvedev A, Scheblyakov D, Artemicheva NM, Logunov DY, Gintsburg AL, Naroditsky BS, Makarov SS, Gudkov AV (2013) Central role of liver in anticancer and radioprotective activities of Toll-like receptor 5 agonist. *Proc Natl Acad Sci U S A* **110:**E1857-E1866. doi: 10.1073/pnas.1222805110

Chen D, Chung Y, Yeh Y, Chaung H, Kuo F, Fu O, Chen H, Hou M, Yuan SF (2006) Serum adiponectin and leptin levels in Taiwanese breast cancer patients. *Cancer Lett* **237:**109-114

Chen J, Bao H, Sawyer S, Kunos G, Gao B (1997) Effects of short and long term ethanol on the activation of signal transducer and activator transcription factor 3 in normal and regenerating liver. *Biochem Biophys Res Commun* **239:**666-669

Chen G, Goeddel DV (2002) TNF-R1 signaling: a beautiful pathway. *Science* **296:**1634-1635. doi: 10.1126/science.1071924 [doi]

Chenard-Neu M, Boudjema K, Bernuau J, Degott C, Belghiti J, Cherqui D, Costes V, Domergue J, Durand F, Erhard J (1996) Auxiliary liver transplantation: regeneration of the native liver and outcome in 30 patients with fulminant hepatic failure–a multicenter European study. *Hepatology* **23:**1119-1127

Cheng C, Gerstein M (2012) Modeling the relative relationship of transcription factor binding and histone modifications to gene expression levels in mouse embryonic stem cells. *Nucleic Acids Res* **40:**553-568. doi: 10.1093/nar/gkr752

Cheng C, Alexander R, Min R, Leng J, Yip KY, Rozowsky J, Yan K, Dong X, Djebali S, Ruan Y, Davis CA, Carninci P, Lassman T, Gingerasi TR, Guigo R, Birney E, Weng Z, Snyder M, Gerstein M (2012) Understanding transcriptional regulation by integrative analysis of transcription factor binding data. *Genome Res* **22:**1658-1667. doi: 10.1101/gr.136838.111

Chiang DJ, Pritchard MT, Nagy LE (2011) Obesity, diabetes mellitus, and liver fibrosis. *Am J Physiol Gastrointest Liver Physiol* **300:**G697-702. doi: 10.1152/ajpgi.00426.2010 [doi]

Choi SS, Diehl AM (2009) Epithelial-to-mesenchymal transitions in the liver. *Hepatology* **50:**2007-2013

Combs TP, Wagner JA, Berger J, Doebber T, Wang W, Zhang BB, Tanen M, Berg AH, O'Rahilly S, Savage DB (2002) Induction of adipocyte complement-related protein of 30 kilodaltons by PPARγ agonists: a potential mechanism of insulin sensitization. *Endocrinology* **143:**998-1007

Cook D, Ogunnaike BA, Vadigepalli R (2015) Systems analysis of non-parenchymal cell modulation of liver repair across multiple regeneration modes. *BMC systems biology* **9:**1

Copple BL, Bustamante JJ, Welch TP, Kim ND, Moon J (2009) Hypoxia-inducible factor-dependent production of profibrotic mediators by hypoxic hepatocytes. *Liver International* **29:**1010-1021

Corpechot C, Barbu V, Wendum D, Kinnman N, Rey C, Poupon R, Housset C, Rosmorduc O (2002) Hypoxia-induced VEGF and collagen I expressions are associated with angiogenesis and fibrogenesis in experimental cirrhosis. *Hepatology* **35:**1010-1021

Correnti JM, Cook D, Aksamitiene E, Swarup A, Ogunnaike B, Vadigepalli R, Hoek JB (2015) Adiponectin fine-tuning of liver regeneration dynamics revealed through cellular network modelling. *J Physiol (Lond)* **593:**365-383

Correnti JM, Juskeviciute E, Swarup A, Hoek JB (2014) Pharmacological ceramide reduction alleviates alcohol-induced steatosis and hepatomegaly in adiponectin knockout mice. *Am J Physiol Gastrointest Liver Physiol* **306:**G959-73. doi: 10.1152/ajpgi.00395.2013 [doi]

Court F, Wemyss-Holden S, Dennison A, Maddern G (2002) The mystery of liver regeneration. *Br J Surg* **89:**1089-1095

Crumm S, Cofan M, Juskeviciute E, Hoek JB (2008) Adenine nucleotide changes in the remnant liver: An early signal for regeneration after partial hepatectomy. *Hepatology* **48:**898-908

Dan R, Creţu O, Mazilu O, Sima L, Iliescu D, Blidişel A, Tirziu R, Istodor A, Huţ E (2012) Postoperative morbidity and mortality after liver resection. Retrospective study on 133 patients. *Chirurgia (Bucur)* **107:**737-741

De Lazzari F, Ravagnan P, Tenderini M, Vicarioto MA, Galliani EA, Lorenzoni U, Popovic A, Floreani A (2002) Circulating soluble-CD30 (sCD30) in patients with HCV-related chronic hepatitis and in patients with alcoholic liver disease. *Hepatogastroenterology* **49:**231-234

De Minicis S, Seki E, Uchinami H, Kluwe J, Zhang Y, Brenner DA, Schwabe RF (2007) Gene expression profiles during hepatic stellate cell activation in culture and in vivo. *Gastroenterology* **132:**1937-1946

de Waal Malefyt R, Abrams J, Bennett B, Figdor CG, de Vries JE (1991) Interleukin 10(IL-10) inhibits cytokine synthesis by human monocytes: an autoregulatory role of IL-10 produced by monocytes. *J Exp Med* **174:**1209-1220

DeAngelis RA, Kovalovich K, Cressman DE, Taub R (2001) Normal liver regeneration in p50/nuclear factor kappa B1 knockout mice. *Hepatology* **33:**915-924. doi: 10.1053/jhep.2001.23192

DeAngelis R, Markiewski M, Taub R, Lambris J (2005) A high-fat diet impairs liver regeneration in C57BL/6 mice through overexpression of the NF-kappa B inhibitor, I kappa B alpha. *Hepatology* **42:**1148-1157. doi: 10.1002/hep.20879

DeLeve LD (2013) Liver sinusoidal endothelial cells and liver regeneration. *J Clin Invest* **123:**1861-1866

Deshmane SL, Kremlev S, Amini S, Sawaya BE (2009) Monocyte chemoattractant protein-1 (MCP-1): an overview. *Journal of interferon & cytokine research* **29:**313-326

Diaz-Munoz M, Canedo-Merino R, Gutierrez-Salinas J, Hernandez-Munoz R (1998) Modifications of intracellular calcium release channels and calcium mobilization following 70% hepatectomy. *Arch Biochem Biophys* **349:**105-112. doi: 10.1006/abbi.1997.0396

Ding B, Nolan DJ, Butler JM, James D, Babazadeh AO, Rosenwaks Z, Mittal V, Kobayashi H, Shido K, Lyden D (2010) Inductive angiocrine signals from sinusoidal endothelium are required for liver regeneration. *Nature* **468:**310-315

Ding X, Saxena NK, Lin S, Xu A, Srinivasan S, Anania FA (2005) The roles of leptin and adiponectin: a novel paradigm in adipocytokine regulation of liver fibrosis and stellate cell biology. *The American journal of pathology* **166:**1655-1669

Doci R, Gennari L, Bignami P, Montalto F, Morabito A, Bozzetti F (1991) One hundred patients with hepatic metastases from colorectal cancer treated by resection: analysis of prognostic determinants. *Br J Surg* **78:**797-801

Dor Y, Brown J, Martinez OI, Melton DA (2004) Adult pancreatic β-cells are formed by self-duplication rather than stem-cell differentiation. *Nature* **429:**41-46

Dueck H, Eberwine J, Kim J (2015) Variation is function: Are single cell differences functionally important? *Bioessays*

DUGUAY L, COUTU D, HETU C, JOLY J (1982) Inhibition of Liver-Regeneration by Chronic Alcohol Administration. *Gut* **23:**8-13. doi: 10.1136/gut.23.1.8

Dutta-Moscato J, Solovyev A, Mi Q, Nishikawa T, Soto-Gutierrez A, Fox IJ, Vodovotz Y (2014) A Multiscale Agent-Based in silico Model of Liver Fibrosis Progression. *Systems Biology* **2:**18

Edgar R, Domrachev M, Lash AE (2002) Gene Expression Omnibus: NCBI gene expression and hybridization array data repository. *Nucleic Acids Res* **30:**207-210. doi: 10.1093/nar/30.1.207

Engelmann JC, Amann T, Ott-Rötzer B, Nützel M, Reinders Y, Reinders J, Thasler WE, Kristl T, Teufel A, Huber CG (2015) Causal Modeling of Cancer-Stromal Communication Identifies PAPPA as a Novel Stroma-Secreted Factor Activating NFκB Signaling in Hepatocellular Carcinoma.

Ezaki H, Yoshida Y, Saji Y, Takemura T, Fukushima J, Matsumoto H, Kamada Y, Wada A, Igura T, Kihara S (2009) Delayed liver regeneration after partial hepatectomy in adiponectin knockout mice. *Biochem Biophys Res Commun* **378:**68-72

Fabrega E, Unzueta M, Cobo M, Casafont F, Amado J, Romero F (2007) Value of soluble CD30 in liver transplantation. **39:**2295-2296

Fausto N (2001) Liver regeneration: from laboratory to clinic. *Liver transplantation* **7:**835-844

Fausto N, Campbell JS (2003) The role of hepatocytes and oval cells in liver regeneration and repopulation. *Mech Dev* **120:**117-130

Fausto N, Campbell JS, Riehle KJ (2006) Liver regeneration. *Hepatology* **43:**

Fausto N (2000) Liver regeneration. *J Hepatol* **32:**19-31. doi: 10.1016/S0168-8278(00)80412-2

Fayad R, Pini M, Sennello JA, Cabay RJ, Chan L, Xu A, Fantuzzi G (2007) Adiponectin deficiency protects mice from chemically induced colonic inflammation. *Gastroenterology* **132:**601-614

Félix M, Barkoulas M (2015) Pervasive robustness in biological systems. *Nature Reviews Genetics* **16:**483-496

Fernandez-Riejos P, Najib S, Santos-Alvarez J, Martin-Romero C, Perez-Perez A, Gonzalez-Yanes C, Sanchez-Margalet V (2010) Role of leptin in the activation of immune cells. *Mediators Inflamm* **2010:**568343. doi: 10.1155/2010/568343 [doi]

Fiorentino DF, Zlotnik A, Mosmann TR, Howard M, O'Garra A (1991) IL-10 inhibits cytokine production by activated macrophages. *J Immunol* **147:**3815-3822

Font-Burgada J, Shalapour S, Ramaswamy S, Hsueh B, Rossell D, Umemura A, Taniguchi K, Nakagawa H, Valasek MA, Ye L (2015) Hybrid periportal hepatocytes regenerate the injured liver without giving rise to cancer. *Cell* **162:**766-779

Fourcot A, Couchie D, Chobert MN, Zafrani ES, Mavier P, Laperche Y, Brouillet A (2011) Gas6 deficiency prevents liver inflammation, steatohepatitis, and fibrosis in mice. *Am J Physiol Gastrointest Liver Physiol* **300:**G1043-53. doi: 10.1152/ajpgi.00311.2010 [doi]

Franceschini B, Ceva-Grimaldi G, Russo C, Dioguardi N, Grizzi F (2006) The complex functions of mast cells in chronic human liver diseases. *Dig Dis Sci* **51:**2248-2256

Freeman K, Staehle MM, Gümüs ZH, Vadigepalli R, Gonye GE, Nichols CN, Ogunnaike BA, Hoek JB, Schwaber JS (2012) Rapid temporal changes in the expression of a set of neuromodulatory genes during alcohol withdrawal in the dorsal vagal complex: molecular evidence of homeostatic disturbance. *Alcoholism: Clinical and Experimental Research* **36:**1688-1700

Friedberg EC, Walker GC, Siede W, Wood RD (2005) *DNA repair and mutagenesis*. American Society for Microbiology Press

Friedman SL (2008a) Hepatic stellate cells: protean, multifunctional, and enigmatic cells of the liver. *Physiol Rev* **88:**125-172. doi: 10.1152/physrev.00013.2007 [doi]

Friedman SL (2008b) Hepatic stellate cells: protean, multifunctional, and enigmatic cells of the liver. *Physiol Rev* **88:**125-172. doi: 10.1152/physrev.00013.2007 [doi]

Friedman SL (2008c) Hepatic stellate cells: Protean, multifunctional, and enigmatic cells of the liver. *Physiol Rev* **88:**125-172. doi: 10.1152/physrev.00013.2007

Fris RJ (2004) Preoperative low energy diet diminishes liver size. *Obesity Surg* **14:**1165-1170

Fujita K, Maeda N, Sonoda M, Ohashi K, Hibuse T, Nishizawa H, Nishida M, Hiuge A, Kurata A, Kihara S, Shimomura I, Funahashi T (2008) Adiponectin protects against

angiotensin II-induced cardiac fibrosis through activation of PPAR-alpha. *Arterioscler Thromb Vasc Biol* **28:**863-870. doi: 10.1161/ATVBAHA.107.156687 [doi]

Furchtgott LA, Chow CC, Periwal V (2009) A Model of Liver Regeneration. *Biophys J* **96:**3926-3935. doi: 10.1016/j.bpj.2009.01.061

Galkina E, Ley K (2007) Vascular adhesion molecules in atherosclerosis. *Arterioscler Thromb Vasc Biol* **27:**2292-2301. doi: ATVBAHA.107.149179 [pii]

Gentleman RC, Carey VJ, Bates DM, Bolstad B, Dettling M, Dudoit S, Ellis B, Gautier L, Ge Y, Gentry J, Hornik K, Hothorn T, Huber W, Iacus S, Irizarry R, Leisch F, Li C, Maechler M, Rossini AJ, Sawitzki G, Smith C, Smyth G, Tierney L, Yang JY, Zhang J (2004a) Bioconductor: open software development for computational biology and bioinformatics. *Genome Biol* **5:**R80. doi: gb-2004-5-10-r80 [pii]

Gentleman R, Carey V, Bates D, Bolstad B, Dettling M, Dudoit S, Ellis B, Gautier L, Ge Y, Gentry J, Hornik K, Hothorn T, Huber W, Iacus S, Irizarry R, Leisch F, Li C, Maechler M, Rossini A, Sawitzki G, Smith C, Smyth G, Tierney L, Yang J, Zhang J (2004b) Bioconductor: open software development for computational biology and bioinformatics. *Genome Biol* **5:**R80. doi: 10.1186/gb-2004-5-10-r80

GERSHBEIN LL (1958) Pregnancy and liver regeneration in partially hepatectomized rats. *Proc Soc Exp Biol Med* **99:**716-717

Gille C, Boelling C, Hoppe A, Bulik S, Hoffmann S, Huebner K, Karlstaedt A, Ganeshan R, Koenig M, Rother K, Weidlich M, Behre J, Holzhuetter H (2010) HepatoNet1: a comprehensive metabolic reconstruction of the human hepatocyte for the analysis of liver physiology. *Molecular Systems Biology* **6:**411. doi: 10.1038/msb.2010.62

Gopalan A, Yu W, Sanders BG, Kline K (2013) Eliminating drug resistant breast cancer stem-like cells with combination of simvastatin and gamma-tocotrienol. *Cancer Lett* **328:**285-296

Goymer P (2007) Synonymous mutations break their silence. *Nature Reviews Genetics* **8:**92-92

Grumm S, Cofan M, Juskeviciute E, Hoek JB (2008) Adenine nucleotide changes in the remnant liver: An early signal for regeneration after partial hepatectomy. *Hepatology* **48:**898-908. doi: 10.1002/hep.22421

Gunawan R, Doyle FJ,3rd (2007) Phase sensitivity analysis of circadian rhythm entrainment. *J Biol Rhythms* **22:**180-194. doi: 22/2/180 [pii]

Haga S, Ogawa W, Inoue H, Terui K, Ogino T, Igarashi R, Takeda K, Akira S, Enosawa S, Furukawa H, Todo S, Ozaki M (2005) Compensatory recovery of liver mass by Akt-mediated hepatocellular hypertrophy in liver-specific STAT3-deficient mice. *J Hepatol* **43:**799-807. doi: 10.1016/j.jhep.2005.03.027

Han L, Qiu P, Zeng Z, Jorgensen JL, Mak DH, Burks JK, Schober W, McQueen TJ, Cortes J, Tanner SD (2015) Single-cell mass cytometry reveals intracellular survival/proliferative signaling in FLT3-ITD-mutated AML stem/progenitor cells. *Cytometry Part A* **87:**346-356

Haque WA, Shimomura I, Matsuzawa Y, Garg A (2002) Serum adiponectin and leptin levels in patients with lipodystrophies. *The Journal of Clinical Endocrinology & Metabolism* **87:**2395-2395

Haruyama T, Ajioka I, Akaike T, Watanabe Y (2000) Regulation and significance of hepatocyte-derived matrix metalloproteinases in liver remodeling. *Biochem Biophys Res Commun* **272:**681-686

Hasegawa T, Ito Y, Wijeweera J, Liu J, Malle E, Farhood A, McCuskey RS, Jaeschke H (2007) Reduced inflammatory response and increased microcirculatory disturbances during hepatic ischemia-reperfusion injury in steatotic livers of ob/ob mice. *Am J Physiol Gastrointest Liver Physiol* **292:**G1385-95. doi: 00246.2006 [pii]

Hayashi H, Sakai K, Baba H, Sakai T (2012) Thrombospondin-1 is a novel negative regulator of liver regeneration after partial hepatectomy through transforming growth factor-beta1 activation in mice. *Hepatology* **55:**1562-1573

Hayden M, Ghosh S (2004) Signaling to NF-kappa B. *Genes Dev* **18:**2195-2224. doi: 10.1101/gad.1228704

Hecker M, Lambeck S, Toepfer S, Van Someren E, Guthke R (2009) Gene regulatory network inference: data integration in dynamic models—a review. *BioSystems* **96:**86-103

Hemmann S, Graf J, Roderfeld M, Roeb E (2007) Expression of MMPs and TIMPs in liver fibrosis–a systematic review with special emphasis on anti-fibrotic strategies. *J Hepatol* **46:**955-975

Hendriks H, Verhoofstad W, Brouwer A, De Leeuw A, Knook D (1985) Perisinusoidal fat-storing cells are the main vitamin A storage sites in rat liver. *Exp Cell Res* **160:**138-149

Herr I, Schemmer P, Büchler MW (2007) On the TRAIL to therapeutic intervention in liver disease. *Hepatology* **46:**266-274

Higgins GM, Anderson RM (1931) Experimental pathology of the liver I Restoration of the liver of the white rat following partial surgical removal. *Arch Pathol* **12:**186-202

Ho JWK, Bishop E, Karchenko PV, Negre N, White KP, Park PJ (2011) ChIP-chip versus ChIP-seq: Lessons for experimental design and data analysis. *BMC Genomics* **12:**134. doi: 10.1186/1471-2164-12-134

Hoehme S, Brulport M, Bauer A, Bedawy E, Schormann W, Hermes M, Puppe V, Gebhardt R, Zellmer S, Schwarz M, Bockamp E, Timmel T, Hengstler JG, Drasdo D (2010) Prediction and validation of cell alignment along microvessels as order principle to restore tissue architecture in liver regeneration. *Proc Natl Acad Sci U S A* **107:**10371-10376. doi: 10.1073/pnas.0909374107

Holland WL, Miller RA, Wang ZV, Sun K, Barth BM, Bui HH, Davis KE, Bikman BT, Halberg N, Rutkowski JM (2011) Receptor-mediated activation of ceramidase activity initiates the pleiotropic actions of adiponectin. *Nat Med* **17:**55-63

Honiden S, Gong MN (2009) Diabetes, insulin, and development of acute lung injury. *Crit Care Med* **37:**2455-2464. doi: 10.1097/CCM.0b013e3181a0fea5 [doi]

Hoo RL, Chow WS, Yau MH, Xu A, Tso AW, Tse HF, Fong CH, Tam S, Chan L, Lam KS (2007) Adiponectin mediates the suppressive effect of rosiglitazone on plasminogen activator inhibitor-1 production. *Arterioscler Thromb Vasc Biol* **27:**2777-2782. doi: ATVBAHA.107.152462 [pii]

Horiguchi N, Ishac EJ, Gao B (2007) Liver regeneration is suppressed in alcoholic cirrhosis: correlation with decreased STAT3 activation. *Alcohol* **41:**271-280

Hsieh M, Chen W, Jiang M, Cheng B, Huang T, Chang M (2006) Interleukin-20 promotes angiogenesis in a direct and indirect manner. *Genes Immun* **7:**234-242

Hu J, Srivastava K, Wieland M, Runge A, Mogler C, Besemfelder E, Terhardt D, Vogel MJ, Cao L, Korn C, Bartels S, Thomas M, Augustin HG (2014) Endothelial cell-derived angiopoietin-2 controls liver regeneration as a spatiotemporal rheostat. *Science* **343:**416-419. doi: 10.1126/science.1244880 [doi]

Huang DW, Sherman BT, Lempicki RA (2009) Systematic and integrative analysis of large gene lists using DAVID bioinformatics resources. *Nature Protocols* **4:**44-57. doi: 10.1038/nprot.2008.211

Huh CG, Factor VM, Sanchez A, Uchida K, Conner EA, Thorgeirsson SS (2004) Hepatocyte growth factor/c-met signaling pathway is required for efficient liver

regeneration and repair. *Proc Natl Acad Sci U S A* **101:**4477-4482. doi: 10.1073/pnas.0306068101 [doi]

Husted T, Blanchard J, Schuster R, Shen H, Lentsch A (2006) Potential role for IL-23 in hepatic ischemia/reperfusion injury. *Inflammation Res* **55:**177-178

Iannelli F, Collino A, Sinha S, Radaelli E, Nicoli P, D'Antiga L, Sonzogni A, Faivre J, Buendia MA, Sturm E, Thompson RJ, Knisely AS, Natoli G, Ghisletti S, Ciccarelli FD (2014) Massive gene amplification drives paediatric hepatocellular carcinoma caused by bile salt export pump deficiency. *Nature Communications* **5:**3850. doi: 10.1038/ncomms4850

Israel Y, Khanna JM, Orrego H, Rachamin G, Wahid S, Britton R, Macdonald A, Kalant H (1979) Studies on metabolic tolerance to alcohol, hepatomegaly and alcoholic liver disease. *Drug Alcohol Depend* **4:**107-118

Issa R, Zhou X, Trim N, Millward-Sadler H, Krane S, Benyon C, Iredale J (2003) Mutation in collagen-1 that confers resistance to the action of collagenase results in failure of recovery from CCl4-induced liver fibrosis, persistence of activated hepatic stellate cells, and diminished hepatocyte regeneration. *FASEB J* **17:**47-49. doi: 10.1096/fj.02-0494fje [doi]

Jaeck D, Bachellier P, Oussoultzoglou E, Weber J, Wolf P (2004) Surgical resection of hepatocellular carcinoma. Post-operative outcome and long-term results in Europe: An overview. *Liver transplantation* **10:**

Jain M, Patel N, Kamani P, Shah N, Kulkarni S, Gautam S, Shah A, Doshi S (2015) Care of patients with liver cirrhosis: How are we doing?

Jiang F, Parsons CJ, Stefanovic B (2006a) Gene expression profile of quiescent and activated rat hepatic stellate cells implicates Wnt signaling pathway in activation. *J Hepatol* **45:**401-409

Jiang F, Parsons CJ, Stefanovic B (2006b) Gene expression profile of quiescent and activated rat hepatic stellate cells implicates Wnt signaling pathway in activation. *J Hepatol* **45:**401-409

Jiao J, Friedman SL, Aloman C (2009) Hepatic fibrosis. *Curr Opin Gastroenterol* **25:**223-229

Jin X, Zimmers TA, Perez EA, Pierce RH, Zhang Z, Koniaris LG (2006) Paradoxical effects of short-and long-term interleukin-6 exposure on liver injury and repair. *Hepatology* **43:**474-484

JOHNSTON D, JOHNSON G, ALBERTI K, MILLWARDSADLER G, MITCHELL J, WRIGHT R (1986) Hepatic Regeneration and Metabolism After Partial-Hepatectomy in Diabetic Rats - Effects of Insulin Therapy. *Eur J Clin Invest* **16:**384-390. doi: 10.1111/j.1365-2362.1986.tb01013.x

Johnston MD, Edwards CM, Bodmer WF, Maini PK, Chapman SJ (2007) Mathematical modeling of cell population dynamics in the colonic crypt and in colorectal cancer. *Proc Natl Acad Sci U S A* **104:**4008-4013. doi: 0611179104 [pii]

Juskeviciute E, Vadigepalli R, Hoek JB (2008) Temporal and functional profile of the transcriptional regulatory network in the early regenerative response to partial hepatectomy in the rat. *BMC Genomics* **9:**527. doi: 10.1186/1471-2164-9-527

Kadowaki T, Yamauchi T, Kubota N, Hara K, Ueki K, Tobe K (2006) Adiponectin and adiponectin receptors in insulin resistance, diabetes, and the metabolic syndrome. *J Clin Invest* **116:**1784-1792. doi: 10.1172/JCI29126 [doi]

KAHN D, HICKMAN R, TERBLANCHE J, VONSOMMOGGY S (1988) Partial-Hepatectomy and Liver-Regeneration in Pigs - the Response to Different Resection Sizes. *J Surg Res* **45:**176-180. doi: 10.1016/0022-4804(88)90062-5

Kaibori M, Kwon A, Nakagawa M, Wei T, Uetsuji S, Kamiyama Y, Okumura T, Kitamura N (1997) Stimulation of liver regeneration and function after partial hepatectomy in cirrhotic rats by continuous infusion of recombinant human hepatocyte growth factor. *J Hepatol* **27:**381-390. doi: 10.1016/S0168-8278(97)80185-7

Kajimura D, Lee HW, Riley KJ, Arteaga-Solis E, Ferron M, Zhou B, Clarke CJ, Hannun YA, DePinho RA, Guo XE (2013) Adiponectin regulates bone mass via opposite central and peripheral mechanisms through FoxO1. *Cell metabolism* **17:**901-915

Kamada Y, Matsumoto H, Tamura S, Fukushima J, Kiso S, Fukui K, Igura T, Maeda N, Kihara S, Funahashi T (2007) Hypoadiponectinemia accelerates hepatic tumor formation in a nonalcoholic steatohepatitis mouse model. *J Hepatol* **47:**556-564

Kamada Y, Tamura S, Kiso S, Matsumoto H, Saji Y, Yoshida Y, Fukui K, Maeda N, Nishizawa H, Nagaretani H (2003) Enhanced carbon tetrachloride-induced liver fibrosis in mice lacking adiponectin. *Gastroenterology* **125:**1796-1807

Kanehisa M, Goto S (2000) KEGG: Kyoto Encyclopedia of Genes and Genomes. *Nucleic Acids Res* **28:**27-30. doi: 10.1093/nar/28.1.27

Kanehisa M, Goto S, Sato Y, Kawashima M, Furumichi M, Tanabe M (2014) Data, information, knowledge and principle: back to metabolism in KEGG. *Nucleic Acids Res* **42:**D199-D205. doi: 10.1093/nar/gkt1076

Karlmark KR, Weiskirchen R, Zimmermann HW, Gassler N, Ginhoux F, Weber C, Merad M, Luedde T, Trautwein C, Tacke F (2009) Hepatic recruitment of the inflammatory Gr1 monocyte subset upon liver injury promotes hepatic fibrosis. *Hepatology* **50:**261-274

Kasama Y, Mizukami T, Kusunoki H, Peveling-Oberhag J, Nishito Y, Ozawa M, Kohara M, Mizuochi T, Tsukiyama-Kohara K (2014) B-Cell-Intrinsic Hepatitis C Virus Expression Leads to B-Cell-Lymphomagenesis and Induction of NF-kappa B Signalling. *Plos One* **9:**e91373. doi: 10.1371/journal.pone.0091373

Kauffmann R, Fong Y (2014) Post-hepatectomy liver failure. *Hepatobiliary surgery and nutrition* **3:**238-246

Kindt TJ, Goldsby RA, Osborne BA, Kuby J (2007) *Kuby immunology*. Macmillan

Kisseleva T, Cong M, Paik Y, Scholten D, Jiang C, Benner C, Iwaisako K, Moore-Morris T, Scott B, Tsukamoto H, Evans SM, Dillmann W, Glass CK, Brenner DA (2012) Myofibroblasts revert to an inactive phenotype during regression of liver fibrosis. *Proc Natl Acad Sci U S A* **109:**9448-9453. doi: 10.1073/pnas.1201840109 [doi]

Kitano H (2002) Systems biology: a brief overview. *Science* **295:**1662-1664. doi: 10.1126/science.1069492 [doi]

Kmieć Z (2001) *Cooperation of Liver Cells in Health and Disease*. Springer Berlin Heidelberg

Kolokotrones T, Savage V, Deeds EJ, Fontana W (2010) Curvature in metabolic scaling. *Nature* **464:**753-756. doi: 10.1038/nature08920

Kopp JL, Grompe M, Sander M (2016) Stem cells versus plasticity in liver and pancreas regeneration. *Nat Cell Biol* **18:**238-245

Kreiman G, Koch C, Fried I (2000) Category-specific visual responses of single neurons in the human medial temporal lobe. *Nat Neurosci* **3:**946-953

Kudo A, Tanaka S, Ban D, Matsumura S, Irie T, Ochiai T, Nakamura N, Arii S, Tanabe M (2014) Alcohol consumption and recurrence of non-B or non-C hepatocellular carcinoma after hepatectomy: a propensity score analysis. *J Gastroenterol* **49:**1352-1361

Kumar R, Clermont G, Vodovotz Y, Chow C (2004) The dynamics of acute inflammation. *J Theor Biol* **230:**145-155. doi: 10.1016/j.jtbi.2004.04.044

Kuttippurathu L, Parrish A, Vadigepalli R (2014) Integrated Computational Model of Intracellular Signaling and microRNA Regulation Predicts the Network Balances and Timing Constraints Critical to the Hepatic Stellate Cell Activation Process. *Processes* **2:**773-794

Kuttippurathu L, Patra B, Hoek JB, Vadigepalli R (2016a) A novel comparative pattern count analysis reveals a chronic ethanol-induced dynamic shift in immediate early NF-κB genome-wide promoter binding during liver regeneration. *Molecular BioSystems* **12:**1037-1056

Kuttippurathu L, Patra B, Hoek JB, Vadigepalli R (2016b) A novel comparative pattern count analysis reveals a chronic ethanol-induced dynamic shift in immediate early NF-κB genome-wide promoter binding during liver regeneration. *Molecular BioSystems* **12:**1037-1056

Kuttippurathu L, Juskeviciute E, Dippold RP, Hoek JB, Vadigepalli R (2016c) A novel comparative pattern analysis approach identifies chronic alcohol mediated dysregulation of transcriptomic dynamics during liver regeneration. *BMC Genomics* **17:**1

Landskroner-Eiger S, Qian B, Muise ES, Nawrocki AR, Berger JP, Fine EJ, Koba W, Deng Y, Pollard JW, Scherer PE (2009) Proangiogenic contribution of adiponectin toward mammary tumor growth in vivo. *Clin Cancer Res* **15:**3265-3276. doi: 10.1158/1078-0432.CCR-08-2649 [doi]

Langrish CL, Chen Y, Blumenschein WM, Mattson J, Basham B, Sedgwick JD, McClanahan T, Kastelein RA, Cua DJ (2005) IL-23 drives a pathogenic T cell population that induces autoimmune inflammation. *J Exp Med* **201:**233-240. doi: jem.20041257 [pii]

Laranjeiro R, Whitmore D (2014) Transcription factors involved in retinogenesis are co-opted by the circadian clock following photoreceptor differentiation. *Development* **141:**2644-2656. doi: 10.1242/dev.104380 [doi]

Lee H, Miau L, Chen C, Chiou L, Huang G, Yang P, Sheu J (2003) Differential role of p38 in IL-1α induction of MMP-9 and MMP-13 in an established liver myofibroblast cell line. *J Biomed Sci* **10:**757-765

Lee SH, Seo GS, Park YN, Yoo TM, Sohn DH (2004) Effects and regulation of osteopontin in rat hepatic stellate cells. *Biochem Pharmacol* **68:**2367-2378

Lee SH, Kim KW, Min KM, Kim KW, Chang SI, Kim JC (2014) Angiogenin reduces immune inflammation via inhibition of TANK-binding kinase 1 expression in human corneal fibroblast cells. *Mediators Inflamm* **2014:**861435. doi: 10.1155/2014/861435 [doi]

Li D, Friedman S (1999) Liver fibrogenesis and the role of hepatic stellate cells: new insights and prospects for therapy. *J Gastroenterol Hepatol* **14:**618-633

Li W, Liang X, Kellendonk C, Poli V, Taub R (2002) STAT3 contributes to the mitogenic response of hepatocytes during liver regeneration. *J Biol Chem* **277:**28411-28417

Lipniacki T, Paszek P, Brasier A, Luxon B, Kimmel M (2004) Mathematical model of NF-kappa B regulatory module. *J Theor Biol* **228:**195-215. doi: 10.1016/j.jtbi.2004.01.001

Liu S, Cheng C, Chang C, Mai F, Wang C, Lee S, Ho A, Chen L, Chang J (2011) Discovery of serum biomarkers of alcoholic fatty liver in a rodent model: C-reactive protein. *J Biomed Sci* **18:**1

Liu Y, Ma Z, Zhao C, Wang Y, Wu G, Xiao J, McClain CJ, Li X, Feng W (2014) HIF-1α and HIF-2α are critically involved in hypoxia-induced lipid accumulation in hepatocytes through reducing PGC-1α-mediated fatty acid β-oxidation. *Toxicol Lett* **226:**117-123

Liu M, Xu Y, Han X, Yin L, Xu L, Qi Y, Zhao Y, Liu K, Peng J (2015) Dioscin alleviates alcoholic liver fibrosis by attenuating hepatic stellate cell activation via the TLR4/MyD88/NF-kappaB signaling pathway. *Sci Rep* **5:**18038. doi: 10.1038/srep18038 [doi]

Livak KJ, Schmittgen TD (2001a) Analysis of relative gene expression data using real-time quantitative PCR and the 2− ΔΔCT method. *Methods* **25:**402-408

Livak KJ, Schmittgen TD (2001b) Analysis of relative gene expression data using real-time quantitative PCR and the 2− ΔΔCT method. *Methods* **25:**402-408

Lovrics A, Csikász-Nagy A, Zsély IG, Zádor J, Turányi T, Novák B (2006) Time scale and dimension analysis of a budding yeast cell cycle model. *BMC Bioinformatics* **7:**1

Loyer P, Glaise D, Cariou S, Baffet G, Meijer L, Guguen-Guillouzo C (1994) Expression and activation of cdks (1 and 2) and cyclins in the cell cycle progression during liver regeneration. *J Biol Chem* **269:**2491-2500

Luo X, Chae M, Krishnakumar R, Danko CG, Kraus WL (2014) Dynamic reorganization of the AC16 cardiomyocyte transcriptome in response to TNFalpha signaling revealed by integrated genomic analyses. *BMC Genomics* **15:**155-2164-15-155. doi: 10.1186/1471-2164-15-155 [doi]

Maeno H, Ono T, Dhar DK, Sato T, Yamanoi A, Nagasue N (2005) Expression of hypoxia inducible factor-1α during liver regeneration induced by partial hepatectomy in rats. *Liver International* **25:**1002-1009

Maher JJ (1993) Cell-specific expression of hepatocyte growth factor in liver. Upregulation in sinusoidal endothelial cells after carbon tetrachloride. *J Clin Invest* **91:**2244-2252. doi: 10.1172/JCI116451 [doi]

Mahony S, Benos PV (2007) STAMP: a web tool for exploring DNA-binding motif similarities. *Nucleic Acids Res* **35:**W253-W258. doi: 10.1093/nar/gkm272

Malato Y, Sander LE, Liedtke C, Al-Masaoudi M, Tacke F, Trautwein C, Beraza N (2008) Hepatocyte-specific inhibitor-of-kappaB-kinase deletion triggers the innate immune response and promotes earlier cell proliferation during liver regeneration. *Hepatology* **47:**2036-2050

Malato Y, Naqvi S, Schurmann N, Ng R, Wang B, Zape J, Kay MA, Grimm D, Willenbring H (2011) Fate tracing of mature hepatocytes in mouse liver homeostasis and regeneration. *J Clin Invest* **121:**4850-4860. doi: 10.1172/JCI59261 [doi]

Malik R, Selden C, Hodgson H (2002) The role of non-parenchymal cells in liver growth. **13:**425-431

Mantzoros CS, Magkos F, Brinkoetter M, Sienkiewicz E, Dardeno TA, Kim SY, Hamnvik OP, Koniaris A (2011) Leptin in human physiology and pathophysiology. *Am J Physiol Endocrinol Metab* **301:**E567-84. doi: 10.1152/ajpendo.00315.2011 [doi]

Marino S, Hogue IB, Ray CJ, Kirschner DE (2008) A methodology for performing global uncertainty and sensitivity analysis in systems biology. *J Theor Biol* **254:**178-196

Marino S, Cilfone NA, Mattila JT, Linderman JJ, Flynn JL, Kirschner DE (2015) Macrophage polarization drives granuloma outcome during Mycobacterium tuberculosis infection. *Infect Immun* **83:**324-338. doi: 10.1128/IAI.02494-14 [doi]

Martinez-Jimenez CP, Odom DT (2016) The mechanisms shaping the single-cell transcriptional landscape. *Curr Opin Genet Dev* **37:**27-35

Matsubara M, Maruoka S, Katayose S (2002) Inverse relationship between plasma adiponectin and leptin concentrations in normal-weight and obese women. *Eur J Endocrinol* **147:**173-180. doi: 147173 [pii]

Matys V, Kel-Margoulis OV, Fricke E, Liebich I, Land S, Barre-Dirrie A, Reuter I, Chekmenev D, Krull M, Hornischer K, Voss N, Stegmaier P, Lewicki-Potapov B, Saxel H, Kel AE, Wingender E (2006) TRANSFAC (R) and its module TRANSCompel (R): transcriptional gene regulation in eukaryotes. *Nucleic Acids Res* **34:**D108-D110. doi: 10.1093/nar/gkj143

McAdams HH, Arkin A (1997) Stochastic mechanisms in gene expression. *Proc Natl Acad Sci U S A* **94:**814-819. doi: 10.1073/pnas.94.3.814

McClain C, Song Z, Barve S, Hill D, Deaciuc I (2004) Recent advances in alcoholic liver disease - IV. Dysregulated cytokine metabolism in alcoholic liver disease. *American Journal of Physiology-Gastrointestinal and Liver Physiology* **287:**G497-G502. doi: 10.1152/ajpgi.00171.2004

McCormack L, Dutkowski P, El-Badry AM, Clavien P (2011) Liver transplantation using fatty livers: always feasible? *J Hepatol* **54:**1055-1062

McGivern DR, Lemon SM (2011) Virus-specific mechanisms of carcinogenesis in hepatitis C virus associated liver cancer. *Oncogene* **30:**1969-1983

Meijer C, Wiezer MJ, Diehl AM, Yang S, Schouten HJ, Meijer S, Rooijen N, Lambalgen AA, Dijkstra CD, Leeuwen PA (2000a) Kupffer cell depletion by CI2MDP-liposomes alters hepatic cytokine expression and delays liver regeneration after partial hepatectomy. *Liver* **20:**66-77

Meijer C, Wiezer M, Diehl A, Yang S, Schouten H, Meijer S, van Rooijen N, van Lambalgen A, Dijkstra C, van Leeuwen P (2000b) Kupffer cell depletion by CI2MDP-liposomes alters hepatic cytokine expression and delays liver regeneration after partial hepatectomy. *Liver* **20:**66-77. doi: 10.1034/j.1600-0676.2000.020001066.x

Melgar-Lesmes P, Edelman ER (2015) Monocyte-endothelial cell interactions in the regulation of vascular sprouting and liver regeneration in mouse. *J Hepatol*

Michalopoulos GK (2013) Principles of liver regeneration and growth homeostasis. *Comprehensive Physiology*

Michalopoulos GK (2007a) Liver regeneration. *J Cell Physiol* **213:**286-300

Michalopoulos GK (1990) Liver regeneration: molecular mechanisms of growth control. *The FASEB Journal* **4:**176-187

Michalopoulos GK, Barua L, Bowen WC (2005) Transdifferentiation of rat hepatocytes into biliary cells after bile duct ligation and toxic biliary injury. *Hepatology* **41:**535-544

Michalopoulos GK (2010) Liver Regeneration after Partial Hepatectomy Critical Analysis of Mechanistic Dilemmas. *Am J Pathol* **176:**2-13. doi: 10.2353/ajpath.2010.090675

Michalopoulos GK (2007b) Liver regeneration. *J Cell Physiol* **213:**286-300. doi: 10.1002/jcp.21172

MICHALOPOULOS G (1990) Liver-Regeneration - Molecular Mechanisms of Growth-Control. *Faseb Journal* **4:**176-187

Michalopoulos G, DeFrances M (1997) Liver regeneration. *Science* **276:**60-66. doi: 10.1126/science.276.5309.60

Mitchell C, Willenbring H (2008) A reproducible and well-tolerated method for 2/3 partial hepatectomy in mice. *Nature protocols* **3:**1167-1170

Miyajima A, Tanaka M, Itoh T (2014) Stem/progenitor cells in liver development, homeostasis, regeneration, and reprogramming. *Cell Stem Cell* **14:**561-574

Monami M, Lamanna C, Marchionni N, Mannucci E (2008) Rosiglitazone and risk of cancer: a meta-analysis of randomized clinical trials. *Diabetes Care* **31:**1455-1460. doi: 10.2337/dc07-2308 [doi]

Monga S, Pediaditakis P, Mule K, Stolz D, Michalopoulos G (2001) Changes in wnt/beta-catenin pathway during regulated growth in rat liver regeneration. *Hepatology* **33:**1098-1109. doi: 10.1053/jhep.2001.23786

Montalto G, Cervello M, Giannitrapani L, Dantona F, Terranova A, Castagnetta LA (2002) Epidemiology, risk factors, and natural history of hepatocellular carcinoma. *Ann N Y Acad Sci* **963:**13-20

Mullhaupt B, Feren A, Fodor E, Jones A (1994) Liver expression of epidermal growth factor RNA. Rapid increases in immediate-early phase of liver regeneration. *J Biol Chem* **269:**19667-19670

Muppidi JR, Tschopp J, Siegel RM (2004) Life and death decisions: secondary complexes and lipid rafts in TNF receptor family signal transduction. *Immunity* **21:**461-465

Murata S, Hashimoto I, Nakano Y, Myronovych A, Watanabe M, Ohkohchi N (2008) Single administration of thrombopoietin prevents progression of liver fibrosis and promotes liver regeneration after partial hepatectomy in cirrhotic rats. *Ann Surg* **248:**821-828. doi: 10.1097/SLA.0b013e31818584c7 [doi]

NAGASUE N, KOHNO H, CHANG Y, TANIURA H, YAMANOI A, UCHIDA M, KIMOTO T, TAKEMOTO Y, NAKAMURA T, YUKAYA H (1993) Liver Resection for Hepatocellular-Carcinoma - Results of 229 Consecutive Patients during 11 Years. *Ann Surg* **217:**375-384. doi: 10.1097/00000658-199304000-00009

Nan Y, Wang R, Fu N (2014) Peroxisome proliferator-activated receptor alpha, a potential therapeutic target for alcoholic liver disease. *World Journal of Gastroenterology* **20:**8055-8060. doi: 10.3748/wjg.v20.i25.8055

Naugler WE (2014) Bile Acid Flux Is Necessary for Normal Liver Regeneration. *Plos One* **9:**e97426. doi: 10.1371/journal.pone.0097426

Naveau S, Chollet-Martin S, Dharancy S, Mathurin P, Jouet P, Piquet M, Davion T, Oberti F, Broet P, Emilie D, AFEF (2004) A double-blind randomized controlled trial of infliximab associated with prednisolone in acute alcoholic hepatitis. *Hepatology* **39:**1390-1397. doi: 10.1002/hep.20206

Nawa T, Nawa MT, Cai Y, Zhang C, Uchimura I, Narumi S, Numano F, Kitajima S (2000) Repression of TNF-α-induced E-selectin expression by PPAR activators: involvement of transcriptional repressor LRF-1/ATF3. *Biochem Biophys Res Commun* **275:**406-411

Nawrocki AR, Rajala MW, Tomas E, Pajvani UB, Saha AK, Trumbauer ME, Pang Z, Chen AS, Ruderman NB, Chen H, Rossetti L, Scherer PE (2006) Mice lacking adiponectin show decreased hepatic insulin sensitivity and reduced responsiveness to peroxisome proliferator-activated receptor gamma agonists. *J Biol Chem* **281:**2654-2660. doi: M505311200 [pii]

Nissen SE, Wolski K (2007) Effect of rosiglitazone on the risk of myocardial infarction and death from cardiovascular causes. *N Engl J Med* **356:**2457-2471

Novak JP, Sladek R, Hudson TJ (2002) Characterization of variability in large-scale gene expression data: implications for study design. *Genomics* **79:**104-113

Novak M, Tyson J (2004) A model for restriction point control of the mammalian cell cycle. *J Theor Biol* **230:**563-579. doi: 10.1016/j.jtbi.2004.04.039

Oe S, Lemmer ER, Conner EA, Factor VM, Levéen P, Larsson J, Karlsson S, Thorgeirsson SS (2004) Intact signaling by transforming growth factor β is not required for termination of liver regeneration in mice. *Hepatology* **40:**1098-1105

Ogawa D, Stone JF, Takata Y, Blaschke F, Chu VH, Towler DA, Law RE, Hsueh WA, Bruemmer D (2005) Liver x receptor agonists inhibit cytokine-induced osteopontin expression in macrophages through interference with activator protein-1 signaling pathways. *Circ Res* **96:**e59-67. doi: 01.RES.0000163630.86796.17 [pii]

Oh DK, Ciaraldi T, Henry RR (2007) Adiponectin in health and disease. *Diabetes, Obesity and Metabolism* **9:**282-289

Ohashi K, Iwatani H, Kihara S, Nakagawa Y, Komura N, Fujita K, Maeda N, Nishida M, Katsube F, Shimomura I, Ito T, Funahashi T (2007) Exacerbation of albuminuria and renal fibrosis in subtotal renal ablation model of adiponectin-knockout mice. *Arterioscler Thromb Vasc Biol* **27:**1910-1917. doi: ATVBAHA.107.147645 [pii]

Oksanen J, Blanchet F, Kindt R, Legendre P, O'Hara R, Simpson G, Solymos P, Stevens M, Wagner H (2013) vegan: Community Ecology Package. *R package* **version 2.0-10:**

Olazabal IM, Muñoz JA, Rodríguez-Navas C, Alvarez L, Delgado-Baeza E, García-Ruiz JP (2009) Prolactin's role in the early stages of liver regeneration in rats. *J Cell Physiol* **219:**626-633

Ono Y, Kawachi S, Hayashida T, Wakui M, Tanabe M, Itano O, Obara H, Shinoda M, Hibi T, Oshima G (2011a) The influence of donor age on liver regeneration and hepatic progenitor cell populations. *Surgery* **150:**154-161

Ono Y, Kawachi S, Hayashida T, Wakui M, Tanabe M, Itano O, Obara H, Shinoda M, Hibi T, Oshima G (2011b) The influence of donor age on liver regeneration and hepatic progenitor cell populations. *Surgery* **150:**154-161

O'shea RS, Dasarathy S, McCullough AJ (2010) Alcoholic liver disease. *Hepatology* **51:**307-328

Paik Y, Schwabe RF, Bataller R, Russo MP, Jobin C, Brenner DA (2003) Toll-like receptor 4 mediates inflammatory signaling by bacterial lipopolysaccharide in human hepatic stellate cells. *Hepatology* **37:**1043-1055

Paik Y, Lee KS, Lee HJ, Yang KM, Lee SJ, Lee DK, Han K, Chon CY, Lee SI, Moon YM (2006) Hepatic stellate cells primed with cytokines upregulate inflammation in response to peptidoglycan or lipoteichoic acid. *Laboratory Investigation* **86:**676-686

Pan S, Wu L, Chen C, Shieh S, Chiu H (2012) Angiogenin expression in burn blister fluid: implications for its role in burn wound neovascularization. *Wound Repair and Regeneration* **20:**731-739

Panzeri S, Petersen RS, Schultz SR, Lebedev M, Diamond ME (2001) The role of spike timing in the coding of stimulus location in rat somatosensory cortex. *Neuron* **29:**769-777

Park J, Ogunnaike B, Schwaber J, Vadigepalli R (2015a) Identifying functional gene regulatory network phenotypes underlying single cell transcriptional variability. *Prog Biophys Mol Biol* **117:**87-98

Park P, Sanz-Garcia C, Nagy LE (2015b) Adiponectin as an Anti-fibrotic and Anti-inflammatory Adipokine in the Liver. *Current pathobiology reports* **3:**243-252

Park J, Brureau A, Kernan K, Starks A, Gulati S, Ogunnaike B, Schwaber J, Vadigepalli R (2014) Inputs drive cell phenotype variability. *Genome Res* **24:**930-941. doi: 10.1101/gr.161802.113 [doi]

Park PH, McMullen MR, Huang H, Thakur V, Nagy LE (2007) Short-term treatment of RAW264.7 macrophages with adiponectin increases tumor necrosis factor-alpha (TNF-alpha) expression via ERK1/2 activation and Egr-1 expression: role of TNF-alpha in adiponectin-stimulated interleukin-10 production. *J Biol Chem* **282:**21695-21703. doi: M701419200 [pii]

Paschos KA, Majeed AW, Bird NC (2010) Role of Kupffer cells in the outgrowth of colorectal cancer liver metastases. *Hepatology Research* **40:**83-94

Paszek P, Ryan S, Ashall L, Sillitoe K, Harper CV, Spiller DG, Rand DA, White MR (2010) Population robustness arising from cellular heterogeneity. *Proc Natl Acad Sci U S A* **107:**11644-11649. doi: 10.1073/pnas.0913798107 [doi]

Pataridis S, Eckhardt A, Mikulíková K, Sedláková P, Mikšík I (2008) Identification of collagen types in tissues using HPLC-MS/MS. *Journal of separation science* **31:**3483-3488

Patel AP, Tirosh I, Trombetta JJ, Shalek AK, Gillespie SM, Wakimoto H, Cahill DP, Nahed BV, Curry WT, Martuza RL, Louis DN, Rozenblatt-Rosen O, Suva ML, Regev A, Bernstein BE (2014) Single-cell RNA-seq highlights intratumoral heterogeneity in primary glioblastoma. *Science* **344:**1396-1401. doi: 10.1126/science.1254257 [doi]

Pearson R (2011) *Exploring data in engineering, the sciences, and medicine*. OUP USA

Periwal V, Gaillard JR, Needleman L, Doria C (2014) Mathematical Model of Liver Regeneration in Human Live Donors. *J Cell Physiol* **229:**599-606. doi: 10.1002/jcp.24482

Perumal TM, Gunawan R (2011) Impulse parametric sensitivity analysis. *IFAC Proceedings Volumes* **44:**9686-9690

Pluznick JL, Zou D, Zhang X, Yan Q, Rodriguez-Gil DJ, Eisner C, Wells E, Greer CA, Wang T, Firestein S, Schnermann J, Caplan MJ (2009) Functional expression of the olfactory signaling system in the kidney. *Proc Natl Acad Sci U S A* **106:**2059-2064. doi: 10.1073/pnas.0812859106

Pomfret E, Pomposelli J, Gordon F, Erbay N, Price L, Lewis W, Jenkins R (2003) Liver regeneration and surgical outcome in donors of right-lobe liver grafts. *Transplantation* **76:**5-10. doi: 10.1097/01.TP.0000079064.08263.8E

Poon RT, Fan S (2004) Hepatectomy for hepatocellular carcinoma: patient selection and postoperative outcome. *Liver transplantation* **10:**

Poss KD (2010) Advances in understanding tissue regenerative capacity and mechanisms in animals. *Nature Reviews Genetics* **11:**710-722

Qiu P, Simonds EF, Bendall SC, Gibbs Jr KD, Bruggner RV, Linderman MD, Sachs K, Nolan GP, Plevritis SK (2011) Extracting a cellular hierarchy from high-dimensional cytometry data with SPADE. *Nat Biotechnol* **29:**886-891

R Core Team (2014) R: A Language and Environment for Statistical Computing.

R Core Team (2012) R: A language and environment for statistical computing. *R Foundation for Statistical Computing*

Ramer MS, Priestley JV, McMahon SB (2000) Functional regeneration of sensory axons into the adult spinal cord. *Nature* **403:**312-316

Reddy JK, Rao MS (2006) Lipid metabolism and liver inflammation. II. Fatty liver disease and fatty acid oxidation. *Am J Physiol Gastrointest Liver Physiol* **290:**G852-8. doi: 290/5/G852 [pii]

Reeves HL, Friedman SL (2002) Activation of hepatic stellate cells-a key issue in liver fibrosis. *Front Biosci* **7:**808-826

Reich P, Tjoelker M, Machado J, Oleksyn J (2006) Universal scaling of respiratory metabolism, size and nitrogen in plants. *Nature* **439:**457-461. doi: 10.1038/nature04282

Reiman RM, Thompson RW, Feng CG, Hari D, Knight R, Cheever AW, Rosenberg HF, Wynn TA (2006) Interleukin-5 (IL-5) augments the progression of liver fibrosis by regulating IL-13 activity. *Infect Immun* **74:**1471-1479. doi: 74/3/1471 [pii]

Ren W, Li X, Wang F, Qiao J, Dang S, Kong H, Wang L, Lu S, Sun X, Xu G (2005) Generation of adiponectin gene knock--out and LacZ gene knock--in mouse model. *Sheng wu hua xue yu sheng wu wu li jin zhan* **33:**846-853

Rhee HS, Pugh BF (2012) ChIP-exo method for identifying genomic location of DNA-binding proteins with near-single-nucleotide accuracy. *Current protocols in molecular biology / edited by Frederick M.Ausubel ...[et al.]* **Chapter 21:**Unit 21.24-Unit 21.24. doi: 10.1002/0471142727.mb2124s100

Ringe B, Pichlmayr R, Wittekind C, Tusch G (1991) Surgical treatment of hepatocellular carcinoma: experience with liver resection and transplantation in 198 patients. *World J Surg* **15:**270-285

Ringelhan M, Schmid RM, Geisler F (2012) The NF-kappa B Subunit RelA/p65 Is Dispensable for Successful Liver Regeneration after Partial Hepatectomy in Mice. *Plos One* **7:**e46469. doi: 10.1371/journal.pone.0046469

Ritsma L, Ellenbroek SI, Zomer A, Snippert HJ, de Sauvage FJ, Simons BD, Clevers H, van Rheenen J (2014) Intestinal crypt homeostasis revealed at single-stem-cell level by in vivo live imaging. *Nature* **507:**362-365

Ronis MJ, Hennings L, Stewart B, Basnakian AG, Apostolov EO, Albano E, Badger TM, Petersen DR (2011) Effects of long-term ethanol administration in a rat total enteral nutrition model of alcoholic liver disease. *Am J Physiol Gastrointest Liver Physiol* **300:**G109-19. doi: 10.1152/ajpgi.00145.2010 [doi]

Rudolph KL, Trautwein C, Kubicka S, Rakemann T, Bahr MJ, Sedlaczek N, Schuppan D, Manns MP (1999) Differential regulation of extracellular matrix synthesis during liver regeneration after partial hepatectomy in rats. *Hepatology* **30:**1159-1166

Saha B, Bala S, Hosseini N, Kodys K, Szabo G (2015) Kruppel-like factor 4 is a transcriptional regulator of M1/M2 macrophage polarization in alcoholic liver disease. *J Leukoc Biol* . doi: jlb.4A1014-485R [pii]

Sahin H, Trautwein C, Wasmuth HE (2010) Functional role of chemokines in liver disease models. *Nature Reviews Gastroenterology and Hepatology* **7:**682-690

Sahin H, Borkham-Kamphorst E, Kuppe C, Zaldivar MM, Grouls C, Al-samman M, Nellen A, Schmitz P, Heinrichs D, Berres M (2012) Chemokine Cxcl9 attenuates liver fibrosis-associated angiogenesis in mice. *Hepatology* **55:**1610-1619

Sakai N, Van Sweringen HL, Schuster R, Blanchard J, Burns JM, Tevar AD, Edwards MJ, Lentsch AB (2012) Receptor activator of nuclear factor-κB ligand (RANKL) protects against hepatic ischemia/reperfusion injury in mice. *Hepatology* **55:**888-897

Sakaida I, Hironaka K, Terai S, Okita K (2003) Gadolinium chloride reverses dimethylnitrosamine (DMN)-induced rat liver fibrosis with increased matrix metalloproteinases (MMPs) of Kupffer cells. *Life Sci* **72:**943-959

Salazar-Montes A, Ruiz-Corro L, Sandoval-Rodriguez A, Lopez-Reyes A, Armendariz-Borunda J (2006) Increased DNA binding activity of NF-kappa B, STAT-3, SMAD3 and AP-1 in acutely damaged liver. *World Journal of Gastroenterology* **12:**5995-6001

Satija R, Farrell JA, Gennert D, Schier AF, Regev A (2015) Spatial reconstruction of single-cell gene expression data. *Nat Biotechnol* **33:**495-502

Saxena NK, Ikeda K, Rockey DC, Friedman SL, Anania FA (2002) Leptin in hepatic fibrosis: evidence for increased collagen production in stellate cells and lean littermates of ob/ob mice. *Hepatology* **35:**762-771

Schmitt WA, Raab RM, Stephanopoulos G (2004) Elucidation of gene interaction networks through time-lagged correlation analysis of transcriptional data. *Genome Res* **14:**1654-1663. doi: 10.1101/gr.2439804

Schümann J, Bluethmann H, Tiegs G (2000) Synergism of Pseudomonas aeruginosa exotoxin A with endotoxin, superantigen, or TNF results in TNFR1-and TNFR2-dependent liver toxicity in mice. *Immunol Lett* **74:**165-172

Schwabe RF, Schnabl B, Kweon YO, Brenner DA (2001) CD40 activates NF-kappa B and c-Jun N-terminal kinase and enhances chemokine secretion on activated human hepatic stellate cells. *J Immunol* **166:**6812-6819

Schwen LO, Krauss M, Niederalt C, Gremse F, Kiessling F, Schenk A, Preusser T, Kuepfer L (2014) Spatio-Temporal Simulation of First Pass Drug Perfusion in the Liver. *Plos Computational Biology* **10:**e1003499. doi: 10.1371/journal.pcbi.1003499

Seki E, Brenner DA (2015) Recent advancement of molecular mechanisms of liver fibrosis. *Journal of hepato-biliary-pancreatic sciences* **22:**512-518

Sheikh-Bahaei S, Kim SH, Sheikhbahaei S, Hunt CA (2009) Understanding the role of liver zonation in toxin elimination. *Int J Intell Control Syst* **14:**33-40

Shestopaloff YK (2014) Method for Finding Metabolic Properties Based on the General Growth Law. Liver Examples. A General Framework for Biological Modeling. *Plos One* **9:**e99836. doi: 10.1371/journal.pone.0099836

Shimabukuro R, Kawanaka H, Tomikawa M, Akahoshi T, Konishi K, Yoshida D, Anegawa G, Uehara H, Hashimoto N, Hashizume M (2009) Effect of thrombopoietin on platelet counts and liver regeneration after partial hepatectomy in a rat model. *Surg Today* **39:**1054-1059

Shu R, Zhang F, Wang F, Feng D, Li X, Ren W, Wu X, Yang X, Liao X, Huang L (2009a) Adiponectin deficiency impairs liver regeneration through attenuating STAT3 phosphorylation in mice. *Laboratory Investigation* **89:**1043-1052

Shu R, Zhang F, Wang F, Feng D, Li X, Ren W, Wu X, Yang X, Liao X, Huang L, Wang Z (2009b) Adiponectin deficiency impairs liver regeneration through attenuating STAT3 phosphorylation in mice. *Laboratory Investigation* **89:**1043-1052. doi: 10.1038/labinvest.2009.63

Sica A, Invernizzi P, Mantovani A (2014) Macrophage plasticity and polarization in liver homeostasis and pathology. *Hepatology* **59:**2034-2042

Silberberg G, Bethge M, Markram H, Pawelzik K, Tsodyks M (2004) Dynamics of population rate codes in ensembles of neocortical neurons. *J Neurophysiol* **91:**704-709. doi: 10.1152/jn.00415.2003 [doi]

Silha JV, Krsek M, Skrha JV, Sucharda P, Nyomba BL, Murphy LJ (2003) Plasma resistin, adiponectin and leptin levels in lean and obese subjects: correlations with insulin resistance. *Eur J Endocrinol* **149:**331-335

Simon-Holtorf J, Mönig H, Klomp H, Reinecke-Lüthge A, Fölsch U, Kloehn S (2006) Expression and distribution of prolactin receptor in normal, fibrotic, and cirrhotic human liver. *Experimental and clinical endocrinology & diabetes* **114:**584-589

Simpson KJ, Henderson NC, Bone-Larson CL, Lukacs NW, Hogaboam CM, Kunkel SL (2003) Chemokines in the pathogenesis of liver disease: so many players with poorly defined roles. *Clin Sci (Lond)* **104:**47-63. doi: 10.1042/ [doi]

Singhania R, Sramkoski RM, Jacobberger JW, Tyson JJ (2011) A Hybrid Model of Mammalian Cell Cycle Regulation. *Plos Computational Biology* **7:**e1001077. doi: 10.1371/journal.pcbi.1001077

Skene NG, Grant SG (2016) Identification of Vulnerable Cell Types in Major Brain Disorders Using Single Cell Transcriptomes and Expression Weighted Cell Type Enrichment. *Frontiers in neuroscience* **10:**

Smith A, Sumazin P, Zhang M (2005) Identifying tissue-selective transcription factor bindings sites in vertebrate promoters. *Proc Natl Acad Sci U S A* **102:**1560-1565. doi: 10.1073/pnas.0406123102

Sobol IM (2001) Global sensitivity indices for nonlinear mathematical models and their Monte Carlo estimates. *Math Comput Simul* **55:**271-280

Spalding KL, Bhardwaj RD, Buchholz BA, Druid H, Frisén J (2005) Retrospective birth dating of cells in humans. *Cell* **122:**133-143

Spurgeon SL, Jones RC, Ramakrishnan R (2008) High Throughput Gene Expression Measurement with Real Time PCR in a Microfluidic Dynamic Array. *Plos One* **3:**e1662. doi: 10.1371/journal.pone.0001662

Stanger BZ (2015) Probing hepatocyte heterogeneity. *Cell Res*

Stefanovic L, Brenner DA, Stefanovic B (2005) Direct hepatotoxic effect of KC chemokine in the liver without infiltration of neutrophils. *Exp Biol Med (Maywood)* **230:**573-586. doi: 230/8/573 [pii]

Stuart JM, Segal E, Koller D, Kim SK (2003) A gene-coexpression network for global discovery of conserved genetic modules. *Science* **302:**249-255. doi: 10.1126/science.1087447 [doi]

Sturm J, Keese M, Zhang H, Bönninghoff R, Magdeburg R, Vajkoczy P, Dono R, Zeller R, Gretz N (2004) Liver regeneration in FGF-2-deficient mice: VEGF acts as potential functional substitute for FGF-2. *Liver International* **24:**161-168

Sun B, Karin M (2012) Obesity, inflammation, and liver cancer. *J Hepatol* **56:**704-713

Sun Y, Lodish HF (2010) Adiponectin deficiency promotes tumor growth in mice by reducing macrophage infiltration. *PLoS One* **5:**e11987

Tanemura A, Mizuno S, Wada H, Yamada T, Nobori T, Isaji S (2012) Donor Age Affects Liver Regeneration during Early Period in the Graft Liver and Late Period in the Remnant Liver after Living Donor Liver Transplantation. *World J Surg* **36:**1102-1111. doi: 10.1007/s00268-012-1496-1

Tang F, Barbacioru C, Bao S, Lee C, Nordman E, Wang X, Lao K, Surani MA (2010) Tracing the derivation of embryonic stem cells from the inner cell mass by single-cell RNA-Seq analysis. *Cell stem cell* **6:**468-478

Tanoue S, Uto H, Kumamoto R, Arima S, Hashimoto S, Nasu Y, Takami Y, Moriuchi A, Sakiyama T, Oketani M, Ido A, Tsubouchi H (2011) Liver regeneration after partial hepatectomy in rat is more impaired in a steatotic liver induced by dietary fructose compared to dietary fat. *Biochem Biophys Res Commun* **407:**163-168. doi: 10.1016/j.bbrc.2011.02.131

Tao L, Wang Y, Gao E, Zhang H, Yuan Y, Lau WB, Chan L, Koch WJ, Ma XL (2010) Adiponectin: an indispensable molecule in rosiglitazone cardioprotection following myocardial infarction. *Circ Res* **106:**409-417. doi: 10.1161/CIRCRESAHA.109.211797 [doi]

Tarrats N, Moles A, Morales A, García-Ruiz C, Fernández-Checa JC, Marí M (2011) Critical role of tumor necrosis factor receptor 1, but not 2, in hepatic stellate cell proliferation, extracellular matrix remodeling, and liver fibrogenesis. *Hepatology* **54:**319-327

Taub R (2004a) Liver regeneration: from myth to mechanism. *Nature reviews Molecular cell biology* **5:**836-847

Taub R (2004b) Liver regeneration: from myth to mechanism. *Nature reviews Molecular cell biology* **5:**836-847

Taub R (2004c) Liver regeneration: From myth to mechanism. *Nature Reviews Molecular Cell Biology* **5:**836-847. doi: 10.1038/nrm1489

Thakar J, Pilione M, Kirimanjeswara G, Harvill ET, Albert R (2007) Modeling systems-level regulation of host immune responses. *Plos Computational Biology* **3:**1022-1039. doi: 10.1371/journal.pcbi.0030109

Thorgeirsson SS, Grisham JW (2006) Hematopoietic cells as hepatocyte stem cells: a critical review of the evidence. *Hepatology* **43:**2-8

Tomiya T, Ogata I, Fujiwara K (1998) Transforming growth factor α levels in liver and blood correlate better than hepatocyte growth factor with hepatocyte proliferation during liver regeneration. *The American journal of pathology* **153:**955-961

Treutlein B, Brownfield DG, Wu AR, Neff NF, Mantalas GL, Espinoza FH, Desai TJ, Krasnow MA, Quake SR (2014) Reconstructing lineage hierarchies of the distal lung epithelium using single-cell RNA-seq. *Nature* **509:**371-375

Tsai C, Bussel JB, Imahiyerobo AA, Sandler SI, Ogunnaike BA (2016) Platelet count control in immune thrombocytopenic purpura patient: Optimum romiplostim dose profile. *J Process Control* **45:**76-83

Tsochatzis E, Papatheodoridis GV, Archimandritis AJ (2006) The evolving role of leptin and adiponectin in chronic liver diseases. *Am J Gastroenterol* **101:**2629-2640

Turer A, Scherer P (2012) Adiponectin: mechanistic insights and clinical implications. *Diabetologia* **55:**2319-2326

Turmelle YP, Shikapwashya O, Tu S, Hruz PW, Yan Q, Rudnick DA (2006) Rosiglitazone inhibits mouse liver regeneration. *FASEB J* **20:**2609-2611. doi: fj.06-6511fje [pii]

TYSON J (1985) The Coordination of Cell-Growth and Division - Intentional Or Incidental. *Bioessays* **2:**72-77. doi: 10.1002/bies.950020208

Venables WN, Ripley BD (2002) *Modern Applied Statistics with S.* Springer, New York

Vendrell J, Broch M, Vilarrasa N, Molina A, Gómez JM, Gutiérrez C, Simón I, Soler J, Richart C (2004) Resistin, adiponectin, ghrelin, leptin, and proinflammatory cytokines: relationships in obesity. *Obes Res* **12:**962-971

Virani S, Michaelson JS, Hutter MM, Lancaster RT, Warshaw AL, Henderson WG, Khuri SF, Tanabe KK (2007) Morbidity and mortality after liver resection: results of the patient safety in surgery study. *J Am Coll Surg* **204:**1284-1292

Wang B, Zhao L, Fish M, Logan CY, Nusse R (2015a) Self-renewing diploid Axin2 cells fuel homeostatic renewal of the liver. *Nature* **524:**180-185

Wang B, Zhao L, Fish M, Logan CY, Nusse R (2015b) Self-renewing diploid Axin2 cells fuel homeostatic renewal of the liver. *Nature* **524:**180-185

Wang H, Keiser JA (2000) Hepatocyte growth factor enhances MMP activity in human endothelial cells. *Biochem Biophys Res Commun* **272:**900-905

Wang M, You Q, Lor K, Chen F, Gao B, Ju C (2014) Chronic alcohol ingestion modulates hepatic macrophage populations and functions in mice. *J Leukoc Biol* **96:**657-665. doi: 10.1189/jlb.6A0114-004RR [doi]

Wang X, Foster M, Al-Dhalimy M, Lagasse E, Finegold M, Grompe M (2003) The origin and liver repopulating capacity of murine oval cells. *Proc Natl Acad Sci U S A* **100 Suppl 1:**11881-11888. doi: 10.1073/pnas.1734199100 [doi]

Wang Y, Lam KS, Xu JY, Lu G, Xu LY, Cooper GJ, Xu A (2005) Adiponectin inhibits cell proliferation by interacting with several growth factors in an oligomerization-dependent manner. *J Biol Chem* **280:**18341-18347. doi: M501149200 [pii]

Weglarz TC, Sandgren EP (2000) Timing of hepatocyte entry into DNA synthesis after partial hepatectomy is cell autonomous. *Proc Natl Acad Sci U S A* **97:**12595-12600. doi: 10.1073/pnas.220430497 [doi]

White C, Seymour R (2003) Mammalian basal metabolic rate is proportional to body mass(2/3). *Proc Natl Acad Sci U S A* **100:**4046-4049. doi: 10.1073/pnas.0436428100

Wilk G, Iwasa M, Fuller PE, Kandere-Grzybowska K, Grzybowski BA (2014) Universal Area Distributions in the Monolayers of Confluent Mammalian Cells. *Phys Rev Lett* **112:**138104. doi: 10.1103/PhysRevLett.112.138104

Winter DR, Song L, Mukherjee S, Furey TS, Crawford GE (2013) DNase-seq predicts regions of rotational nucleosome stability across diverse human cell types. *Genome Res* **23:**1118-1129. doi: 10.1101/gr.150482.112

Xing Z, Tremblay GM, Sime PJ, Gauldie J (1997) Overexpression of granulocyte-macrophage colony-stimulating factor induces pulmonary granulation tissue formation and fibrosis by induction of transforming growth factor-beta 1 and myofibroblast accumulation. *Am J Pathol* **150:**59-66

Xu J, Murphy SL, Kochanek KD, Bastian BA (2016) Deaths: Final Data for 2013. *Natl Vital Stat Rep* **64:**1-119

Xu L, Hui AY, Albanis E, Arthur MJ, O'Byrne SM, Blaner WS, Mukherjee P, Friedman SL, Eng FJ (2005) Human hepatic stellate cell lines, LX-1 and LX-2: new tools for analysis of hepatic fibrosis. *Gut* **54:**142-151. doi: 54/1/142 [pii]

Yamauchi T, Kadowaki T (2013) Adiponectin receptor as a key player in healthy longevity and obesity-related diseases. *Cell metabolism* **17:**185-196

Yang L, Jung Y, Omenetti A, Witek RP, Choi S, Vandongen HM, Huang J, Alpini GD, Diehl AM (2008) Fate-mapping evidence that hepatic stellate cells are epithelial progenitors in adult mouse livers. *Stem Cells* **26:**2104-2113

Yang L, Magness ST, Bataller R, Rippe RA, Brenner DA (2005) NF-kappa B activation in Kupffer cells after partial hepatectomy. *American Journal of Physiology-Gastrointestinal and Liver Physiology* **289:**G530-G538. doi: 10.1152/ajpgi.00526.2004

Yang SQ, Lin HZ, Yin M, Albrecht JH, Diehl AM (1998a) Effects of chronic ethanol consumption on cytokine regulation of liver regeneration. *Am J Physiol* **275:**G696-704

Yang S, Lin H, Yiu M, Albrecht J, Diehl A (1998b) Effects of chronic ethanol consumption on cytokine regulation of liver regeneration. *American Journal of Physiology-Gastrointestinal and Liver Physiology* **275:**G696-G704

Yang ZF, Poon RT, Luo Y, Cheung CK, Ho DW, Lo CM, Fan ST (2004) Up-regulation of vascular endothelial growth factor (VEGF) in small-for-size liver grafts enhances macrophage activities through VEGF receptor 2-dependent pathway. *J Immunol* **173:**2507-2515. doi: 173/4/2507 [pii]

Yanger K, Zong Y, Maggs LR, Shapira SN, Maddipati R, Aiello NM, Thung SN, Wells RG, Greenbaum LE, Stanger BZ (2013) Robust cellular reprogramming occurs spontaneously during liver regeneration. *Genes Dev* **27:**719-724. doi: 10.1101/gad.207803.112 [doi]

Yao Y, Liu R, Shin MS, Trentalange M, Allore H, Nassar A, Kang I, Pober JS, Montgomery RR (2014) CyTOF supports efficient detection of immune cell subsets from small samples. *J Immunol Methods* **415:**1-5

Ye J, Coulouris G, Zaretskaya I, Cutcutache I, Rozen S, Madden TL (2012) Primer-BLAST: a tool to design target-specific primers for polymerase chain reaction. *BMC Bioinformatics* **13:**134-2105-13-134. doi: 10.1186/1471-2105-13-134 [doi]

Yeo L, Toellner KM, Salmon M, Filer A, Buckley CD, Raza K, Scheel-Toellner D (2011) Cytokine mRNA profiling identifies B cells as a major source of RANKL in rheumatoid arthritis. *Ann Rheum Dis* **70:**2022-2028. doi: 10.1136/ard.2011.153312 [doi]

Yimlamai D, Christodoulou C, Galli GG, Yanger K, Pepe-Mooney B, Gurung B, Shrestha K, Cahan P, Stanger BZ, Camargo FD (2014) Hippo pathway activity influences liver cell fate. *Cell* **157:**1324-1338

Young LH, Periwal V (2015a) Metabolic Scaling Predicts Post-Hepatectomy Liver Regeneration after Accounting for Hepatocyte Hypertrophy. *Liver Transplantation*

Young LH, Periwal V (2015b) Metabolic Scaling Predicts Post-Hepatectomy Liver Regeneration after Accounting for Hepatocyte Hypertrophy. *Liver Transplantation*

Yue F, Cheng Y, Breschi A, Vierstra J, Wu W, Ryba T, Sandstrom R, Ma Z, Davis C, Pope BD, Shen Y, Pervouchine DD, Djebali S, Thurman RE, Kaul R, Rynes E, Kirilusha A, Marinov GK, Williams BA, Trout D, Amrhein H, Fisher-Aylor K, Antoshechkin I, DeSalvo G, See L, Fastuca M, Drenkow J, Zaleski C, Dobin A, Prieto

P, Lagarde J, Bussotti G, Tanzer A, Denas O, Li K, Bender MA, Zhang M, Byron R, Groudine MT, McCleary D, Pham L, Ye Z, Kuan S, Edsall L, Wu Y, Rasmussen MD, Bansal MS, Kellis M, Keller CA, Morrissey CS, Mishra T, Jain D, Dogan N, Harris RS, Cayting P, Kawli T, Boyle AP, Euskirchen G, Kundaje A, Lin S, Lin Y, Jansen C, Malladi VS, Cline MS, Erickson DT, Kirkup VM, Learned K, Sloan CA, Rosenbloom KR, De Sousa BL, Beal K, Pignatelli M, Flicek P, Lian J, Kahveci T, Lee D, Kent WJ, Santos MR, Herrero J, Notredame C, Johnson A, Vong S, Lee K, Bates D, Neri F, Diegel M, Canfield T, Sabo PJ, Wilken MS, Reh TA, Giste E, Shafer A, Kutyavin T, Haugen E, Dunn D, Reynolds AP, Neph S, Humbert R, Hansen RS, De Bruijn M, Selleri L, Rudensky A, Josefowicz S, Samstein R, Eichler EE, Orkin SH, Levasseur D, Papayannopoulou T, Chang K, Skoultchi A, Gosh S, Disteche C, Treuting P, Wang Y, Weiss MJ, Blobel GA, Cao X, Zhong S, Wang T, Good PJ, Lowdon RF, Adams LB, Zhou X, Pazin MJ, Feingold EA, Wold B, Taylor J, Mortazavi A, Weissman SM, Stamatoyannopoulos JA, Snyder MP, Guigo R, Gingeras TR, Gilbert DM, Hardison RC, Beer MA, Ren B, Mouse ENCODE Consortium (2014) A comparative encyclopedia of DNA elements in the mouse genome. *Nature* **515:**355-+

Zak DE, Stelling J, Doyle FJ (2005) Sensitivity analysis of oscillatory (bio) chemical systems. *Comput Chem Eng* **29:**663-673

Zaldivar MM, Pauels K, von Hundelshausen P, Berres M, Schmitz P, Bornemann J, Kowalska MA, Gassler N, Streetz KL, Weiskirchen R (2010) CXC chemokine ligand 4 (Cxcl4) is a platelet-derived mediator of experimental liver fibrosis. *Hepatology* **51:**1345-1353

Zeisel A, Munoz-Manchado AB, Codeluppi S, Lonnerberg P, La Manno G, Jureus A, Marques S, Munguba H, He L, Betsholtz C, Rolny C, Castelo-Branco G, Hjerling-Leffler J, Linnarsson S (2015a) Brain structure. Cell types in the mouse cortex and hippocampus revealed by single-cell RNA-seq. *Science* **347:**1138-1142. doi: 10.1126/science.aaa1934 [doi]

Zeisel A, Munoz-Manchado AB, Codeluppi S, Lonnerberg P, La Manno G, Jureus A, Marques S, Munguba H, He L, Betsholtz C, Rolny C, Castelo-Branco G, Hjerling-Leffler J, Linnarsson S (2015b) Brain structure. Cell types in the mouse cortex and hippocampus revealed by single-cell RNA-seq. *Science* **347:**1138-1142. doi: 10.1126/science.aaa1934 [doi]

ZETTERBERG A, LARSSON O (1985) Kinetic-Analysis of Regulatory Events in G1 Leading to Proliferation Or Quiescence of Swiss 3t3 Cells. *Proc Natl Acad Sci U S A* **82:**5365-5369. doi: 10.1073/pnas.82.16.5365

Zhang C, Lu L, Li Y, Wang X, Zhou J, Liu Y, Fu P, Gallicchio MA, Bach LA, Duan C (2012) IGF binding protein-6 expression in vascular endothelial cells is induced by

hypoxia and plays a negative role in tumor angiogenesis. *International journal of cancer* **130:**2003-2012

Zhao X, Sato A, Dela Cruz CS, Linehan M, Luegering A, Kucharzik T, Shirakawa AK, Marquez G, Farber JM, Williams I, Iwasaki A (2003) CCL9 is secreted by the follicle-associated epithelium and recruits dome region Peyer's patch CD11b+ dendritic cells. *J Immunol* **171:**2797-2803

Zhou B, Fan Y, Rao J, Xu Z, Liu Y, Lu L, Li G (2015) Matrix metalloproteinases-9 deficiency impairs liver regeneration through epidermal growth factor receptor signaling in partial hepatectomy mice. *J Surg Res*

Zhu X, Zellweger R, Ayala A, Chaudry IH (1996) Prolactin inhibits the increased cytokine gene expression in Kupffer cells following haemorrhage. *Cytokine* **8:**134-140

Zhu GQ, Shi KQ, Huang S, Huang GQ, Lin YQ, Zhou ZR, Braddock M, Chen YP, Zheng MH (2015) Network meta-analysis of randomized controlled trials: efficacy and safety of UDCA-based therapies in primary biliary cirrhosis. *Medicine (Baltimore)* **94:**e609. doi: 10.1097/MD.0000000000000609 [doi]

Zhu LJ, Gazin C, Lawson ND, Pages H, Lin SM, Lapointe DS, Green MR (2010) ChIPpeakAnno: a Bioconductor package to annotate ChIP-seq and ChIP-chip data. *BMC Bioinformatics* **11:**237-2105-11-237. doi: 10.1186/1471-2105-11-237 [doi]

Appendix A

MODEL PARAMETERS

Table A.1 Model parameters for the Cell Growth Model of liver regeneration (Chapter 6)

Parameters

Name	Nominal or Starting Value	Approximate Biological Correlate
M	20.8 (rat)	Relative nutrient and toxin delivery/absorption rate in the liver
G	3.5×10^{-4} (rat)	Growth rate of hepatocyte mass [mass equivalent doublings/min]
k_{IL6}	1.5	Rate at which non-parenchymal cells (primarily Kupffer cells) are able to modify the cytokine milieu post-PHx
κ_{IL6}	0.9	Rate of cytokine degradation
V_{JAK}	2×10^4	Maximum JAK activation rate
K_m^{JAK}	10^4	JAK Michaelis concentration
κ_{JAK}	0.4	Rate of JAK degradation
[STAT3]	2	Relative concentration of monomeric STAT3 in the liver

V_{STAT3}	$7.5x10^{2}$	Maximum STAT3 phosphorylation rate
K_m^{STAT3}	0.4	pSTAT3 Michaelis concentration
κ_{STAT3}	0.1	Rate of pSTAT3 dephosphorylation
V_{SOCS3}	$2.4x10^{4}$	Maximum SOCS3 activation rate
K_m^{SOCS3}	$7x10^{-4}$	SOCS3 Michaelis concentration
κ_{SOCS3}	0.4	Rate of SOCS3 degradation
K_I^{SOCS3}	$1.5x10^{-2}$	SOCS3 Inhibition effect on STAT3 phosphorylation
V_{IE}	$2.5x10^{2}$	Maximum IE gene activation rate
K_m^{IE}	18	IE gene Michaelis concentration
κ_{IE}	5	Rate of IE gene degradation
κ_{DEG}	7	Rate of ECM degradation by MMPs
κ_{ECM}	33	Rate of constitutive ECM degradation
k_{GF}	0.113	Rate at which non-parenchymal cells (primarily hepatic stellate cells) directly & indirectly produce growth factors post-PHx
κ_{GF}	0.23	Rate of growth factor degradation
k_{up}	$6x10^{-2}$	Rate of growth factor absorption/binding to the ECM
k_Q	$7x10^{-3}$	Maximum rate of hepatocyte transition from Quiescence to Primed [cells/min]

k_P	$4.4x10^{-3}$	Maximum rate of hepatocyte transition from Primed to Replicating [cells/min]
k_R	$5.4x10^{-3}$	Maximum rate of hepatocyte transition from Replicating to Quiescence [cells/min]
k_{prol}	$2x10^{-2}$	Rate of hepatocyte progression through the cell cycle [doublings/min]
k_{req}	0.1	Requiescence rate of Primed hepatocytes [cells/min]
θ_{req}	8	None
β_{req}	3	None
k_{ap}	0.1	Apoptosis rate of damaged hepatocytes
θ_{ap}	$9x10^{-3}$	None
β_{ap}	$4.5x10^{-3}$	None
k_{MBF}	1	Rate of release of matrix bound factors during ECM remodeling
κ_{MBF}	1	Degradation rate of matrix bound factors once they are released from the ECM

Variables

Name	Nominal or Starting Value	Approximate Biological Correlate
Q	1	Fraction of hepatocytes in the Quiescent state
P	0	Fraction of hepatocytes in the Primed state
R	0	Fraction of hepatocytes in the Replicating state

[IL-6]	1	Cytokine microenvironment of the liver
[JAK]	1	Relative levels of activated receptors for cytokine signals in hepatocytes
[pSTAT3]	1	Relative levels of phosphorylated STAT-3 compared to monomeric STAT-3 or other downstream effectors of cytokine signaling (i.e. NF-κB)
[SOCS3]	1	Relative levels of SOCS3 or other inhibitors of cytokine signaling
[IE]	1	Relative levels of immediate early genes induced in hepatocytes (e.g. cFOS, cJUN, and AP-1)
[GF]	1	Relative bioavailability of growth factors promoting hepatocyte proliferation
[ECM]	1	Relative levels of extracellular matrix buildup of matrix composed of collagens inhibitory to regeneration
$[MBF_{ECM}]$	50	Relative levels of matrix bound factors priming hepatocytes
$[MBF_{Free}]$	0	Relative levels of free matrix bound factors that were initially bound by ECM

Table A.2 Hepatocyte model parameters for the Non-Parenchymal Cell Model of liver regeneration (Chapter 7)

Parameter	Value	Physiological Interpretation
M	Species-specific	Metabolic demand
$k_{IL6}^{Hepatocyte}$	0.3	IL-6 production rate by hepatocytes
V_{JAK}	$6x10^{4}$	JAK activation rate
K_m^{JAK}	10^{4}	JAK Michaelis constant
κ_{JAK}	0.4	JAK degradation rate
[STAT]	2	Concentration of monomeric STAT3
V_{STAT}	$7.5x10^{2}$	STAT3 activation rate
K_m^{STAT}	0.4	STAT3 Michaelis constant
κ_{STAT}	0.1	STAT3 degradation rate
V_{SOCS}	$2.4x10^{4}$	SOCS3 activation rate
K_m^{SOCS}	$7x10^{-4}$	SOCS3 Michaelis constant
κ_{SOCS}	0.4	SOCS3 degradation rate
K_I^{SOCS}	$1.5x10^{-2}$	SOCS3 inhibition of STAT3 signaling

V_{IE}	$2.5x10^{2}$	Immediate early (IE) gene expression rate
K_m^{IE}	18	IE gene Michaelis constant
κ_{IE}	5	IE gene degradation
$k_{Q\rightarrow P}$	$7x10^{-3}$	Hepatocyte priming rate
$k_{P\rightarrow R}$	$4.4x10^{-3}$	Hepatocyte replication transition rate
$k_{R\rightarrow Q}$	$5.4x10^{-2}$	Hepatocyte requiescence of replicating cells
k_{prol}	$2x10^{-2}$	Hepatocyte proliferation rate
k_{req}	0.1	Hepatocyte requiescence of primed cells
θ_{req}	8	Requiescence shape parameter
β_{req}	3	Requiescence scale parameter
k_{ap}	0.1	Hepatocyte apoptosis rate
θ_{ap}	$9x10^{-3}$	Apoptosis shape parameter
β_{ap}	$4.5x10^{-3}$	Apoptosis scale parameter

Table A.3 Kupffer cell model parameters for the Non-Parenchymal Cell Model of liver regeneration (Chapter 7)

Parameter	Value	Physiological Interpretation
M	Species-specific	Metabolic demand
HL	2	Hypoxia load
k_{TNF}	16	TNFa production rate
κ_{TNF}	2	TNFa degradation rate
k_{IL6}^{KC}	180	IL-6 production rate by Kupffer cells
κ_{IL6}	0.9	IL-6 degradation rate
k_{IL10}	20	IL-10 production rate
κ_{IL10}	0.9	IL-10 degradation rate
K_I^{IL10}	3	IL-10 inhibition of TNFa production
k_{TGF}^{KC}	30	TGF-β production rate by Kupffer cells
k_{PDGF}	15	PDGF production rate
κ_{PDGF}	0.9	PDGF degradation rate
$k_{Q\rightarrow A}^{KC}$	$7x10^{-3}$	Kupffer cell activation rate
$k_{A\rightarrow R}^{KC}$	$2.2x10^{-2}$	Kupffer cell replication transition rate

$k_{R \rightarrow Q}^{KC}$	5.4×10^{-2}	Kupffer cell requiescence of replicating cells
k_{prol}^{KC}	2×10^{-2}	Kupffer cell proliferation rate
k_{req}^{KC}	0.3	Kupffer cell requiescence of primed cells
θ_{req}^{KC}	8	Kupffer cell requiescence shape parameter
β_{req}^{KC}	3	Kupffer cell requiescence scale parameter
k_{ap}^{KC}	0.1	Kupffer cell apoptosis rate
θ_{ap}^{KC}	9×10^{-3}	Kupffer cell apoptosis shape parameter
β_{ap}^{KC}	4.5×10^{-3}	Kupffer cell apoptosis scale parameter

Table A.4 Hepatic stellate cell model parameters for the Non-Parenchymal Cell Model of liver regeneration (Chapter 7)

Parameter	Value	Physiological Interpretation
M	Species-specific	Metabolic demand
k_{HGF}	25	HGF production rate
κ_{HGF}	0.23	HGF degradation rate
k_{up}	0.6	HGF uptake by ECM
k_{TGF}^{HSC}	8	TGF-β production rate by hepatic stellate cells
κ_{TGF}	0.9	TGF-β degradation rate
K_I^{TGF}	5	TGF-β inhibition of HGF production
k_{ECM}	100	ECM production rate
k_{degrad}	7	ECM degradation rate by MMPs
κ_{ECM}	3	Constitutive ECM degradation rate
$k_{Q\rightarrow PR}$	$7x10^{-2}$	State transition rate: Quiescent to Pro-regenerative
$k_{Q\rightarrow AR}$	$3x10^{-2}$	State transition rate: Quiescent to Anti-regenerative
$k_{PR\rightarrow PRR}$	$4.4x10^{-3}$	State transition rate: Pro-regenerative to Replicating
$k_{AR\rightarrow ARR}$	$4.4x10^{-3}$	State transition rate: Anti-regenerative to Replicating

$k_{PRR \rightarrow PR}$	$5.4x10^{-2}$	State transition rate: Replicating to Pro-regenerative
$k_{ARR \rightarrow AR}$	$5.4x10^{-2}$	State transition rate: Replicating to Anti-regenerative
k_{prol}	$8.5x10^{-3}$	Hepatic stellate cell proliferation rate
k_{req}	0.2	Requiescence rate of pro- and anti-regenerative cells
θ_{req}^{HSC}	8	Hepatic stellate cell requiescence shape parameter
β_{req}^{HSC}	3	Hepatic stellate cell requiescence scale parameter
k_{ap}^{HSC}	0.1	Hepatic stellate cell apoptosis rate
θ_{ap}^{HSC}	$9x10^{-3}$	Hepatic stellate cell apoptosis shape parameter
β_{ap}^{HSC}	$4.5x10^{-3}$	Hepatic stellate cell apoptosis scale parameter

Appendix B

SEGMENTATION METHOD FOR CALCULATING CORRELATIONS FROM TIME-SERIES BIOLOGICAL DATASETS: MITIGATING THE EFFECTS OF TERMINAL SAMPLES, FEW TIME POINTS, AND LIMITED REPLICATES

This work was performed under the supervision of Arun K. Tangirala.

B.1 Introduction

Systems biology uses high-throughput data gathering techniques coupled with computational modeling to interrogate the complex biological mechanisms underlying physiology. One of the key tools used in systems biology is the construction of gene regulatory networks (Kitano, 2002). Often, these networks rely on the pair-wise correlation between the expression of genes to identify co-regulation and mutual antagonism (Hecker et al, 2009). These networks can then be interrogated to identify how progression of a disease can be associated with imbalances within gene regulatory networks. To identify imbalances in networks during disease progression, researchers take high-throughput measurements from animals over a time course of disease progression. To collect these high-throughput measurements, a typical procedure involves sacrificing an animal, flash freezing its tissue, and subjecting that tissue to biological assays (e.g. high-throughput qPCR or microarrays). This brings up a serious challenge for the calculation of correlation from these data: one animal is not followed throughout the time-series, but rather biological replicates are sacrificed at each time point to construct a pseudo-time series of biological response.

Typically, correlation is calculated between expression of gene pairs by calculating correlation of mRNA levels across all animal replicates (Stuart et al, 2003). One constraint of this method is that calculating correlation across animals rather than across time points gives up the temporal nature of the data. Another challenge for calculating correlation from biological replicates is that, due to time and money constraints, often only a limited number of samples can be taken (Freeman et al, 2012). Thus the number of replicates at each time point and the number of time points investigated is highly limited. Often, as few as 3 replicates per time point and 2-5 time points are used in biological experiments. This gives 6-15 animals with which to calculate correlation, which may not give an accurate estimate of true correlation (Bonett & Wright, 2000).

In light of these challenges, this study presents a novel method of estimating pair-wise correlation between biological assays from terminal, pseudo-time series measurements which takes into account the time-series nature of the data. This method segments the data into pseudo time-series profiles, then estimates pairwise gene correlation by averaging correlation estimates for two mRNA levels between all pairs of their pseudo time-series profiles. The segmentation method of estimating correlation gives a more accurate estimate of true correlation for datasets with few time points and limited replicates and is more robust to biological noise than standard correlation estimation methods.

B.2 Materials and Methods

B.2.1 Standard Method to calculate correlation

To calculate correlation between a pair of genes using the standard method, the gene expression data are arranged according to animal ID for each mRNA, as shown in Figure B.1A. In this method, the order of the data does not affect the calculation as long as the order is the same for each mRNA. The Pearson product moment correlation coefficient is then estimated between pairs of mRNA across N animals according to Equation B.1. Notice that the standard method does not take into account the time-series nature of the data.

$$E\{p_{xy}\} = \frac{\sum_{i=1}^{N}(x_i - \bar{x})(y_i - \bar{y})}{\sqrt{\sum_{i=1}^{N}(x-\bar{x})^2} * \sqrt{\sum_{i=1}^{N}(y-\bar{y})^2}} \quad \text{(B.1)}$$

B.2.2 Segmentation Method to calculate correlation

To calculate correlation between a pair of mRNA using the segmentation method, the gene expression data are arranged according to the time at which the sample was taken after treatment. The data are then segmented into k vectors, each containing the mRNA expression levels of one animal per time point. This gives a pseudo time-series with expression levels from one animal at each time point in a vector with N/k elements, as shown in Figure B.1B. Between each pair of pseudo time-series for two mRNA, the Pearson product moment correlation coefficient is estimated. This gives k^2 estimates of correlation between two mRNA. These k^2 estimates are then averaged to give one estimate of correlation, according to Equation B.2.

$$E\{p_{xy}\} = \frac{1}{k^2}\sum_{j=1}^{k^2} \frac{\sum_{i=1}^{N/k}(x_i - \bar{x}_j)(y_i - \bar{y}_j)}{\sqrt{\sum_{i=1}^{N/k}(x-\overline{x_j})^2} * \sqrt{\sum_{i=1}^{N/k}(y-\overline{y_j})^2}} \quad \text{(B.2)}$$

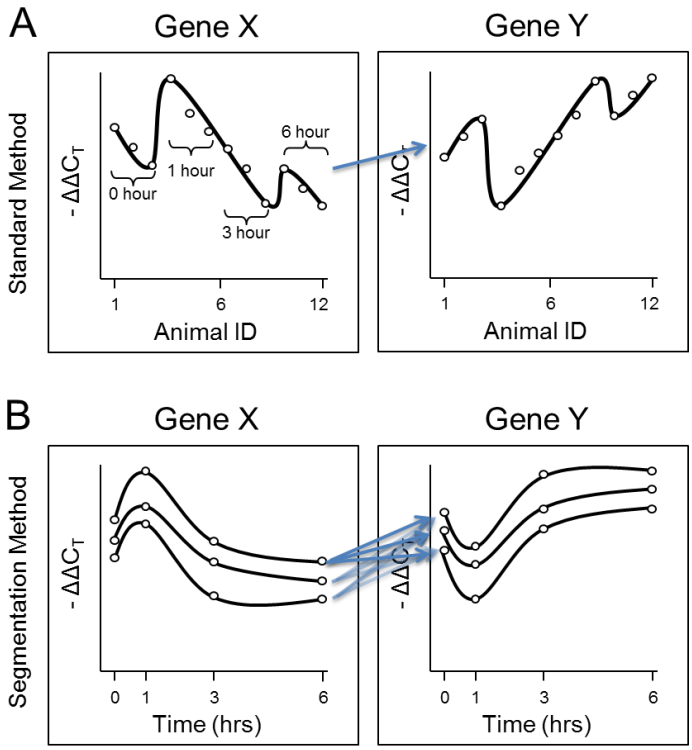

Figure B.1 Procedure for calculating estimates of correlation based on (A) the standard method and (B) the segmentation method (with k=3 segments). Gene expression values are based on the –ΔΔCT method; 12 animals were used over a time series of 6 hours post stimulus, with 3 biological replicates at each time point.

B.2.3 Definition of high correlation

A cutoff of $\rho \geq 0.5$ was used to define high correlation. This cutoff was chosen so that genes identified as highly correlated would have greater than half of their expression pattern linearly related to each other. Because it is likely that correlated genes are regulated by the same regulatory mechanisms, the majority of their relationship should be able to be explained by a linear relationship.

B.3 Results and Discussion

B.2.4 Calculating Correlation from Standard Method and Segmentation Method

To ensure that the segmentation method does not degrade the accuracy of the correlation estimate in the absence of noise, correlation between phase-shifted sine waves was calculated using both the standard method and the segmentation method. Two sine waves were generated using 40 data points to span one period. One sine wave was phase shifted from the other between 0 and 180 degrees, as shown in Figure B.2A. Three simulated biological replicates were used such that each estimate of correlation used 120 data points. Figure B.2B shows that, in the absence of noise, the standard method and the segmentation method give the same estimate of correlation. These results are robust to changes in number of data points per period, number of periods, and number of segments used.

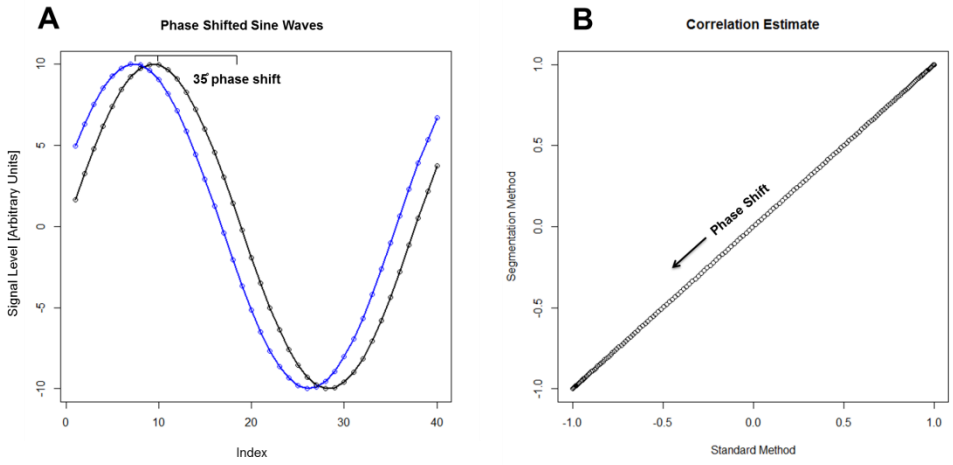

Figure B.2 Correlation estimates between sine waves phase-shifted between 1-180˚ using the standard method and the segmentation method are equal in the absence of noise.

B.3.1 Application of Segmentation Method to a Simulated Dataset

A simulated sinusoidal profile of gene expression with a magnitude of 10 was generated spanning a period of four hours, as shown by the solid line in Figure B.3A. To simulate biological sampling, the value of the sin wave at 1, 2, 3, and 4 hours was taken 3 times, for a total of 12 samples. Noise was added to each of these samples by introducing random fluctuations from a normal distribution with mean 0 and standard deviation 5. This corresponds to sampling from a gene expression profile like that shown by the data points in Figure B.3A. The resulting gene expression profile has a signal to noise ratio (SNR) of 4, which is representative of the level of noise commonly seen in biological experiments. To test the efficacy of the segmentation method to estimate correlation, this sampling procedure was performed on (1) two sine waves to simulate an experiment on two genes with a true correlation of 1 (Figure B.3B), (2) one sin wave and one cosine wave to simulate an experiment on two genes with a true correlation of 0 (Figure B.3C), and (3) one sine wave and one negative sine wave to simulate an experiment on two genes with a true correlation of -1 (Figure B.3D). Correlation was then calculated using both the standard method and the segmentation method for each condition. This process was repeated 1,000 times for each sampling procedure. Figure B.3E shows a scatterplot of correlation estimates calculated by the standard and segmentation methods for each trial. If all points lay along the x=y line, as in Figure B.2B, the two estimates of correlation would be equivalent. However, the segmentation method estimates a higher correlation when true correlation is 1 and a lower correlation when true correlation is -1. When true correlation is 0, there appears to be no difference in the estimates of the two methods.

When the number of samples taken and the number of segments used increase, these trends become even more pronounced, Figure B.3F.

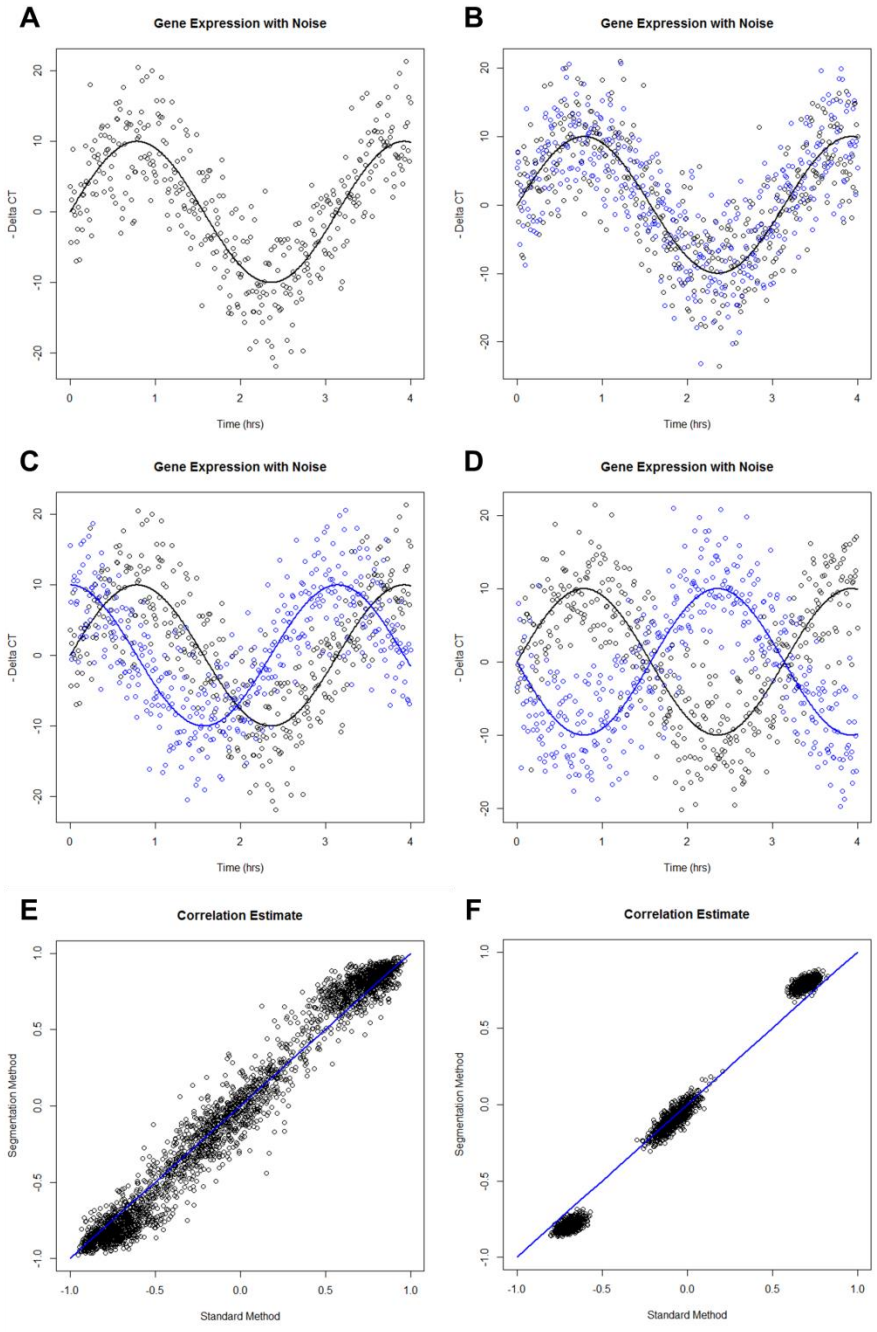
A
Gene Expression with Noise
- Delta CT
Time (hrs)
B
Gene Expression with Noise
- Delta CT
Time (hrs)
C
Gene Expression with Noise
- Delta CT
Time (hrs)
D
Gene Expression with Noise
- Delta CT
Time (hrs)
E
Correlation Estimate
Segmentation Method
Standard Method
F
Correlation Estimate
Segmentation Method
Standard Method

Figure B.3 (A) Gene expression with white noise introduced around the mean expression level, (B) two genes with a correlation = 1 prior to the introduction of noise, (C) correlation of 0, (D) correlation of -1, (E) scatterplot of correlation estimate comparing the standard method and segmentation method with 12 simulated animals and 3 segments, (F) the same correlation comparison with 120 simulated animals and 30 segments.

To ensure that the trends seen in the data are statistically significant, histograms of the estimated correlations for the standard method and segmentation method were generated, as shown in Figure B.4A-F.

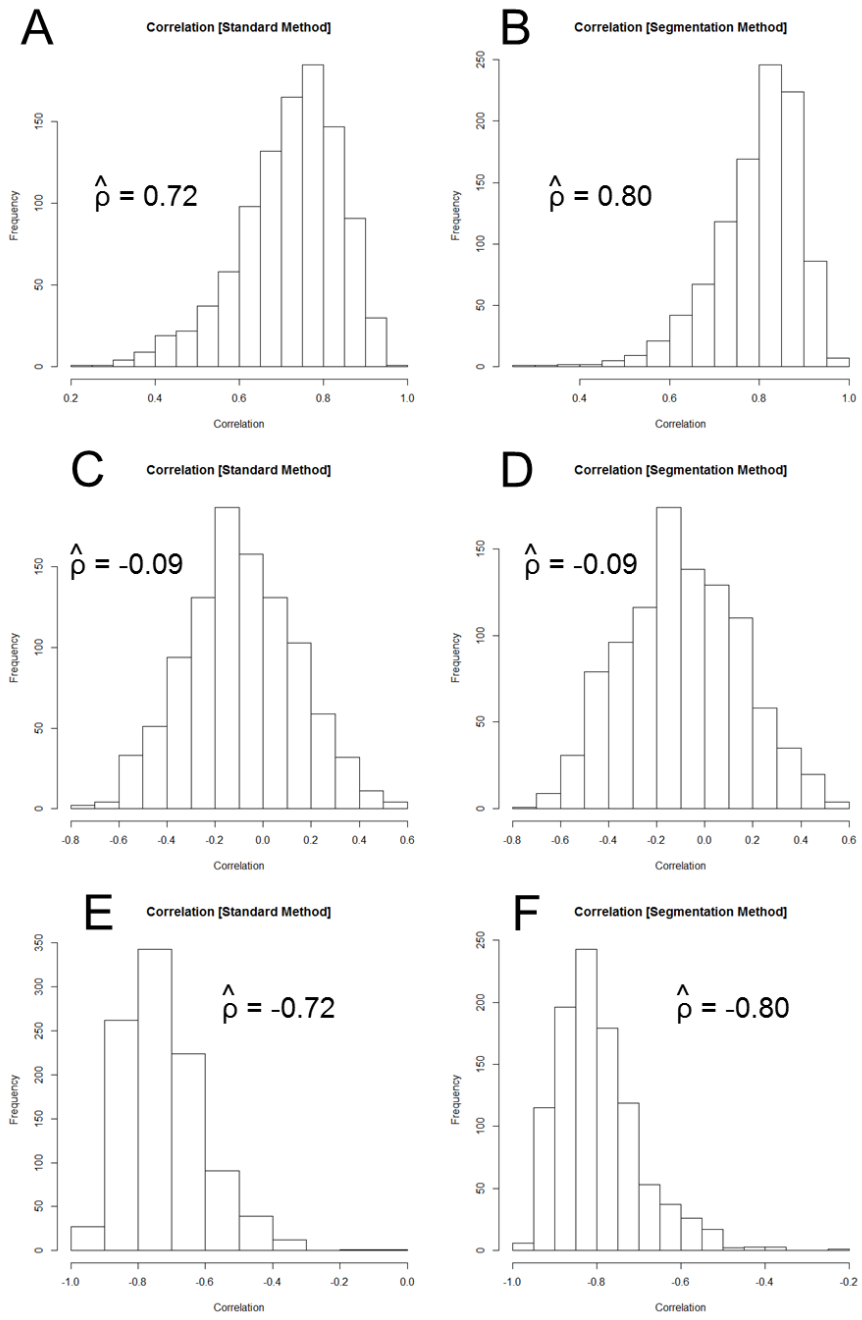

Figure B.4 Estimates of correlation for the standard method and segmentation method when (A-B) true correlation = 1, (C-D) true correlation = 0, and (E-F) true correlation = -1.

The histograms for true correlation = 1 suggest the segmentation method yields a more accurate estimate of correlation than the standard method. Using Fisher's transformation to shift the distribution to an approximate t-distribution and using a 2 sample t-test confirmed that the two distributions are significantly different (p-value < 2.2e-16). However, an F-test showed no difference in variance between the two transformed distributions (p-value = 0.625). The same tests on the histograms for true correlation = -1 confirmed that the two distributions are significantly different (p-value = < 2.2e-16) with no difference in variance (p-value = 0.228). It has been shown that the distribution of correlation estimates when true correlation is zero follows a normal distribution (Pearson, 2011). Therefore, in this case no transformation of the data was necessary. A t-test identified no difference between the means of these two populations (p-value = 0.871); however, the segmentation method has a slightly higher standard deviation – 0.248 vs. 0.228 – identified as significant using an F-test (p-value = 0.025).

B.3.2 Robustness of the Segmentation Method

Often in biological datasets, the signal to noise ratio is lower than desired. This is partly due to variability between animals or culture conditions and partly due to the often large number of processing steps needed to generate the dataset (Novak et al, 2002). To test the robustness of the segmentation method to high noise systems, the Signal to Noise Ratio (SNR, defined as the signal divided by the variance) was varied between high levels of noise (SNR ~ 0.5) and low levels of noise (SNR ~ 100). At all levels of noise, the segmentation method outperformed the standard method with a more accurate estimate of correlation regardless of the sample size and number of segments used (Table B.1). However, at low noise levels this difference became

biologically insignificant. The performance of the segmentation method improves when using a larger number of samples and a larger number of segments for all signal to noise levels.

Table B.1: Correlation estimates using the standard and segmentation methods (true correlation is 1)

			Correlation Coefficient		Standard Deviation		
Sample #	Segment #	SNR	Std	Seg	Std	Seg	p-value
12	2	111.11	0.999	0.999	0.001	0.000	1.16E-04
12	2	40.00	0.996	0.997	0.002	0.001	5.07E-03
12	2	20.41	0.992	0.994	0.004	0.003	8.27E-04
12	2	12.35	0.988	0.990	0.006	0.005	1.61E-02
12	2	8.26	0.982	0.985	0.009	0.007	2.84E-04
12	2	5.92	0.976	0.979	0.012	0.009	7.96E-03
12	2	4.44	0.965	0.973	0.015	0.012	1.03E-03
12	2	3.46	0.960	0.967	0.022	0.016	1.32E-04
12	2	2.77	0.946	0.956	0.024	0.018	3.15E-03
12	2	2.27	0.934	0.945	0.028	0.022	1.21E-03
12	2	1.89	0.932	0.940	0.034	0.026	3.02E-02
24	2	111.11	0.998	0.999	0.001	0.000	2.63E-02
24	2	40.00	0.996	0.996	0.001	0.001	1.07E-01
24	2	20.41	0.991	0.993	0.003	0.002	3.09E-03
24	2	12.35	0.986	0.987	0.004	0.003	1.04E-01
24	2	8.26	0.981	0.982	0.006	0.005	2.42E-02
24	2	5.92	0.971	0.974	0.009	0.008	3.08E-02
24	2	4.44	0.964	0.967	0.011	0.009	2.87E-02
24	2	3.46	0.951	0.955	0.015	0.012	2.11E-02
24	2	2.77	0.943	0.945	0.017	0.014	6.91E-02
24	2	2.27	0.933	0.937	0.023	0.018	1.62E-02
24	2	1.89	0.918	0.925	0.025	0.022	1.71E-01
48	2	111.11	0.998	0.998	0.000	0.000	1.17E-01
48	2	40.00	0.995	0.996	0.001	0.001	8.54E-02
48	2	20.41	0.991	0.991	0.002	0.002	4.83E-01

48	2	12.35	0.986	0.986	0.003	0.002	9.81E-03
48	2	8.26	0.979	0.980	0.004	0.004	2.34E-01
48	2	5.92	0.970	0.971	0.006	0.005	1.82E-01
48	2	4.44	0.961	0.963	0.009	0.008	1.01E-01
48	2	3.46	0.950	0.951	0.009	0.008	3.80E-01
48	2	2.77	0.936	0.941	0.013	0.011	6.37E-02
48	2	2.27	0.926	0.927	0.016	0.013	1.50E-01
48	2	1.89	0.911	0.912	0.019	0.017	7.35E-01
12	3	111.11	0.999	0.999	0.001	0.000	5.20E-13
12	3	40.00	0.997	0.998	0.001	0.001	7.56E-21
12	3	20.41	0.993	0.997	0.003	0.002	1.92E-14
12	3	12.35	0.988	0.993	0.005	0.004	8.34E-14
12	3	8.26	0.984	0.990	0.008	0.005	1.01E-10
12	3	5.92	0.977	0.987	0.011	0.006	2.13E-16
12	3	4.44	0.974	0.982	0.014	0.008	3.39E-09
12	3	3.46	0.961	0.977	0.017	0.011	7.20E-09
12	3	2.77	0.951	0.970	0.022	0.014	1.63E-13
12	3	2.27	0.943	0.965	0.025	0.016	7.54E-13
12	3	1.89	0.930	0.959	0.031	0.019	2.42E-14
24	3	111.11	0.998	0.999	0.000	0.000	2.36E-05
24	3	40.00	0.995	0.996	0.001	0.001	8.86E-07
24	3	20.41	0.992	0.993	0.003	0.002	5.05E-05
24	3	12.35	0.986	0.989	0.004	0.003	2.70E-06
24	3	8.26	0.978	0.982	0.006	0.004	2.27E-05
24	3	5.92	0.971	0.976	0.008	0.006	1.78E-07
24	3	4.44	0.962	0.970	0.012	0.010	8.57E-06
24	3	3.46	0.953	0.961	0.014	0.010	1.40E-04
24	3	2.77	0.940	0.951	0.020	0.015	1.25E-05
24	3	2.27	0.929	0.939	0.026	0.020	3.28E-04
24	3	1.89	0.919	0.929	0.027	0.021	2.12E-03
48	3	111.11	0.998	0.999	0.000	0.000	1.54E-03
48	3	40.00	0.995	0.996	0.001	0.001	8.60E-04
48	3	20.41	0.991	0.992	0.002	0.001	3.93E-03
48	3	12.35	0.985	0.987	0.004	0.003	2.90E-03
48	3	8.26	0.978	0.981	0.004	0.004	2.03E-04
48	3	5.92	0.970	0.972	0.007	0.005	1.15E-03
48	3	4.44	0.960	0.962	0.010	0.007	8.75E-02
48	3	3.46	0.950	0.953	0.012	0.008	2.72E-02

48	3	2.77	0.936	0.941	0.013	0.011	7.87E-03
48	3	2.27	0.927	0.932	0.018	0.013	9.85E-02
48	3	1.89	0.910	0.915	0.022	0.017	1.00E-02
12	4	111.11	0.999	1.000	0.001	0.000	1.81E-34
12	4	40.00	0.996	0.998	0.002	0.001	6.28E-32
12	4	20.41	0.992	0.997	0.004	0.002	2.55E-28
12	4	12.35	0.986	0.995	0.006	0.003	6.46E-32
12	4	8.26	0.980	0.992	0.009	0.005	3.72E-26
12	4	5.92	0.975	0.990	0.013	0.007	2.92E-26
12	4	4.44	0.965	0.985	0.015	0.008	5.64E-26
12	4	3.46	0.957	0.982	0.019	0.010	2.49E-25
12	4	2.77	0.943	0.977	0.025	0.013	8.17E-28
12	4	2.27	0.935	0.975	0.028	0.016	1.20E-27
12	4	1.89	0.914	0.967	0.033	0.018	3.30E-28
24	4	111.11	0.998	0.999	0.001	0.000	1.14E-11
24	4	40.00	0.996	0.997	0.002	0.001	9.96E-11
24	4	20.41	0.992	0.994	0.003	0.002	8.00E-15
24	4	12.35	0.986	0.989	0.004	0.003	4.38E-12
24	4	8.26	0.980	0.985	0.006	0.005	1.19E-09
24	4	5.92	0.970	0.978	0.008	0.006	5.27E-15
24	4	4.44	0.962	0.972	0.011	0.008	1.44E-09
24	4	3.46	0.951	0.964	0.014	0.010	1.96E-10
24	4	2.77	0.939	0.954	0.018	0.013	1.63E-07
24	4	2.27	0.928	0.945	0.020	0.017	4.56E-10
24	4	1.89	0.910	0.934	0.027	0.019	9.33E-11
48	4	111.11	0.998	0.999	0.000	0.000	3.64E-07
48	4	40.00	0.996	0.996	0.001	0.001	5.19E-05
48	4	20.41	0.991	0.992	0.002	0.001	6.42E-05
48	4	12.35	0.985	0.987	0.003	0.002	1.65E-05
48	4	8.26	0.978	0.981	0.005	0.004	4.68E-07
48	4	5.92	0.972	0.974	0.005	0.004	1.78E-05
48	4	4.44	0.961	0.966	0.008	0.006	4.39E-06
48	4	3.46	0.951	0.956	0.011	0.007	4.85E-04
48	4	2.77	0.939	0.948	0.012	0.008	9.15E-07
48	4	2.27	0.929	0.939	0.017	0.012	1.14E-04
48	4	1.89	0.910	0.924	0.018	0.014	3.74E-07

Another challenge posed by biological datasets is missing data, which can have many causes. Assays fail, animals die prematurely, cultures are contaminated, and sensors break. To test the robustness of the segmentation to missing data, between 1-4 measurements were randomly selected and removed from the simulated dataset prior to calculating correlation (Table B.2).

Table B.2: Correlations calculated from missing data study

Missing data points	**1**	**2**	**3**	**4**
Standard Method Corr. **Standard Method Stdev**	0.728 0.128	0.727 0.139	0.725 0.147	0.729 0.153
Segmentation Method Corr. **Segment Method Stdev**	0.795 0.120	0.792 0.145	0.763 0.200	0.707 0.247
P-value : 2 sample t-test on Fisher transformed data	~0	~0	~0	0.001
P-value: F-test for equal variance on Fisher transformed data	0.002	~0	~0	~0

For 1 missing data point, the segmentation method still provides a better estimate of correlation, with the deletion affecting the variability of the segmentation method less than that of the standard method. For 2 or 3 missing data points, the segmentation method gives a more accurate but less precise estimate of correlation. The accuracy of the segmentation method makes it the better choice for this scenario. For $\geq$ 4 missing data points, the segmentation method provides a worse correlation estimate with higher variability. Because there are only 4 data points in each pseudo-time series, when greater than 3 data points are missing it becomes highly likely that at least 1 pseudo-time series will have only 2 data points. Estimating correlation from only 2 points is a poor way to estimate, which is why the performance of the

segmentation method suffers more than the standard method's performance for many missing data points. For no true correlation, there is no difference between the distributions of the correlation estimate for the two methods with 1-4 missing data points.

To ensure that these results were not specific to the use of sin waves as a model, the above analyses were repeated for linear profiles of gene expression. Similar results were obtained.

B.4 Conclusion

The segmentation method provides a robust, accurate estimation of correlation for time series biological data. Compared to the standard method used to calculate correlation from biological data, the segmentation method is less susceptible to noise and is more accurate in identifying correlations. However, because of the segmentation the data is subject to, it is less robust to missing data points after a certain threshold of missing data is reached. This study focused on calculating Pearson correlation, the underlying mathematics, however, may be applied to other methods of calculating relationships between time-series data, such as Spearman's rank correlation or mutual information.

Appendix C

PRIMER SEQUENCES FOR HIGH-THROUGHPUT QPCR EXPERIMENTS

Table C.1 Primer sequences and RefSeq IDs of mRNA measured in Chapter 8

Gene	RefSeq ID	Forward Sequence	Reverse Sequence
Actb	NM_031144	AAGGCCAACCGTGAAAAGAT	ACCAGAGGCATACAGGGACA
Adamts1	NM_024400	GGACAGGTGCAAGCTTACCT	CACAGCCAGCTTTCACACAC
Adamts13	XM_006233879	ACCCTCTCAGGAGGCTAAAT	GTGACTGGGATTCTGGTTAGTG
Adh1a	NM_019286	GATGCCGACTTGGACATTGC	TGGCTCGCTCAACACTCTTT
Alb	NM_134326	TGGCACAATGAAGTGGGTAA	GGGCGATCTCACTCTTGTGT
Aldh1a1	NM_022407	GCCATCACTGTGTCTTCTGC	CATCTTGAATCCACCGAAGG
Aldh2	NM_032416	TTACCTGTCCCAAGCTCTGC	GCACGCCACTTTACGAGTTC
Aldh7a1	NM_001271105	GGAATCATCACTGCCTTCAAC	AGTTGTTGGTGCTCCTTTCC
Ang1	NM_001006992	CGTCCTCTGTTGTCGGTTTT	CGTGTACCTGGGGTCGTC
Apoa4	NM_012737	AGCCCCTGGGGGATAAGT	CCAGCTGCTGCCTGAACT
Arg1	NM_017134	GGTAGAGAAAGGTCCCGCAG	CAGACCGTGGGTTCTTCACA
Bambi	NM_139082	AGCAGAAACCTCATCACTAAGG	GCTGTAGTGCAAACGAGAGA
Bmp6	NM_013107	CAG CAA CAA TCG CAACAG AC	GGG AGT TGT AGA GATCCA GCA
Casp3	NM_012922	TCTACCGCACCCGGTTACTA	TGACTGGATGAACCATGACC
Ccl3	NM_013025	CGC CAT ATG GAG CTG	GTG GAA TTT GCC GTC

		ACA C	CAT AG
Ccnd1	NM_171992	TGTGATATGTACCAGCC ACAGG	CGAACAGACGACGGCA TACT
Cdkn1a	NM_080782	GCGCCCTCCGTTTCTTA CTT	TCGCAGACCTCTAGCAT CCA
Ch25h	NM_001025415	CTGCACTGGAACAGGG CTAA	ACTGCCCAGCAGGAAC AAAT
Clcn3	NM_053363	GACTGTCTCTCTGGTGG TTATTG	GCCAGGGTTGTATGAGT GAA
Col14a1	NM_001130548	CAG GCC AGA GGG GAT TTC	AAT GCC AAT TGG TCC AGG T
Col3a1	NM_032085	ATGTGGGACCTGGTTTC TTC	CAGTCTAGTGGCTCATC ATCAC
Col4A1	NM_001135009	CCA GCG GTG GTT ATG ACT TC	GGC CAC CAT CTT GAG ACT TC
Col4A2	XM_001076134	CTG TCA GCA AAT GGG CAC T	TTA GGA GGT GGG TGT TAG CAG
Csf1	NM_023981	CTGACTCTGGTAGGGAA GGATA	GAGACCAAGGAGCAAG TAAGAG
Csf2	NM_053852	CTA ATG AGT TCT CCA TCC AGA GG	CCC GTA GAC CCT GCT TGT AT
Csf3	NM_017104	GGTTTTCCTGACCCCGT AGG	TAGGCCAGCAAGCGCT AAAA
Csrp2	NM_177425	ACATGGACCGTGGTGA GAG	GTAGGCCTGTGAGGTTG AGC
Cxcl1	NM_030845	ACTCAAGAATGGTCGCG AGG	ACGCCATCGGTGCAATC TAT
Cxcl12	NM_001033882	GGC CTC TGG GCA CAG TTA	TGG TGG AAG GTT GCT ACT CC
Cyp1a1	NM_012540	CTCCCTGGGGTCCTAGA GAACA	CTCTGTGGCTGATGTGA AGGC
Cyp1a2	NM_012541	GGAACACTATCAAGACT TCAACAAGA	AATCCAGCTCCAAAGAT GTCA
Cyp27b1	NM_053763	GGCTCCTATGCCCACCT C	CACAGCCTTTAGCAGGG GTA
Cyp2b1	NM_001134844	CGGACCTTTTCCCTCCT AAG	GGAACCCAGAGAAGAA CTCAAA
Cyp2e1	NM_031543	CTGACTGTCTCCTCATA GAGATGG	TCACAGAAACATTTTCC ATTGTGT
Dcn	NM_024129	CGGTGGCAAATACCCG GATTA	TCTGCTCAAATGGTCCA GCC
Ecm1	NM_053882	TGACCCGTGACCAGTTC	GGTGCTGCATAGCCTAC

		TTAC	TTC
Erlin2	NM_001106088	CCCAGAAACAGAAGGTGGTG	GCAACCTGTGCCACTTTTTC
Fap	NM_138850	GAA GAG GAA ATG CTT GCT ACA AA	TGG TAT GTC CGA ATC ATT AAA TTC
Fn1	NM_019143	CAGCCCCTGATTGGAGTC	TGGGTGACACCTGAGTGAAC
Fos	NM_022197	GGGACAGCCTTTCCTACTACC	GATCTGCGCAAAAGTCCTGT
Gapdh	NM_017008	TGGCCTCCAAGGAGTAAGAA	GGCCTCTCTCTTGCTCTCAG
Gfap	NM_017009	AAGATCCCGAGGCAAAGAAT	TCGTCAGGGTTCTTCCAGAT
Got1	NM_012571	ACGAATCACCTGGTCCAATC	GCCATTGTCTTCACGTTTCC
Hgf	NM_017017	TGATCCAAACATCCGAGTTG	CCATTGCCACGATAACAATCT
Hif1a	NM_024359	CATGATGGCTCCCTTTTTCA	CATAGTAGGGGCACGGTCAC
Igf1	NM_001082477	CACACTGACATGCCCAAGAC	TCTCCTTTGCAGCTTCCTTT
Il10	NM_012854	CAGATTCCTTACTGCAGGACTTTA	CAAATGCTCCTTGATTTCTGG
Il1a	NM_017019	AAATACTCAGCTCTTTGTGAGTGC	TGTGATGAGTTTTGGTGTTTCC
Il1r1	NM_013123	ATAGACAGACATAGAGGCTTTGGGG	CAGTGTAGCTTGGGATTTCACC
Il6	NM_012589	CACTTCACAAGTCGGAGGCT	TCTGACAGTGCATCATCGCT
Irf1	NM_012591	GAGCTGGGCCATTCACAC	CGATGTCTGGTAGGGAGTTCA
Itgad	NM_031691	CCGGTGGAGTTGTGATCCTC	CGATGGGTTCCTCCACATCC
Itgam	NM_012711	ATTGGGGCCCCTCATCACTA	CCACCGTGCTCTCCCCCTA
Klf6	NM_031642	TTGAAAGCACATCAGCGCAC	AGGTGGTCAGACCTGGAGAA
Kras	NM_031515	GGAGGGCTTTCTTTGTGTATTTG	CCCATAACTCCTTGCTAACTCC
Lama1	NM_001108237	AGATTGGCTAAGACCGCACA	AGCTGCTTCAGCATTAGGGG
Lep	NM_013076	TGTCTTCAACGGAGGAG	GTCCCGAGCACTTTGGA

		AAAG	TAA
Lrat	NM_022280	TCCTGATAGTCAATTTG CTAGGC	CAACCAATCCAAACTTC CTTACA
Mapk1	NM_053842	GGCATGGTTTGTTCTGC TTATG	GTCTCCATGAGGTCCTG TACTA
Mmp13	NM_133530	TTG AGT TGG ACT CAC TGT TGG T	CTT CCT CAG ACA AGT CAT CAT CA
Mmp14	NM_031056	ACA AAG ATG CCC CCT CAA C	CCA TAG GTG GGG TTT CTG G
Mmp2	NM_031054	CTG GTT GGA GGA GAA CCA AG	TCC CAT GGG GAA CTG TTA AA
Mmp3	NM_133523	TGTGTTTCAGCTGACCC TGAT	TGCTAGAGTAAGGAAA CCACTTCA
Mrc1	NM_001106123	CCCTGCTCCTGGCTTTT ATCT	CTGAACGGAGATGGCG CTTA
Nfkb2	NM_001008349	CCACTGCATCTAGCCAC AGA	ATTCACATTAGCATGGA GCTTG
Npy	NM_012614	TGTGAAACCAGTCTGCC TGT	GAAATGGGTCGGAATC CAG
Pdgfa	NM_012801	GGACAGGACGCGTAGA ACAA	CGGGTTGCTCGAGGTCT TAG
Pdgfc	NM_031317	GCAAGTTGCAGCTCTCC AG	TGGATGCTCCCATTACC AG
Pecam1	NM_031591	GCCTCACCAAGAGAAC GGAA	ATTGGATGGCTTGGCCT GAA
Pklr	NM_012624	GATACGAACCGGAGTCT TGC	ACCTGTGAGCCCTTCAC AAT
Ppara	NM_013196	CTGTCCCCAAAATGCCT GTG	ATTTTTCGCAAGGCCAC GTT
Ptn	NM_017066	GAAGCAGTTTGGAGCTG AGTG	GCTTGGGCTTGGTGAGT TTG
Rara	NM_031528	CGGCTGAGTGACGAGA GC	GACTTCTACACTTTCGT ACATCTTGC
Rbp1	NM_012733	CACGCTGAGCACTTTTC G	CCCAGCTCACTGTGGTC A
Rbp2	NM_012640	AGTGGGTCGAGGGAGA CAA	TTGAACACTTGTCGACA CACC
Rdh10	NM_181478	TTCAGAGGCTGCCGAAT CAG	GTACATGAGACGAGGG GTGC
Serpine1	NM_012620	CACCCTTTGAAAAAGAT GTGC	ATGAGCTCAGCGTCCAA AAT
Serpinh1	NM_017173	TTTTTGAGTTTTTCAAG	TGTTTTGAAAGCAATAA

		GAATGG	AGGCTTC
Smad1	NM_013130	AGAAAGGGGCCATGGAAG	AGCGAGGAATGGTGACACA
Smad4	NM_019275	TCA CAA TGA GCT TGC ATT CC	TCA AAG TAA GCA ATG GAA CAC C
Smad7	NM_030858	CCCTGCTGTTGTTGCTGTC	ATGACCTCCGCACACCAT
Sosc3	NM_053565	AATCCAGCCCCAATGGTC	GGCCTGAGGAAGAAGCCTAT
Spp1	NM_012881	ATCGACAGTCAGGCGAGTTC	GCTGTGAAACTCGTGGCTCT
Stat3	NM_012747	GGGCCATCCTAAGCACAAA	AGACTGGATCTGGGTCTTGC
Tbp	NM_001004198	CCCACCAGCAGTTCAGTAGC	CAATTCTGGGTTTGATCATTCTG
Tgfb1	NM_021578	GTCAACTGTGGAGCAACACG	GACAGCCACTCAGGCGTATC
Tgfb2	NM_031131	CCATACAGTCCCAGGTGCTC	GCAAGCGAAAGACCCTGAAC
Tgfbr2	NM_031132	AGAAGCCGCAGGAAGTCTG	GGCAAACGGTCTCCAGAGTA
Timp2	NM_021989	GTAGTGATCAGGGCCAAAGC	GATGGGGTTGCCATAGATGT
Tlr9	NM_198131	ACCTGTCTCGGAACAACCTG	AGATGGGAGAGGTTGACGAA
Tnf	NM_012675	CCCTGGTACTAACTCCCAGAAA	TGTATGAGAGGGACGGAACC
Tnfr1	NM_013091	AATGAGTGCACCCCTTGC	CCTGGGGGTTTGTGACATT
Ubqln1	NM_053747	GAAGGAAGAGTTCGCTGTGC	TGAAACGTTTTGAGATTTCCTCT
Vcl	NM_001107248	TACCAAGCGGGCACTTATTC	CCTTCACTGTGGACAGGATTT
Vegfa	NM_001110333	AAAAACGAAAGCGCAAGAAA	TTTCTCCGCTCTGAACAAGG
Vim	NM_031140	CGA GAA AAA TTG CAG GAG GA	GAA TGA CTG CAG GGT GCT CT

Appendix D

MATLAB CODE FOR MATHEMATICAL MODELS DEVELOPED IN THIS THESIS

D.1 Cell Growth Model of Liver Regeneration

```
function [t,cell,conc,G] = HepatRegenGrowth(initialFraction)
% Author:       Daniel Cook
% Date:         10/08/2015
% Copyright:    Creative Commons Share Alike
% To run, use:  [t,cell,conc,G] = HepatRegenGrowth(0.3);
% Modified from "A Model of Liver Regeneration" (2009) by Furchtgott et al.

% Citation: Cook, D.; Ogunnaike, B.A.; Vadigepalli, R.
% Systems Analysis of Non-Parenchymal Cell Modulation of Liver Repair
% across Multiple Regeneration Modes, BMC Systems Biology, 2015

% Set species: 1=rats, 2=mice, 3=humans
setSpecies = 1;

% Set disease (for use only with rats)
% 1= no disease
% 2= non-alcoholic steatohepatitis (NASH)
% 3= alcoholic steatohepatitis (ASH)
% 4= cirrhosis
% 5= toxin-induced diabetes
setDisease = 1;

% Set alternate hypotheses (for use only with humans)
% Hypothesis 5 is the default human parameter set
% 1= altered stress response
% 2= altered ECM remodeling and storage of GFs
% 3= altered transition times
% 4= longer cell cycle, higher apoptosis rate, et al.
% 5= lower metabolic demand
setHypotheses = 5;
```

```
% Plot results: 1=yes, 2=no
shouldPlot = 1;

% Define model parameters
k = zeros(41,1);
% Table 1: Molecular parameters
k(1) = initialFraction; % Fraction of liver mass remaining (N)
k(2) = 16.8; % Metabolic load (M)
k(3) = 1.5; % TNF production
k(4) = 0.9; % TNF mRNA degrad
k(5) = 2e4; % JAK activation rate (V_JAK)
k(6) = 1e4; % Km JAK
k(7) = 0.4; % JAK degrad
k(8) = 2; % Conc. of monomeric STAT3
k(9) = 7.5e2; % STAT3 activation rate
k(10) = 0.4; % Km STAT3
k(11) = 0.1; % STAT3 degrad
k(12) = 2.4e4; % SOCS activation rate
k(13) = 7e-4; % Km SOCS3
k(14) = 0.4; % SOCS3 degrad.
k(15) = 1.5e-2; % SOCS3 inhibition constant
k(16) = 2.5e2; % IE response gene expression rate
k(17) = 18; % Km for IE genes
k(18) = 5; % IE gene degrad
k(19) = 7; % ECM degrad by MMPs
k(20) = 33; % ECM degrad

% Table 2: Cellular parameters
k(21) = 0.113; % GF production
k(22) = 0.23; % GF degrad
k(23) = 6e-2; % k_up - GF uptake/production rate by ECM
k(24) = 7e-3; % k_Q
k(25) = 4.4e-3; % k_P
k(26) = 5.4e-2; % k_R
k(27) = 2e-2; % k_prol - specifies length of mitotic cycle
k(28) = 0.1; % k_req - requiescence rate
k(29) = 8; % theta_req (for sigma_req)
k(30) = 3; % beta_req (for sigma_req)
k(31) = 1e-1; %1e-2; % k_ap - apoptosis rate
k(32) = 9e-3; % theta_ap
k(33) = 4.5e-3; % beta_ap
```

```
% Growth rate and metabolic load for rats
if setSpecies == 1
   k(2) = 20.8217; % Metabolic demand
   k(41) = 3.4742e-4; % Growth rate
end

% Growth rate and metabolic load for mice
if setSpecies == 2
   k(2) = 23.0294; % Metabolic demand
   k(41) = 9.6607e-4; % Growth rate
   k(32) = k(32)*21.3671/k(2); % Scaled apoptosis rate
end

% Growth rate and metabolic load for humans
if setSpecies == 3
   k(2) = 5.8507; % For fitting data from Pomfret
   k(41) = 6.5675e-4; % For fitting data from Pomfret
   k(32) = k(32)*20.8217/k(2); % Scale the apoptosis response
end

% Set parameters for fructose-induced steatosis (NASH)
if setDisease == 2
   k(2) = 23.1645;
   k(41) = 0.0025;
   k(3) = 0.3095;
   k(4) = 2.3633;
   k(19) = 1.7312;
   k(20) = 9.5395;
   k(21) = 0.0793;
   k(22) = 0.1679;
   k(23) = 0.0075;
end

% Set parameters for Alcohol-induced steatosis (ASH)
if setDisease == 3
   k(2) = 14.4017;
   k(41) = .0014;
   k(3) = 0.79;
   k(4) = 0.2073;
   k(19) = 10.5646;
   k(20) = 77.7923;
   k(21) = 0.0002;
   k(22) = 0.1196;
```

```
    k(23) = 0.0071;
end

% Parameters for cirrhosis-impaired regeneration (rat)
if setDisease == 4
    k(2) = 18.0454;
    k(41) = 4.358e-06;
    k(3) = 2.1565;
    k(4) = 1.043;
    k(19) = 0;
    k(20) = 83.5649;
    k(21) = 0.069;
    k(22) = 0.2456;
    k(23) = 0.0027;
end

% Set parameters for Diabetes-impaired regeneration
if setDisease == 5
    k(2) = 16.4539;
    k(41) = 8.92e-4;
    k(3) =  1.5892;
    k(4) =  0.3699;
    k(19) = 6.4571;
    k(20) = 1.8271e-6;
    k(21) = 1.7519e-7;
    k(22) = 0.5044;
    k(23) = 0.1218;
end

% Hypothesis testing (humans)
% Hyp1: humans have a higher stress response than rats
if setHypotheses == 1
    k(2) = 20.8217; % Metabolic demand
    k(41) = 3.4742e-4; % Growth rate
    k(32) = 9e-3; % theta_ap
    k(3) = 0.1435; % TNF production
    k(4) = 0.4942; % TNF mRNA degrad
    k(5) = 1.3637e3; % JAK activation rate (V_JAK)
    k(6) = 7.5654e3; % Km JAK
    k(7) = 0.0398; % JAK degrad
    k(8) = 2.031; % Conc. of monomeric STAT3
    k(9) = 1.1091e3; % STAT3 activation rate
    k(10) = 0.5178; % Km STAT3
```

```
    k(11) = 0.035; % STAT3 degrad
    k(12) = 6.3042e3; % SOCS activation rate
    k(13) = 6.8196e-4; % Km SOCS3
    k(14) = 0.1682; % SOCS3 degrad.
    k(15) = 0.0569; % SOCS3 inhibition constant
    k(16) = 18.6019; % IE response gene expression rate
    k(17) = 88.1259; % Km for IE genes
    k(18) = 1.1482; % IE gene degrad
end
% Hyp2: humans store a greater quantitiy of GFs in ECM & Potentially
% altered ECM synthesis
if setHypotheses == 2
    k(2) = 20.8217; % Metabolic demand
    k(41) = 3.4742e-4; % Growth rate
    k(32) = 9e-3; % theta_ap
    k(19) = 4.9548; % ECM degrad by MMPs
    k(20) = 56.2986; % ECM degrad
    k(21) = 3.288e-7; % GF production
    k(22) = 2.1389e-7; % GF degrad
    k(23) = 0.1008; % k_up - GF uptake/production rate by ECM
end
% Hyp3: humans have a higher transition time
if setHypotheses == 3
    k(2) = 20.8217; % Metabolic demand
    k(41) = 3.4742e-4; % Growth rate
    k(32) = 9e-3; % theta_ap
    k(24) = 1.4e-3; % k_Q
    k(25) = 1.5e-3; % k_P
    k(26) = 70.9e-3; % k_R
end
% Hyp4: longer cell cycle, higher apoptosis rate, et al.
if setHypotheses == 4
    k(2) = 20.8217; % Metabolic demand
    k(41) = 3.4742e-4; % Growth rate
    k(32) = 9e-3; % theta_ap
    k(28) = 0.00417; %k_req
    k(27) = 0.00833; %k_prol
    k(31) = 0.00417; %k_apop
    k(24) = 1.1e-3; %k_q
    k(25) = 2.6e-3; %k_p
    k(26) = 135e-3; %k_r
end
```

```
% Table 3: Steady-State parameters
k(34) = -k(3)*k(2) + k(5)/(1+k(6)) + k(4); %-22.3; % TNF production
k(35) = -k(5)/(1+k(6)) + k(7); %-1.6; % JAK production
k(36) = -k(9)*k(8)^2/(k(8)^2+k(10)*(1+1/k(15))) + ...
   k(16)/(1+k(17)) + k(12)/(1+k(13)) + k(11); %2.39e4; % STAT3 production
k(37) = -k(12)/(1+k(13)) + k(14); %2.4e4; % SOCS production
k(38) = -k(16)/(1+k(17)) + k(18); %-8.16; % IE gene production
k(39) = k(19) + k(20); %40; % ECM production
k(40) = -k(21)*k(2) + k(23) + k(22); %-1.6; % GF production

% Set initial hepatocyte states, cell = (Q,P,R)
% and concentrations, conc = [IE,GF,ECM,TNF,JAK,STAT3,SOCS3]
cell = [k(1),0,0];
conc = ones(1,7);
G = 1;
x0 = [cell,conc,G]';

tStart = 0;
if setSpecies == 3
   tEnd = 400*24; % for humans
else tEnd = 300; % for rats/mice
end

% Call ODE solver
[t,x] = ode15s(@(t,x)odefun(t,x,k,x0), [tStart:.1:tEnd], x0);

% Organize results
cell = x(:,1:3);
% Remove negative values not used in calculations
cell(cell(:,2) < 0,2) = 0;
cell(cell(:,3) < 0,3) = 0;
% End of removing negative values
conc = x(:,4:10);
G = x(:,11);

% Plot results here
if shouldPlot == 1

   Stylez = 'k-'; % How to plot results
   Stylez2 = '-';
   if setSpecies == 3
      xAxisText = 'Time post-PHx (days)';
      t = t/24;
```

```
    else xAxisText = 'Time post-PHx (hrs)';
    end

    figure(1); hold on;

plot(t,cell(:,2),Stylez2,t,cell(:,3),Stylez2,t,cell(:,1)+cell(:,2)+cell(:,3),Stylez,'linewidth',
3)
    set(gca,'FontSize',12)
    xlabel(xAxisText,'FontSize',14);ylabel('Fraction of Liver','FontSize',14);
    ylim([0 1.10000001])
    title('Regeneration Profile','FontSize',18);
    legend('Primed','Replicating','Total','Location','Best');

    figure(2)
    plot(t,(conc),'linewidth',3)
    set(gca,'FontSize',12)
    xlabel(xAxisText,'FontSize',14);ylabel('Fold Change','FontSize',14);
    title('Molecular Levels','FontSize',18);
    legend('IE','GF','ECM','TNF','JAK','STAT3','SOCS3','location','best')

    figure(3);hold on;
    plot(t,cell(:,1)+G.*(cell(:,2)+cell(:,3)),Stylez,'linewidth',3)
    set(gca,'FontSize',12)
    xlabel(xAxisText,'FontSize',14);ylabel('Fraction of Liver','FontSize',14);
    ylim([0 1.10000001])
    title('Regeneration Profile','FontSize',18);

    brdu = cell(:,3)./(sum(cell')');
    brduMax = find(brdu >= max(brdu),1);
    disp('Maximum Brdu Incorporation is at')
    disp(t(brduMax))

    figure(4);hold on;
    plot(t,brdu,Stylez,'linewidth',3)
    set(gca,'FontSize',12)
    xlabel(xAxisText,'FontSize',14);ylabel('Fraction of Cells Replicating','FontSize',14);
    title('Replicating Hepatocytes','FontSize',18);
end %Ends plotting if statement
end

%% ODE Function to solve
function dxdt = odefun(t,x,k,x0)
% Set variable names
```

```
G = x(11);
Q=max(0,x(1)); P=max(0,x(2)); R=max(0,x(3)); N=Q+G*(P+R);
IE=x(4); GF=max(1,x(5)); ECM=x(6); TNF=x(7); JAK=x(8); STAT=x(9);
SOCS=x(10);
IE0=x0(4); GF0=x0(5); ECM0=x0(6); TNF0=x0(7); JAK0=x0(8); STAT0=x0(9);
SOCS0=x0(10);

% Calculate sigmas
sr = 0.5*(1+tanh((k(29)-GF)/k(30))); % sigma_req
sa = 0.5*(1+tanh((k(32)-((N)/k(2)))/k(33))); % sigma_ap

% Calculate reaction rates
r1 = k(24)*(IE-IE0)*Q; % Priming of Quiescent cells
r2 = k(26)*ECM*R; % Replicating cell returning to Quiescence
r3 = k(28)*sr*P; % Requiescence of Primed cells
r4 = k(25)*(GF-GF0)*P; % Primed cells begining Replication
r5 = k(27)*R; % Doubling of Replicating cells
ra1 = k(31)*sa*Q; % Apoptosis of Quiescent cells
ra2 = k(31)*sa*P; % Apoptosis of Primed cells
ra3 = k(31)*sa*R; % Apoptosis of Replicating cells

r6 = k(3)*k(2)/(N); % TNF production by stimulus
r7 = k(5)*TNF/(TNF+k(6)); % TNF production of JAK
r8 = k(4)*TNF; % TNF degradation
r9 = k(7)*JAK; % JAK degredation
r10 = k(9)*JAK*k(8)^2/(k(8)^2+k(10)*(1+SOCS/k(15))); % STAT3 production by
JAK
r11 = k(16)*STAT/(STAT+k(17)); % IE production by STAT3
r12 = k(12)*STAT/(STAT+k(13)); % SOCS3 production by STAT3
r13 = k(11)*STAT; % STAT3 degredation
r14 = k(14)*SOCS; % SOCS3 degredation
r15 = k(18)*IE; % IE degredation
r16 = k(19)*TNF*ECM; % ECM degredation by TNF activated MMPs
r17 = k(20)*ECM; % ECM degredation
r18 = k(21)*k(2)/N; % GF production by stimulus
r19 = k(23)*GF*ECM; % GF uptake/production by ECM
r20 = k(22)*GF; % GF degredation

% Set differential equations
dxdt(1) = -r1 + r2 + r3 - ra1; % Q Phase
dxdt(2) = r1 - r4 - r3 - ra2; % P Phase
dxdt(3) = r4 - r2 + r5 - ra3; % R Phase
```

```
dxdt(4) = r11 - r15 + k(38); % IE genes
dxdt(5) = r18 - r19 - r20 + k(40); % GF
dxdt(6) = -r16 - r17 + k(39); % ECM

dxdt(7) = r6 - r7 - r8 + k(34); % TNF
dxdt(8) = r7 - r9 + k(35); % JAK
dxdt(9) = r10 - r11 - r12 - r13 + k(36); % STAT3
dxdt(10) = r12 - r14 + k(37); % SOCS3

dxdt(11) = (k(2)/(N))*k(41) - k(2)*k(41); % Cell Mass (M)

dxdt = dxdt';
end
```

D.2 Non-parenchymal Cell Model of Liver Regeneration

```
function [t,cellh,conch,cellk,conck,cells,concs,IL6,TGFb,celle,G] =
LiverRegenGrowthFull(initialFraction,para)
% Author:       Daniel Cook
% Date:         08/08/2016
% Copyright:    Creative Commons Share Alike

% This function computes cellular regeneration following PHx
% It is an extension of the model from "A Model of Liver Regeneration" (2009) by
Furchtgott et al.
% Initial fraction is the fraction of liver removed (ie 0.7)
% To run this code: [t,cellh,conch,cellk,conck,cells,concs,IL6,TGFb,celle,G] =
LiverRegenGrowthFull(0.7);

% Plot results (1=plot, 2=do not plot)
shouldPlot = 2;

% Set species (1=rat, 2=mouse, 3=human)
setSpecies = 1;

% Set disease state (1=healthy, 2=ALD)
setDisease = 1;

% Set para to a default value of 0 if the "para" input is missing
if nargin == 1
   para = 0;
end

% Call parameter setting functions (also set disease states)
[cellh0,conch0,kh] =
hepatocyteParameters(initialFraction,para,setSpecies,setDisease);
[cellk0,conck0,kk] = kupfferParameters(initialFraction,para,setSpecies,setDisease);
[cells0,concs0,ks] = stellateParameters(initialFraction,para,setSpecies,setDisease);
[celle0,ke] = endothelialParameters(initialFraction,para);
G = 1;

% Set initial conditions vector
x0 = [cellh0,conch0,cellk0,conck0,cells0,concs0]';
x0(end+1) = (x0(5) + x0(15))/2; % Combined IL6
x0(end+1) = (x0(17) + x0(25))/2; % Combined TGFb
```

```
x0(end+1) = celle0; % Endothelial cells
x0(end+1) = G; % Hepatocyte size

% Set start, step, and end time
tStart = 0;
tStep = 1;
if setSpecies == 3
   tEnd = 10000; % for humans
else
   tEnd = 300; % for rats/mice
end

% Run ODE solver
[t,x] = ode15s(@(t,x)odefun(t,x,kh,kk,ks,ke,x0), [tStart:tStep:tEnd], x0);

% Split output results into readable components
split1=length(cellh0)+length(conch0);
split2=split1+length(cellk0); split3=split2+length(conck0);
split4=split3+length(cells0); split5=split4+length(concs0);

cellh=x(:,1:length(cellh0)); conch=x(:,(length(cellh0)+1):split1);
cellk=x(:,(split1+1):split2); conck=x(:,(split2+1):split3);
cells=x(:,(split3+1):split4); concs=x(:,(split4+1):split5);
IL6=x(:,split5+1); TGFb=x(:,split5+2); celle = x(:,split5+3); G=x(:,split5+4);

%% Plot Results

% Plot results
if shouldPlot == 1

   % Change time scale to days for humans
   xAxisLabel = 'Time post-PHx (hrs)';
   if setSpecies == 3
      t = t/24;
      xAxisLabel = 'Time post-PHx (days)';
   end

   % Plot hepatocyte mass recovery
   if setDisease == 1
      figure(1);hold on; plot(t,cellh(:,1)+G.*(cellh(:,2)+cellh(:,3)),'k-','linewidth',3);
   end
   if setDisease == 2
```

```
    figure(1);hold on; plot(t,cellh(:,1)+G.*(cellh(:,2)+cellh(:,3)),'-','color',[.5 .5
.5],'linewidth',3);
  end
  title('Liver Mass Recovery','fontsize',22)
  xlabel(xAxisLabel,'fontsize',18);ylabel('Mass Recovery','fontsize',18);
  set(gca,'fontsize',18,'linewidth',2);box off; xlim([0 t(end)])

  % Plot experimental results
  controlTime = [0,1,3,7]*24;
  controlMean = [0.3,0.447,0.757,0.923];
  control95CI = [0,0.089,0.135,0.21];
  ashTime = [0, 24, 48];
  ashMean = [0.3,0.4,0.424];
  ash95CI = [0,0.082,0.028];
  if setDisease == 1 && setSpecies == 1;
    errorbar(controlTime,controlMean,control95CI,'ko','linewidth',3);
  end
  if setDisease == 2 && setSpecies == 1;
    errorbar(ashTime,ashMean,ash95CI,'o','color',[.5 .5 .5],'linewidth',3);
  end

  % Plot cell states
  figure(2); hold on; plot(t,cellh(:,2),'b-','linewidth',3);
  plot(t,cellh(:,3),'-','linewidth',3,'color',[.25 .75 .25]);
  plot(t,cellh(:,1)+cellh(:,2)+cellh(:,3),'k-','linewidth',3);
  legend('Primed','Replicating','Total');set(gca,'fontsize',18);
  title('Hepatocyte Dynamics','fontsize',22)
  xlabel(xAxisLabel,'fontsize',18);ylabel('Fraction Recovery','fontsize',18);
  set(gca,'fontsize',18,'linewidth',2);box off; xlim([0 t(end)])

  % Generate Figures from paper
  figure(3); hold on; plot(t,cells(:,2)./sum(cells')','-','color',[.25 .75 .25],'linewidth',2)
  figure(3); hold on; plot(t,cells(:,4)./sum(cells')','r-','linewidth',2)
  set(gca,'fontSize',18,'linewidth',2);box off
  xlabel('Time post-PHx (hrs)'); ylabel('Fraction of total')
  title('Stellate Cell Dynamics','fontsize',22)

  figure(4); hold on; plot(t,conck(:,3),'k-','linewidth',2)
  figure(4); hold on; plot(t,IL6,'b-','linewidth',2)
  set(gca,'fontSize',18,'linewidth',2);box off
  xlabel('Time post-PHx (hrs)'); ylabel('Fold Change')
  title('Cytokine Dynamics','fontsize',22)
```

```
    figure(5); hold on; plot(t,cellh(:,2),'k-','linewidth',2)
    set(gca,'fontSize',18,'linewidth',2);box off
    xlabel('Time post-PHx (hrs)'); ylabel('Fraction of Original Mass')
    title('Hepatocyte Priming','fontsize',22)

    figure(6); hold on; plot(t,cellh(:,3),'k-','linewidth',2)
    set(gca,'fontSize',18,'linewidth',2);box off
    xlabel('Time post-PHx (hrs)'); ylabel('Fraction of Original Mass')
    title('Replicating Hepatocytes','fontsize',22)

    figure(7); hold on; plot(t,(G-1).*(cellh(:,2)+cellh(:,3)),'k-','linewidth',2)
    set(gca,'fontSize',18,'linewidth',2);box off
    xlabel('Time post-PHx (hrs)'); ylabel('Fraction of Original Mass')
    title('Liver Hypertrophy','fontsize',22)

end

end

function dxdt = odefun(t,x,kh,kk,ks,ke,x0)
%% Call cellular subfunctions
% Combine variables of secreted factors
x(end-3) = (x(5) + x(15))/2; % Combined IL6
x(end-2) = (x(17) + x(25))/2; % Combined TGFb

% Call hepatocyte cellular & molecular equations
dx1 = hepatocyteEquations(t,x,x0,kh);
dx2 = kupfferEquations(t,x,x0,kk);
dx3 = stellateEquations(t,x,x0,ks);
dxe = endothelialEquations(t,x,x0,ke);
dxg = growthEquations(t,x,x0,kh);

dxdt = [dx1;dx2;dx3;dx1(5)+dx2(5);dx2(7)+dx3(7);dxe;dxg];
end

function [cellh,conch,kh] =
hepatocyteParameters(initialFraction,para,setSpecies,setDisease)
%% Set Hepatocyte Parameters
kh = zeros(41,1);
% Table 1: Molecular parameters
kh(1) = 1-initialFraction; % Fraction of liver mass remaining (N)
kh(2) = 16.8; % Metabolic load (M)
kh(3) = 0.3; % IL6 production (Changed from Vipul)
```

```
kh(4) = 0; % IL6 mRNA degrad (Changed from Vipul)
kh(5) = 6e4; %2e4; % JAK activation rate (V_JAK)
kh(6) = 1e4; % Km JAK
kh(7) = 0.4; % JAK degrad
kh(8) = 2; % Conc. of monomeric STAT3
kh(9) = 7.5e2; % STAT3 activation rate
kh(10) = 0.4; % Km STAT3
kh(11) = 0.1; % STAT3 degrad
kh(12) = 2.4e4; % SOCS activation rate
kh(13) = 7e-4; % Km SOCS3
kh(14) = 0.4; % SOCS3 degrad.
kh(15) = 1.5e-2; % SOCS3 inhibition constant
kh(16) = 2.5e2; % IE response gene expression rate
kh(17) = 18; % Km for IE genes
kh(18) = 5; % IE gene degrad

% Table 2: Cellular parameters
kh(19) = 7e-3; % k_Q
kh(20) = 4.4e-3; % k_P
kh(21) = 5.4e-2; % k_R
kh(22) = 2e-2; % k_prol - specifies length of mitotic cycle
kh(23) = 0.1; % k_req - requiescence rate
kh(24) = 8; % theta_req (for sigma_req)
kh(25) = 3; % beta_req (for sigma_req)
kh(26) = 1e-1; %1e-2; % k_ap - apoptosis rate
kh(27) = 9e-3; % theta_ap
kh(28) = 4.5e-3; % beta_ap

% Set metabolic demand and growth rates
if setSpecies == 1
   kh(2) = 23.21; %M, Metabolic Load Rat
   kh(42) = 8.29e-4; %G, Growth Rate Rat
elseif setSpecies == 2
   kh(2) = 25.24; %M, Metabolic Load Mouse
   kh(42) = 16.83e-4; %G, Growth Rate Mouse
elseif setSpecies == 3
   kh(2) = 1.432; %M, Metabolic Load Human
   kh(42) = 12.56e-4; %G, Growth Rate Human
end

% Scale the apoptosis response
kh(27) = kh(27)*23.21/kh(2);
```

```
% Alter Hepatocyte parameters (ALD)
if setDisease == 2
   kh(8) = kh(8)*.7; % JAK activation rate (V_JAK)
end

% Table 3: Steady-State parameters
kh(29) = -kh(3)*kh(2) + kh(5)/(1+kh(6)) + kh(4); %-22.3; % IL6 production
kh(30) = -kh(5)/(1+kh(6)) + kh(7); %-1.6; % JAK production
kh(31) = -kh(9)*kh(8)^2/(kh(8)^2+kh(10)*(1+1/kh(15))) + ...
   kh(16)/(1+kh(17)) + kh(12)/(1+kh(13)) + kh(11); %2.39e4; % STAT3 production
kh(32) = -kh(12)/(1+kh(13)) + kh(14); %2.4e4; % SOCS production
kh(33) = -kh(16)/(1+kh(17)) + kh(18); %-8.16; % IE gene production

% Parameters for Production of VEGF
kh(34) = 2; % Hypoxia Load (HL)
kh(35) = 15; % HIF production rate
kh(36) = 0.9; % HIF degradation rate
kh(37) = 2e4; % VEGF activation rate
kh(38) = 1e4; % Km VEGF
kh(39) = 0.4; % VEGF degradation rate
kh(40) = kh(37)/(1+kh(38)) + kh(36); % Steady state of HIF
kh(41) = -kh(37)/(1+kh(38)) + kh(39); % Steady state of VEGF

% Set initial hepatocyte states, cell = (Q,P,R)
% and concentrations, conc = [IE,IL6,JAK,STAT3,SOCS3,HIF,VEGF]
cellh = [kh(1),0,0];
conch = ones(1,7); %mRNA levels all start at a FC value of 1
end

function dx1 = hepatocyteEquations(t,x,x0,kh)
%% Hepatocyte Equations
% Set aliases
G = x(30);
Q=x(1); P=x(2); R=x(3); N=Q+G*(P+R);
IE=x(4); HGF=x(24); ECM=x(26); IL6=x(27); JAK=x(6); STAT=x(7); SOCS=x(8);
IE0=x0(4); HGF0=x0(24); ECM0=x0(26); IL60=x0(27); JAK0=x0(6); STAT0=x0(7);
SOCS0=x0(8);
HIF=x(9); VEGF=x(10); HIF0=x0(9); VEGF0=x0(10);
k=kh;
EC = x(29);

sr = 0.5*(1+tanh((k(24)-HGF)/k(25))); % sigma_req
sa = 0.5*(1+tanh((k(27)-(N/k(2)))/k(28))); % sigma_ap
```

```
if (IE >= IE0)
   r1 = k(19)*(IE-IE0)*Q; % Priming of Quiescent cells
else r1 = 0; end;
r2 = k(21)*ECM*R; % Replicating cell returning to Quiescence
r3 = k(23)*sr*P; % Requiescence of Primed cells
if (HGF >= HGF0)
r4 = k(20)*(HGF-HGF0)*P; % Primed cells begining Replication
else r4 = 0; end;
r5 = k(22)*R; % Doubling of Replicating cells
ra1 = k(26)*sa*Q; % Apoptosis of Quiescent cells
ra2 = k(26)*sa*P; % Apoptosis of Primed cells
ra3 = k(26)*sa*R; % Apoptosis of Replicating cells

r6 = k(3)*k(2)/N; % IL6 production by stimulus
r7 = k(5)*IL6/(IL6+k(6)); % IL6 production of JAK
r8 = k(4)*IL6; % IL6 degradation
r9 = k(7)*JAK; % JAK degradation
r10 = k(9)*JAK*k(8)^2/(k(8)^2+k(10)*(1+SOCS/k(15))); % STAT3 production by
JAK
r11 = k(16)*STAT/(STAT+k(17)); % IE production by STAT3
r12 = k(12)*STAT/(STAT+k(13)); % SOCS3 production by STAT3
r13 = k(11)*STAT; % STAT3 degradation
r14 = k(14)*SOCS; % SOCS3 degradation
r15 = k(18)*IE; % IE degradation
% r16 = (N-k(1))/k(34)*k(35)*(1-tanh(3*(x(11)+x(12)+x(13)))); % HIF production
(Uses KC growth as a surrigate for blood vessel growth)
r16 = (N-k(1))/k(34)*k(35)*(1-tanh(3*EC)); % HIF production (Uses EC growth as a
surrigate for blood vessel growth)
r17 = k(37)*HIF/(HIF+k(38)); % HIF activation of VEGF
r18 = k(36)*HIF; % HIF degradation
r19 = k(39)*VEGF; % VEGF degradation

dx1(1) = -r1 + r2 + r3 - ra1; % Q Phase
dx1(2) = r1 - r4 - r3 - ra2; % P Phase
dx1(3) = r4 - r2 + r5 - ra3; % R Phase
dx1(4) = r11 - r15 + k(33); % IE genes
dx1(5) = r6 - r7 - r8 + k(29); % IL6
dx1(6) = r7 - r9 + k(30); % JAK
dx1(7) = r10 - r11 - r12 - r13 + k(31); % STAT3
dx1(8) = r12 - r14 + k(32); % SOCS3
dx1(9) = r16 - r17 - r18 + k(40); % HIF1a
dx1(10) = r17 - r19 + k(41); % VEGF
```

```
% Set differential equations
dx1 = dx1';
end

function [cellk,conck,kk] =
kupfferParameters(initialFraction,para,setSpecies,setDisease)
%% Set Kupffer cell parameters
kk = zeros(30,1);
% Table 1: Molecular parameters
kk(1) = 1-initialFraction; % Fraction of liver mass remaining (N)
kk(2) = 16.8; % Metabolic load (M)
kk(3) = 2; % Hypoxic load (HL)
kk(4) = 16; %8; % TNF production
kk(5) = 2; % TNF mRNA degrad
kk(6) = 180; %90; % IL6 production
kk(7) = 0.9; % IL6 degradation
kk(8) = 20; %1; % IL10 production
kk(9) = 0.9; % IL10 degradation
kk(10) = 30; %3; % TGFb production
kk(11) = 0; % TGFb degradation
kk(12) = 15; % PDGF production
kk(13) = 0.9; % PDGF degradation

% Table 2: Cellular parameters
kk(14) = 7e-3; % k_Q
kk(15) = 2.2e-2; % k_A
kk(16) = 5.4e-2; % k_R
kk(17) = 2e-2; % k_prol - specifies length of mitotic cycle
kk(18) = 0.3; % k_req - requiescence rate
kk(19) = 8; % theta_req (for sigma_req)
kk(20) = 3; % beta_req (for sigma_req)
kk(21) = 1e-1; % k_ap - apoptosis rate
kk(22) = 9e-3; % theta_ap
kk(23) = 4.5e-3; % beta_ap
kk(24) = 0.1; % IL10 antagonism to IL6 (This parameter no longer used)

% IL10 inhibition of TNFa
kk(30) = 3; %1.5; % IL10 inihbition of TNFa

% Increase both pro- and anti-inflammation
if setDisease == 2
   kk(4) = kk(4)*2;
```

```
    kk(6) = kk(6)*1.25;
    kk(8) = kk(8)*3;
    kk(10) = kk(10)*3;
end

% Table 3: Steady-State parameters
kk(25) = kk(5); % TNF production
kk(26) = kk(7) + kk(24); % IL6 production
kk(27) = kk(9) + kk(24); % IL10 production
kk(28) = kk(11); % TGFb production
kk(29) = kk(13); % PDGF production

% Set metabolic demand
if setSpecies == 1
    kk(2) = 23.21; %M, Metabolic Load Rat
elseif setSpecies == 2
    kh(2) = 25.24; %M, Metabolic Load Mouse
elseif setSpecies == 3
    kk(2) = 1.432; %M, Metabolic Load Human
end

% Scale the apoptosis response
kk(22) = kk(22)*23.21/kk(2);

% Set initial hepatocyte states, cell = (Q,P,R)
% and concentrations, conc = [TNF, IL6, IL10, TGFb, PDGF]
cellk = [kk(1),0,0];
conck = ones(1,5); % mRNA levels all start at a FC value of 1
end

function dx2 = kupfferEquations(t,x,x0,kk)
%% Kupffer Cell Equations
% Set aliases
Q=x(11); A=x(12); R=x(13); % Kupffer cell states
N=x(1)+x(30)*(x(2)+x(3)); % N is based on the total number of hepatocytes
TNF=x(14); IL6=x(27); IL10=x(16); TGFb=x(28); PDGF=x(18); VEGF=x(10);
ECM=x(26);
TNF0=x0(14); IL60=x0(27); IL100=x0(16); TGFb0=x0(28); PDGF0=x0(18); VEGF0
= x0(10);
HGF=x(24);
k=kk;
EC=x(30);
```

```
sr = 0.5*(1+tanh((k(19)-(k(2)/N/10 + TNF))/k(20))); % sigma_req
sa = 0.5*(1+tanh((k(22)-(N/k(2)))/k(23))); % sigma_ap

if (TNF >= TNF0)
   r1 = k(14)*((TNF-TNF0) + (k(2)/N-k(2)))*Q; % Activation of Quiescent cells
else r1 = 0; end;
r2 = k(16)*ECM*R; % Replicating cell returning to Activation
r3 = k(18)*sr*A; % Requiescence of Activated cells
if (VEGF >= VEGF0)
   r4 = k(15)*(VEGF - VEGF0)*A; % Activated cells begining Replication
else r4 = 0; end;
r5 = k(17)*R; % Doubling of Replicating cells
ra1 = k(21)*sa*Q; % Apoptosis of Quiescent cells
ra2 = k(21)*sa*A; % Apoptosis of Activated cells
ra3 = k(21)*sa*R; % Apoptosis of Replicating cells

r6 = k(4)*A*((k(30)+IL10)/IL10); % TNF production by Activated cells
r7 = k(5)*TNF; % TNF degradation
r8 = k(6)*A; % IL6 production
r9 = k(7)*IL6; % IL6 degradation
r10 = k(8)*A; % IL10 production
r11 = k(9)*IL10; % IL10 degradation
r12 = k(10)*A; % TGFb production
r13 = k(11)*TGFb; % TGFb degradation
r14 = (N-k(1))/k(3)*k(12)*(1-tanh(3*EC)); % PDGF production in response to
hypoxia (Uses EC as a surragate for blood vessel growth)
r15 = k(13)*PDGF; % PDGF degradation

dx2(1) = -r1 + r3 - ra1; % Q Phase
dx2(2) = r1 + r2 - r4 - r3 - ra2; % A Phase
dx2(3) = r4 - r2 + r5 - ra3; % R Phase

dx2(4) = r6 - r7 + kk(25); % TNF
dx2(5) = r8 - r9 + kk(26); % IL6
dx2(6) = r10 - r11 + kk(27); % IL10
dx2(7) = r12 - r13 + kk(28); % TGFb
dx2(8) = r14 - r15 + kk(29); % PDGF

% Set differential equations
dx2 = dx2';
end
```

```
function [cells,concs,ks] =
stellateParameters(initialFraction,para,setSpecies,setDisease)
%% Set Stellate cell parameters
ks = zeros(27,1);
% Table 1: Molecular parameters
ks(1) = 1-initialFraction; % Fraction of liver mass remaining (N)
ks(2) = 16.8; % Metabolic load (M)
ks(3) = 25; % HGF production
ks(4) = 0.23; % HGF degrad
ks(5) = 60e-2; %6e-2; % k_up - HGF uptake/production rate by ECM
ks(6) = 8; %1.5; % TGFb production
ks(7) = 0.9; % TGFb degradation
ks(8) = 100; %50; % ECM production
ks(9) = 7; % ECM degrad by MMPs
ks(10) = 3; % ECM degrad

% Table 2: Cellular parameters
ks(11) = 7e-2; % 7e-3; % k_QP (Quiescent to Pro-proliferative)
ks(12) = 3e-2; %7e-3; % k_QA (Quiescent to Anti-proliferative)
ks(13) = 4.4e-3; % k_AP
ks(14) = 4.4e-3; % k_AA
ks(15) = 5.4e-2; % k_RP
ks(16) = 5.4e-2; % k_RA
ks(17) = 0.85e-2; %2e-2; % k_prol - specifies length of mitotic cycle
ks(18) = 0.2; %0.1; % k_req - requiescence rate
ks(19) = 8; % theta_req (for sigma_req)
ks(20) = 3; % beta_req (for sigma_req)
ks(21) = 1e-1; %1e-2; % k_ap - apoptosis rate
ks(22) = 9e-3; % theta_ap
ks(23) = 4.5e-3; % beta_ap
ks(24) = 5; % TGFb inhibition of HGF production

% Matrix preconditioning and GF deficiency (with increased macrophage activation)
if setDisease == 2
   ks(11) = ks(11)*.65;
%     ks(12) = ks(12)*.35;
   ks(12) = ks(12)*.25;
   ks(5) = ks(5)*.7;
   ks(8) = ks(8)*4;
   ks(9) = ks(9)*0.1;
end

% Table 3: Steady-State parameters
```

```
ks(25) = ks(4) + ks(5); %-22.3; % HGF production
ks(26) = ks(7); % TGFb production
ks(27) = ks(9) + ks(10); % ECM production

% Set metabolic demand
if setSpecies == 1
   ks(2) = 23.21; %M, Metabolic Load Rat
elseif setSpecies == 2
   kh(2) = 25.24; %M, Metabolic Load Mouse
elseif setSpecies == 3
   ks(2) = 1.432; %M, Metabolic Load Human
end

% Scale the apoptosis response
ks(22) = ks(22)*23.21/ks(2);

% Set initial stellate cell states, cell = (Q,Pro-R,Pro-R-Rep,Anti-R,Anti-R-Rep)
% and concentrations, conc = [HGF,TGFb,ECM]
cells = [ks(1),0,0,0,0];
concs = ones(1,3); %mRNA levels all start at a FC value of 1
end

function dx3 = stellateEquations(t,x,x0,ks)
%% Stellate Cell Equations
% Set aliases
Q=x(19); AP=x(20); RP=x(21); AA=x(22); RA=x(23); % Stellate cell states
N=x(1)+x(30)*(x(2)+x(3)); % N is based on the total number of hepatocytes
HGF=x(24); TGFb=x(28); ECM=x(26); PDGF=x(18); TNF=x(14);
HGF0=x0(24); TGFb0=x0(28); ECM0=x0(26); PDGF0=x0(18); TNF0=x0(14);
IL6=x(27); IL60=x0(27);
k=ks;

sr = 0.5*(1+tanh((k(19)-PDGF)/k(20))); % sigma_req
sa = 0.5*(1+tanh((k(22)-(N/k(2)))/k(23))); % sigma_ap

if (IL6 >= IL60)
r1 = k(11)*(IL6-IL60)*Q; % Pro-proliferative (PP) Activation of Quiescent cells
else r1 = 0; end;
r2 = k(15)*ECM*RP; % Replicating cell returning to PP Activation
r3 = k(18)*sr*AP; % Requiescence of PP Activated cells
if (PDGF >= PDGF0)
   r4 = k(13)*(PDGF-PDGF0)*AP; % PP Activated cells begining Replication
%%%%%%%%%%% This should be k(13) %%%%%%%%%%%
```

```
else r4 = 0; end;
r5 = k(17)*RP; % Doubling of PP Replicating cells
ra1 = k(21)*sa*Q; % Apoptosis of Quiescent cells
ra2 = k(21)*sa*AP; % Apoptosis of PP Activated cells
ra3 = k(21)*sa*RP; % Apoptosis of PP Replicating cells

if (TGFb >= TGFb0)
   r6 = k(12)*(TGFb-TGFb0)*Q; % Anti-proliferative (AP) Activation of Quiescent
cells
else r6 = 0; end;
r7 = k(16)*ECM*RA; % Replicating cell returning to AP Activation
r8 = k(18)*sr*AA; % Requiescence of AP Activated cells
if (PDGF >= PDGF0)
   r9 = k(14)*(PDGF-PDGF0)*AA; % AP Activated cells begining Replication
%%%%%%%%%%% This should be k(14) %%%%%%%%%%%
else r9 = 0; end;
r10 = k(17)*RA; % Doubling of AP Replicating cells
ra4 = k(21)*sa*AA; % Apoptosis of AP Activated cells
ra5 = k(21)*sa*RP; % Apoptosis of AP Replicating cells

r11 = k(3)*AP*((k(24)+TGFb)/TGFb); % HGF production by Activated cells
r12 = k(4)*HGF; % HGF degradation
r13 = k(5)*HGF*ECM; % HGF uptake by ECM
r14 = k(6)*AA; % TGFb production by Activated cells
r15 = k(7)*TGFb; % TGFb degradation
r16 = k(8)*AA; % ECM production by Activated cells
r17 = k(9)*ECM*TNF; % ECM degradation by TNF actived MMPs
r18 = k(10)*ECM; % ECM degradation rate

dx3(1) = -r1 + r3 - r6 + r8 - ra1; % Q Phase
dx3(2) = r1 + r2 - r4 - r3 - ra2; % PA Phase
dx3(3) = r4 - r2 + r5 - ra3; % RP Phase
dx3(4) = r6 + r7 - r9 - r8 - ra4; % AA Phase
dx3(5) = r9 - r7 + r10 - ra5; % RA Phase

dx3(6) = r11 - r12 - r13 + k(25); % HGF
dx3(7) = r14 - r15 + k(26); % TGFb
dx3(8) = r16 - r17 - r18 + k(27); % ECM

% Set differential equations
dx3 = dx3';
end
```

```
function [celle,ke] = endothelialParameters(initialFraction,para)
%% Set Endothelial Cell Parameters
ke = zeros(2,1);
ke(1) = 1 - initialFraction; % Fraction of liver mass remaining (N)
ke(2) = 2e-2; % k_prol - specifies length of mitotic cycle
celle = ke(1); % Fraction of initial endothelial cells
end

function dxe = endothelialEquations(t,x,x0,ke)
%% Hepatocyte Equations
% Set aliases
VEGF=x(10); VEGF0=x0(10);

if (VEGF >= VEGF0)
   r1 = ke(2)*(VEGF - VEGF0); % Endothelial Cell proliferation
else r1 = 0; end;

dxe = r1; % Endothelial cell proliferation
end

function dxg = growthEquations(t,x,x0,kh)
G = x(30);
Q=x(1); P=x(2); R=x(3); N=Q+G*(P+R);

dxg(1) = (kh(2)/N)*kh(42) - kh(2)*kh(42);
end
```

D.3 Liver Homeostatic Renewal Model

```
function [t,cellh,k] = Hepat_HR_full(feedBackInput,insultInput,startBal)
% Author: Daniel Cook
% Date: 01/01/2016
% Copyrighted under Creative Commons Share Alike

% To run, use: [t,cellh,k] = Hepat_HR_full([1,1,1,0],1,[.05 .95]);
% k = parameter values, R1-R4 = Robustness per disturbance, OR = overall
robustness

% Set plotting and printing (1=show results, 2=suppress results)
shouldPlot = 1; colorChoice = 'k';
shouldPrint = 2;

% Feedback mechanisms
% F(1) = implicit competition (Model A)
% F(2) = product inhibition of proliferation (Model B)
% F(3) = product inhibition of transitions (Model C)
% F(4) = alternate populations (i.e. stem cells) (Model D)

% Insults
% 0 = no insult
% 1 = increased apoptosis, 2 = decreased apoptosis
% 3 = increased proliferation, 4 = decreased proliferation
% 5 = periodic apoptosis increase
% 6 = periodic apoptosis increase w/ same width
% 7 = Periodic apoptosis increase w/ differing magnitudes
% 8 = Periodic apoptosis decrease
% 9 = Sinusoidal apoptosis rate
% 10= Unit step change in apoptosis rate

%% Section 1: Set parameter values given which feedbacks are present
% Declare global variables & input values
global F y0 insult insultFrequency
F = feedBackInput;
insult = insultInput;

% Set insult frequency
% Natural frequencies = 1.4224 & 0.3086
insultFrequency = 2.0; % 2 = 1/2 day on, 1/2 day off
```

```
% Use blue for high frequency (>1), red for low frequency (<1)


% Set time (in days)
tStart = 0;
tEnd = 365*1; % Number of years to run simulation

% Table 1: Initial hepatocyte states, cell = (A2+,A2-)
init_A2plus = .05; % Initial level
cellh = [init_A2plus,1-init_A2plus];
x0 = cellh;
% Set steady-state conditions for changing starting points
y0 = x0;

% Change starting concentrations if startBal parameter is used
x0(1) = startBal(1);
x0(2) = startBal(2);

% Define model parameters
k = zeros(13,1);

% Table 2: Physiological parameters
% Rates are in doublings/day
k(1) = (1/14);  % k_prol^A2+
k(2) = .05*1.5; % K_cap^A2+ (carrying capacity of A2+ hepatocytes)
k(3) = .95*1.5; % K_cap^A2- (carrying capacity of A2- hepatocytes)

% Table 3: Literature and steady-state constrained parameters
k(4) = .5*k(1); % k_prol^A2- (Proliferation rate is half of A2+) (Lit.)

% Additional parameters for specific feedbacks
k(8) = 1;       % k_P-env: Tissue microenvironment effect Axin2+ proliferation
k(9) = 0.95;    % k_T-env: Tissue microenvironment effect on cell transition
k(10) = 0.1;    % k_A
k(11) = 100;    % C1
k(12) = 8;      % C2 (This starts renewing H+ cells at ~.025)
k(13) = 8;      % kRenew

% Set feedback conditions
if F(1) == 0
   feedBack1a = 1; feedBack1b = 1;
elseif F(1) == 1
   feedBack1a = (1-cellh(1)/k(2));
```

```
    feedBack1b = (1-cellh(2)/k(3));
end
if F(2) == 0
    feedBack2 = 1;
elseif F(2) == 1
    feedBack2 = k(8)/(cellh(1)+k(10)*cellh(2));
end
if F(3) == 0
    feedBack3 = 1;
elseif F(3) == 1
    feedBack3 = (k(9))/cellh(2);
%     hillCoeff = 1;
%     feedBack3 = 2*k(9)^hillCoeff/(k(9)^hillCoeff+cellh(2)^hillCoeff); % Alternate
feedback
end
if F(4) == 0
    feedBack4 = 0;
elseif F(4) == 1
    feedBack4 = k(13)*(1/(1+exp(k(11)*cellh(1)+k(12))));
end

% Set steady-state constrained parameters
% Set effective proliferation rate equal to observed proliferation rate
if F(1) == 1 && F(2) == 0
    solverfun1a = @(x)abs(x*feedBack1a*feedBack2 - k(1));
    [k(1),fval] = fminsearch(solverfun1a,1);
    solverfun1b = @(x)abs(x*feedBack1b - k(4));
    [k(4),fval] = fminsearch(solverfun1b,1);
end
if F(2) == 1 && F(1) == 0
    solverfun1c = @(x)abs(k(1)*feedBack1a*x/(cellh(1)+k(10)*cellh(2)) - k(1));
    [k(8),fval] = fminsearch(solverfun1c,1);
    feedBack2 = k(8)/(cellh(1)+k(10)*cellh(2));
    solverfun1b = @(x)abs(x*feedBack1b - k(4));
    [k(4),fval] = fminsearch(solverfun1b,1);
end
if F(2) == 1 && F(1) == 1
    solverfun1a = @(x)abs(x*feedBack1a - k(1));
    [k(1),fval] = fminsearch(solverfun1a,1);
    solverfun1c = @(x)abs(k(1)*feedBack1a*x/(cellh(1)+k(10)*cellh(2)) - k(1));
    [k(8),fval] = fminsearch(solverfun1c,1);
    feedBack2 = k(8)/(cellh(1)+k(10)*cellh(2));
    solverfun1b = @(x)abs(x*feedBack1b - k(4));
```

```
    [k(4),fval] = fminsearch(solverfun1b,1);
end
% Solve for kapPlus (using the sum of equations 1 and 2)
solverfun = @(x)abs(k(1)*cellh(1)*feedBack1a*feedBack2 + feedBack4 - cellh(1)*x
+ k(4)*cellh(2)*feedBack1b - cellh(2)*x);
[k(5),fval] = fminsearch(solverfun,1);
k(6) = k(5); % set kapMinus = kapPlus
% Solve for kT (using equation 1)
solverfun2 = @(x)abs(k(1)*cellh(1)*feedBack1a*feedBack2 + feedBack4 -
cellh(1)*k(5) - cellh(1)*x*feedBack3);
[k(7),fval2] = fminsearch(solverfun2,1);


%% Section 2: Run model
% Call ODE solver
timeStep = 0.1; % Days
[t,x] = ode15s(@(t,x)odefun(t,x,k,x0), [tStart:timeStep:tEnd], x0);
cellh = x(:,1:2);

%% Section 3: Plot results
% Plot results
if shouldPlot == 1
    % Hepatocyte Populations
    figure(1); hold on; plot(t,cellh(:,1),'-','color',colorChoice,'linewidth',2);
    plot(t,cellh(:,2),'--','color',colorChoice,'linewidth',2);
    set(gca,'fontsize',18,'linewidth',2); box off
    xlabel('Time (Days)'); ylabel('Hepatocyte Populations')
    legend('Axin2+','Axin2-')

    % Hepatocyte Population Phase Plane
    figure(2); hold on; plot(cellh(:,1),cellh(:,2),'-','color',colorChoice,'linewidth',2);
    set(gca,'fontsize',18,'linewidth',2); box off
    ylabel('Axin2- Hepatocytes')
    xlabel('Axin2+ Hepatocytes')

    % If insult is periodic, plot insult period
    if insult == 5 || insult == 8
        yTime = 0:.1:tEnd;
        yInsult = zeros(1,length(yTime));
        yInsult(-sin(insultFrequency*3.14*yTime) > 0) = 1;
        figure(3); hold on; plot(yTime,yInsult,'-','color',colorChoice,'linewidth',3)
        set(gca,'fontsize',18,'linewidth',2); box off
        ylabel('Relative apoptosis Rate'); xlabel('Time (Days)')
```

```
        xlim([0 30])
    end

    % If insult is periodic, plot insult period
    if insult == 6
        yTime = 0:.1:tEnd;
        yInsult = zeros(1,length(yTime));
        yInsult(-sin(insultFrequency*3.14*yTime) > sin(pi/4*(2-insultFrequency))) = 1;
        figure(3); hold on; plot(yTime,yInsult,'-','color',colorChoice,'linewidth',3)
        set(gca,'fontsize',18,'linewidth',2); box off
        ylabel('Relative apoptosis Rate'); xlabel('Time (Days)')
        xlim([0 30])
    end

    % If insult is periodic, plot insult period
    if insult == 7
        yTime = 0:.1:tEnd;
        yInsult = zeros(1,length(yTime));
        yInsult(-sin(insultFrequency*3.14*yTime) > 0) = 2;
        figure(3); hold on; plot(yTime,yInsult,'-','color',colorChoice,'linewidth',3)
        set(gca,'fontsize',18,'linewidth',2); box off
        ylabel('Relative apoptosis Rate'); xlabel('Time (Days)')
        xlim([0 30])
    end

    % If insult is sinusoidal, plot insult period
    if insult == 9 || insult == 10
        yTime = 0:.01:tEnd;
        yInsult = sin(insultFrequency*3.14*yTime)*k(6) + k(6);
        figure(3); hold on; plot(yTime,yInsult,'-','color',colorChoice,'linewidth',3)
        set(gca,'fontsize',18,'linewidth',2); box off
        ylabel('Apoptosis Rate'); xlabel('Time (Days)')
        xlim([0 30])
    end
end

%% Section 4: Print results
% Calculate recovery time
% y0 is the steady-state value for cellh
recoveryTime = 1;
temp = length(find(cellh((40/timeStep+1):end,1)./y0(1)>=.99 &
cellh((40/timeStep+1):end,1)./y0(1)<= 1.1,1));
if temp > 0
```

```
   temp = length(find(cellh((40/timeStep+1):end,2)./y0(2)>=.99 &
cellh((40/timeStep+1):end,2)./y0(2)<= 1.1,1));
   if temp > 0
      tRecovery(1) = t((40/timeStep+1)+find(cellh((40/timeStep+1):end,1)./y0(1)>=.99
& cellh((40/timeStep+1):end,1)./y0(1)<= 1.1,1))-40;
      tRecovery(2) = t((40/timeStep+1)+find(cellh((40/timeStep+1):end,2)./y0(2)>=.99
& cellh((40/timeStep+1):end,2)./y0(2)<= 1.1,1))-40;
      recoveryTime = max(tRecovery);
   end
end

% Calculate overall deviation
deviation = zeros(size(cellh,1),size(cellh,2));
for i=1:size(cellh,1)
   deviation(i,:) = abs(cellh(i,:) - y0)*timeStep;
end
sumDeviation = sum(deviation);

% Calculate robustness
if insult == 0
   R = 'No insult';
elseif insult ~= 0
   R = sumDeviation(1)*sumDeviation(2)*recoveryTime;
end

% Print results
if shouldPrint == 1
   fprintf('\n Robustness metric score follows: \n');
   R
end
end

function dxdt = odefun(t,x,k,x0)
% Set global parameters
global F y0 insult insultFrequency

% Set aliases
A2Plus = x(1); A2Minus = x(2);
A2PlusIC = y0(1); A2MinusIC = y0(2);
kprolPlus = k(1); kCapPlus = k(2); kapPlus = k(5);
kCapMinus = k(3); kprolMinus = k(4); kapMinus = k(6);
kT = k(7);
kPenv = k(8); kTenv = k(9); kA = k(10);
```

```
kRenew = k(13); C1 = k(11); C2 = k(12);

% Set insults
% Insult 1: Increased apoptosis rate (50% for 30 days)
if insult == 1
   if t >= 10 && t <= 40
      kapMinus = 1.5*k(6);
      kapPlus = 1.5*k(5);
   end
end

% Insult 2: Decreased apoptosis rate (50% for 30 days)
if insult == 2
   if t >= 10 && t <= 40
      kapMinus = 0.5*k(6);
      kapPlus = 0.5*k(5);
   end
end

% Insult 3: Increased proliferation rate (50% for 30 days)
if insult == 3
   if t >= 10 && t <= 40
      kprolMinus = 1.5*k(4);
      kprolPlus = 1.5*k(1);
   end
end

% Insult 4: Decreased proliferation rate (50% for 30 days)
if insult == 4
   if t >= 10 && t <= 40
      kprolMinus = 0.5*k(4);
      kprolPlus = 0.5*k(1);
   end
end

% Insult 5: Periodic apoptosis increase
if insult == 5
   if -sin(insultFrequency*3.14*t) > 0
      kapMinus = 1.5*k(6);
      kapPlus = 1.5*k(5);
   end
end
```

```
% Insult 6: Periodic apoptosis increase w/ same width
if insult == 6
   if -sin(insultFrequency*3.14*t) > sin(pi/4*(2-insultFrequency))
      kapMinus = 1.5*k(6);
      kapPlus = 1.5*k(5);
   end
end

% Insult 7: Periodic apoptosis increase w/ differing magnitudes
if insult == 7
   if -sin(insultFrequency*3.14*t) > 0
      kapMinus = 0.25*(0.5)*k(6)+k(6);
      kapPlus = 0.25*(0.5)*k(5)+k(5);
   end
end

% Insult 8: Periodic apoptosis decrease
if insult == 5
   if -sin(insultFrequency*3.14*t) > 0
      kapMinus = 0.5*k(6);
      kapPlus = 0.5*k(5);
   end
end

% Insult 9: Sinusoidal apoptosis rate
if insult == 9
   kapMinus = sin(insultFrequency*3.14*t)*k(6) + k(6);
   kapPlus = sin(insultFrequency*3.14*t)*k(5) + k(6);
end

% Insult 10: Unit step change in apoptosis rate
if insult == 10
   if t >= 10
      kapMinus = 0.5*k(6)+k(6);
      kapPlus = 0.5*k(5)+k(5);
   end
end

% Feedback mechanisms
% F(1) = implicit competition (Model A)
% F(2) = product inhibition of proliferation (Model B)
% F(3) = product inhibition of transitions (Model C)
% F(4) = alternate populations (i.e. stem cells) (Model D)
```

```
% Set feedback conditions
if F(1) == 0
   feedBack1a = 1; feedBack1b = 1;
elseif F(1) == 1
   feedBack1a = (1-A2Plus/kCapPlus);
   feedBack1b = (1-A2Minus/kCapMinus);
end
if F(2) == 0
   feedBack2 = 1;
elseif F(2) == 1
   feedBack2 = kPenv/(A2Plus + kA*A2Minus);
end
if F(3) == 0
   feedBack3 = 1;
elseif F(3) == 1
   feedBack3 = kTenv/A2Minus;
%    hillCoeff = 1;
%    feedBack3 = 2*kTenv^hillCoeff/(kTenv^hillCoeff+A2Minus^hillCoeff); %
Alternate feedback
end
if F(4) == 0
   feedBack4 = 0;
elseif F(4) == 1
   feedBack4 = kRenew*(1/(1+exp(C1*A2Plus+C2)));
end

% Equations
r1 = A2Plus*kprolPlus*feedBack1a*feedBack2 + feedBack4; % A2Minus growth
r2 = A2Plus*kT*feedBack3; % Transition from A2Plus to A2Minus
r3 = A2Plus*kapPlus; % A2Plus Hepatocyte apoptosis
r4 = A2Minus*kprolMinus*feedBack1b; % A2Minus growth
r5 = A2Minus*kapMinus; % A2Minus Hepatocyte apoptosis

% Differential equations
dxdt(1) = r1 - r2 - r3; % A2+ Hepatocytes
dxdt(2) = r4 + r2 - r5; % A2- Hepatocytes

dxdt = dxdt';
end
```

Appendix E

R CODE USED TO EVALUATE SINGLE HEPATIC STELLATE CELL DATA

```
##########  Import Data  ##########
setwd("C:/Users/…")

# Import data from SH1-HSC-3-2
hsc.cells <- read.delim("HSC-SingleCell-
SampleData.txt",stringsAsFactors=F,header=T)
hsc.cells.data <- hsc.cells[,9:dim(hsc.cells)[2]]
sample.info <- hsc.cells[,1:8]

##########  Perform Quality Control  ##########
# Identify high fidelity genes
high.fid.genes <-
names(which(apply(is.na(hsc.cells.data),2,sum)/dim(hsc.cells.data)[1] <= 0.55))
semi.fid.genes <-
names(which(apply(is.na(hsc.cells.data),2,sum)/dim(hsc.cells.data)[1] <= 0.80))

# Identify high fidelity samples
sample.fid.cutoff <- 0.75
hsc.cells.high.fid.samples <-
hsc.cells.data[which(apply(is.na(hsc.cells.data[,semi.fid.genes]),1,sum)/dim(hsc.cells.
data[,semi.fid.genes])[2] <= sample.fid.cutoff),]

##########  Normalize Data  ##########
# Median center each sample by high fidelity genes
hsc.cells.neg.dct <- -hsc.cells.data +
apply(hsc.cells.data[,high.fid.genes],1,median,na.rm=T)

# Median center each gene within a Chip
hsc.cells.neg.ddct <- t(t(hsc.cells.neg.dct) -
apply(hsc.cells.neg.dct,2,median,na.rm=T))

# Combine high fidelity data into a single data frame (& combine sample info)
hsc.cells.neg.ddct <-
hsc.cells.neg.ddct[as.numeric(rownames(hsc.cells.high.fid.samples)),semi.fid.genes]
rownames(hsc.cells.neg.ddct) <- 1:dim(hsc.cells.neg.ddct)[1]
```

```
sample.info <- sample.info[as.numeric(rownames(hsc.cells.high.fid.samples)),]

##########  Semi-Manually Classify States  ##########
# Activate libraries
library(cluster);library(rgl);library(plotrix)
library('MASS');library(vegan);library(pcaMethods)

# Manual state classification
cells.gf.high <-
which(apply(hsc.cells.neg.ddct[,c("HGFa.b","Vegfa","IGF1")],1,max,na.rm=T) >= -
0.01)
cells.col.high <-
which(apply(hsc.cells.neg.ddct[,c("Col3a1","Col14a1","Ecm1")],1,max,na.rm=T) >= -
0.01)

cells.act.mixed <- intersect(cells.gf.high,cells.col.high)
cells.act.pro <- cells.gf.high[!cells.gf.high %in% cells.act.mixed]
cells.act.anti <- cells.col.high[!cells.col.high %in% cells.act.mixed]
cells.other <- as.numeric(intersect(rownames(hsc.cells.neg.ddct)[!
rownames(hsc.cells.neg.ddct) %in% cells.gf.high],rownames(hsc.cells.neg.ddct)[!
rownames(hsc.cells.neg.ddct) %in% cells.col.high]))

# Cluster additional samples based on similarity to mixed activation state
r <-
cor(apply(hsc.cells.neg.ddct[cells.act.mixed,],2,median,na.rm=T),t(hsc.cells.neg.ddct[
cells.other,]),use="pairwise",method="pearson")
sigma <- 1/sqrt(length(r)-3)
r.z <- .5*log((1+r)/(1-r))
cells.act.mixed.corr <- which(pnorm(r.z,mean=0,sd=sigma) >= 0.975)

# Cluster additional samples based on similarity to pro-regen activation state
r <-
cor(apply(hsc.cells.neg.ddct[cells.act.pro,],2,median,na.rm=T),t(hsc.cells.neg.ddct[cell
s.other,]),use="pairwise",method="pearson")
sigma <- 1/sqrt(length(r)-3)
r.z <- .5*log((1+r)/(1-r))
cells.act.pro.corr <- which(pnorm(r.z,mean=0,sd=sigma) >= 0.975)

# Cluster additional samples based on similarity to anti-regen activation state
r <-
cor(apply(hsc.cells.neg.ddct[cells.act.anti,],2,median,na.rm=T),t(hsc.cells.neg.ddct[cel
ls.other,]),use="pairwise",method="pearson")
```

```
sigma <- 1/sqrt(length(r)-3)
r.z <- .5*log((1+r)/(1-r))
cells.act.anti.corr <- which(pnorm(r.z,mean=0,sd=sigma) >= 0.975)

# Generate clusters [1=quiescent,2=pro,3=anti,4=mixed]
cluster.vector <- matrix(0,dim(hsc.cells.neg.ddct)[1],1)
cluster.vector[sort(c(cells.act.pro,cells.other[cells.act.pro.corr])),1]<- 2
cluster.vector[sort(c(cells.act.anti,cells.other[cells.act.anti.corr])),1]<- 3
cluster.vector[sort(c(cells.act.mixed,cells.other[cells.act.mixed.corr])),1]<- 4
cluster.vector[cells.other[!c(1:length(cells.other)) %in%
c(cells.act.anti.corr,cells.act.pro.corr,cells.act.mixed.corr)]] <- 1

# Identify numbers of samples in each cluster
cluster.table <- matrix(0,4,4)
rownames(cluster.table) <- c("Quiescent","Pro-R","Anti-R","Mixed")
colnames(cluster.table) <- c("Control 0h","Control 24h","Ethanol 0h","Ethanol 24h")
cluster.table[c(2,3,4),1] <-
summary(as.factor(cluster.vector[intersect(which(sample.info[,'Treatment'] ==
'Control'),which(sample.info[,'Time'] == '0h'))]))
cluster.table[,2] <-
summary(as.factor(cluster.vector[intersect(which(sample.info[,'Treatment'] ==
'Control'),which(sample.info[,'Time'] == '24h'))]))
cluster.table[c(2,3,4),3] <-
summary(as.factor(cluster.vector[intersect(which(sample.info[,'Treatment'] ==
'Ethanol'),which(sample.info[,'Time'] == '0h'))]))
cluster.table[,4] <-
summary(as.factor(cluster.vector[intersect(which(sample.info[,'Treatment'] ==
'Ethanol'),which(sample.info[,'Time'] == '24h'))]))

#write.table(cbind(sample.info,cluster.vector,hsc.cells.neg.ddct), file="SH1-HSC-3-
singleCell-data-manualSorted.txt", row.names=F, sep="\t")

# Impute missing data using (min - 1) for each gene
hsc.cells.neg.ddct.min <- hsc.cells.neg.ddct
gene.mins <- apply(hsc.cells.neg.ddct.min,2,min,na.rm=T) - 1
for (i in 1:dim(hsc.cells.neg.ddct.min)[1]){
  hsc.cells.neg.ddct.min[i,is.na(hsc.cells.neg.ddct.min[i,])] <-
gene.mins[is.na(hsc.cells.neg.ddct.min[i,])]
}

# Plot Cells as Growth Factors vs. Fibrous collagens (with mins)
```

```
x11();plot(apply(hsc.cells.neg.ddct.min[,c("HGFa.b","Vegfa","IGF1")],1,max,na.rm=
T),apply(hsc.cells.neg.ddct.min[,c("Col3a1","Col14a1","Ecm1")],1,max,na.rm=T),pch
=19,cex=1.5,col='black',xlab="",ylab="")
lines(c(-.01,-.01),c(-30,30),col='black');lines(c(-30,30),c(-.01,-.01),col='black')

# LDA to identify cluster distributions
fit <- lda(x=as.matrix(hsc.cells.neg.ddct.min),grouping=cluster.vector,CV=F)

# Plot LDA results
color.scale <-
c('blue','darkolivegreen','red','orange','lightskyblue','gray','black','magenta','brown')
x11();plot(hsc.cells.neg.ddct.min %*% fit$scaling, pch=19,
col=color.scale[cluster.vector],cex=1.5) # Plot results on LD1 and LD2
points(fit$means %*%
fit$scaling,type='p',pch=10,col=color.scale[as.numeric(levels(as.factor(cluster.vector))
)],cex=2.5,lwd=2)
spheres3d(hsc.cells.neg.ddct.min %*% fit$scaling, type='s',pch=19,
col=color.scale[cluster.vector],radius=0.15) # Plot results on LD1, LD2, and LD3
axes3d()

# Plot Linear Discriminants
x11();plot(fit$scaling,type="p",pch=19,cex=1.5)
text(fit$scaling[,1:2],rownames(fit$scaling),pos=4,offset=0.5)


# Represent clusters as a minimum spanning tree
pc.hsc.all.clusters.span <- spantree(daisy(hsc.cells.neg.ddct.min %*%
fit$scaling,metric = 'euclidean'),toolong=0)
x11();plot(pc.hsc.all.clusters.span,type='p',pch=19,col=color.scale[as.numeric(as.facto
r(cluster.vector))],cex=1.5,lwd=2)

# Find BIC score & Sihouette score for random data cluster
set.seed(10)
silhouette.score.randomized <- matrix(0,1,1000)
for (k in 1:1000){
  #     Reshuffle data and rerun PCA for shuffled data
  data.randomized <- 0*hsc.cells.neg.ddct.min
  for (j in 1:dim(hsc.cells.neg.ddct.min)[1]){
    data.randomized[j,] <-
hsc.cells.neg.ddct.min[j,order(floor(runif(dim(hsc.cells.neg.ddct.min)[2])*10))]
  }
  for (j in 1:dim(hsc.cells.neg.ddct.min)[2]){
```

```
   data.randomized[,j] <-
data.randomized[order(floor(runif(dim(hsc.cells.neg.ddct.min)[1])*10)),j]
  }
  fit.rand <- lda(x=as.matrix(data.randomized),grouping=cluster.vector,CV=F)
  silhouette.score.randomized[1,k] <-
mean(silhouette(cluster.vector,daisy(data.randomized %*% fit.rand$scaling,metric =
'euclidean'),full=T)[,'sil_width'])
}

silhouette.score <- mean(silhouette(cluster.vector,daisy(hsc.cells.neg.ddct.min %*%
fit$scaling,metric = 'euclidean'),full=T)[,'sil_width'])

x11();plot(density(silhouette.score.randomized),type='l',col='black',lwd=1.5,xlim=c(0,
0.7),ylim=c(.7,20))
lines(c(silhouette.score,silhouette.score),c(0,5),col='black',lwd=1.5)
points(silhouette.score,5,pch=19,col='black',cex=1.5)

##########  Classify Effect of Ethanol on Transcriptional State-Space  ##########
# Mesh energy wells for last figure
library(plot3D)
control.0h.cells <- intersect(which(sample.info[,'Treatment'] ==
'Control'),which(sample.info[,'Time'] == '0h'))
control.24h.cells <- intersect(which(sample.info[,'Treatment'] ==
'Control'),which(sample.info[,'Time'] == '24h'))
ethanol.0h.cells <- intersect(which(sample.info[,'Treatment'] ==
'Ethanol'),which(sample.info[,'Time'] == '0h'))
ethanol.24h.cells <- intersect(which(sample.info[,'Treatment'] ==
'Ethanol'),which(sample.info[,'Time'] == '24h'))

# Plot Contours and cells from each state
color.scale <-
c('blue','darkolivegreen','red','orange','lightskyblue','gray','black','magenta','brown')
all.density <- kde2d((hsc.cells.neg.ddct.min %*%
fit$scaling)[,1],(hsc.cells.neg.ddct.min %*% fit$scaling)[,2])
x11();contour(all.density$x,all.density$y,all.density$z,drawlabels=F,col='gray')
points(hsc.cells.neg.ddct.min[control.0h.cells,] %*% fit$scaling, pch=19,
col=color.scale[cluster.vector[control.0h.cells]],cex=2.5)
points(hsc.cells.neg.ddct.min[ethanol.0h.cells,] %*% fit$scaling, pch=19,
col=color.scale[cluster.vector[ethanol.0h.cells]],cex=2.5)
points(hsc.cells.neg.ddct.min[control.24h.cells,] %*% fit$scaling, pch=19,
col=color.scale[cluster.vector[control.24h.cells]],cex=2.5)
points(hsc.cells.neg.ddct.min[ethanol.24h.cells,] %*% fit$scaling, pch=19,
col=color.scale[cluster.vector[ethanol.24h.cells]],cex=2.5)
```

```
##########  Plot activation state densities in radians  ##########
cells.ld <- hsc.cells.neg.ddct.min %*% fit$scaling
cells.ld.1.cent <- cells.ld[,1] - apply(cells.ld,2,mean)[1]
cells.ld.2.cent <- cells.ld[,2] - apply(cells.ld,2,mean)[2]

quad.1 <- intersect(which(cells.ld.1.cent >= 0),which(cells.ld.2.cent >= 0))
cells.angle.1 <- atan(abs(cells.ld.1.cent[quad.1]/cells.ld.2.cent[quad.1]))
quad.2 <- intersect(which(cells.ld.1.cent >= 0),which(cells.ld.2.cent <= 0))
cells.angle.2 <- pi/2+atan(abs(cells.ld.1.cent[quad.2]/cells.ld.2.cent[quad.2]))
quad.3 <- intersect(which(cells.ld.1.cent <= 0),which(cells.ld.2.cent <= 0))
cells.angle.3 <- pi+atan(abs(cells.ld.1.cent[quad.3]/cells.ld.2.cent[quad.3]))
quad.4 <- intersect(which(cells.ld.1.cent <= 0),which(cells.ld.2.cent >= 0))
cells.angle.4 <- 3*pi/2+atan(abs(cells.ld.1.cent[quad.4]/cells.ld.2.cent[quad.4]))

cells.angle <-
c(cells.angle.1,cells.angle.2,cells.angle.3,cells.angle.4)[order(c(quad.1,quad.2,quad.3,q
uad.4))]

x11();plot(density(cells.angle[cluster.vector ==
1])$x,density(cells.angle[cluster.vector ==
1])$y,col='blue',lwd=3,type='l',ylim=c(0,5),xlim=c(-0.5,6.5),cex.axis=2)
lines(density(cells.angle[cluster.vector == 2])$x,density(cells.angle[cluster.vector ==
2])$y,col='forestgreen',lwd=3)
lines(density(cells.angle[cluster.vector == 3])$x,density(cells.angle[cluster.vector ==
3])$y,col='red',lwd=3)
lines(density(cells.angle[cluster.vector == 4])$x,density(cells.angle[cluster.vector ==
4])$y,col='orange',lwd=3)


##########  Cluster genes and samples (within a state)  using min-1 ##########
# Calculate correlation / distance to find functional gene modules
gene.cor.min <-
cor(hsc.cells.neg.ddct.min,use='pairwise.complete.obs',method='pearson')
gene.cor.min.dist <- as.dist((1-gene.cor.min))
x11();plot(hclust(gene.cor.min.dist),main="Dist = (1 - Correlation)", xlab="")

# Calculate correlation / distance within each cell state
# Cluster IDs [1=quiescent,2=pro,3=anti,4=mixed]
clust.1.cor.min <- cor(t(hsc.cells.neg.ddct.min[which(cluster.vector ==
1),]),use='pairwise.complete.obs',method='pearson')
clust.1.cor.min.dist <- as.dist(1-clust.1.cor.min)
```

```
clust.2.cor.min <- cor(t(hsc.cells.neg.ddct.min[which(cluster.vector ==
2),]),use='pairwise.complete.obs',method='pearson')
clust.2.cor.min.dist <- as.dist(1-clust.2.cor.min)

clust.3.cor.min <- cor(t(hsc.cells.neg.ddct.min[which(cluster.vector ==
3),]),use='pairwise.complete.obs',method='pearson')
clust.3.cor.min.dist <- as.dist(1-clust.3.cor.min)

clust.4.cor.min <- cor(t(hsc.cells.neg.ddct.min[which(cluster.vector ==
4),]),use='pairwise.complete.obs',method='pearson')
clust.4.cor.min.dist <- as.dist(1-clust.4.cor.min)

# Create order vector for samples
sample.order.min <- NULL
sample.order.min <- cbind(which(cluster.vector ==
1),hclust(clust.1.cor.min.dist)$order+100)
sample.order.min <- rbind(sample.order.min,cbind(which(cluster.vector ==
2),hclust(clust.2.cor.min.dist)$order+200))
sample.order.min <- rbind(sample.order.min,cbind(which(cluster.vector ==
3),hclust(clust.3.cor.min.dist)$order+300))
sample.order.min <- rbind(sample.order.min,cbind(which(cluster.vector ==
4),hclust(clust.4.cor.min.dist)$order+400))

sample.sort.min <- sample.order.min[order(sample.order.min[,1]),2]

# Save results and ordering
results.ordered.min <-
cbind(sample.info,cluster.vector,sample.sort.min,hsc.cells.neg.ddct[,hclust(gene.cor.m
in.dist)$order])

# Identify modules of coexpressed genes from the dendogram & Plot
groups <- cutree(hclust(gene.cor.min.dist), k=6) # cut tree into 6 clusters
x11();plot(hclust(gene.cor.min.dist),main="Dist = (1 - Correlation)", xlab="")
rect.hclust(hclust(gene.cor.min.dist), k=6, border="blue") # draw blue borders around
clusters on dendrogram
```

Appendix F

SAMPLE (TOY) SINGLE CELL DATA

The real data used in this thesis will be published with the manuscript corresponding to Chapter 8. Until then, the following data can be used to test the script in Appendix E.

Table F.1 Sample single cell data for use with the script in Appendix E (Genes 1-6)

Treatment	Time	Col14a1	Col3a1	Ecm1	HGFa.b	IGF1	Vegfa
Ethanol	24h	NA	19	15	12	18	27
Ethanol	24h	24	29	9	NA	NA	23
Ethanol	24h	17	NA	NA	NA	10	NA
Ethanol	24h	10	27	24	24	NA	NA
Ethanol	24h	24	16	10	19	20	22
Ethanol	24h	24	18	21	23	14	NA
Control	0h	28	18	NA	29	NA	12
Control	0h	27	27	12	12	11	18
Control	24h	25	23	11	24	13	NA
Control	24h	26	13	26	29	19	NA
Control	24h	18	25	NA	11	14	NA
Control	24h	9	NA	21	NA	12	12
Control	24h	17	17	17	14	26	14
Control	24h	11	19	NA	19	19	13
Control	24h	13	NA	29	NA	12	28
Control	24h	15	NA	17	10	NA	NA
Ethanol	0h	26	19	13	25	18	14
Ethanol	24h	29	19	15	20	14	19
Ethanol	24h	NA	NA	NA	NA	22	29
Ethanol	24h	19	28	27	14	25	27
Control	0h	20	13	28	13	NA	NA
Control	24h	13	NA	10	29	22	28

Control	24h	29	18	10	28	20	NA
Ethanol	0h	NA	27	20	NA	10	14
Ethanol	0h	26	28	27	18	28	NA
Ethanol	24h	26	20	18	26	16	NA
Control	0h	20	18	17	28	NA	24
Control	0h	20	26	29	24	23	NA
Control	0h	20	NA	19	20	28	NA
Control	0h	13	9	23	12	17	NA
Ethanol	0h	NA	13	22	24	16	27
Ethanol	0h	NA	17	24	24	27	22
Ethanol	24h	19	25	23	27	NA	27
Ethanol	24h	27	26	NA	10	11	13
Ethanol	24h	22	9	NA	19	18	16
Ethanol	24h	13	NA	NA	9	20	NA
Ethanol	24h	NA	NA	11	11	NA	16
Control	0h	16	NA	23	12	15	9
Control	0h	21	19	18	25	NA	NA
Control	0h	10	18	29	29	10	10
Control	0h	NA	10	29	NA	19	NA
Control	0h	20	21	NA	12	24	25
Control	24h	11	29	NA	23	10	25
Control	24h	17	14	22	NA	NA	10
Control	0h	NA	NA	NA	NA	NA	17
Control	0h	NA	21	13	NA	15	22
Control	0h	NA	NA	22	NA	24	28
Ethanol	24h	17	27	20	NA	NA	29
Ethanol	24h	9	22	19	24	NA	15
Ethanol	24h	28	25	17	10	10	18
Control	24h	22	10	NA	NA	NA	NA
Ethanol	0h	NA	15	18	NA	25	18
Ethanol	0h	25	11	26	26	18	NA
Ethanol	0h	22	18	29	17	29	NA
Ethanol	0h	18	17	NA	10	19	28
Ethanol	0h	NA	15	16	13	NA	14
Ethanol	24h	NA	10	NA	16	24	26
Ethanol	24h	NA	11	NA	11	14	26
Ethanol	24h	24	NA	13	18	21	NA
Ethanol	24h	12	24	23	29	NA	NA
Control	0h	9	18	NA	15	11	17

Control	0h	9	26	19	29	NA	17
Control	0h	24	19	24	NA	27	NA
Control	0h	18	29	10	28	16	NA
Control	0h	29	NA	NA	NA	17	24
Control	0h	NA	14	18	NA	NA	NA
Control	0h	22	28	27	9	25	NA
Control	0h	NA	23	12	26	23	26
Control	0h	28	NA	12	12	16	15
Control	24h	NA	29	18	17	NA	NA
Control	24h	12	29	21	NA	29	27
Control	24h	17	10	14	21	22	21
Control	24h	23	16	NA	10	14	23
Control	24h	18	NA	NA	12	10	19
Control	24h	19	16	14	15	27	24
Control	24h	23	21	19	NA	21	NA
Ethanol	0h	21	10	26	23	11	9
Ethanol	0h	NA	15	22	28	NA	NA
Ethanol	0h	9	28	NA	NA	28	19
Ethanol	0h	29	NA	19	13	9	9

Table F.2 Sample single cell data for use with the script in Appendix E (Genes 7-12)

Treatment	Time	Actb	Tgfb1	Spp1	Rdh10	IL6	IL10
Ethanol	24h	18	21	NA	25	14	25
Ethanol	24h	NA	25	27	NA	28	22
Ethanol	24h	13	NA	11	23	27	10
Ethanol	24h	23	24	17	21	21	29
Ethanol	24h	20	NA	18	23	15	14
Ethanol	24h	20	NA	9	17	29	NA
Control	0h	24	28	24	16	29	20
Control	0h	NA	18	10	25	NA	21
Control	24h	20	24	25	NA	19	11
Control	24h	28	17	13	20	15	9
Control	24h	10	NA	12	NA	9	13
Control	24h	9	NA	13	24	NA	NA
Control	24h	11	13	NA	25	28	14
Control	24h	NA	12	13	24	NA	17
Control	24h	NA	NA	27	27	NA	NA
Control	24h	10	NA	27	NA	22	10
Ethanol	0h	17	16	18	26	17	17
Ethanol	24h	NA	28	NA	NA	11	14
Ethanol	24h	12	9	19	NA	NA	NA
Ethanol	24h	27	15	23	19	24	12
Control	0h	29	23	20	27	14	23
Control	24h	13	13	24	29	11	16
Control	24h	17	10	23	18	NA	9
Ethanol	0h	12	29	13	27	13	9
Ethanol	0h	NA	14	26	17	18	14
Ethanol	24h	NA	17	16	NA	26	NA
Control	0h	15	21	20	NA	NA	19
Control	0h	22	28	NA	11	10	16
Control	0h	NA	18	29	NA	NA	24
Control	0h	27	NA	21	28	23	NA
Ethanol	0h	16	18	NA	22	NA	19
Ethanol	0h	26	9	21	NA	10	22
Ethanol	24h	9	20	26	23	23	18
Ethanol	24h	21	9	20	NA	22	NA
Ethanol	24h	28	NA	27	NA	28	NA
Ethanol	24h	NA	24	15	NA	29	27
Ethanol	24h	NA	18	13	12	NA	9

Control	0h	NA	27	12	10	10	18
Control	0h	22	9	9	24	26	NA
Control	0h	NA	18	NA	18	24	NA
Control	0h	29	NA	25	9	16	9
Control	0h	19	NA	NA	NA	27	12
Control	24h	21	19	20	16	10	NA
Control	24h	19	29	21	20	24	28
Control	0h	19	16	27	14	15	NA
Control	0h	NA	18	22	NA	17	16
Control	0h	29	29	12	20	11	11
Ethanol	24h	17	14	12	21	NA	18
Ethanol	24h	NA	23	10	10	27	25
Ethanol	24h	10	25	NA	23	19	22
Control	24h	24	23	NA	15	18	10
Ethanol	0h	26	22	20	NA	20	12
Ethanol	0h	20	NA	21	19	15	13
Ethanol	0h	20	17	11	29	10	NA
Ethanol	0h	NA	NA	13	24	22	19
Ethanol	0h	18	22	NA	20	20	26
Ethanol	24h	17	22	11	NA	23	17
Ethanol	24h	20	23	NA	NA	26	NA
Ethanol	24h	12	20	NA	18	15	NA
Ethanol	24h	NA	15	10	21	NA	20
Control	0h	10	18	27	20	13	NA
Control	0h	NA	25	19	18	15	NA
Control	0h	NA	11	29	16	29	NA
Control	0h	NA	23	15	13	13	9
Control	0h	NA	NA	18	21	16	NA
Control	0h	29	17	28	NA	14	NA
Control	0h	NA	10	16	NA	17	28
Control	0h	15	27	NA	NA	NA	21
Control	0h	NA	18	25	17	21	21
Control	24h	10	NA	NA	NA	15	14
Control	24h	12	9	NA	18	11	9
Control	24h	19	26	12	12	23	29
Control	24h	NA	16	16	18	NA	25
Control	24h	NA	NA	16	10	NA	26
Control	24h	15	9	NA	11	25	17
Control	24h	16	29	NA	19	13	24

Ethanol	0h	29	NA	21	12	NA	24
Ethanol	0h	29	15	14	18	13	25
Ethanol	0h	29	22	NA	27	13	29
Ethanol	0h	20	NA	11	25	23	24

Appendix G

VERTEBRATE ANIMAL PLAN (F31) AND IACUC PROTOCOL

All signed copies of the documents contained in this appendix are on file with the appropriate institutions.

G.1 Vertebrate Animal Plan (F31)

Summary of Procedure

Two-thirds partial hepatectomy (PHx) will be performed following the standard protocol of Higgins and Anderson (1931), Arch. Pathol. 12, 186-202, with modifications to comply with current IACUC guidelines. The rats will be brought under anesthesia with 5% isoflurane using a dedicated anesthesia chamber. Animals will be transferred to surgical table with continued anesthesia using a nose cone containing 2.5% isoflurane. Complete anesthesia will be assessed by lack of response to tail and toe pinch. The abdomens, from above the sternum to 1 cm below the surgical incision will be shaved using Andis AGC clippers, and removed fur discarded. The shaved and cleaned area will then be sterilized using betadine-soaked 3x3 gauze pads, with repeated applications, followed by a 70% ethanol wash. All laboratory personnel conducting or assisting in surgical procedures will wear designated animal lab coats and surgical gloves. A small incision will be made with a feather #10 sterile scalpel through the skin and muscle layer beginning at the sternum. This incision will then be opened with sterilized scissors. The left-lateral and medial lobes will be exposed and tied off at the base of each lobe using sterile SP117 non-absorbable black braided silk surgical thread. The lobes will then be resected with a scalpel and snap frozen by submersion in liquid nitrogen for assay of baseline levels of protein and mRNA levels. Following PHx, the muscle layer will be sutured using sofsilk 8-0 non-absorbable coated, braided silk and the skin will be surgically stapled using micron autoclip 9mm wound clips. Following surgery, but while under anaesthesia, animals will receive 1 ml intraperitoneal (IP) injections of lactated ringers solution (LRS) that has been prewarmed to 37°C to ensure hydration following surgery. The anesthesia will be removed at the end of the surgical procedure and the animal returned to its cage. After the animal recovers and starts moving, it will be monitored closely for signs of distress for the first hour (and for 10 minutes hourly thereafter) while it is kept in its cage with access to food and water ad libitum until time of sacrifice. Cages will be kept warm with heating lamps for the first 3 hours

following surgery. At time of sacrifice, the animal will again be anesthetized, the original incision will be reopened and the remnant liver will be removed and frozen. The animal will then be euthanized by cervical dislocation and opening of the chest cavity.

Performance Site:

All work related to experimental treatment, animal handling, single-cell and tissue sample collection will be performed at Thomas Jefferson University (TJU).

Proposed Use of Animals:

This study will use 64 8-14 week old, male rats of the Sprague Dawley strain of Rattus Norvegicus.

Justification of Animal Use, Species, and Number:

The molecular signaling systems under study herein are relatively conserved across mammalian species; therefore it is possible to extrapolate from animal models to human liver. It is not possible to study the gene expression of liver regeneration in lower animals, and, as the system under study involves a dynamic, systemic response to several factors (chronic alcohol consumption and partial hepatectomy), it is not possible to replicate *in vitro*. Because the procedures are invasive, terminal, and destructive (tissue is destroyed in processing), it is not possible to use human tissue on the large scale required herein. Further, due to the need for dynamic data following the partial hepatectomy, human postmortem tissue is also not a viable source. Finally a large body of existing rat-based data is available in scientific literature to serve as reference for the proposed studies.

The Sprague Dawley strain of Rattus Norvegicus is the preferred model system for several reasons. First, the regenerative response of these animals is highly reproducible. Second, the animals are robust in recovery from survival surgery allowing for increased chances of survival. Third, the TJU alcohol center and animal facility have strong expertise in rat models and the Lieber-DeCarli model specifically allowing for high quality animal care and handling. Finally, the large size of rat livers simplifies the procedures and provides ample amounts of tissue because the samples are neither too large to be analyzed as a single unit nor too small to be useful.

Animal requirements are greatly reduced by the use of PCR amplification technology. The number of animals actually used will be the minimum required to generate statistically valid data. Previous work in our lab was able to detect statistically significant changes to gene expression and protein levels in a slightly impaired regeneration phenotype using three animals per time point. Any fewer than three biological replicates provides only limited information about the variability of the data. We propose to use four rats at each time point for several reasons. First, the use of an additional animal provides a built-in backup in case of animal death, errors in tissue processing, or other experimental errors. Second, the use of four rats per time point will allow us to detect a 20-30% change in molecular levels using a standard

two-tailed t-test of log-transformed data, assuming a high standard deviation of 10% between animals, power of 0.95, and alpha of 0.05 (Power analysis performed using G*power: http://www.psycho.uni-duesseldorf.de/abteilungen/aap/gpower3). This is well below what many consider of threshold of biological significance (50% change) and below expected changes based on published literature and previous work in our lab (Correnti, Cook, et al., *In Preparation,* 2014,). The estimate of 64 total animals includes testing multiple biological assays (protein and gene expression at the tissue and single-cell level) at 8 time points early post-PHx in 2 conditions (see table below).

Time post-PHx	**1h**	**2h**	**3h**	**4h**	**5h**	**6h**	**9h**	**12h**	**Total**
Control Rats	4	4	4	4	4	4	4	4	32
Alcohol-Fed Rats	4	4	4	4	4	4	4	4	32

Veterinary Care of Animals Involved

The animals will be maintained in an AAALAC approved facility under direction of a licensed veterinarian and skilled staff. Animals in the study will be fed ad libitum (alcohol or control diet). The long-established Leiber-deCarli alcohol pair-feeding protocol will be used to match alcohol and control fed animals, with alcohol-fed animals receiving 36% of total calories from alcohol for a period of 5 weeks. All animals will be housed in standard shoebox cages in a dedicated temperature- and humidity-controlled room on a 12/12 day/night cycle. Animals will be bred within this facility or imported from a local outside supplier.

Description of Procedures Limiting Discomfort, Distress, Pain, and Injury

Following PHx, animals will be allowed to recover from anesthesia and surgery without access to analgesics. Analgesics are generally metabolized in the liver and affect cell signaling processes and cellular redox state in a manner that interferes with the processes under study. In addition, research from our group and others has shown that treatment with different classes of analgesics alters the normal course of regeneration. Treatment with Acetaminophen following PHx leads to increases in liver weight compared to controls and increased liver microsomal enzymes (White & Gershbein, Research Communications in Chemical Pathology and Pharmacology, 1985; 48(2):275-289). Corticosteroid treatment was shown to suppress DNA synthesis in rats following PHx (Tsukamoto & Kojo, Gut, 1989; 30:387-390). Opiate treatment has been shown to be hepatotoxic (Zhang et al., Basic and Clinical Pharmacology and Toxicology, 2004, 95:53-58), and buprenorphine in particular has been shown to interfere in hepatocyte mitochondrial function (Berson et al., Journal of Hepatology, 2001; 34:261-269). Our lab has also tested the topical analgesic EMLA cream in the context of partial hepatectomy, and found that 30 min following surgery, there was significant elevation in phospho-p38 and phospho-Jun kinase in animals

receiving treatment, indicating activation of stress signaling pathways that are critical for the onset of regeneration following PHx. In addition, animals showed behavioral signs of increased irritation and stress after treatment with EMLA cream.

Animals will be closely monitored visually during the first hour post-PHx for normal locomotive activity, guarding, abnormal behavior or appearance including normal consumption of food and water, urination, piloerection, unkempt coat/rough hair, hunched posture, aggression, and self-mutilation. The surgical wound will be monitored for evidence of dehiscence and to ensure that none of the wound clips have been removed. The animals will then be monitored for 10 minutes every hour thereafter prior to sacrifice. Animal food consumption will be monitored as well as signs of dehydration. Any animals that display inability to eat and drink as listed above will be given nutragel (Bioserv, Frenchtown, NJ) and lactated ringers solution (LRS) at a rate of 100ml/kg/day.

Any animal that exhibits any of the following – dehiscence, bleeding from the surgical wound or is moribund, not moving, weight loss > 20%, not eating, significant lethargy, hunched posture (evidence of dehydration) not responsive to fluid administration will be euthanized by pentobarbital injection. Pentobarbital injection was chosen to minimize pain and time to euthanasia and is consistent with the recommendations of the AVMA Guidelines for Euthanasia of Animals.

G.2 IACUC Protocol

ANIMAL USE PROTOCOL

Institutional Animal Care and Use Committee of Thomas Jefferson University

Martin Building, 203 South 11th St. Rm. 317A Website: http://www.jefferson.edu/oar/iacuc.cfm
Office: 215-503-4745 Email: IACUC@jefferson.edu Revised: 1/07

FOR OFFICE USE ONLY	
IACUC #	Approval Date:

Blue text indicates a hyperlink (with the exception of Emergency Contact(s) which is in red text) and also a pop-up screen tip.

Background

(General instructions about the form)

Protocol Title: (Expands to fit text)	Alcohol and the control of liver regeneration/preparation of isolated cells or subcellular fractions from liver				
Principal Investigator:	Joannes (Jan) B. Hoek, PhD.				
Department:	Pathology, Anatomy and Cell Biology				
Address:	Building: Jefferson Alumni Hall	Room: 222	Phone: 3-5106		
E-mail Address:	Jan.hoek@jefferson.edu				
Pre-reviewer:	Micheal Oshinsky				

Emergency Contact(s) (Not required to be PI; contact has authority to make all decisions concerning the animals. (Add rows as needed)

Name	Phone Numbers: TJU	Phone Numbers: Off Campus
Jan Hoek	3-5106	267-670-1229
Jason Correnti	3-5022	
Anil Antony	3-5022	

Protocol Type: [ ] New [ ] Revision* [x] 3Yr. Renewal*; *Protocol Number: 208C

Category: [x] Research [ ] Teaching/Training

Species: (1 species per form) Rat Age: 8-14 weeks Gender: M

Strain(s): (Expands to fit text) *Sprague Dawley, Tp53(-/-)*

Checklist: This protocol involves; (Check all that apply)

[x]	Survival Surgery	[x]	Hazards (Section 11)	Animal Transport	
[x]	Non-survival Surgery	[ ]	Neuromuscular Blocking Agents	(Does not pertain to required distribution of animals for NIH "sharing" guidelines.)	
[x]	Pain/Distress without analgesia	[ ]	Complete Freund's Adjuvant		
[x]	Anesthesia	[ ]	Mouse Ascites Production	[x]	Between/Within TJU Building
[ ]	Analgesia	[x]	Non-pharmaceutical compounds	[ ]	Off TJU, No Return
[ ]	Conditionally Accepted Euthanasia	[ ]		[ ]	Off TJU, Return to TJU

Number of Animals Involved in Protocol: (Must match total in Section 5)

Year 1	Year 2	Year 3	Total
484	484	484	1452

Funding Information (if applicable)

Funding Agency/Source: NIH/NIAAA (ongoing support)
Submission Date: Start Date: IACUC Approval Deadline:

1. Support Personnel (Add rows as needed; Boxes expand to fit text)

Name	Position	RO-4B	
		Attached	On File
Egle Juskeviciute	Postdoctoral Fellow		X
Jason Correnti	Graduate student		X
Sara Crumm	Postdoctoral fellow		X
Anil Antony	Graduate Student		X
Lauren Rouleau	MD/PhD student		X
Aditi Swarup	Research assistant		X

Comments: Sara Crumm is currently a part-time postdoctoral fellow who works at TJU for three months during the summer. She has been a PhD student and a full-time postdoctoral fellow in Dr. Hoek's Laboratory for the past 11 years and has been involved in all the animal protocols described here during those years.

NOTE: As of January 1, 2007 all TJU personnel, including the PI, listed on an Animal Use Protocol must complete the web-based training **before** this form can be submitted. Training Policy Link

2. Animal Supplier(s) (Check all boxes that apply and provide appropriate information)

[x] **Approved Vendor** — List vendor(s) – Consult with OAR for list of approved vendors.

Harlan, Charles River

[x] **TJU Source** — Indicate Protocol Number and PI, if PI on Protocol is other than you.

Protocol # 208I **PI** Dr. Jan B. Hoek

TJU Core Facility

[X] **Other** — List source and justify why a non-approved vendor or source must be used. (See Animal Importation Form) (Box expands to fit text)

Sigma-Aldrich, INC. The Tp53 knockoput transgenic rats have been generated using proprietary technology developed by Sigma. These animals are not available from any approved vendors.

Purpose and Procedures

3. Lay Explanation of Study Objectives and Impact:

Using easily understandable **LAY TERMS**, briefly describe the objectives of the study and the relevance to advancing scientific knowledge and/or the benefits to human and/or animal health. (Box expands to fit text)

The purpose of these studies is to understand the processes involved in liver repair after injury and in the regeneration of damaged tissues, and how alcohol consumption affects these repair/regeneration processes to promote liver disease. Studies have shown that alcohol consumption alters the energy balance in the liver, and this may have important implications for liver repair as alcohol also inhibits normal liver regeneration. In these proposed studies, we will be examining rats that are treated to interfere with factors that regulate the maintenance of energy levels and how these treatments impact on repair/regeneration processes. Specifically, we will: a) analyze the response to acute liver injury and liver energy status in normal and ethanol-treated rats, b) study the cellular signaling processes that mediate the response of liver cells to injury and c) study the functional changes in cellular components that mediate energy production, ie mitochondria. The results potentially provide important insight into how alcohol-induced damage to energy homeostasis limits the liver's intrinsic repair capacity.

4. Procedures and Experiments: (additional tip)

Provide a purpose and describe all procedures to be used. (*Box expands to fit text*)

A. Purpose:

The purpose of these studies is to understand the cellular signaling processes and energetics that drive liver cell function and liver regeneration after 70%partial hepatectomy (PHx). These studies will focus on two main areas. The first area stems from work done in our laboratory that has identified substantial changes in adenine nucleotides immediately following PHx, indicative of hepatocyte energy stress and a potent activating stimulus for AMP-activated protein kinase (AMPK). AMPK is a heterotrimeric kinase that senses cellular energy status and initiates energy production under conditions of increased demand. Rats express 2 isoforms of the catalytic α subunit, α1 and α2. AMPK has been shown to be dysregulated under conditions of chronic alcohol consumption, highlighting the importance of understanding its normal biological function. Following PHx, we have observed two peaks of AMPK activation in rats. The first one coincides with the loss of adenine nucleotides from the liver, peaking at 5 minutes after PHx and then gradually declining over the first hour following surgery. In addition to the observed early activation, our laboratory also has evidence that there is a broad peak of AMPK activation beginning at about 8 h following PHx and continuing from 18-24 h. This time is critical in the regeneration process as the increase preceeds hepatocyte entry into S phase, and we have evidence that this activation helps drive the expression of certain cell cycle proteins. In addition, this late AMPK activation peak coincides with increased serum levels of adiponectin, which has been shown to activate AMPK through hepatic adiponectin receptors, and we hypothesize that this serum increase plays a causative role in late-phase activation of AMPK. The experiments proposed in this protocol have been designed to directly address the role of AMPK and its potential activation by adiponectin signaling on both liver energy status and hepatocyte proliferation during the regeneration process. To do this, we will perform PHx on control and ethanol-fed rats and compare the role of AMPKα1, AMPKα2, adiponectin, and adiponectin receptor (adipoR), and compare how pharmacological agents that affect the activity of these proteins alter signaling, cell energetics and markers of proliferation during regeneration. In addition we will monitor the time course of gene expression and microRNA changes that reflect the functional response of tissue to PHx.

As a function of its response to increased energy demands, AMPK activation, in conjunction with the genes PGC-1α and Sirt1, has also been shown to control mitochondrial replication, and studies in the second area of research will address how deficiencies in these key proteins affect the course of mitochondrial biogenesis during regeneration following partial hepatectomy. Understanding this is critical for understanding hepatic energetics as hepatectomy imposes not only greater demand per unit mass, but also imposes the synthetic demands of cell replication on remaining hepatocytes. In addition, mt dysfunction is a hallmark of chronic alcohol exposure. These experiments will be performed as described in the next section, and in addition to assessing these parameters in control and ethanol-fed rats described above, it will include studies on rats treated with pharmaceutical agents that imapir the early loss of ATP/NAD+ and its signalling pathway and/or that affect the activity of PPARα, PPARγ and Sirt1 proteins, all of which have been shown to be involved in mitochondrial replication and importantly are dysregulated under conditions of chronic alcohol exposure.

B. Experimental Design with Endpoints:

The experimental design incorporates three distinct sets of studies with corresponding experimental protocols and endpoints: 1) *In Vivo* studies designed to characterize the processes involved in the maintanence of cellular energy levels and redox potential as animals transition from the quiescent state to the G1 phase of the cell cycle, as they progress through G1 and into S phase (where DNA replication occurs), and as they carry out metabolic and other functional adaptations required to maintain differentiated liver functions dring these transitions. Studies will also be carried out to assess the role of AMPK and adiponectin on these same parameters. Animals undergoing sham surgery (i.e. without liver resection) will be used as controls to adjust for the effects of surgical stress. 2) Studies on isolated hepatocytes for detailed biochemical analysis of signaling in the regulation of metabolism, cell proliferation and apoptosis. For these

studies, cells will be used immediately after isolation or placed in culture for 24-48 hours, stimulated with hormones or growth factors in the presence or absence of inhibitors of specific cellular processes, and analyzed at different timepoints for gene expression or changes in the functional state of signaling proteins. 3) Studies on isolated mitochondria to test changes in their function in response to cellular signals associated with tissue damage and apoptosis. In some experiments, these different experimental designs may be combined, e.g., hepatocyes or mitochondria will be isolated at various timepoints following PHx to assess function.

Endpoints for protocol 1: *In vivo analysis of liver regeneration.* An important set of experiments that will be performed will be to establish baseline parameters for cell signaling and energetics during liver regeneration. This includes two distinct sets of timepoints for analysis: The first timepoint incorporates early signaling event that occur <1hr following PHx. Work from our lab has identified dramatic changes in adenine nucleotides (ATP, ADP and AMP)(Crumm et al., Hepatol., 48:3, 898-908) and redox metabolism (NAD+ levels) that occur immediately following PHx (<1min), reaching a new steady-state at 30 min following PHx, accompanied by an activation and deactivation cycle of AMPK. The studies in this section will characterize parameters downstream of AMPK activation, including analysis of the mTOR system, genes controlling oxidative metabolism, as assessed by western blotting. We will also look at global changes in gene expression as measured by microarray analysis followed by qRT-PCR validation. Experimentally, rats will undergo 2/3 PHx, and remnant livers will be removed and freeze clamped 0, 1, 5, 15, 30 and 60 minutes following, and animals will be euthanized. Because the adenine nucleotide changes fluctuated vastly in the rat over the first hour, it is necessary to assess changes in cellular energetics at all of these time points. Data from our laboratory has also identified a later peak of AMPK activation that precedes hepatocyte replication, and the later time points in this protocol incorporate events critical to the onset and progression of the cell cycle in rats. Studies at this time point will include 4 and 8 hours for analysis of adenine nucleotides, AMPK activation status and cell signaling parameters. 12, 18 24, 36 and 48 hours following PHx will be analyzed for these same parameters, and in addition animals will also be treated with 100 mg/kg BrdU 1 and 3 hours before sacrifice to measure hepatocyte DNA replication. Again, because data from our laboratory has identified such a broad peak of activation for AMPK in rats it is necessary to assay a wide range of times to properly assess downstream events following PHx. Once these parameters have been fully established in normal rats, we will then choose specific timepoints to assess these parameters in animals that have undergone an alcohol-feeding regimen.

Endpoints for protocol 2: *In vitro analysis of mitochondrial biogenesis and energy status in hepatocytes isolated from wt and ko animals.* The genes that control energy balance in the cell also play important roles in maintaining cellular mitochondrial (mt) content. Isolation of hepatocytes in these experiments serves two major purposes:

1) The first is to examine changes in mt mass as a measure of biogenesis and mt membrane potential as a measure of mt activity. To do this, at the time points listed above, hepatocytes will be isolated from anaesthetized animals by liver perfusion, isolated hepatocytes will be fixed and stained with mitochondrial-specific dyes and assayed by flow cytometry. Animals are euthanized in these experiments by bleeding out under anesthesia.

2) In addition to measuring mitochondrial biogenesis in regenerating livers, we will also do detailed biochemical analysis of hepatocyte replication and mt biogenesis *in vitro* and the effects of acute alcohol exposure using primary hepatocyte cultures. To measure these parameters, hepatocytes will be isolated from naïve mice (no PHx) and placed in culture. The hepatocytes will be stimulated with growth factors that induce proliferation in primary hepatocytes and biogenesis will be assessed as a function of hepatocyte proliferation. In addition to proliferation, these cells will be treated with chemical agents that enhance biogenesis, or transduced with genes that have been shown to enhance biogenesis in the presence and absence of growth factors. Once biogenesis parameters have been assessed, these experiments will be repeated in the presence and absence of alcohol, to determine in an *in vitro* setting how alcohol affects both hepatocyte proliferation and biogenesis. Cells will be assayed for changes in cell signaling parameters by western blotting, assessed for changes in gene expression by RT-PCR and

western blotting, and mt biogenesis will be assayed by immunohistochemistry and flow cytometry as previously described.

Endpoints for protocol 3: *Ex vivo analysis of mt function*. In order to test changes in mt function in response to cellular signals associated with tissue damage outlined in endpoint protocols 1 and 2, it will be necessary to isolate hepatocyte mt from control- and alcohol-fed animals, with and without PHx. This analysis will provide more detailed information on mt function which will complement and expand our understanding from measurements of mt membrane potential described in endpoints for protocol 2. Naïve or remnant livers will be removed from anaesthetized animals, and animals will be euthanized following organ harvest by cervical dislocation. Following mt isolation, *ex vivo* analysis will assess activity and degree of coupling of oxidative phosphorylation, TCA cycle activity, electron transport complex activities, calcium uptake, formation of reactive oxygen species, mt permeabilization and release of intermembrane space proteins.

C. Description of Procedure(s):

1) Partial Hepatectomy. Two-thirds partial hepatectomy (PHx) will be performed following the standard protocol of Higgins and Anderson (1931), Arch. Pathol. 12, 186-202, with modifications to comply with current IACUC guidelines. Rats will be brought under anesthesia with 2% isoflurane using a dedicated anesthesia chamber. Animals will be transferred to surgical table where body temperature will be maintained with circulating warm water heater pad, and continued anesthesia using a nose cone with 2% isoflurane. Complete anesthesia is assessed by lack of response to tail and toe pinch. The abdomens, from above the sternum to 1 cm below the surgical incision will be shaved using Andis AGC clippers, and removed fur is discarded. The shaved and cleaned area will then be sterilized using betadine-soaked 3x3 gauze pads, with repeated applications, followed by a 70% ethanol wash. All laboratory personnel conducting or assisting in surgical procedures will wear designated animal lab coats and surgical gloves. A small incision (3-4cm) is made with a feather #10 sterile scalpel through the skin and muscle layer beginning at the sternum. This incision is opened with scissors that have been washed with bacdown soap and sterilized by autoclave. For batch surgeries, instruments will be washed with soap, sprayed with 70% ethanol and sterilized with a hot-bead sterilizer. The left-lateral and medial lobes are exposed and are tied off at the base of each lobe using sterile SP117 non-absorbable black braided silk surgical thread. The lobes are then resected with a scalpel and snap frozen by submersion in liquid nitrogen for assay of baseline levels of proteins and transcription. For measurements of adenine nucleotides, it is essential that the remnant be uniformly frozen rapidly, so custom made clamps that have been pre-cooled in liquid nitrogen will be used to ensure uniform rapid freezing (referred to as freeze-clamping). Following PHx, the muscle layer is sutured using sofsilk 8-0 non-absorbable coated, braided silk and the skin is surgically stapled using micron autoclip 9mm wound clips. Following surgery, but while under anaesthesia, animals will receive 1 ml intraperitoneal (IP) injections of lactated ringers solution (LRS) that has been prewarmed to 37°C to ensure hydration following surgery. For short-term studies (<15 min), animals are kept under anesthesia until time of sacrifice. For longer term studies of the liver regeneration response, the anesthesia is removed at the end of the surgical procedure and the animal is returned to its cage. After the animal recovers and starts moving, it is monitored closely for signs of distress while it is kept in its cage with access to food and water ad libitum until time of sacrifice, and cages will be kept warm with heating lamps for the first 3 hours following surgery. In addition, hydrogel will be placed on the floor of the cage for animals unable to reach the water because of the abdominal incision. Animals will be monitored to ensure that they are drinking 100 ml/kg/day, and are urinating normally At time of sacrifice, the animal is again anesthetized and original incision is reopened and the remnant liver is removed either for immediate homogenization (mt isolation) or freeze claming (metabolite measurements, cell signaling studies). The animal is euthanized by cervical dislocation and opening of the chest cavity.

2)Bleeding: In order to monitor blood glucose levels and serum adiponectin levels, blood will be

drawn on PHx or sham treated animals. All bleeding will not exceed 1% of the total blood volume of the animal over the time between PHx and sacrifice. There is some variation in size of the rats, but they average 350g. Therefore, blood drawn from one animal will not exceed 0.25ml. Assuming that each blood draw will be 0.05ml, each animal will have blood drawn no more than 5 times over the course of the experiment. After consultation with the veterinarian, we will use tail clips to take blood from the animals. Animals will be anesthetized using isoflurane and the tails will be cut 2 mM from the end. Blood will be collected into sterile tubes, and bleeding will be stopped by applying pressure to the tail with sterile gauze pads. For any further bleeds, the animals will again be anesthetized, and blood will be collected by removing scab tissue.

3) **Hepatocyte isolation.** For hepatocyte isolation, animals are injected IP with 50-90 mg/kg of pentobarbital ensuring complete anesthesia. Sometimes, animals are injected with a mix of 1ml of Ketamine (100mg/ml) and 5 ml of xylazine (20mg/ml) will be added to 0.6 ml of sterile water to obtain the k/x cocktail. This cocktail will be administered IP at a dose of 100µl/20g body weight

The abdominal cavity is opened, the portal vein is cannulated and the liver is perfused with Krebs-Ringer solution. The vena cava is cut as soon as the perfusion is started, and the animal is sacrificed without recovering from anesthesia by exsanguination. The liver is removed from the body cavity for further perfusion. Isolation of hepatocytes involves the treatment of the isolated perfused liver with collagenase and dissociation of the tissue following standard procedures of cell isolation.

4) **Mitochondrial Isolation.** Homogenates for mt isolation are prepared from liver tissue following removal following procedures described above or from untreated animals. The animals are brought under anesthesia and the body cavity is opened, liver tissue is removed and placed in a suitable buffer for homogenization. Subcellular fractions are prepared from the homogenate by differential centrifugation.

5) **Injections**: For animals that are being monitored for hepatocyte proliferation (i.e. 24, 36 and 48 animals) will receive IP injections of 100mg/kg BrdU (BD pharmagen) resuspended in sterile saline (0.9%) 2 h prior to sacrifice.

For the study of the role of microRNAs rats will be injected with 10mg/kg of microRNA antagonists - antisense oligonucleaotide (Exiqon) in saline in a volume of 1ml.. The rats will receive 2 injections, the first 72hrs prior to PHx and the second immediately following PHx. Saline and scrambled oligo injections of 1ml each will be used as a vehicle control and administered in the same way as well.

For the study of early signaling processes that depend on the loss of ATP or NAD+, animals will be injected with adrenergic antagonists (phentolamine – 7mg/kg), or with purinergic receptor antagonists (suramin, PPADS – both at 6mg/kg), the α1-adrenergic antagonist phentolamine (10 mg/kg), L-NAME, (N-arginine methyl ester, an inhibitor of nitric oxide synthase, 10 mg/kg body wt), the nitric oxide donor SIN-1 (3-morpholino sydnonamine, 7 mg/kg), NOC-5(7mg/kg), the gap junction inhibitor α-glycerrhetinic acid (7 mg/kg), or GAP26/GAP27 peptides that are reported to inhibit connexin hemichannels. These agents are administered intraperitoneally

dissolved in PBS (0.1-0.5 ml) and control animals receive a corresponding volume of PBS. No signs of discomfort have been noted when carrying out the partial hepatectomy following treatment with these agents

5. Justification of Animal Numbers: (Must match totals in Background Section)

The best justification is based on statistical analysis. If statements, such as, "Standard in the field" or "Based on previous experience" are used, then citation(s) of published material is (are) required. **The number of animals per experimental group must be justified. See Instructions!!!** (Box expands to fit text.)

1) PHx:

In order to determine animal numbers for PHx experiments, a power analysis was done using G*power (http://www.psycho.uni-duesseldorf.de/abteilungen/aap/gpower3/program-handling), set on a two-tailed t-test analyzing the difference between two independent means. AMPK activity data previously generated in the lab was used to estimate animal numbers. It was shown that in rats, AMPK activity 12 h following PHx was 27 nmol/min/g liver, with a standard deviation of 3.5 nmol/min/g. We hope to detect a difference of 7 units and assume that the sigma for the experimental group will be the same. This yields an effect size of 2. Assuming $\alpha = 0.05$ and a power value of 0.95, we calculate that we will need 8 rats per group for biochemical and metabolite analysis. In addition, animals that have undergone PHx will be used for isolation of hepatocytes for assessment of mt biogenesis/mt function. Based on previous studies conducted in the lab using mt DNA content as a measure of mt biogenesis, we know that the ratio of mt DNA to nuclear DNA increases in rats to a peak 1.4 +/- 0.07. We want to detect a change of 0.2 in the ratio at any time point, assuming the same standard deviation in the experimental group and using power analysis with the same settings as described above, we need five mice per group. For PHx experiments with control animals we are doing 6 early time points and 9 late time points for a total of 15 time points, and each time point needs an equal number of sham operated control animals. In addition, following experiments with chow fed animals, we will need to do these experiments in isocalorically pair-fed, littermate alcohol and control animals. Animals fed an alcohol diet are being transferred from the alcohol feeding protocol (2081) maintained by Dr. Hoek. Briefly, animals are fed ad libitum with a special liquid diet containing alcohol or isocalorically matched control liquid diet.

PHx summary:
8 rats for biochemical analysis and 5 for mt biogenesis analysis= 13 rats/time point
13 rats/time point x 13 time points= 195 rats experimental group
195 experimental + 195 sham control animals= 390 rats
390 mice x 3 (1=chow fed, 2=alcohol fed 3= isocaloric alcohol control) and control animals total strains mutant strains= 1170 rats for PHx studies.

2) Hepatocyte isolation:
For the hepatocyte isolation and culture experiments, we estimate based on our experience that we will need 4 preps each to work out experimental conditions for 1) proliferation with growth factors, 2) biogenesis with chemical agents, 3) transduction of genes for the initiation of biogenesis, and 4) establishing a dose response for the treatment of alcohol. Once the experimental conditions have been established, we will need to do 3 experiments for each condition with and without alcohol to establish reproducibility. In addition, we estimate based on our experiences with rat hepatocytes that approximately 20% of the preps are not functional due to lack of viability.

3)Tp53 knockout animals:
Because these are novel animals, we would like to do 3 isolations of tp53 KO and control rats to establish baseline levels of proliferation of isolated hepatocytes in both monolayer and collagen sandwich culture.

For our proposed experiments, we will use the MTT assay to determine proliferation levels in vitro. Baseline values we have found are 0.06 AU570 (Absorbance units) +/- 0.008 and after 48 h of proliferation the values are 0.092 +/- 0.008. Using G*power, we estimate an effect size of 4, and using a two-tailed test we require 4 animals per group to attain p values <0.05.

Therefore, we need 3 animals for establishment of baseline values and 4 animals for our experiments, totaling 7 ko. We also need an equivalent number of control animals for a total of 14 animals.

Summary:
4 conditions to be established x 4 preps= 16 animals
3 replicates x 3 conditions= 9 animals
25 animals + 5 animals (20% prep failure)= 30 total animals/ genotype
30 animals/genotype x 8 genotypes= 240 animals.
14 tp53(-/-) animals

Totals:
1170 PHx + 240 hepatocyte isolation + 42 Tp53(-/-) = 52
470 year 1
470 year 2
470 year 3

Condition	Class	Year 1	Year 2	Year 3	Totals/group
PHx	E	390	390	390	1170
Hepatocyte isolation	D	80	80	80	240
Hepaocyte isolation from Tp53(-/-)	D	14	14	14	42
Totals/year		484	484	484	1452

6. Restraint Devices (does not pertain to **anesthetized** animal under restraint)

[x] No restraint or restraint less than 5 minutes [ ] Restraint more than 5 minutes

Provide required information below if restraint is more than 5 minutes. (Boxes expand to fit text)

Device:
Frequency:
Duration:
Justification:

7. Pain/Distress Classifications:

This classification system is required by the Animal Welfare Act. It is only a reporting mechanism and does not alter IACUC or veterinary oversight. Issues of assessment and minimization of pain and distress are addressed in other sections throughout this protocol form. (There is no class A – it's a USDA thing)

Class B. No Procedures: Animals bred, conditioned, or held for use in teaching, testing, experiments, research, or surgery but not yet needed for such purposes.

Class C. Non-Painful/Non-Stressful Procedures: Animals upon which teaching, research, experiments, or tests will be conducted involving no pain, distress, or use of pain-relieving drugs. (Routine procedures causing only slight or momentary discomfort such as: venipuncture, injections, use of non-inflammatory adjuvants, tail clip and ear notching on pre-weaning age mice. NOT for toxicology-type studies.)

Class D. Painful/Stressful Procedures WITH Analgesia/Anesthesia/Tranquilizers: Animals upon which experiments, teaching, research, **surgery**, or tests will be conducted involving pain or distress to the animals and for which appropriate anesthetic, analgesic, or tranquilizing drugs **will be** used.

Class E. Painful/Stressful Procedures WITHOUT Pain or Stress Relieving Measures: Animals upon which teaching, experiments, **surgery** or tests will be conducted involving pain or distress for which the use of appropriate anesthetic, analgesic, or tranquilizing drugs **will not be used** as such use **will** adversely affect results of the procedure(s). Withholding post-surgery analgesia is a Class E procedure.

7. A) Procedure Classification List all procedures (breeding is a procedure – Class B) to be performed and the pain/distress class by checking the appropriate box. (Add rows as needed, boxes expand to fit text)

List of Procedures	Class				Comments:
	B	C	D	E	
Injections		x			
PHx				x	
Hepatocyte isolation			x		
Tail clipping		x			

B) Number of Animals in Class D and E

Must match totals in Section 5.

	Year 1	Year 2	Year 3	Total
Class D	94	94	94	282
Class E	390	390	390	1170

C) Veterinary Consultation. If animals in class D or E are USDA covered species (USDA Animal), the attending veterinarian must be consulted *before* submission of this form.

Date veterinary consultation occurred for USDA covered species in Class D or E

8. Survival, Non-Survival, and Multiple Surgical Procedures Summary: Use of Anesthesia:

Animal Care and Use Policies 102.03, 104.01, 104.02, 104.03, 104.05, 104.06

A) Survival Surgery and Use of Anesthesia

List procedures in which anesthsia is administered, whether the procedure is surgical or not, using 1 row per anesthetic and procedure. Add rows as needed. Boxes expand to fit text.

Procedure	Anesthetic & Concentration	Dose	Route/Device
Partial Hepatectomy	Isoflurane	2%	Inhalation chamber/nose cone
Preperation of liver homogenates	Isoflurane	2%	Inhalation/nose cone

Comments: (Procedures are to be described in Section 4). It was noted by Dr. Daviau that some strains of rats/mice are more sensitive to isoflurane than others. Each strain will be tested individually for the percentage needed to ensure anesthesia by tail pinch without endangering the welfare of the animal.

B) Non-Survival Surgery

List procedures using 1 row per surgical procedure. Add rows as needed. Boxes expand to fit text.

Surgical Procedure	Anesthetic & Concentration	Dose	Route/Device
Liver perfusion for hepatocyte isolation	Pentobarbital	50-90 mg/kg	IP
Liver perfusion for hepatocyte isolation	Ketamine/Xylazine	100µl mix/20g	IP
Partial Hepatectomy	Isoflurane	2%	Inhalation chamber, nose cone

Comments: (Surgical Procedures are to be described in Section 4)

C) Multiple Surgeries

If multiple surgeries are to be performed on the same animal, list the surgeries and justify why multiple surgeries are required. (Box expands to fit text)

Animals that undergo partial hepatectomy for periods more than 15 minutes are allowed to recover from the anesthesia until the time the remnant liver samples are to be harvested (up to 72 hours). The animals are then undergoing surgery to remove the remnant/ isolate hepatocytes and then are euthanized.

9. Animal Monitoring Plan:

AN ANIMAL MONITORING PLAN IS REQUIRED FOR ALL PROCEDURES WITH THE POTENTIAL TO CAUSE MORE THAN MOMENTARY PAIN/ DISTRESS AND ALL SURVIVAL SURGERY. Policy 104.03

A) Post-Procedure Analgesia: Class D procedures (One row per procedure: Add rows as needed; boxes expand to fit text.)

Procedure	Analgesic & Concentration	Dose	Route/Device
No analgesia will be used			

B) Pain/Stress Criteria: List the criteria that determine pain/stress -- Classes D & E. (Box expands to fit text)

Animals will be monitored visually for normal locomotive activity, guarding, abnormal behavior or appearance including piloerection, unkempt coat/rough hair, hunched posture, aggression, and self-mutilation. Blood glucose will be monitored as mentioned above to ensure proper remnant function, and the surgical wound will be monitored for evidence of dehiscence and to ensure that none of the wound clips have been removed.

C) Euthanasia Criteria: List criteria that will result in euthanasia of the animal or removal of the animal from the study – Classes D & E (Box expands to fit text.)

Any animal that exhibits dehiscence or bleeding from the surgical wound or is moribund, not moving or if any of the pain criteria mentioned in section B is not relieved in 24hrs, will be euthanized by pentobarbital injection.

D) Monitors: List animal monitors and their decision authorization regarding use of analgesics and euthanasia to relieve pain/stress – Classes D & E (Add rows as needed, boxes expand to fit)

Name	Decision Authorization		Comments:
	Analgesia	Euthanasia	
Jason Correnti	x	X	
Anil Antony	x	x	
Aditi Swarup	x	X	

E) Monitoring Plan: Provide the monitoring plan. Include analgesia (for Class D) schedule and other post-procedure components (suture removal, additional care, etc.) – Classes D & E – (Box expands to fit text)

After recovery from anesthesia animals are monitored for signs of distress. Animals will only be observed visually and will not be removed from their cages during the first 12 h following PHx. They will be monitored twice daily on successive days post surgery, and detailed post-surgical records will be kept. Animal food consumption will be monitored as well as signs of dehydration.

.

F) Class E Justification: Provide a justification for Class E procedures: (Box expands to fit text)

Analgesics are generally metabolized in the liver and affect cell signaling processes and cellular redox state in a manner that interferes with the processes under study. In addition, research from our group and others has shown that treatment with different classes of analgesics alters the normal course of regeneration. Treatment with Acetaminophen following PHx leads to increases in liver weight compared to controls and increased liver microsomal enzymes (White & Gershbein, Research Communications in Chemical Pathology and Pharmacology, 1985; 48(2):275-289). Corticosteroid treatment was shown to suppress DNA synthesis in rats following PHx (Tsukamoto & Kojo, Gut, 1989; 30:387-390). Opiate treatment has been shown to be hepatotoxic (Zhang et al., Basic and Clinical Pharmacology and Toxicology, 2004, 95:53-58), and buprenorphine in particular has been shown to interfere in hepatocyte mitochondrial function (Berson et al., Journal of Hepatology, 2001; 34:261-269). Our lab has also tested the topical analgesic EMLA cream in the context of partial hepatectomy, and found that 30 min following surgery, there was significant elevation in phospho-p38 and phospho-Jun kinase in animals receiving treatment, indicating activation of stress signaling pathways that are also critical for the onset of regeneration following PHx. In addition, animals showed behavioral signs of increased irritation and stress after treatment with EMLA cream. We believe that this data provides sufficient scientific justification for class E procedures.

10. **Euthanasia**

Euthanasia methods must be in accord with the AVMA Panel on Euthanasia for adult animals and/or NIH guidelines for rodent embryos and neonates. For chemical agents and gases, provide dosages and route of administration. For physical methods include anesthesia (dose, route). Perfusion and exsanguination are also euthanasia methods. Boxes expand to fit text.

Method(s): cervical dislocation, under 2% isoflurane anesthesia; pentobarbital, 50-90 mg/kg IP
How is euthanasia assured? Opening the chest cavity, animals monitored for 30 seconds following cervical dislocation for breathing.

Justification for Conditionally Acceptable Euthanasia Methods

Provide a scientific justification for the use of any conditionally acceptable methods of euthanasia, as defined by the AVMA (examples: **decapitation or cervical dislocation without anesthesia**). (Box expands to fit text)

Hazardous and Regulated Materials and Procedures

11. Hazard Identification: Are any of the following to be used in, or performed on, animals?

Yes	No	Hazard	Specify (Boxes expand to fit text)
x		Carcinogen	Brdu
x		Teratogen	Brdu
X		Chemical	Glycyrrhetinic acid, L-NAME, phentolamine, suramin, PPADS, SIN-1, NOC-5
	x	Toxin	
	x	Irradiation	
	x	Radioisotope	
	x	Human Origin Tissue	
x		Recombinant DNA	Anti-sense oligonucleotides – a locked nucleic acid (LNA)-modified oligo antisense to microRNAs (Exiqon)
	x	Biohazard	

12. Hazardous Material Approval: (Box expands to fit text)

Attach approval letters to this form or cite IBC or RSO approval number.

Letter attached

13. Use of Non-Pharmaceutical and/or Biological Material in Animals:

Non-pharmaceutical/biological material is any compound whether biological (e.g. protein, peptide, DNA, recombinant virus, cells, cell extract, etc.), or chemical not certified for *in vivo* use. Also includes use of out-of-date pharmaceuticals.

A) Identify the source of the material (Manufacturer or production system, such as, bacteria, tissue-culture cells, plants, etc). **For cells or tissues**, including cells used to produce recombinant virus or any other biological material, identify species, cell type (also primary culture or cell line), and source (supplier).

Brdu will be purchased from BD pharmagen in a sterile saline solution (0.9%) intended for in vivo use.

The antisense oligos and its scrambled oligos will be purchased from Exiqon. Glycyrrhetinic acid, L-NAME and PPADS will be obtained from Sigma

B) Justify the use of non-pharmaceutical grade chemicals, drugs, or similar compounds.

Brdu, oligos, Glycyrrhetinic acid, SIN-1, NOC-5, L-NAME and PPADS are currently not available as a pharmaceutical grade chemical.

C) Indicate how the non-pharmaceutical material is sterilized or determined to be pathogen-free. For animal cells, tissues, or organs, and/or derivative material, including, but not limited to, viral vectors, antibodies, proteins, etc., MAP or IMPACT testing may be required. Attach the test result(s) and date(s) of most recent test(s). Provide a justification if biological material is not sterilized or MAP or IMPACT tested.

BD pharmagen supplies Brdu in a sterile saline solution (0.9%). The stock will be handled under aseptic conditions to prepare IP injections, of 100mg/kg (body weight) BrdU, resuspended in sterile saline (0.9%)

The oligonucleotides are supplied by Exiqon as HPLC purified and lyophilized powder, which will be reconstituted in saline aseptically. IP injections are prepared in saline (0.9%) aseptically.

Glycyrrhetinic acid, SIN-1, NOC-5, L-NAME and PPADS are obtained from sigma as HPLC/tissue culture grade. IP injections are prepared in saline (0.9%) aseptically.

14. Other Regulated Materials and Procedures:

A. Will neuromuscular blocking agent(s) be used? ☐ Yes ☒ No

If **Yes,** state the agent and provide a detailed justification: (Box expands to accommodate text)

B. Will hybridomas/ascites be produced? ☐ Yes ☒ No **If "Yes" See Policies 104.08 & 104.09**

a) For ascites fluid production, describe **1)** method of induction including amount of pristane, **2)** duration of ascites production, **3)** degree of abdominal distension **4)** frequency, number of taps, needle size and **5)** criteria for identifying a moribund condition so that euthanasia can be performed immediately.

b) If ascites fluid is used to produce a monoclonal antibody, **justify** why *in vitro* methods cannot be used.

C. Will any adjuvant(s) be used? ☐ Yes ☒ No **If "Yes", See Policies 104.08 & 104.09**

a) If yes, identify the adjuvant(s), and provide requested information. (Add rows if needed, boxes expand)

Adjuvant	Volume/Dose	Route	Site(s)	Frequency

b) Provide justification if Complete Freund's Adjuvant (CFA) is used beyond the initial injection or used in a manner differing from IACUC Policy 104.08.

Animal Housing

15. Animal Housing and Location Where Procedures are Performed:

A. Indicate where animals will be housed: (Add rows if more than 1 TJU location)

Building: Jefferson Alumni Hall Room Number: 234, 222

B. Describe special animal husbandry requirements: (Boxes expand to fit text)

Caging or housing:	
Diets:	
Environment:	
Care:	

C-1. Identify the procedure(s) and location(s) where procedures are performed on living or dead animals on the TJU/TJUH Campus, including procedures performed in your laboratory. (Add rows as needed)

Procedure List	TJU/TJUH Building	Room Number	Is this location within an animal facility?			
Partial hepatectomy	JAH	Rm. 222		Yes	x	No
Hepatocyte isolation	JAH	Rm. 222		Yes	x	No

C–2. Identify the procedure(s) and the location(s) for procedures involving living or dead animals that are performed off of the TJU/TJUH Campus. (Also answer D to H. Add rows for multiple locations.)

Procedure List	Address of Non-TJU/TJUH Site
N/A	

If all procedures and all transportation occur within the TJU Animal Facilities, then skip to Section 16.
(**Note:** If living or dead animals are removed from the Animal Facility for any reason, then answer the following questions. Not all core facilities are located within the TJU Animal Facilities and may involve transportation between the Animal Facility and the Core Facility. Answer question E if any transportation uses public corridors or elevators, even within the same building.)

D. Justification for use of non-Animal Facility, and/or off-campus location(s): (Box expands to fit text)

The laboratory is outfitted with dedicated equipment necessary for the surgical procedures described, including anesthesia, surgical procedures, instrument sterilization, and hepatocyte isolation. There is no room or equipment in the animal facilities to carry out these procedures.

IACUC has previously approved post-surgical housing of animals in our laboratory. Because we had approval in the past, animals have been routinely housed in a designated area in our laboratory comprising a light source fitted to a timer to maintain 12/12 dark light cycle. This area is adjacent to the surgical area, in a room designated largely for animal work, and as such does not have much foot traffic. Animals are transferred to fresh cages following surgery, and appropriate food and water levels maintained. After recovery from anesthesia animals are monitored for signs of distress. Animals will only be observed visually and will not be removed from their cages during the first 12 h following PHx. They will be monitored twice daily on successive days post-surgery, and detailed post-surgical records will be kept. Animal food consumption will be monitored as well as signs of dehydration. Since we hold the animals only for a maximum of 72hours, bedding will be changed only if required. A key to the lab will be made available to the animal support staff in case they need to check on the animals.
We believe that maintaining this is important for a number of reasons. First of all, it expedites the monitoring process, as the animals are checked frequently in the first hours following surgery. This allows for timely reaction

to any pain or distress that animals may experience following PHx. In addition, the transportation of animals following surgery, and then returning them to the laboratory for organ harvest adds another stress following PHx. We think it is important to avoid adding stress both for the welfare of the animal as well as the continuity of our research. In particular, animals fed an alcoholic diet are sensitized to added stress, and there is a baseline mortality associated with stress in these animals. The third reason we would like to house these animals in the lab is the guarantee that these animals will be undisturbed by traffic, noise and any other activitites that may occur in the animal facility. As mentioned before, these animals are stressed following surgery and the minimization of this stress is critical for the animals and the experiments.

E. Describe route to be taken and time during which transport may occur: (Box expands to fit text)

Currently, rats are taken from our animal room on the second floor of JAH through the corridor on the North and West sides of the building to reach 222. Animals are transported in the mornings between 8 am and 12 pm.

F. Describe container/caging used to transport the animals. Only OAR approved containers/cages may be used for transport of animals. (Box expands to fit text)

Standard OAR-approved containers will be used.

G. How long will live animals be held outside the animal facility?

Permission is required from OAR and IACUC if animals are held outside the facility longer than 12 hours.

H. Will live animals be returned to TJU animal facilities? ☐ Yes ☒ No

OAR authorization is required to return live animals to the animal facilities

I. Will living or dead animals enter or travel through patient care areas? ☐ Yes ☒ No

If "Yes" consult Policy 103.04 and attach permission letter from Epidemiological Officer to this form

Comments Regarding Animal Transport: The majority of animals are held for less than 12 hours. For longer time points (up to 72 hours) animals will be housed in a dedicated space in JAH 222 with food and water ad libitum, with cage changes as needed.

Justifications and Assurances

16. Search for Alternatives to Animal Use, Alternate Species, Less Painful/Distressful Procedures, and for Research Duplication:

A. USDA considers a computer-assisted literature search as the best method to check for non-painful/ stressful alternatives. However, an alternate search strategy can be described (in Database/Search Engine box) to determine that no alternatives were available to the painful/ distressful procedure. Link to USDA Policy 12.
NOTE: Part A must be completed regardless of Pain/Distress classification – This search is also necessary to be able to answer subsections B, C, D, and E.
Use 1 row per search method; add rows as needed, boxes expand to fit text.

Date of Search	Database/Search Engine	Period Covered
2/27/13	Altweb, pain management	All available
2/27/13	Altex	All available
2/27/13	Pubmed	1990-present

Keywords:	Altweb and Altex-hepatectomy; Pubmed- hepatectomy, alcohol, ampk
Description of Search	Altweb- a search for alternate procedures for hepatectomy produced one result,

Results:	where they used lidocaine following liver resection. Work in our lab has shown that EMLA cream, which contains lidocaine alters cell signaling in hepatocytes following PHx. **Altex**- one study on the creation of immortalized kupfer cells (liver-specific immune cells), which are not currently under investigation in our laboratory. **Pubmed**- individual search strategies are detailed below: 1)keywords: hepatectomy, alcohol and ampk: yielded no results 2) keywords: hepatectomy, AMPK yielded 5 results, these studies that showed that AMPK was activated following PHx, which is consistent with data obtained in our laboratory. No one has tested the effects of alcohol on ampk activation following PHx

B. Justify the use of animals for these experiments (Box expands to fit text):

Liver regeneration involves the concerted actions of multiple cell types in the liver, integrated with contributions from circulating hormones and other physiological stimuli. This process cannot be reproduced in vitro.

C. Justify why this particular species, and sex if limited to one sex, were chosen (Box expands to fit text):

The rat has been chosen for studies in liver regeneration because of the effective response peak of DNA synthesis at 12-24 h following PHx. This has also been the model we have used for alcohol feeding. In addition, there are many differences between alcohol feeding between male and female rats. This is due to differences in the uptake and metabolism of alcohol between the sexes, due to mechanisms that are still not fully understood. Because all of our studies have been done in males, it would require that many more female animals be used to identify baseline parameters in female rats, which is beyond the scope of our funding at this point.

D. Provide justification(s) if less painful/stressful alternatives for **any of the painful/stressful procedures** described are known but not used. Also describe if the alternatives search revealed a less painful/stressful model that has been implemented.(Box expands to fit text)

N/A

E. Does this research unnecessarily duplicate previous work? [ ] **Yes, See b.** [x] **No, See a.**

a. If NO, document that this work is not an unnecessary duplication of previous work by completing a literature search, or web-based search (Part A, above).

b. If YES, the duplicated work must be cited or described, and provide justification(s) for this unnecessarily duplicated study in the box below. (Box expands to fit text)

I certify that:

All information within this form is true and accurate to the best of my knowledge.

I will comply with the NIH Guide for the Care and Use of Laboratory Animals (National

Academy of Sciences, 1996), the Animal Welfare Act, and Standard Operating Procedures and Policies as described in the TJU Animal Care and Use Manual.

I acknowledge full responsibility for the conduct and training of all support personnel on this project. All support personnel and I are qualified (or will be adequately trained) to perform our role on this Protocol and to provide humane care for the animals.

I acknowledge that any change(s) to this protocol must be approved by the IACUC before implementation. Failure to do so may result in loss of animal use privileges.

All support personnel listed on this protocol and I have *read* this document in its entirety.

I acknowledge that animal use for research is a privilege, not a right, and I realize that my, or any of my support personnel's, animal use privileges and/or that my Animal Use Protocols can be suspended and revoked for animal use violations, at the discretion of the IACUC or Attending Veterinarian.

Signature, Principal Investigator	Date

Upon completion, submit a copy electronically as an E-mail attachment to IACUC@jefferson.edu and provide a signed copy to the IACUC Regulatory Office, Martin Building, Room 317A

List Attachments Send PDF or other electronic versions of attachments if available. If only paper copies are available, send a paper copy of the attachment with the signed paper copy of the Animal Use Protocol. List all attachments here regardless of whether submitted electronically or as a paper document. Indicate whether the form is electronic or is a paper document. Box expands to fit text.

For Office Use Only

Date of Animal Facility Orientation:	**Orientation Trainer Initials:**
Date of Bio-Techniques Training:	**Bio-Techniques Trainer Initials:**
Date of University Health Services Visit:	

Thomas Jefferson University Animal Utilization (RO-4, 05/09)
Personnel Qualifications in Animal Care and Use (A separate form is required for each person)

NAME: **Daniel J. Cook**

DEPARTMENT: **Pathology, Anatomy and Cell Biology**

OFFICE ADDRESS: **1020 Locust St. Philadelphia, PA 19107, Rm 318 PHONE #: 215-503-2969**

LABORATORY ADDRESS: **1020 Locust St. Philadelphia, PA 19107, Rm 316 PHONE #: NA**

PRINCIPAL INVESTIGATOR: **Joannes Hoek**

JOB TITLE: **Graduate Student**

1. *Describe your academic training, credentials, (e.g. degrees, AALAS certifications) and previous experience in animal research activities.*
   I have a B.S. in Chemical Engineering and a B.A. in Chemistry from Virginia Tech. I am pursuing my PhD in Chemical Engineering from the University of Delaware. I have no previous experience in animal research activities.

2. *Briefly describe your role in animal activities related to the protocol(s).*
   My role in animal activities will be: animal feeding, animal injections, assisting in partial hepatectomies, animal sacrifice, and harvesting liver post-sacrifice.

3. *It is required that you attend bio-techniques training with an LAS veterinary technician. Please indicate what animal procedures you will be performing and any other specific technical training you would like to receive.*
   I will be performing animal injections, animal sacrifice, and harvesting liver post-sacrifice. I would like to receive training on animal handling, IP injections, and alcohol feeding.

I have reviewed the Thomas Jefferson University Institutional Guidelines on the Care and Use of Laboratory Animals and have completed an animal facility orientation and bio-techniques training through the Office of Animal Resources.

Signature of Support Person *Date*

List below all IACUC protocol numbers this person will be working on or associated with.

208C, 208I, 208G

List below all animal activities that this person will be trained in by the PI or his/ her support personnel.

Partial hepatectomy (performance & assistance), harvesting liver, animal sacrifice, general surgery

I certify that the above named person has adequate training or I will arrange for necessary training to qualify this individual to perform the assigned animal activities related to my protocol(s).

Signature of Principal Investigator *Date*

Please note that all Principal Investigators and Support Personnel must complete the required IACUC Online Training before access can be granted to the animal facility.

Appendix H

LICENSING FOR PREVIOUSLY PUBLISHED ARTICLES INCLUDED IN THIS DISSERTATION

H.1 BMC Systems Biology

Cook, Daniel, Babatunde A. Ogunnaike, and Rajanikanth Vadigepalli. "Systems analysis of non-parenchymal cell modulation of liver repair across multiple regeneration modes." *BMC systems biology* 9.1 (2015): 1.

Licensing

License agreement

In submitting an article to any of the journals published by BioMed Central, I certify that:

1. I am authorized by my co-authors to enter into these arrangements.

2. I warrant, on behalf of myself and my co-authors, that:

- the article is original, has not been formally published in any other peer-reviewed journal, is not under consideration by any other journal and does not infringe any existing copyright or any other third party rights;
- I am/we are the sole author(s) of the article and have full authority to enter into this agreement and in granting rights to BioMed Central are not in breach of any other obligation;
- the article contains nothing that is unlawful, libellous, or which would, if published, constitute a breach of contract or of confidence or of commitment given to secrecy;
- I/we have taken due care to ensure the integrity of the article. To my/our - and currently accepted scientific - knowledge all statements contained in it purporting to

be facts are true and any formula or instruction contained in the article will not, if followed accurately, cause any injury, illness or damage to the user.

3. I, and all co-authors, agree that the article, if editorially accepted for publication, shall be licensed under the Creative Commons Attribution License 4.0. In line with BioMed Central's Open Data Policy, data included in the article shall be made available under the Creative Commons 1.0 Public Domain Dedication waiver, unless otherwise stated. If the law requires that the article be published in the public domain, I/we will notify BioMed Central at the time of submission, and in such cases not only the data but also the article shall be released under the Creative Commons 1.0 Public Domain Dedication waiver. For the avoidance of doubt it is stated that sections 1 and 2 of this license agreement shall apply and prevail regardless of whether the article is published under Creative Commons Attribution License 4.0 or the Creative Commons 1.0 Public Domain Dedication waiver.

[End of BioMed Central’s license agreement]

H.2 Journal of Physiology

Correnti, Jason M., et al. "Adiponectin fine-tuning of liver regeneration dynamics revealed through cellular network modelling." *The Journal of physiology* 593.2 (2015): 365-383.

JOHN WILEY AND SONS LICENSE TERMS AND CONDITIONS

Nov 04, 2016

This Agreement between Daniel Cook ("You") and John Wiley and Sons ("John Wiley and Sons") consists of your license details and the terms and conditions provided by John Wiley and Sons and Copyright Clearance Center.

License Number	3982120208987
License date	Nov 04, 2016
Licensed Content Publisher	John Wiley and Sons
Licensed Content Publication	Journal of Physiology
Licensed Content Title	Adiponectin fine-tuning of liver regeneration dynamics revealed through cellular network modelling
Licensed Content Author	Jason M. Correnti,Daniel Cook,Edita Aksamitiene,Aditi Swarup,Babatunde Ogunnaike,Rajanikanth Vadigepalli,Jan B. Hoek
Licensed Content Date	Jan 15, 2015
Licensed Content Pages	19
Type of use	Dissertation/Thesis
Requestor type	Author of this Wiley article
Format	Electronic
Portion	Full article
Will you be translating?	No
Title of your thesis / dissertation	LIVER REGENERATION AND CELLULAR ADAPTATION TO CHRONIC DISEASES: A SYSTEMS BIOLOGY INVESTIGATION
Expected completion date	Nov 2016
Expected size (number of pages)	550
Requestor Location	Daniel Cook 1020 Locust St. JAH Room 301 PHILADELPHIA, PA 19107 United States Attn: Daniel Cook
Publisher Tax ID	EU826007151
Billing Type	Invoice
Billing Address	Daniel Cook 1020 Locust St. JAH Room 301 PHILADELPHIA, PA 19107 United States Attn: Daniel Cook
Total	0.00 USD
Terms and Conditions	

TERMS AND CONDITIONS

("Marks") of WILEY or its licensors is granted hereunder, and you agree that you shall not assert any such right, license or interest with respect thereto

- NEITHER WILEY NOR ITS LICENSORS MAKES ANY WARRANTY OR REPRESENTATION OF ANY KIND TO YOU OR ANY THIRD PARTY, EXPRESS, IMPLIED OR STATUTORY, WITH RESPECT TO THE MATERIALS OR THE ACCURACY OF ANY INFORMATION CONTAINED IN THE MATERIALS, INCLUDING, WITHOUT LIMITATION, ANY IMPLIED WARRANTY OF MERCHANTABILITY, ACCURACY, SATISFACTORY QUALITY, FITNESS FOR A PARTICULAR PURPOSE, USABILITY, INTEGRATION OR NON-INFRINGEMENT AND ALL SUCH WARRANTIES ARE HEREBY EXCLUDED BY WILEY AND ITS LICENSORS AND WAIVED BY YOU.

- WILEY shall have the right to terminate this Agreement immediately upon breach of this Agreement by you.

- You shall indemnify, defend and hold harmless WILEY, its Licensors and their respective directors, officers, agents and employees, from and against any actual or threatened claims, demands, causes of action or proceedings arising from any breach of this Agreement by you.

- IN NO EVENT SHALL WILEY OR ITS LICENSORS BE LIABLE TO YOU OR ANY OTHER PARTY OR ANY OTHER PERSON OR ENTITY FOR ANY SPECIAL, CONSEQUENTIAL, INCIDENTAL, INDIRECT, EXEMPLARY OR PUNITIVE DAMAGES, HOWEVER CAUSED, ARISING OUT OF OR IN CONNECTION WITH THE DOWNLOADING, PROVISIONING, VIEWING OR USE OF THE MATERIALS REGARDLESS OF THE FORM OF ACTION, WHETHER FOR BREACH OF CONTRACT, BREACH OF WARRANTY, TORT, NEGLIGENCE, INFRINGEMENT OR OTHERWISE (INCLUDING, WITHOUT LIMITATION, DAMAGES BASED ON LOSS OF PROFITS, DATA, FILES, USE, BUSINESS OPPORTUNITY OR CLAIMS OF THIRD PARTIES), AND WHETHER OR NOT THE PARTY HAS BEEN ADVISED OF THE POSSIBILITY OF SUCH DAMAGES. THIS LIMITATION SHALL APPLY NOTWITHSTANDING ANY FAILURE OF ESSENTIAL PURPOSE OF ANY LIMITED REMEDY PROVIDED HEREIN.

- Should any provision of this Agreement be held by a court of competent jurisdiction to be illegal, invalid, or unenforceable, that provision shall be deemed amended to achieve as nearly as possible the same economic effect as the original provision, and the legality, validity and enforceability of the remaining provisions of this Agreement shall not be affected or impaired thereby.

- The failure of either party to enforce any term or condition of this Agreement shall not constitute a waiver of either party's right to enforce each and every term and condition of this Agreement. No breach under this agreement shall be deemed waived or excused by either party unless such waiver or consent is in writing signed by the party granting such waiver or consent. The waiver by or consent of a party to a breach of any provision of this Agreement shall not operate or be construed as a waiver of or consent to any other or subsequent breach by such other party.

- This Agreement may not be assigned (including by operation of law or otherwise) by you without WILEY's prior written consent.

- Any fee required for this permission shall be non-refundable after thirty (30) days from receipt by the CCC.

- These terms and conditions together with CCC's Billing and Payment terms and conditions (which are incorporated herein) form the entire agreement between you and WILEY concerning this licensing transaction and (in the absence of fraud) supersedes all prior agreements and representations of the parties, oral or written. This Agreement may not be amended except in writing signed by both parties. This Agreement shall be binding upon and inure to the benefit of the parties' successors, legal representatives, and authorized assigns.

- In the event of any conflict between your obligations established by these terms and conditions and those established by CCC's Billing and Payment terms and conditions, these terms and conditions shall prevail.

- WILEY expressly reserves all rights not specifically granted in the combination of (i) the license details provided by you and accepted in the course of this licensing transaction, (ii) these terms and conditions and (iii) CCC's Billing and Payment terms and conditions.

- This Agreement will be void if the Type of Use, Format, Circulation, or Requestor Type was misrepresented during the licensing process.

- This Agreement shall be governed by and construed in accordance with the laws of the State of New York, USA, without regards to such state's conflict of law rules. Any legal action, suit or proceeding arising out of or relating to these Terms and Conditions or the breach thereof shall be instituted in a court of competent jurisdiction in New York County in the State of New York in the United States of America and each party hereby consents and submits to the personal jurisdiction of such court, waives any objection to venue in such court and consents to service of process by registered or certified mail, return receipt requested, at the last known address of such party.

WILEY OPEN ACCESS TERMS AND CONDITIONS

Wiley Publishes Open Access Articles in fully Open Access Journals and in Subscription journals offering Online Open. Although most of the fully Open Access journals publish open access articles under the terms of the Creative Commons Attribution (CC BY) License only, the subscription journals and a few of the Open Access Journals offer a choice of Creative Commons Licenses. The license type is clearly identified on the article.

The Creative Commons Attribution License

The Creative Commons Attribution License (CC-BY) allows users to copy, distribute and transmit an article, adapt the article and make commercial use of the article. The CC-BY license permits commercial and non-

Creative Commons Attribution Non-Commercial License

The Creative Commons Attribution Non-Commercial (CC-BY-NC)License permits use, distribution and reproduction in any medium, provided the original work is properly cited and is not used for commercial purposes.(see below)

Creative Commons Attribution-Non-Commercial-NoDerivs License

The Creative Commons Attribution Non-Commercial-NoDerivs License (CC-BY-NC-ND) permits use, distribution and reproduction in any medium, provided the original work is properly cited, is not used for commercial purposes and no modifications or adaptations are made. (see below)

Use by commercial "for-profit" organizations

H.3 Frontiers in Physiology

Cook, Daniel J., et al. "A novel, dynamic pattern-based analysis of NF-κB binding during the priming phase of liver regeneration reveals switch-like functional regulation of target genes." *Frontiers in physiology* 6 (2015).